DIMENSIONAL AND CRYSTALLOGRAPHIC FABRIC DEVELOPMENT IN EXPERIMENTALLY DEFORMED SYNTHETIC AGGREGATE AND NATURAL ROCKS

by

John Robert McArthur ©

Submitted in partial fulfilment
of the requirements for the degree
of

Masters of Science

Geology Department
Lakehead University
Thunder Bay, Ontario, Can.

ISBN 0-315-63183-X

Canada

Abstract

Calcite Portland-cement aggregate samples were deformed triaxially at 25° with confining pressures of 200 Mpa. The samples were deformed under experimental approximations of pure shear (dry and wet experimental conditions), transpressional shear and simple shear. The pore fluid pressure during the wet pure shear test was less than 195 MPa. Extensive grain rotation accompanied by twinning of the calcite grains occurred.

Optical analyses of calcite crystallographic fabrics have been used to infer the orientation of the maximum principal compressive stress (σ_1). Stress orientations in the deformed specimens agree well with the externally imposed stresses. A new method has been successfully used to determine the σ_1 orientation. The method uses contouring of the lamellae index associated with the compression direction determined from Turner's Dynamic analysis method.

In pure shear, preferred dimensional orientation (PDO) of the calcite grains are produced more efficiently in the presence of a pore fluid pressure. In dry specimens, transpressional shear is more effective in producing a PDO in the calcite grain than either pure shear or simple shear. Grain shape fabrics do not conform to the symmetry of the bulk deformation when extensive rotation of calcite grains is involved. Mean grain alignment is perpendicular to the shortening in pure shear, initially inclined and later parallel to the shear zone wall in transpressional shear, and inclined to the shear zone wall in simple shear. The mean orientation of the grain-alignment fabrics is, therefore, a reliable kinematic indicator under the conditions investigated. Transpressional shear and dry pure shear exhibit higher lamellae indices than either wet pure shear or simple shear.

Strain analysis of calcite grains by Robin's method (1977), the linearization method (Yu and Zheng, 1984) and Harmonic mean method (Lisle, 1977) yields overestimates of the experimental bulk strain in wet pure shear. These methods fail to take into account interparticle motions that occur in the presence of a high pore fluid pressure.

The triaxial deformation of the Ancaster oolitic limestone was preformed with a confining pressure of 200 Mpa, a natural strain rate of 10^{-5}/s and at a temperature of 135°C. The samples were deformed under dry and wet experimental conditions. The pore fluid pressure, during the wet test, was less than 60 % of the confining pressure.

The deformation process of ooids in the dry experimental

test is rigid rotation of the ooid particles. In the case of wet experimental conditions, it appears that the pore fluid pressure produces particulate flow in the fine grained ooid matrix.

Due to a viscosity contrast, between ooids and cement matrix, strain analysis on the ooids exhibits an overestimate of strain compared to the experimental bulk strain. This holds true for both wet and dry experimental conditions.

Experimental triaxial deformation was conducted on the China Beach sandstone by pure shear for dry experimental conditions. The temperature was held constant at 25°C, with computer controlled natural strain rates of 10^{-5}/s and a confining pressure of 200 Mpa.

Mechanical heterogeneities in the grains of the China Beach sample play an important role in the development of cleavage. Altered feldspar grains and lithic fragments deform by ductile processes, while unaltered feldspar and quartz grain deform by rigid rotation and brittle processes. Strain analysis of each grain type in the China Beach sandstone yield a range of strain estimates depending on the deformation process compared to the experimental bulk strain.

Comparison of Robin's method, the linearization method and Harmonic mean method suggest that Robin's method generates the best estimates of the bulk experimental strain ratio.

Acknowledgments

This study represents the authors M.Sc. Thesis, which has been supervised by Dr. Graham J. Borradaile who provided financial support from his NSERC operating grant (no. A6861). The author is indebted to Dr. Borradaile for running of the triaxial deformation experiments and also for his guidance and constructive criticism. The manuscript was greatly improved from comments by Dr. G.J. Borradaile and Dr. P.J. Hudleston.

The author owes a debt of gratitude to A. Hammond and R. Viitala for thin section preparation and S. Spivak for the drafting of figures and microphotograph development and printing.

The author also gratefully acknowledges two Ontario Graduate Scholarships for 1988-89 and 1989-90.

Table of Contents

Chapter 1: Dimensional and crystallographic fabric development in experimentally deformed synthetic aggregate and natural rocks

1.1 Introduction

This study focuses on low temperature experimental triaxial deformation and associated petrofabric development of an artificial calcite Portland-cement aggregate (a) and two natural rocks, the Ancaster oolitic limestone (Jurassic, Lincolnshire, county U.K.) (b) and the China Beach sandstone (Oligocene, Vancouver Island B.C.) (c). This permits observations of petrofabric development for low temperature deformation processes as well as petrofabric development between grains of different rheological behaviour.

a) Calcite Portland-Cement Aggregate

The development of preferred dimensional and crystallographic orientation at low temperature (25°C) in calcite grains is addressed for both coaxial and non-coaxial deformation. The deformation tests consist of experimental approximations of pure shear (axial symmetrical compression (Fig. 1.2a)) under (P_f=0) and wet (P_f>>0) experimental conditions, transpressional shear in a (55° oblique shear assemblage (Fig. 1.2b)) and simple shear (longitudinal shear assemblage (Fig. 1.2c)). The orientation of the σ_1 in figure 1.2 is that imposed on the sample by the hydraulic ram during deformation. In pure shear tests the role of a pore fluid pressure in the development of a preferred dimensional orientation of calcite grains is also addressed.

Optical analyses of calcite grain crystallographic fabrics are used to infer the orientation of the maximum principal compressive stress (σ_1). Methods for this determination, using *c*-axes and e-twin lamellae, involve the procedures developed

by Turner (1953), Friedman and Conger (1964) and Dietrich and Song (1984). The effect of the different deformation type on degree and frequency of twinning in calcite grains as well as the use of twinning information in the dynamic analysis methods are also addressed.

Strain analysis for the coaxial deformation experiments are conducted on the calcite grains to infer an estimate of the bulk strain of the test sample. The methods of bulk strain determination include Robin's method (1977), the linearization method (Yu and Zheng, 1984) and the harmonic mean method (Lisle, 1977).

b) Ancaster Oolitic Limestone

The development of a preferred dimensional orientation in ooid grains of the deformed Ancaster oolitic limestone under dry (P_f=0) and wet (P_f>>0) pure shear experimental conditions is addressed. From this an understanding of the deformation processes in ooid grains and calcite-cement matrix at low temperature (135°) is obtained. The role of a pore fluid pressure in the development of preferred dimensional orientation of ooid grains is also discussed.

Strain analysis of the coaxial deformation experiments are conducted on the ooid grains to infer an estimate of the bulk strain of the test sample. The methods of bulk strain determination include Robin's method, the linearization method and the harmonic mean method. Strain heterogeneity between the ooid grain and the calcite-cement matrix is also discussed.

c) China Beach Sandstone

The experimental triaxial deformation of the China Beach sandstone limestone focuses on the development of preferred

dimensional orientations with increasing bulk strain in the 5 major grain types. The development of preferred dimensional orientation in grains at low temperature (25°C) deformation of the polymictic sandstone aggregate under pure shear conditions is addressed as well as an understanding of the deformation processes in the sandstone grains. The significance of mechanical heterogeneities between grain types and its influence in the formation of cleavage are discussed.

Strain analysis of the coaxial deformation experiments are conducted on each grain type as well as the entire sample to infer an estimate of the bulk strain of the test sample. The methods of bulk strain determination include Robin's method, the linearization method and the harmonic mean method. Strain heterogeneity between the different sandstone grain types is discussed.

1.2 Plastic Deformation of calcite

Twinning of calcite has been studied extensively (Griggs, 1938; Turner and Ch'ih, 1951; Griggs *et.al.*, 1951, 1953, 1960; Turner *et.al.*, 1953, Friedman and Conger, 1964; Paterson and Turner, 1970). Twinning on $e=\{01\bar{1}2\}$ planes (Fig. 1.1a) is the most common mode of deformation in calcite and is readily induced at room temperature by a compression. The crystal structure and its association to twinning is presented in figure 1.1b.

Below 500°C, twin lamellae tend to exist as thin sharply bounded planar surfaces extending across the full width of the deformed grain. However as strain increases the lamellae index (*i.e.*, number of grains per mm) also increases until the lamellae finally coalesce and the crystal becomes completely twinned. These grains can only be recognized by the presence of small triangular shaped relics of the host lattice on the boundaries of the deformed calcite crystal.

At higher temperatures, between 700 and 800°C, lamellae are few, thick and have irregular boundaries. At 800°C complete twinning is never attained even in the most favourably oriented crystals. As first suggested by Turner (1953) this is due to the lowering of the critical resolved shear stress associated with slip on r-planes $\{10\bar{1}1\}$ which becomes more favourably than e-twin gliding. Friedman and Higgs (1981) have shown in experimental deformation of calcite gouge that this transition in deformation mechanism occurs between 400 and 650°C, in this temperature regime fabric changes are produced by twinning and rotation by slip on *r*-planes. Griggs *et.al.* (1960) reported that *f*-slip tends to be dominant at temperatures between 500 and 800°C.

a)

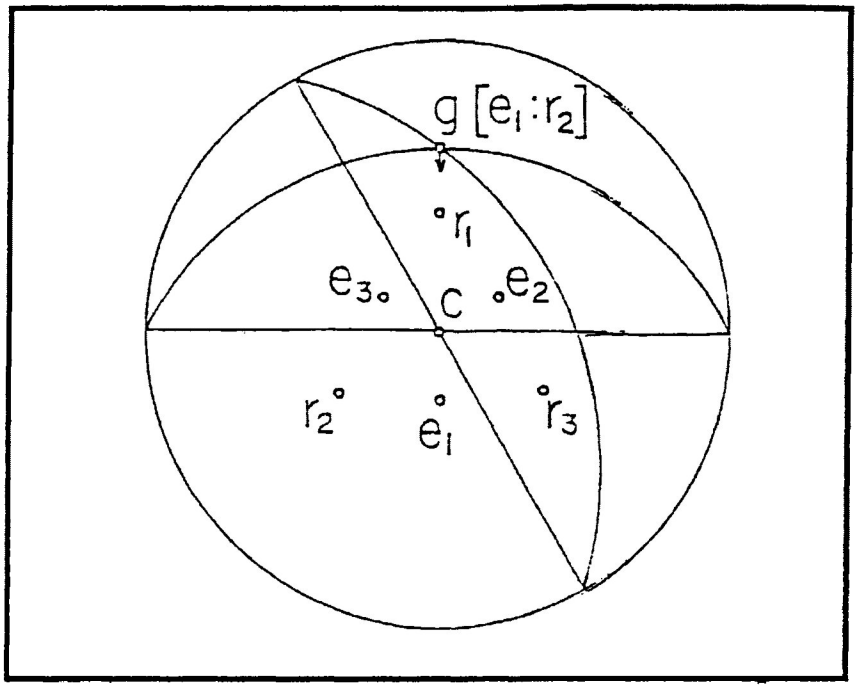

b)

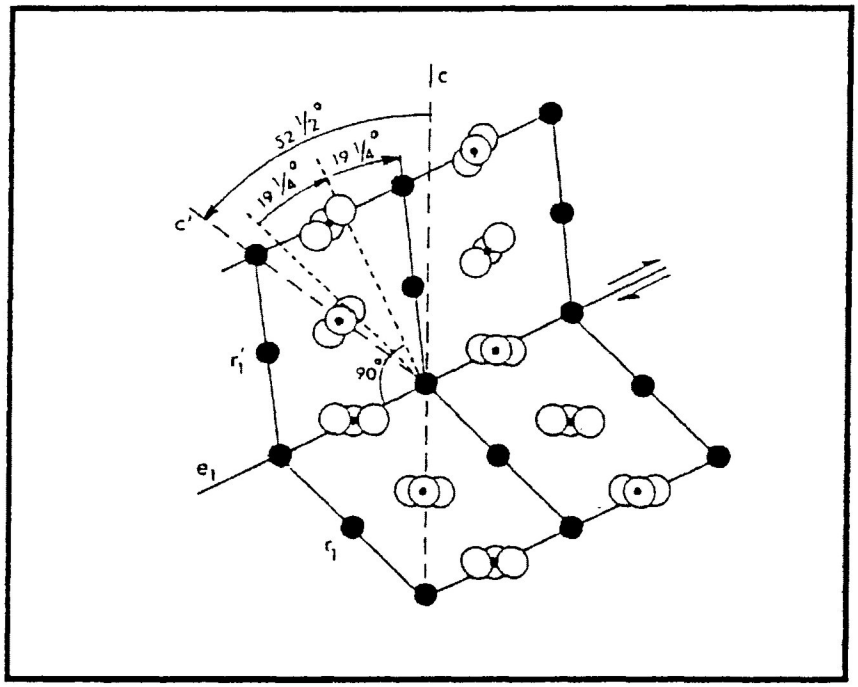

Figure 1.1a The crystallographic orientation of the twin glide direction $e_1:r_2$. Twin glide occurs parallel to g, the line of intersection of the e and r-planes, to give a positive sense of shear. (from Turner and Weiss, 1963).

1.1b Twinning in calcite. The sense of shear is indicated by the arrows. Closed circles = calcium ions; grouped circles = CO_3 (from Turner et.al., 1954)

The flow properties of calcite have also been extensively studied, beginning with Griggs (1936, 1938). The steady state flow of Yule marble has been studied by Heard (1963) and Heard and Raleigh (1972). In these experiments steady state creep occurred in a temperature range of 500 to 800°C under a confining pressure of 5 kbars. Schmid *et.al.* (1977) have shown that grain size is a very important variable influencing the flow of rocks at high temperature, low stresses and strain rates. These experiments used fine-grained Solnhofen limestone and showed that below a certain temperature dependent stress threshold (1000 bars at 600°C, 300 bars at 900°C), there is a marked change in flow behaviour. This change in behaviour was representative of a superplastic flow regime. Such a superplastic flow regime was not observed in the coarser-grained Yule marble by Heard and Raleigh (1972) or the Carrara marble by Schmid *et.al.* (1980).

1.3 Development of non-coaxial strain histories in experimental deformation experiments on calcite

In order to understand preferred crystallographic and dimensional orientation, developed as a result of intracrystalline glide in natural tectonites, it is necessary to conduct experiments in which the deformation history is non-coaxial. The advancement of experimental technique has allowed for the progressive development of improved approximations of simple shear and for a better understanding of calcite petrofabric.

The first approximation of shearing in calcite rocks was conducted by Rutter and Rusbridge (1977), in which non-coaxial strain of Carrara marble was accomplished by a 2 stage deformation. This resulted in a state of finite strain whose principal axes are always inclined to the superposed directions of the maximum stress and incremental strain.

Friedman and Higgs (1981) produced shear strains which ranged up to 5.7 in triaxial deformation experiments involving calcite gouge. These shear strains were accomplished by deforming cylindrical assemblies consisting of more competent material with a thin layer of crushed calcite along a precut surface at 35° to the experimental σ_1 orientation. This method allowed for the development of strain histories with non-coaxial incremental stress/strain and finite strain axis during shearing, within the calcite gouge. However, the strain history was not representative of simple shear in that a component of axial compression has occurred normal to the shear zone. These experiments have, therefore, produced transpressional shear strains, a combination of pure and simple shear.

The method developed by Friedman and Higgs (1981) has also been employed by Schmid *et.al.* (1987). Borradaile and Alford

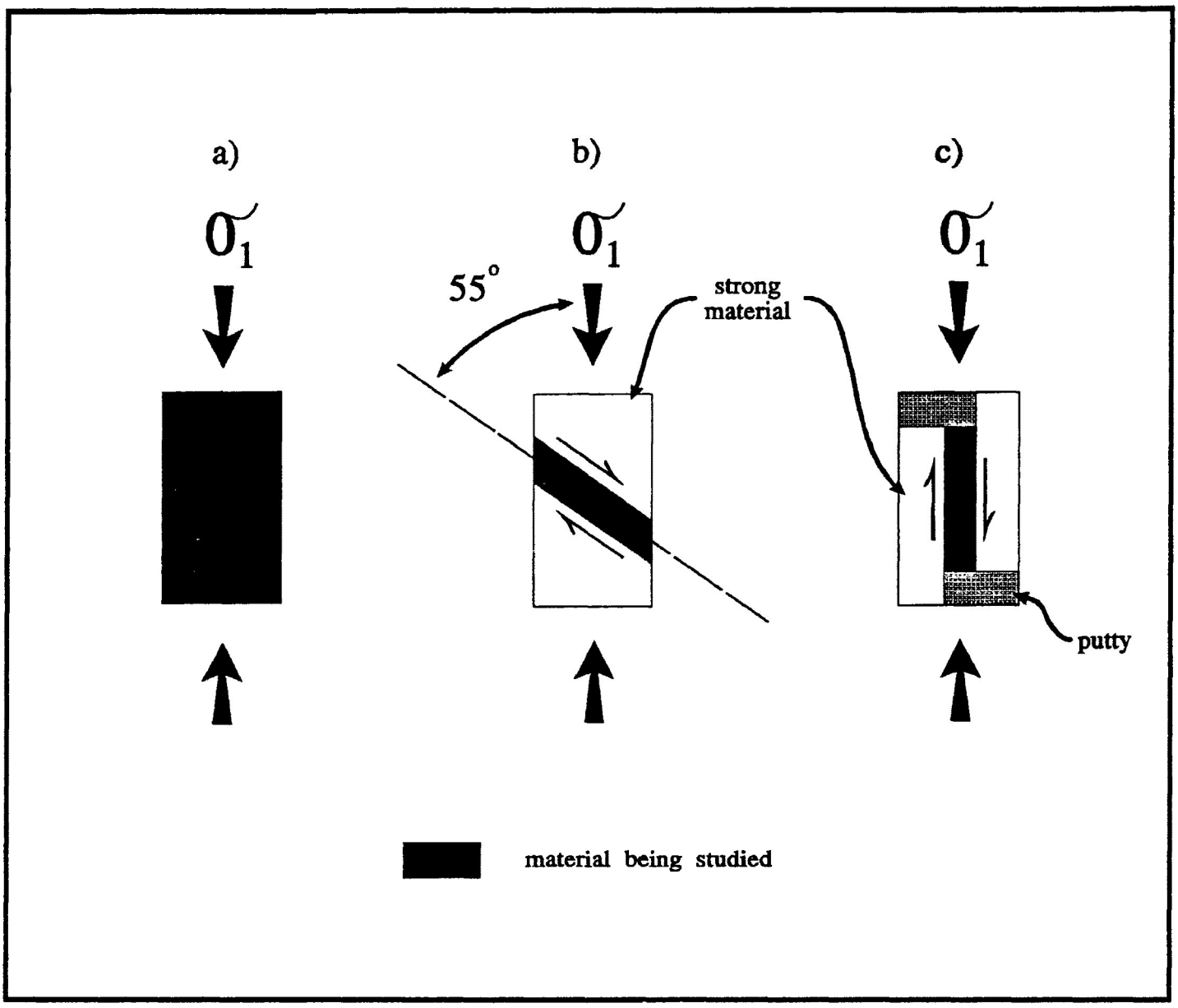

Figure 1.2 Sample assemblies of the deformable material investigated in the various arrangements. Left: to produce coaxial (approximately pure shear). Middle: to produce transpressional shear (oblique assembly). Right: to produce simple shear (longitudinal assembly). (modified from Borradaile and McArthur, 1990)

(1988) have also used the Friedman and Higgs's method for the development on non-coaxial strain histories. These tests were conducted on a synthetic magnetite containing calcite Portland-cement aggregate on which magnetic susceptibility measurements were made after deformation. Because of the limitations in the experimental method for obtaining magnetic susceptibilities the sandstone cylinder was precut at 55° to the experimental σ_1 orientation (Fig. 1.2b). As a result, large transpressional shears strains were produced in the deformable calcite-cement.

A better approximation to simple shear deformation has recently been developed from experimentation on clay gouge (developed by J. Logan personal communication, New Brunswick, August 1988)) and can be used for deformation of calcite rocks. The method involves the use of cylinders of sandstone in which the deformable sample is placed in a precut parallel to the axis of compression (Fig. 1.2c). The sandstone assemblage is then offset on either side of the sample with clay putty filling the voids produced during the offsetting procedure. When the assemblage experiences axial compression differential movement occurs between the 2 offset sandstone sections and a shear zone develops. Since no component of pure shear is expressed normal to the shear direction the non-coaxial deformation is simple shear.

CHAPTER 2: Apparatus used in experimental study

2.1 Introduction

The apparatus employed in the present investigation consists of a Donath type triaxial rig, a Ziess Fedorov (four axial) universal rotary stage attached to a Ziess AMPLIVAL pol-d polarization research microscope and a Ziess Videoplan digital analyzer. The use and operation of these apparatuses will be discussed separately.

2.2 Triaxial Rig System

Triaxial deformation experiments were conducted on the calcite Portland-cement aggregate by Dr. G. Borradaile for this study (Borradaile and McArthur, (1990)) and also previous studies involving magnetic susceptibility (Borradaile and Alford, (1988) and Alford, (1988)). Experimental deformation of the Ancaster Oolitic limestone and China Beach sandstone were also conducted by Dr. G. Borradaile.

The system was developed by Dr. G. Borradaile from a simple triaxial rig supplied from Dr. F. Donath of the Earth Technology Corporation, 3777 Long Beach, California 90807 (c.f. 1970). This was purchased by Dr. G. Borradaile using funds supplied, to him by B.I.L.D. (Ontario) and developed using his operating grant (NSERC 6861). The triaxial rig and the data gathering systems are controlled by an IBM model 20 computer. This advancement was developed and built by Dr. G. Borradaile. The software used to operate the triaxial rig system and reduce and plot data was written by Dr. G. Borradaile. This software also includes on-line correction for apparatus distortion and specimen shape change. The triaxial rig system as a whole was upgraded to a 5 kbar (500 MPa), 250°C system by Dr. G. Borradaile using NSERC funds and L.U.

grants.

The triaxial rig system consists of the following components:

1) Pressure Vessel Assembly

The current (500 MPa) pressure vessel (Fig. 2.1) consists of a cylinder of tool steel which is 11.4 cm in diameter by 25.4 cm in length. The centre of the cylinder has been machined to provide a pressure chamber and to admit the upper and lower retaining plugs. The upper piston specimen assembly consists of the test specimen, upper piston, load-cell sleeve and the upper retaining plug. Test specimens are jacketed to prevent the confining pressure medium (very low viscosity silicon oil) from entering into pore spaces and to hold the specimen together during deformation. In this study a double jacket of teflon and heat-shrink tubing was used.

The active lower assembly consists of the hydraulic ram, the ram piston and the equalization chamber. Axial stress in applied to the sample by the hydraulic ram via the lower piston. The equalization chamber, which is connected to the pressure chamber, allows for a constant confining pressure in the pressure chamber during deformation.

2) Pressure Generator and Confining Pressure System

Priming confining pressures up to 10,000 psi can be achieved in the triaxial rig using a hand pump as presented in figure 2.2. Higher confining pressures (< 60,000 psi) are generated with the use of a hand-turned pressure generator or by a motor driven syringe pump in combination with a pressure intensifier. The magnitude of the confining pressure is registered on a pressure gauge, and electronically via an

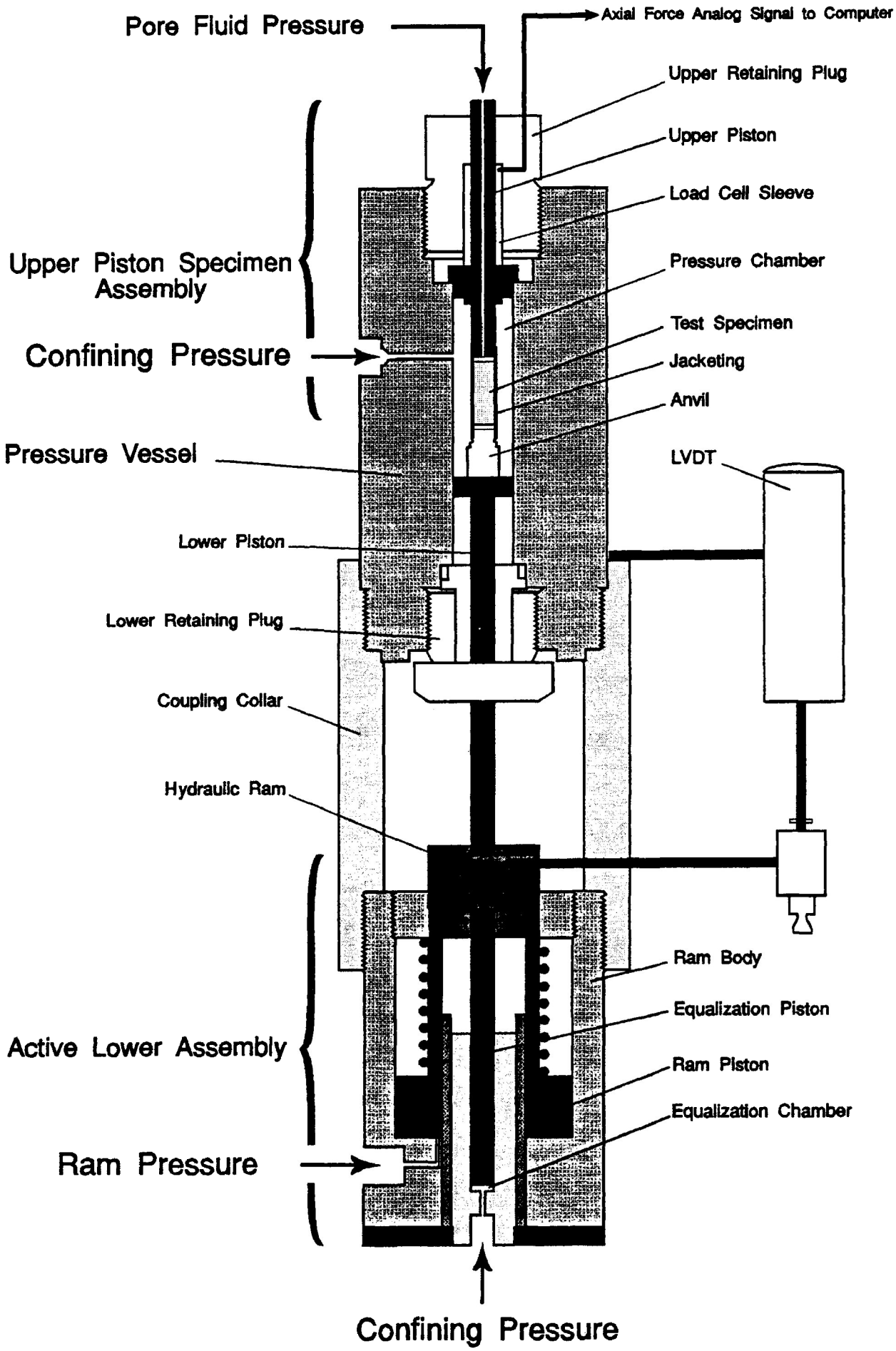

Figure 2.1 Schematic drawing of the pressure vessel assembly. (modified from Donath (1970))

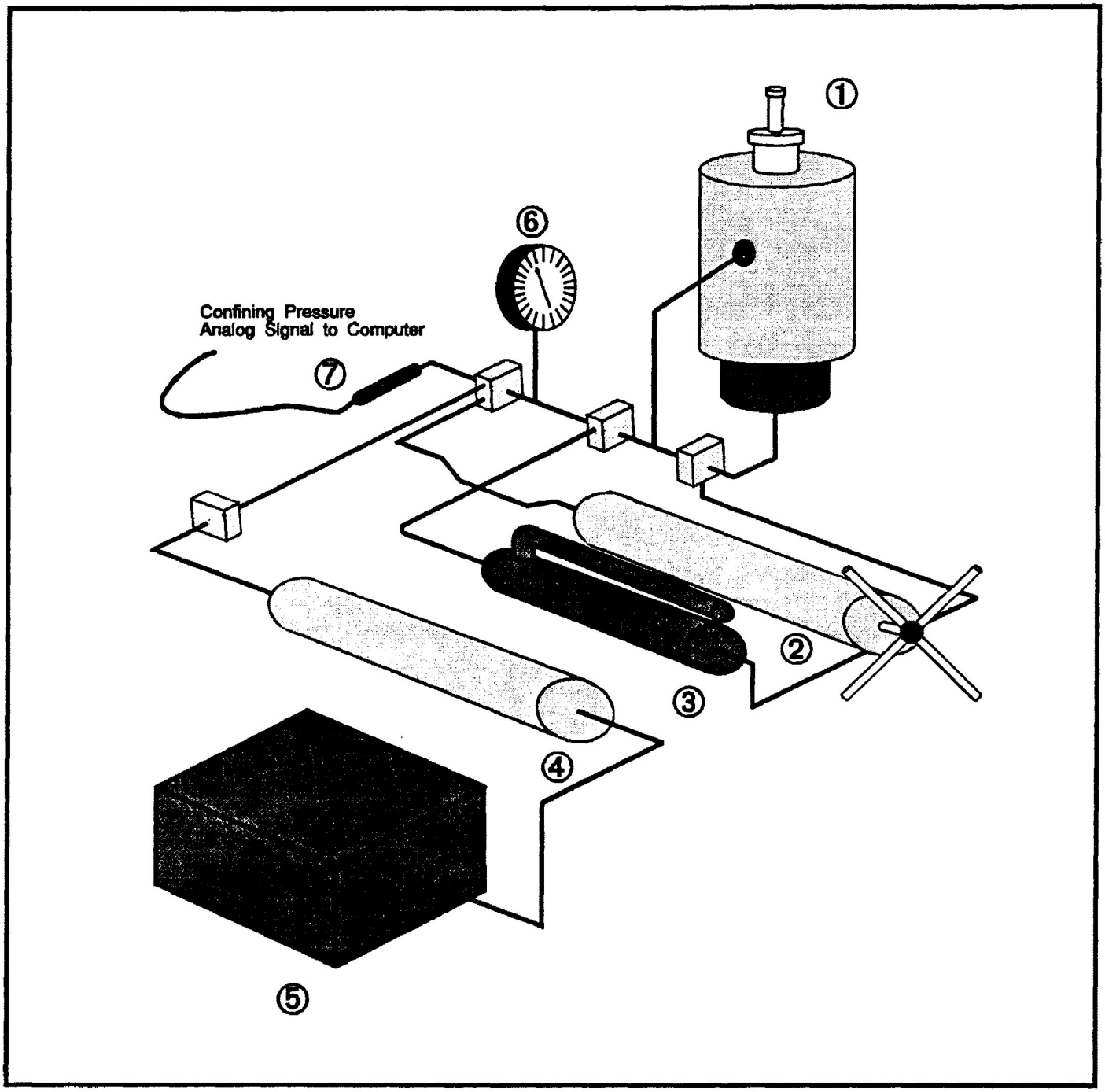

Figure 2.2 Pressure Generator and Confining Pressure System.

1) Pressure vessel assembly
2) Hand-turned pressure generator (PPT, 600 MPa)
3) Hand pump (Enerpac; 10,000 psi)
4) Pressure intensifier (AUTOCLAVE)
5) Motor driven multi-rate syringe pump
6) Pressure gauge (ASTRA)
7) Pressure sensor (ASTRA)

Pressure valves are represented by the small stippled boxes. (modified from Alford, 1988)

ASTRA electronic pressure gauge.

The confining pressure, within the pressure vessel, is applied laterally by the hydraulic fluid surrounding the sample in the pressure chamber. The confining pressure is also applied axially through the hydraulic ram which drives the lower piston. The combination of the lateral and axial confining pressure on the cylindrical test specimen produces nearly true hydrostatic pressure during deformation of the sample material. The confining pressure also acts as a constant component of the axial stress producing the deformation in the test specimen.

3) Ram Hydraulic Pressure System

The axial stress used to deform the test specimen is proportional to the axial force applied to the lower piston by the hydraulic ram. The lower piston is mechanically coupled to the ram pressure system and confining pressure system. The force produced by the ram system is determined by the pressure of the ram and confining pressure fluid pumped into the active lower assembly (Fig. 2.1). Combination of the two hydraulic pressures produces a differential axial stress (σ_1-σ_3). Since the confining pressure is held constant, variations in the hydraulic ram pressure is used to control increasing and decreasing differential axial stress.

As presented in figure 2.3 the hydraulic pressure is provided by an electric motor through a multi-rate gear box. The gear box rate is computer controlled to provide accurate computed axial displacements, in order to simulate constant natural strain rates.

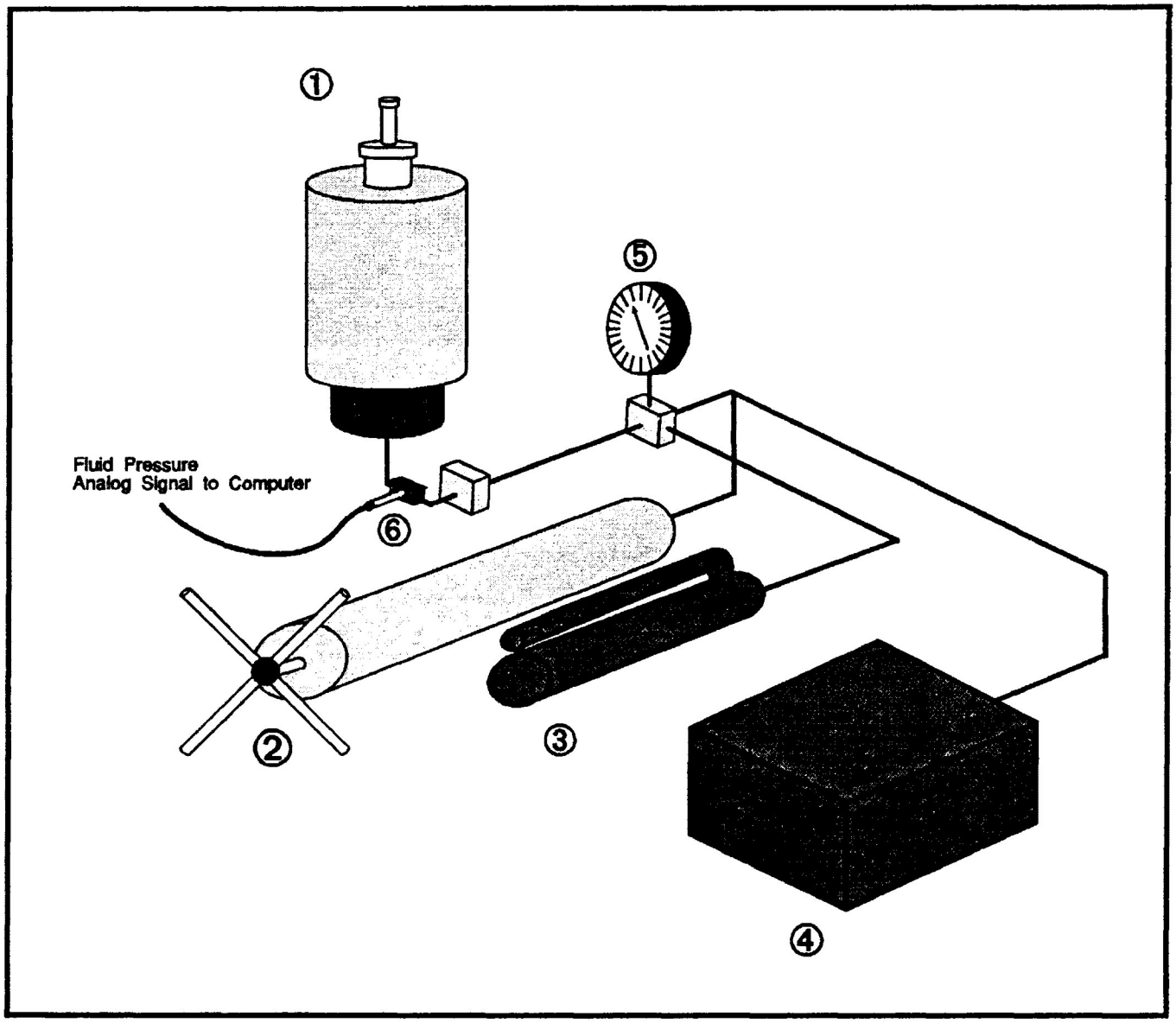

Figure 2.3 Ram Hydraulic Pressure System

1) Pressure vessel assembly
2) Hand-turned pressure generator (PPT, 600 MPa)
3) Hand pump (Enerpac; 10,000 psi)
4) Multi-rate gear box
5) Pressure gauge (ASTRA)
6) Pressure sensor (PSI-TRONIC)

Pressure valves are represented by the small stippled boxes. (modified from Alford, 1988)

4) Pore Fluid Pressure Control Equipment

The pore fluid pressure control equipment is presented in figure 2.4. The high pressure fluid (*eg.*, distilled water) is generated by hand-turned pressure generator. A hole in the upper piston allows the injection the fluid into the test specimen. The selective injection of a fluid allows for the creation and control of a constant pore fluid pressure in the specimen during a triaxial experiment. Deformation under wet experimental conditions can produce a pore fluid pressure close to the experimental confining pressure in the pressure chamber. The magnitude of the pore fluid pressure is registered on a pressure gauge. The analog signal is sent to a computer for storage.

5) Temperature Control Equipment

The temperature control equipment consists of an insulated thermal jacket which surrounds the pressure vessel. The control of temperature is accomplished by a thermostat, which has a maximum operating temperature of 650°C. However, only moderate temperatures can be accurately maintained in this type of open heating system.

6) Force and Displacement Measuring-Recording System

Axial shortening of the test specimen during the deformation experiment is determined from the movement of the ram piston relative to the pressure vessel body. The displacement is registered by a linear variable differential transformer (LVDT in Fig. 2.1). Analog signals are sent to a chart recorder (Fig. 2.5).

Differential axial load is measured with strain gauges affixed to the load cell. For high temperature experiments

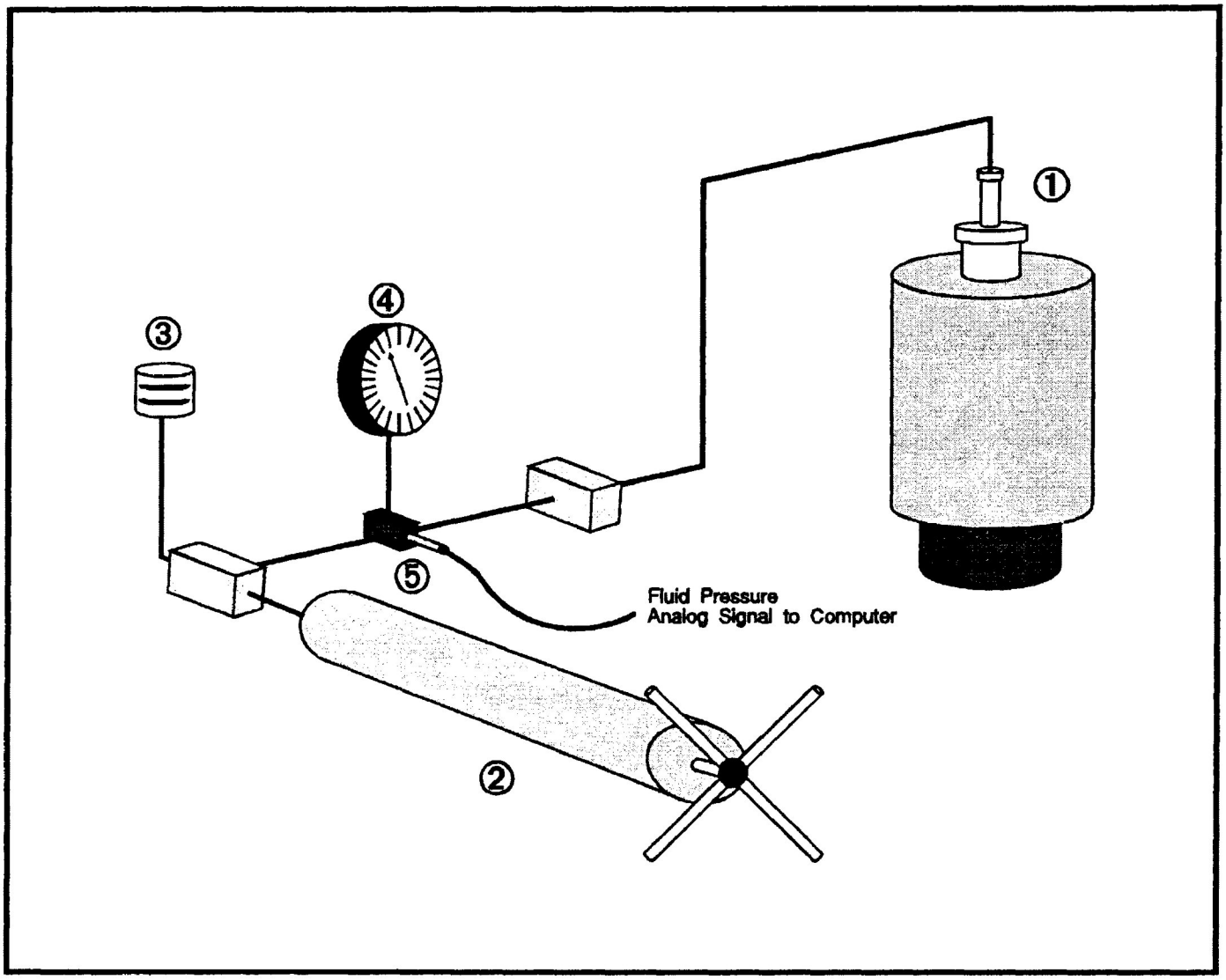

Figure 2.4 Pore Fluid Pressure Control Equipment

1) Pressure vessel assembly
2) Hand-turned pressure generator (PPT, 600 MPa)
3) Pore pressure fluid container
4) Pressure gauge (ASTRA)
5) Pressure sensor (PSI-TRONIC)

Pressure valves are represented by the small stippled boxes. (modified from Alford, 1988)

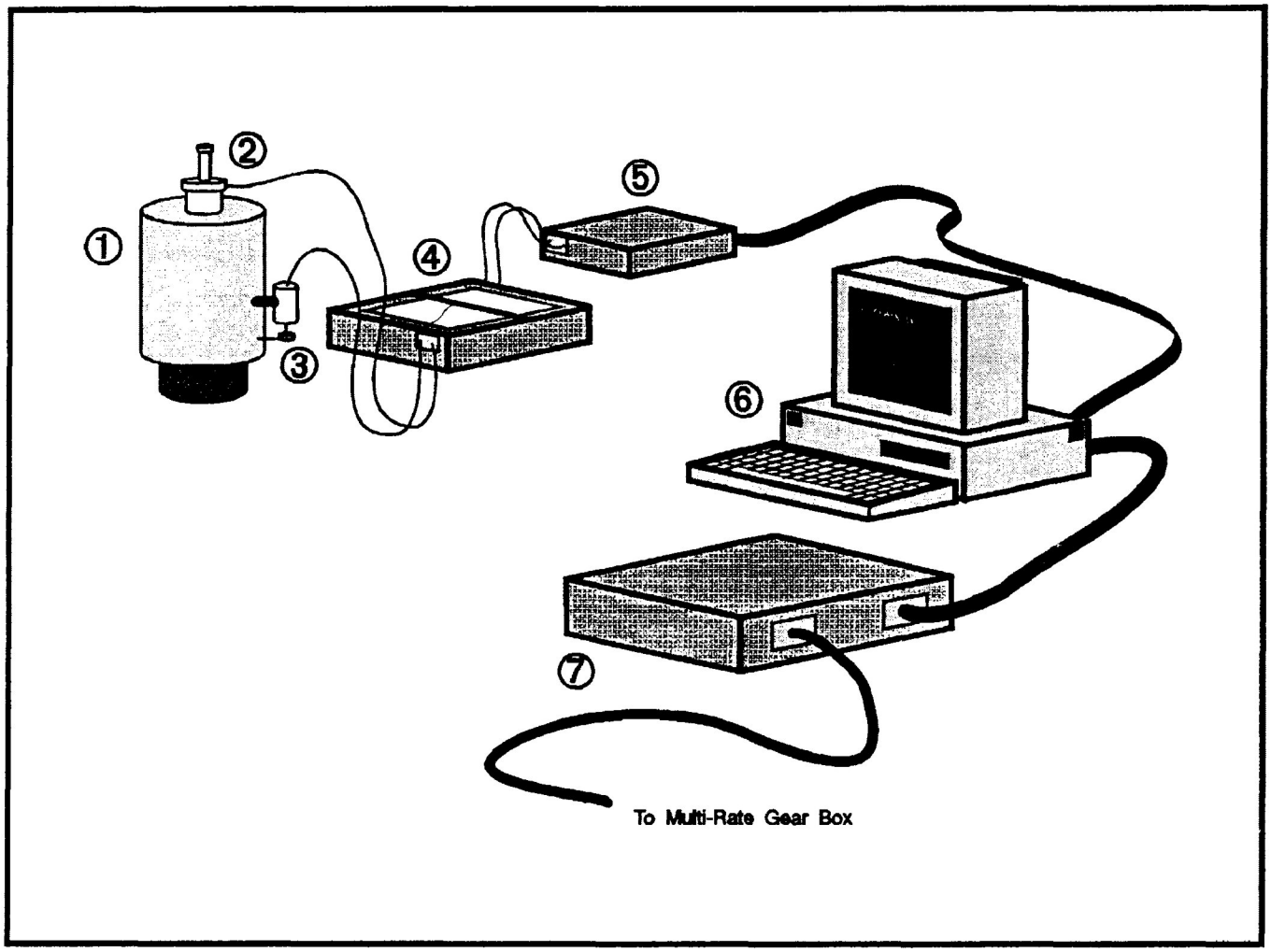

Figure 2.5 Force Displacement Measuring-Recording System; Computer and Analog Digital Converter for the Control of Loading

1) Pressure Vessel Assembly
2) Load cell
3) LVDT (COLLINS INC.)
4) Chart recorder
5) Analog to digital converter (TAURUS)
6) IBM model 20 computer
7) Motor speed control unit (PARAJUST)

(modified from Alford, 1988)

(T>100°C) the axial force is measured electronically by a PSI-TRONIC pressure gauge on the Ram pressure line. (Fig. 2.3). The load cell strain gauges or pressure monitor emit analog signals which are sent to a chart recorder (Fig. 2.5).

7) Computer and Analog Digital Converter for the Control of Loading

After the analog signals are read by the chart recorder, as presented in figure 2.5, the signal is converted to a digital signal by a 12-bit analog to digital converter (resolution 1 in 2^{12}). The digital signal is sent to an IBM model 20 computer where it is recorded and used to periodically compute the amount of strain and strain rate during the deformation experiment.

If changes in the strain rate are monitored, during the deformation of the sample, then the computer sends a signal to a motor speed control unit. This unit sends a voltage signal to the multi-rate gear box (Fig. 2.3) which controls the ram hydraulic pressure. The control of the ram hydraulic pressure allows for the simulation of a natural strain rate during experimental deformation.

2.3 Ziess polarizing microscope with an attached Ziess universal stage

3.2.1 Introduction

Universal-stage measurements were made on the orientations of the optic axes of the host crystals (*c*-axes) and the pole to the *e*-twin planes for calcite grains in the calcite-cement aggregate. The number of twin lamellae and the thickness of the calcite grain parallel to the pole to the twin plane were measured for the determination of the lamellae index. The necessary optical techniques use in this study are modified from those described by Turner and Weiss (1963) and Shelley (1983) and are presented in the following section.

2.3.2 Method for the determination of c-axis orientation in calcite

The following step by step method deals with the determination of the *c*-axis orientation from thin sections cut parallel to the X/Z and X/Y principal plane. The method is best suited for horizontal (*i.e.*, parallel to the A_4 axis) *c*-axes determinations, however, it is still applicable for vertical (*i.e.*, perpendicular to the A_4 axis) *c*-axes determinations. The steps for the *c*-axes determination procedure for calcite grains are as follows:

Step 1) For the determination of the calcite grain *c*-axis use cross polarized light with a low to medium power objective. The long axis of the thin section should be oriented parallel to 0° on A_1. Following the insertion of the thin section onto the universal stage the section should be squared using a small set square. Next the desired calcite grain is located and centred in the cross wires. Set the graduated circles of A_1, A_2, A_3, A_4 and the microscope stage equal to 0° as presented in figure 2.6. Check to see if the thin section is still squared, it is important that this is checked continually throughout the determination procedure.

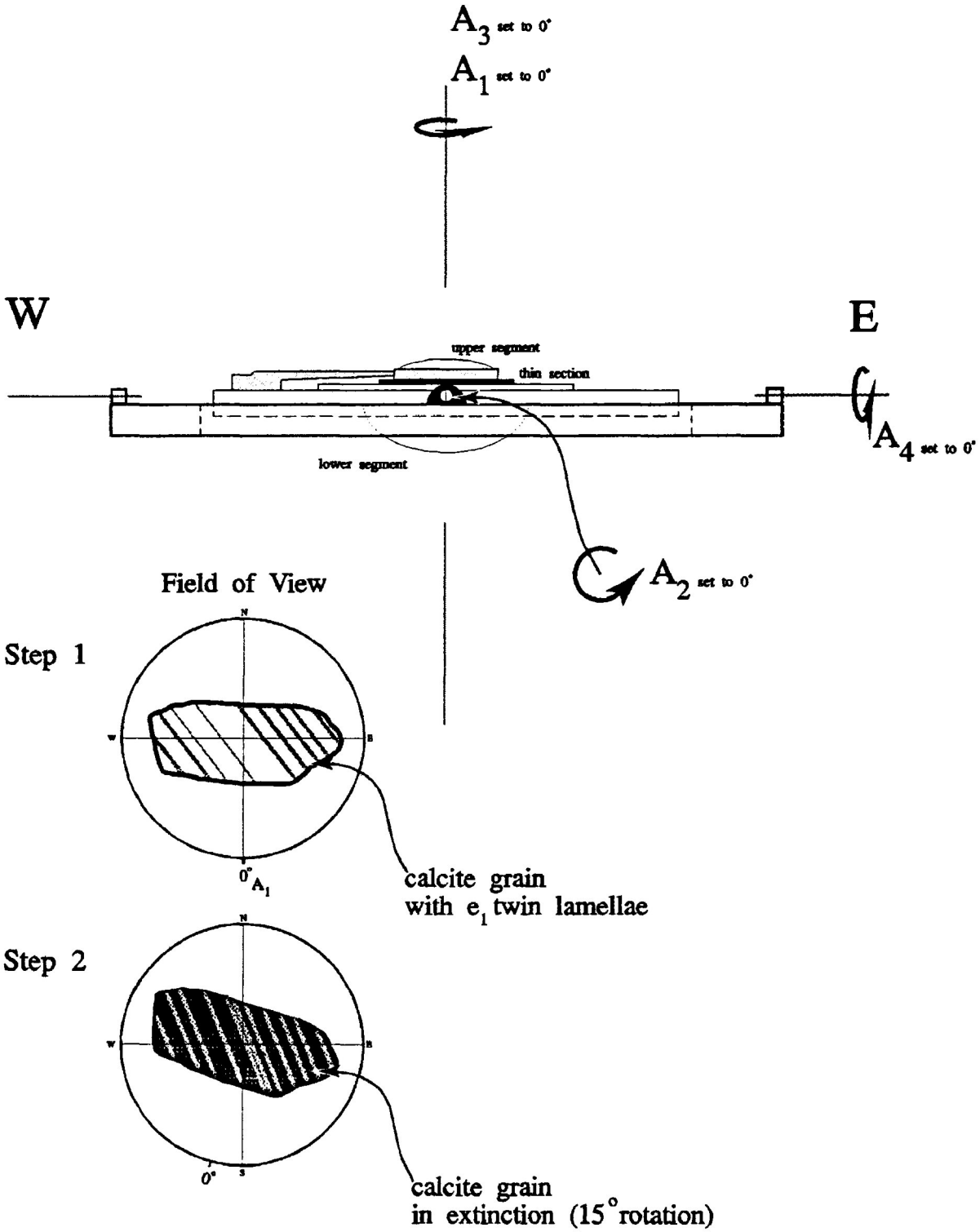

Figure 2.6 Schematic representation of a universal stage with A_1, A_2, A_3, A_4 and the microscope stage set to 0°. Step 1 and 2 involve finding the desired calcite grain and rotating it about A_1 until the host lattice of the grain is in extinction (for the hypothetical grain a 15° rotation about A_1 is needed (note orientation of twin lamellae in field of view)).

Step 2) Rotate the host lattice of the calcite grain into its extinction direction on A_1 (Fig. 2.6). There are two possible choices for the extinction direction orientation, called the slow and fast vibration direction. When the calcite grain is in extinction the host lattice slow vibration direction is either parallel to the N-S or E-W polarizer direction. For the *c*-axis determination, the slow vibration direction (parallel to the *c*-axis) must be parallel to the E-W polarizer direction.

Twin lamellae can sometimes be used to quickly determine the correct extinction direction orientation. The fact that the *c*-axis is approximately 26° away from the pole to the *e*-twin plane allows one to orient the calcite grain in an extinction direction in which the *e*-twin plain boundary is closest to the N-S polarizer direction (Fig. 2.7a). In the case where a calcite grain has two sets of twin lamellae the *c*-axis will lie in the obtuse angle between them (Fig. 2.7b). In both cases the *c*-axis will be parallel to the E-W polarizer. In the hypothetical calcite grain of figure 2.6 the correct extinction direction is obtained by a 15° clockwise rotation of A_1.

Step 3) Rotate the calcite grain through the maximum arc on A_2 to determine if the slow vibration direction is actually in the E-W orientation (Fig. 2.8). Rotate the calcite grain either to the right (east) or left hand side (west) of the universal stage (it is best to check this on both sides of the universal stage). Turner and Weiss (1963) have stated that calcite grains will show minimum relief when the slow vibration direction is aligned with the E-W polarizer. Observations on the synthetic calcite aggregates, however, suggest that this may not always be correct. The following method can be used to determine the slow vibration direction:

a) If the host lattice of the calcite grain remains in extinction when rotated through the maximum arc on A_2 then the slow direction is in the E-W position (Fig. 2.8). Go to step 3c if the above observation is found to be true. Calcite grains may, in some cases, light up on the east of west side of the stage when in maximum arc because of the high birefringence of calcite and also the rotating surfaces of *e*-

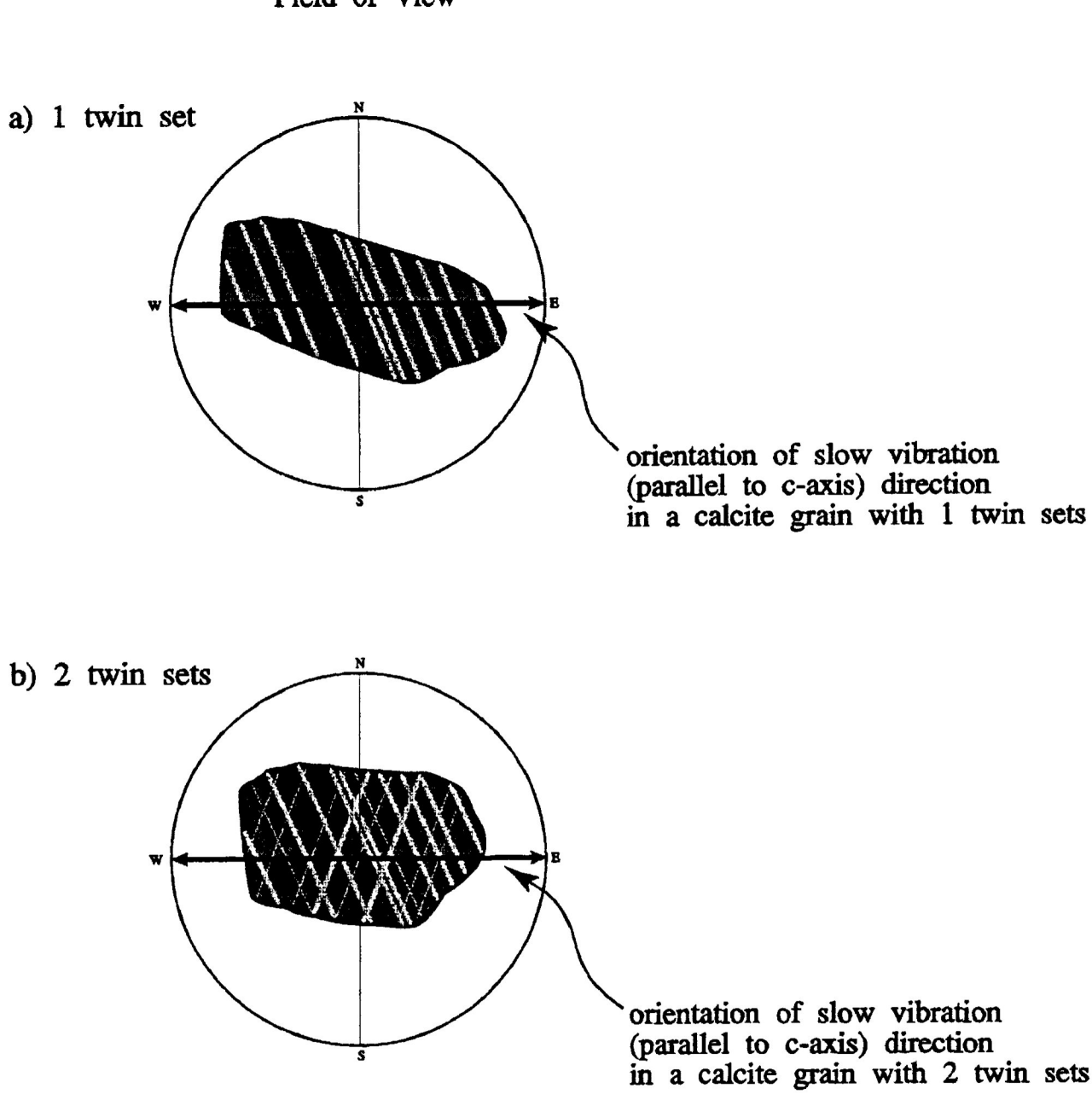

Figure 2.7a,b The orientation of the slow vibration direction (parallel to the *c*-axis) in the host lattice of a calcite grains with 1 and 2 sets of twin planes. a) In the case a calcite grain with 1 set of twin planes the correct extinction direction will have e-twin plain boundaries close to the N-S polarizer direction. b) In the case where a calcite grain has two sets of twin lamellae the slow vibration direction will lie in the obtuse angle between them.

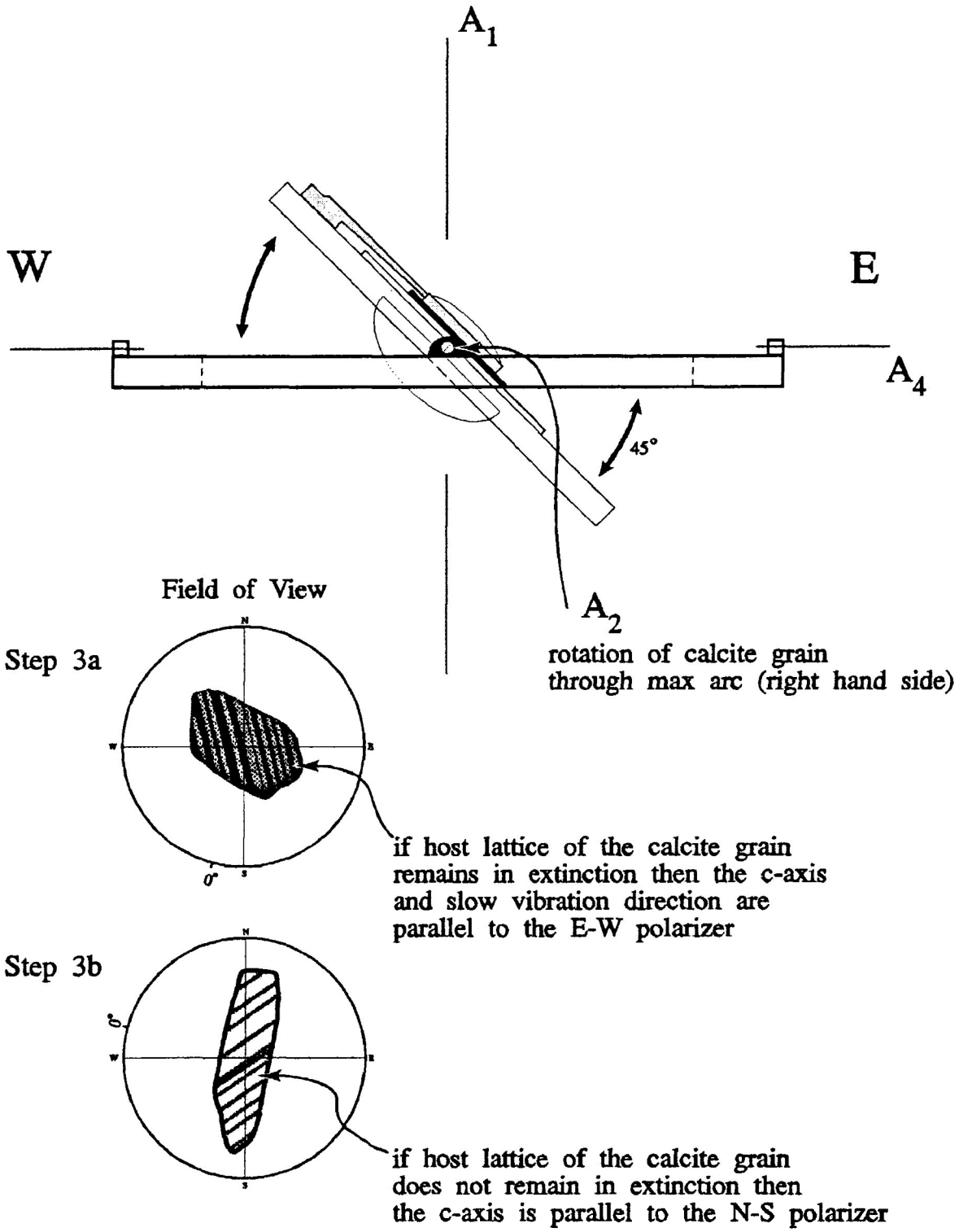

Figure 2.8 Step 3 involves rotating the grain through a maximum arc about A_2 to determine if the slow vibration direction is oriented correctly. Step 3a illustrates the observed result if the host lattice of the calcite grain is in the correct extinction orientation. Step 3b illustrates the observed result if the host lattice of the calcite grain is in the incorrect extinction orientation (a 90° rotation about A_1 is needed).

twin planes. There is one exception to this observation which deals with a c-axis that is horizontal or vertical to the thin section, determination of the slow vibration direction in this case is explained in step 4.

b) If the host lattice of the calcite grain lights up (*i*.e., reduction in the degree of extinction) on the east and west sides of the stage when rotated through the maximum arc on A_2 (Fig. 2.8) then rotate the grain 90° on A_1, so that the host lattice is in the other extinction direction. Return to 3a to check if the slow vibration direction is in the E-W position.

c) Reset the graduated circle of A_2 equal to zero and go to step 4.

Step 4) Rotate the calcite grain through the maximum arc on A_4 to the south and north sides of the universal stage. The calcite grain should light up with low to moderate birefringence in the north and south position on the stage (Fig. 2.9a and c). If the host lattice of the calcite grain remains in extinction then it is possible that the c-axis is horizontal or vertical to the universal stage. To check this the following can be used (Shelley, 1983):

The correct vibration direction is chosen by first tilting A_4 and then tilting A_2. If the host lattice of the calcite grain remains in extinction then the c-axis is in the N-S direction and the alternative extinction direction must be used (90° rotation about A_1). If the host lattice of the calcite grain does not remain in extinction then the slow vibration direction is in the correct orientation (parallel E-W polarizer). Reset the graduated circles A_2 and A_4 equal to zero.

Step 5) Rotate calcite grain forward on A_4 to the maximum arc in the south direction (Fig. 2.10).

Step 6) Rotate A_2 until maximum extinction is obtained in the host lattice of the calcite grain (Fig. 2.10). When maximum extinction is obtained the fast vibration direction will be parallel to the N-S polarizer and perpendicular to the microscope stage. It will be noticed that on rotation of A_2 one side of the calcite grain will show high birefringence

Step 4

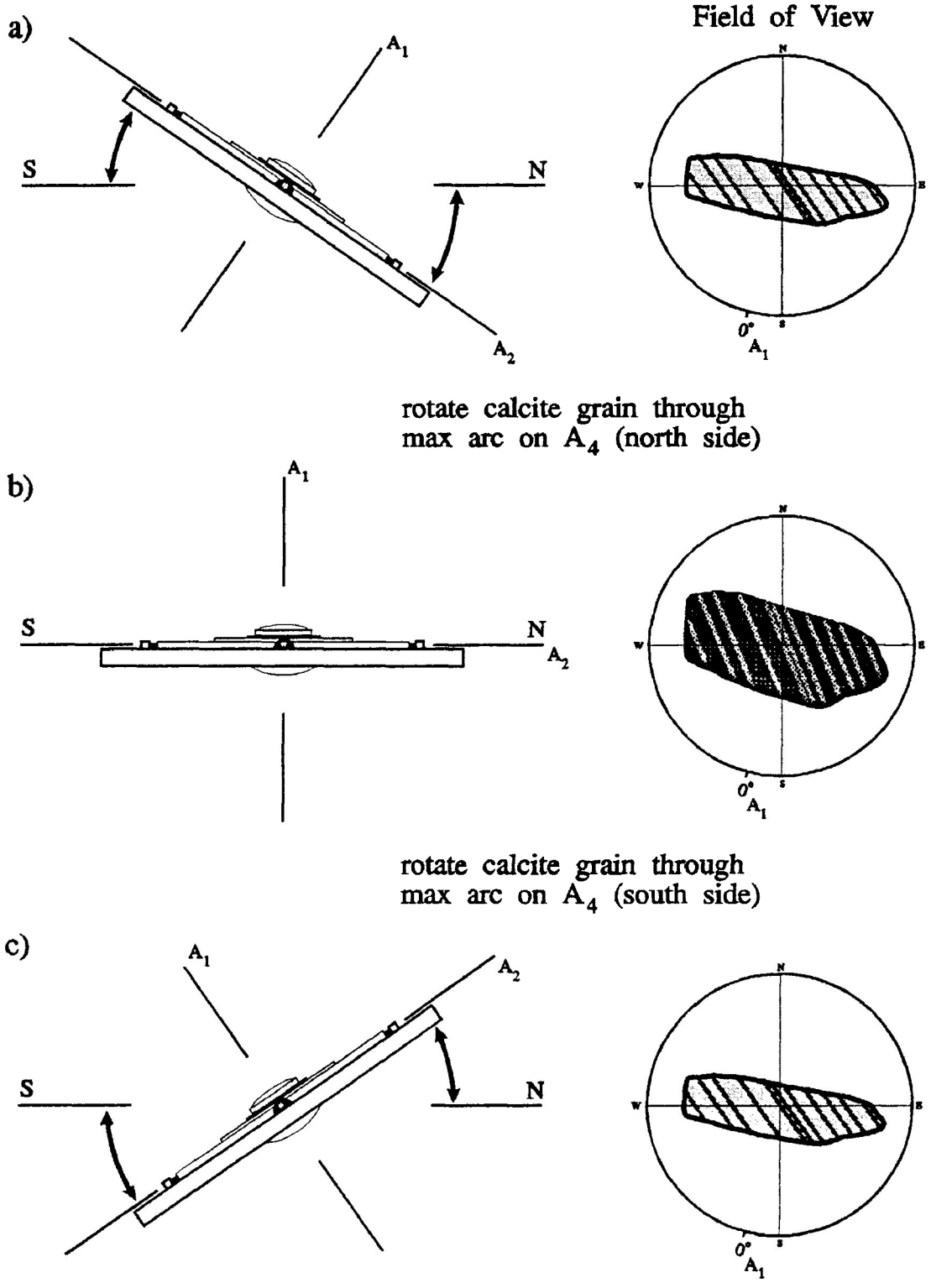

Figure 2.9 Step 4 involves rotating the calcite grain through a maximum arc about A_4 to determine if the slow vibration direction is oriented correctly (parallel to E-W polarizer) or if the *c*-axis is parallel or perpendicular to A_4. As illustrated in the field of view the host lattice of the calcite grain should light up (decrease in extinction) on the north (a) and south (c) side of the universal stage and remain in extinction when A_2 is horizontal (b).

Figure 2.10 Step 5 involves rotating the calcite grain forward on A_4 to a maximum arc. Step 6 involves rotating the calcite grain through a maximum arc on A_2 in order to orientate the fast vibration direction perpendicular to the stage and parallel to the N-S polarizer (*i.e.*, maximum extinction of the host calcite lattice). Step 6a) represent calcite grain in the left hand maximum arc with high birefringence (*i.e.*, bright appearance). Step 6b) represents the calcite grain in the right hand maximum arc with low birefringence (*i.e.*, dull appearance). Step 6c) represents the calcite grain in a orientation in which the fast vibration direction is perpendicular to the stage (for the hypothetical calcite grain a 25° rotation to the east side is needed).

Step 5

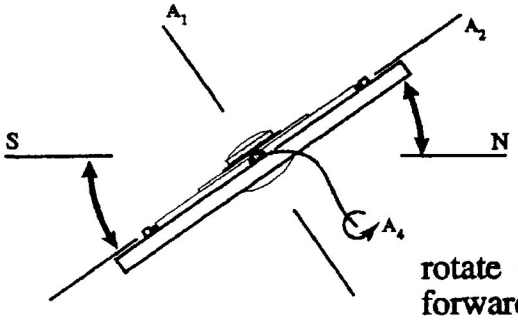

rotate calcite grain forward to max arc on A_4

Field of View

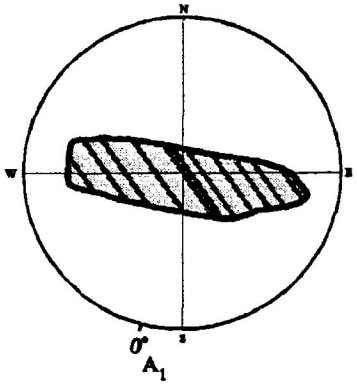

Step 6

a)

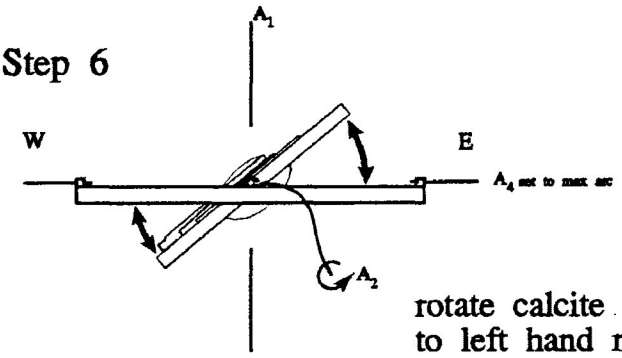

rotate calcite grain to left hand max arc on A_2

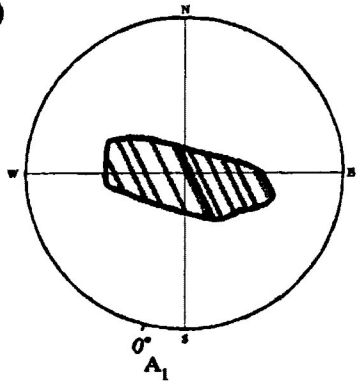

b)

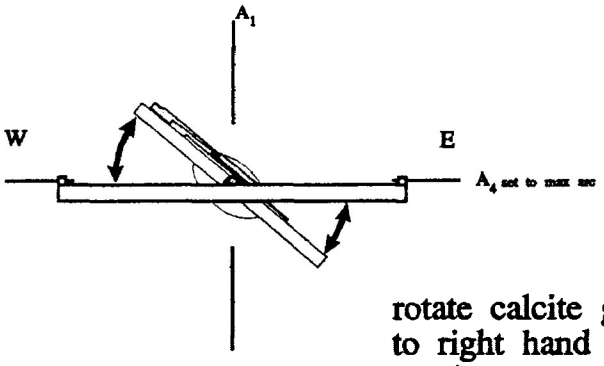

rotate calcite grain to right hand max arc on A_2

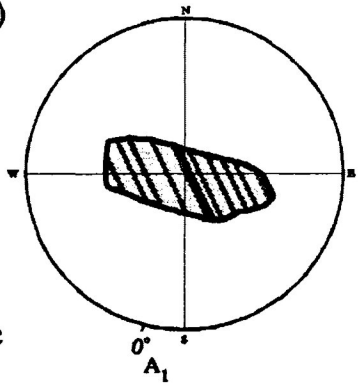

c)

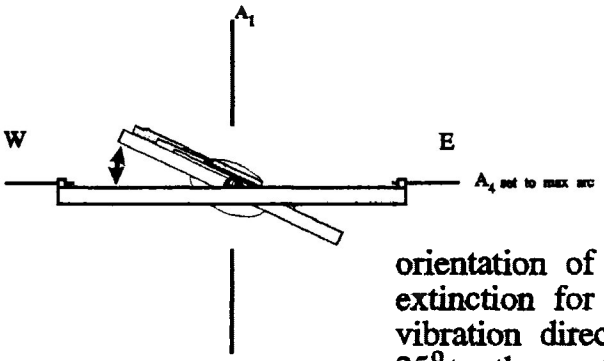

orientation of max extinction for fast vibration direction 25° to the east side

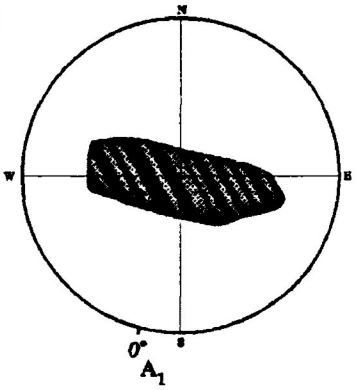

(*i.e.*, bright (Fig. 2.10a)) and on the other the calcite grain will show low birefringence (*i.e.*, dull (Fig. 2.10b)), either of which may have an extinction position.

It is preferable to use the maximum extinction position that exists in the low birefringence side of the calcite grain (Fig 2.10c). If this extinction direction is used then the c-axis will be horizontal to the universal stage (Fig. 2.11a). If the high birefringence side is used then the c-axis will normal to the universal stage (Fig. 2.11b). The choice, however, depend on the orientation of the *c*-axis and the rotational limits of the universal stage. In the calcite grain of figure 2.10 the extinction direction for a horizontal *c*-axis is obtained by a 25° clockwise rotation of A_2.

Step 7) Rotate backwards on A_4 to the maximum arc in the north position. The host lattice of the calcite grain should remain extinct, if so then rotate A_4 to 0° and go to step 8. If the extinction is not sufficiently good (*i.e.*, degree of host lattice extinction decreases) then return the graduated circle A_4 to 0° and rotate A_1 until maximum extinction is obtained. If the extinction is good on the second rotation of A_4 through the north and south maximum arc then go to step 8. If extinction is not sufficiently good during rotation about A_4 then return to step 5 and redetermine the fast vibration orientation.

Step 8) If the c-axis is horizontal to the universal stage (Fig. 2.11a) then the host lattice of the calcite grain will alternate in extinction on rotation of the microscopic stage. If the c-axis is normal to the universal stage (Fig. 2.11b) then the calcite grain will remain in extinction.

Step 9a-b) Angular measurements are taken from the graduated circle on A_1 and A_2 and recorded in the arrowhead convention presented in figure 2.11a-b. Plotting the orientation of the *c*-axis on a stereogram from data recorded in the arrowhead convention first involves rotating the top reference orientation of the thin section (A_1 initially equal to 0°) to the new orientation of A_1. Since the thin section is most likely tilted during the determination, the *c*-axis is rotated away from the periphery of the stereogram for a horizontal *c*-axis or rotated away from the centre of the stereogram for a vertical *c*-axis.

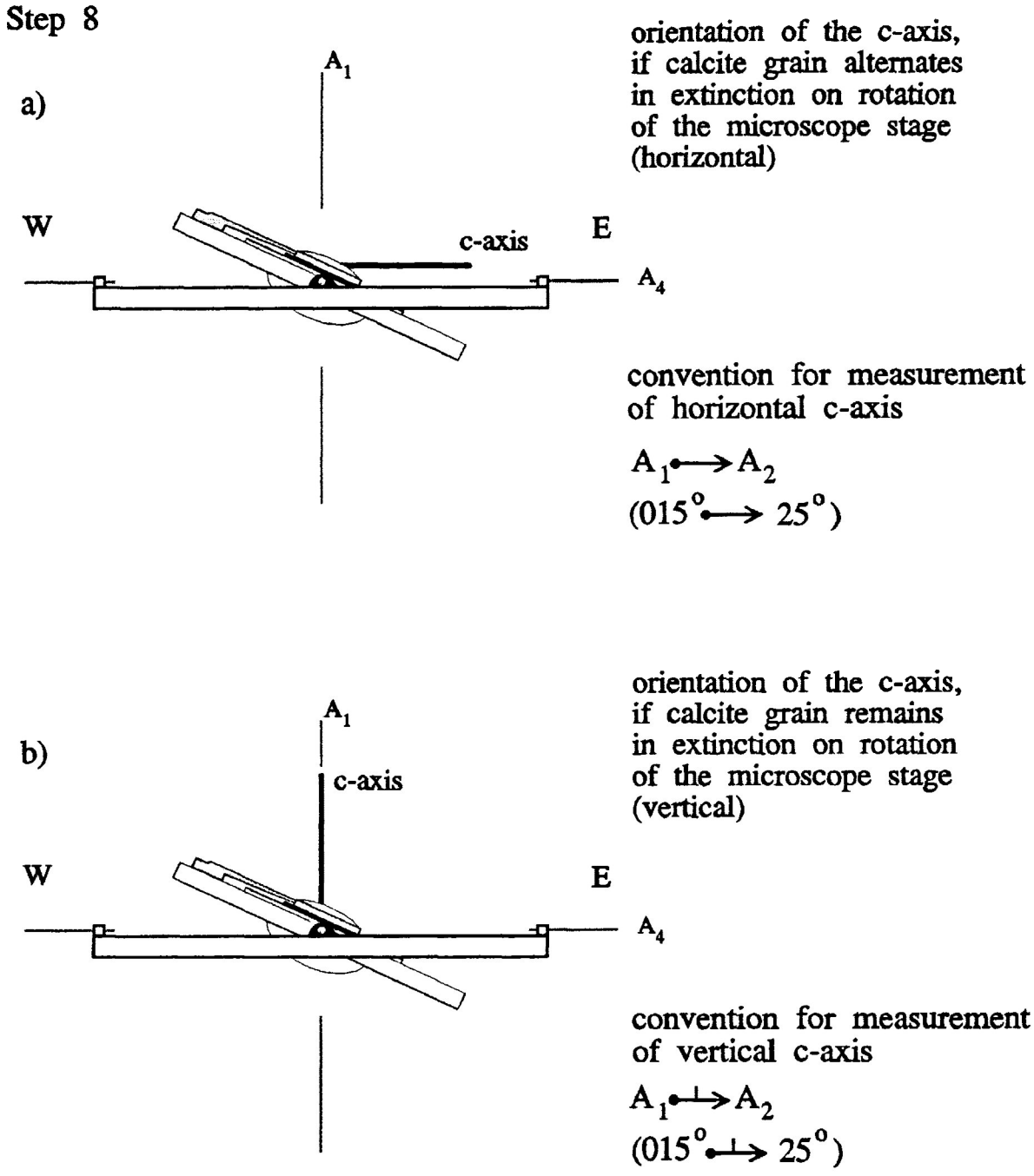

Figure 2.11 Step 8 a) If the c-axis is horizontal to the universal stage then the host lattice of the calcite grain will alternate in extinction on rotation of the microscopic stage. Step 8 b) If the c-axis is normal to the universal stage then the host lattice of the calcite grain will remain in extinction on rotation of the microscope stage. Also presented in the figure is the arrowhead convention for recording of the orientation data needed for the plotting of the *c*-axis on a stereogram.

Step 9a

Stereographic projection
(equal area, lower hemisphere)

a) horizontal c-axis

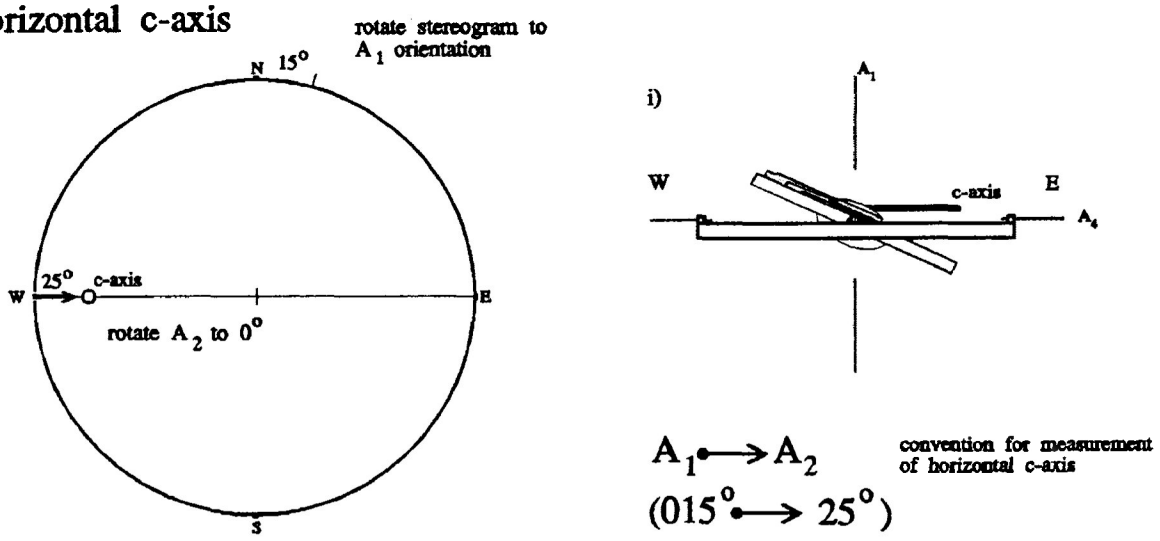

b) vertical c-axis

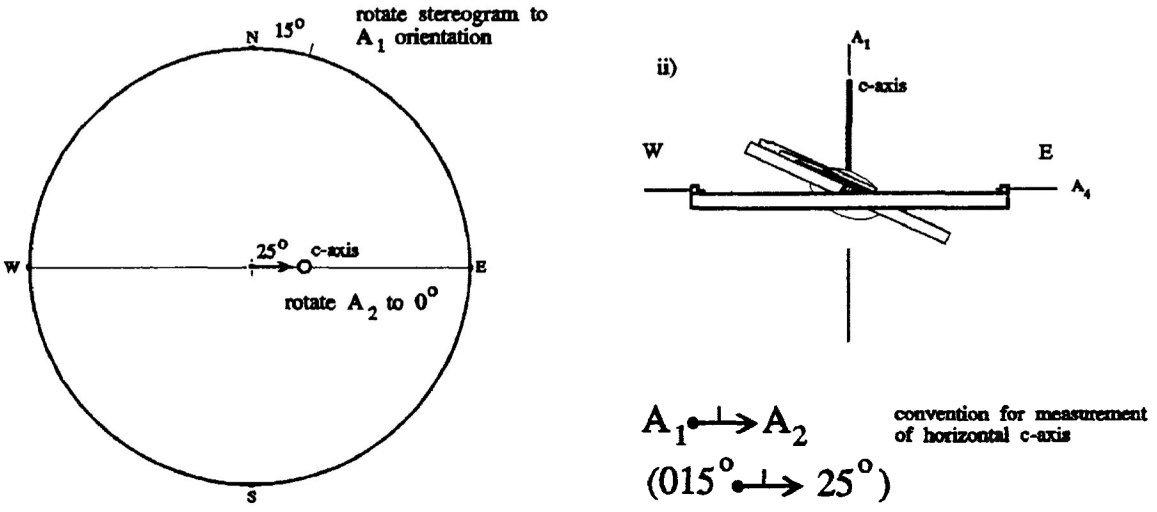

Figure 2.12a-b Plotting of a horizontal (a) and vertical (b) *c*-axes for a east dipping A_2 measurements. Stereographic projection is equal area and lower hemisphere.

Step 9b

Stereographic projection
(equal area, lower hemisphere)

a) horizontal c-axis

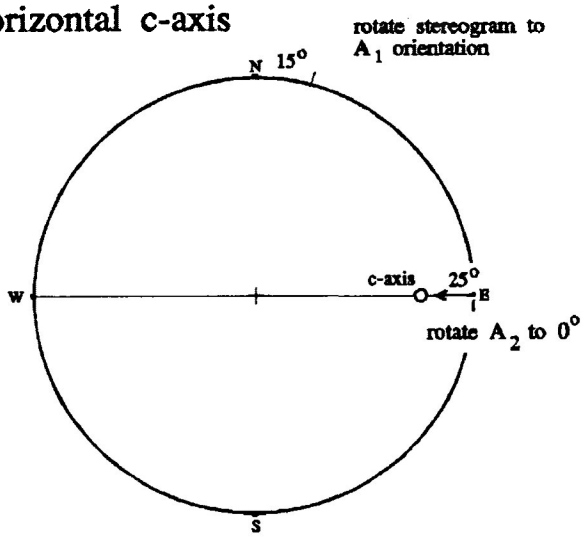

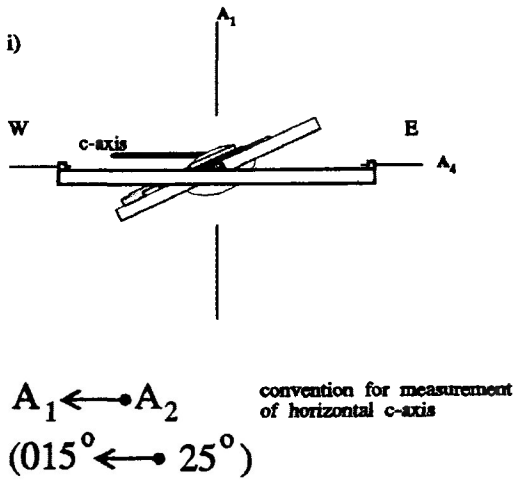

$A_1 \longleftarrow A_2$ convention for measurement of horizontal c-axis

$(015^\circ \longleftarrow 25^\circ)$

b) vertical c-axis

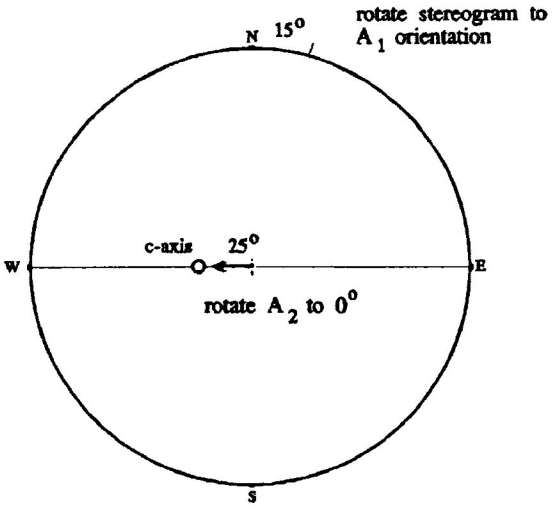

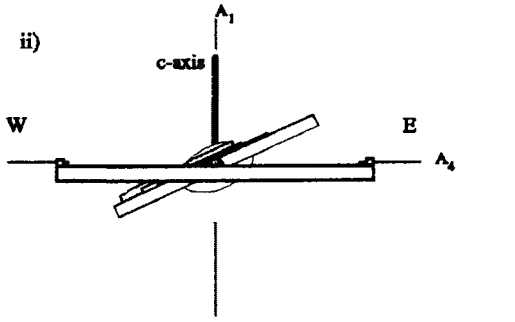

$A_1 \longleftarrow\!\!\perp A_2$ convention for measurement of horizontal c-axis

$(015^\circ \longleftarrow\!\!\perp 25^\circ)$

Figure 2.13a-b Plotting of a horizontal (a) and vertical (b) *c*-axes for a west dipping A_2 measurements. Stereographic projection is equal area and lower hemisphere.

The rotation is represented by counting off the angle of A_2 along the E-W small circle depending on the direction of dip on A_2 (Fig. 2.12a-b (Step 9a) and 2.13a-b (Step 9b)). Figure 2.12a-b represents the measured calcite grain with a *c*-axis dipping to the east for a horizontally (i) and vertically (ii) measurement. Figure 2.13a-b represents the measured calcite grain with a *c*-axis dipping to the west for a horizontally (i) and vertically (ii) measurement.

2.3.3 Determination of the orientation of pole to an e-twin in calcite

The following method was used in the present study for the determination of the pole to the *e*-twin plane and also information needed for the calculation of the lamellae index.

Step 1) Rotate the desired twin set of the calcite grain so that the twin plane boundaries are parallel into the E-W polarizer direction on A_1 (Fig 2.14, for the hypothetical calcite grain a rotation of A_1=130° is needed). It is best to use plane light and a low to medium objective.

Step 2) Rotate the calcite grain with A_4 so that the twin lamellae boundaries exhibit the sharpest thinnest appearance (Fig. 2.14, for the hypothetical calcite grain a rotation of A_4=20° (south dipping) is needed). The pole to the *e*-twin plane is now parallel to the N-S polarizer (Fig. 2.14). If the twin lamellae are microtwins then they will appear as a thin black line.

Measurement of the lamellae index of the calcite grain should be made at this point. The lamellae index is calculated by the number of twin lamellae in the calcite grain divided by the length of the calcite grain parallel to the N-S polarizer.

Step 3) Angular measurements are taken from the graduated circle on A_1 and A_4 and recorded in the arrowhead convention presented in figure 2.15. Plotting the orientation of the pole to the e-twin plane on a stereogram first involves rotating the top orientation of the thin section (A_1 initially equal to 0°) to the new orientation of A_1. Since the thin section is most likely tilted during the determination, the orientation of the pole to the e-twin plane is rotated away from the periphery of the stereogram. The rotation is represented by counting off the angle of A_4 along the N-S great circle (Fig. 2.14a (south dipping) and Fig. 2.14b (north dipping)).

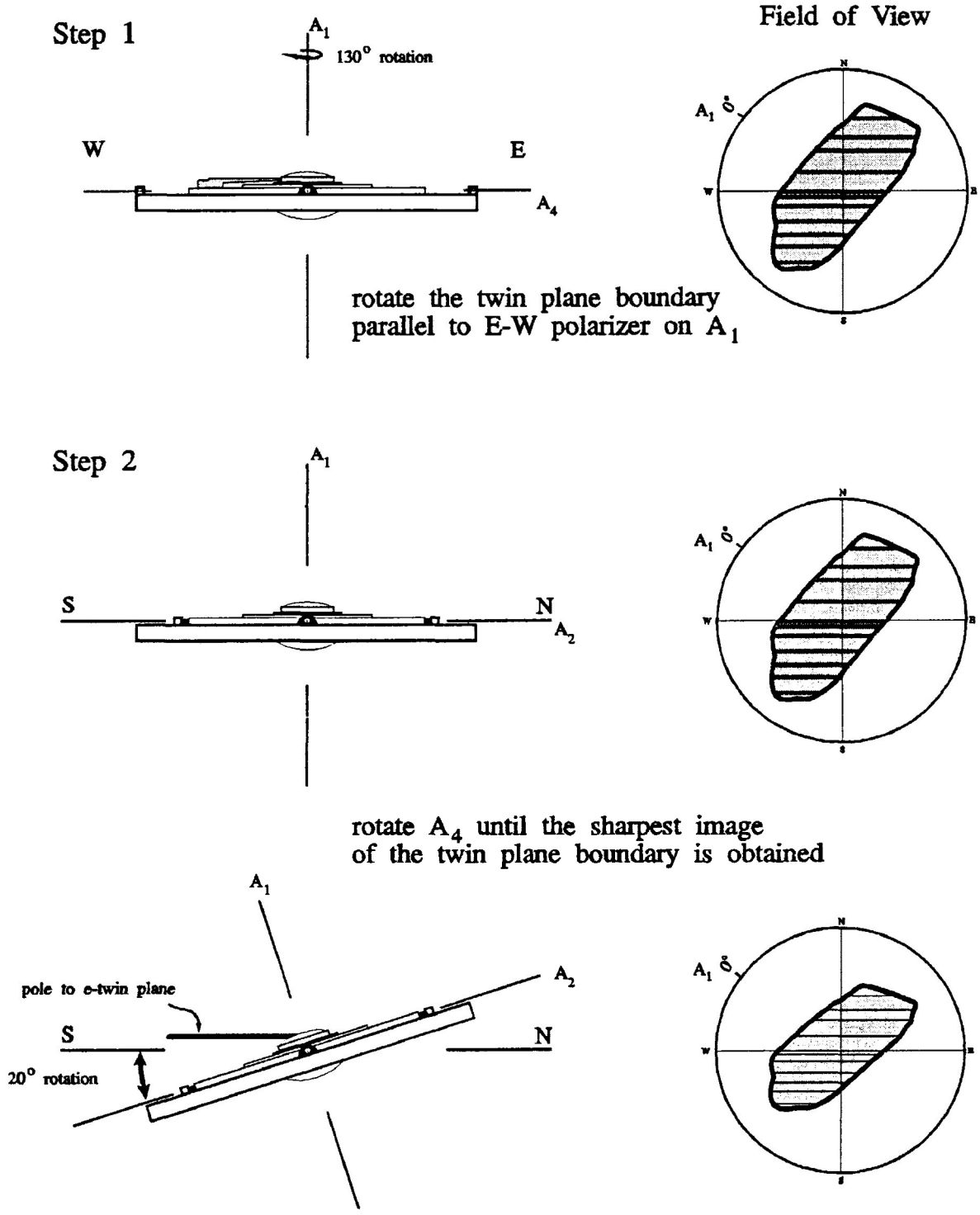

Figure 2.14 Determination of the orientation of the pole to an e-twin plane of a calcite grain using a universal stage. Step 1 involves rotating the calcite grain about A_1 until the e-twin plane boundaries are parallel to the E-W polarizer (for the hypothetical calcite grain a 130° rotation about A_1 is needed). Step 2 involves rotation of the calcite grain about A_4 until the sharpest thinnest appearance of the twin lamellae boundaries are obtained (for the hypothetical calcite grain a 20° rotation about A_4 to the south is needed).

Step 3

Stereographic projection
(equal area, lower hemisphere)

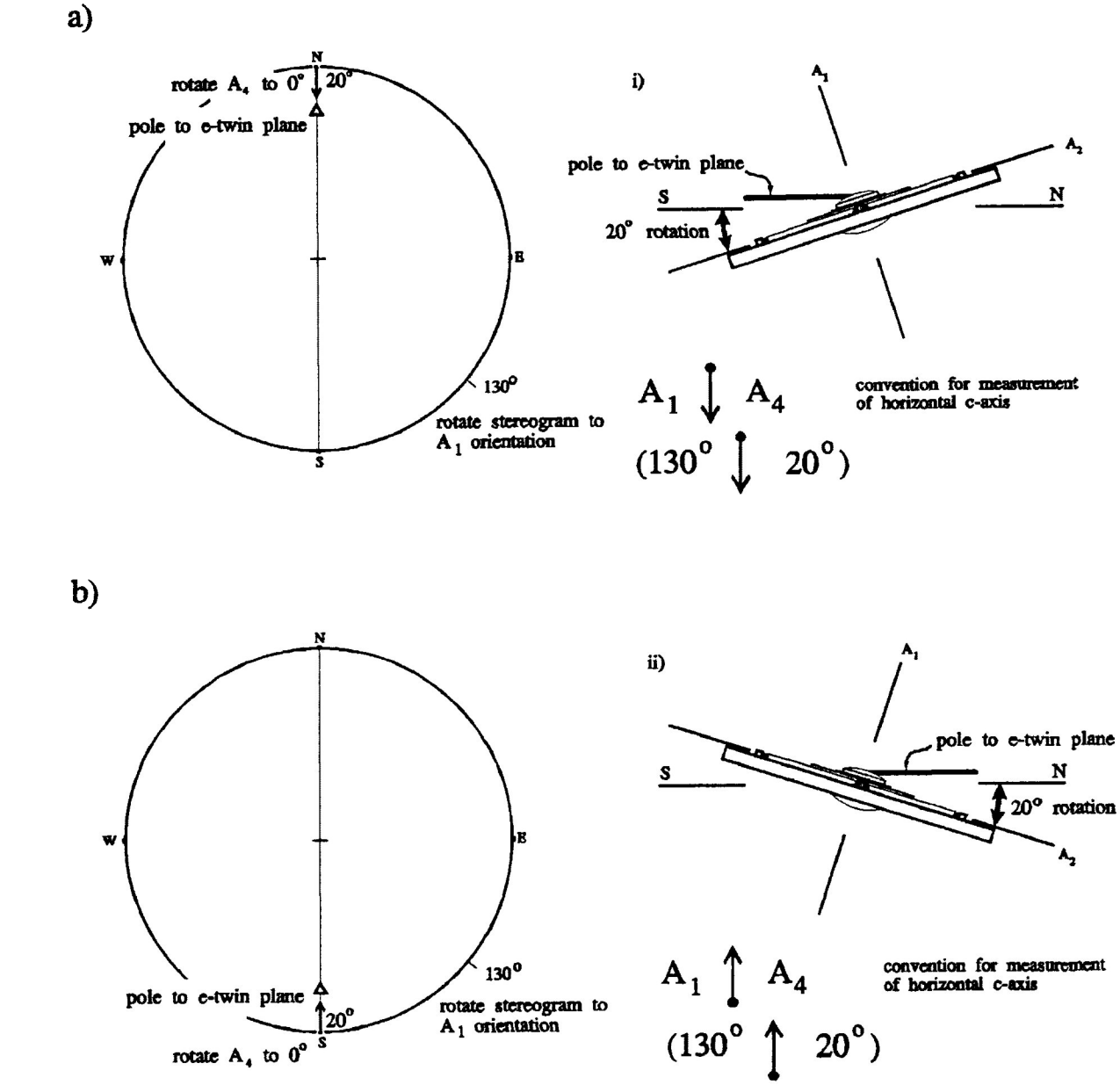

Figure 2.15a-b Plotting of a pole to an e-twin plane for a south dipping (a) and west dipping (b) for A_4 measurements. Stereographic projection is equal area and lower hemisphere.

2.4 Determination of the dimensional and angular parameter of deformed particles with a Ziess Videoplan digital analyzer

A Ziess Videoplan digital analyzer was used in this study to determine dimensional parameters (*i.e.*, maximum (DELLIP-A) and minimum (DELLIP-B) dimensional axes, R_i (FORM ELL^{-1}) and R_f (FORM ELL^{-1})) and angular parameters (theta (ANGLE AX), ϕ (ANGLE AX)) for computer generated elliptical approximations of traced particles. The elliptical approximations were calculate from the best-fit of the moment-of-inertia for each traced particle. The parameter information was digitized from photocopies of thin section micrographs or in some cases tracings of micrographs. The scale of all the photographs were 38:1.

As presented in figure 2.16 the photocopies or tracings of thin section micrographs for coaxial deformation were aligned so that the cleavage trace (S_1, defined by overall grain shape orientation) was perpendicular to the X reference line. In undeformed samples they were aligned so that the X reference line was taken to be parallel to the long axis of the text cylinder. Undeformed and deformed non-coaxial samples were aligned so that the X reference line was perpendicular to the shear zone. Angle Ax was measured counterclockwise from the X reference line from 0° to 180°. Subtracting 90° from Angle Ax allows for the orientation data to be recorded between -90° and 90° with 0° being the orientation of S_1.

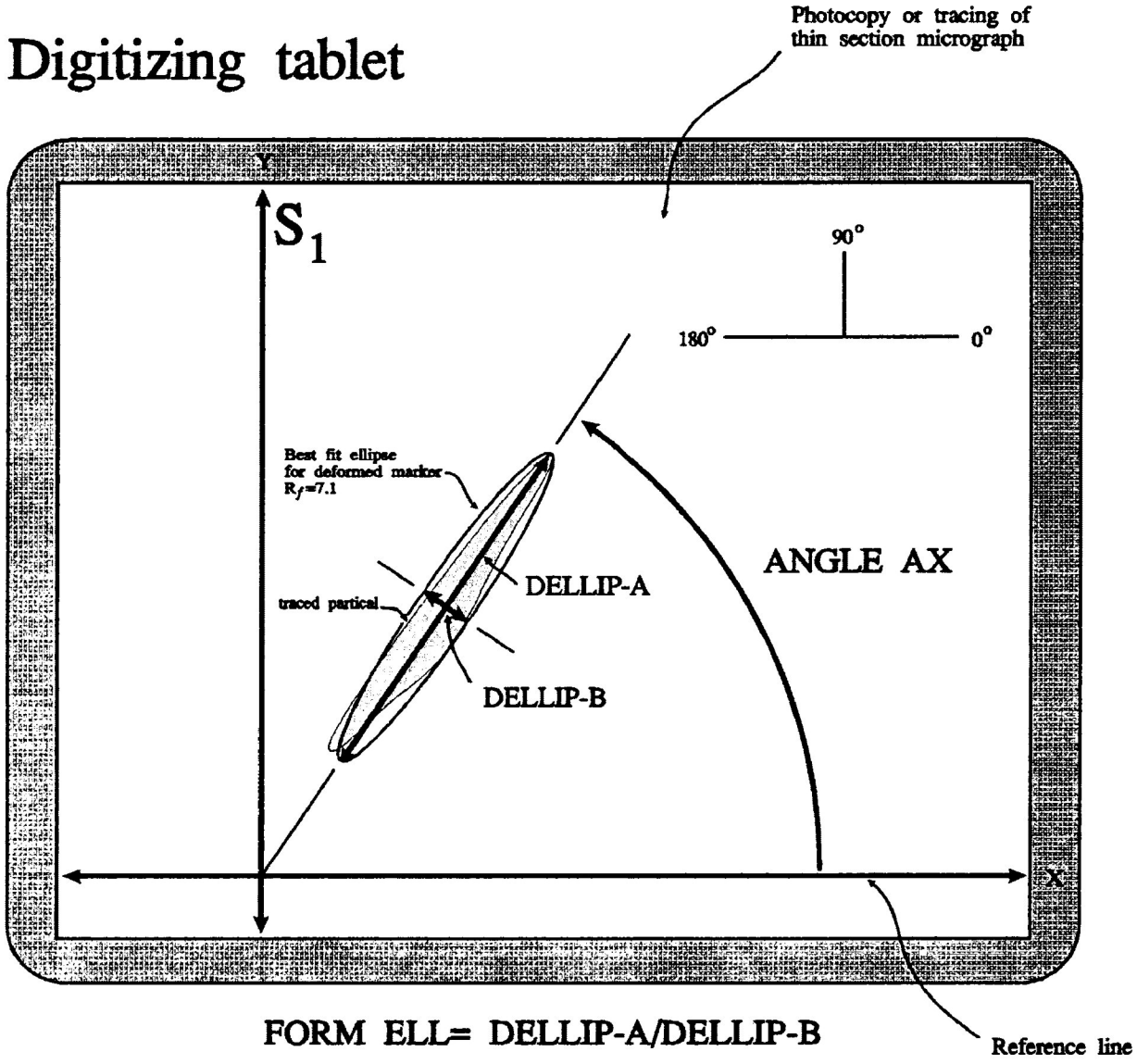

Figure 2.16 Schematic representation of a digitization tablet. Photocopy or tracing of thin section micrographs aligned so that the cleavage trace (S_1, defined by overall grain shape orientation) is perpendicular to the X reference line in coaxial deformation. Best fit elliptical approximation of deformed particle (shaded) is used to calculate R_f (FORM ELL^{-1}) and ϕ (ANGLE AX). Angle Ax is measured counterclockwise from the X reference line from 0° to 180°.

Chapter 3: Robin's, Harmonic and Linearization strain analysis methods

3.1 Introduction

Three numerical strain analysis methods were used in this study for the determination of estimates of experimental bulk strain. The first method is Robin's method (1977) for determining ratios of the longitudinal finite strain in rocks by using passive strain markers of any shape. The second is the harmonic mean method (Lisle, 1977) which uses harmonic mean of the strain markers axial ratios. The third method in the linearization method (Yu and Zheng, 1984) involves the linearization of Dunnet (1969) R_f/ϕ "onion skin" equation. These three methods are discussed in detail in the following sections.

3.2 Robin's method for strain analysis

3.2.1 Introduction

Robin (1977) devised a simple method of determining ratios of perpendicular radii of the strain ellipse, using axial ratios of passively deformed particles of possibly unknown and highly-irregular shape. Robin's method (1977) has not been that pervasive in geological literature, compared with graphical strain analysis methods. Studies that have included strain estimates based on Robin's method include Bau (1979) on strained cordierite porphyroblasts crystals, Schnorr and Schwerdtner (1981) on deformed granite, Schwerdtner *et.al.* (1983) on deformed granite, Van Berkel *et.al.* (1986) on deformed anhydrite nodules and Borradaile and McArthur (1990) on experimentally deformed calcite-cement aggregate. Several studies have compared Robin's method to other methods, including Paterson (1983) and Babaie (1986).

3.2.2 Assumptions necessary for Robin's Method

Robin's Method (1977) was developed as an numerical technique for determining ratios of finite strain in a rock by using passive strain markers of any shape. As well as the necessity of homogeneous strain and perfectly continuous particle deformation, two other considerations must be taken into account when using this method:

1) The first is that there must be no significant competency contrast between the markers and the host rock.

2) The second consideration is that the markers may have any shape provided their original orientation is random.

These assumptions are less restrictive than other method such as Ramsay (1967) and Dunnet (1969), in that initial and final particle shapes are not necessarily ellipsoidal. However, Robin's Method is still applicable if the markers are elliptical.

3.2.3 Technique for determining strain from Robin's Method

In Robin's method the strain ratio can be calculated from passive markers of a given rock section. Initially, the location of the centre of gravity for each of the markers under study is located or calculated. Secondly, measurements of the two diameters (a_j, c_j, Fig. 3.1), which are parallel to each of two principal directions of the sectional strain (X and Z in figure 3.1), is determined from each marker. The marker's ratio $r_j=a_j/c_j$ and its logarithm $l_j=\ln r_j$ are then calculated. The estimate of logarithm of the sectional strain ellipse is calculated as the arithmetic mean of the logarithmic r_j ratios.

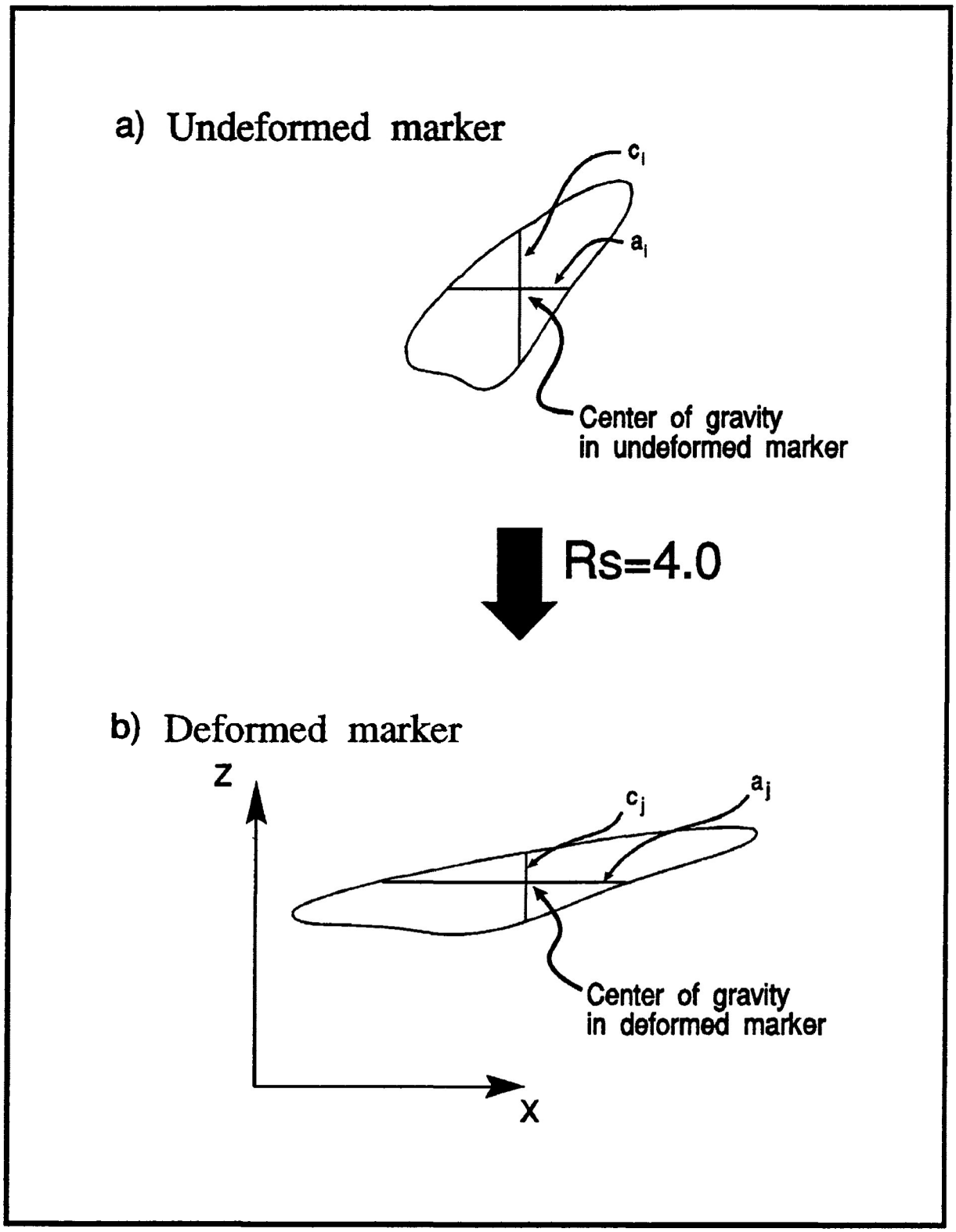

Figure 3.1 a) undeformed irregular shaped marker with undeformed a_i/c_i ratio, as well as the centre of gravity of the marker. b) irregular shaped marker deformed by a R_s=4, with principle strain axes oriented horizontally (X) and vertically (Y). Presented are the deformed a_j/c_j ratio and the centre of mass of the deformed marker. Note that the centre of mass in the deformed marker is in the same material location as the undeformed marker for passive homogenious

3.2.4 Statistical Analysis of the strain estimate

As suggested by Robin and Torrance (1987) a confidence interval of the strain estimate can be calculated from the simple statistical formula of standard deviation (σ_m). A confidence bracket can be determined, in which there is a 68.26% likelihood that the actual strain ratio of the deformed sample falls in the range of $R_s+\sigma_c$ to $R_s-\sigma_c$ around the calculated strain estimate.

3.2.5 Problem in determining strain from r_j ratios

Robin's method requires that the principal directions of strain be known or can be determined by visual inspection. Incorrect interpretation of these directions can lead to significant error in the calculation of strain. However, in principle these directions can always be found by determining the maximum value of strain using the calculation of Robin's method (1977). However, it may also be possible to estimate the direction of the maximum principal strain from a histogram of the orientations of the longest diameter of each deformed marker (assuming that no initial dimensional fabric is present), or from the trace of a foliation associated with the deformation in the X/Z principal section. In this study the angular mean was calculated from the distribution of the directions of the long diameter of each deformed marker.

The problems associated with determining the centre of mass of the marker are alleviated if the markers are assumed to be centrosymetrical, such as ellipsoids. Although, Robin's method (1977) was developed for markers of any irregular shape, it can also be used for elliptical markers (or elliptical approximations of the irregular shapes, Fig. 3.2a). Therefore, data can be collected in the R_f/ϕ form. For R_f/ϕ data, with the principal directions of the maximum sectional

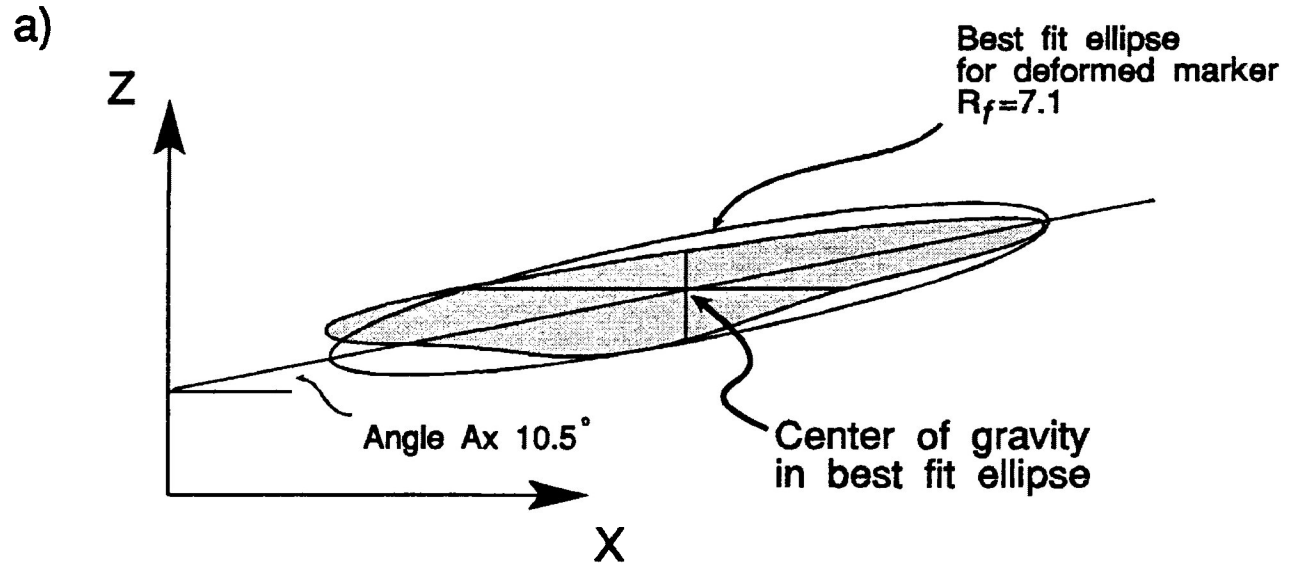

b)

$$\frac{a_i}{c_i} = \sqrt{\frac{\tan^2\phi_i + R_{fi}^2}{R_{fi}^2 \tan^2\phi_i + 1}}$$

Figure 3.2 a) Computer generation of a best fit ellipse (R_f) and associated orientation (Angle Ax (ϕ)) of the irregular particle.

b) Equation for the calculation of the a_j/c_j ratio from the best fit ellipse and orientation.

strain used as a reference direction, the r_i ratio needed to determine the strain ellipse can be calculated using the formula of figure 3.2b.

3.3 Harmonic mean method for strain analysis

The inaccuracies arising from estimating strain as an arithmetic mean of axial ratios has been pointed out by Ramsay (1967), Dunnet (1969), Elliot (1970), Lisle (1977b) and Pfiffner (1980). Closer approximations, but still overestimates of strain, are given by geometric mean (Dunnet, 1969) and Harmonic mean (Lisle, 1977b, 1979).

Lisle (1977b) compared inaccuracies arising from arithmetic (R), geometric (G) and harmonic (H) means and found harmonic mean to be the best approximation of finite strain value, so that the estimates of strain are consistent with R > G > H (Lisle, 1977b).

The results of Lisle (1977b, 1979), Borradaile (1984) and Babaie (1987) are consistent with the suggestion that application of the harmonic mean method provides a good estimate of the strain ration in the cases where strain is larger than 2.5 and where immediate application of other methods is not applicable.

3.4 Linearization Method of strain analysis

3.4.1 Introduction

A method of statistical analysis of R_f/ϕ data, developed by Yu and Zheng (1984), has been used in this study for strain analysis of the experimentally deformed synthetic calcite-cement aggregate, Ancaster Oolitic limestone and China Beach sandstone. This method provides estimates of the strain ratio (R_s in the X/Z principal plane), initial shape ratio (R_i) and original strain marker orientation (theta) from R_f and non-random ϕ of strain markers in the deformed state. To test the determination of R_s by the linearization method a series computer simulations of homogeneous deformation, were conducted on a computer program (version 1.25) developed by Dr. G.J. Borradaile (@1989).

3.4.2 Theory

Dunnet (1969) developed an equation (Fig. 3.3b), based on Ramsay (1967, Fig. 3.3a), which relates the two measurable parameters R_f and ϕ to R_i and R_s. These equations can be used to construct the classic "onion skin" R_f/ϕ curves on a R_f/ϕ diagram, where each curve represents a sample of strain markers, of constant R_i and initially random in orientation, deformed to a fixed finite strain ratio. If a suite of randomly oriented and constant R_i particles are homogeneously deformed, except where the initial shape were circular, the deformed particles will lie on a hyperbolic curve around the finite strain value on a R_f/ϕ diagram. These curves can, therefore, be compared to measured R_f/ϕ data in natural and experimentally deformed rocks, in order to determine an estimate of the finite strain ratio. The estimation of finite strain ratio by this method, from field and experimental R_f/ϕ data, is subjective and difficult, especially where the

Figure 3.3a-c

a) R_f / ϕ equations developed by Ramsay (1967)

$$\tan 2\theta = \frac{2R_s^{1/2}(R_i - 1)\sin 2\theta}{(R_i+1)(R_s-1) + (R_i-1)(R_s+1)\cos 2\theta}$$

$$R_f = \frac{\tan^2\phi(1+R_i\tan^2\theta) - R_s(\tan^2\theta + R_i)}{R_s\tan^2\phi(\tan^2\theta + R_i) - (1+R_i\tan^2\theta)}$$

b) "Onion skin" equation developed by Dunnet (1969)

$$\cos 2\phi = \frac{\cosh 2\epsilon_f \cosh 2\epsilon_s - \cosh 2\epsilon_i}{\sinh 2\epsilon_f \sinh 2\epsilon_s}$$

c) Linearization equation developed by Yu and Zheng (1984)

$$\cosh 2\epsilon_f = \tanh 2\epsilon_s \sinh 2\epsilon_f \cos 2\phi + \frac{\cosh 2\epsilon_i}{\cosh 2\epsilon_s}$$

$$y = mx + b$$

initial shape ratio was not constant.

Yu and Zheng (1984) have shown that the relationship developed by Dunnet (1969) can be rewritten as the equation of a line (Fig. 3.3c). The equation shows a linear relationship between the values $x=\sinh(2e_f)\cos(2\phi)$ and $y=\cosh(2e_f)$, where e_f is the $\ln R_f$. The slope of the linear relationship ($\tanh(2e_s)$, where e_s is the $\ln R_s$) can be used to determine the finite strain ratio (R_s). The slope of the linear relationship is determined by the linear regression of the x and y data obtained from R_f/ϕ information. The graph, representing the x-y linear relationship, will be called a linearization diagram.

For a group of deformed strain markers (>50), using standard statistical methods, a confidence level can be calculated on either side of the slope (m) of the linear regression. In this study a confidence bracket was determined, in which there is a 68.26% likelihood that the actual strain ratio of the deformed sample falls in the range of $R_s+\sigma_c$ to $R_s+\sigma_c$ around the calculated strain estimate. The determined R_s from linear regression of the above x and y hyperbolic equations can be used to determine an estimate of the original average shape ratio by substitution into the equation of figure 3.3c.

a) <u>Simple case of the deformed constant R_i samples</u>

Figure 3.4a presents a R_f/ϕ diagram for the simple case of a sample of elliptical strain markers, with a R_i of 1.3 and initially random in orientation (uniform angular distribution), which have been deformed to a R_s of 1.5 by a computer simulation of homogeneous pure shear. From the R_f/ϕ diagram it is observed that the deformed strain markers delineate an "onion skin" hyperbolic curve. This curve is

Figure 3.4 a) R_f/ϕ diagram for a sample of 250 strain markers with R_i equal to 1.3 and initially random in orientation (uniform angular distribution). The markers have been deformed by a computer simulation of homogeneous pure shear to a R_s of 1.5. The R_f/ϕ diagram is representative of the X/Z principal plane. (Semilog Y-axis for R_f)

b) Corresponding linearization diagram for the above R_f/ϕ sample of 250 strain markers with R_i equal to 1.3 and initially random in orientation (uniform angular distribution). The markers have been deformed by a computer simulation of homogeneous pure shear to a R_s of 1.5. The linearization diagram is representative of the X/Z principal plane.

The figure also illustrates the corresponding location of data between the R_f/ϕ and linearization diagrams. The linear relationship of figure b is constructed by the linear transformation of the R_f/ϕ data from both the left ($\phi < 0^\circ$) and right ($\phi > 0^\circ$) halves of the R_i/ϕ diagram of figure a. The up slope transverse of the linear relationship corresponds to movement along both halves the R_f/ϕ "onion skin" curve from low to high R_f

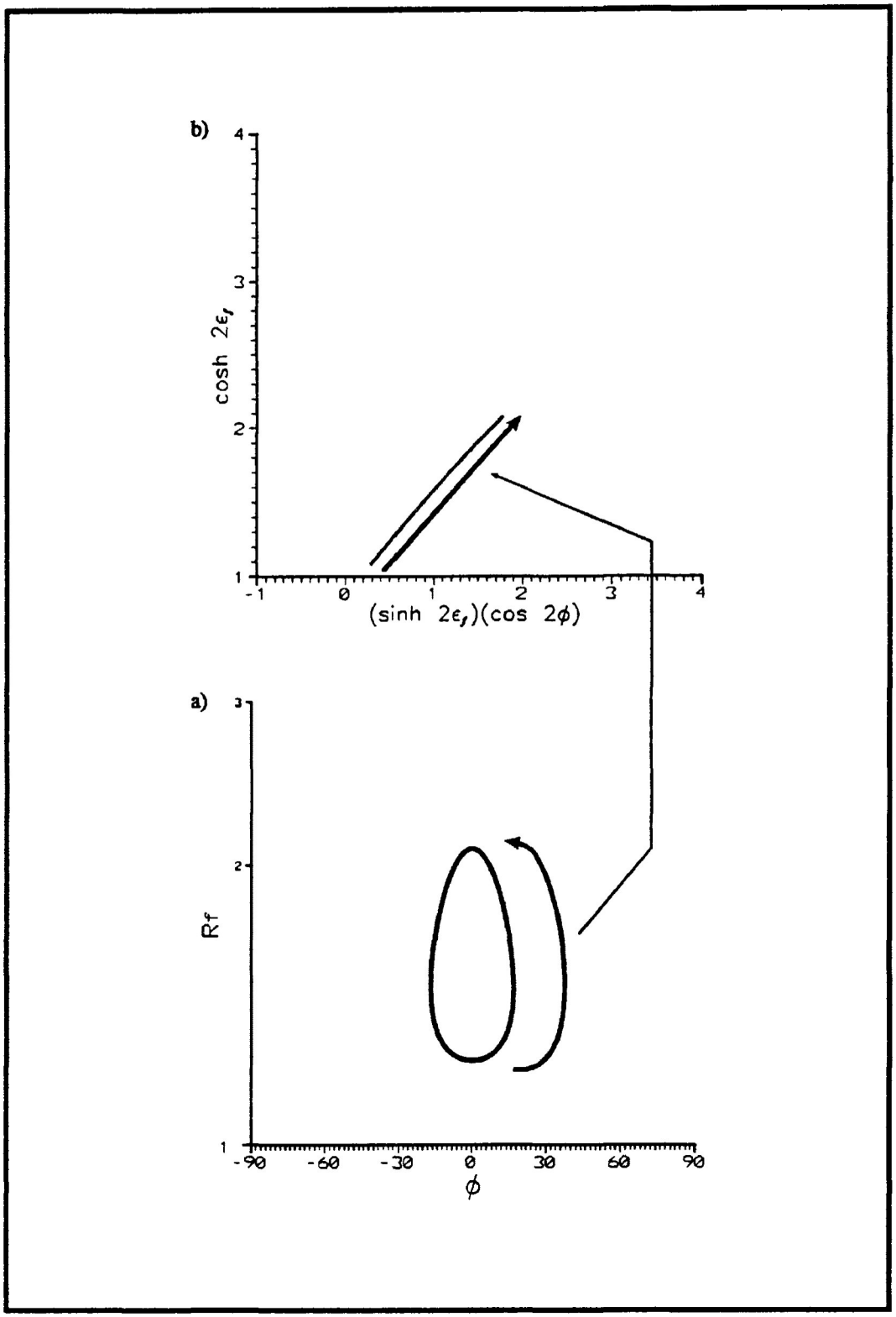
b)
4
3
2
1
cosh 2ε_f
-1
0
1
2
3
4
(sinh 2ε_f)(cos 2φ)
a)
3
2
1
Rf
-90
-60
-30
0
30
60
90
φ

centred on the finite strain ratio of 1.5. Transformation of the R_f/ϕ data, by the equation of figure 3.3c, yields the linear relationship presented in the linearization diagram of figure 3.4b. The slope of the linear regression gives an estimate for the finite strain ratio of 1.500 (±0.001).

Comparison of the plotted data of the R_f/ϕ diagram and linearization diagram exhibits a relationship, in which corresponding R_f data with equal and opposite ϕ, are located in the same x-y coordinates of the linearization diagram. The linear transformation of the R_f/ϕ data is characterized by increasing R_f values in the up slope direction of the linear relationship. This means that the linear regression is constructed by both the left ($\phi < 0^\circ$) and right ($\phi > 0^\circ$) halves of the R_i/ϕ diagram, in which the up slope transverse of the linear relationship corresponds to the movement up the right and left portion R_f/ϕ "onion skin" curve from low to high R_f (Fig. 3.4a,b).

Figure 3.5a-j and 3.6a-j present a comparison between coincident R_f/ϕ (semilog R_f-axis) and linearization diagrams for the previous sample group for finite strain ratios of 1.1 to 2.0, increasing at 0.1 intervals. The linearization diagrams are characterized by increasing slope, increasing length and an increasing X-axis intercept as strain increases. The increasing slope and X-axis intercept is produced by the shape of the "onion skin" curves observed in the R_f/ϕ diagram, in response to increasing strain. The increasing length of the linear relationship is the result of an increasing range of R_f values (1.18 to 1.43 for R_s=1.1 to 1.54 to 2.60 for R_s=2.0) as the markers become more deformed.

Strain ratio estimates from linear regression range from 1.100 (±0.100) to 1.997 (±0.080) for a simulated strain of 1.1 to 2.0, respectively (Fig. 3.7). The strain estimate closely

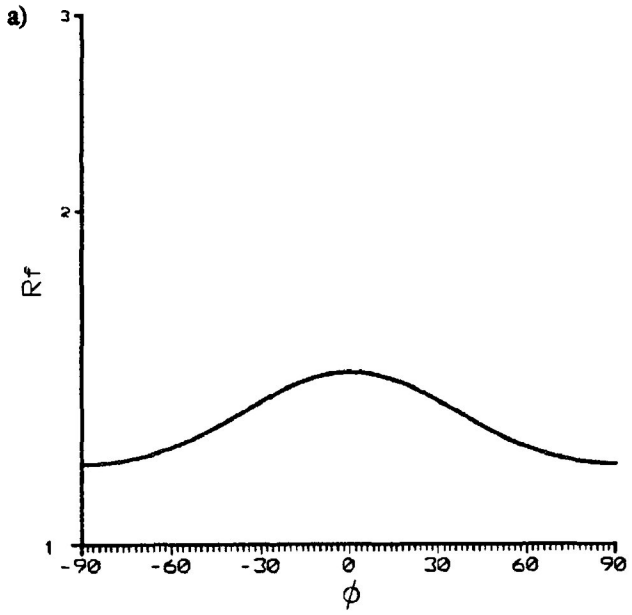

Rs = 1.1, n = 250

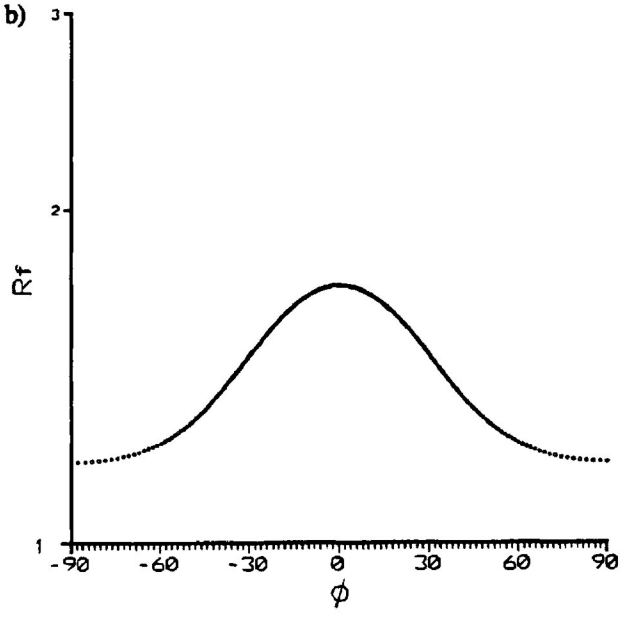

Rs = 1.2, n = 250

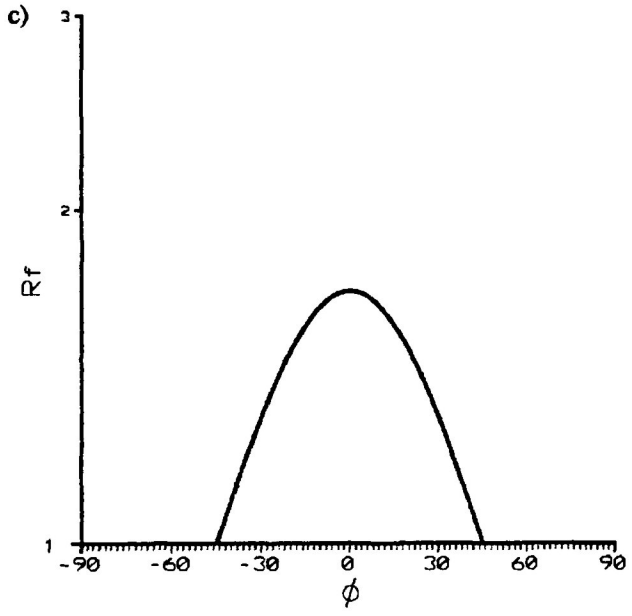

Rs = 1.3, n = 250

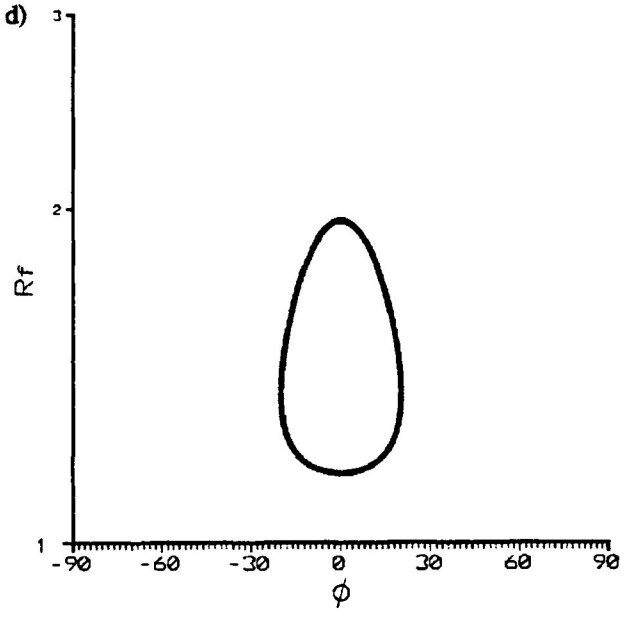

Rs = 1.4, n = 250

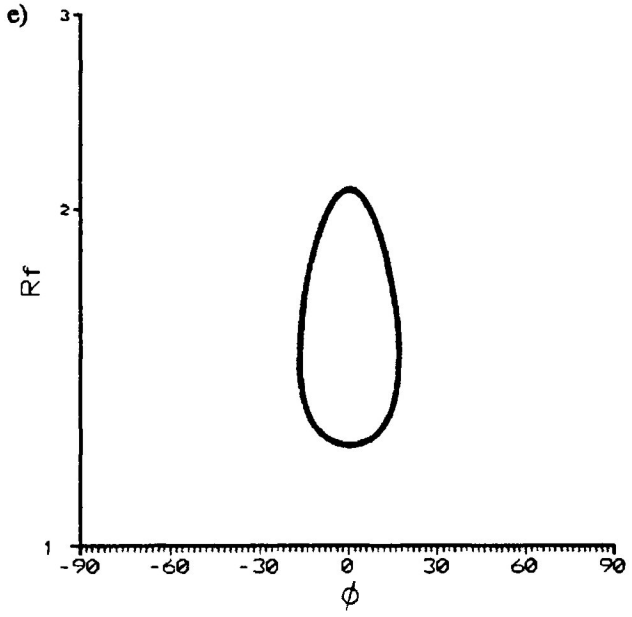

Rs = 1.5, n = 250

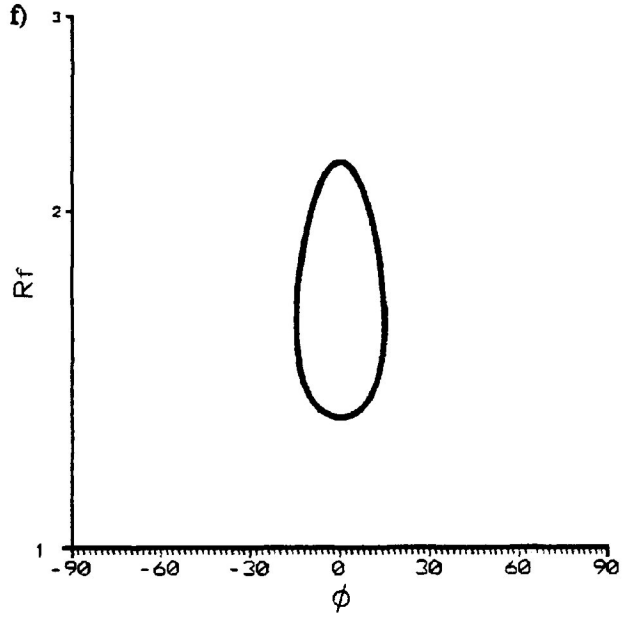

Rs = 1.6, n = 250

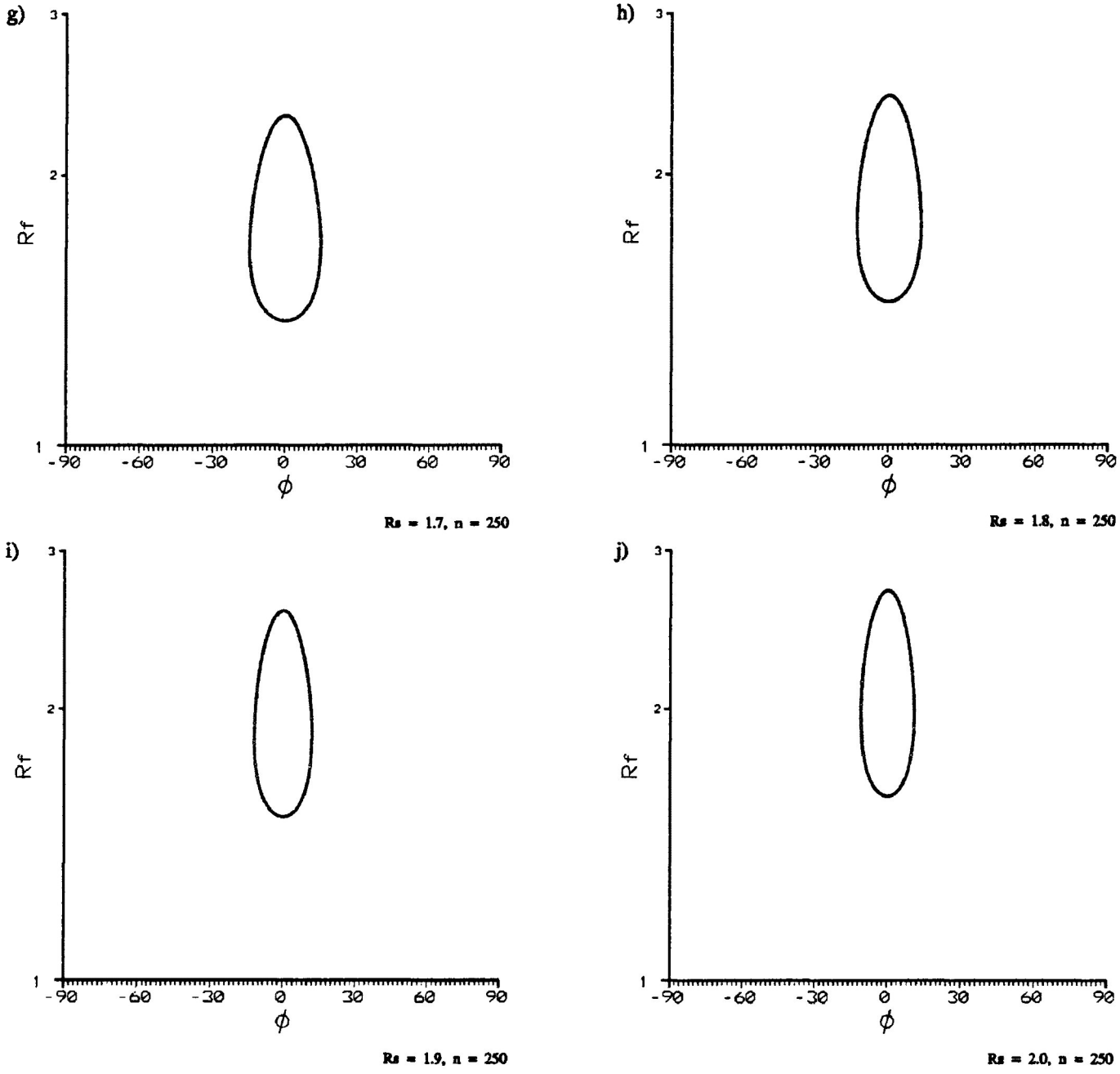

Figure 3.5a-j R_f/ϕ diagrams for the deformation of a sample of 250 strain markers with R_i equal to 1.3 and initially random in orientation (uniform angular distribution). The markers have been deformed by a computer simulation of homogeneous pure shear to a R_s of 1.1 to 2.0, increasing at 0.1 intervals. The R_f/ϕ diagrams are representative of the X/Z principal plane. (Semilog Y-axis for R_f)

a)

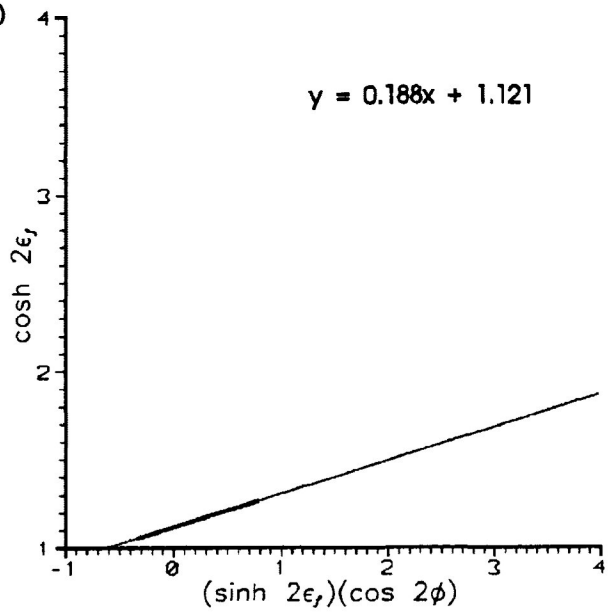

Rs = 1.1, n = 250

b)

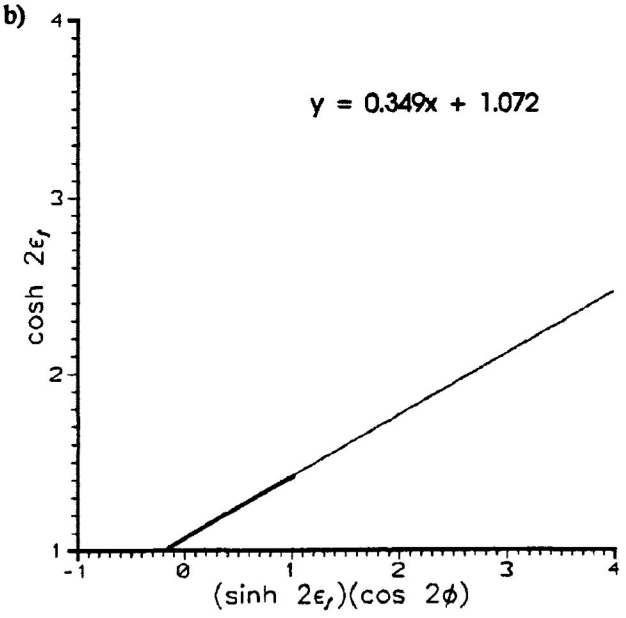

Rs = 1.2, n = 250

c)

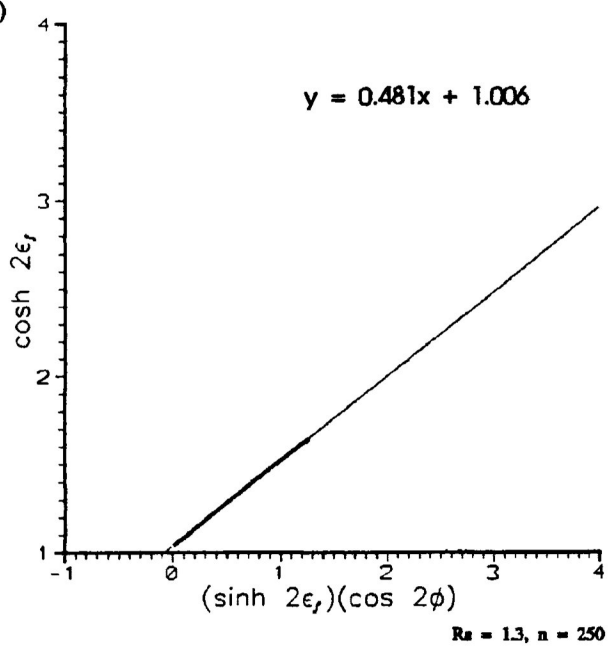

Rs = 1.3, n = 250

d)

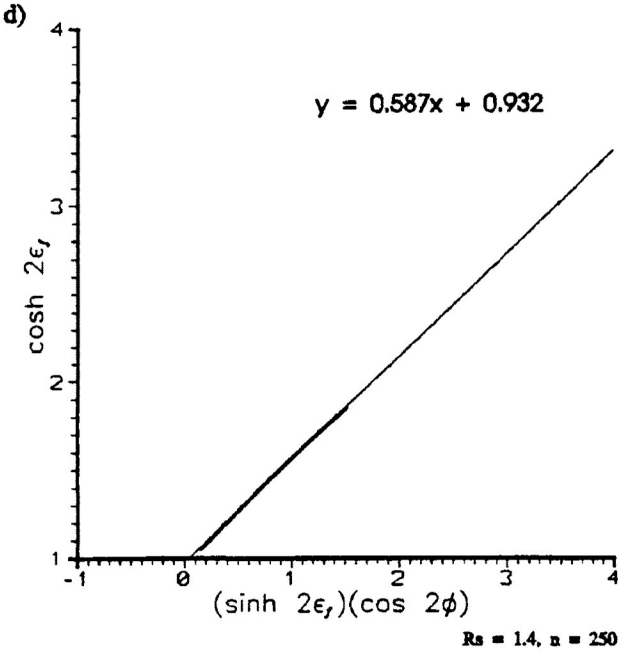

Rs = 1.4, n = 250

e)

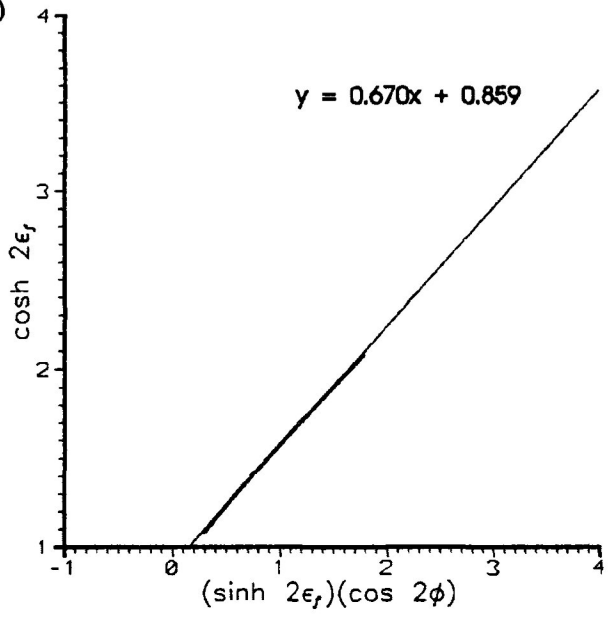

Rs = 1.5, n = 250

f)

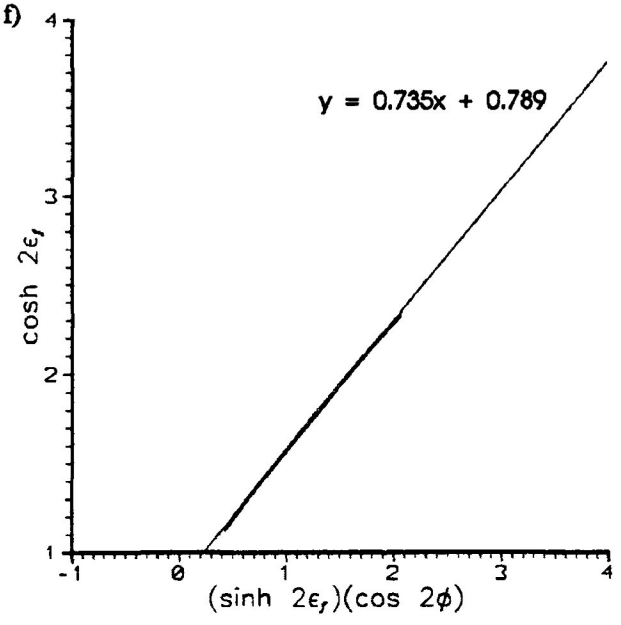

Rs = 1.6, n = 250

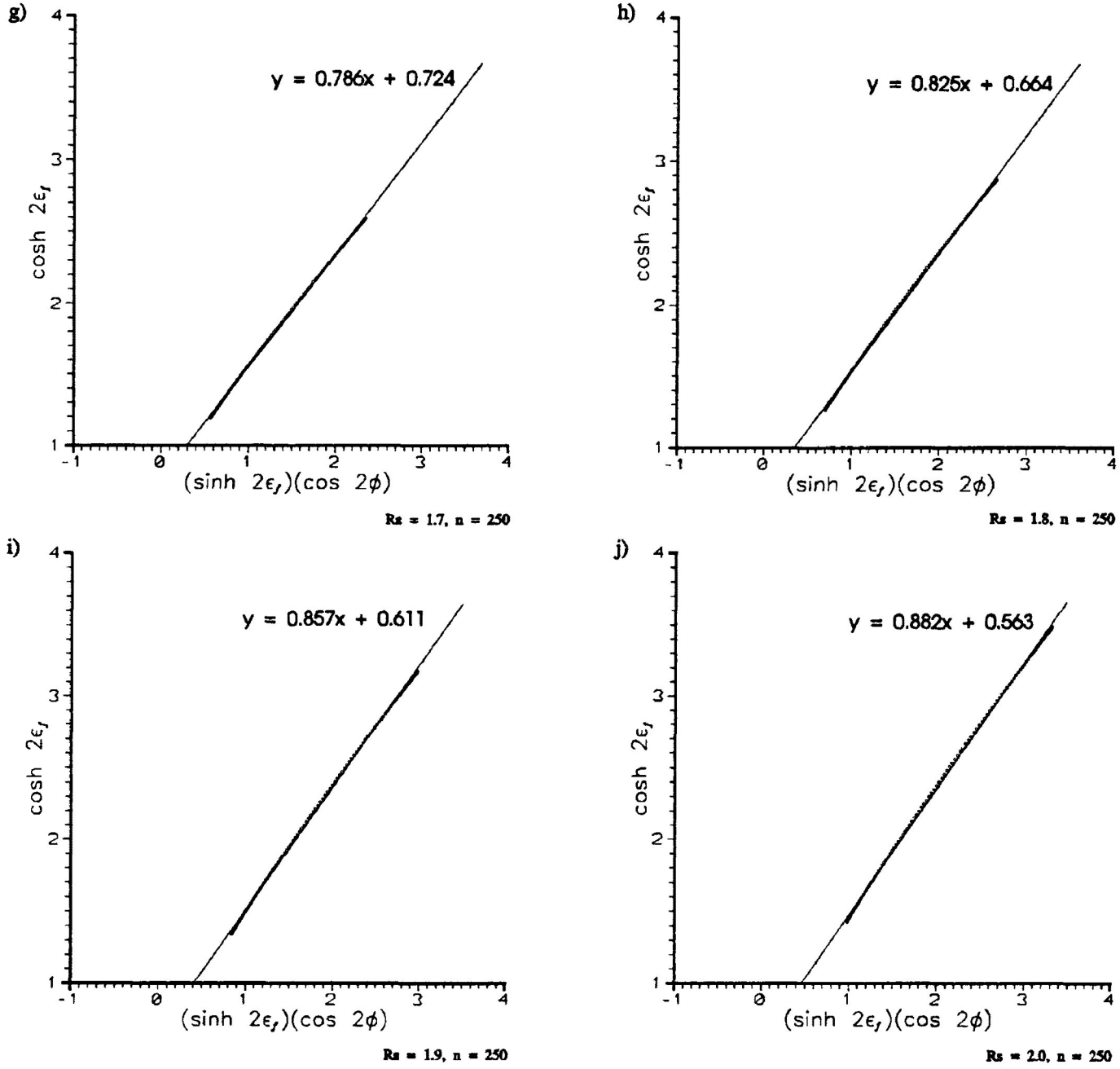

Figure 3.6a-j Linearization diagrams for the deformation of a sample of 250 strain markers with R_i equal to 1.3 and initially random in orientation (uniform angular distribution). The markers have been deformed by a computer simulation of homogeneous pure shear to a R_s of 1.1 to 2.0, increasing at 0.1 intervals. The linearization diagrams are representative of the X/Z principal plane. Linear equation needed for the determination of the finite strain estimate are given in each diagram.

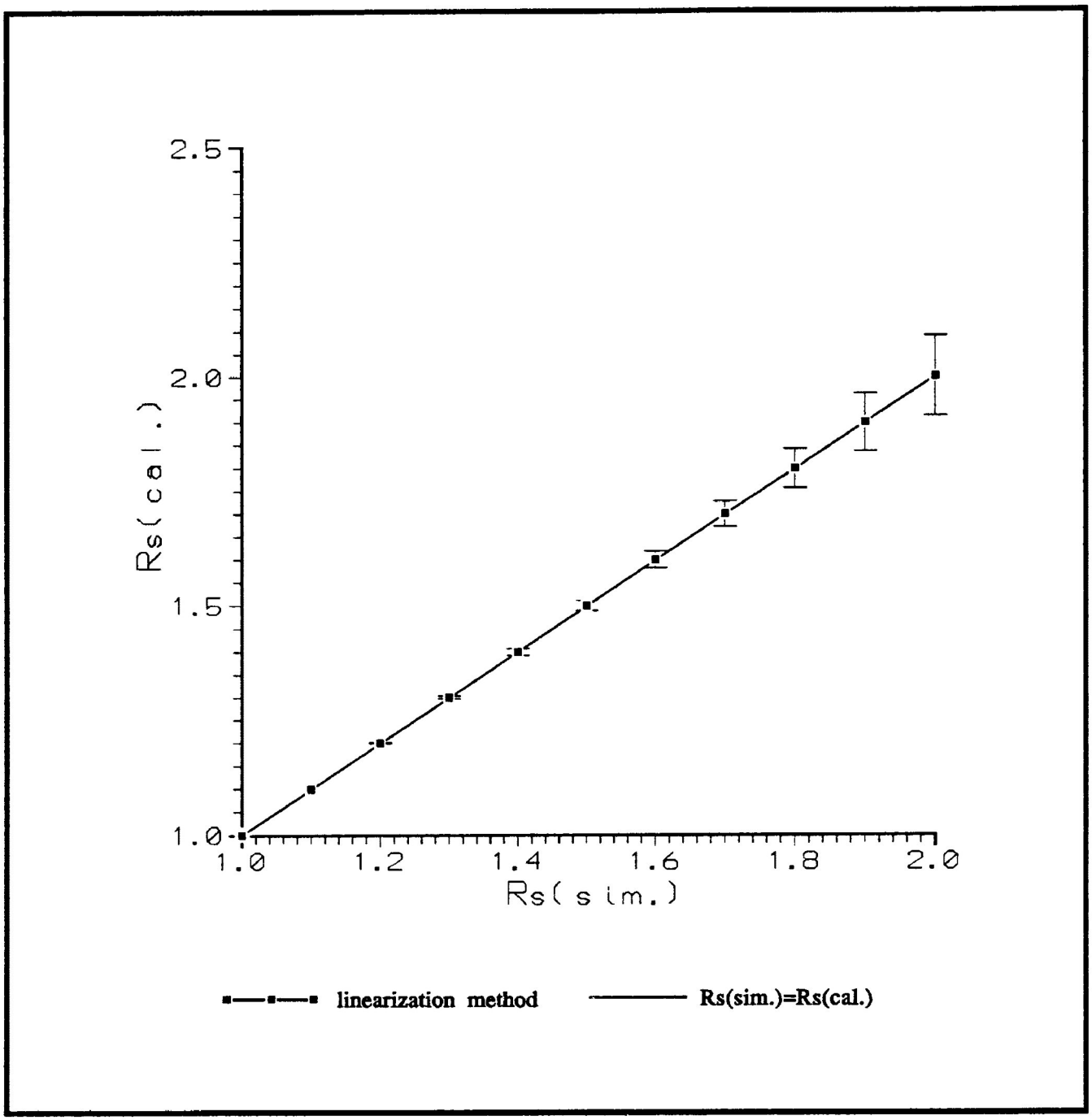

Figure 3.7 Comparison of the estimate of strain from the linearization method (R_s (cal.)) to the simulated strain (R_s (sim.)) for the data of figure 5.4a-j. A confidence bracket is given for each R_s with a 68.26% likelihood that the actual strain ratio falls in the range of Rs+σ_c to Rs+σ_c around the calculated strain ratio estimate.

approximates the actual simulated strain. However, the estimate becomes a slight underestimate as strain increases. Calculation of the estimate of R_i, from the deformed particles for each sample, is presented in figure 3.14. From the figure it is observed that the calculated R_i closely approximates the arithmetic mean of the actual R_i in the undeformed state for low strains, but becomes an overestimate as strain increases. Furthermore, the overestimate of R_i increases as strain increases.

b) Deformation of a series of constant R_i samples

Figure 3.8 and 3.9 presents the linearization diagram and the corresponding R_f/ϕ diagram for samples of particles, initially random in orientation (uniform angular distribution) and deformed to a simulated finite strain ratio of 1.5, for R_i equal to 1.1, 1.3, 1.5, 1.7 and 1.9. It is observed from the linearization diagram that the slopes of the linear regressions for each sample are approximately the same. The linear regression for each sample generates estimates of the strain ratio that range form 1.500 (±0.002 (R_i=1.1)) to 1.497 (±0.008 (R_i=1.9)).

The decrease in the estimate of the strain ratio is the result of a noticeably increasing curvature of the linear data, suggesting that higher R_i values are slightly less precise for strain analysis with the linearization method. This curvature is also observed with increasing R_f at high strain, for example a constant R_i sample such as in figure 3.6a-j. This curving effect, may be the result of the sensitivity of hyperbolic equations to slight variations in data, mainly in the range of R_f. This variation may be the result of computer inaccuracy. Also observed in figure 3.8 is an increase in the X-axis intercept as R_i increases.

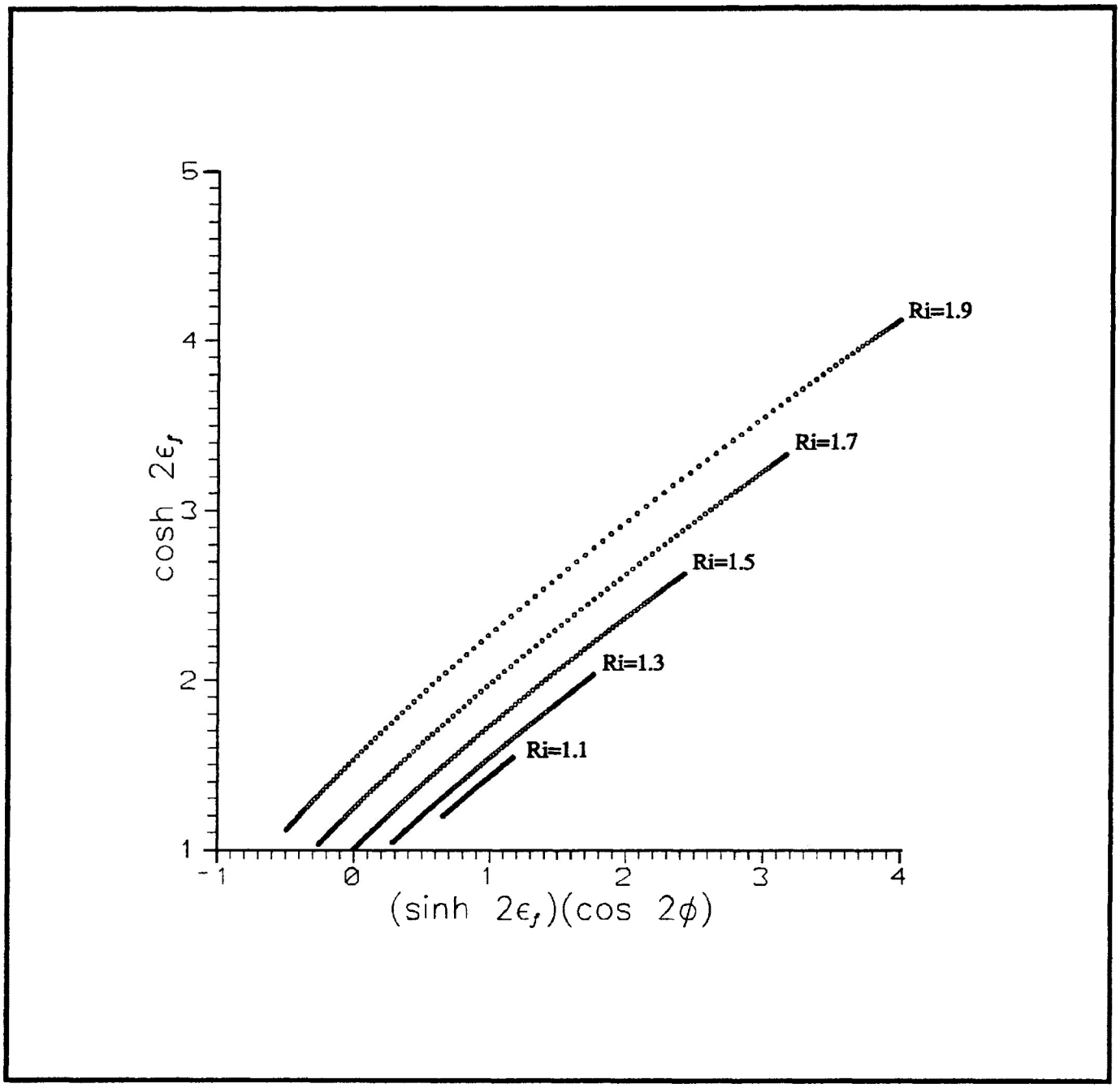

Figure 3.8 Linearization diagrams for the deformation of 5 samples of 250 strain markers with each sample having a constant R_i equal to 1.1 to 1.9 at 0.2 intervals. The strain markers were initially random in orientation with an uniform angular distribution. The markers have been deformed by a computer simulation of homogeneous pure shear to a R_s of 1.5. The linearization diagram is representative of the X/Z principal plane.

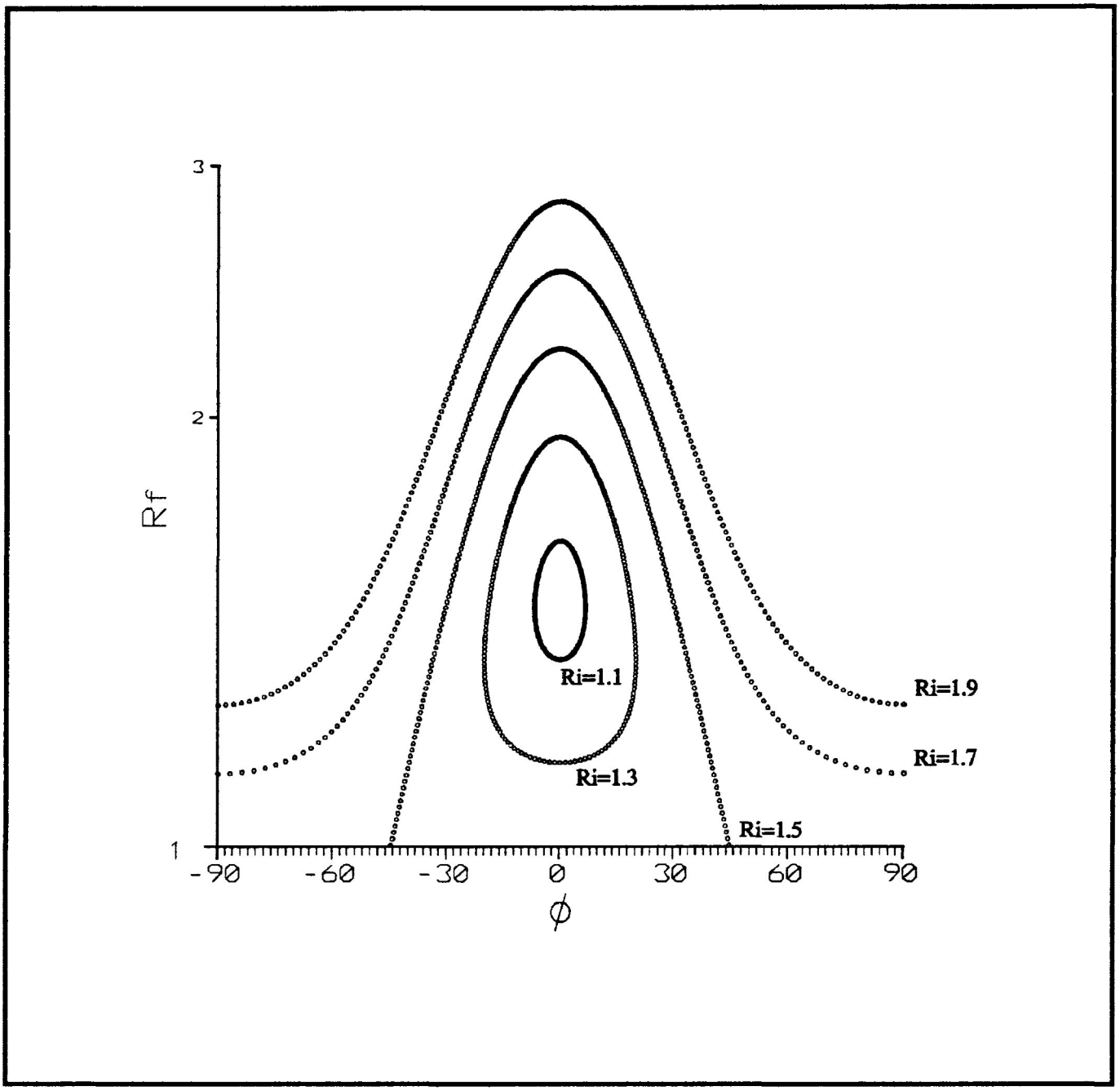

Figure 3.9 R_f/ϕ diagram for the deformation of 5 samples of 250 strain markers with each sample having a constant R_i equal to 1.1 to 1.9 at 0.2 intervals. The strain markers were initially random in orientation with an uniform angular distribution. The markers have been deformed by a computer simulation of homogeneous pure shear to a R_s of 1.5. The R_f/ϕ diagram is representative of the X/Z principal plane. (Semilog Y-axis for R_f)

Comparison of the R_f/ϕ distributions (Fig. 3.9) with that of the linearization diagram illustrates that the particles with values of R_i, that are greater than R_s (fluctuation (F (Ramsay, 1967)) >90° in the deformed state), will generate a linear relationship to the left of the line of data containing R_i equal to R_s (F=90°). Those values of R_i, that are less than R_s (F<90°), will generate a linear relationship to the right of the line of data containing R_i equal to R_s (F=90°).

The separation between the linear relationships of each constant R_i sample and the length of the linear relationship becomes less as R_i decreases. Moreover, for a continuous range of R_i data from 1.1 to 1.9 a progression of linearization data would be observed, representing increasing initial R_i values, as one moves from left to right on the linearization diagram of figure 3.8. This situation would produce a "lensoidal" shape distribution derived from x and y values on the linearization diagram. Also developed, at least in the case where some R_i data was less than the R_s, is a parabolic like distribution in the lower portion of the linearization diagram.

Also noted, is the increase in the lowest y value ($y=\cosh(2e_f)$) of the linearization data, for samples with R_i values greater than and less than R_i equal to R_s. If the value of y is equal to 1 the initial R_i was equal to R_s. The lowest y values of each sample represents deformed particles having the minimum and maximum ϕ values in the case where R_i is greater than or equal to R_s, and the lowest R_f values in the case where R_i is less than R_s. The parabolic like distribution discussed in the previous paragraph in the result of these values.

The previous comparisons are important in understanding the distribution of data in linearization diagrams for

deformed samples of particles, that contained random and lognormal R_i distributions. This will be discussed in the following sections, which involved more complex situations.

c) **Complex case of deformed random R_i samples.**

Figure 3.10e presents a R_f/ϕ diagram (semilog R_f-axis) for a sample of strain markers, with a range of R_i between 1 and 1.3 (mean= 1.152), which were initially random in orientation and have been deformed to a R_s of 1.500 by a computer simulation of homogeneous pure shear. From the figure it is observed that the deformed strain markers delineate a continuous range of partially formed "onion skin" hyperbolic curves. The outer most partially formed curve is represented by deformed particles with R_i approximately equal to 1.3. The partially formed "onion skin" curves are centred on the finite strain ratio of 1.500, marked by the location of those particles with a R_i approximately equal to 1.

Transformation of the R_f/ϕ data, by the equations of figure 3.3c, are used to yield a linear relationship as presented in the linearization diagram of figure 3.11e. The best fit slope of the linear regression through the data of figure 3.11e gives an estimate for the finite strain ratio of 1.514 (±0.051). The linear relationship of the R_f/ϕ data is again characterized by increasing R_f values in the up slope direction of the linear regression. However, the distribution of $x=\sinh(2e_f)\cos(2\phi)$ and $y=\cosh(2e_f)$ data on the linearization diagram is lens shaped in appearance and not in contact with the X-axis.

Figure 3.10a-j and 3.11a-j presents a comparison between coincident R_f/ϕ diagrams (semilog R_f-axis) and linearization diagrams, for the previous sample group for finite strains ratios of 1.1 to 2.0 increasing at 0.1 intervals. The

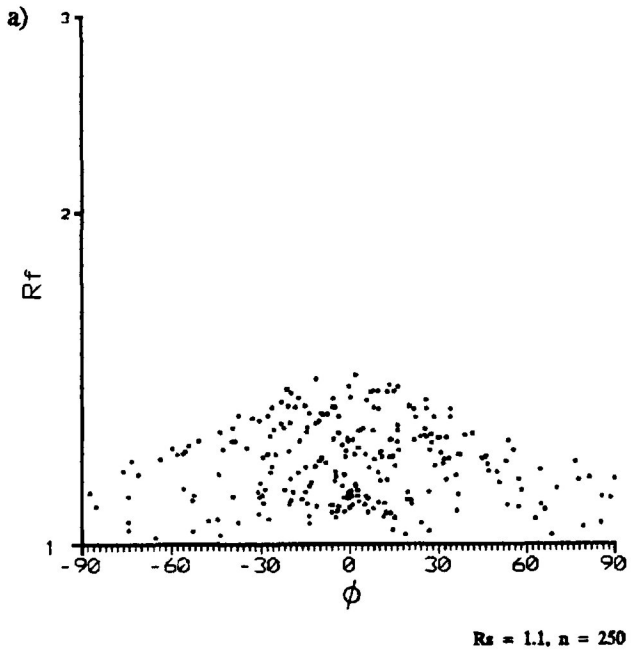

Rs = 1.1, n = 250

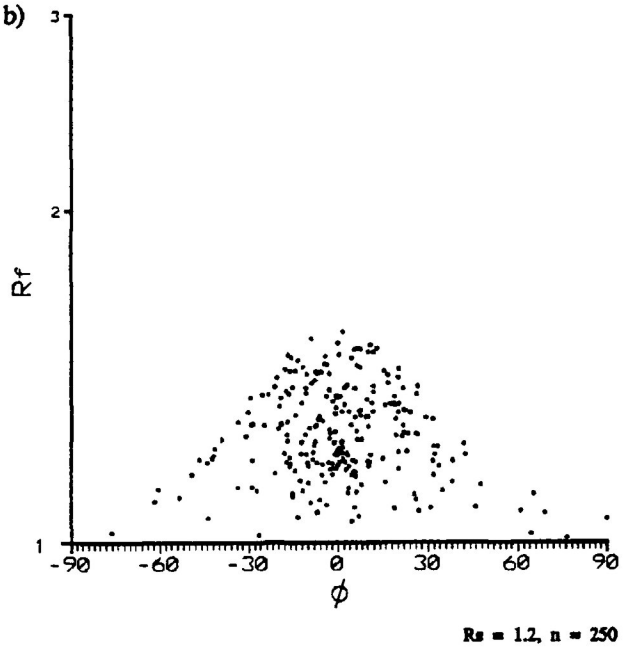

Rs = 1.2, n = 250

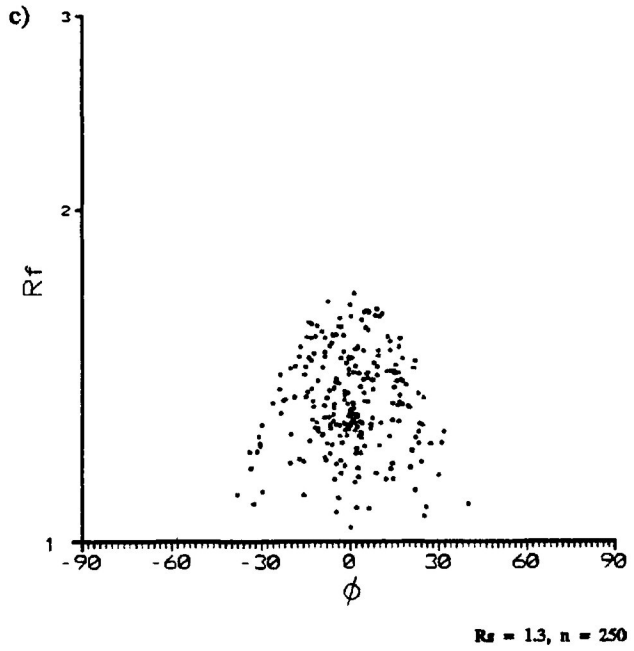

Rs = 1.3, n = 250

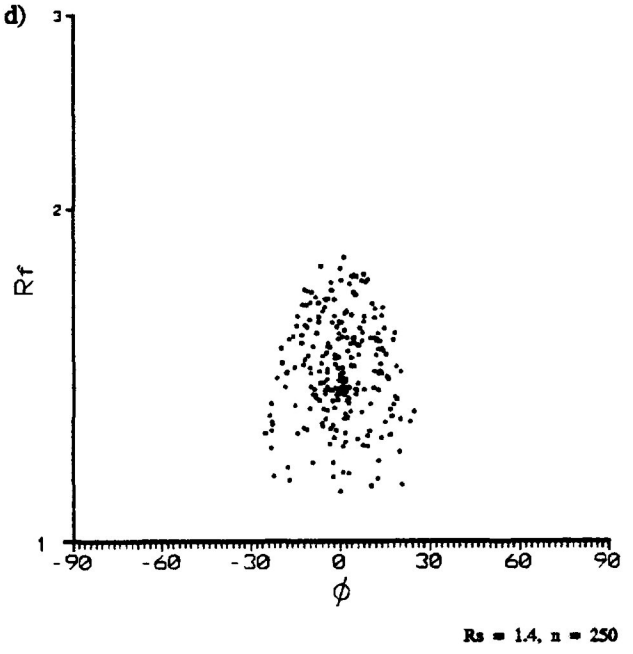

Rs = 1.4, n = 250

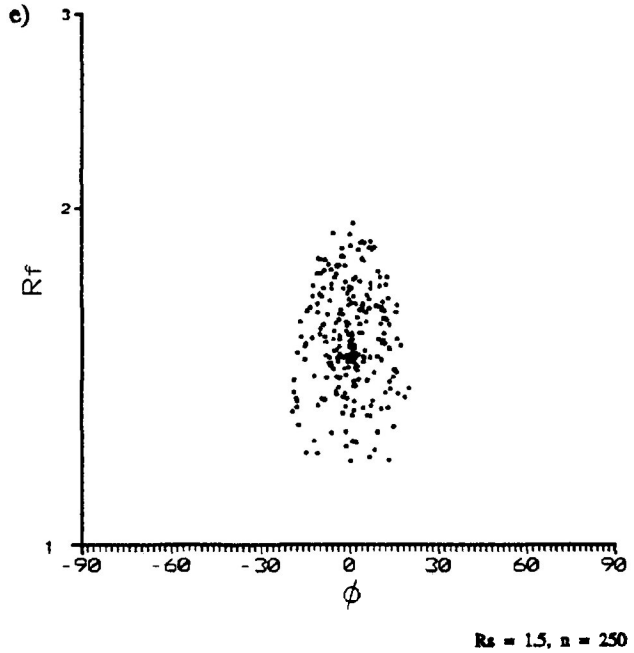

Rs = 1.5, n = 250

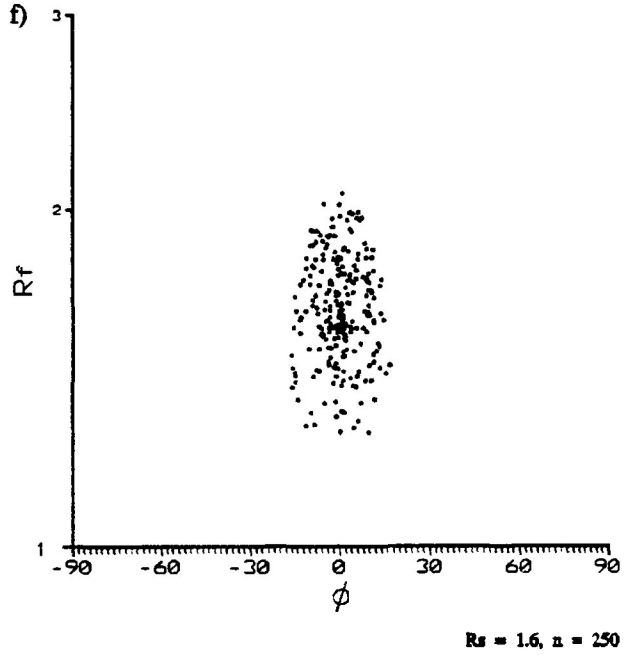

Rs = 1.6, n = 250

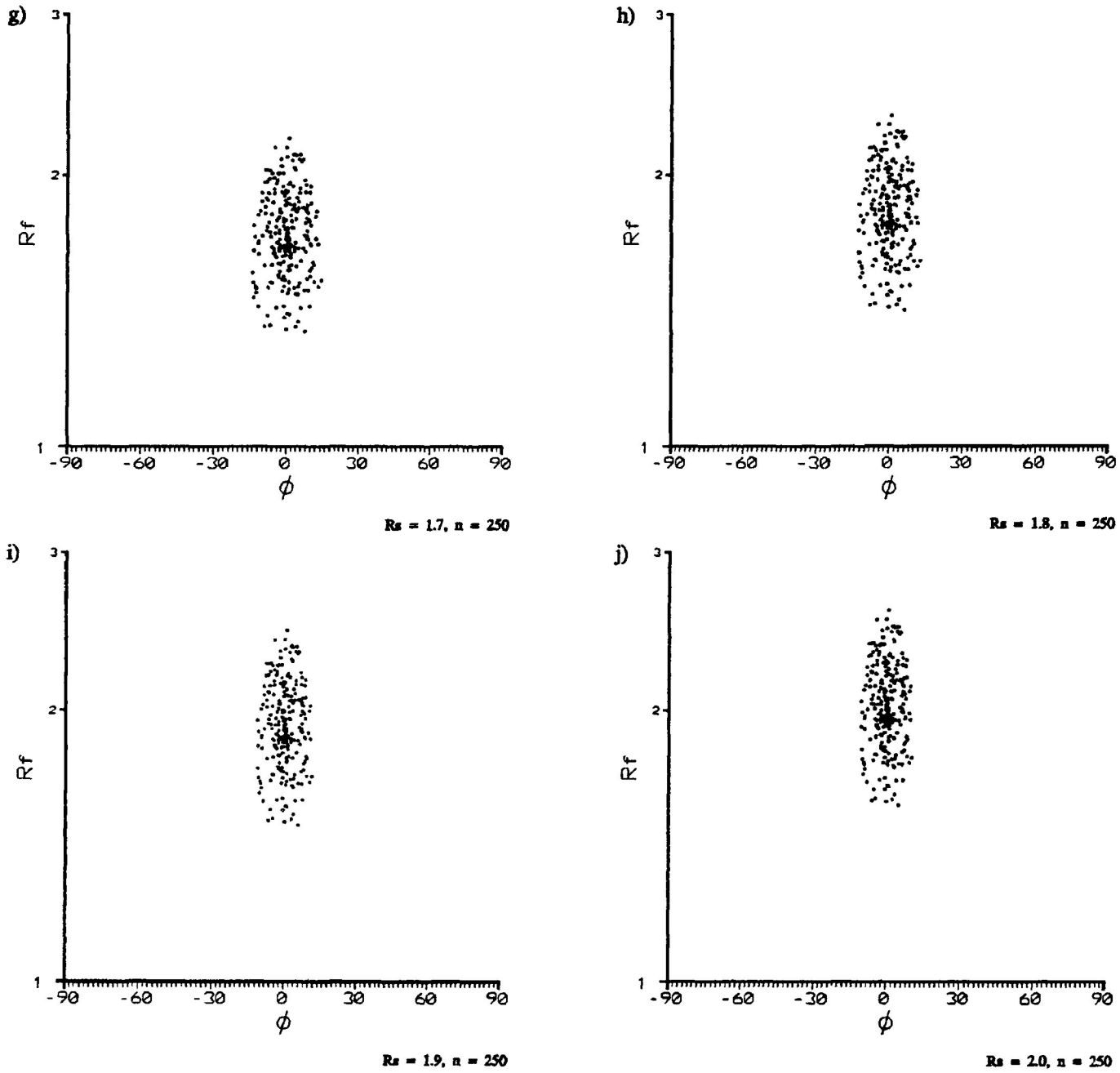

Figure 3.10a-j R_f/ϕ diagrams for the deformation of a sample of 250 strain markers with a range of R_i equal to 1.0 to 1.3 and initially random in orientation (uniform angular distribution). The markers have been deformed by a computer simulation of homogeneous pure shear to a R_s of 1.1 to 2.0, increasing at 0.1 intervals. The R_f/ϕ diagrams are representative of the X/Z principal plane. (Semilog Y-axis for R_f).

a)

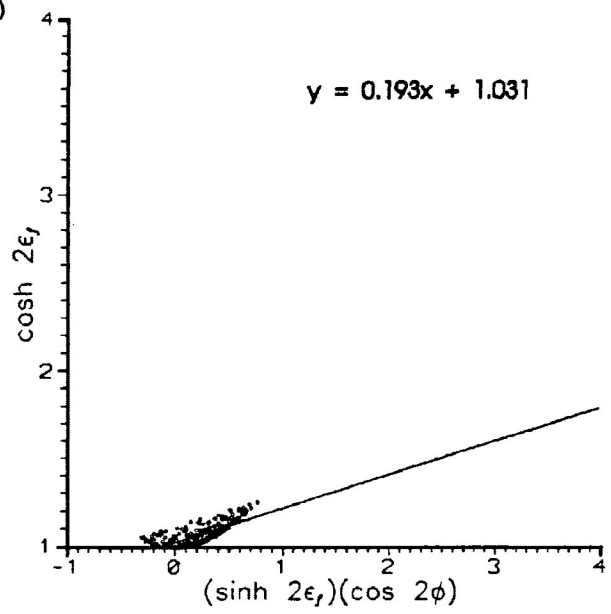

Rs = 1.1, n = 250

b)

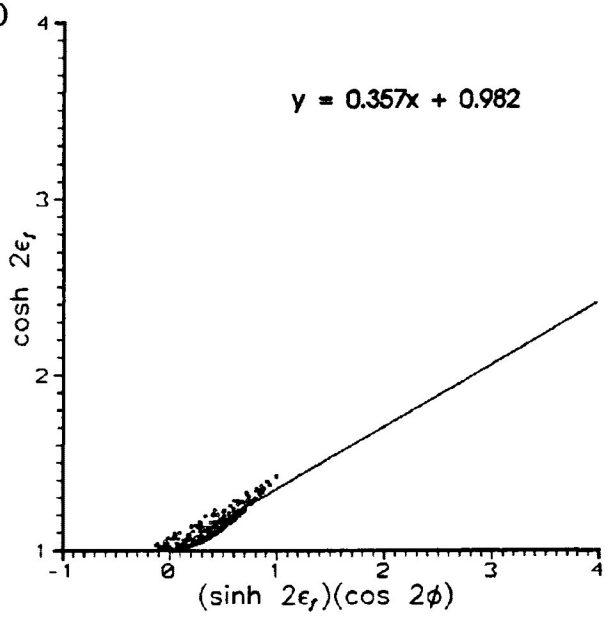

Rs = 1.2, n = 250

c)

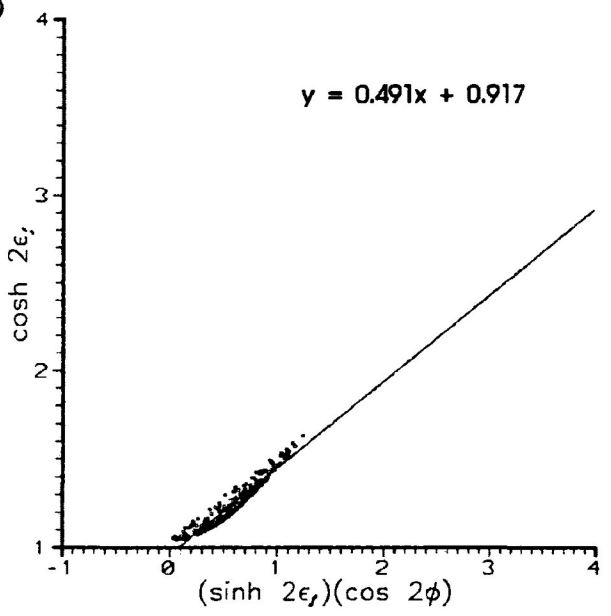

Rs = 1.3, n = 250

d)

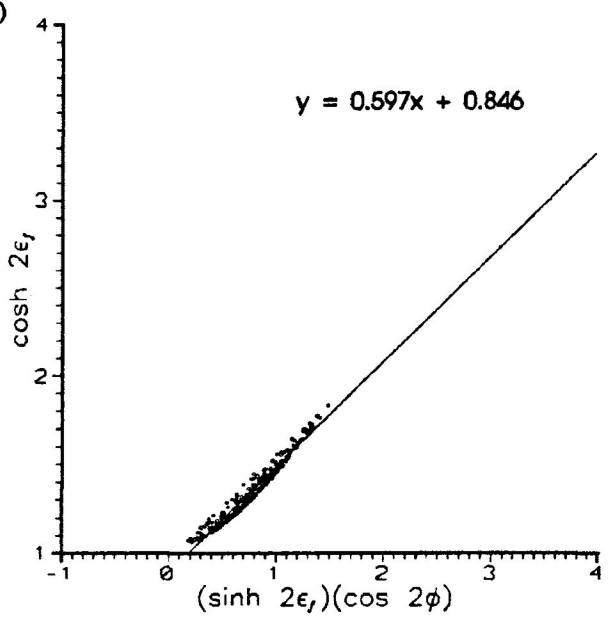

Rs = 1.4, n = 250

e)

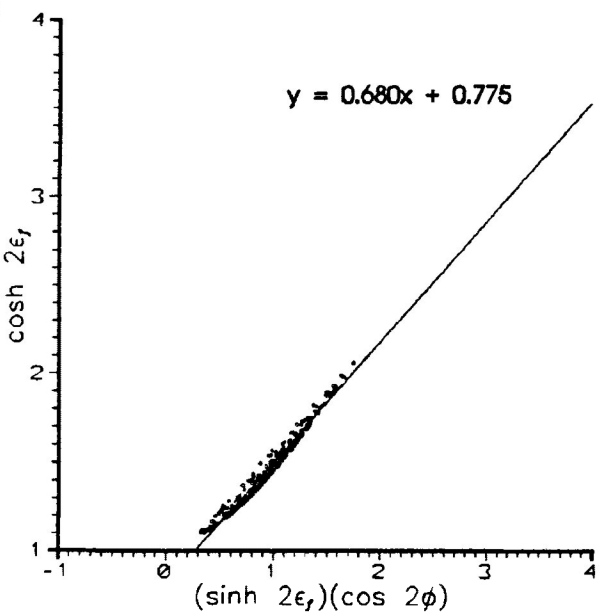

Rs = 1.5, n = 250

f)

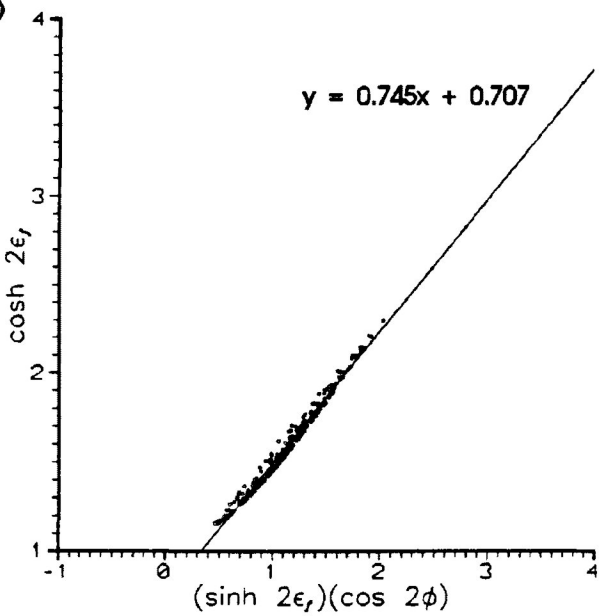

Rs = 1.6, n = 250

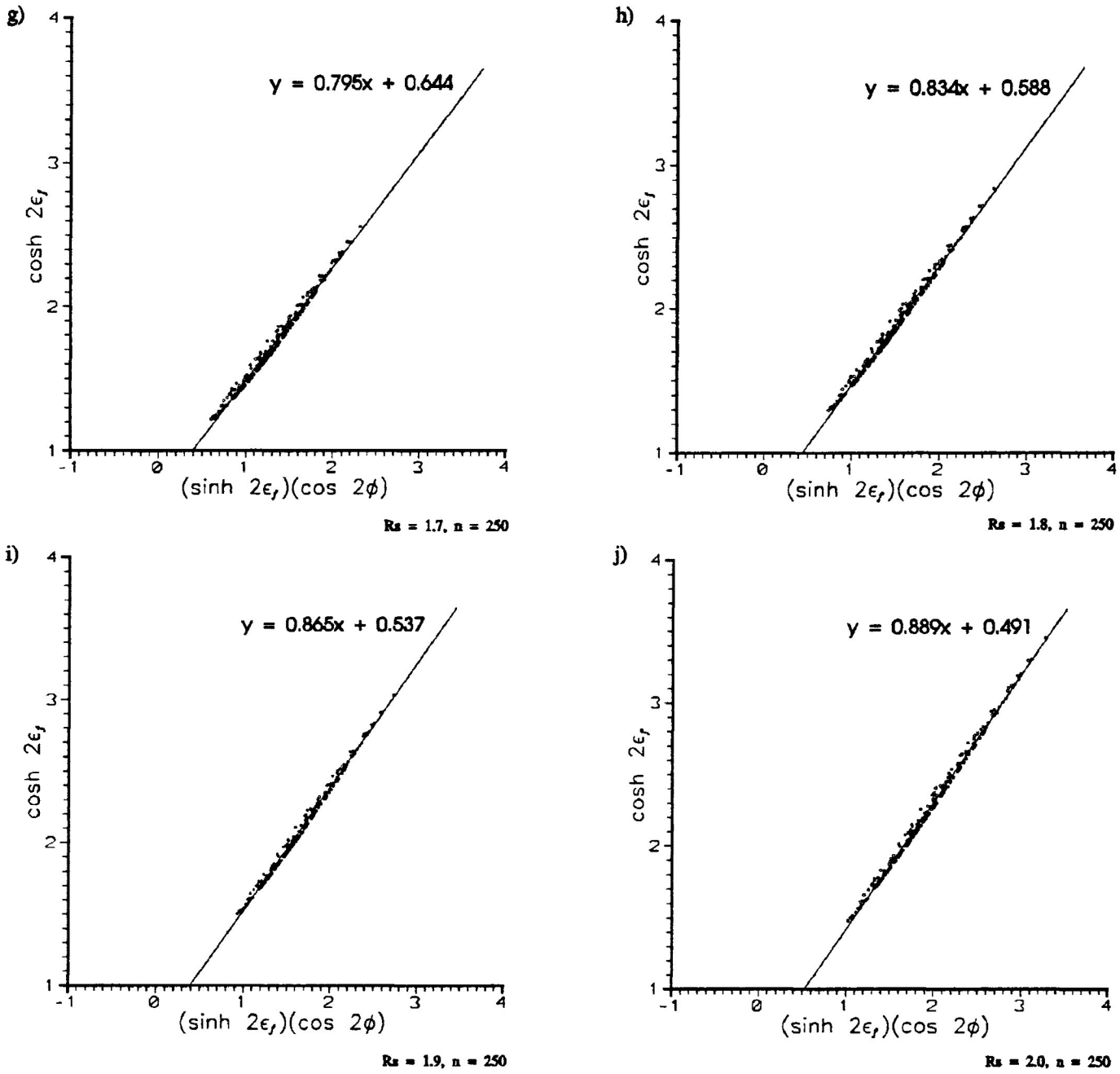

Figure 3.11a-j Linearization diagrams for the deformation of a sample of 250 strain markers with a range of R_i equal to 1.0 to 1.3 and initially random in orientation (uniform angular distribution). The markers have been deformed by a computer simulation of homogeneous pure shear to a R_s of 1.1 to 2.0, increasing at 0.1 intervals. The linearization diagrams are representative of the X/Z principal plane. Linear equation needed for the determination of the finite strain ratio estimate are given in each diagram.

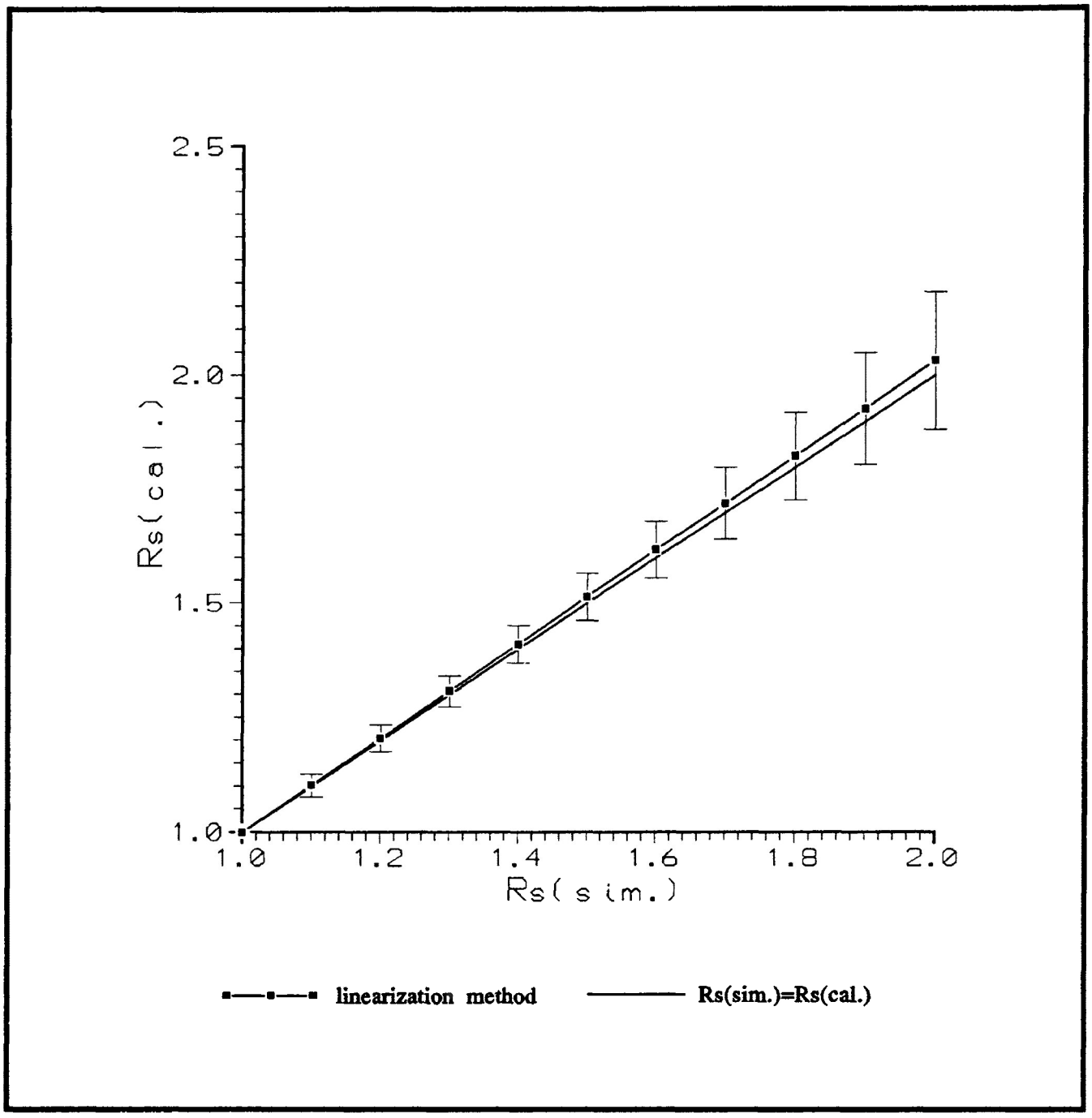

Figure 3.12 Comparison of the estimate of strain from the linearization method (R_s (cal.)) to the simulated strain (R_s (sim.)) for the data of figure 5.10a-j. A confidence bracket is given for each R_s with a 68.26% likelihood that the actual strain ratio falls in the range of $Rs+\sigma_c$ to $Rs+\sigma_c$ around the calculated strain ratio estimate.

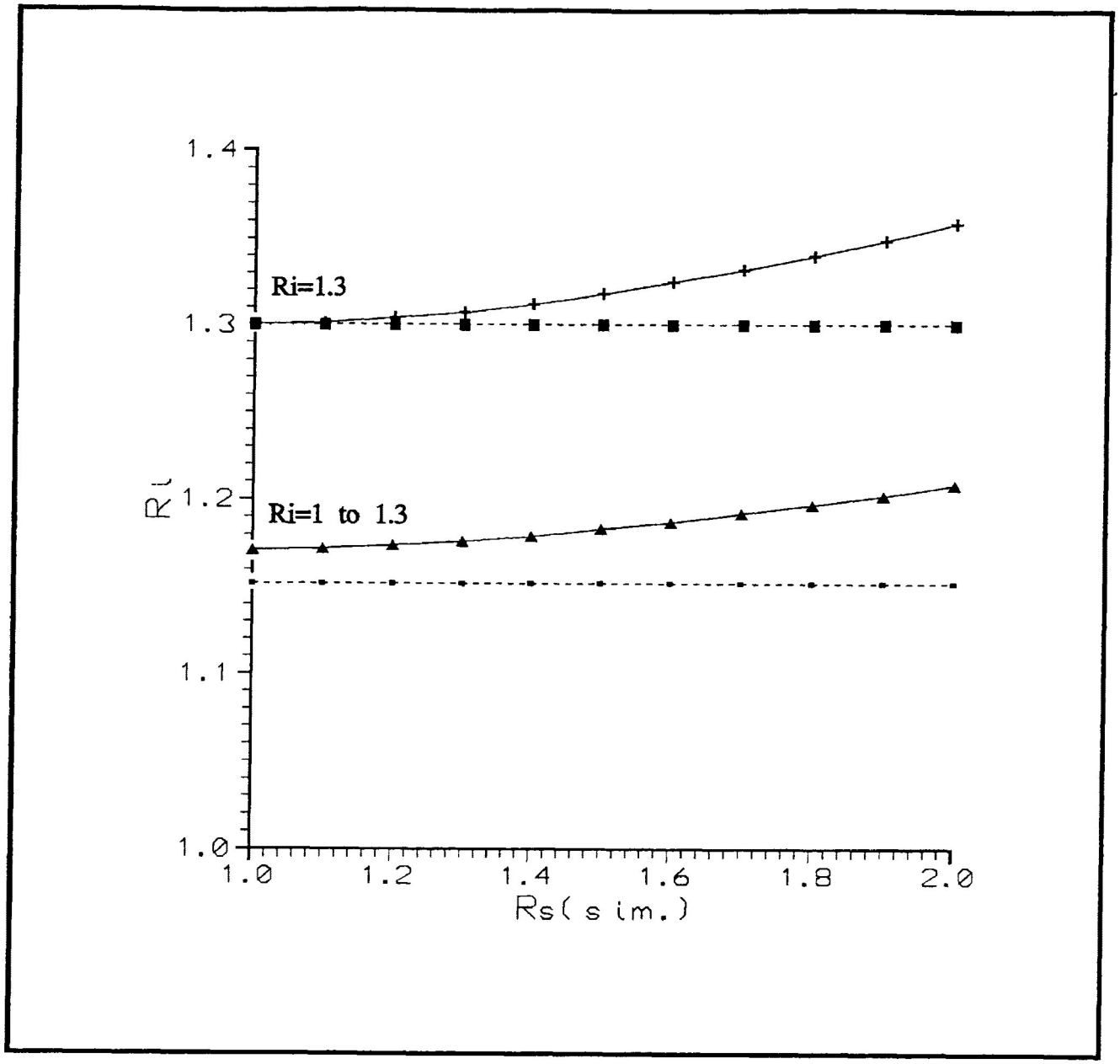

Figure 3.13 The estimates of the average R_i determined by the calculated strain ratio from linear regressions of Figure 5.10a-j as the simulated strain increases. Lines (a) Crosses represent R_i estimates for a sample of 250 strain markers with R_i equal to 1.3 and initially random in orientation (uniform angular distribution). The markers have been deformed by a computer simulation of homogeneous pure shear to a R_s of 1.1 to 2.0 at 0.1 intervals. Squares represent the actual mean of the R_i distribution in the undeformed state. Lines (b) Triangles represent R_i estimates for a sample of 250 strain markers with a range of R_i equal to 1.0 to 1.3 and initially random in orientation (uniform angular distribution). The markers have been deformed by a computer simulation of homogeneous pure shear to a R_s of 1.1 to 2.0, increasing at 0.1 intervals. Small solid squares represent the actual mean of the R_i distribution in the undeformed state.

linearization diagrams are characterized by increasing best fit slope, increasing length, thinning of the "lensoidal" shape distribution and an increasing X-axis intercept with increasing strain. Note the contact of the "lensoidal" linearization distribution with the X-axis, for strains less than 1.300. This represents the values of R_i that are equal to R_s and have maximum and minimum ϕ values. This contact with the X-axis moves along the lower parameter of the linearization distribution as strain increases from 1.1 to 1.3, until it separates from the X-axis at strains greater than 1.3 (i.e., all R_i are less than R_s).

Strain estimates from the best fit linear regression range from 1.103 (±0.025) to 2.031 (±0.149) for a simulated strain of 1.1 to 2.0, respectively (Fig. 3.12). The estimate of strain becomes an increasing overestimate as simulated strain increases. The calculation of the estimate of R_i from the deformed particles for each sample is presented in figure 3.13. From the figure, it is observed that the calculated R_i overestimates the arithmetic mean of the simulated R_i for all strain ratios. The overestimate of R_i increases as strain increases.

d) <u>Deformation of a lognormal R_i distribution</u>

At higher strains a much larger difference in the estimate of R_s, by the linearization method, is observed in the sample that contained a range of R_i values compared with that of the sample with a constant R_i (section 3.4.2a). This suggests that R_i distributions will produce an estimate of R_s (cal.) that will deviate from the simulated R_s producing the deformation. In other words, the shape of the "lensoidal" distribution of linearization data (a result of the range of R_i and the R_s), may cause a deviation from the actual strain ratio estimate by linear regression. Many rocks in nature have distributions

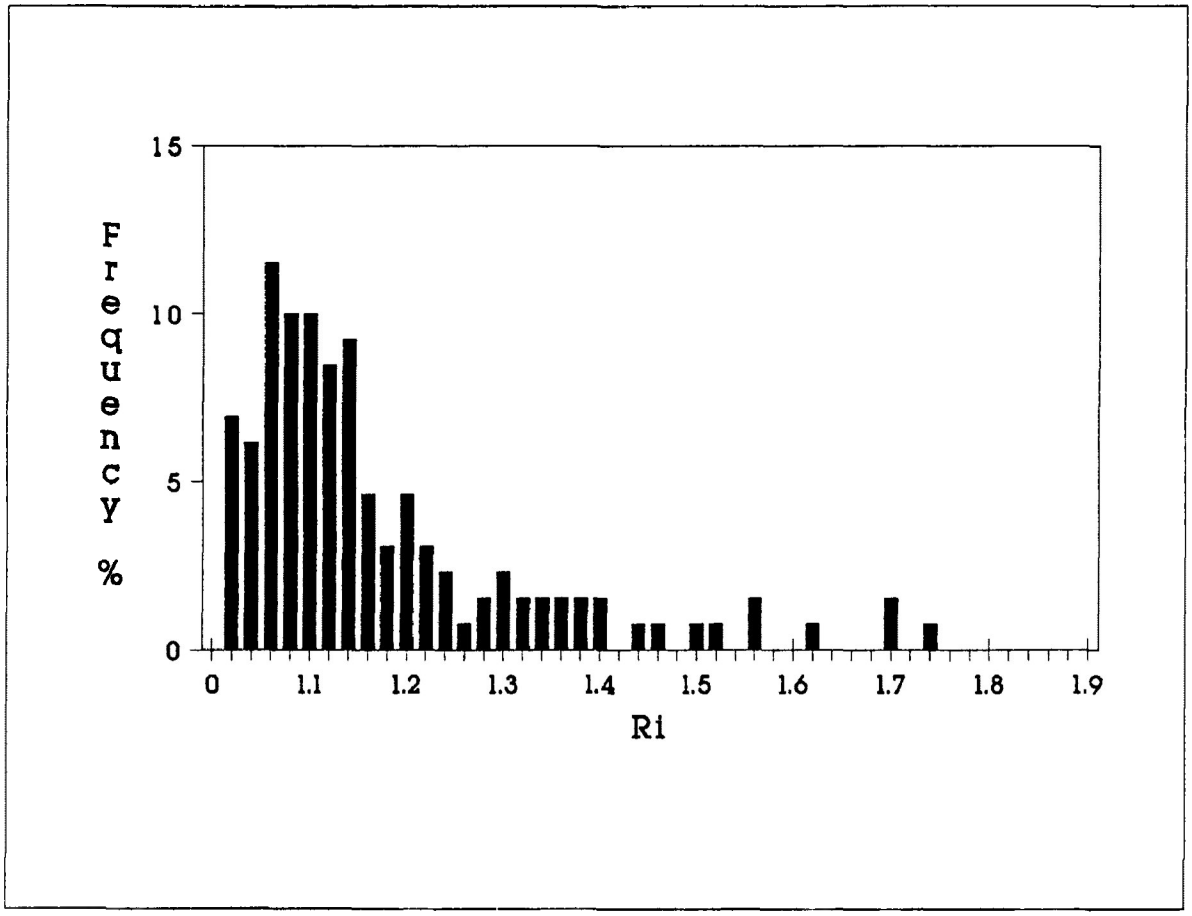

Figure 3.14 Simulated lognormal distribution of R_i for a 130 strain markers of random uniform orientation with a range of R_i between 1.0 and 1.8. This sample is used in the simulated deformation presented in Figure 5.14 and 5.15.

Figure 3.15 a) R_f/ϕ diagram for a sample of 130 strain markers with a lognormal range of R_i between 1.0 to 1.8 and initially random in orientation (uniform angular distribution). The markers have been deformed by a computer simulation of homogeneous pure shear to a R_s of 1.5. The R_f/ϕ diagram is representative of the X/Z principal plane. (Semilog Y-axis for R_f)

b) Corresponding linearization diagram for the above R_f/ϕ sample of 130 strain markers with a lognormal range of R_i between 1.0 to 1.8 and initially random in orientation (uniform angular distribution). The markers have been deformed by a computer simulation of homogeneous pure shear to a R_s of 1.5. The linearization diagram is representative of the X/Z principal plane. Linear equation needed for the determination of the finite strain ratio estimate is given the diagram.

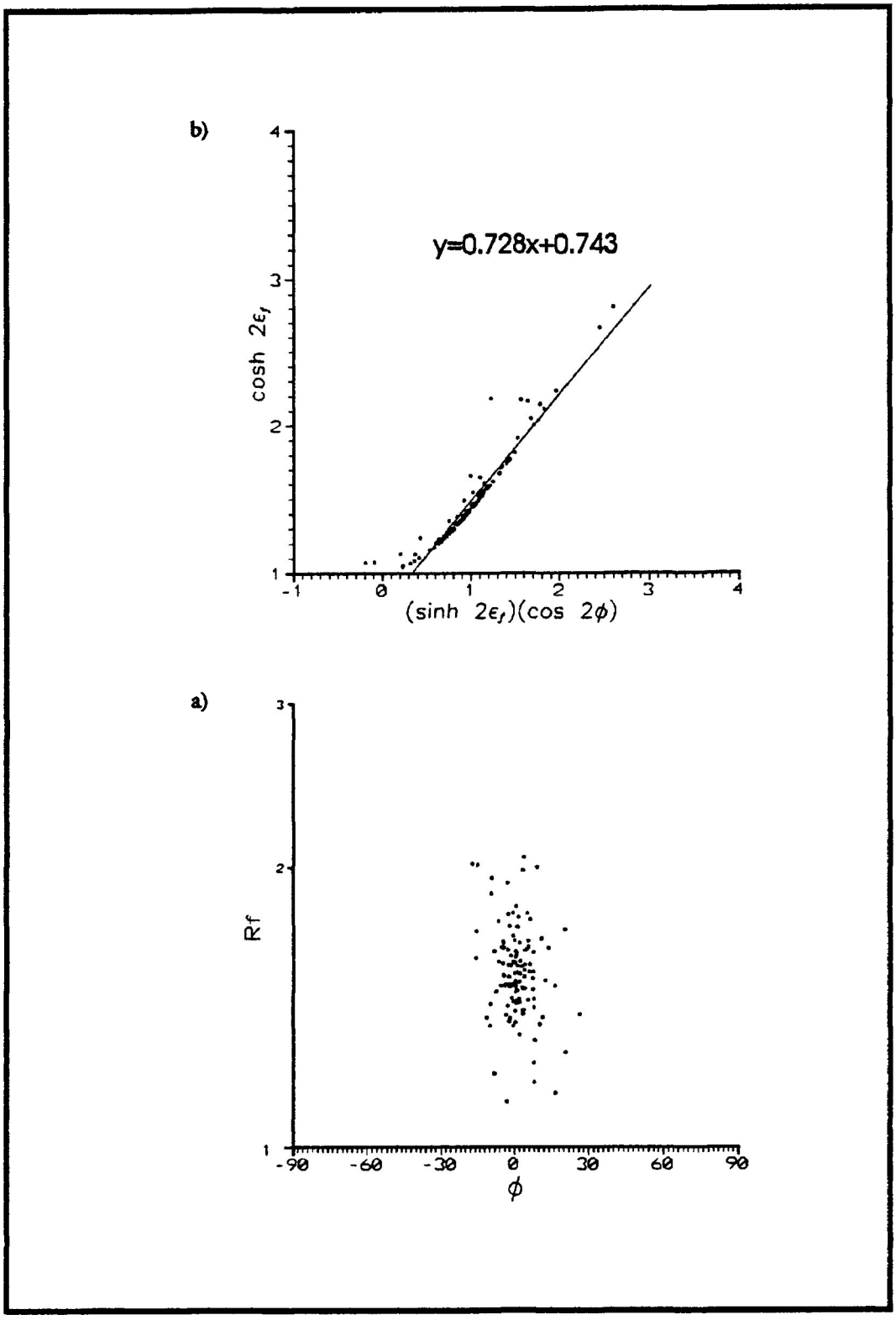
b)
y=0.728x+0.743
cosh 2ε_f
(sinh 2ε_f)(cos 2φ)
a)
Rf
φ

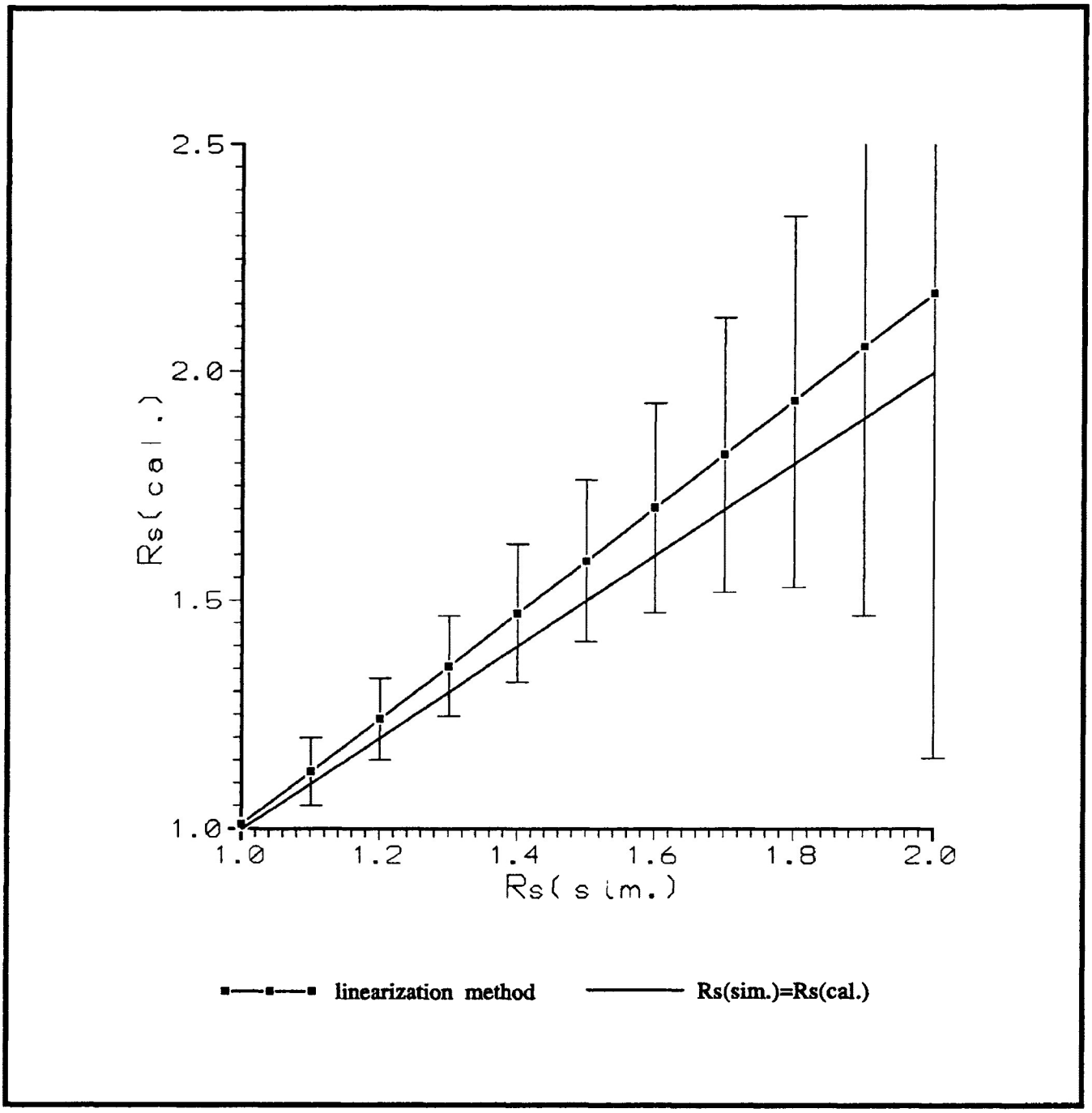

Figure 3.16 Comparison of the estimate of strain from the linearization method (R_s (cal.)) to the simulated strain (R_s (sim.)) for lognormal sample of figure 5.13. A confidence bracket is given for each R_s with a 68.26% likelihood that the actual strain ratio falls in the range of $Rs+\sigma_c$ to $Rs+\sigma_c$ around the calculated strain ratio estimate.

of R_i in their undeformed state. For example, most natural undeformed pebbles and lapilli occur with grain shape distributions that are lognormal (Borradaile, 1987).

The simulated homogeneous deformation (R_s=1.5) of a sample of particles with an approximate lognormal distribution of R_i (ranging between 1.0 and 1.8 (mean= 1.162) and random orientations of theta (Fig. 3.14) was conducted. The R_f/ϕ and corresponding linearization diagram is presented in figure 3.15a,b. The linearization method yields an estimate of the strain ratio to be equal to 1.581 (±0.173). This deviation from the simulated strain ratio is observed to increase as strain increases (Fig. 3.16). The possible reason for this increase is discussed in the next section.

3.5 Comparison between strain analysis methods.

Comparison of the linearization method of strain analysis with that of Robin's method and Harmonic mean methods are presented in figure 3.17, 3.19 and 3.21 for the previous simulated deformed samples. Figures 3.18, 3.20 and 3.22 illustrate percent variation $((R_s(\text{cal.})-R_s(\text{sim.}))/R_s(\text{sim.})\times 100)$ in the estimate of the strain ratio to the actual simulated R_s for the linearization and Robin's method. Standard deviation for Robin's method, linearization method and the harmonic mean method were calculated and are presented in Table 3.1. For the linearization method the calculations of standard deviation that yield confidence brackets that extend into bulk strains estimates less than 1.000 are not given.

Figure 3.17 illustrates the estimates of strain ratio, between the three methods of strain analysis, as the simulated strain ratio increases from 1.0 to 2.0, for a sample of particles initially randomly oriented with R_i equal to 1.3. From the figure, it is observed that in the case where R_i was constant the estimate of strain by the linearization method is a better approximation of the simulated R_s than the Robin's and Harmonic mean strain ratio estimate. However, as strain increases the deviation from the simulated strain increases for all methods.

A closer inspection of the variation in the strain ratio estimates, determined by the linearization and Robin's methods, from the simulated R_s is presented in figure 3.18. The figure shows the percent variation of the strain ratio estimate from the simulated strain ratio producing the deformation. In this sample, it is apparent that the linearization method gives a much better approximation of the strain ratio than Robin's method. It is also apparent that the estimate of the strain ratio from both methods is an

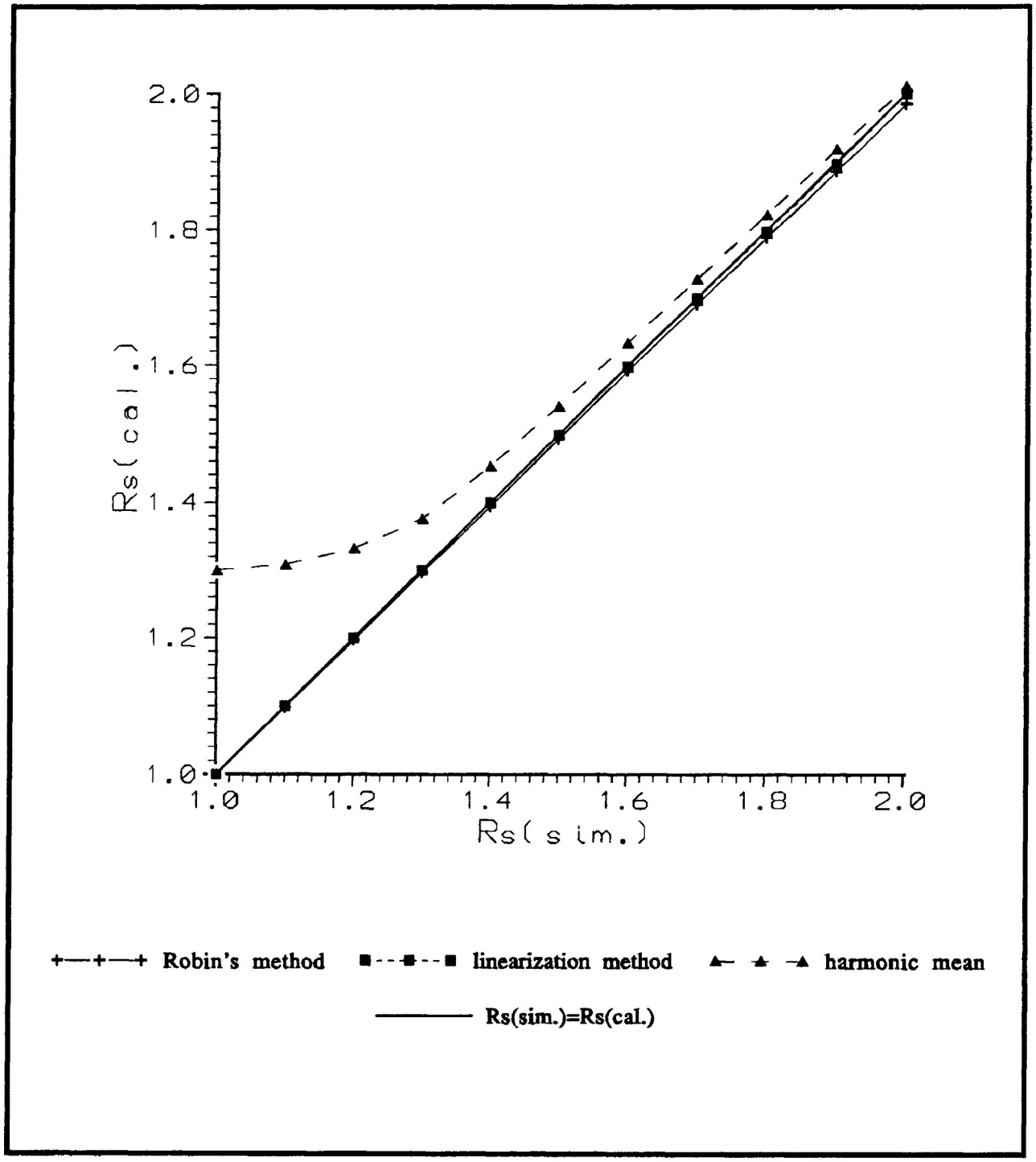

Figure 3.17 Comparison of the estimate of strain ratio (R_s (cal.)) from linearization method (square), Robin's method (cross) and harmonic mean (triangle) to the simulated strain (R_s (sim.)). The estimates are for a sample of 250 strain markers with R_i equal to 1.3 and initially random in orientation (uniform angular distribution). The markers have been deformed by a computer simulation of homogeneous pure shear in the X/Z principal plane to a R_s of 1.1 to 2.0 at 0.1 intervals.

TABLE 3.1

Ri=1.3

sample	Rs(exp.)	Robin's error (s.d.)	Harmonic error (s.d.)	Linear error (s.d.)	n
SIM1	1.100	0.076	0.051	0.000	250
SIM2	1.200	0.076	0.094	0.001	250
SIM3	1.300	0.076	0.123	0.003	250
SIM4	1.400	0.076	0.123	0.007	250
SIM5	1.500	0.076	0.119	0.011	250
SIM6	1.600	0.076	0.113	0.019	250
SIM7	1.700	0.076	0.107	0.028	250
SIM8	1.800	0.076	0.102	0.043	250
SIM9	1.900	0.076	0.097	0.063	250
SIM10	2.000	0.076	0.092	0.089	250

Ri=1 TO 1.3

sample	Rs(exp.)	Robin's error (s.d.)	Harmonic error (s.d.)	Linear error (s.d.)	n
SIM1	1.100	0.070	0.069	0.025	250
SIM2	1.200	0.070	0.076	0.029	250
SIM3	1.300	0.070	0.077	0.034	250
SIM4	1.400	0.070	0.074	0.041	250
SIM5	1.500	0.070	0.070	0.051	250
SIM6	1.600	0.070	0.066	0.063	250
SIM7	1.700	0.070	0.062	0.079	250
SIM8	1.800	0.070	0.059	0.096	250
SIM9	1.900	0.070	0.056	0.121	250
SIM10	2.000	0.070	0.053	0.149	250

LOGNORMAL

sample	Rs(exp.)	Robin's error (s.d.)	Harmonic error (s.d.)	Linear error (s.d.)	n
SIM1	1.100	0.101	0.077	0.074	250
SIM2	1.200	0.101	0.086	0.089	250
SIM3	1.300	0.101	0.087	0.11	250
SIM4	1.400	0.101	0.083	0.151	250
SIM5	1.500	0.101	0.079	0.177	250
SIM6	1.600	0.101	0.074	0.229	250
SIM7	1.700	0.101	0.070	0.301	250
SIM8	1.800	0.101	0.066	0.408	250
SIM9	1.900	0.101	0.063	0.588	250
SIM10	2.000	0.101	0.060	1.02	250

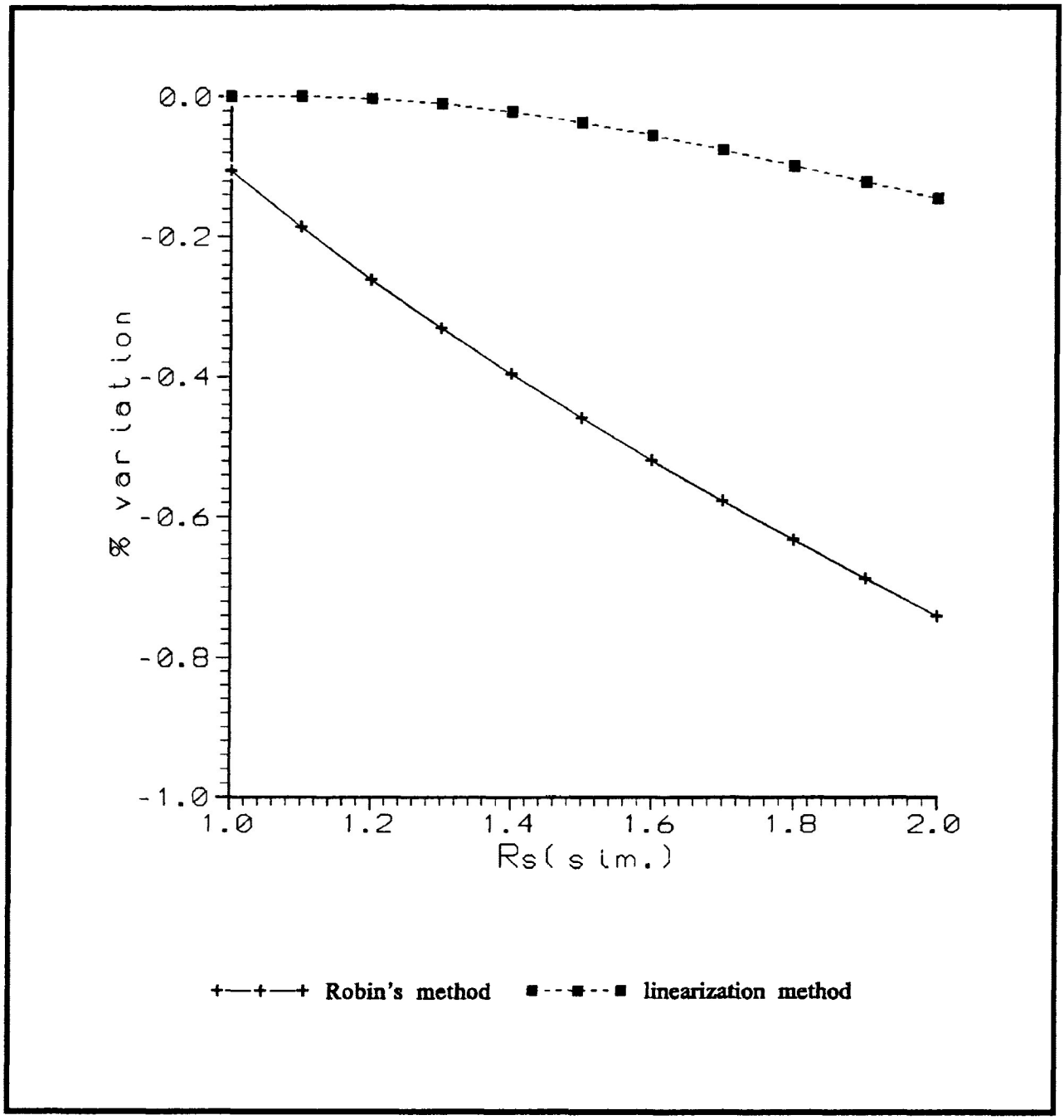

Figure 3.18 Percent variation between the simulated strain ratio and the calculated strain ratio for the linearization and Robin's methods (%variation = $(R_s(\text{cal.})-R_s(\text{sim.}))/R_s(\text{sim.})$ ×100). The estimates are for a sample of 250 strain markers with R_i equal to 1.3 and initially random in orientation (uniform angular distribution). The markers have been deformed by a computer simulation of homogeneous pure shear in the X/Z principal plane to a R_s of 1.1 to 2.0 at 0.1 intervals.

underestimate of R_s. The underestimates of the strain increases as the experimental strain increases, with Robin's method exhibiting the greater increase.

Figure 3.19 illustrates the estimates of strain ratio, between the three methods of strain analysis, as the simulated strain increases from 1.0 to 2.0, for a sample of particles initially random orientation with a range of R_i between to 1.0 and 1.3. From the figure, it is observed that the estimate of strain by Robin's method is closer to the simulated strain than in the case of the both linearization and harmonic mean strain ratio estimates.

A closer inspection of the deviation of the strain ratio estimate, determined by the linearization and Robin's method, from the simulated R_s is presented in figure 3.20. The figure shows the percent variation of the strain ratio estimate from the simulated strain ratio producing the deformation. It is again apparent that Robin's method gives a much better approximation of the strain ratio than the linearization method. The deviation of the strain ratio estimate of the linearization method from the simulated R_s is represented as an increasing overestimate of the strain ratio. In the case of Robin's method, the calculated strain ratio is represented by a lower overestimate of the strain ratio below the simulated R_s of 1.73. For calculated strain ratios, above a simulated R_s of 1.73, the value is an underestimate of R_s, which increases as strain increases.

Figure 3.21 illustrates the estimates of strain ratio, between the three methods of strain analysis, as the simulated strain increases from 1.0 to 2.0, for a sample of particles initially random orientation with an approximation of a lognormal range of R_i between to 1.0 and 1.8. The estimate of the strain ratio by Robin's method is the best estimate of

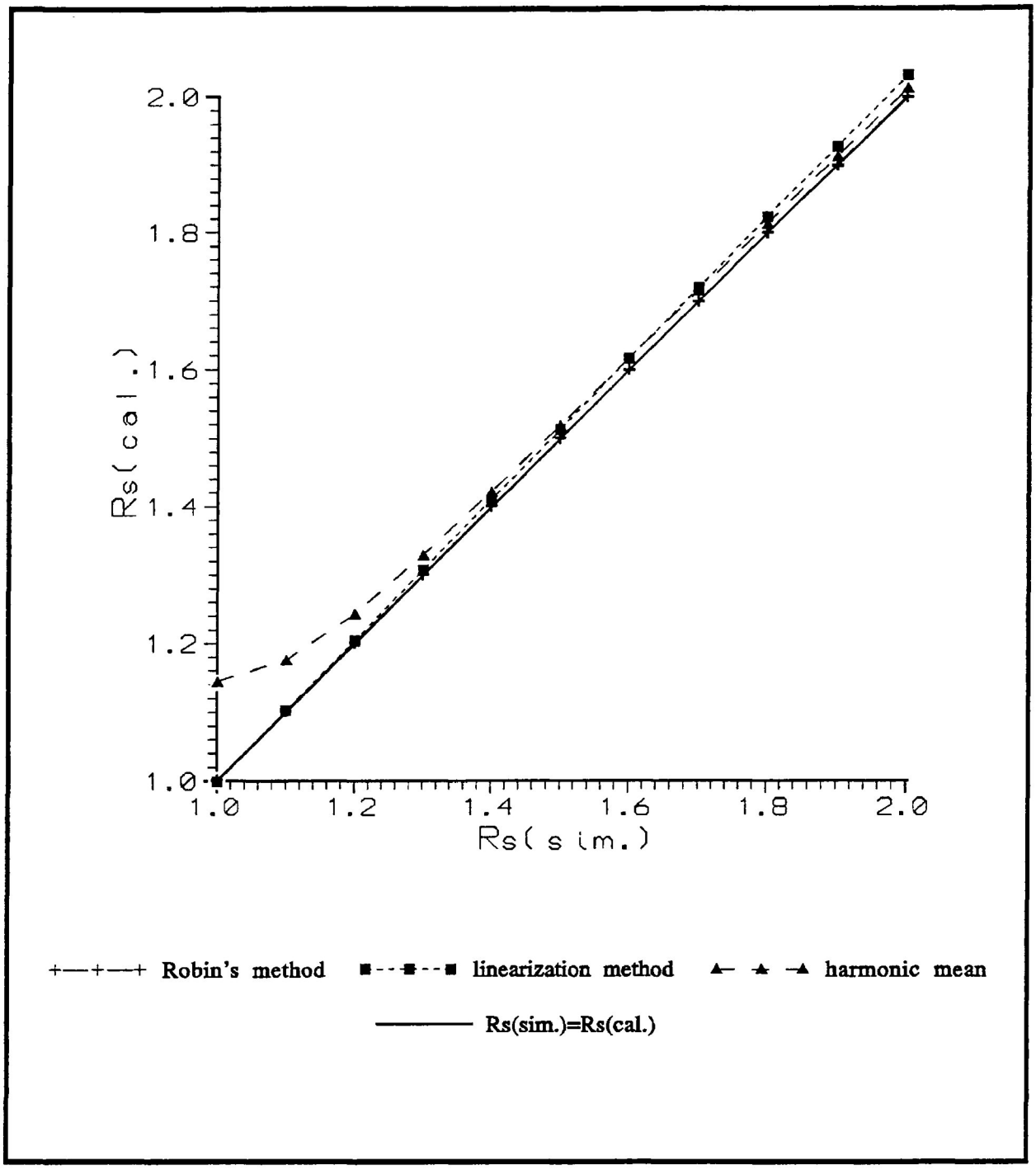

Figure 3.19 Comparison of the estimate of strain ratio (R_s (cal.)) from linearization method (square), Robin's method (cross) and harmonic mean (triangle) to the simulated strain (R_s (sim.)). The estimates are for a sample of 250 strain markers with a range of R_i equal to 1.0 to 1.3 and initially random in orientation (uniform angular distribution). The markers have been deformed by a computer simulation of homogeneous pure shear in the X/Z principal plane to a R_s of 1.1 to 2.0, increasing at 0.1 intervals.

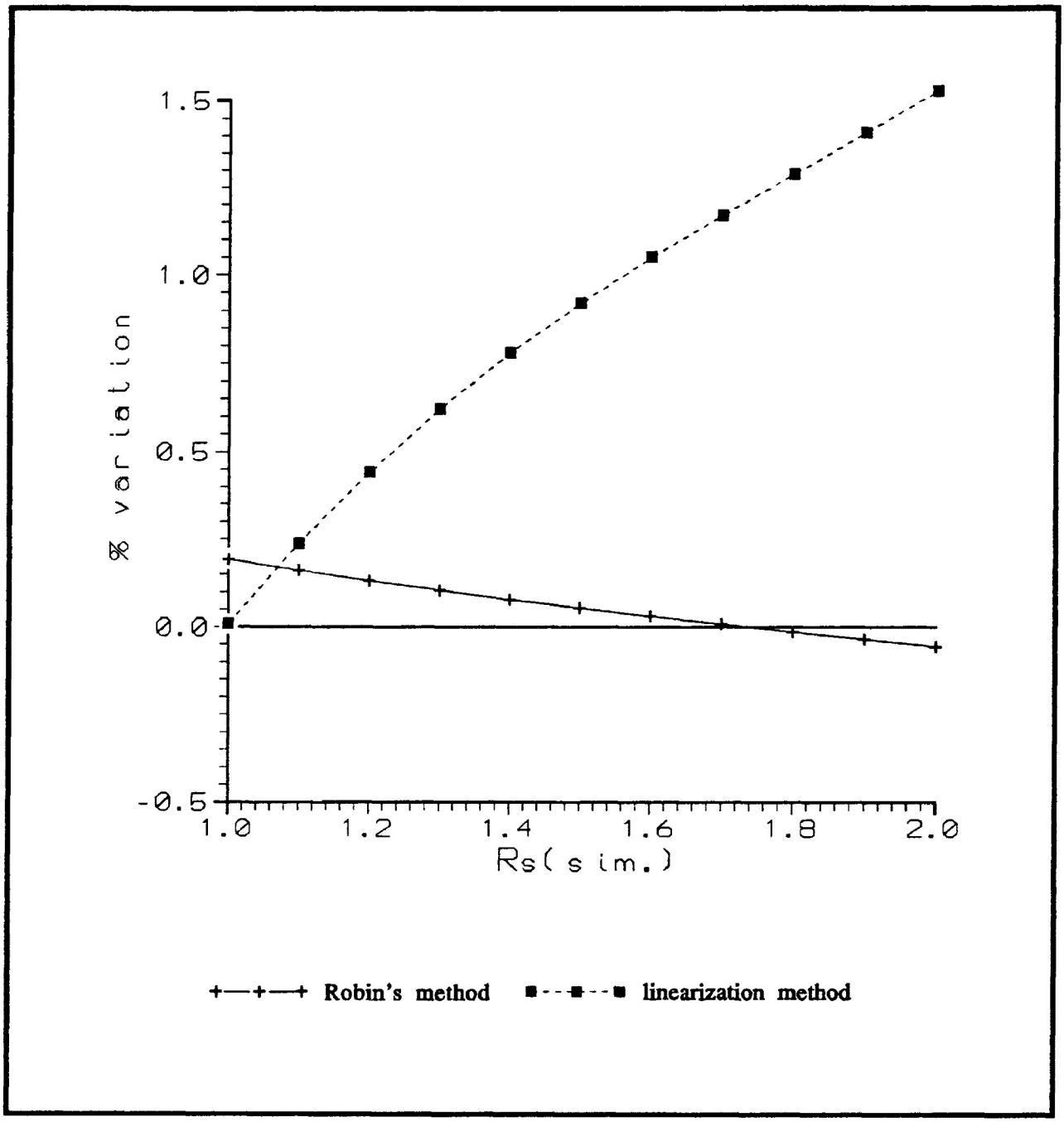

Figure 3.20 Percent variation between the simulated strain ratio and the calculated strain ratio for the linearization and Robin's methods (%variation = $(R_s(\text{cal.})-R_s(\text{sim.}))/R_s(\text{sim.})$ ×100). The estimates are for a sample of 250 strain markers with a range of R_i equal to 1.0 to 1.3 and initially random in orientation (uniform angular distribution). The markers have been deformed by a computer simulation of homogeneous pure shear in the X/Z principal plane to a R_s of 1.1 to 2.0, increasing at 0.1 intervals.

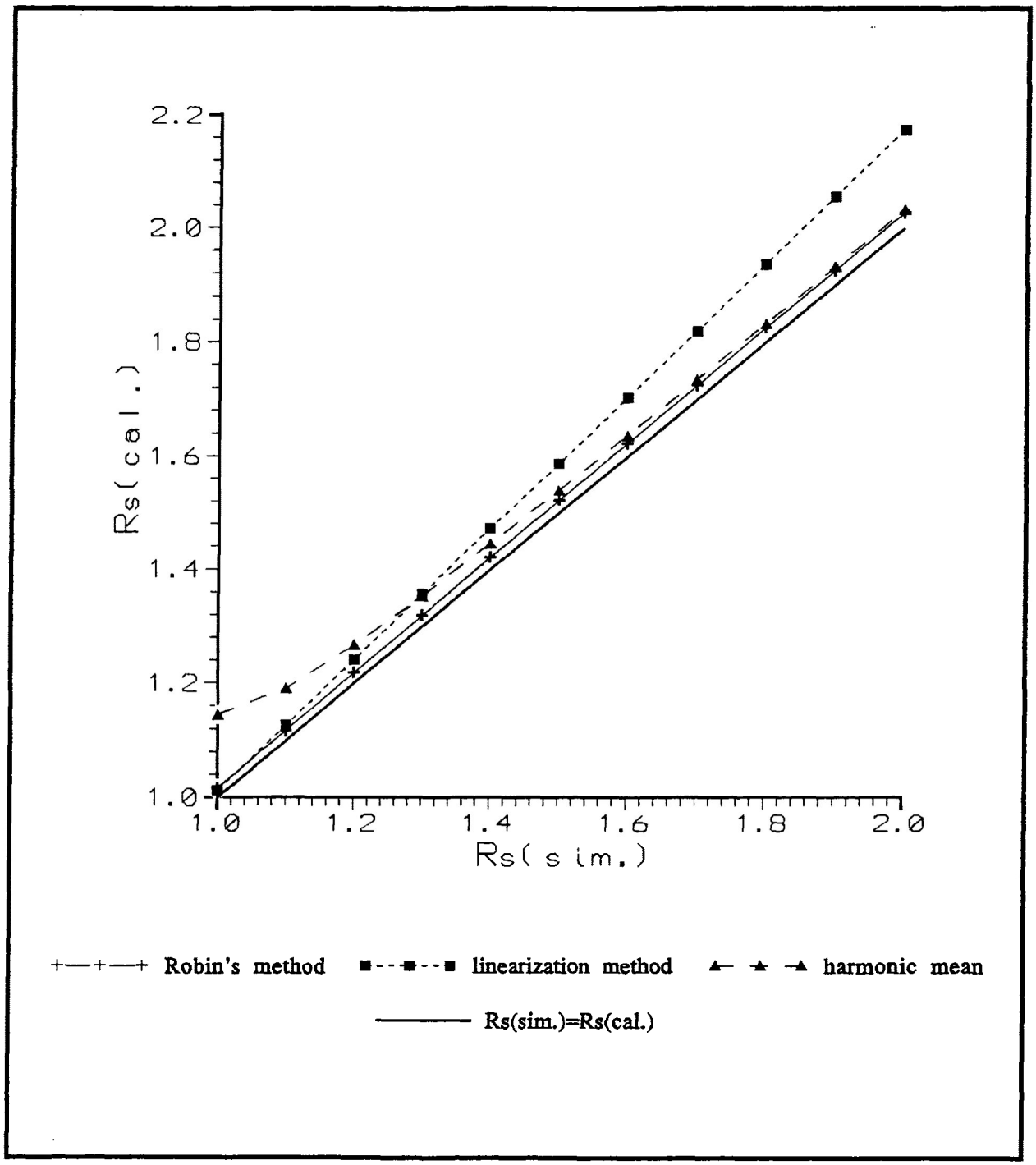

Figure 3.21 Comparison of the estimate of strain ratio (R_s (cal.)) from linearization method (square), Robin's method (cross) and harmonic mean (triangle) to the simulated strain (R_s (sim.)). The estimates are for a sample of 130 strain markers with a lognormal range of R_i equal to 1.0 to 1.8 and initially random in orientation (uniform angular distribution). The markers have been deformed by a computer simulation of homogeneous pure shear in the X/Z principal plane to a R_s of 1.1 to 2.0, increasing at 0.1 intervals.

strain. The estimate of the strain ratio by the linearization method, for R_s above 1.3, is more of an overestimate than the strain ratio calculated by Robin's and Harmonic mean methods.

A closer inspection of the deviation of the strain ratio estimate, determined by the linearization and Robin's method, from the simulated R_s is presented in figure 3.22. It is observed in the figure, that the percent variation of the linearization method is much greater than in the case of Robin's method. The percent variation increases as strain increases for the linearization method. For Robin's method the percent variation decreases as strain increases, suggesting that the estimate of strain ratio will be an underestimate at higher strains.

It is apparent, from the discussion of the simulated examples, that the linearization method is very useful in determining an accurate estimate of strain, where the initial R_i was constant or the range in R_i values is very small (i.e., $R_s > 1 < 1.2$). However, when the sample has a range of R_i which is relatively large, the variation in the estimate of strain in the method of linear regression become significant. The estimate of strain in samples, with large R_i, may lead to an overestimate of strain. These overestimates can be greater than the estimates of the strain ratio from Robin's and Harmonic mean methods. It is also apparent, that increasing strain yield an increasing deviation from the actual R_s producing the deformation. It is, therefore, suggested that the linearization method should be used for low strains where R_i is greater than R_s, and where the R_i range is very small.

The reason that the linearization method gives a less accurate result, for samples that have a range of R_i values, is due to the sensitivity of this method to high R_i particles, that had theta values close to the orientation of the

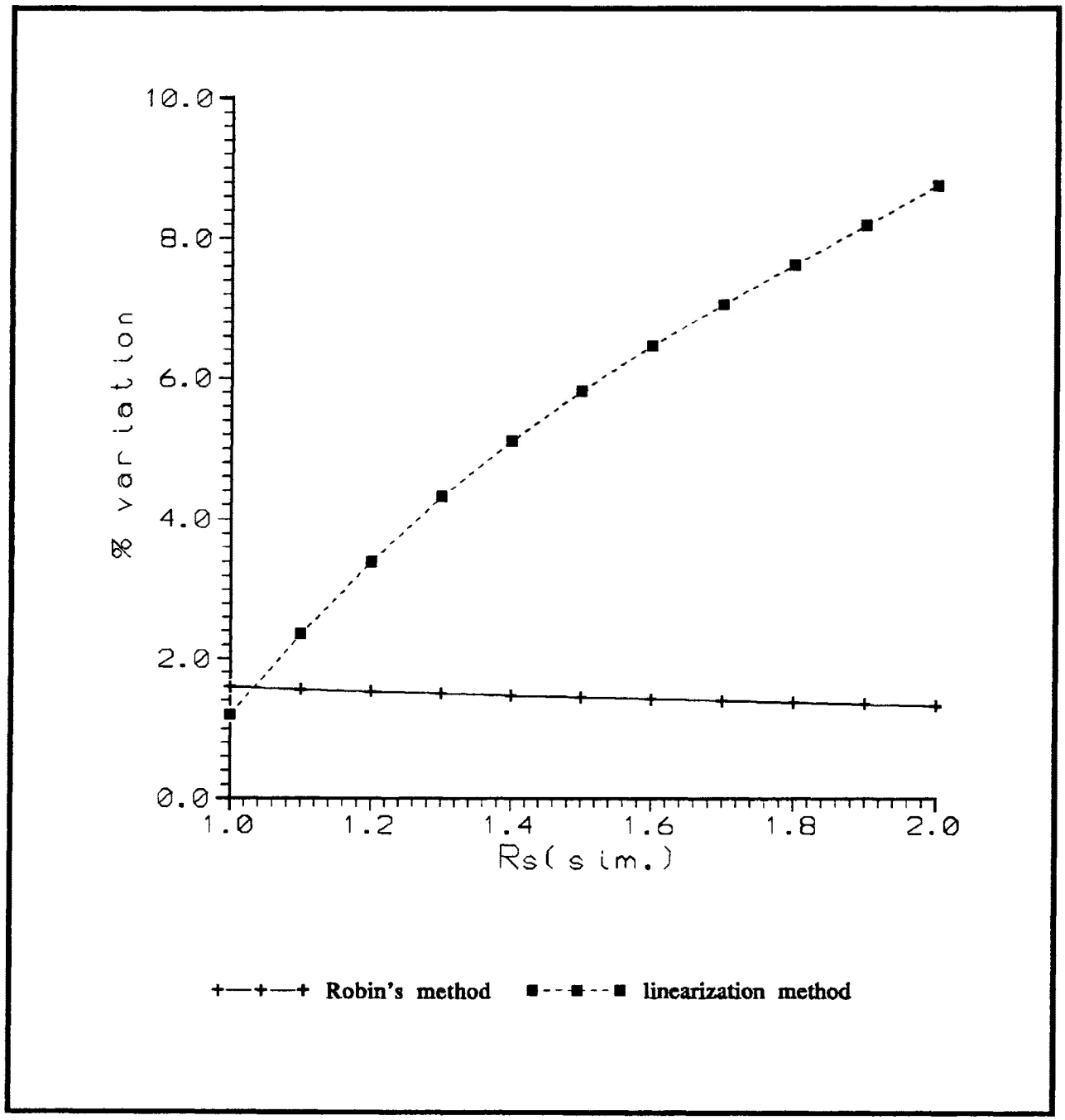

Figure 3.22 Percent variation between the simulated strain ratio and the calculated strain ratio for the linearization and Robin's methods (%variation = (R_s(cal.)-R_s(sim.))/R_s(sim.) ×100). The estimates are for a sample of 130 strain markers with a lognormal range of R_i equal to 1.0 to 1.8 and initially random in orientation (uniform angular distribution). The markers have been deformed by a computer simulation of homogeneous pure shear in the X/Z principal plane to a R_s of 1.1 to 2.0, increasing at 0.1 intervals.

principal extension direction. These values allow for the calculation of overestimates of strain by means of linear regression through the data. In other words, these values, which are located in the upper top of the "lensoidal" distribution pull the linear regression away from the actual R_s, which is more accurately represented by the lower, down slope portion of the "lensoidal" distribution. Robin's method is less susceptible to these particles since it is a calculation based on the arithmetic mean of dimensional ratios in the principal strain directions. The significance of these particles, which are part of the strain equation, is reduced.

Figure 3.23 illustrate the effect of data with high R_f, with ϕ values approximately parallel to the extension direction, on the strain ratio estimate calculated from the linearization method. The figure exhibits the linearization diagram for a sample of particles with a lognormal distribution of R_i (ranging between 1.0 and 1.8 (mean= 1.162) and random in initial orientations which has been deformed to a R_s of 1.5. The solid line represents the linear regression through all the linearization data. The regression gives a strain ratio estimate of 1.587 (±0.191). The dashed line represents the linear regression through all the linearization data except the three highest y-values. The regression gives a better strain ratio estimate of 1.487 (±0.125). Removal of these high y-values may, therefore, improve the estimate of strain for higher strained samples. The linearization method may be useful as a tool for determining the finite strain ratio by the subjective graphic analysis method of Dunnet (1969).

The effect of rigid rotation of particles, which had large R_i (increase in rotational inertia), into orientations approximately parallel to the extension direction may also lead to an overestimate of strain. The particles that have

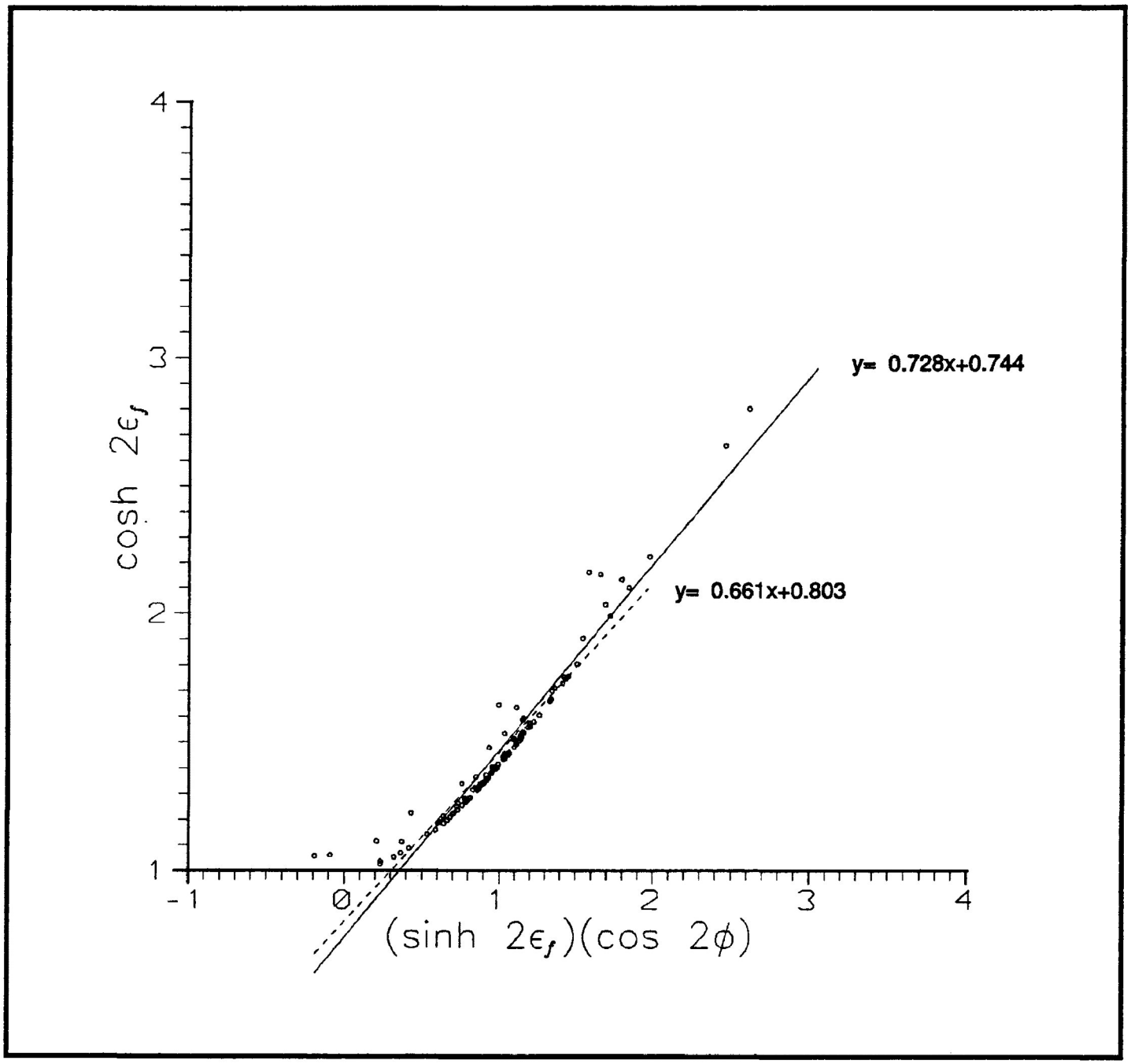

Figure 3.23 Linearization diagram for a sample of particles with a lognormal distribution of R_i (ranging between 1.0 and 1.8 (mean= 1.162) and random in initial orientations which has been deformed to a R_s of 1.5. The solid line represents the linear regression (y=0.728x+0.743) through all of the linearization data (R_s (cal.) 1.587 (±0.191)). The dashed line represents the linear regression (y=0.661x+0.803) through all the linearization data except the three highest y-values (R_s (cal.) 1.487 (±0.125)).

experienced rigid rotation and possible simultaneous deformation, will be located in the upper portion of the linearization diagram.

Chapter 4: Crystallographic fabric development in an experimentally deformed calcite Portland-cement aggregate in pure shear, transpressional shear and simple shear

4.1 Introduction

The calcite Portland-cement samples were deformed under confining pressures of 200 Mpa and at room temperature (25°C). In dry (P_f=0) and wet (P_f>>0) experimental pure shear deformation, the samples were deformed by a computer controlled natural strain rate of 10^{-5}/s. Strains were produced in the X/Z principal plane up to 21.7% (R_s=1.443) and 24.0% (R_s=1.1.509) shortening, respectively. The pore fluid pressure (P_f) in wet experimental conditions was between 180 and 195 Mpa. For transpressional shear and simple shear computer controlled slip rates were 0.73×10^{-4} mm/s. Shear strains less than 0.189 were obtained in the transpressional shear tests. For simple shear tests the shear strains were less than 1.000 (2 mm shear zone) and 1.220 (5 mm shear zone). The shear strains in the deformed samples were determined by displacement of the rigid portion of the deformation assemblages (Fig 1.2).

The known σ_1 orientation, parallel to the axis of the cylinder during deformation, is given in related figures unless otherwise stated. The term theoretical σ_1 orientation is based on the geometry of the shear zone. In simple shear this will be $\sim 45^\circ$ from the known σ_1 orientation. The term inferred σ_1 orientation is based on crystallographic fabric determination.

Errors on the calculation of experimental strain from the test cylinder shortening after triaxial deformation are considered to be negligible. Sample preparation is discussed in detail in Borradaile and McArthur (1990).

The calcite grains present in the calcite Portland-cement aggregate are coarse enough (0.17 to 0.25 mm) for optical determinations of crystallographic axes. Universal-stage measurements were made on the orientations of the optic axis of the host crystal (*c*-axis) and the pole to the *e*-twin plane. The number of twin lamellae and the thickness of the calcite grain parallel to the pole to the twin plane were measured for the determination of the lamellae index recorded as lamellae per millimetre (L/mm). The twin set e_1 is taken to be the most dominant in occurrence (*i*.e., highest L/mm) within in a given calcite grain, e_2 and e_3 are increasingly less dominant in occurrence.

4.2 Microscopic observations of calcite twin lamellae

a) Undeformed

In the undeformed samples (7C-3C, BB8808) the calcite grains exhibit twin lamellae in approximately 55% of the grains. Most of the twin lamellae were well developed and broad enough to allow twinning to be clearly recognized by symmetrical differences in optical behaviour (*i*.e., extinction) of adjacent lamellae in the host calcite grain (Plate 4.1). The diagnostic angle of 26° (±3°), determined by Universal stage measurements, between pole of the twin lamellae and the corresponding *c*-axis identifies the *e*-twin crystallographic plane. Twinning is present as one twin set (e_1) in 55% of the twinned grains. Also present are calcite grains exhibiting two and three twin sets in 43% and 2% of the twinned grains, respectively (Fig. 4.7a). The remaining 45% of the calcite grains in the undeformed sample are not twinned and show minor strained extinction.

Twin lamella thickness in the undeformed sample ranged from 1 to 20 microns. The twin lamellae present in these

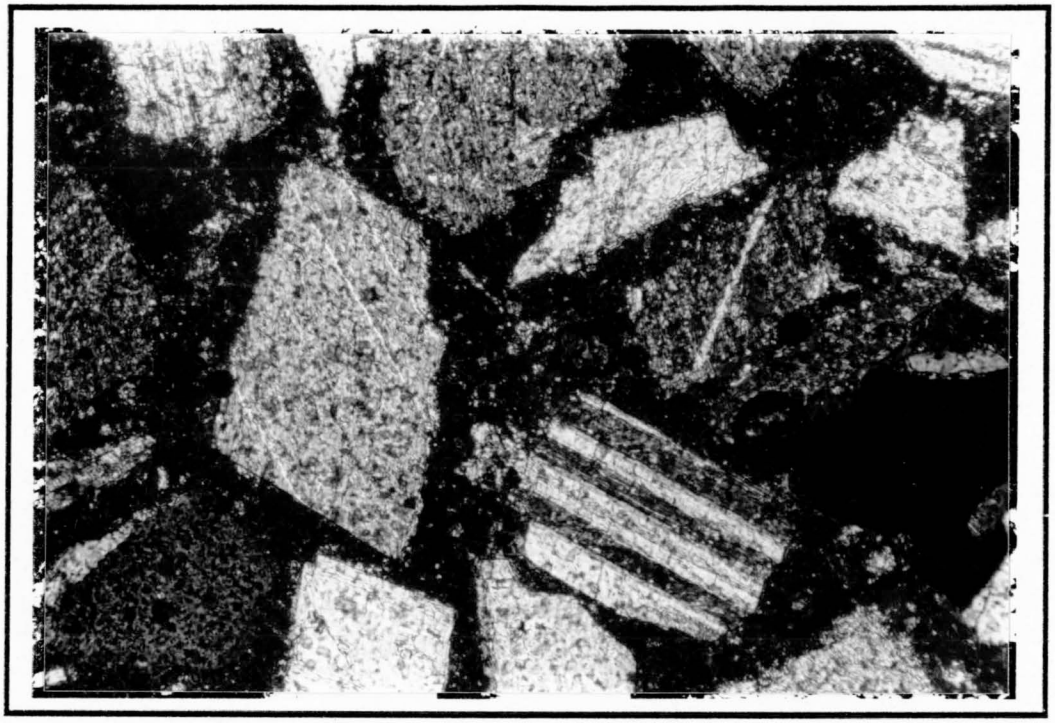

Plate 4.1 Microphotograph illustrating twin lamellae in calcite grains of the undeformed sample 7C-3C. Mechanical twinning in calcite grains recognized by symmetrical differences in optical extinction. Lamellae are of low lamellae index, broad, thick and well developed. Photo taken in partial cross polarized light. (scale 38:1)

samples, most likely represents the original mechanical twinning produced during the preparation of the sample material. Microtwins (Conel, 1962 (*i.e.*, very thin twin lamellae with no measurable thickness), common in natural marbles, were also observed in the calcite grains. The thickness of microtwins in marble has been calculated by Groshong (1972), given by the ratio of 0.50 micron of twin per micron of black lines observed in the host crystal. In the undeformed sample (7C-3C) approximately 5% of the twinned calcite grains contained microtwins as e_2 and e_3 and to a lesser degree as e_1.

The undeformed sample has a very limited range of e_1 and e_2-lamellae index values as presented in the frequency distribution of figure 4.1a,b. The average lamellae index for twinned calcite grains in the undeformed state was determined to be 23.3 L/mm (±16.9 s.d.) for e_1 and 10.1 L/mm (±7.1 s.d.) for e_2.

b) Pure Shear (dry experimental conditions (P_c=200 Mpa))

As experimental strain by axial compression advances under dry experimental conditions, the percentage of calcite grains that exhibit mechanical twinning on e-twin planes increases (Fig. 4.2). At an experimental strain of 4.4% (R_s=1.070) approximately 80% of the calcite grains are twinned to some degree and this increases to 100% at an experimental strain of 12.0% (R_s=1.211). Those calcite grains that are not twinned at lower experimental strains exhibit undulose extinction. Micrographs of sample AC-8 (18.03% (R_s=1.347)) for the centre area of the XZ principal plane is presented in Borradaile and McArthur (1990, Fig.5a).

The thickness of the twin lamella in the deformed samples ranged from 1 to 10 microns and were present as e_1 and e_2 twin

a)

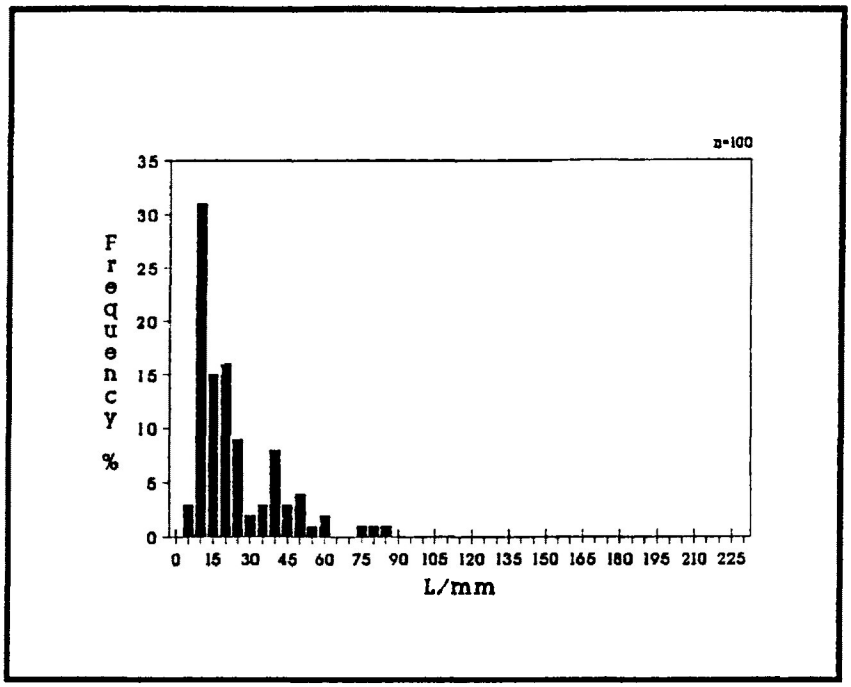

b)

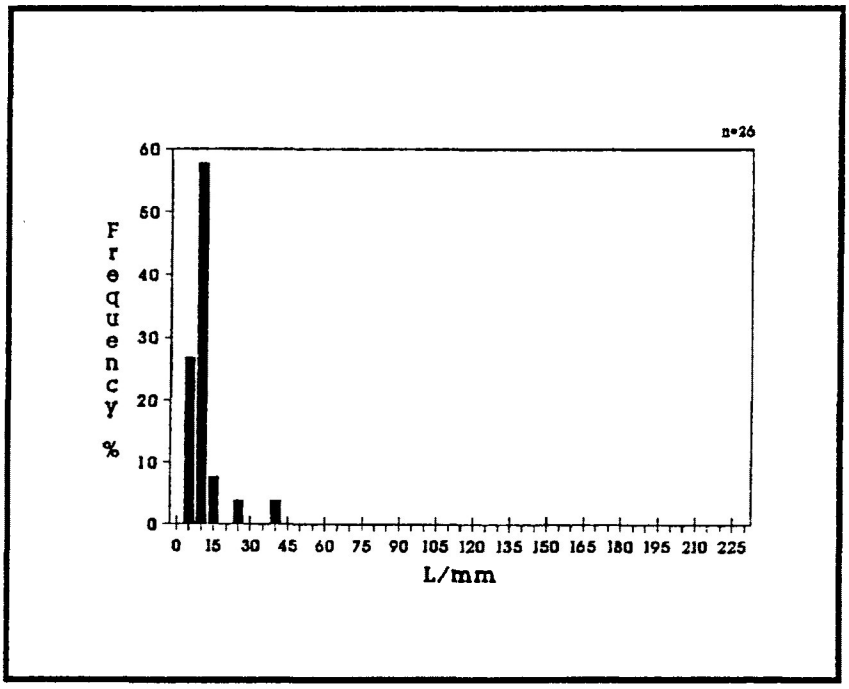

Figure 4.1 Frequency distribution of lamellae indices for individual calcite grains in an undeformed calcite cement aggregate (Sample 7C-3C).
a) e_1-lamellae indices
b) e_2-lamellae indices

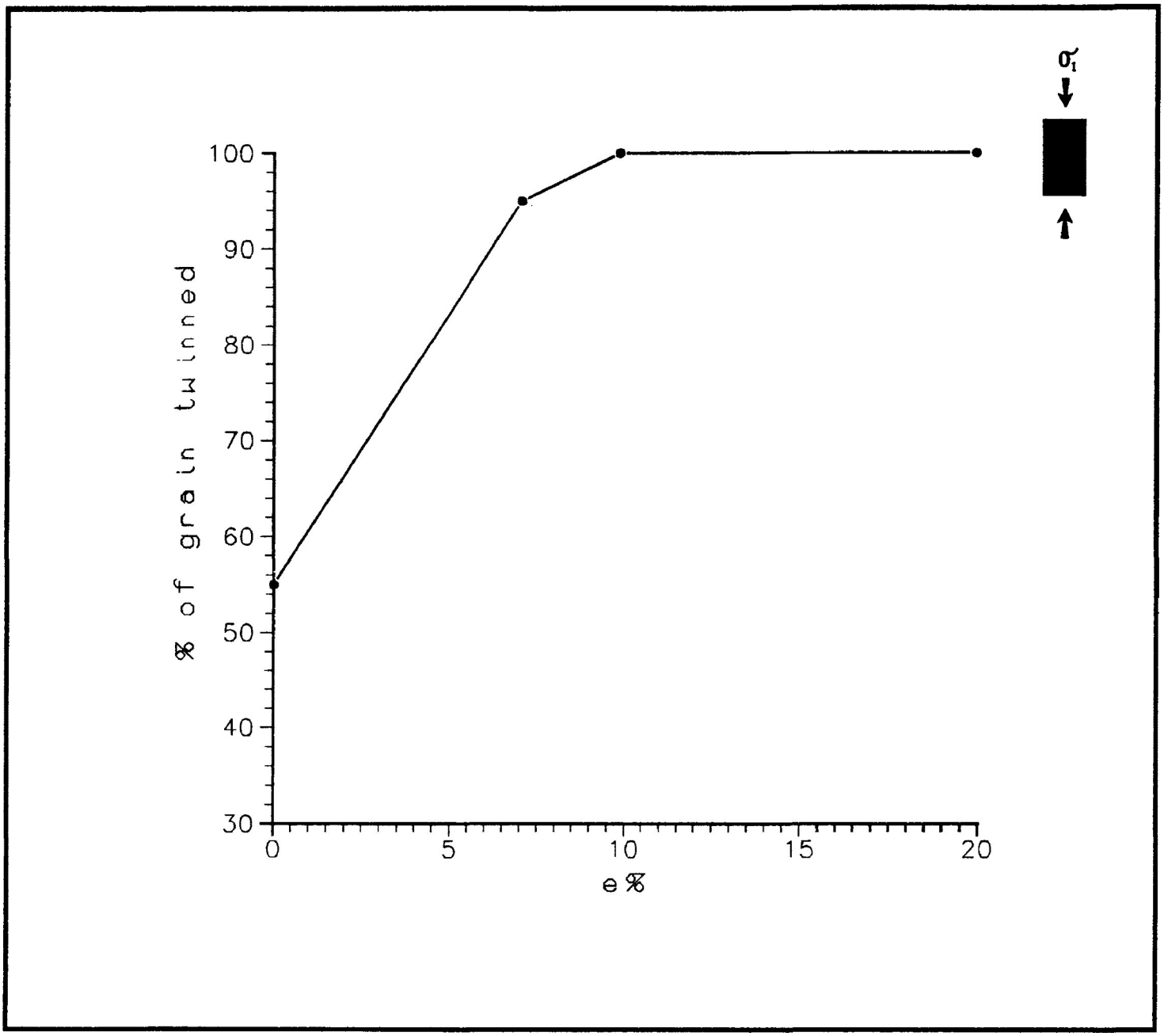

Figure 4.2 Percentage of calcite grains in total aggregate that exhibit twinning in pure shear under dry experimental conditions (P_c=200 Mpa, de/dt=10^{-5}/s) for strains of 0% (R_s=1.000), 4.4% (R_s=1.070), 10.2% (R_s=1.175) and 18.03% (R_s=1.347).

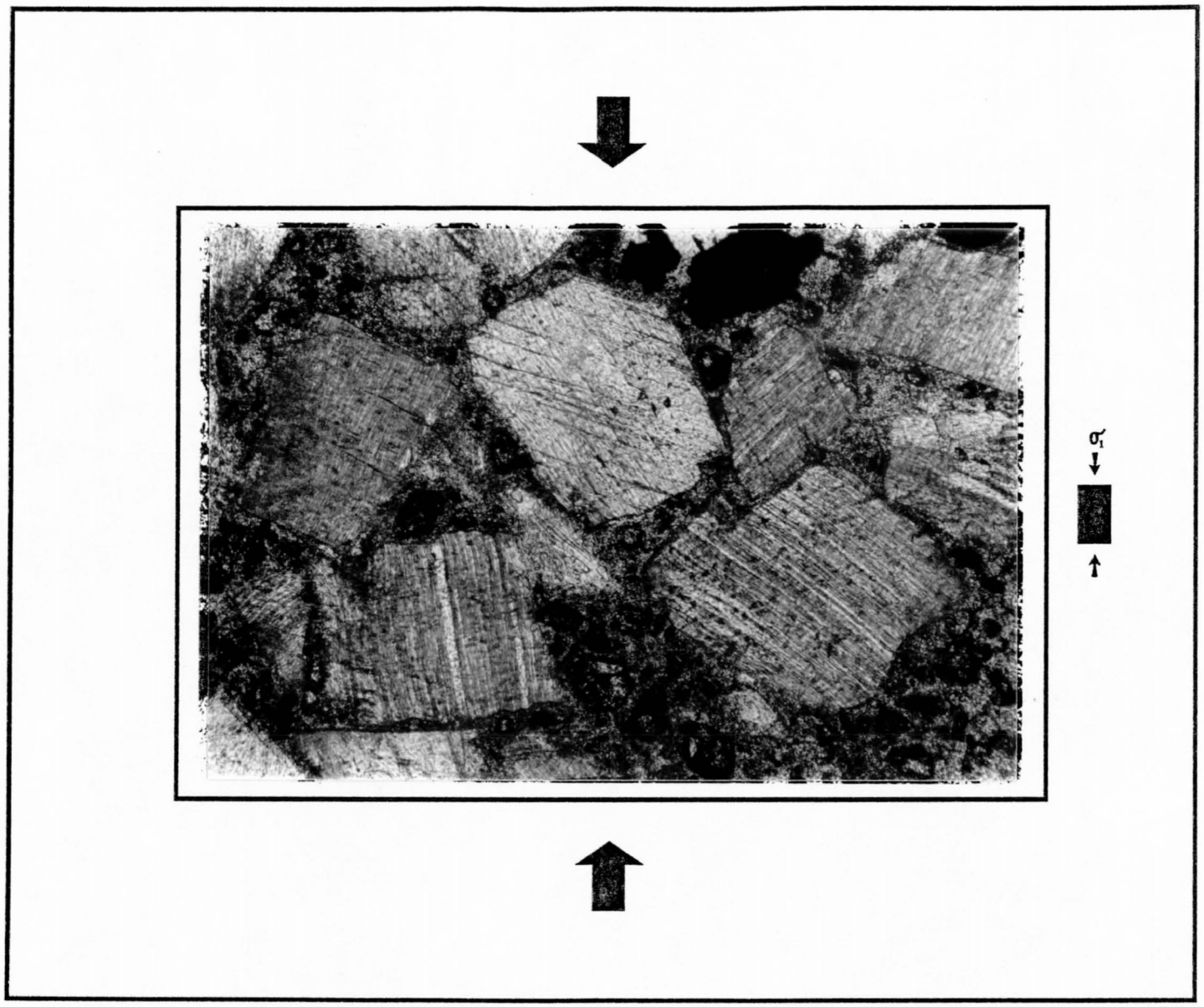

Plate 4.2 Microphotograph of twin lamellae in sample (AC-8 (e=18.03%)) in the X/Z principal plane deformed by dry pure shear (P_c=200 Mpa, de/dt=10^{-5}/s). Twin lamellae exhibit high lamellae index values. Broad arrows indicate orientation of σ_1 during triaxial deformation. Photo taken in partial cross polarized light. (scale 38:1)

sets. However, the majority of calcite grains show lamella thicknesses between 1 and 2 microns. The individual lamellae were sharp and well developed (Plate 4.2).

Microtwins were also observed, usually as e_2 and e_3 twin sets, and were present in 20 percent of the twinned calcite grain at 18.03% (R_s=1.347) shortening. Microtwins have been observed at grain to grain contacts where twin lamella grade into microtwins in a direction of the contact. Microtwins may, therefore, represent twinning in conditions of high stress. Borg and Turner (1953) suggested that microtwins are the result of large compressive stresses operating at high angles to the twin lamellae.

The frequency distributions of e_1-lamellae indices in dry pure shear, for experimental strains of 4.4% (R_s=1.070), 10.2% (R_s=1.175) and 18.03% (R_s=1.347), are presented in figure 4.3. From the histograms it is evident that there is an increase in the range of lamellae index values and also an increase in the maximum lamellae index with advancing strain. The average lamellae index increases with experimental strain from 57.6 L/mm (±32.4 s.d.) at 4.4% (R_s=1.070) to 108.8 L/mm (±75.2 s.d.) at 18.03% (R_s=1.347) shortening (Fig. 4.4). The increase in average lamellae index is reflected by the decrease in twin lamellae thicknesses from the undeformed to deformed state.

The frequency distributions of e_2-lamellae indices in dry pure shear is presented in figure 4.5. In the figure an increase in the range of e_2-lamellae index is observed to a lesser degree than that observed in e_1. The average lamellae indices range from 24.7 L/mm (±11.4 s.d.) to 34.8 L/mm (±14.8 s.d.) as experimental strain increases from 4.4% (R_s=1.070) to 18.03% (R_s=1.347) shortening (Fig 4.6). The increase in the average lamellae index for e_2 is less than that of e_1 twin lamellae, suggesting that deformation of calcite grains in

Figure 4.3 Frequency distribution of e_1-lamellae indices for individual calcite grains in the calcite Portland-cement aggregate. Samples were deformed by pure shear under dry experimental conditions (P_c=200 Mpa, de/dt=10^{-5}/s).

a) Sample AC-3 (e=4.4% (R_s=1.070))
b) Sample AC-5 (e=10.2% (R_s=1.175))
c) Sample AC-8 (e=18.0% (R_s=1.347)

a)

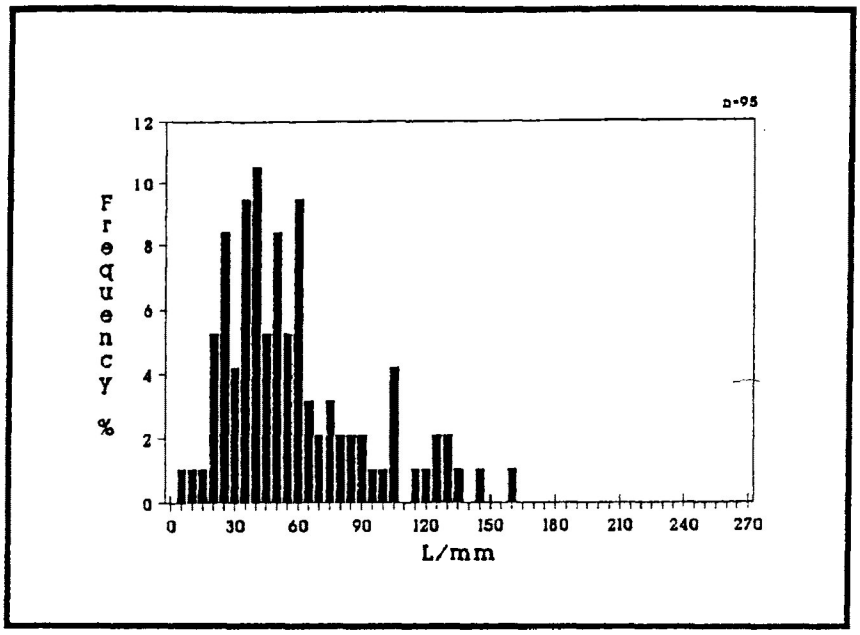
n=95
Frequency %
0
2
4
6
8
10
12
0
30
60
90
120
150
180
210
240
270
L/mm

b)

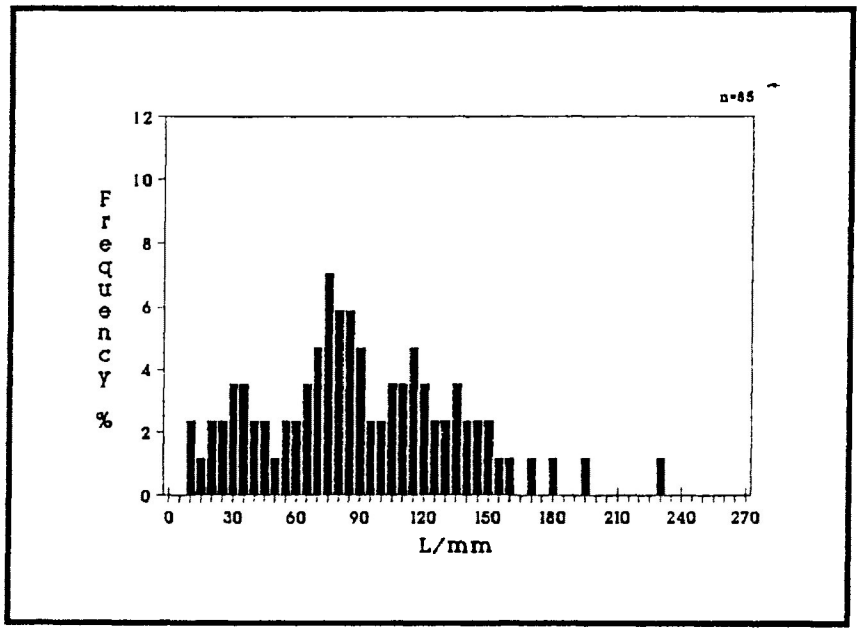
n=85
Frequency %
0
2
4
6
8
10
12
0
30
60
90
120
150
180
210
240
270
L/mm

c)

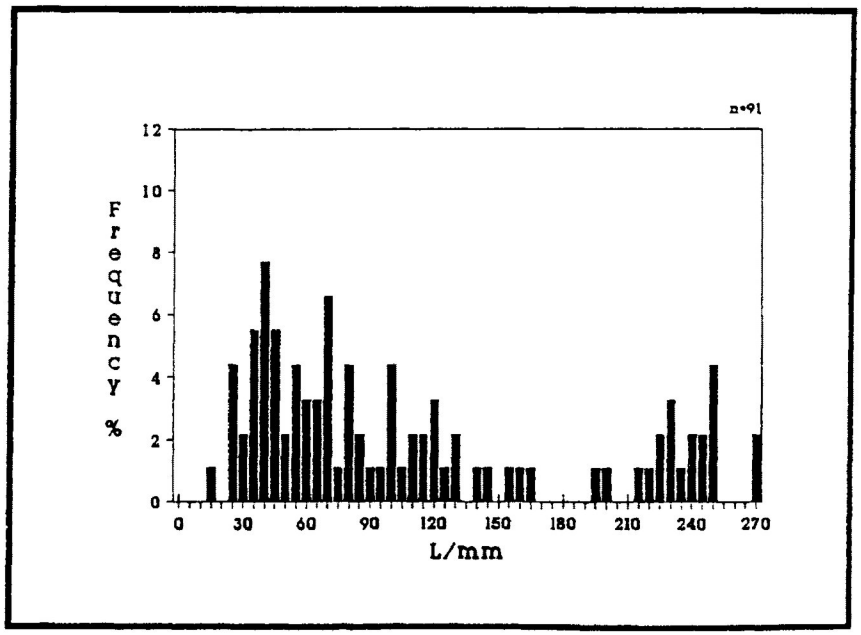
n=91
Frequency %
0
2
4
6
8
10
12
0
30
60
90
120
150
180
210
240
270
L/mm

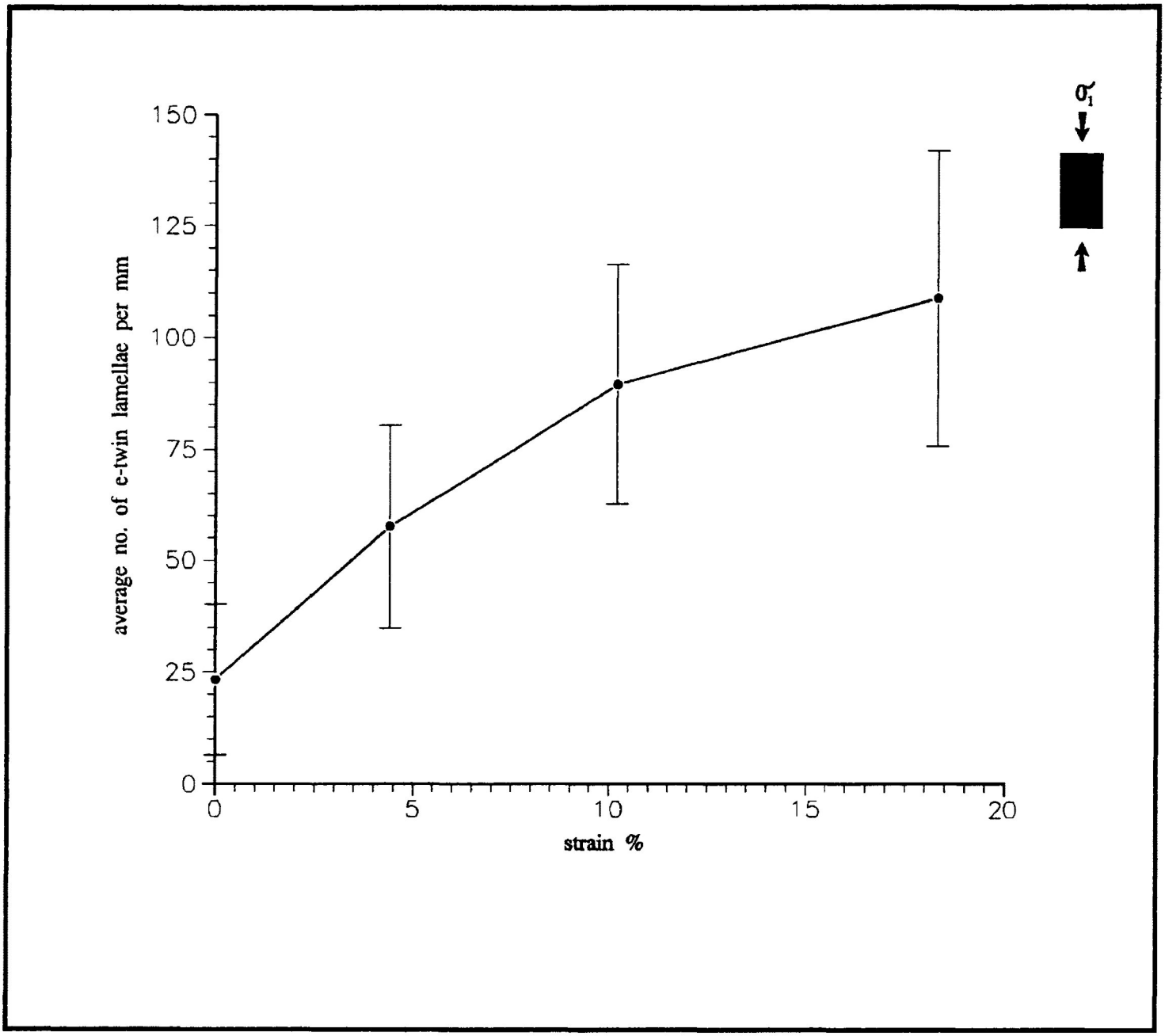

Figure 4.4 Variation in average e_1-lamellae index and associated standard deviation (error bars) for the frequency distributions of measurements on individual calcite grains. The samples were deformed by pure shear under dry experimental conditions (P_c=200 Mpa, de/dt=10^{-5}/s) for experimental strains of 0% (R_s=1.000), 4.4% (R_s=1.070), 10.2% (R_s=1.175) and 18.03% (R_s=1.347).

Figure 4.5 Frequency distribution of e_2-lamellae indices for individual calcite grains in the calcite Portland-cement aggregate. Samples were deformed by pure shear under dry experimental conditions (P_c=200 Mpa, de/dt==10^{-5}/s).

a) Sample AC-3 (e=4.4% (R_s=1.070))
b) Sample AC-5 (e=10.2% (R_s=1.175))
c) Sample AC-8 (e=18.0% (R_s=1.347)

a)

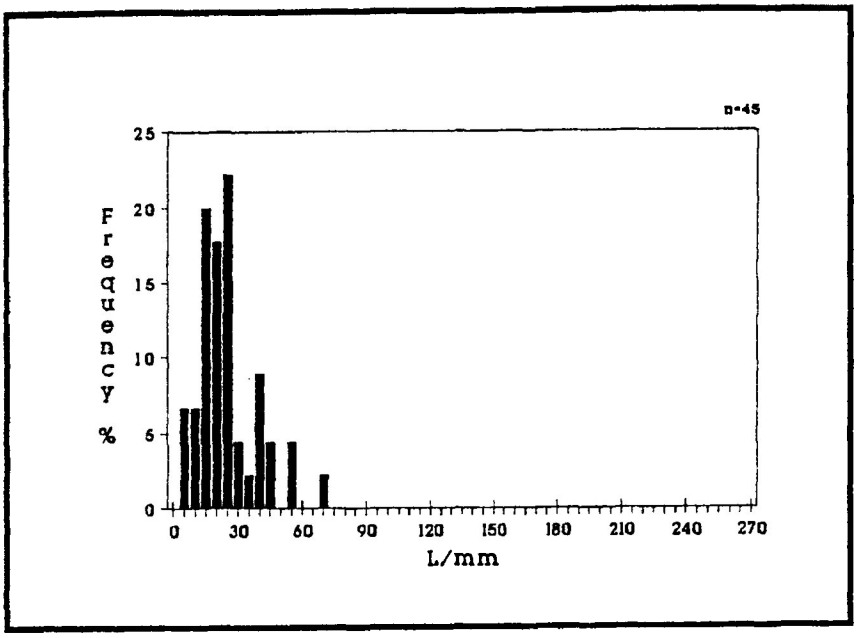
n=45
Frequency %
25
20
15
10
5
0
0 30 60 90 120 150 180 210 240 270
L/mm

b)

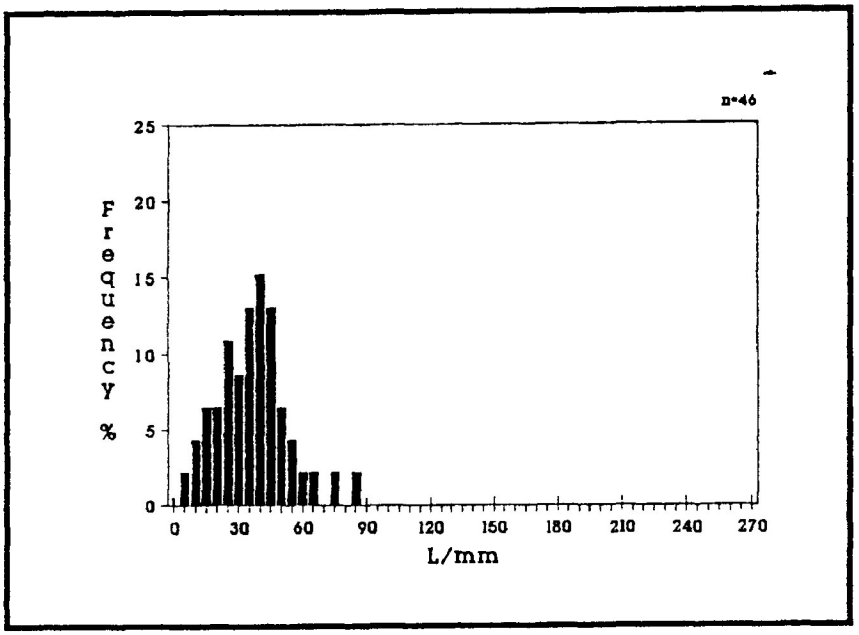
n=46
Frequency %
25
20
15
10
5
0
0 30 60 90 120 150 180 210 240 270
L/mm

c)

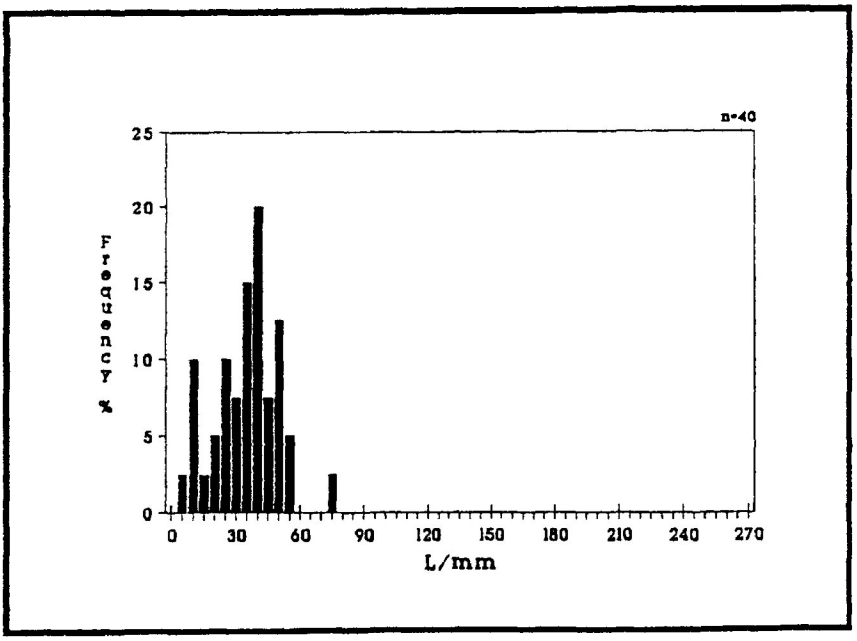
n=40
Frequency %
25
20
15
10
5
0
0 30 60 90 120 150 180 210 240 270
L/mm

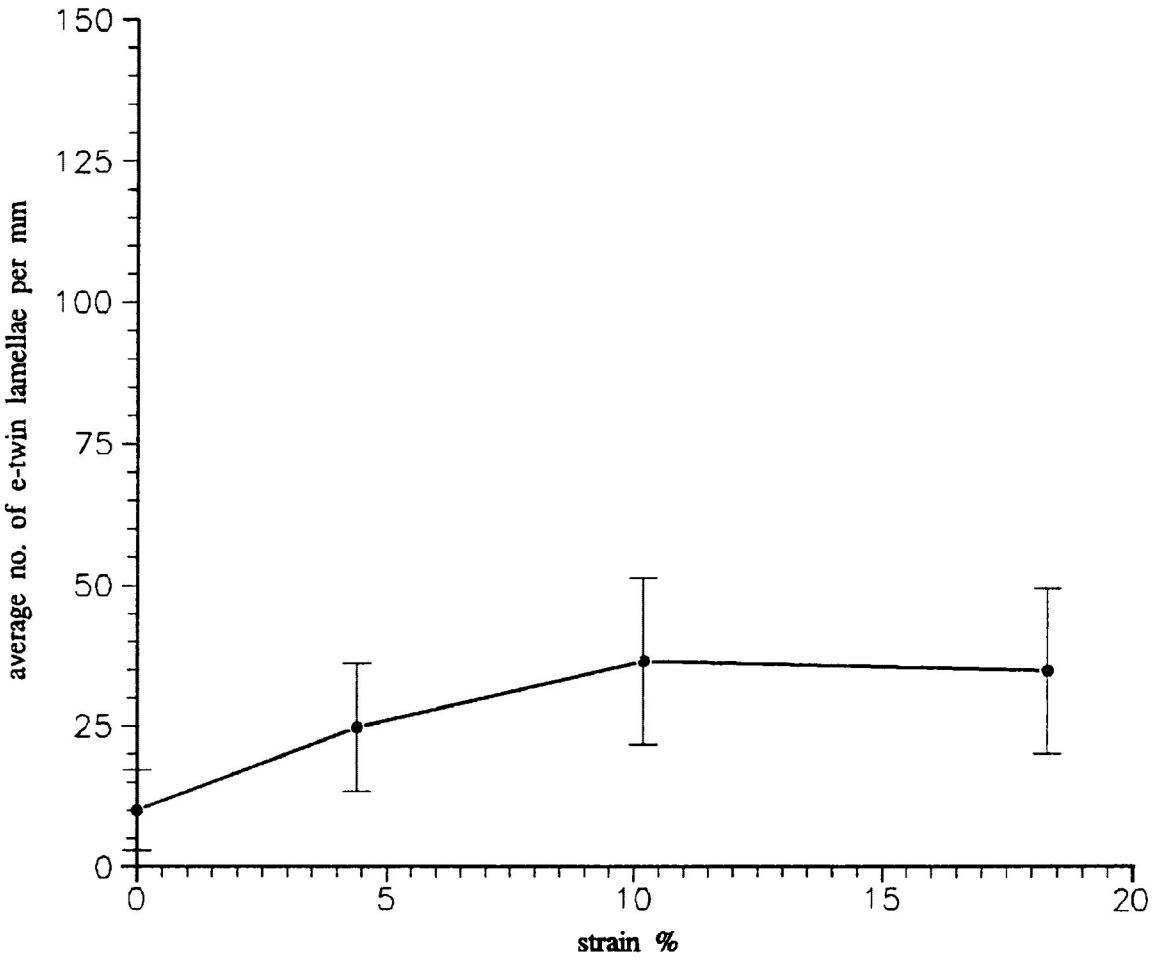

Figure 4.6 Variation in average e_2-lamellae index and associated standard deviation (error bars) for the frequency distribution of measurements on individual calcite grains. The samples were deformed by pure shear under dry experimental conditions (P_c=200 Mpa, de/dt=10^{-5}/s) for experimental strains of 0% (R_s=1.000), 4.4% (R_s=1.070), 10.2% (R_s=1.175) and 18.03% (R_s=1.347).

pure shear is dominated by the latter. However, the increase in the average e_2 lamellae index may be the result of the rotation of calcite grains in which the resolved shear stress on e_2 becomes greater allowing for an increase in e_2 twin development. Studies involving the determination of strain from e-twin lamellae (Teufel, 1980) have observed increases in e_2 over e_1 in 2 stage deformation, where σ_1 was mutually perpendicular.

In this study there is observed an increase in the percentage of calcite grains exhibiting two twin sets (e_1 and e_2) over those grains with only one (e_1) as experimental strain increases under pure shear. Figure 4.7b,c illustrates the increasing development of calcite grains containing 2 twin sets for experimental strains of 4.4% (R_s=1.070) and 18.03% (R_s=1.347) shortening. There is also a slight increase in the development of calcite grains containing three twin sets.

Progressive deformation of the calcite grains by axial compression is reflected by an increase in the development of kink and deformation bands. Kink bands are observed to occur in calcite grains that have e_1 oriented perpendicular and parallel to the compression direction and also in grains which are restricted in their ability to undergo rotation by neighbouring grains. Furthermore, bending of twin lamellae is also observed in the deformed samples. This is especially true for calcite grains that are oriented with e-twin lamellae parallel of sub-parallel to the known compression direction in highly strained samples.

c) <u>Pure Shear (wet experimental conditions) wet conditions (P_c=200 Mpa, P_f=180 to 195 Mpa)</u>

An increase in the percentage of calcite grains that are twinned during increasing experimental strain is also evident in the wet experimental tests (Fig. 4.8). The figure

Figure 4.7 Variation in the percentage of grains that exhibit 1, 2 and 3 twin sets with increasing strain in dry pure shear experimental conditions (P_c=200 Mpa, de/dt=10^{-5}/s)

a) Sample AC-3 (e=4.4% (R_s=1.070))
b) Sample AC-5 (e=10.2% (R_s=1.175))
c) Sample AC-8 (e=18.0% (R_s=1.347)

a)

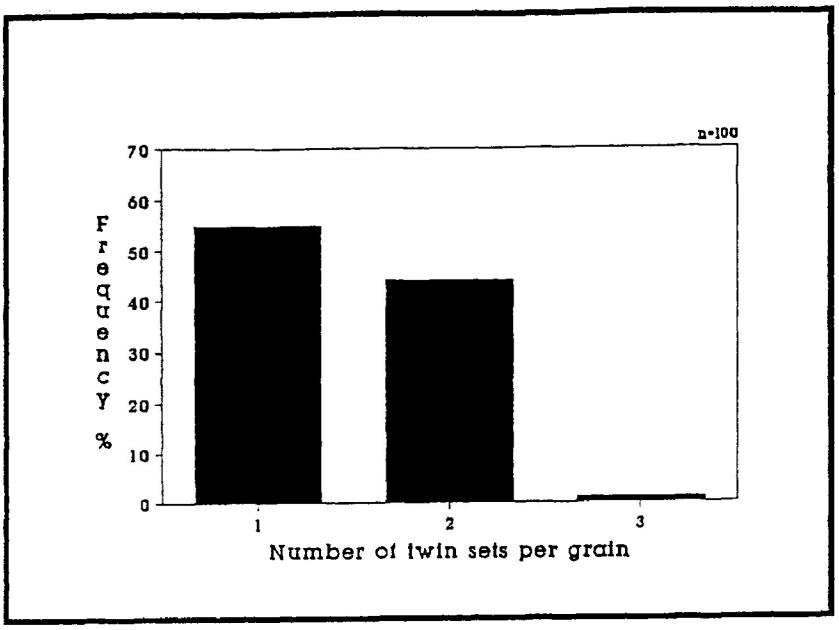
n=100
70
60
50
40
30
20
10
0
Frequency %
1
2
3
Number of twin sets per grain

b)

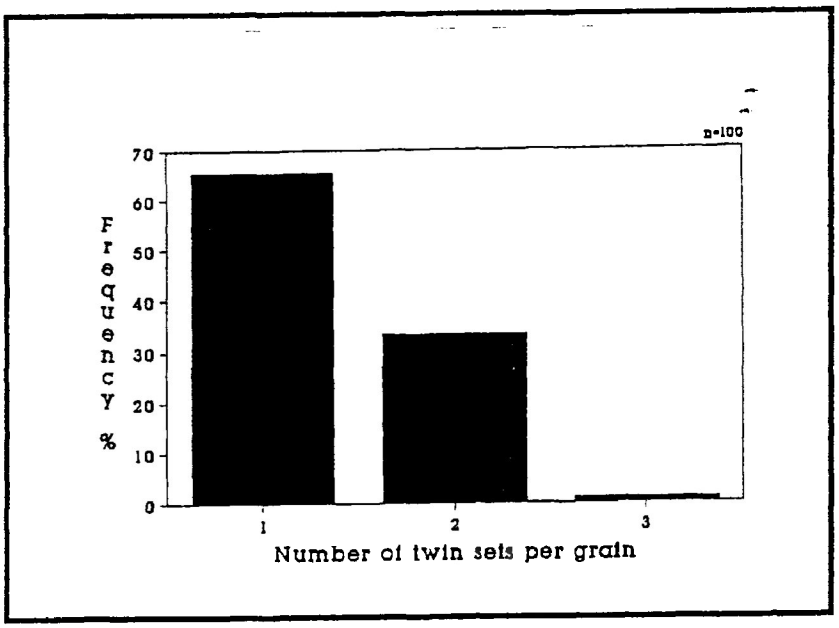
n=100
70
60
50
40
30
20
10
0
Frequency %
1
2
3
Number of twin sets per grain

c)

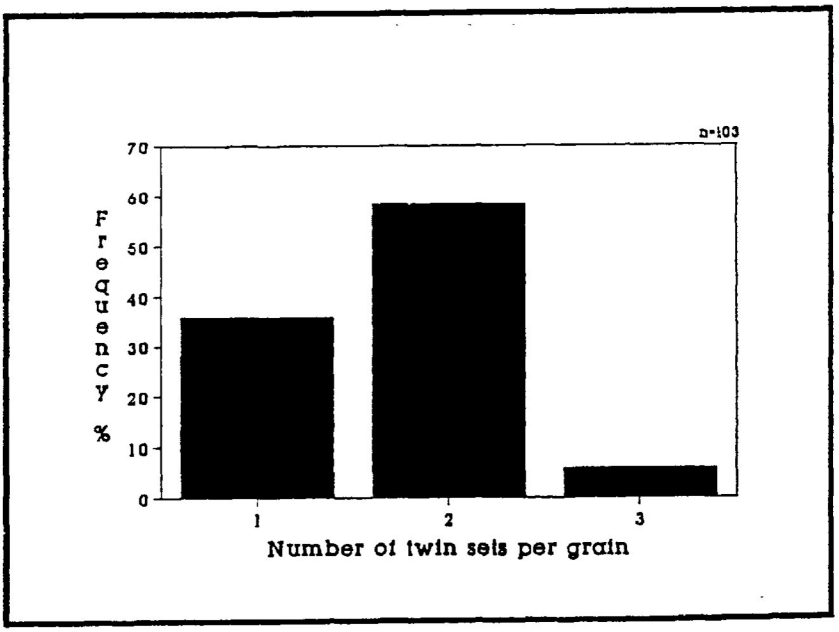
n=103
70
60
50
40
30
20
10
0
Frequency %
1
2
3
Number of twin sets per grain

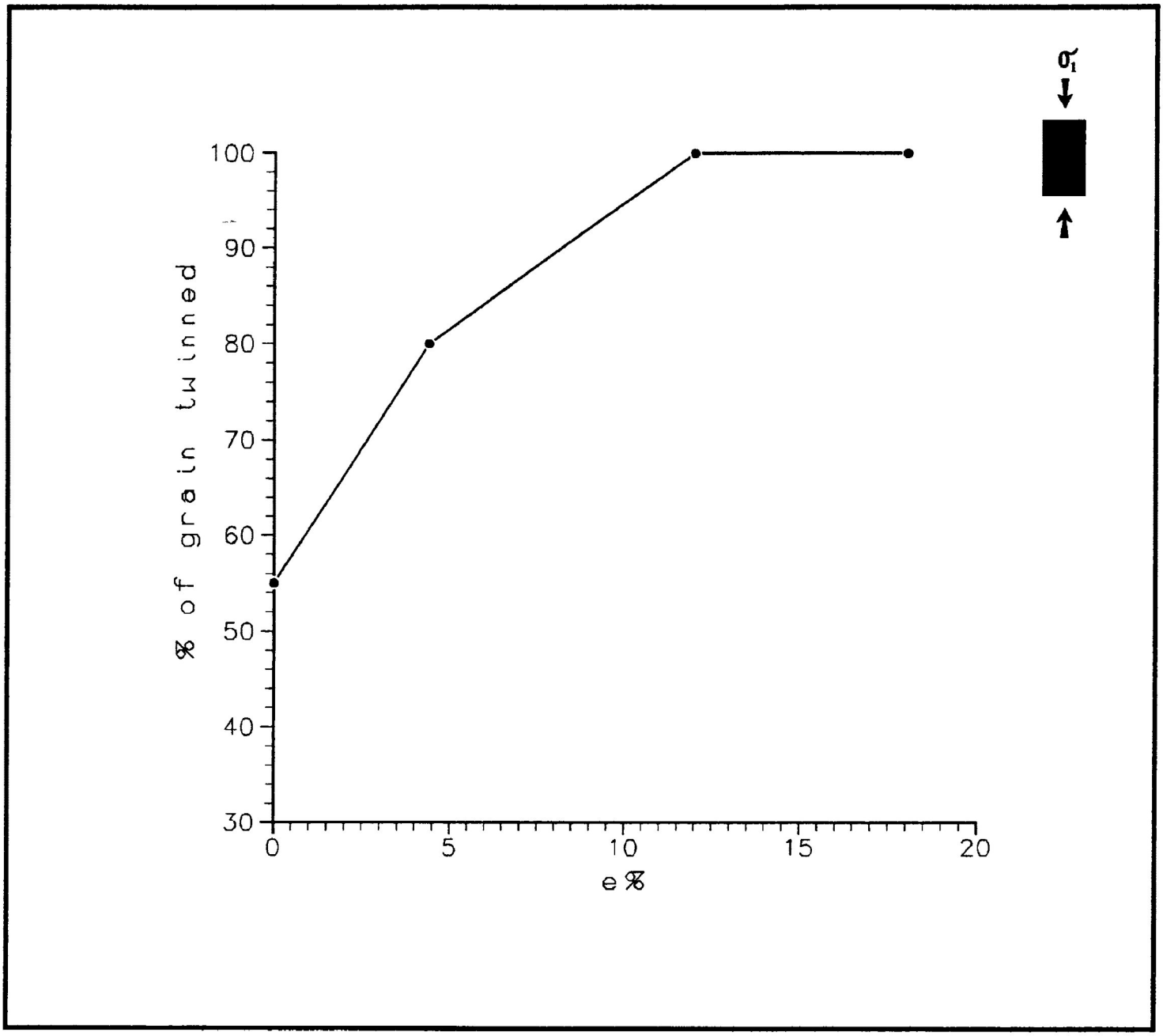

Figure 4.8 Percentage of calcite grains in total aggregate that exhibit twinning in pure shear under wet experimental conditions (P_f=195 Mpa, de/dt=10^{-5}/s) for experimental strains of 0% (R_s=1.000), 6.8% (R_s=1.111), 10.9% (R_s=1.189) and 17.8% (R_s=1.342).

illustrates that at low experimental strains of 6.8% (R_s=1.111) approximately 95% of the calcite grains are twinned and this value reaches 100% at an experimental strain of 8.8% (R_s=1.148). Those calcite grains that are not twinned below experimental strains of 8.8% (R_s=1.148) exhibit moderate to low strained extinction.

The thickness of the twin lamellae in the wet deformed samples ranges from 1 to 20 microns and are present as e_1 and e_2 twin sets. Most of the range of lamellae thicknesses are found to be between 1 to 5 microns. Samples that have deformed under wet experimental conditions exhibit twin lamellae that are not as sharp or as well developed as those observed in dry conditions. Often the twin lamellae are diffuse and discontinuous within the host calcite grain (Plate 4.3). Microtwins are observed as e_2 and e_3 twin sets, and are present in approximately 10% of the twinned calcite grains at 17.8% (R_s=1.342) shortening.

The frequency distribution of e_1-lamellae indices in wet pure shear for experimental strains of 6.8% (R_s=1.111), 10.9% (R_s=1.189) and 17.8% (R_s=1.342) shortening are presented in figure 4.9. From these histograms it is evident that there is a limited range of lamellae index values and a lack of the high lamellae indices that were observed in dry pure shear tests. The average lamellae index increases with increasing experimental strain from 49.3 (±30.1 s.d.) at 6.8% (R_s=1.111) to 83.4 (±23.8 s.d.) at 17.8% (R_s=1.342) shortening (Fig. 4.10).

The frequency distributions of e_2-lamellae indices in wet pure shear is presented in figure 4.11. The increase in the range of e_2-lamellae index is observed to a lesser degree than that observed in the distribution e_1. The average lamellae indices range from 23.8 L/mm (±12.9 s.d.) to 39.8 L/mm (±18.5

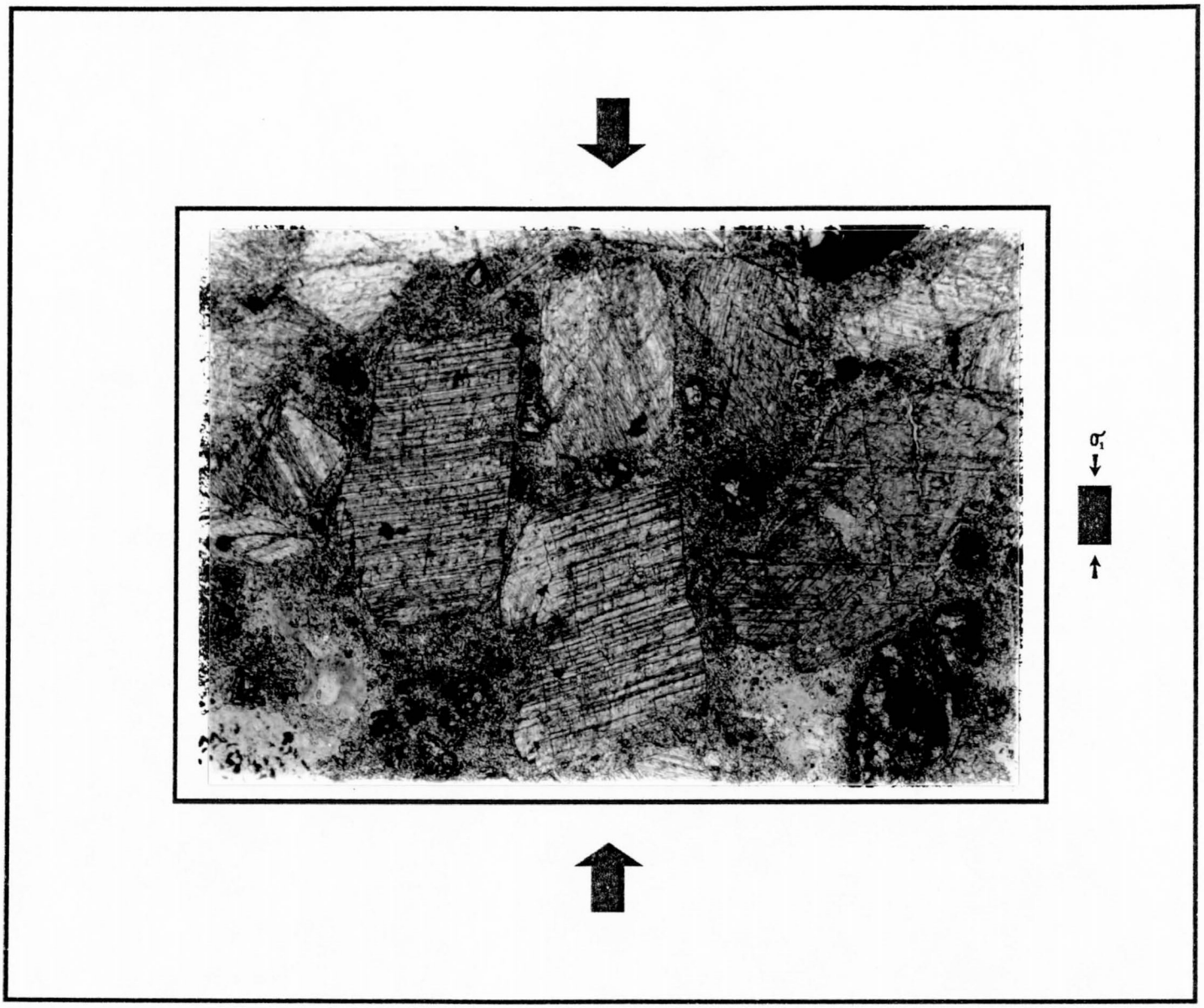

Plate 4.3 Microphotograph of twin lamellae in sample CPF-13 (e=17.86%) in the X/Z principal plane deformed by wet pure shear (P_f=200 Mpa, de/dt=10^{-5}/s). The majority of twin lamellae are orientated perpendicular to the σ_1 direction (note also the high lamellae index, approximately 80 L/mm). Broad arrows indicate orientation of the σ_1 during triaxial deformation. Photo taken in partial cross polarized light. (scale 38:1)

Figure 4.9 Frequency distribution of e_1-lamellae indices for individual calcite grains in the calcite Portland-cement aggregate. Samples were deformed by pure shear under wet experimental conditions (P_f=195 Mpa, de/dt=10^{-5}/s).

a) Sample CPF-12 (e=6.8% (R_s=1.111))
b) Sample CPF-04 (e=10.9% (R_s=1.189))
c) Sample CPF-13 (e=17.8% (R_s=1.342))

a)

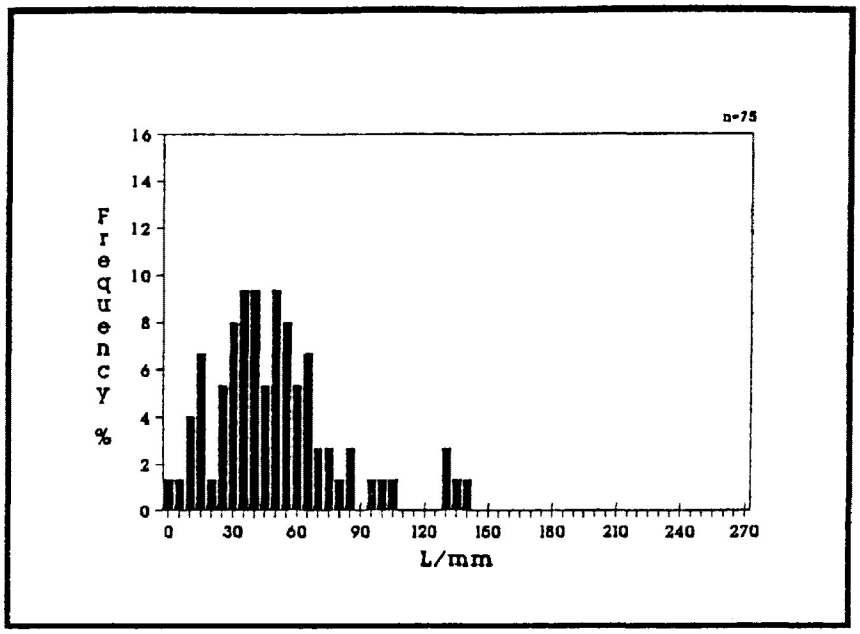
n=75
Frequency %
0
2
4
6
8
10
12
14
16
0 30 60 90 120 150 180 210 240 270
L/mm

b)

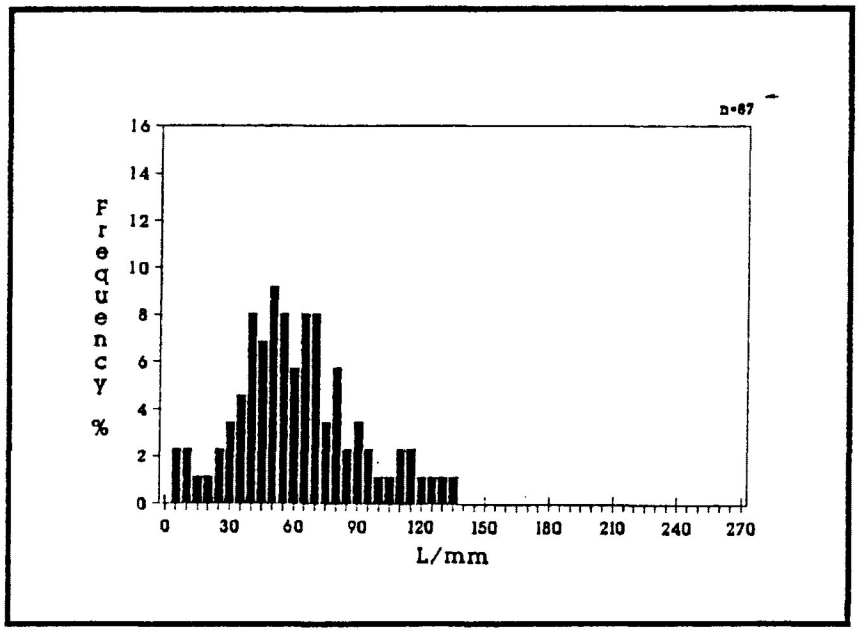
n=87
Frequency %
0
2
4
6
8
10
12
14
16
0 30 60 90 120 150 180 210 240 270
L/mm

c)

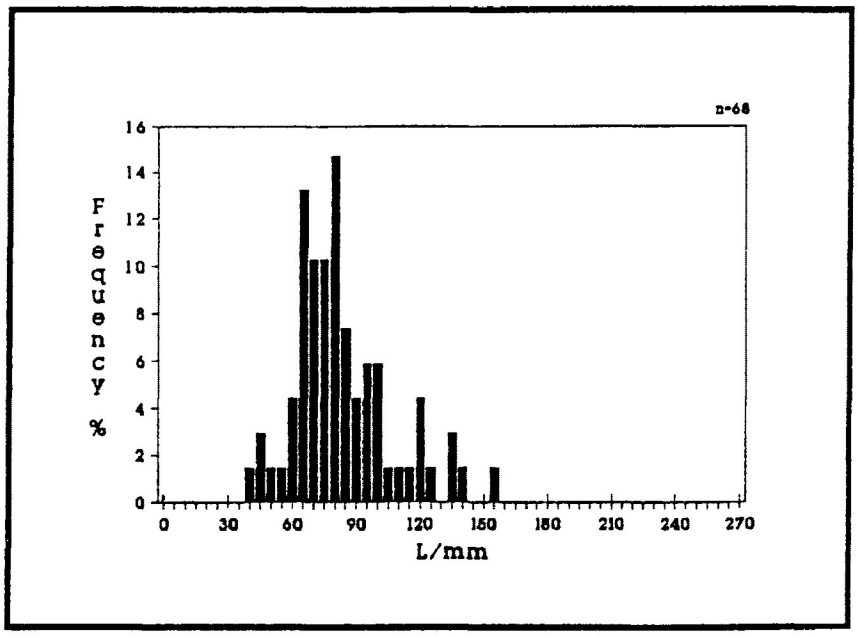
n=68
Frequency %
0
2
4
6
8
10
12
14
16
0 30 60 90 120 150 180 210 240 270
L/mm

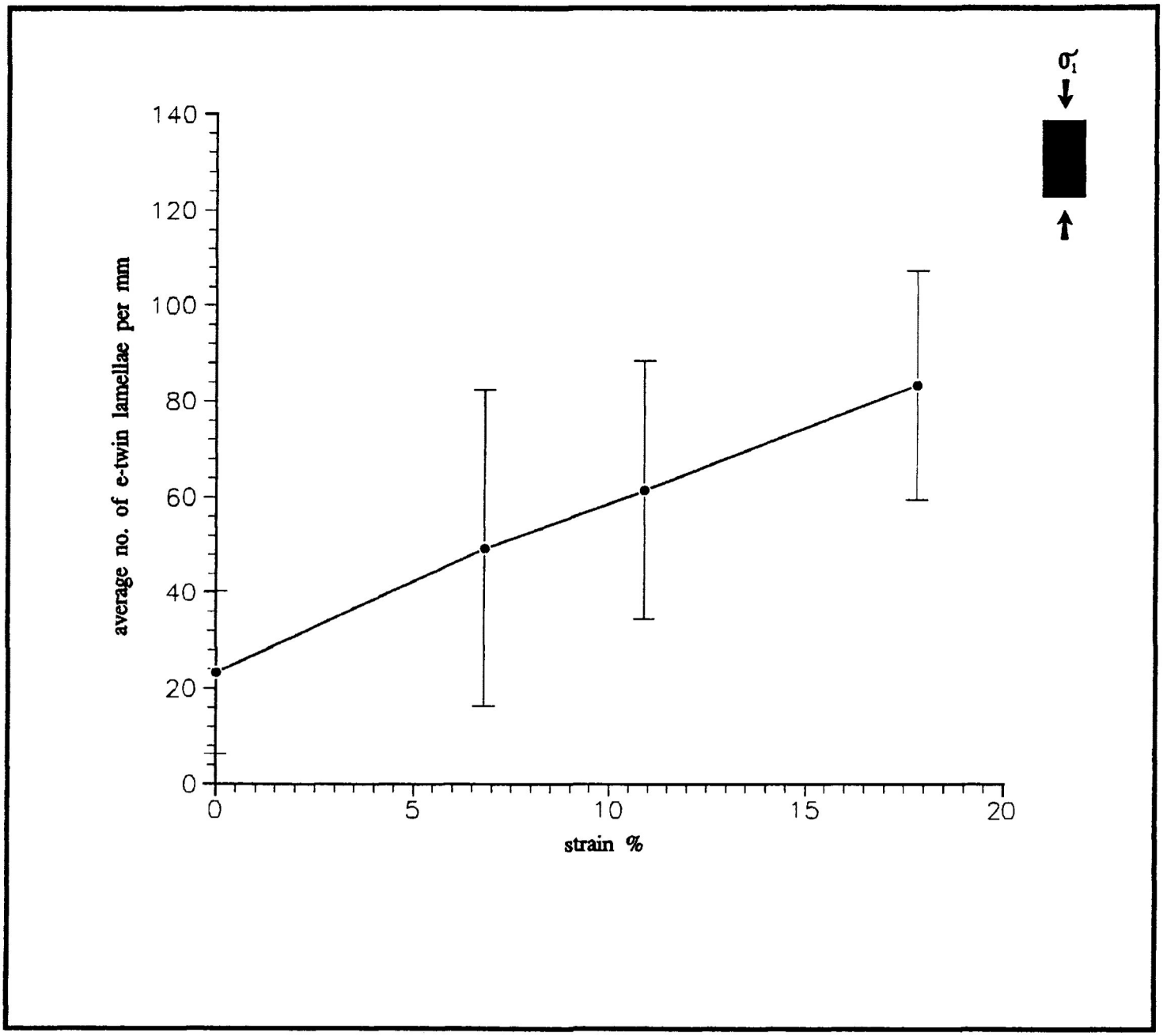

Figure 4.10 Variation in average e_1-lamellae index and associated standard deviation (error bars) for the frequency distribution of measurements on individual calcite grains. The samples were deformed by pure shear under wet experimental conditions (P_f=195 Mpa, de/dt=10^{-5}/s) for experimental strains of 0% (R_s=1.000), 6.8% (R_s=1.111), 10.9% (R_s=1.189) and 17.8% (R_s=1.342).

Figure 4.11 Frequency distribution of e_2-lamellae indices for individual calcite grains in the calcite cement aggregate deformed by pure shear under wet experimental conditions (P_f=195 Mpa, de/dt=10^{-5}/s).

a) Sample CPF-12 (e=6.8% (R_s=1.111))
b) Sample CPF-04 (e=10.9% (R_s=1.189))
c) Sample CPF-13 (e=17.8% (R_s=1.342))

a)

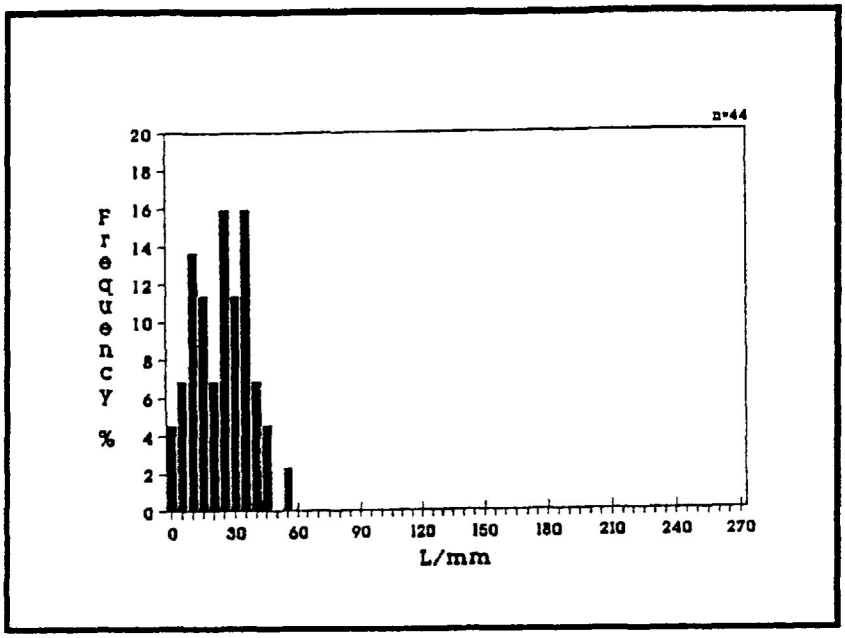
n=44
Frequency %
0
2
4
6
8
10
12
14
16
18
20
0
30
60
90
120
150
180
210
240
270
L/mm

b)

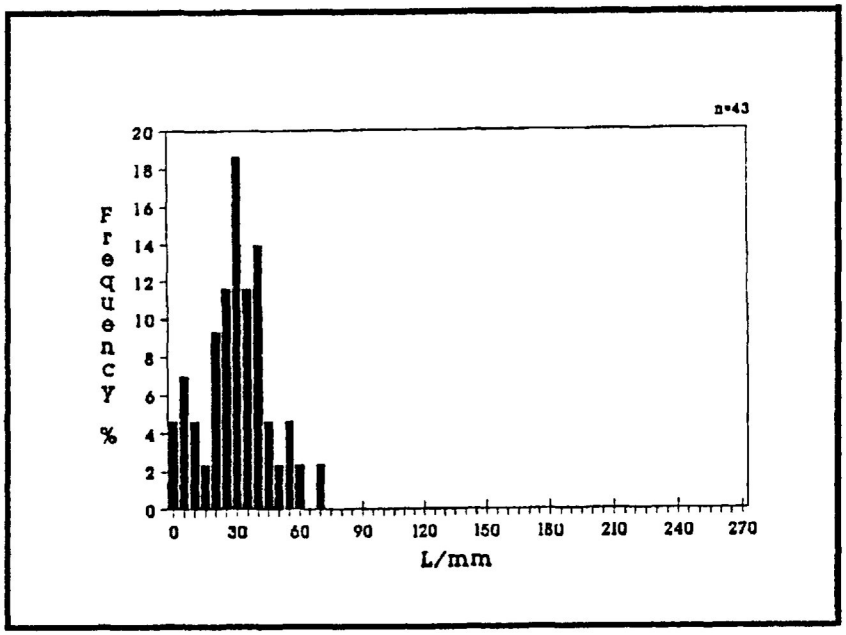
n=43
Frequency %
0
2
4
6
8
10
12
14
16
18
20
0
30
60
90
120
150
180
210
240
270
L/mm

c)

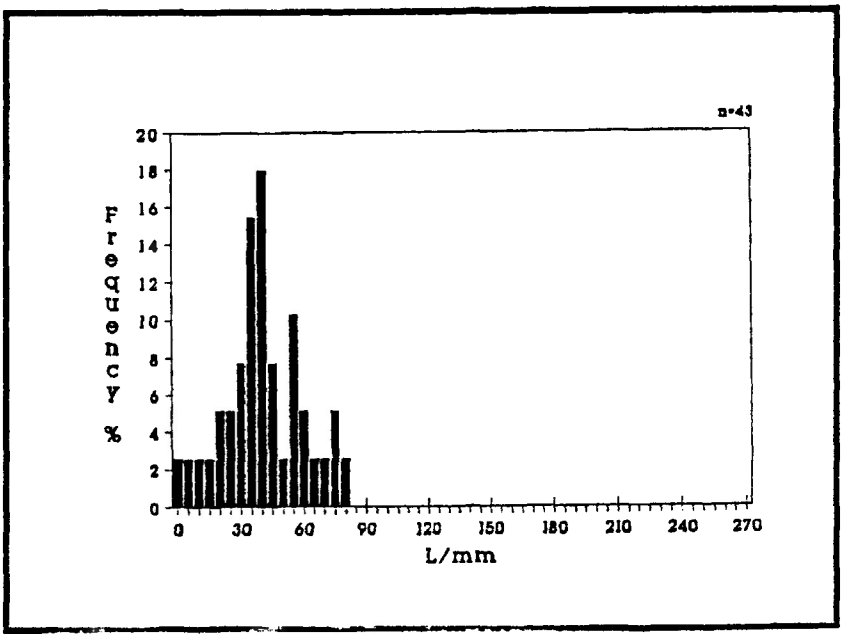
n=43
Frequency %
0
2
4
6
8
10
12
14
16
18
20
0
30
60
90
120
150
180
210
240
270
L/mm

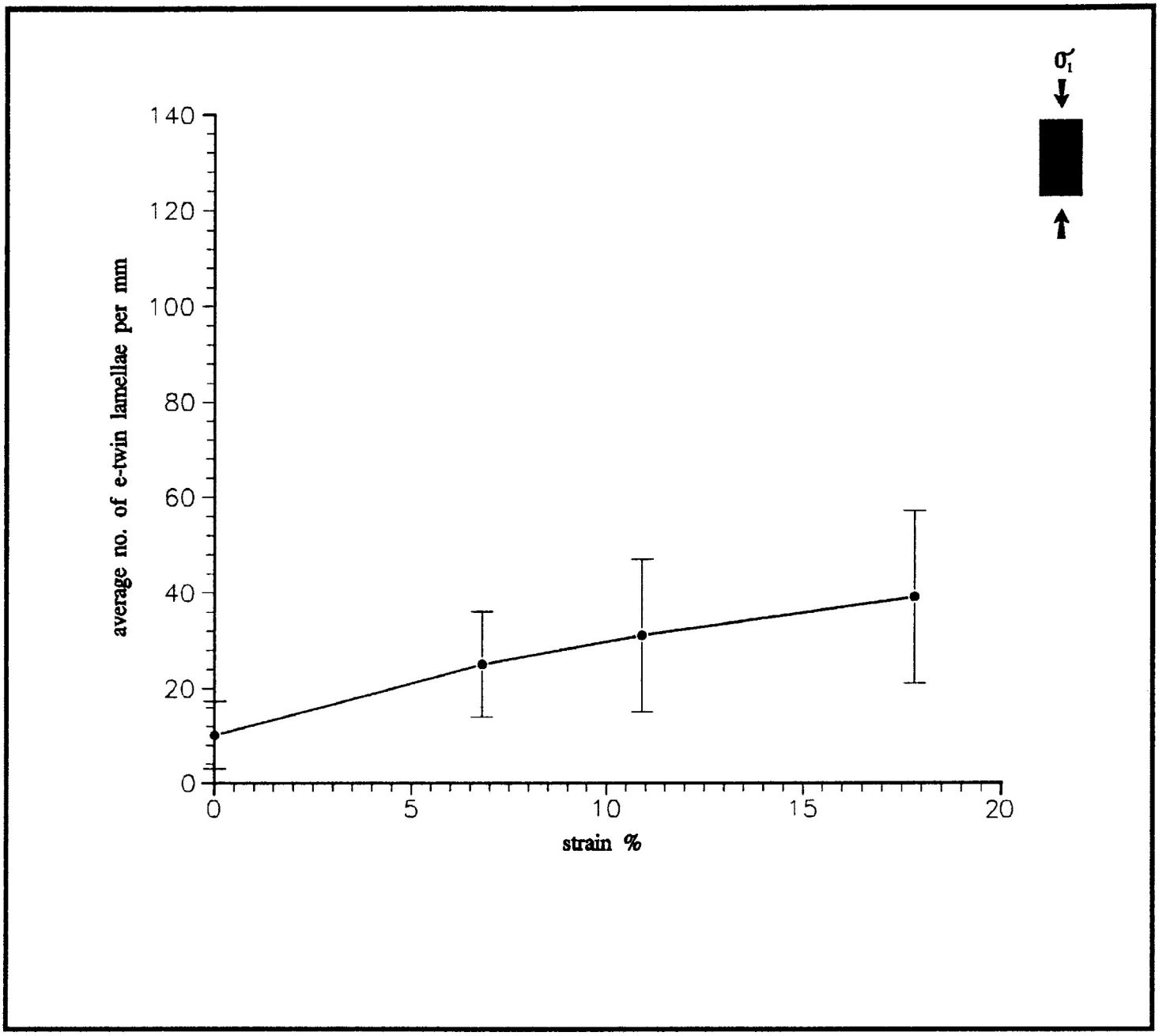

Figure 4.12 Variation in average e_2-lamellae index and associated standard deviation (error bars) for the frequency distribution of measurements on individual calcite grains. The samples were deformed by pure shear under wet experimental conditions (P_f=190 Mpa, de/dt=10^{-5}/s) for experimental strains of 0% (R_s=1.000), 6.8% (R_s=1.111), 10.9% (R_s=1.189) and 17.8% (R_s=1.342).

Figure 4.13 Variation in the percentage of grains that exhibit 1, 2 and 3 twin sets with increasing strain in wet pure shear experimental conditions (P_c=200 Mpa,P_f=190 Mpa, de/dt=10^{-5}/s)

a) Sample CPF-12 (e=6.8% (R_s=1.111))
b) Sample CPF-04 (e=10.9% (R_s=1.189))
c) Sample CPF-13 (e=17.8% (R_s=1.342))

a)

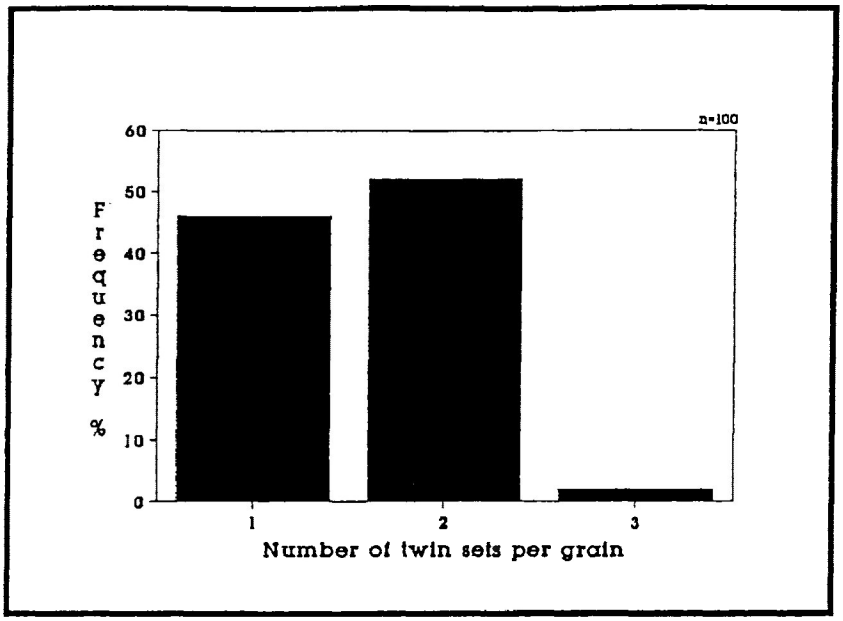
n=100
60
50
40
30
20
10
0
Frequency %
1
2
3
Number of twin sets per grain

b)

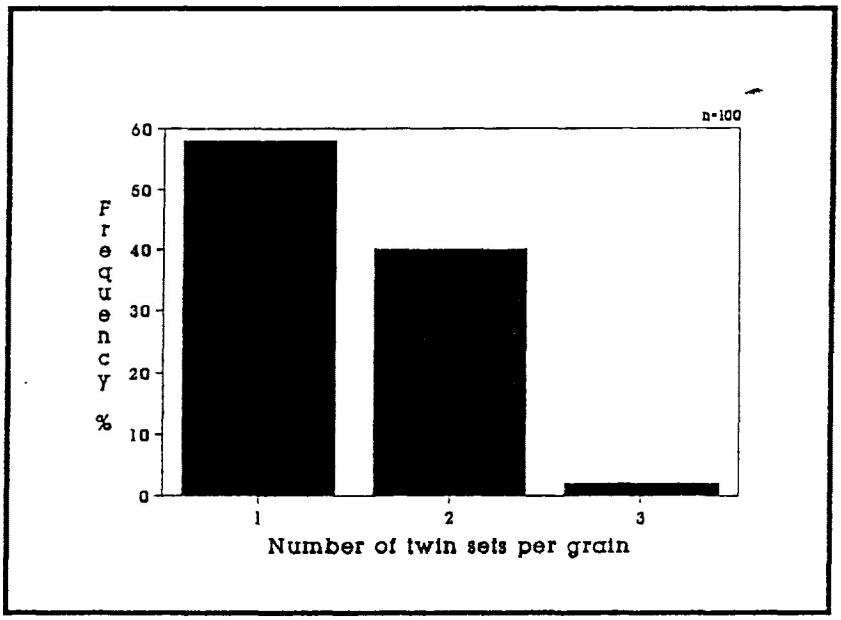
n=100
60
50
40
30
20
10
0
Frequency %
1
2
3
Number of twin sets per grain

c)

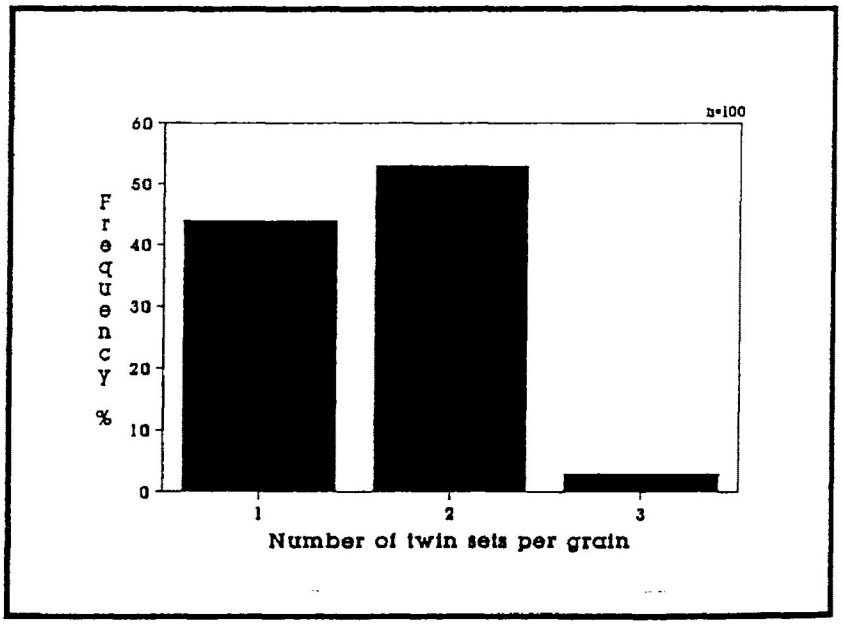
n=100
60
50
40
30
20
10
0
Frequency %
1
2
3
Number of twin sets per grain

s.d.) as the experimental strain increases from 6.8% (R_s=1.111) to 17.8% (R_s=1.342) shortening (Fig. 4.12).

Figure 4.13a-c illustrates the increasing development of calcite grains containing 2 twin sets for experimental strains of 6.8% (R_s=1.111) and 17.86% (R_s=1.342) shortening. There is also a slight increase in the development of calcite grains containing three twin sets.

Progressive deformation under wet conditions is also reflected by the development of kink and deformation bands. There are noticeably more calcite grains exhibiting kink band and deformation bands at experimental strains of 10.9% (R_s=1.189) than in the dry tests. The kink bands are concentrated in the central portion of the thin-section and tend to have a wide range of orientations. At higher experimental strain these kink bands increase in number and exhibit bending. Bending of twin lamellae is also observed to a greater degree than that of the dry experimental conditions. The combination of bending of kink and twinning lamellae leads to cataclasis of some calcite grain. A small zone of cataclastic flow in the centre of the thin-section is first observed at 10.9% (R_s=1.189) shortening.

d) <u>Transpressional Shear (Dry tests) in oblique shear zones</u>

At low experimental shear strains of 0.051 (sample SZ-C4) approximately 85% of the calcite grains are twinned by 1 to 2 twin sets. The remaining 15% of calcite grains are not twinned but show strained extinction. At slightly higher experimental shear strains of 0.111, 0.129 and 0.189 approximately 100% of the calcite grains are twinned. The variation in the percentage of calcite grains that are twinned with increasing experimental shear strain is presented in figure 4.14. A micrograph of sample SZ-C3-1 (shear

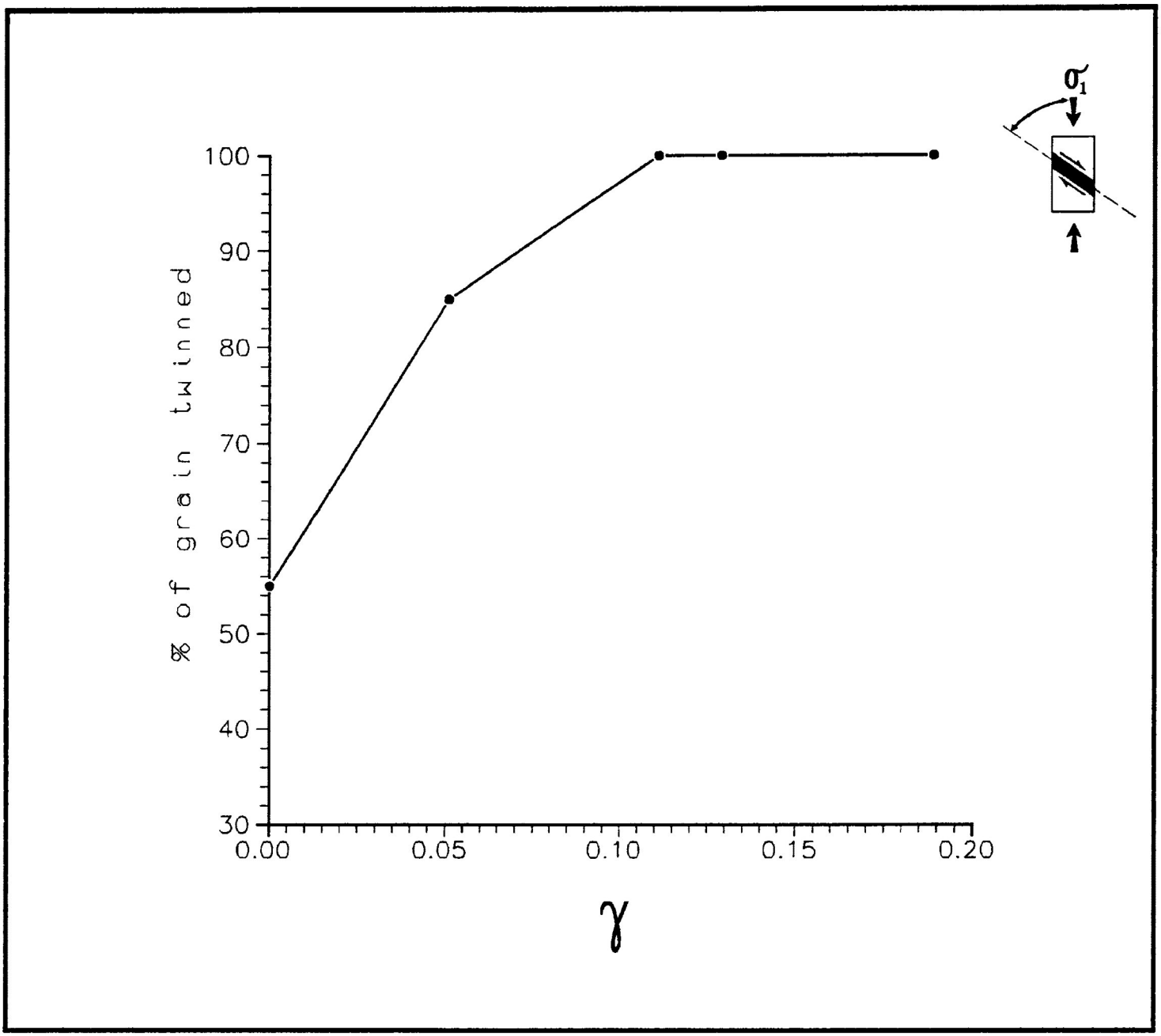

Figure 4.14 Percentage of calcite grains in total aggregate that exhibit twinning in oblique shear zone under dry experimental conditions (P_c=200 Mpa, de/dt=10^{-5}/s) for experimental shear strain of 0.000, 0.111, 0.129 and 0.189.

strain=0.111), for the centre area of the XZ principal plane, is presented in Borradaile and McArthur (1990, Fig. 5b).

The twin lamellae range in thickness from 1 to 10 microns with the majority being less than 2 microns thick. This decrease in the thickness of the lamellae is reflected in an increase in the lamellae index with increasing experimental shear strain. The individual lamellae, present in calcite grains as e_1 and e_2 twin sets, were sharp and well developed (Plate 4.4). Approximately 30% of the calcite grains exhibit microtwins as e_2 and e_3 twin sets and to a lesser degree as e_1 at an experimental shear strain of 0.189.

The frequency distributions of the e_1-lamellae index for calcite grains in sample SZ-C4 is presented in figure 4.15a. In the figure it is evident that the lamellae index values are skewed to the lower end of the lamellae index range reflecting the low experimental shear strain (0.051). The average lamellae index is 55 L/mm (±37.1 s.d.). At higher experimental shear strains frequency distributions of the e_1-lamellae index for calcite grains is presented in figure 4.15b-d. In each of these histograms there is a wide range of twinning deformation which is consistent throughout the transpressional deformation. Figure 4.16 illustrates an increase in the average lamellae index from 55 L/mm (±49.4 s.d.) to 116 L/mm (±45.9 s.d.) at experimental shear strains of 0.051 to 0.189, respectively.

The frequency distribution of e_2-twin lamellae index is presented in figure 4.17. In these histograms it is apparent that the e_2-lamellae are less dominant than the e_1-lamellae. However, as presented in figure 4.18, there is an increase in the average lamellae index from 28.3 L/mm (±19.0 s.d.) at a shear strain of 0.051 to 47.1 L/mm (±18.5 s.d.) at 0.189. The average e_2-lamellae index is higher in the transpressional

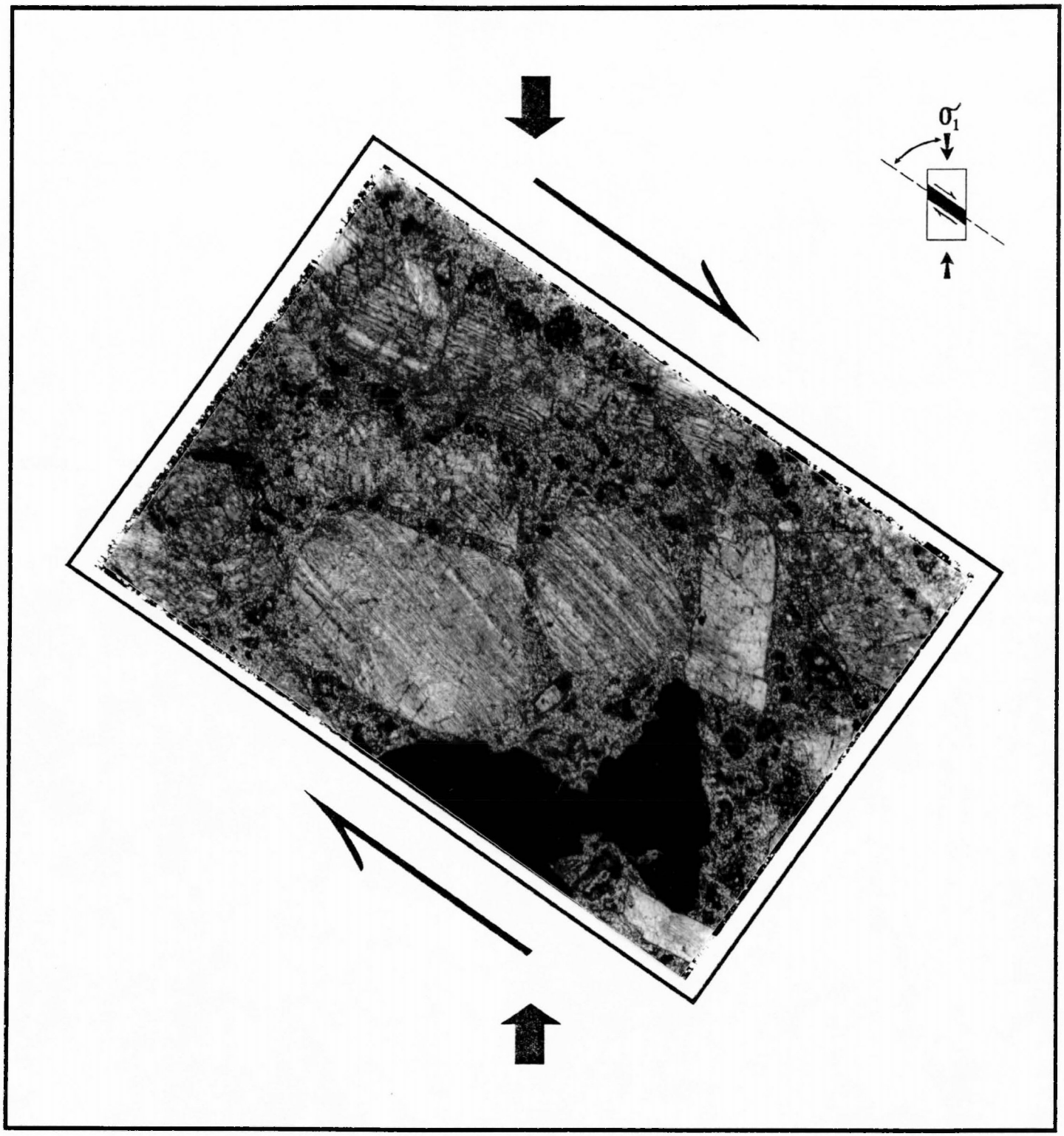

Plate 4.4 Microphotograph of twin lamellae in sample SZ-C1 (shear strain=0.111) in the X/Z principal plane. Sample deformed by dry transpressional shear in an oblique shear zone (P_c=200 Mpa, de/dt=10^{-5}/s). Note majority of twin lamellae are parallel to the direction of shear. Broad arrows indicate orientation of the σ_1 during triaxial deformation and small arrows indicate the direction of shear. shear. Photo taken in partial cross polarized light. (scale 38:1)

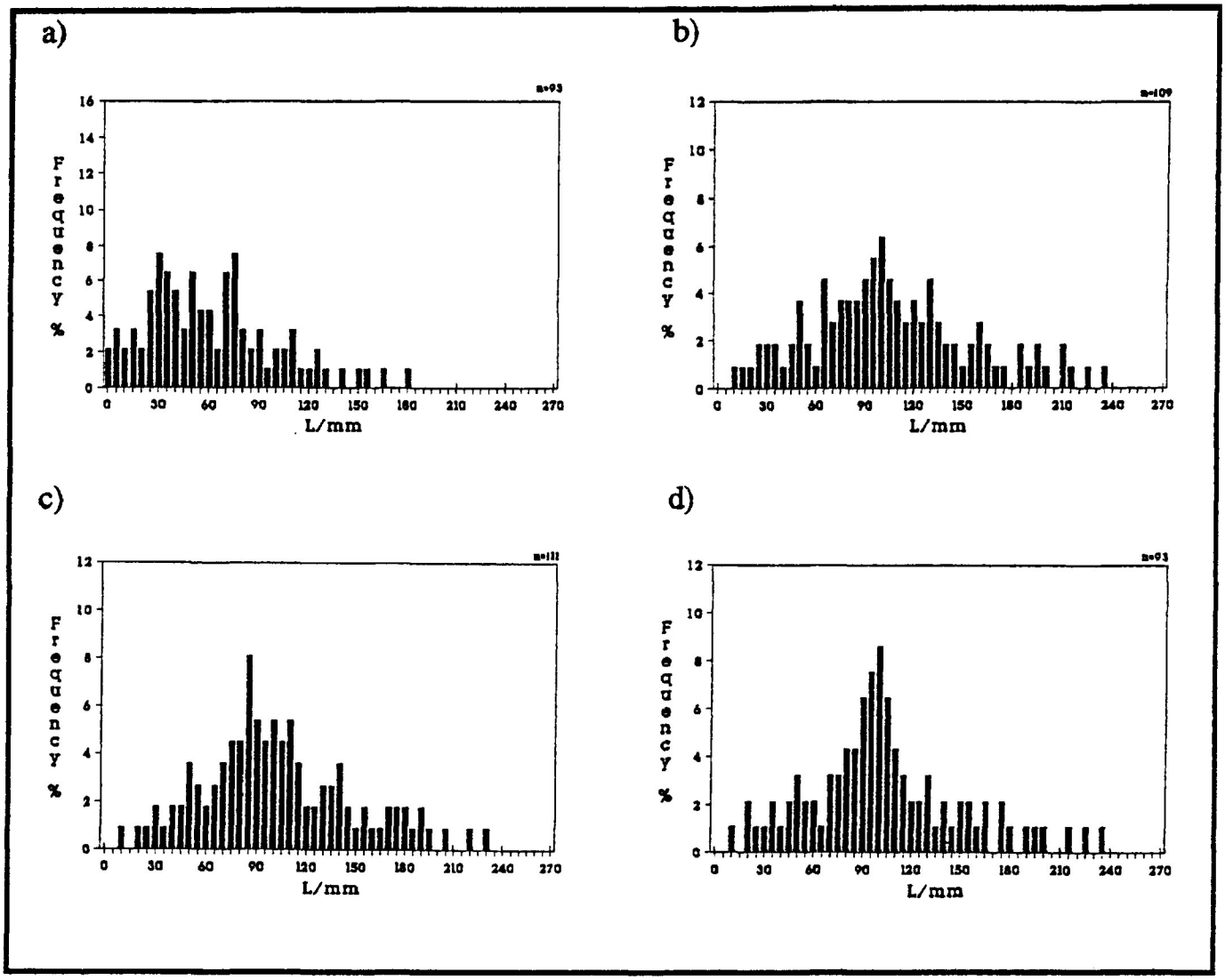

Figure 4.15 Frequency distribution of e_1-lamellae indices for individual calcite grains in the calcite cement aggregate. Samples were deformed in an oblique shear zone under dry experimental conditions (P_c=200 Mpa, $de/dt=10^{-5}$/s).

a) Sample SZ-C4 shear strain=0.051
b) Sample SZ-C1 shear strain=0.111
c) Sample SZ-C3 shear strain=0.129
d) Sample SZ-C3-1 shear strain=0.189

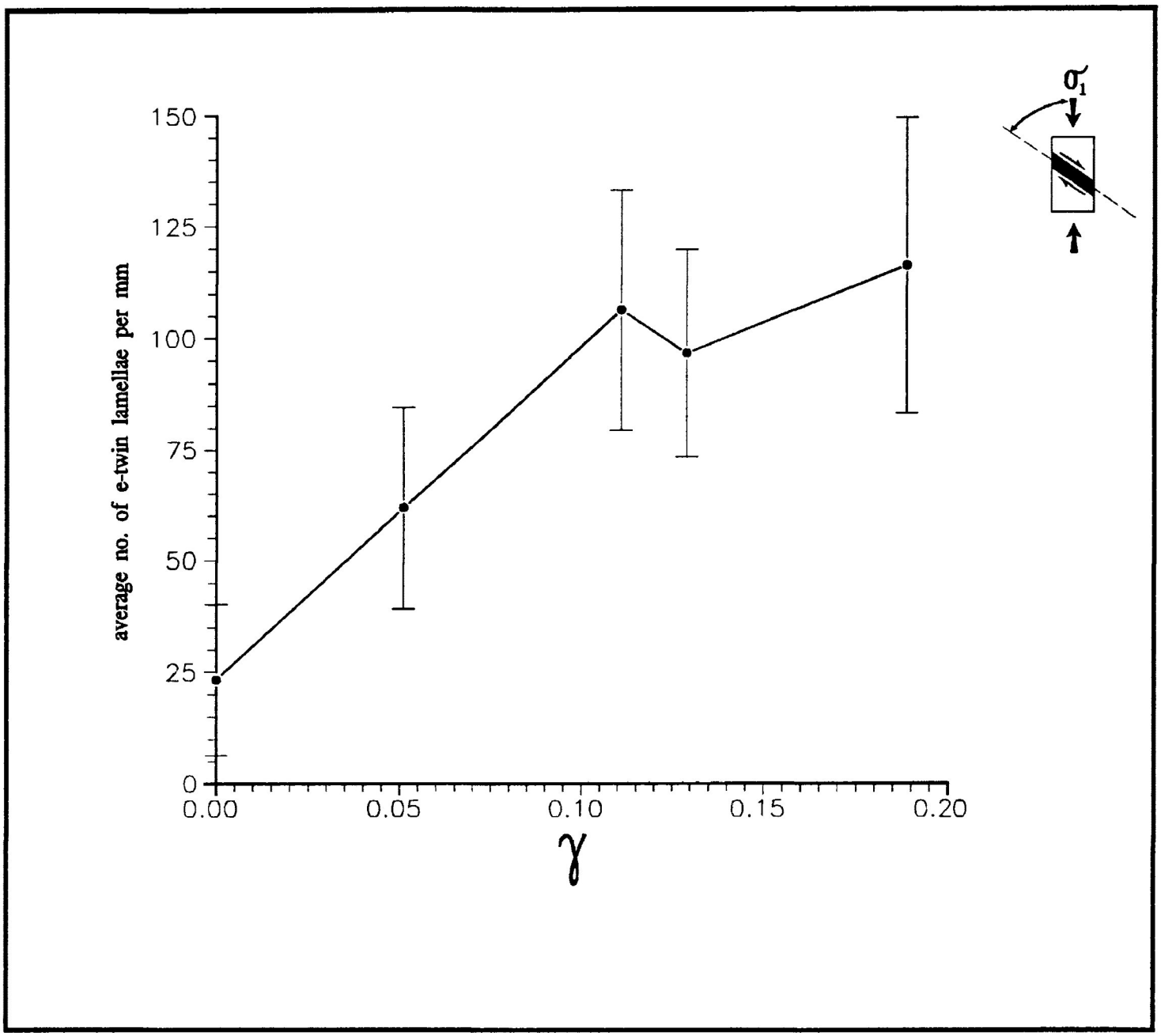

Figure 4.16 Variation in average e_1-lamellae index and associated standard deviation (error bars) for the frequency distribution of measurements on individual calcite grains. The samples were deformed in an oblique shear zone under dry experimental conditions (P_c=200 Mpa, de/dt=10^{-5}/s) for experimental shear strain of 0.051, 0.111, 0.129 and 0.189.

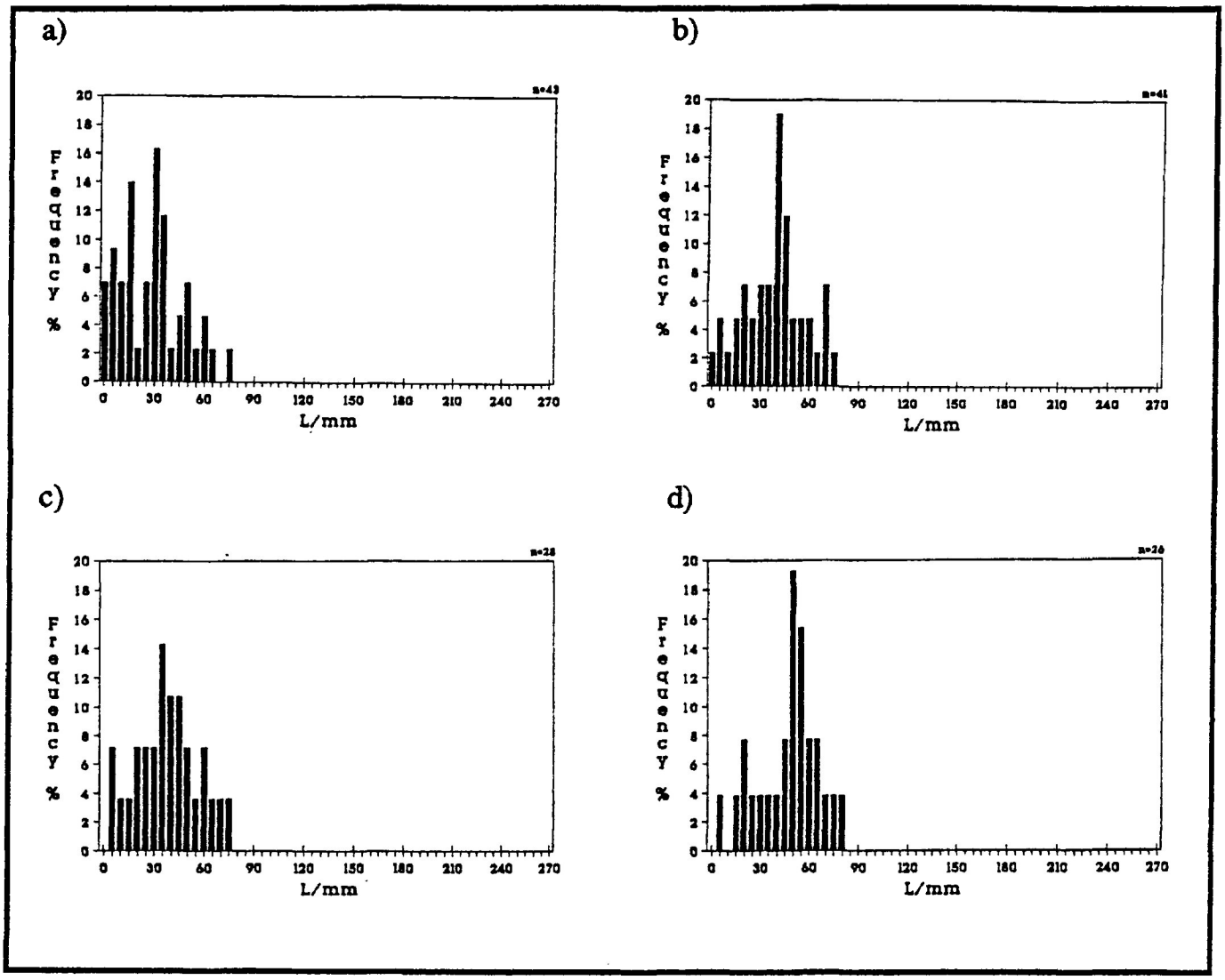

Figure 4.17 Frequency distribution of e_2-lamellae indices for individual calcite grains in the calcite cement aggregate. Samples were deformed in an oblique shear zone under dry experimental conditions (P_c=200 Mpa, $de/dt=10^{-5}$/s).

a) Sample SZ-C4 shear strain=0.051
b) Sample SZ-C1 shear strain=0.111
c) Sample SZ-C3 shear strain=0.129
d) Sample SZ-C3-1 shear strain=0.189

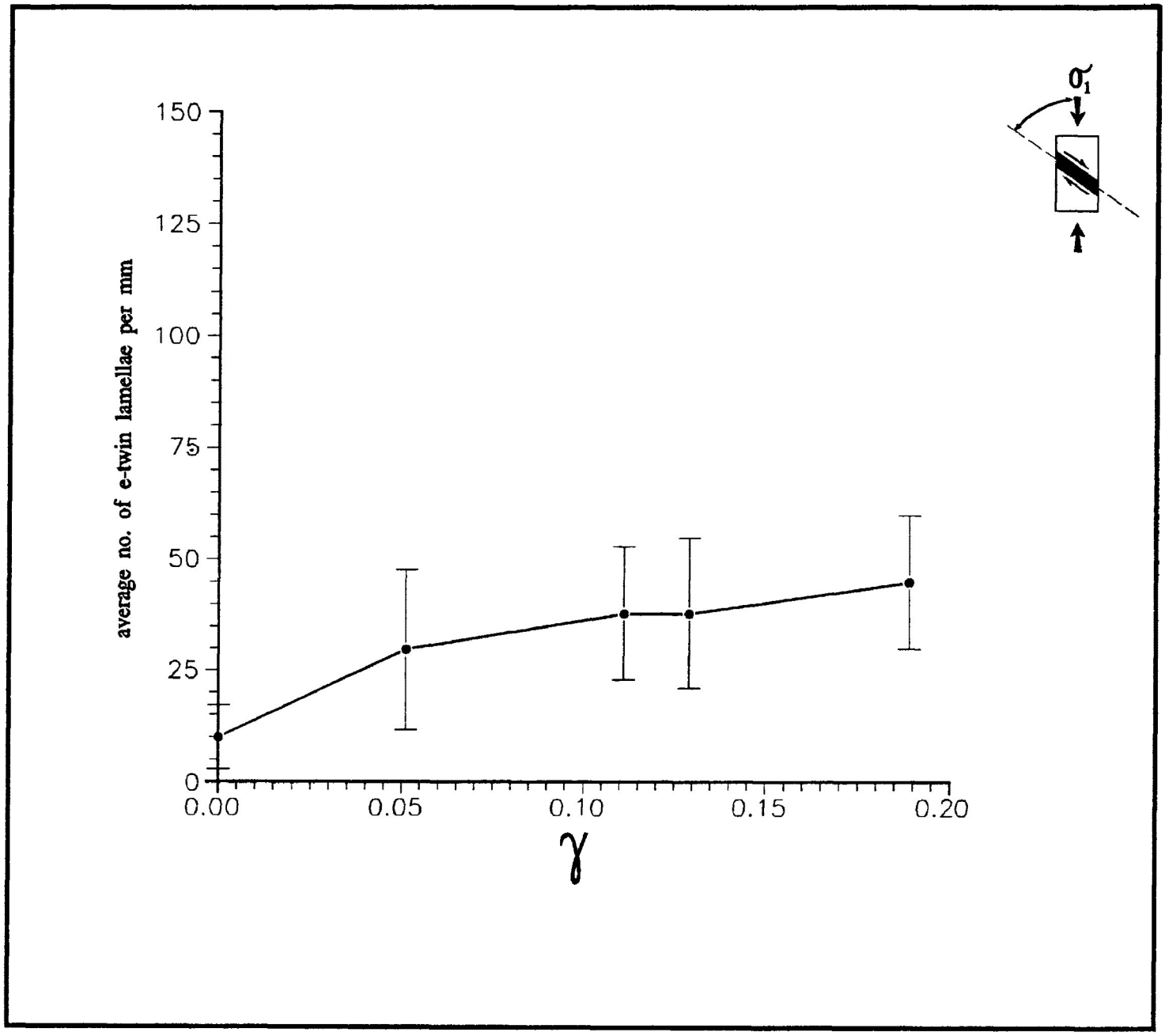

Figure 4.18 Variation in average e_2-lamellae index and associated standard deviation (error bars) for the frequency distribution of measurements on individual calcite grains. The samples were deformed in an oblique shear zone under dry experimental conditions (P_c=200 Mpa, de/dt=10^{-5}/s) for experimental shear strain of 0.051, 0.111, 0.129 and 0.189.

shear experiments compared with that of pure shear under dry and wet conditions.

Figure 4.19 illustrates the variation in development of calcite grains containing 2 twin sets for increasing experimental shear strain. From this figure it is observed that at low experimental shear strains the number of calcite grains exhibiting 2 twin set increases to a greater extent than that of pure shear. However, at strains where the development of a strong preferred dimensional orientation (PDO) is evident the number of calcite grains containing 2 twin sets decreases with the increased dominance of grains containing only e_1 parallel to the shear zone walls.

Samples that have been deformed by transpressional shear exhibit an increase in the percentage of calcite grains that have developed kink and deformation bands compared with that observed in dry and wet pure shear experiments. In strained samples for experimental shear strains of 0.111 to 0.189 approximately 5% of the calcite grains contain kink bands. The majority of kink bands in the least deformed of these samples (SZ-C1) are oriented within 30° of the known compression direction and are skewed towards the perpendicular to the shear zone wall in the direction of shear (Fig. 4.20). The kink bands appear to develop in calcite grains that have twin lamellae parallel and perpendicular to the walls of the shear zone.

In higher experimental strained sample (SZ-C3-1, shear strain of 0.189) there is observed a rotation of the kink bands, so they are oriented within 50° of the known σ_1 orientation (Fig. 4.21). A larger number of calcite grains display bending of twin lamellae compared with that observed in the dry and wet pure shear experimental tests. Often the twin lamellae are sigmoidally bent in a way that represents

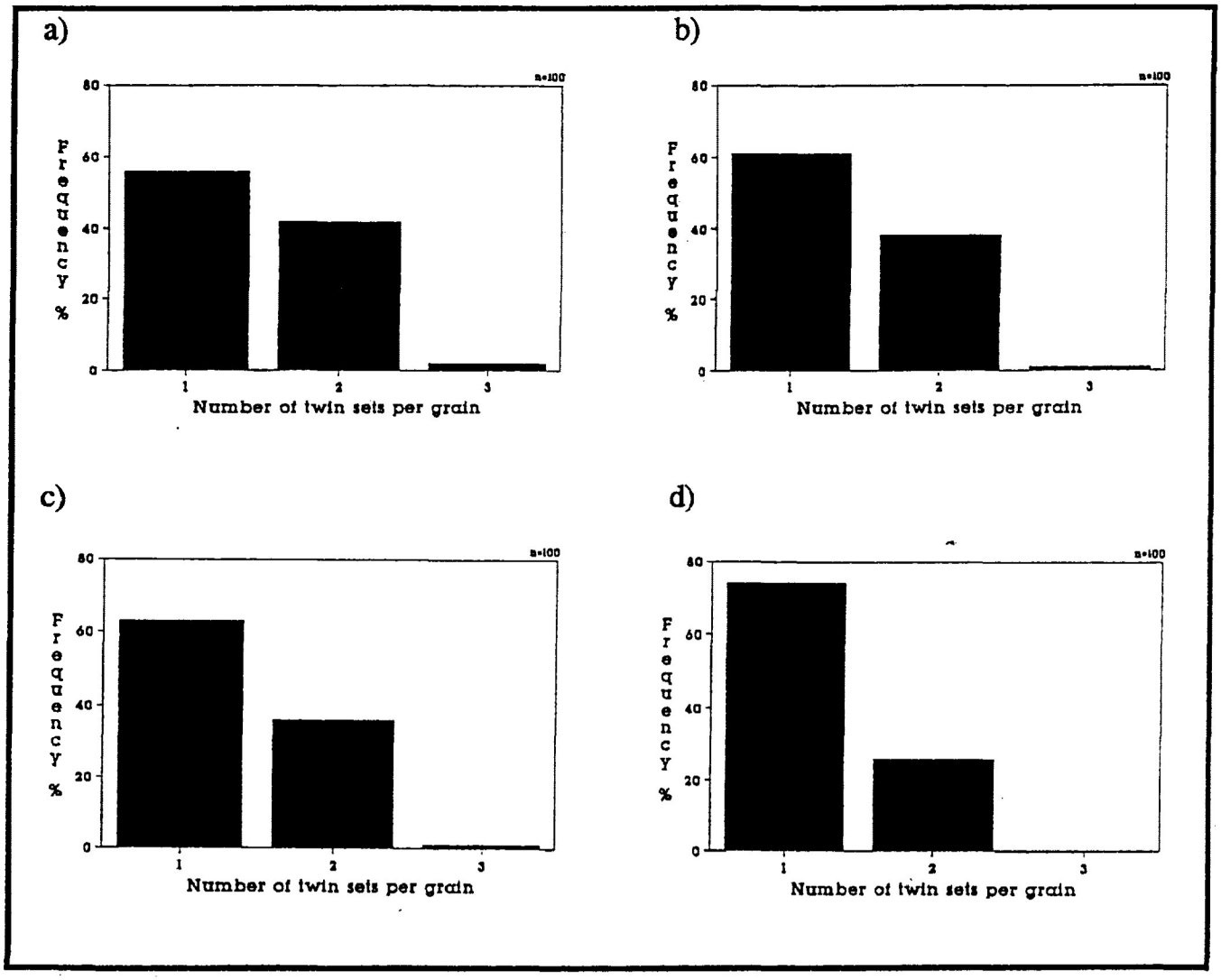

Figure 4.19 Variation in the percentage of grains that exhibit 1, 2 and 3 twin sets with increasing experimental shear strain in the oblique shear zone under dry experimental conditions (P_c=200 Mpa, de/dt=10^{-5}/s)

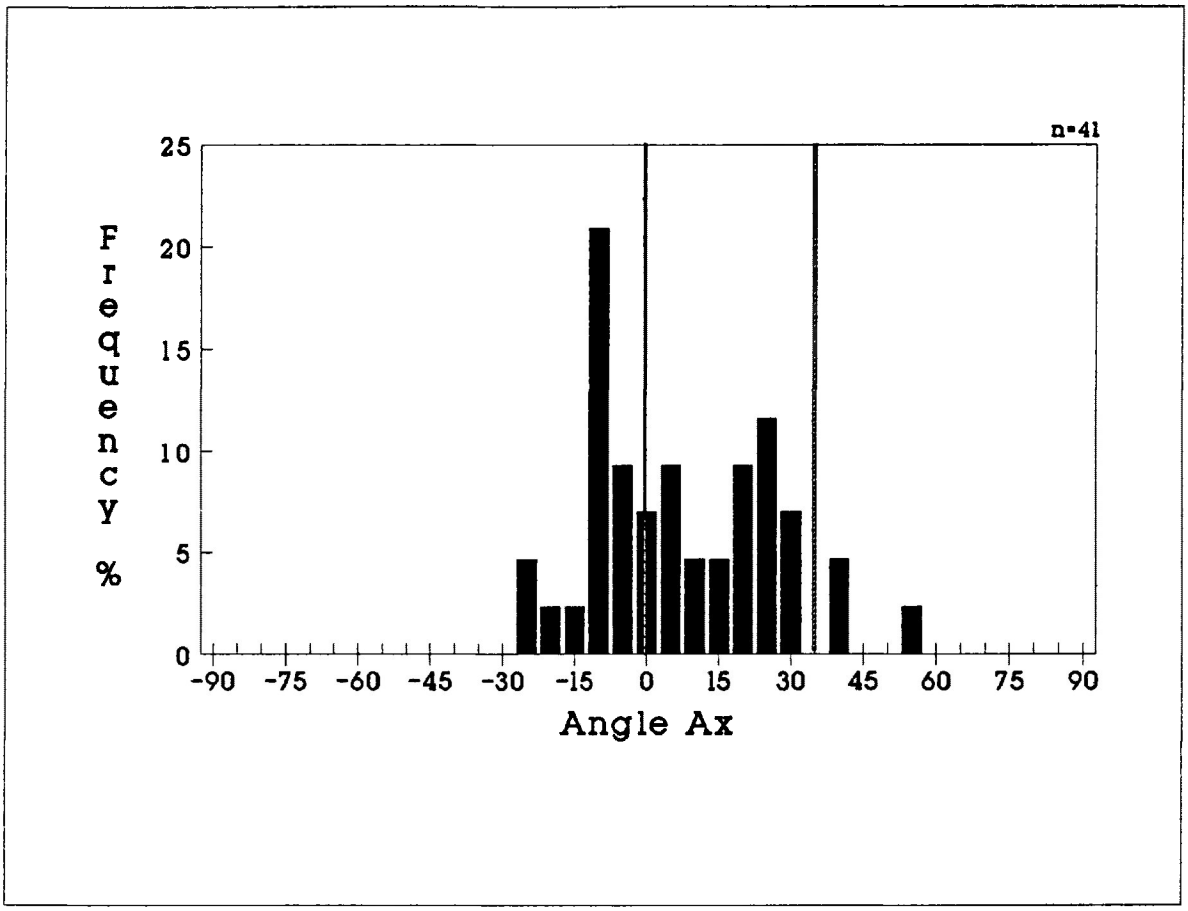

Figure 4.20 Orientational frequency of kink bands in calcite grains within the oblique shear zone of sample SZ-C1, shear strain=0.111. Solid line represents the orientation of σ_1 at 0° and the dash line represents the orientation of the perpendicular to the shear direction. Sample were deformed under dry experimental conditions (P_c=200 Mpa, de/dt=10^{-5}/s).

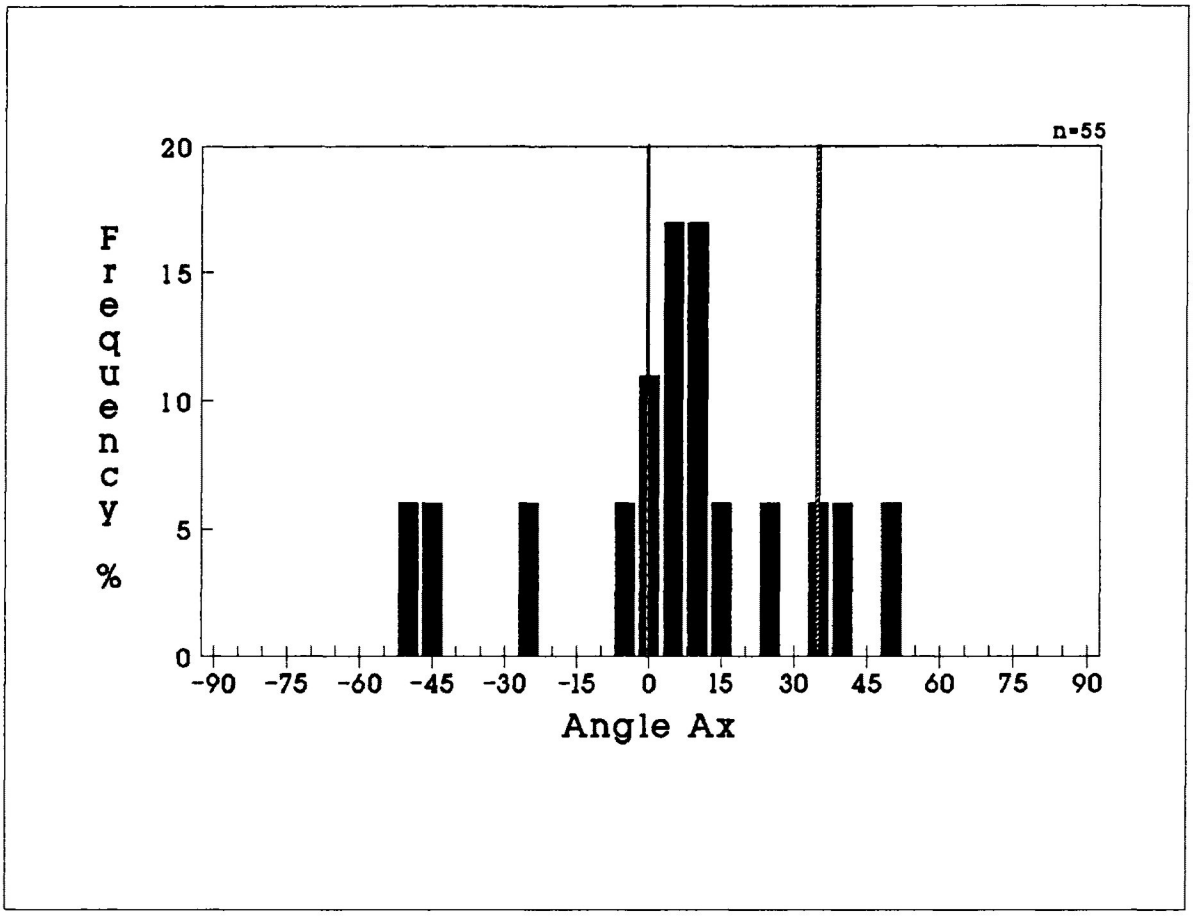

Figure 4.21 Orientational frequency of kink bands in calcite grains within the oblique shear zone of sample SZ-C3-1, shear strain=0.189. Solid line represents the orientation of σ_1 at 0° and the dash line represents the orientation of the perpendicular to the shear direction. Sample deformed under dry experimental conditions (P_c=200 Mpa, de/dt=10^{-5}/s).

the sense of shear imposed on the sample. The combination of bending of kink bands and twin lamellae has produce cataclasis in some calcite grains (approximately 5%) at higher strains.

e) Simple Shear (longitudinal shear zones 2 and 5 mm wide)

i) 2 mm Shear Zone

In simple shear for 2 mm longitudinal shear zones there is no notable increase in the percentage of calcite grains that are twinned as the experimental shear strain increases from 0.23 to 1.00 (Samples LS8811 and LS8807, respectively). The number of calcite grains that are twinned in the deformed state are approximately 75 to 80%; an increase of 36 to 45% over the original undeformed state. The calcite grains that are not twinned at the above range of experimental shear strains exhibit little or no strained extinction (Borradaile and McArthur, 1990 (Fig 5c)).

The thickness of the twin lamellae in the deformed samples ranged from 1 to 20 microns and were present as e_1 and e_2 twin sets. The individual lamellae were sharp and well developed. Microtwins were also observed, usually as e_2 and e_3 twin sets, and are present in approximately 5% of the twinned calcite grains.

The frequency distributions of e_1-lamellae indices in simple shear, for experimental shear strains of 0.23 and 0.933, is presented in figure 4.22. From the histograms it is evident that twinning involved in the simple shear deformation is not as extreme as that observed in dry and wet pure shear or transpressional shear. The average lamellae indices are relatively constant through the deformation with values of 51.1 L/mm (±17.2 s.d.) and 58.9 L/mm (±16.6 s.d.) for experimental shear strains of 0.023 and 0.933 respectively

a)

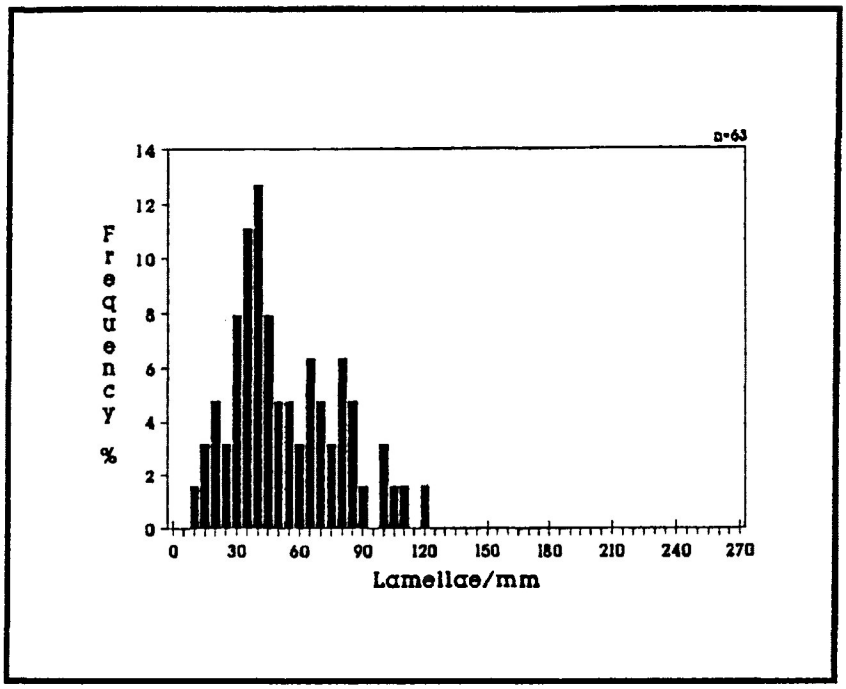

b)

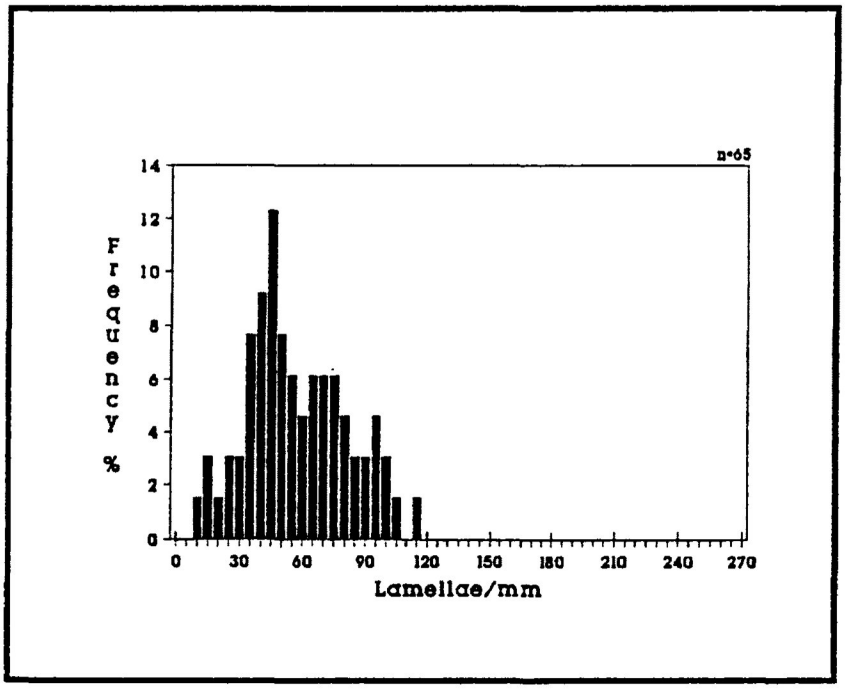

Figure 4.22 Frequency distribution of e_1-lamellae indices for individual calcite grains in the calcite cement aggregate. Samples were deformed in 2mm thick longitudinal shear zones by simple shear under dry experimental conditions (P_c=200 Mpa, $de/dt=10^{-5}$/s).

a) Sample LS8811 shear strain=0.23
b) Sample LS8807 shear strain=0.933

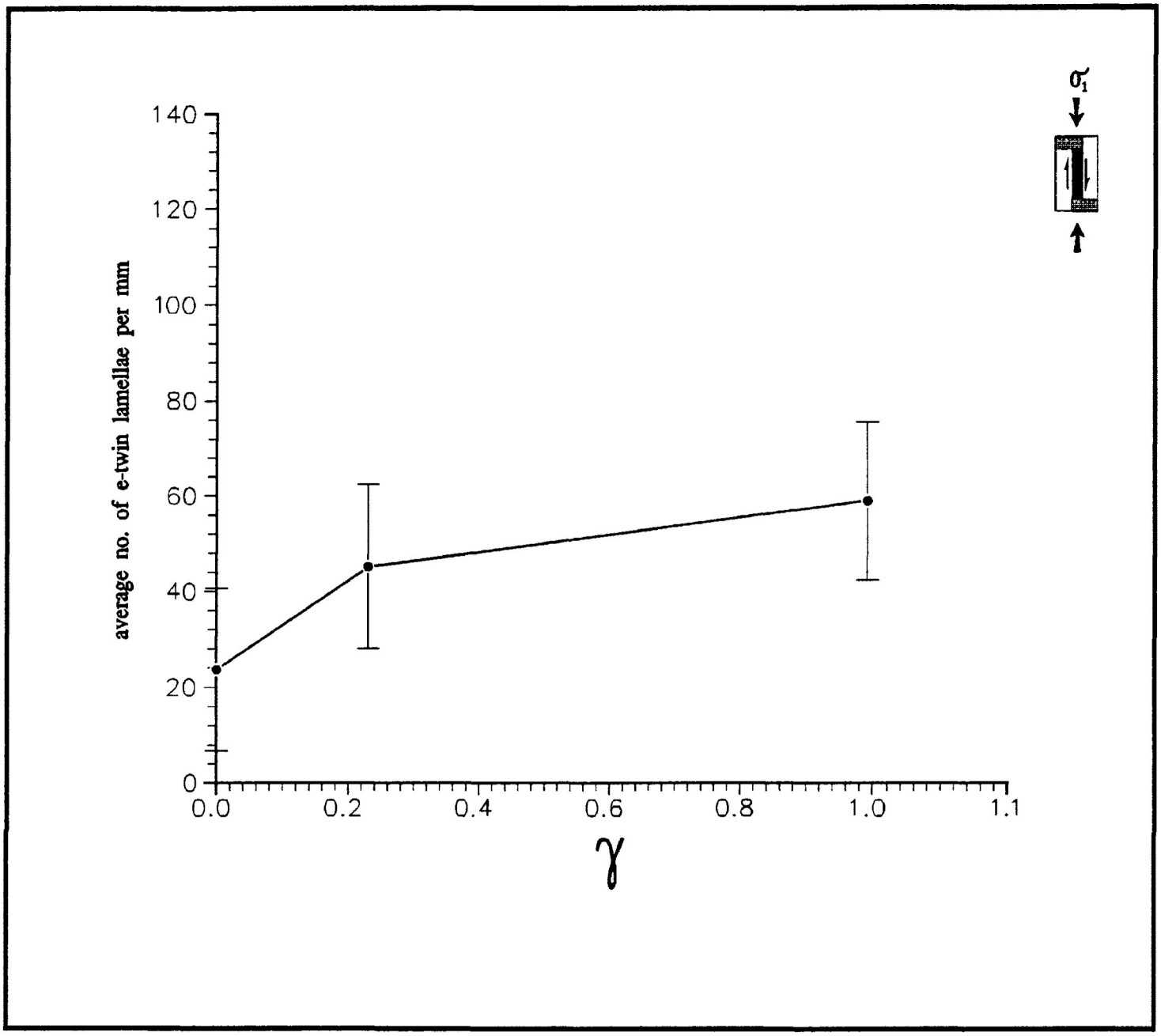

Figure 4.23 Variation in average e_1-lamellae index and associated standard deviation (error bars) for the frequency distribution of measurements on individual calcite grains. The samples were deformed by simple shear in 2mm thick longitudinal shear zones under dry experimental conditions (P_c=200 Mpa, de/dt=10^{-5}/s) for experimental shear strain of 0.23 and 0.933.

a)

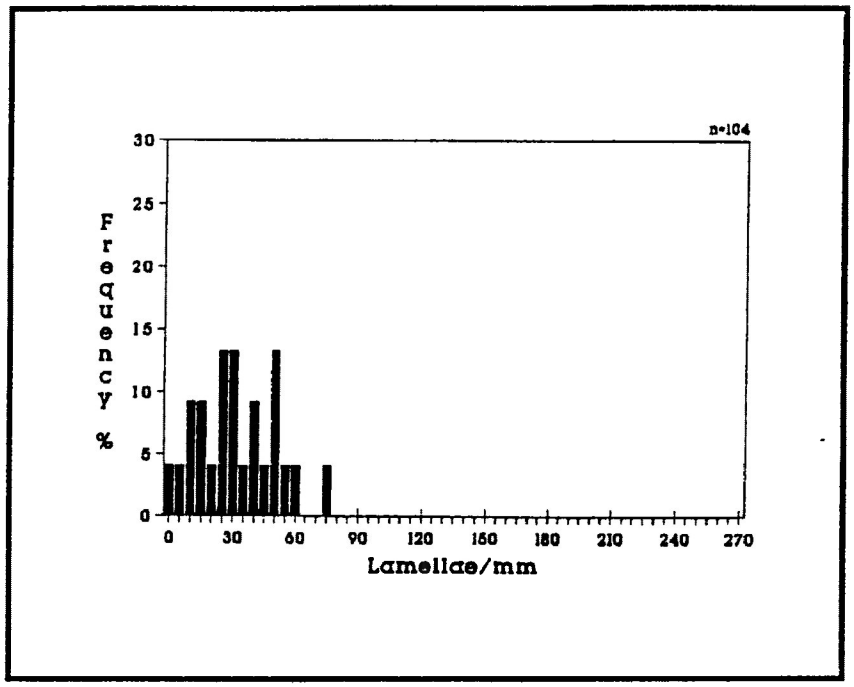

b)

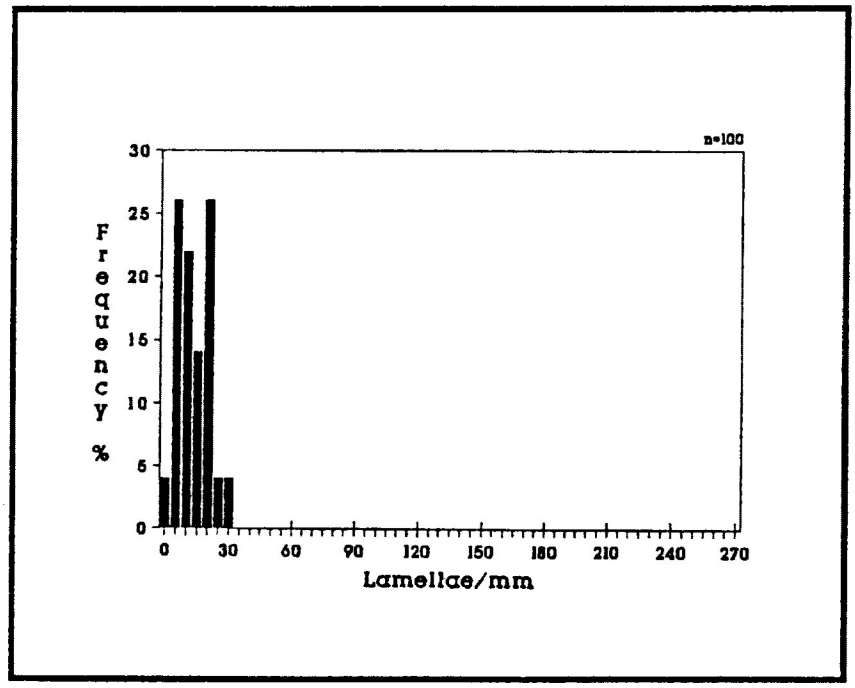

Figure 4.24 Frequency distribution of e_2-lamellae indices for individual calcite grains in the calcite cement aggregate. Samples were deformed in 2mm thick longitudinal shear zones by simple shear under dry experimental conditions (P_c=200 Mpa, de/dt=10^{-5}/s).

a) Sample LS8811 shear strain=0.23
b) Sample LS8807 shear strain=0.933

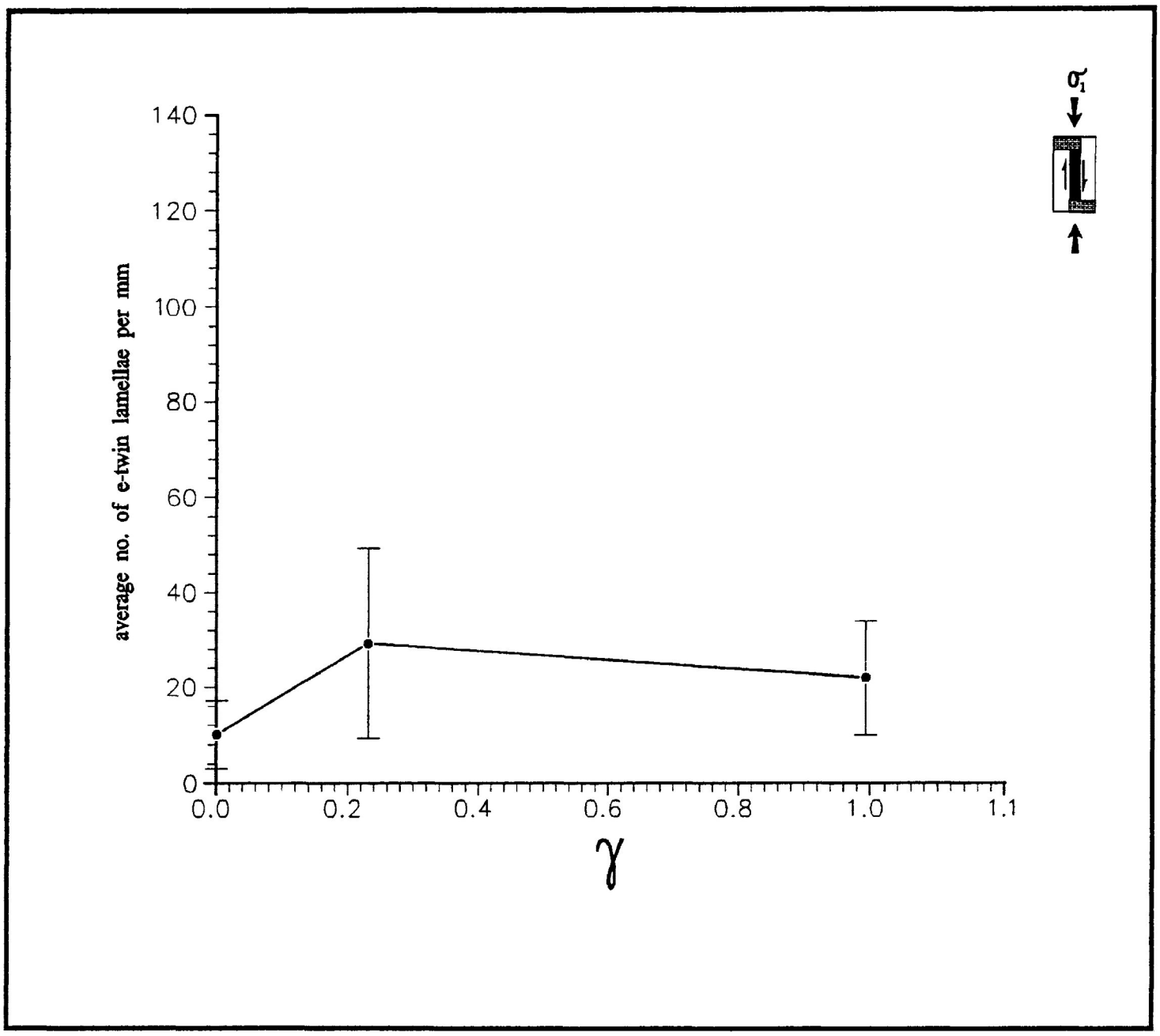

Figure 4.25 Variation in average e_2-lamellae index and associated standard deviation (error bars) for the frequency distribution of measurements on individual calcite grains. The samples were deformed by simple shear in 2mm thick longitudinal shear zones under dry experimental conditions (P_c=200 Mpa, de/dt=10^{-5}/s) for experimental shear strain of 0.23 and 0.933.

(Fig. 4.23). Frequency distributions of e_2-lamellae indices in simple shear are presented in figure 4.24. The average lamellae indices range from 29.3 L/mm (±20.1 s.d.) to 22.0 L/mm (±12.0 s.d.) (Fig. 4.25).

Kink band development during the simple shear deformation did not occur within the range of experimental shear strains studied. Bending of twin lamellae is not observed in the deformed samples.

ii) 5 mm Longitudinal Shear Zones

In simple shear for 5 mm longitudinal shear zones there is increase in the percentage of calcite grains that are twinned as experimental shear strain increases from 0.101 to 1.22 as presented in figure 4.26. At experimental shear strains of 0.101 approximately 90% of the calcite grains are twinned and this increases to 100% at an experimental shear strain of 0.6. The calcite grains that are not twinned at lower experimental shear strains exhibit moderate to high strained extinction.

The thickness of the twin lamellae for experimental shear strains less than 0.6 ranged from 1 to 20 microns and were present as e_1 and e_2 twin sets. The majority of these lamellae are found to be between 1 to 10 microns. In higher strained samples (shear strain=0.6 to 1.22) there is a more limited range of lamellae thicknesses which were found to be between 1 to 2 microns. At both low and high experimental shear strains the individual lamella are sharp and well developed. Microtwins were also observed, usually as e_1, e_2 and e_3 twin sets, and were present in 10 percent of the twinned calcite grains at lower experimental strains which increased to 35% at an experimental shear strains of 1.22. The variation in the lamellae thickness is most likely the result of an increasing

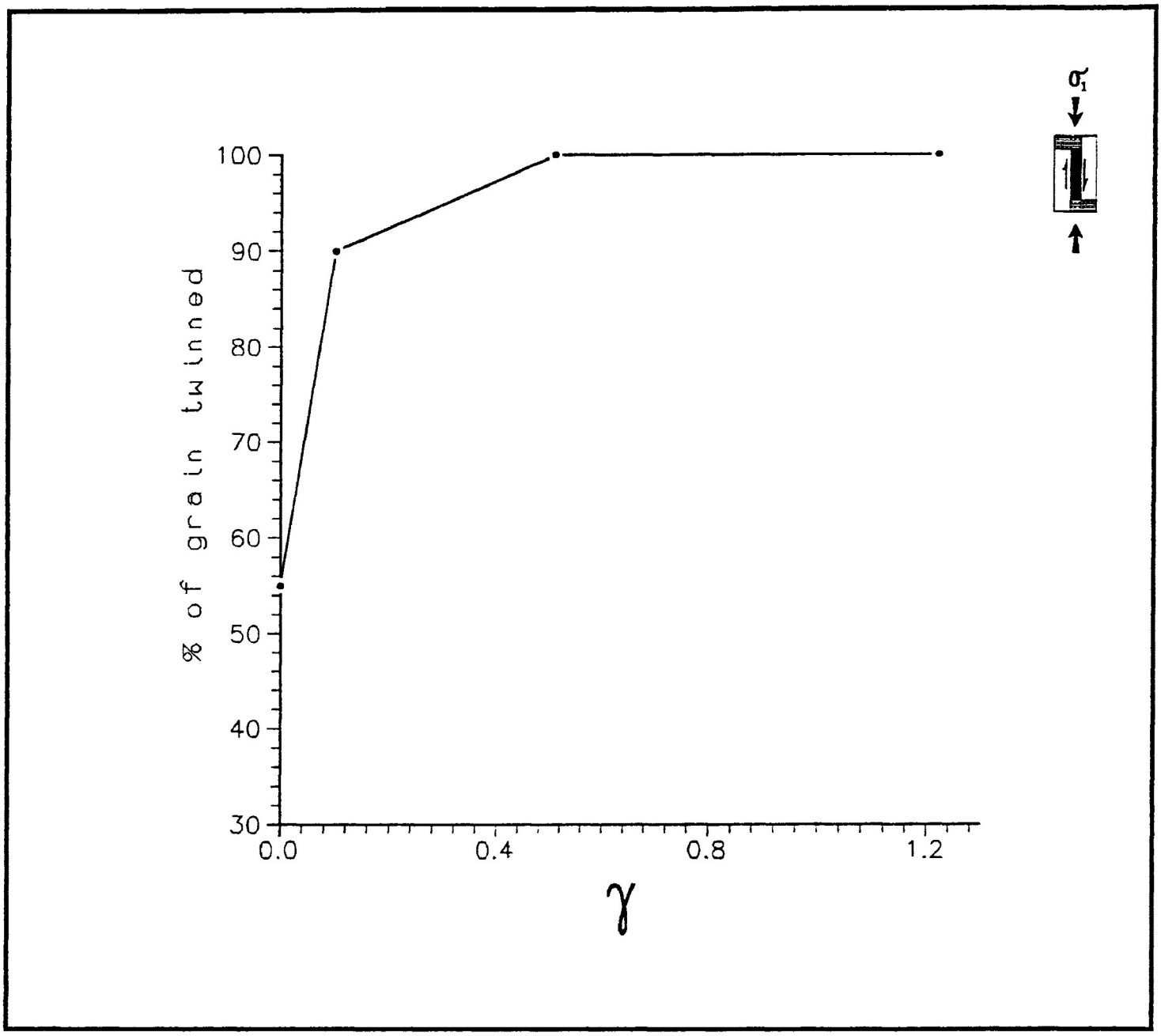

Figure 4.26 Percentage of calcite grains in total aggregate that exhibit twinning. The samples were deformed by simple shear in 5mm thick longitudinal shear zones under dry experimental conditions (P_c=200 Mpa, de/dt=10^{-5}/s).

Figure 4.27 Frequency distribution of e_1-lamellae indices for individual calcite grains in the calcite cement aggregate. Samples were deformed in 5mm thick longitudinal shear zones by simple shear under dry experimental conditions (P_c=200 Mpa, de/dt=10^{-5}/s).

a) Sample LS8803 shear strain=0.101
b) Sample LS8804 shear strain=0.52
c) Sample LS8801 shear strain=1.22

a)

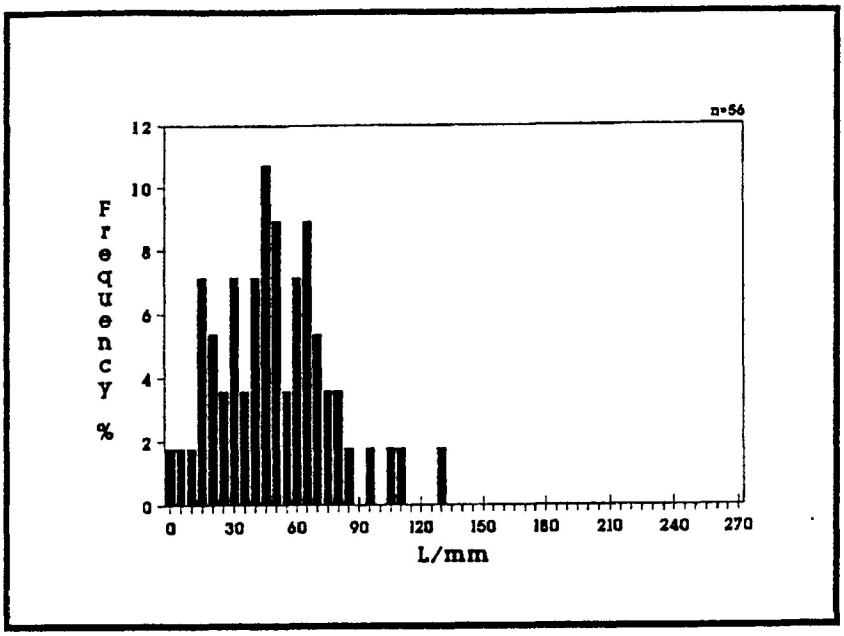
n=56
Frequency %
0
2
4
6
8
10
12
0 30 60 90 120 150 180 210 240 270
L/mm

b)

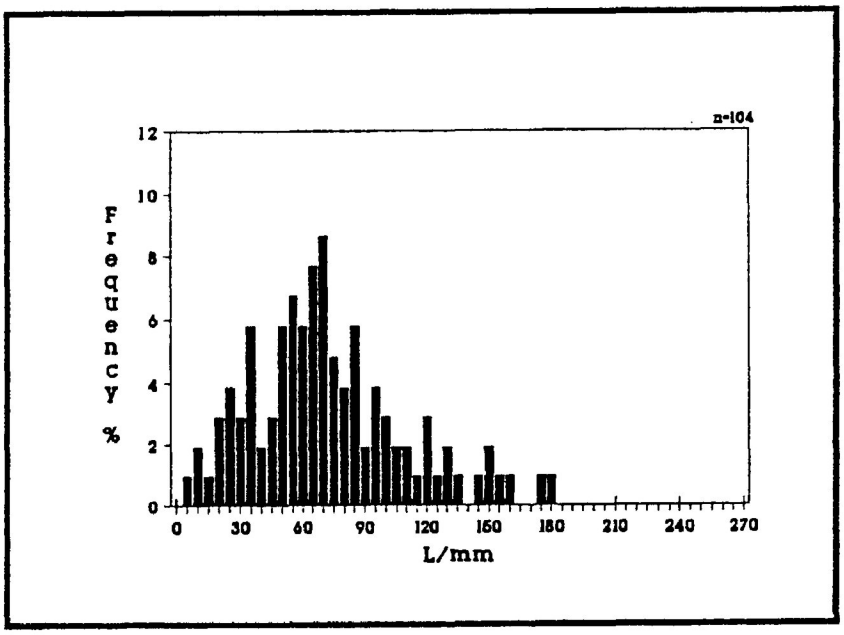
n=104
Frequency %
0
2
4
6
8
10
12
0 30 60 90 120 150 180 210 240 270
L/mm

c)

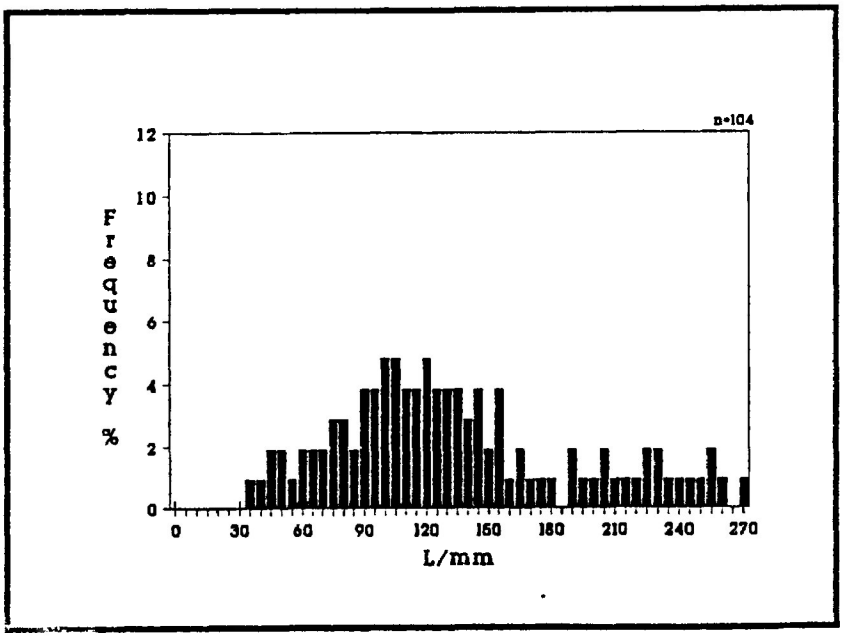
n=104
Frequency %
0
2
4
6
8
10
12
0 30 60 90 120 150 180 210 240 270
L/mm

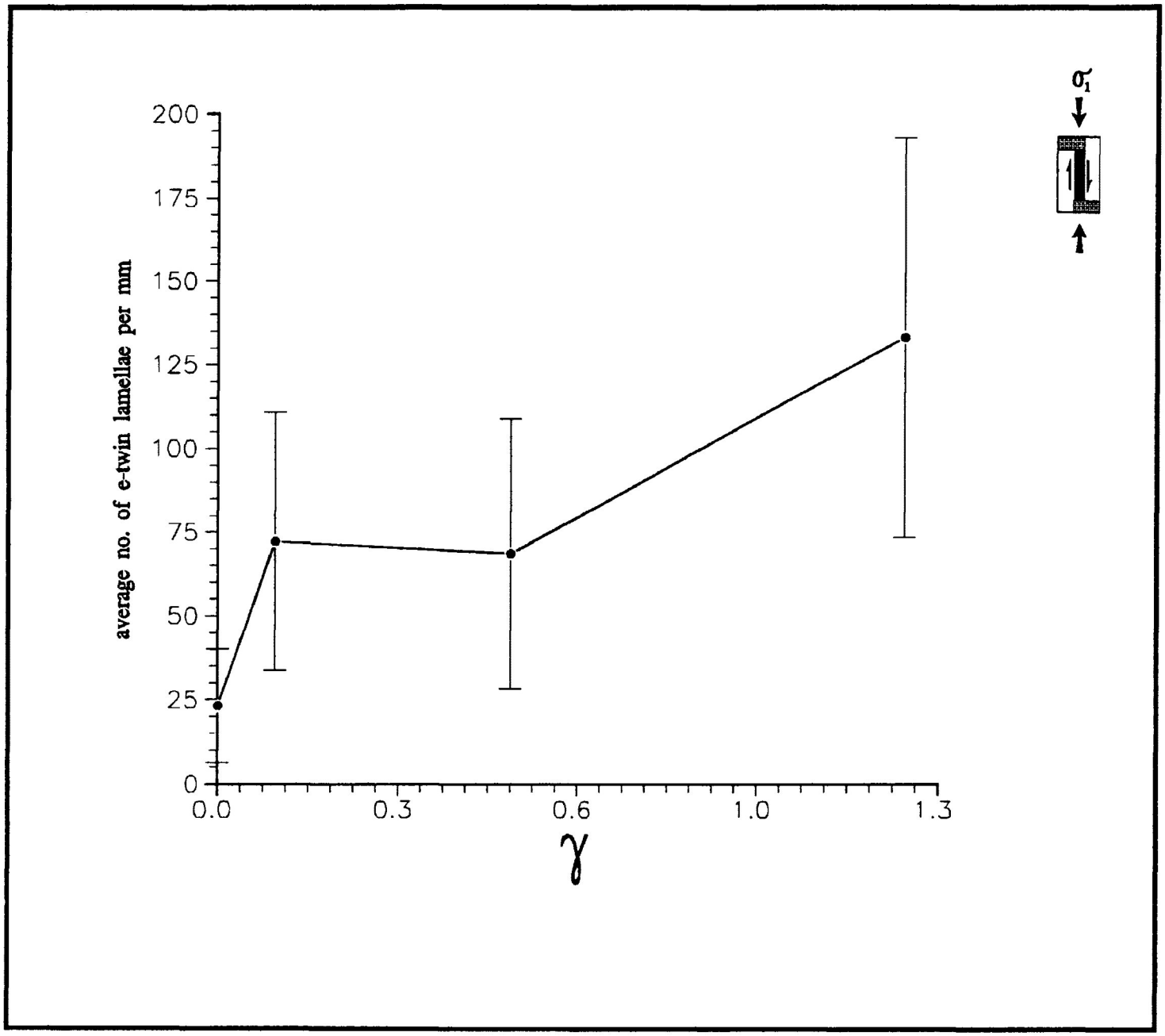

Figure 4.28 Variation in average e_1-lamellae index and associated standard deviation (error bars) for the frequency distribution of measurements on individual calcite grains. The samples were deformed by simple shear in 5mm thick longitudinal shear zones under dry experimental conditions (P_c=200 Mpa, de/dt=10^{-5}/s) for experimental shear strain of 0.101, 0.52 and 1.22.

component of pure shear, causing shortening of the shear zone, in the later stages of the deformation experiments.

The frequency distributions of e_1-lamellae indices in simple shear, for increasing experimental shear strains are presented in figure 4.27. From the figure it is evident that the degree of twinning involved in the 5 mm longitudinal shear zones is greater than that of the 2 mm shear zone at similar experimental shear strains. Furthermore, the intensity and range of the twin lamellae indices increases as a greater component of pure shear is added to the deformed shear assemblage (shear strains of 0.51 to 1.22). The average lamellae indices increase through the deformation with values of 72.3 L/mm (±38.4 s.d.) and 124.7 (±51.4 s.d.) for experimental shear strains of 0.101 to 1.22, respectively (Fig. 4.28).

Kink band development during the simple shear deformation is not observed to a great degree in low experimental shear strain samples. However, at higher strains the number of kink bands increases until approximately 10% of the calcite grains exhibit kink banding at an experimental shear strain of 1.22. Furthermore, there is observed bending of kink bands and twin lamellae. In some cases the twin lamellae are sigmoidally bent in a way that represents the sense of shear acting on the assembly. Cataclasis is also observed in many calcite grains at high experimental shear strains.

4.3 Dynamic analysis methods for the determination of the axis of maximum principal compressive stress for twinned calcite grains

4.3.1 Introduction

Since mechanical twinning in calcite grains can be used to infer the orientation of the principal compressive stress a number of methods for dynamic interpretation have been developed. These methods include Turner's method (1953), Spang's method (1972), Dietrich and Song's method (1984) and the lamellae index method (Borradaile and McArthur, 1990).

4.3.2 Methods for the determining the maximum principal compressive stress orientation

a) Turner's Method

Turner (1953) was the first to make a dynamic interpretation of the twin lamellae in naturally deformed marbles to determine the principal compression and extension orientations that most favoured the development of twin lamellae. Turner's dynamic analysis method was used in this study to locate the most favourably oriented maximum principal compressive stress (σ_1) needed to produce the observed twinning in the calcite grains. This was accomplished by determining the orientations of the ideal compression axes necessary to produce twinning on e-plane in each suitably oriented calcite grain.

For twin gliding to become operative the magnitude of the resolved shear stress (t_r), along the glide line in the twin plane, must reach a critical value (t_c). The t_r on a calcite twin plane can be calculated from the equation that relates the resolved shear stress coefficient, differential stress and the critical resolved shear stress:

$$t_r = S_1 \quad \sigma \qquad (1)$$

$$S_1 = (\cos x_1 \cdot \cos y_1) \qquad (2)$$

$$\Delta\sigma = (\sigma_1 - \sigma_3) \qquad (3)$$

where:

t_r = resolved shear stress
S_1 = resolved shear stress coefficient (Schmid factor)
$\Delta\sigma$ = differential stress
x_1 = angle between the *e*-twin plane pole and the compression direction
y_1 = angle between the glide line and the compression direction
σ_1 = maximum principal compressive stress
σ_3 = minimum principal compressive stress

As presented in figure 4.29a twinning in calcite is restricted to a gliding plane (e) and a glide direction (*n*) resulting in simple shear with no volume change (Friedman, 1964). Since the sense of shear for twin gliding in calcite is fixed (+) and the critical resolved shear stress for twinning remains constant for temperatures below 500°C (Turner *et.al.*, 1954), it is possible to determine the ideal compression axis orientation necessary for twin formation from the crystal geometry presented in figure 4.29a. As discussed by Handin and Griggs (1951) the maximum resolved shear stress will occur when S_1 reaches a maximum value of 0.5 as defined by equation (4.2). The maximum S_1 in obtained when the compression axis is inclined 45° to the e_1 plane ($x_1=y_1=45°$), and coplanar to the *e*-pole and *c*-axis.

The ideal compression axis will, therefore, be located on a stereogram 45° from e_1 along the great circle containing the pole to the *e*-plane and the *c*-axis in a direction away from the *c*-axis (Fig. 4.29b). Turner (1953) has shown that when the compression axis orientations for large numbers of twinned calcite grains are plotted on a stereogram the location of centres of concentration indicates the σ_1 best able to produce

Figure 4.29 a) Twin gliding in calcite is restricted to a glide plane (the twin plane, e) and a glide direction within the glide plane (the glide line, n) which exhibits a positive sense of shear. The σ_1 is oriented at 45° to the pole of the twin plane in the direction of shear. The *c*-axis of the host lattice is oriented at 26.¼° to the pole to the *e*-twin plane. The *c*-axis, the pole to the twin plane and the σ_1 orientation are all coplanar, perpendicular to the twin plane (e) and parallel to the glide line (n). (modified from R. Jamison and H. Sprang, 1976)

b) Turner's dynamic analysis method: Stereogram representing part of the great circle containing the *c*-axis (circle), pole to the e_1-twin plane (small broad arrow) and the compression axis (small arrow) for an individual calcite grain favourably oriented for twinning with the σ_1 (broad arrow) oriented vertically. The short solid line represents the angle of 26.¼° from the *c*-axis to the pole to the twin plane. The longer solid line represents the angle of 45° between pole to the e_1-twin plane and the compressive axis. Stereonet is equal area and lower hemisphere.

a)

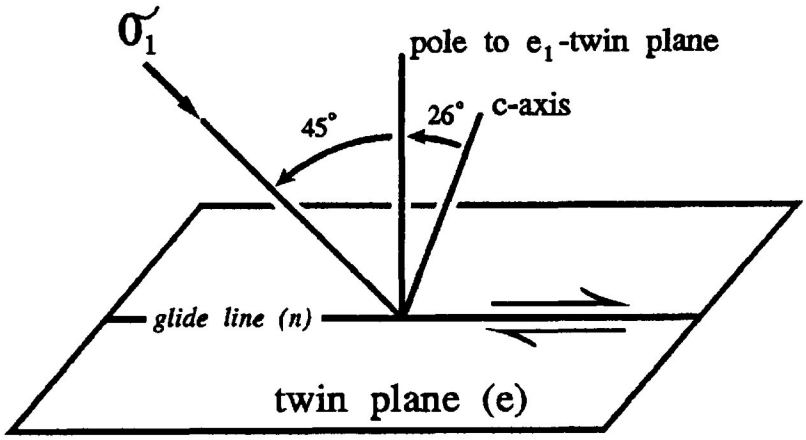
σ1
pole to e1-twin plane
45°
26°
c-axis
glide line (n)
twin plane (e)

b)

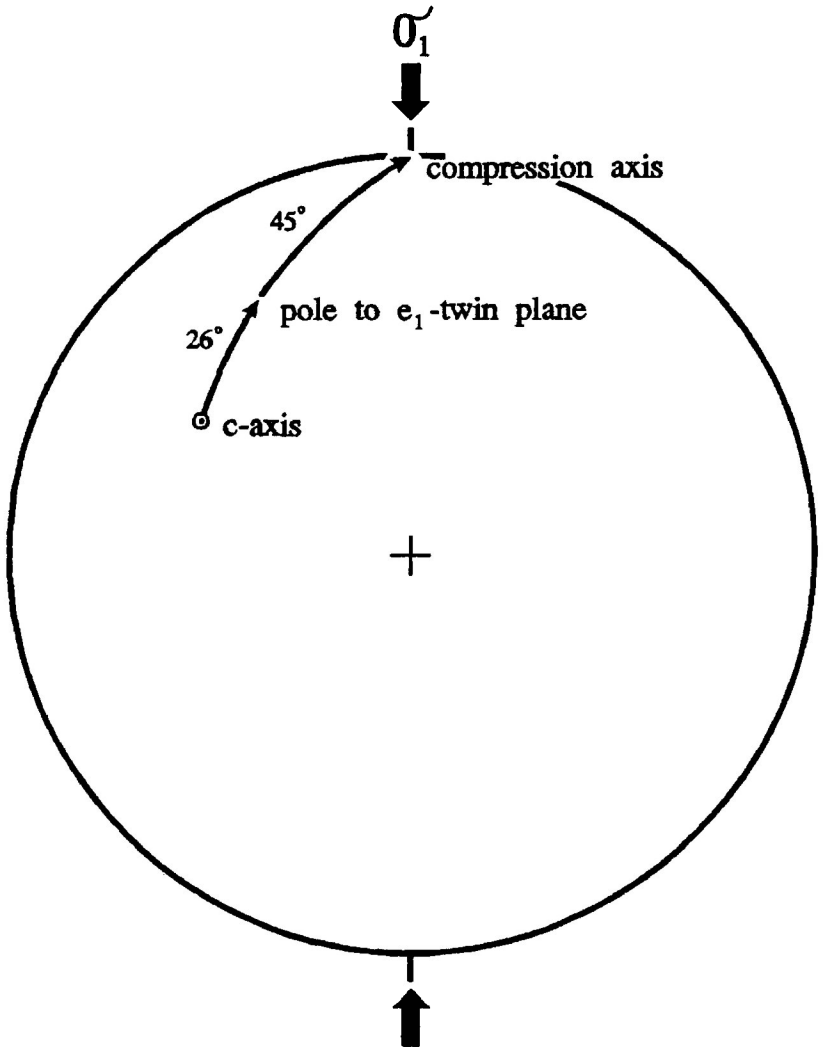
σ1
compression axis
45°
pole to e1-twin plane
26°
c-axis

the twinning in favourably oriented calcite grains. Spiers (1979) has shown that the volume of the host lattice that is twinning will depend on the magnitude of the S_1 (Schmid factor).

Depending on the magnitude of the $\Delta\sigma$ the compression axis does not necessarily have to be at 45° to the e-twin plane to induce twinning, therefore, scatter is usually observed in the compression axes distribution about the σ_1 orientation. An enhancement has been made to Turner's method to elevate this problem. Friedman and Conger (1964) have shown that the analysis of data by Turner's method from only those calcite grains with a high lamellae index sharpens the concentration of the compression axes around the σ_1 direction. Spang (1972) has developed a numerical method of dynamic interpretation using second order tensor translation formula. Principal orientation of stress can be calculated from compression and extension direction determined from Turner's Method.

Studies using Turner's dynamic analysis methods have been conducted on many naturally deformed rocks. These include petrofabric analyses of marble by Turner (1953), McIntyre and Turner (1953), Gilmour and Carman (1954), Clark (1954), Weiss (1954), Schmid *et.al.* (1987) and Rowe and Rutter (1990). Limestones have been studied in the same way by Friedman and Stearns (1971), Dietrich and Song (1984), Schmid *et.al.* (1987) and Jackson *et.al.* (1989). Calcite in a naturally deformed gastropod fossil has been used to determine the maximum compressive stress direction by Friedman and Conger (1964). Modifications of Turner's technique have been used in the study of deformed crinoids (Nissen, 1964*a*) and also in deformed ooids (Nissen, 1964*b*). Studies have also involved artificial calcite Portland-cemented sandstone by Hansen and Borg (1962) and Friedman (1963).

b) Dietrich and Song's Method

Dietrich and Song (1984) developed an analysis method for the determination of the σ_1 orientation. This was also used in this study for samples which experienced high strains. The method is based on the premise that axial symmetrical compression at high strains results in the development of a preferred orientation of *e*-twin planes normal to the σ_1 orientation (Fig. 4.30a). This in turn allows *c*-axes to lie on a small circle girdle oriented at 26° to the maximum compression direction (Turner *et.al.*, 1956; Rutter and Rusbridge, 1977).

Schmid *et.al.* (1987) summarized the method as finding the small circle representing a cone with an opening angle of 26° around the σ_1 orientation, such that: (1) no *c*-axis positions for host calcite grains are found within the small circle; and (2) the arrowheads point away from the cone axis (Fig. 4.30b). On the stereogram the open circle locates the orientation of the pole to the *e*-twin plane and the arrowhead points towards the *c*-axis along the *c-e* great circle. The pole to the *e*-twin plane plots parallel to the σ_1 direction. The compression axis is located on a 45° small circle about the σ_1 orientation. As presented in figure 4.30b the *c*-axis arrowhead represents the direction of positive shear in each *e*-twin set measured in the calcite grains.

c) Lamellae Index method

A variation of Turner's method has been developed in this study to determine the orientation of the maximum compressive stress direction (Borradaile and McArthur, 1990). This method uses contours of lamellae index values for calcite e-twin sets. The index values are plotted on the stereogram at the position of the compression axis as determined by Turner's

Figure 4.30 a) In highly strained calcite grains the σ_1 is oriented parallel to the pole of the twin plane. The *c*-axis of the host lattice is oriented at 26.¼° to the pole to the *e*-twin plane. The *c*-axis, the pole to the twin plane and the σ_1 orientation are all coplanar, perpendicular to the twin plane (e) and parallel to the glide line (n).

b) Dietrich and Song's analysis method: Stereogram representing part of the great circle containing the *c*-axis (small broad arrow), pole to the e_1-twin plane (circle) and the compression axis (small arrow) for an individual calcite grain favourably oriented for twinning with the σ_1 (broad arrow) oriented vertically. 45° and 26° small circle girdles given. Stereonet is equal area and lower hemisphere.

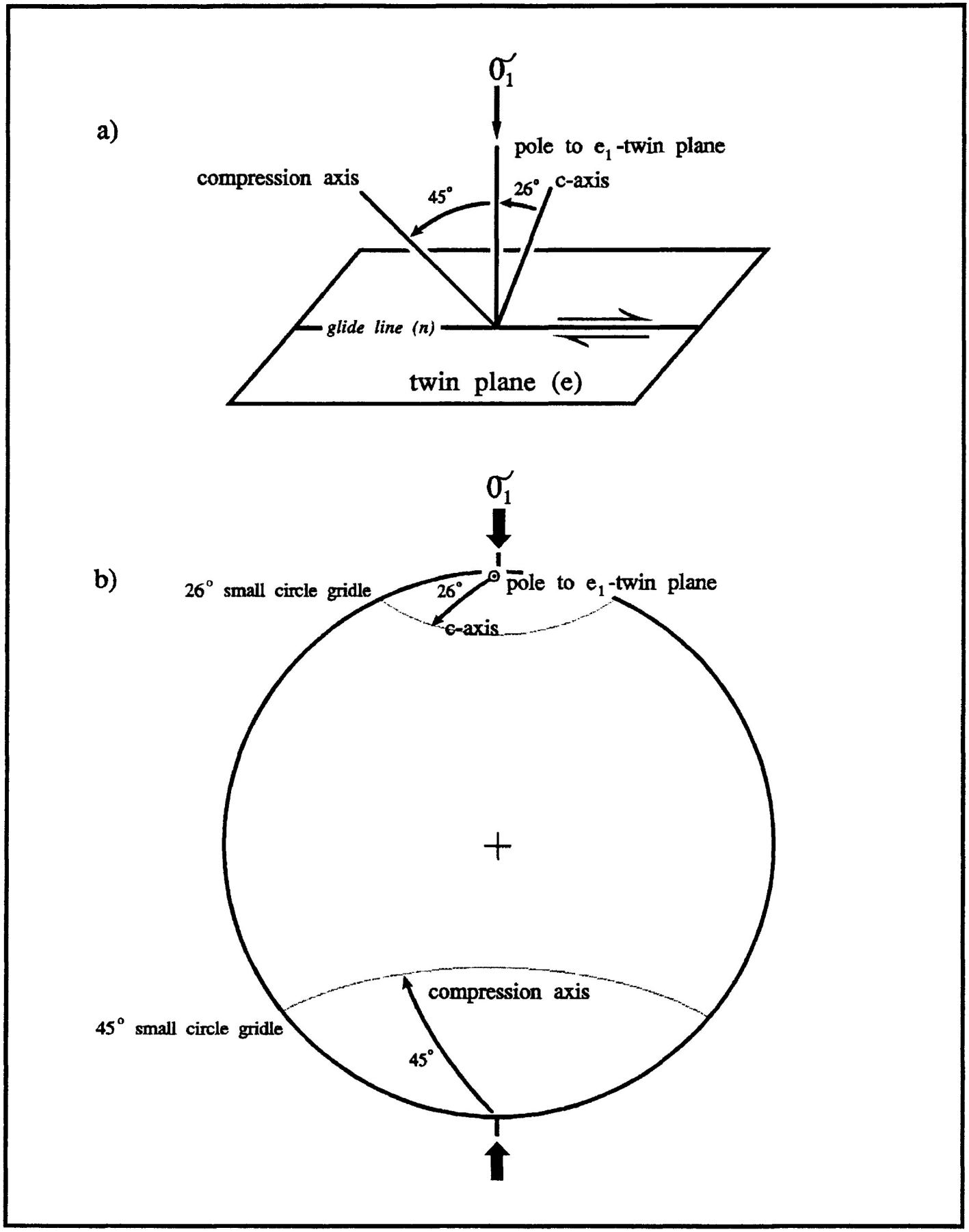
a)
σ_1
pole to e_1-twin plane
compression axis
45°
26°
c-axis
glide line (n)
twin plane (e)
b)
σ_1
26° small circle gridle
26°
pole to e_1-twin plane
c-axis
compression axis
45° small circle gridle
45°

method for individual calcite grains. The location of the highest lamellae contour locates the orientation of the σ_1 most favourably oriented to produce the twinning observed in the calcite grains.

The use of contoured lamella indices on stereograms allows for the twin sets that are the most profusely developed (designated as e_1) to be represented by the highest contoured values of the lamellae indices. This was first suggested by Friedman and Conger (1964) in which they showed, in naturally deformed specimens, that using data containing the highest-spacing index in Turner's Method sharpens the inferred σ_1 orientation when the compression axes were contoured. Turner and Ch'ih (1951) found experimentally that the number of twin lamellae per millimetre is directly related to the magnitude of the shear-stress coefficient (S_1) for a given calcite grain orientation.

Since the value of S_1 will depend on the orientation of the twin plane in question (equation 4.2), the intensity of twinning will vary with orientation of the calcite grain. If a calcite grain is in the ideal compression orientation it will exhibit a high lamellae index. Calcite grains that do not have this orientation will have lower lamellae index values. The contoured equal values of S_1 around a potential e-twin plane is presented in the stereogram of figure 4.31 (Handin and Griggs, 1951). For any fixed orientation of calcite crystals the value of S_1 for any hypothetical σ_1 orientation can be determined. From the figure is observed that for randomly oriented calcite grains the lamellae index values will decrease in intensity in small circle distributions away from the σ_1 orientation.

In this study deformed calcite Portland-cement aggregate contain calcite grains with e-twin plane in a wide range of

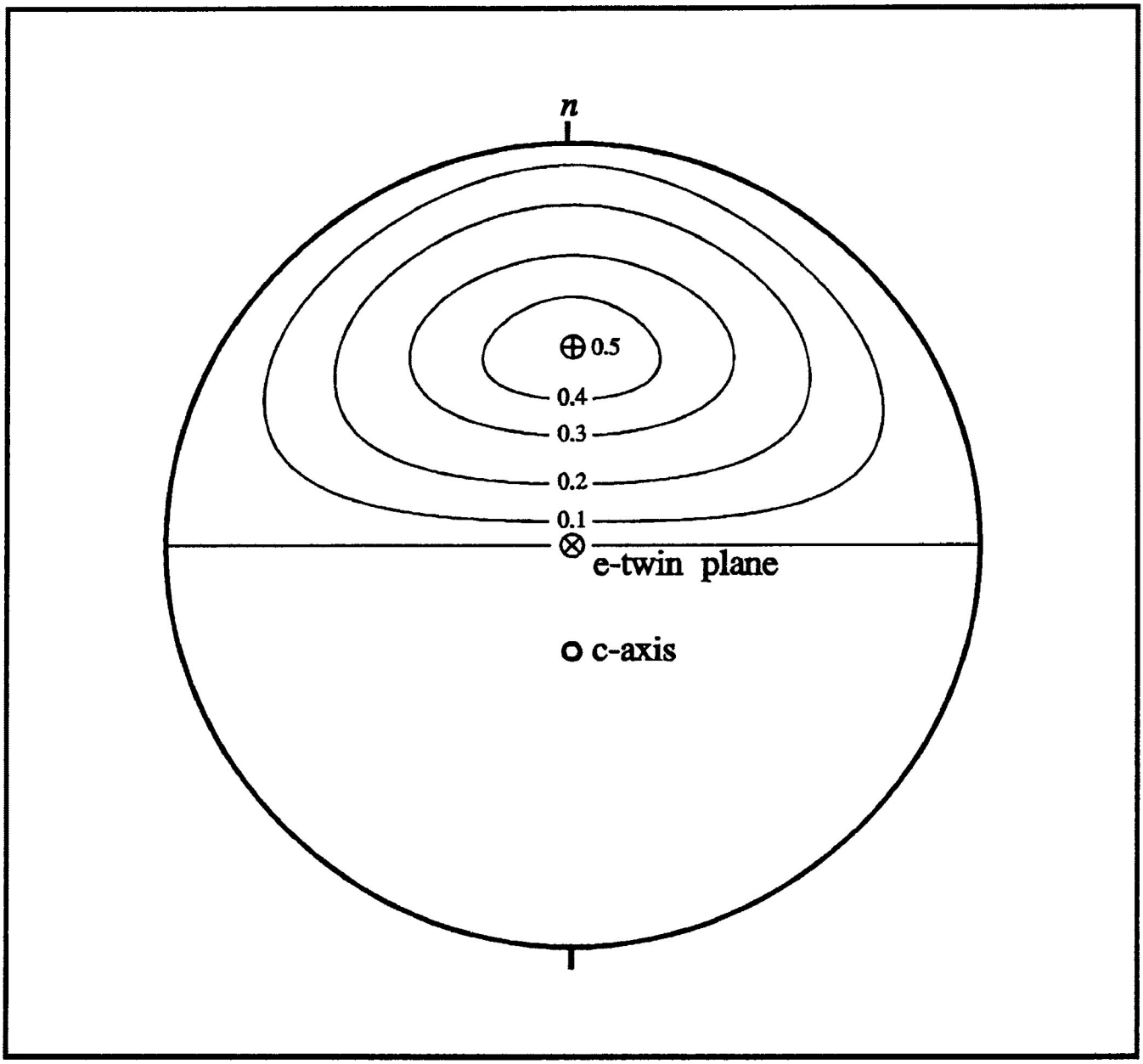

Figure 4.31 Contoured values of S_1 for a horizontal e_1 twin plane. Compressive stress oriented at S_1=0.5 (circled +). Stereogram equal area and lower hemisphere (modified from Handin and Griggs (1951)).

Plate 4.5 Microphotograph of calcite grains (centre) in sample AC-8 (e=18.03%) exhibiting an orientations of e_1-twin lamellae at 80° to σ_1 (lamellae index=15 L/mm). Broad arrows indicate orientation of the principal compressive stress during triaxial deformation. Photo taken in partial cross polarized light. (scale 38:1)

Figure 4.32 Stereogram representing part of the great circle containing the *c*-axis, pole to the e_1-twin plane and the compression axis for a calcite grain (Plate 4.5) with e_1-twin planes oriented at approximately 80° to σ_1.

The maximum principal compressive stress (large broad arrow) oriented vertically. The short solid line represents the angle of 26.¼° from the *c*-axis to the pole to the twin plane. The longer solid line represents the angle of 45° between pole to the e_1-twin plane and the compressive axis. Stereonet is equal area and lower hemisphere.

a)

b)

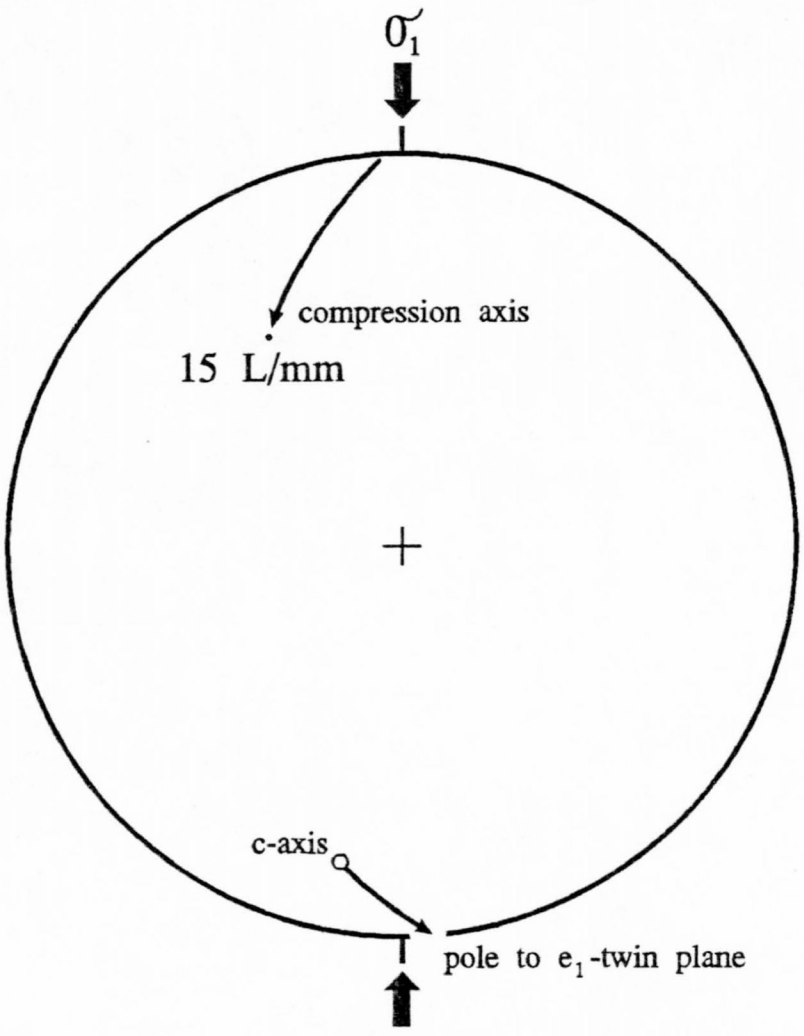

Plate 4.6 Microphotograph of calcite grains (centre) in sample AC-8 (e=18.03%) exhibiting an orientations of e_1-twin lamellae at 45° to σ_1 (lamellae index=180 L/mm). Broad arrows indicate orientation of the principal compressive stress during triaxial deformation. Photo taken in partial cross polarized light. (scale 38:1)

Figure 4.33 Stereogram representing part of the great circle containing the *c*-axis, pole to the e_1-twin plane and the compression axis for a calcite grain (Plate 4.6) with e_1-twin planes oriented at approximately 45° to σ_1.

The maximum principal compressive stress (large broad arrow) oriented vertically. The short solid line represents the angle of 26.¼° from the *c*-axis to the pole to the twin plane. The longer solid line represents the angle of 45° between pole to the e_1-twin plane and the compressive axis. Stereonet is equal area and lower hemisphere.

a)

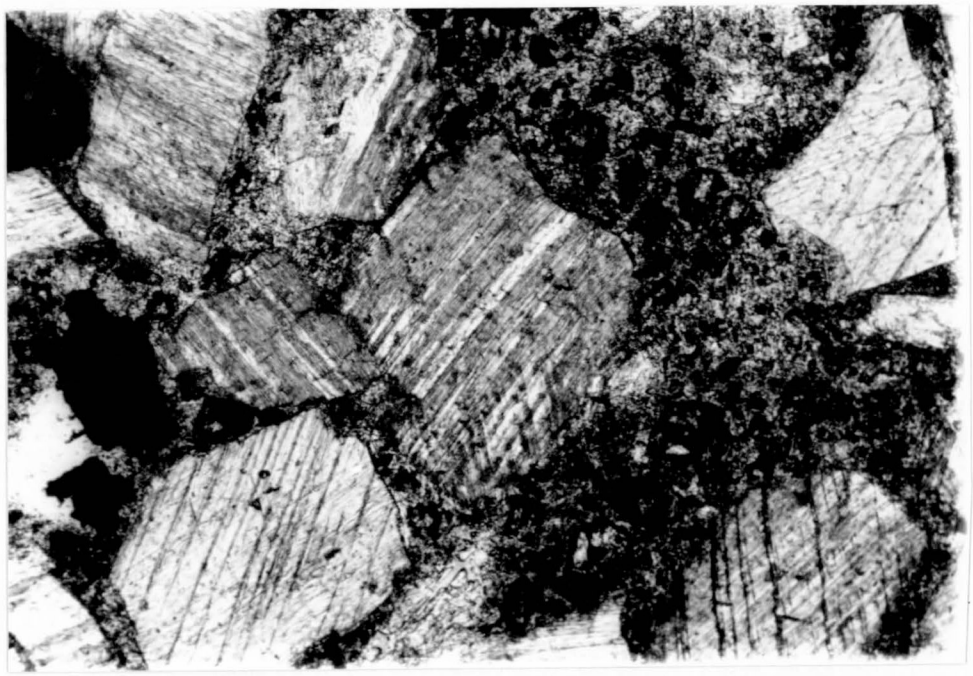

σ_1

b)

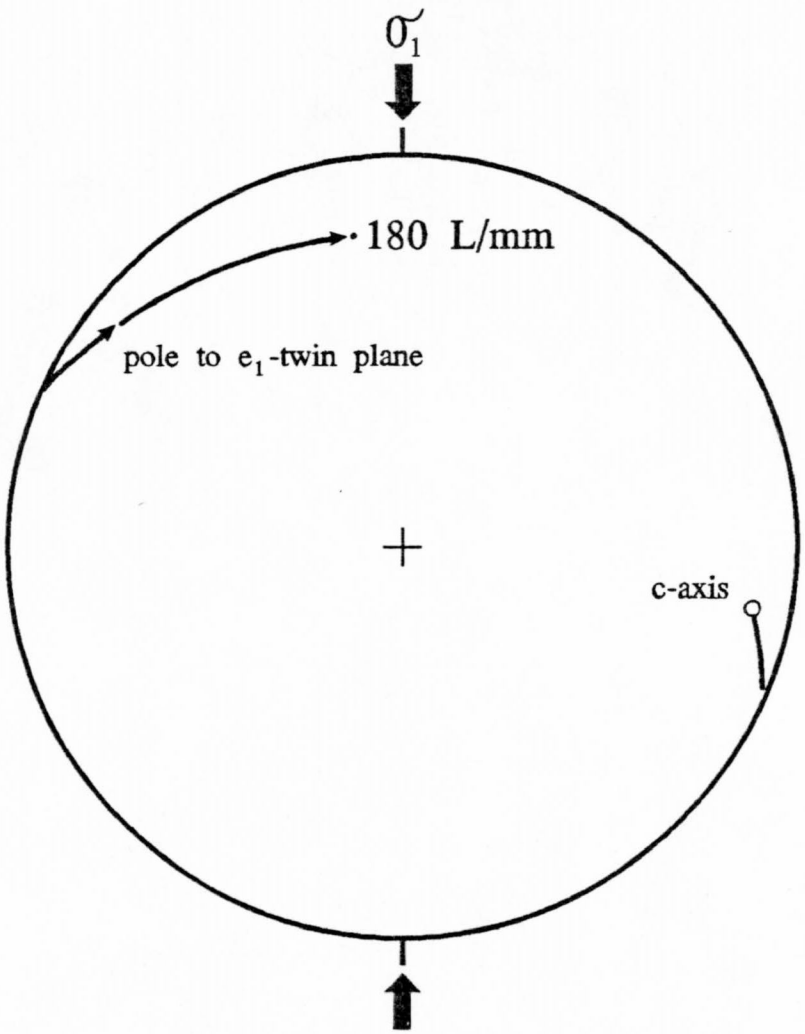

Plate 4.7 Microphotograph of calcite grains (centre) in sample CPF-13 (e=17.8%) exhibiting an orientations of e_1-twin lamellae at 70° to σ_1 (lamellae index=180 L/mm). Broad arrows indicate orientation of the principal compressive stress during triaxial deformation. Photo taken in partial cross polarized light. (scale 38:1)

Figure 4.34 Stereogram representing part of the great circle containing the *c*-axis, pole to the e_1-twin plane and the compression axis for a calcite grain (Plate 4.7) with e_1-twin planes oriented at approximately 70° to σ_1. Grain may have experienced rigid body rotation.

The maximum principal compressive stress (large broad arrow) oriented vertically. The short solid line represents the angle of 26.¼° from the *c*-axis to the pole to the twin plane. The longer solid line represents the angle of 45° between pole to the e_1-twin plane and the compressive axis. Stereonet is equal area and lower hemisphere.

a)

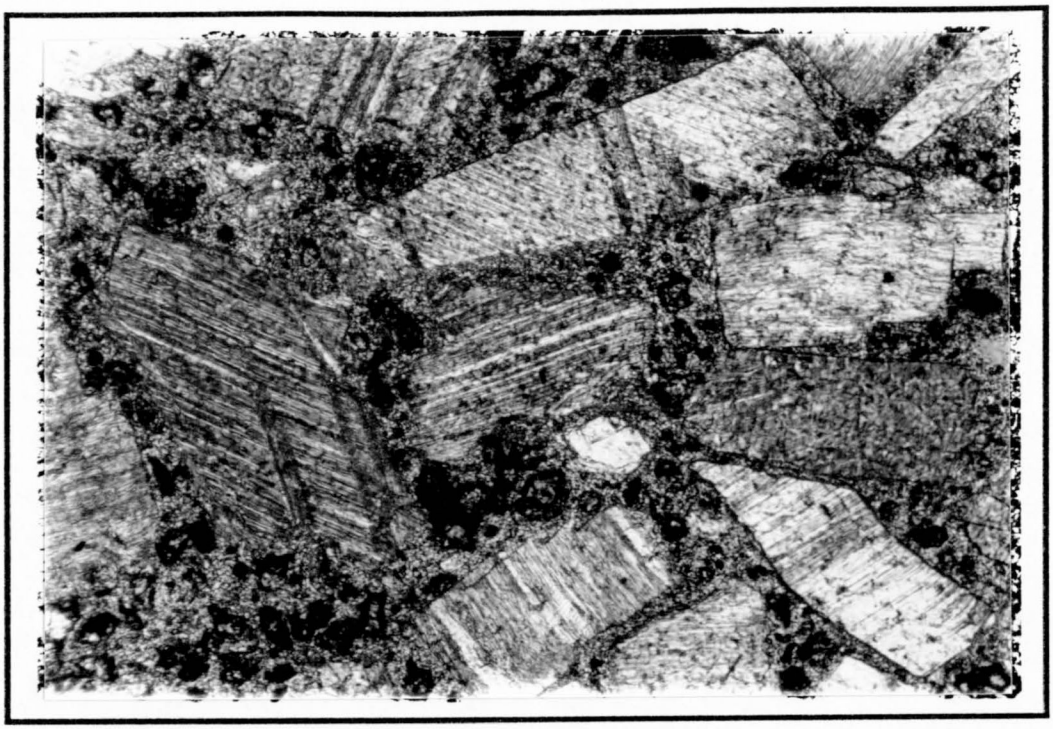

b)

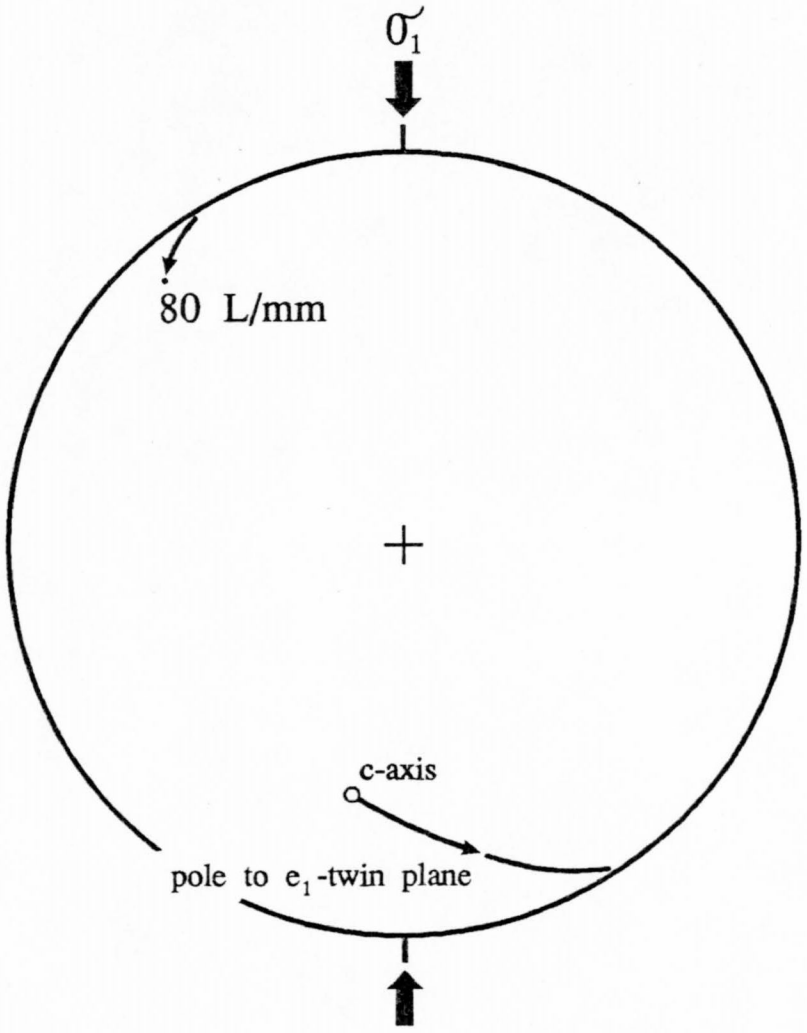

orientations. Plates 4.5 and 4.6 illustrates calcite grains with e_1-twin plane oriented at approximately 45° and 80° to the known σ_1 orientation (sample AC-8, e=18.03% (R_s=1.347)). The lamellae index of these two calcite grains are 180 L/mm (45°, high S_1) and 15 L/mm (80°, low S_1). Stereograms exhibiting the orientation of the *c*-axis (empty circle) and the pole to the *e*-twin plane (arrowhead) for each calcite grain are presented in figures 4.32 and 4.33, respectively. In the figures the solid circle locates the orientation of the compression axis directions, derived from Turner's method (1953). The higher lamellae index grain has a compression axis direction which is oriented much closer to the known σ_1 orientation than the calcite grain with the lower lamellae index.

A problem exists in the lamellae index method (as well as Turner's method) dealing with calcite grains that may undergo rigid body rotation as strain increases. This process may cause calcite grains which were originally in orientations favourably for twinning (high lamellae index) to rotate into orientation unfavourable for twinning. Plate 4.7 illustrates a calcite grain (CPF-13, e=17.8% (R_s=1.342)) which has a relatively high lamellae index 80 L/mm, however, is in an orientation that is not favourable for twinning (e_1 70° from the known σ_1, low S_1). Rigid rotation is suggested by the strong alignment of calcite grain approximately parallel to the extension direction.

The stereogram exhibiting the orientation of the *c*-axis and the pole to the *e*-twin plane for the calcite grain is presented in figure 4.34. The orientation of the compression axis is similar to that of the 15 L/mm calcite grain. Rigid rotation of the calcite grain pulls the compression axis away from the orientation of the known σ_1.

4.4 Dynamic analysis of the compression axis orientation for pure, transpressional and simple shear

4.4.1 Introduction

The following section deals with the interpretation of the maximum principal compressive stress orientation based on the previous 3 dynamic analysis methods. All three methods were used for data obtained from experimentally deformed calcite Portland-cement aggregates in pure shear (dry and wet), transpressional shear, and simple shear. Also a control specimen (7C-3C) was used to determine the nature of the twin lamellae that existed in the original undeformed state.

The *c*-axis in the host crystal and the normal to the twin plane, for each of the possible three twin sets (e_1, e_2 and e_3), was measured in 50 to 75 calcite grain from each deformed sample. In order to prevent the "blind spot" for data orientations, as described by Turner (1953), two mutually perpendicular thin-sections were used.

Only the calcite grains exhibiting a coplanar angular separation, between *c*-axis and pole to *e*-twin plane, of 23 to 29° were used during the analysis (the precise value is 26°¼'). Maximum errors of ±3° occur only in calcite grains of samples that were highly deformed in pure and transpressional shear because of associated high lamellae indices, usually errors were less than ±2°.

All data were plotted and contoured on equal area stereographic projections and are lower hemisphere. Some data were plotted and contoured with the help of an orientation analysis and plotting program (STEREO™) written for an IBM compatible computer by Rockware™, Inc.. Statistical analysis on stereographic data was also determined with aid of Stereo™.

4.4.2 Preferred crystallographic orientation of c-axes and poles to e_1-twin planes

Pole figures for *c*-axes and e_1-twin planes were made to examine the development of preferred crystallographic orientation (PCO) in the samples used to inferred σ_1 orientation. The following section examines the development of crystallographic fabrics in calcite grains during dry and wet pure shear, transpressional shear and in simple shear.

a) Undeformed

In the undeformed state (7C-3C) there is no observed preferred orientation of *c*-axes and e_1-twin planes and the distribution is random (Fig. 4.35a,b). The random nature of the crystallographic fabric suggests that no PCO was produced in the calcite grains during the preparation of the sample or as a result of settling of calcite grains during the drying of the calcite Portland-cement mixture.

b) Pure Shear (dry experimental conditions)

The *c*-axis and e_1-twin plane pole figures for dry pure shear, samples AC-3 (e=4.4% (R_s=1.070)) and AC-8 (e=18.03% (R_s=1.347)), are presented in figure 4.36a,b and 4.37a,b, respectively. The *c*-axes distribution for the lower strained sample AC-3 is similar to that of the undeformed state, in that no PCO was observed (Fig. 4.36a). At higher experimental strains (AC-8) the *c*-axes are found to be located in a broad point maximum at 25 to 30° to the known σ_1 orientation (Fig 4.36b).

In the lower experimentally strain sample the poles of e_1-lamellae are also observed to be random in orientation (Fig. 4.37a). However, at higher experimental strains a distribution has developed that exhibits a weak preferred orientation

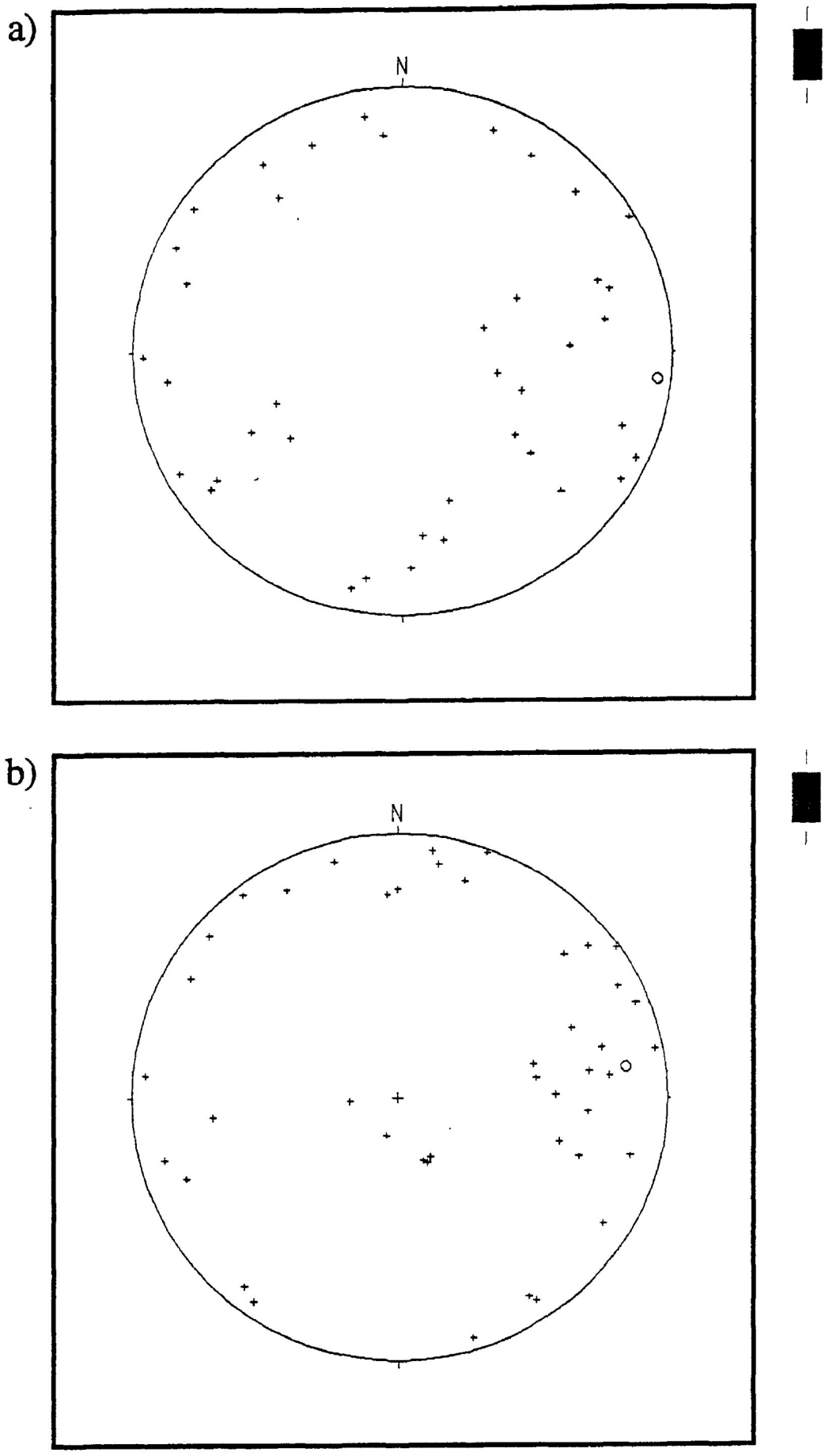

Figure 4.35 Pole figures for a) *c*-axes and b) e_1 twin planes in the undeformed sample 7C-3C. The figures illustrate the random fabric present in the specimens before deformation. Open circle represents mean directional vector of pole distribution.

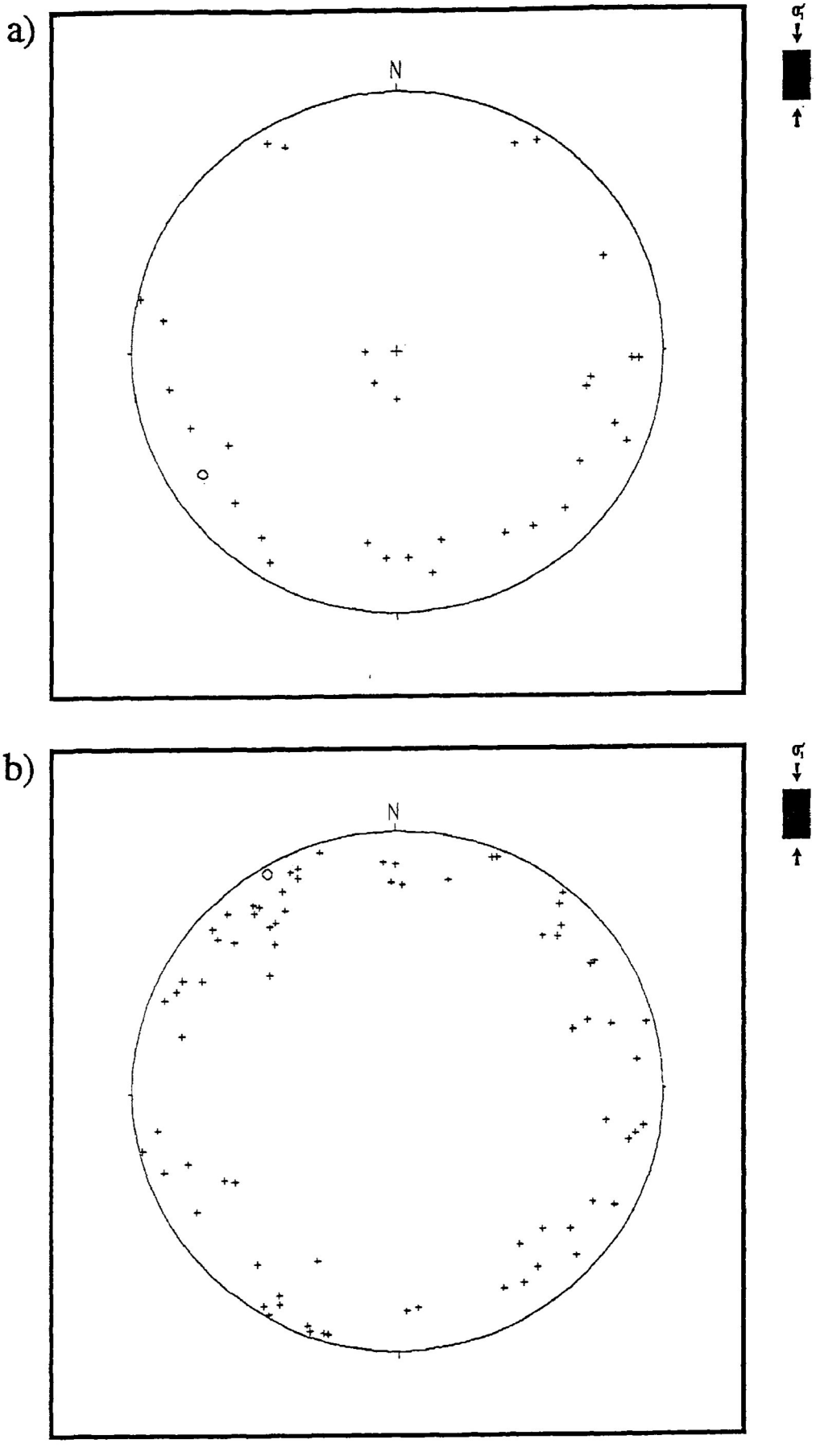

Figure 4.36 Pole figures for *c*-axes in pure shear under dry experimental conditions. Open circle represents mean directional vector of pole distribution.

a) Sample AC-3 (e=4.4% (R_s=1.070))
b) Sample AC-8 (e=18.03% (R_s=1.347))

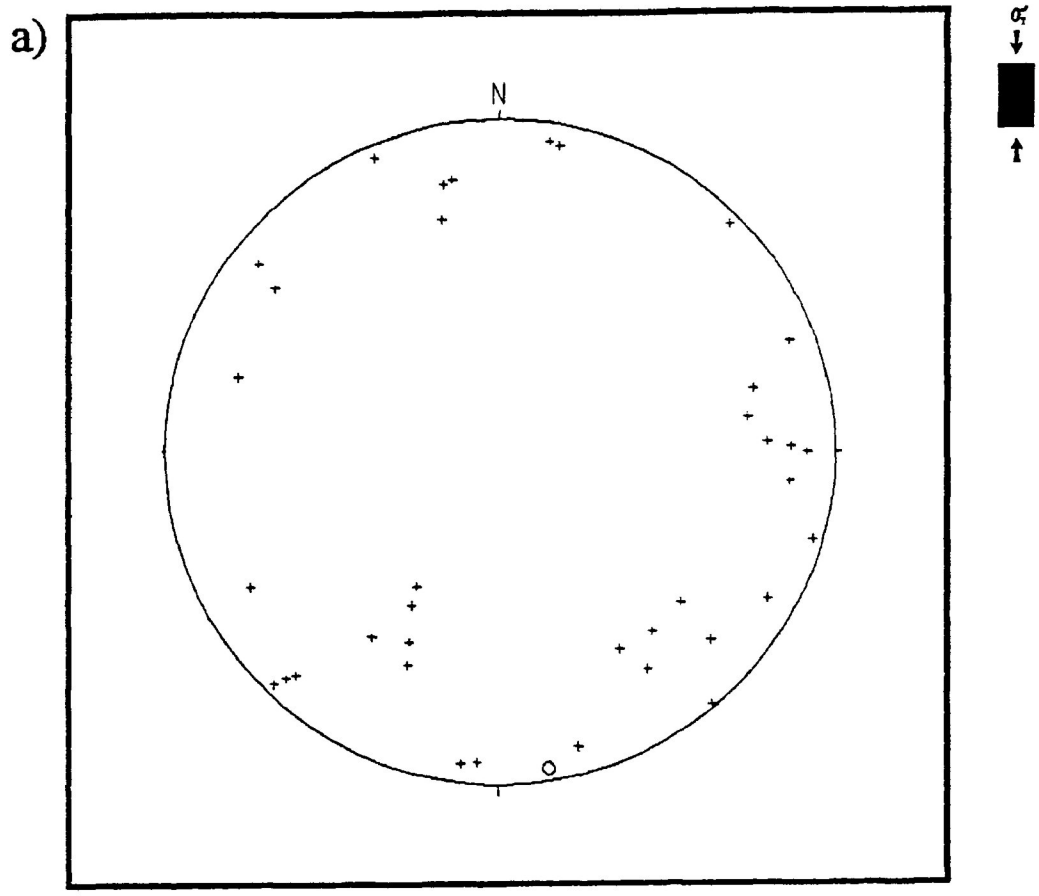

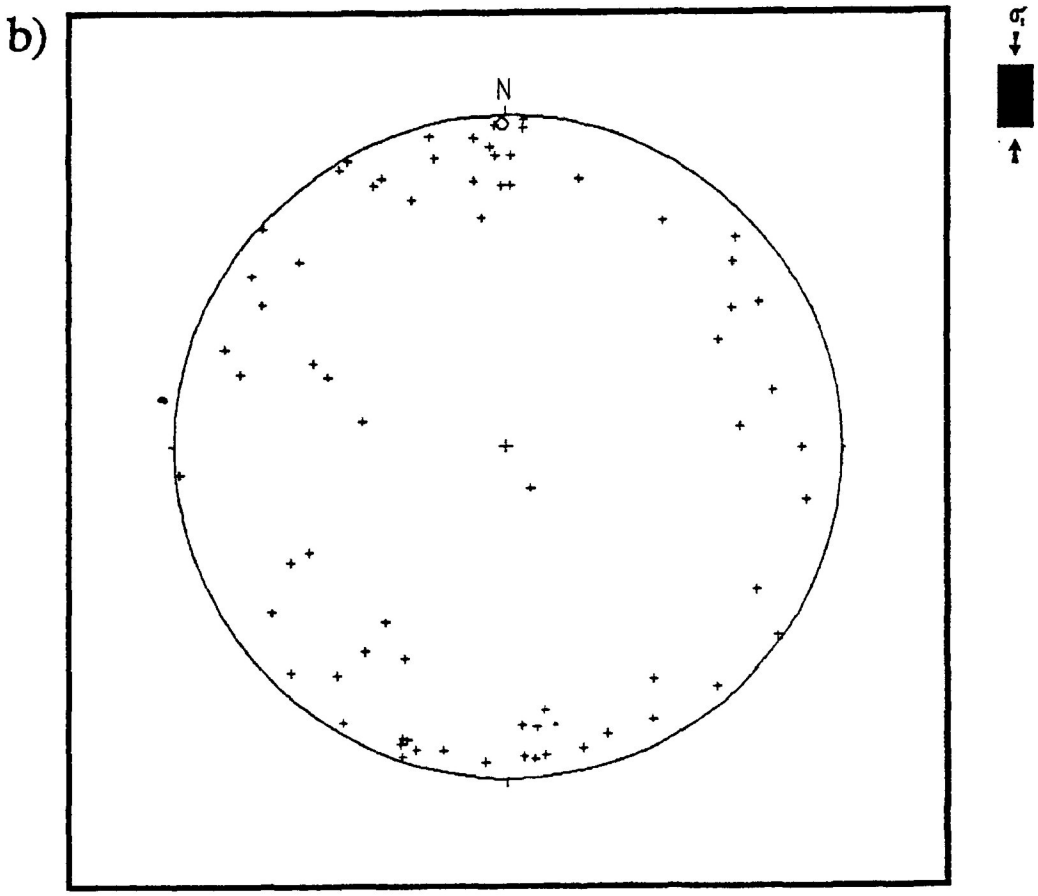

Figure 4.37 Pole figures for e_1 twin planes in pure shear under dry experimental conditions. Open circle represents mean directional vector of pole distribution.

a) Sample AC-3 (e=4.4% (R_s=1.070))
b) Sample AC-8 (e=18.0% (R_s=1.347))

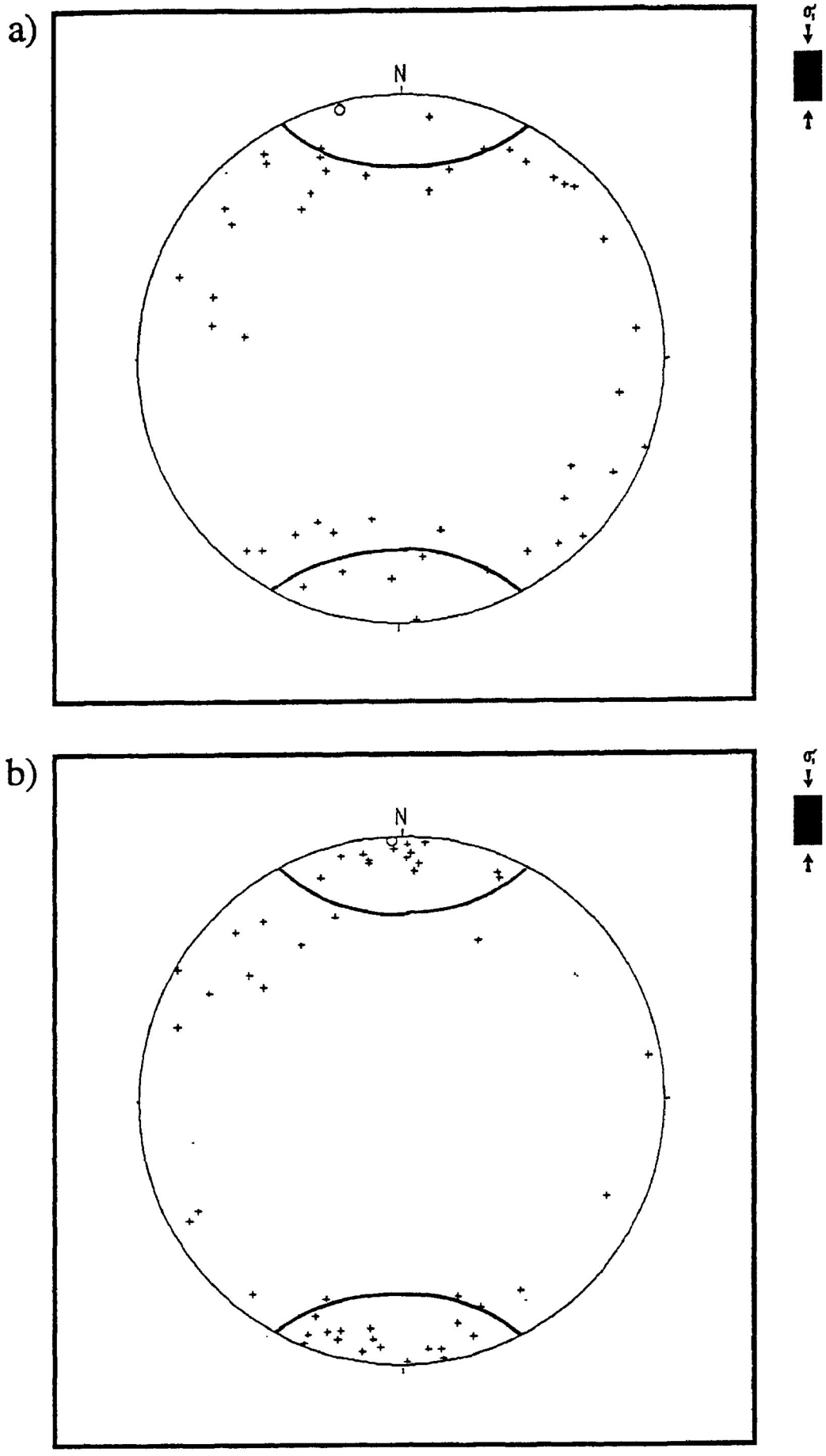

Figure 4.38 Pole figures for a) *c*-axes and b) e_1 twin planes in sample CPF-13 (e=17.8% (R_s=1.342)) deformed by pure shear under wet experimental conditions. 26° small circle girdle given by solid line. Open circle represents mean directional vector of pole distribution.

perpendicular to the known σ_1 orientation (Fig. 4.37b).

c) Pure Shear (wet experimental conditions)

For the case of wet pure shear, sample CPF-13 (e=17.86% (R_s=1.342)), the pole figures for the *c*-axes and e_1-twin planes are presented in figure 4.38a,b. In the *c*-axis pole figure a weak small circle girdle distribution is observed at 20 to 40° around the known σ_1 orientation. The e_1-twin planes pole figure shows the development of a point maximum at the orientation of the known σ_1 direction. The solid line on figure 4.38a represents the 26° small circle centred on the known σ_1 orientation. The development of a point maximum of poles to e_1-twins and the corresponding cone of *c*-axes at 26° to the point maximum is in accordance with the geometric conditions of twinning in calcite.

d) Transpressional Shear (Dry tests) in oblique shear zones

The pole figures of *c*-axes for transpressional shear in oblique shear zones, samples SZ-C1 (shear strain=0.111) and SZ-C3-1 (shear strain=0.189), are presented in figure 4.39a-b. In the case of *c*-axis pole figures both samples exhibit broad maxima slightly oblique to the known σ_1 orientation in the direction of shear. The degree of obliquity is greater in the higher strained sample.

The pole figures of e_1-twin planes for the above sample are presented in figure 4.40a,b. In the e_1-twin plane pole figures there is also the development of broad maximum rotated away from the known σ_1 orientation. The rotation of the maximum is in a direction compatible with the sense of shear operating on the shear assemblage. The degree of rotation is greater in the higher strained sample. The rotation away from the known σ_1 orientation of the *c*-axis and e_1-twin plane point

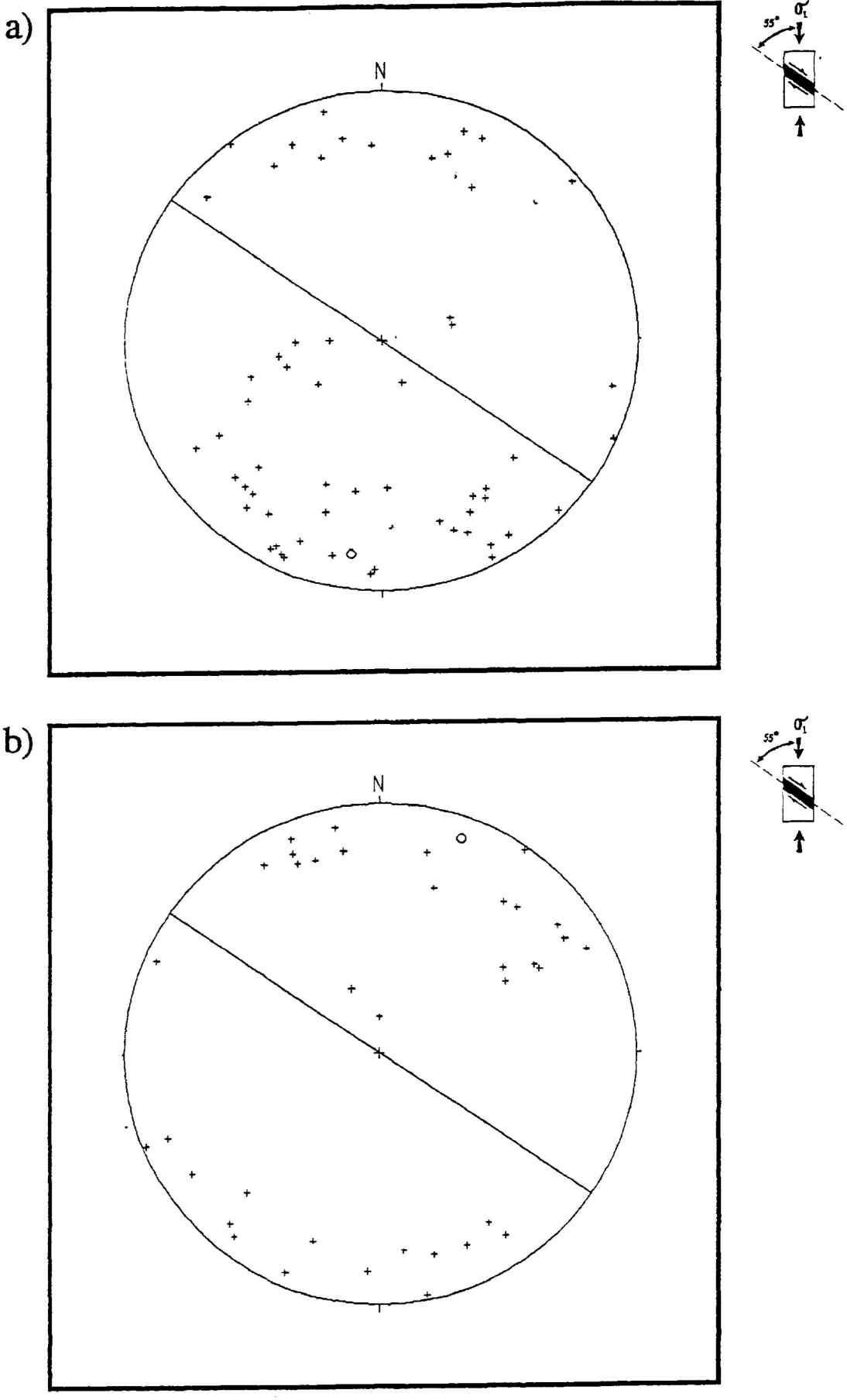

Figure 4.39 Pole figures for *c*-axes in samples deformed by transpressional shear in oblique shear zone under dry experimental conditions. Open circle represents mean directional vector of pole distribution.

a) Sample SZ-C1 shear strain 0.111
b) Sample SZ-C3-1 shear strain 0.189

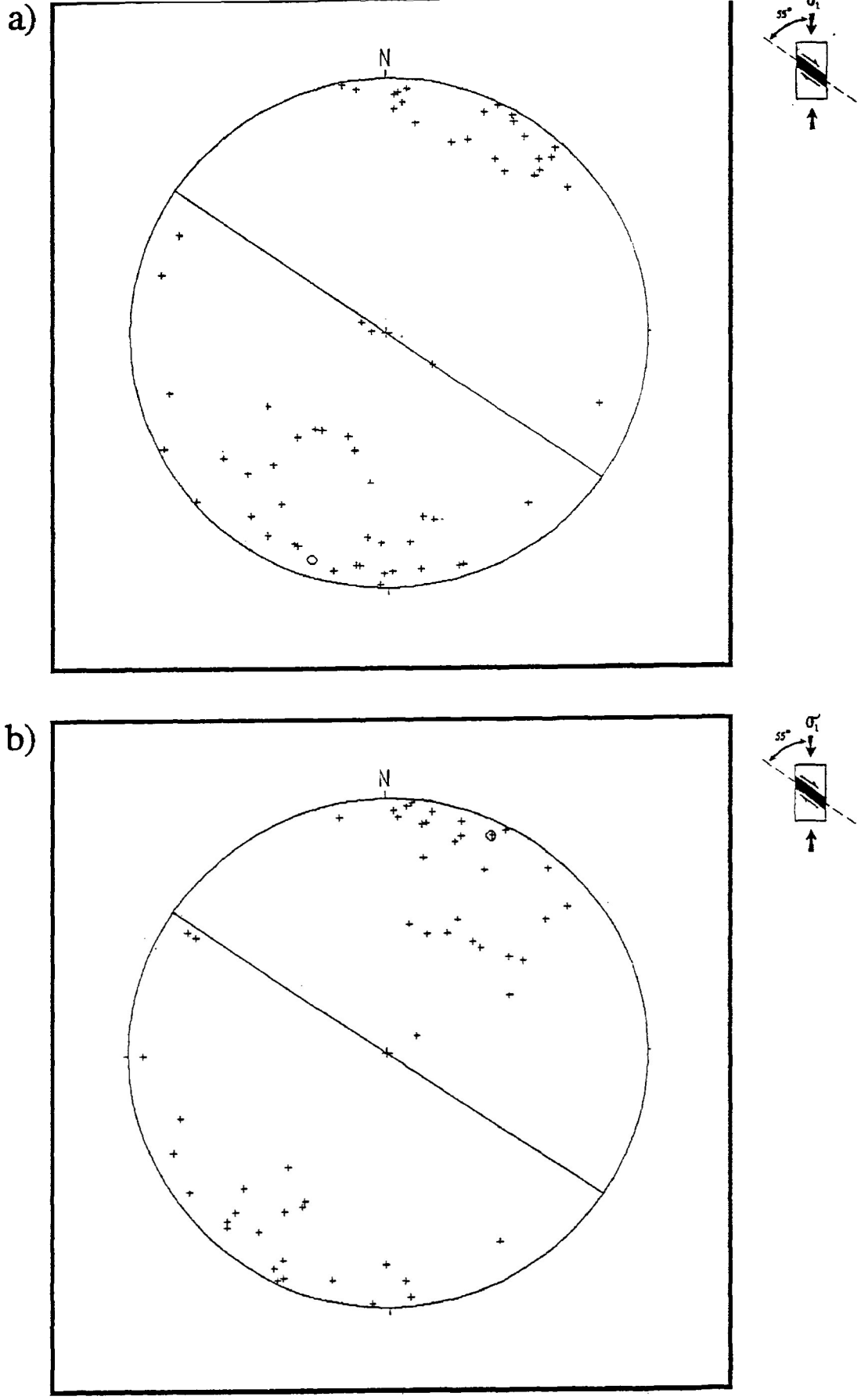

Figure 4.40 Pole figures for e_1 twin planes in samples deformed by transpressional shear in oblique shear zone under dry experimental conditions. Open circle represents mean directional vector of pole distribution.

a) Sample SZ-C1 shear strain 0.111
b) Sample SZ-C3-1 shear strain 0.189

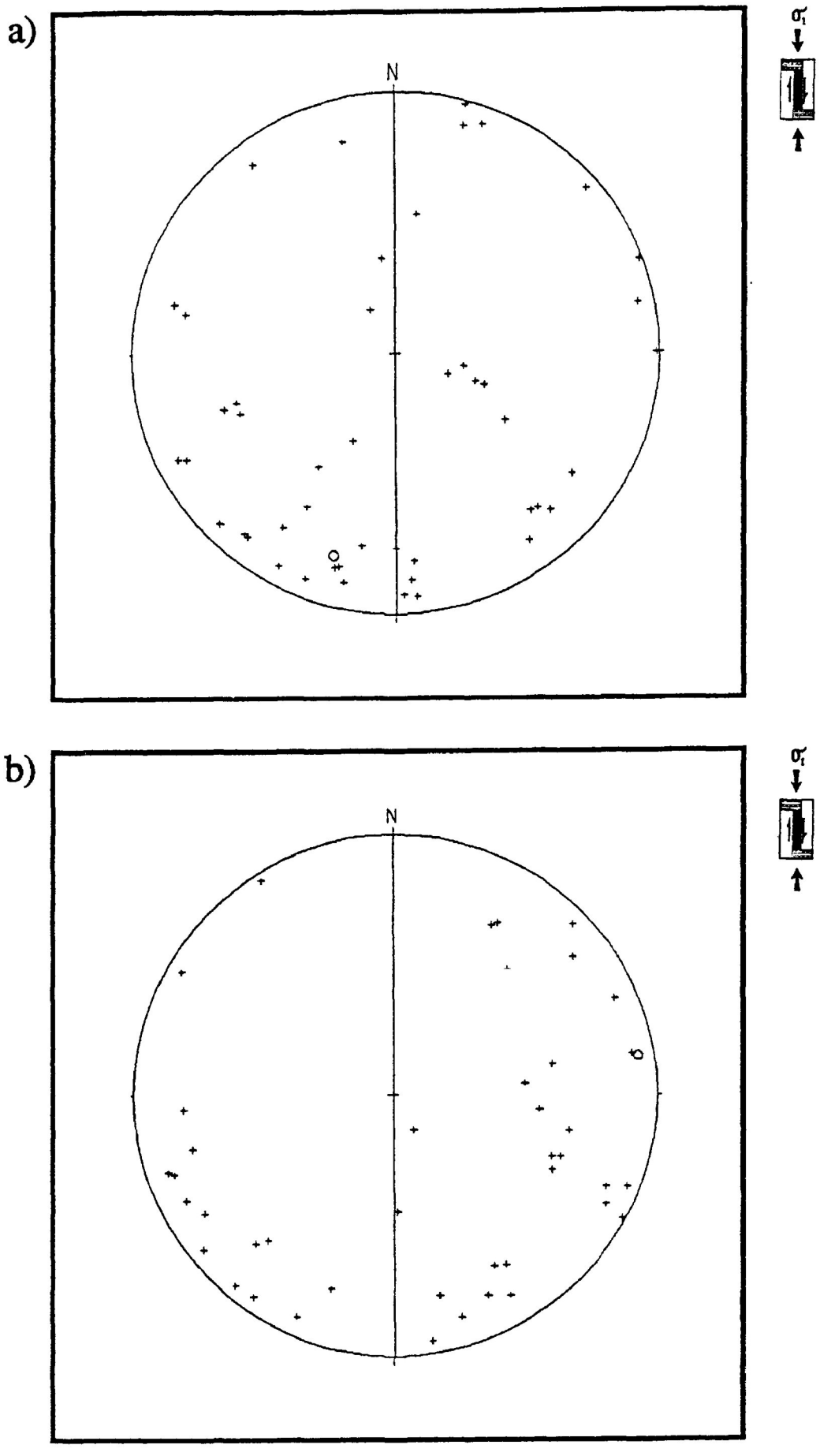

Figure 4.41 Pole figures for a) *c*-axes and b) e_1 twin planes in sample LS8811 deformed by simple shear in a 2mm longitudinal shear zone under dry experimental conditions. Open circle represents mean directional vector of pole distribution. (Shear strain=0.233)

maximum distribution has been observed by Rutter and Rusbridge (1977), Friedman and Higgs (1981) and Schmid *et.al.* (1987).

e) Simple Shear (longitudinal shear zone 2 mm wide)

In the case of the 2 mm longitudinal shear zone, sample LS8811 the *c*-axis pole figure distribution exhibits no preferred orientation and the distribution is random (Fig. 4.41a). The e_1-twin plane poles exhibit very broad distributions on either side of the shear zone direction as presented in figure 4.41b.

4.4.3 Determination of the σ_1 orientation by dynamic analysis

a) Undeformed

In the undeformed state the distribution of compression axes directions as determined by Turner's method is random and no distinct maximum is present in the stereographic projection (Fig.4.42b). This is reflected in a lack of a point concentration of high lamellae index values in the contoured lamellae index stereogram of figure 4.42c. Dietrich and Song's method is presented in figure 4.42a. As expected the stereogram does not exhibit a small circle distribution and the direction of shear in the individual calcite grains has no systematic direction (represented by the direction of arrowheads on the great circles). This suggests that the crystallographic fabric was originally random orientation within the undeformed sample.

b) Pure Shear (dry experimental conditions)

Interpretation of the σ_1 orientation was conducted on samples AC-3 and AC-8 (with experimental strains of 4.4% (R_s=1.070) and 18.03% (R_s=1.347) shortening, respectively) for dry pure shear tests. The contoured stereogram of sample AC-3 (e=4.4% (R_s=1.070)) for Turner's method is presented in figure 4.43a. The distribution of compression axes for AC-3 exhibit no concentration in the orientation of the known σ_1 (broad arrow).

Contouring of the lamellae index value associated with the compression direction derived from Turner's method does generate a broad distribution of lamellae index values greater than 40 L/mm near the orientation of the known σ_1 (Fig. 4.43b). Lamellae index values greater than 40 L/mm are representative of e_1-twin lamellae in this study since the

Figure 4.42 Preferred crystallographic and dynamic orientations in an undeformed sample (7C-3C). (Borradaile and McArthur, 1989)

a) Direction of shear in individual twin sets as defined by the arrowhead which represents the orientation of the pole to the *e*-twin plane and points away from the *c*-axis along the *c*-*e* great circle. Figure shows random nature of shear direction.

b) Turner's method for the determination of the orientation of the compressive stress direction from individual twin sets in calcite grains. Figure shows random distribution of compression directions.

c) Lamellae index method for the determination of the orientation of the maximum principal compressive stress. Figure shows random distribution of compression direction lamellae index values.

Sample 7C-3C (undeformed)

a)

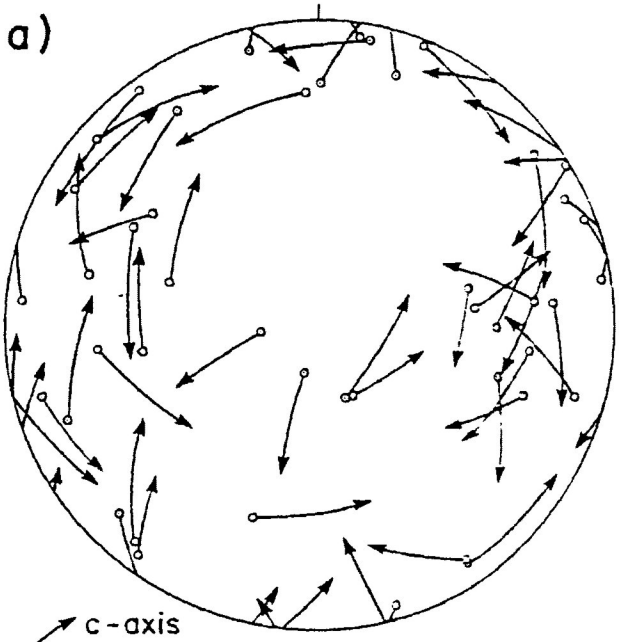

c-axis

pole to e-twin plane

Dominant e-twin planes + c-axis

n = 45

b)

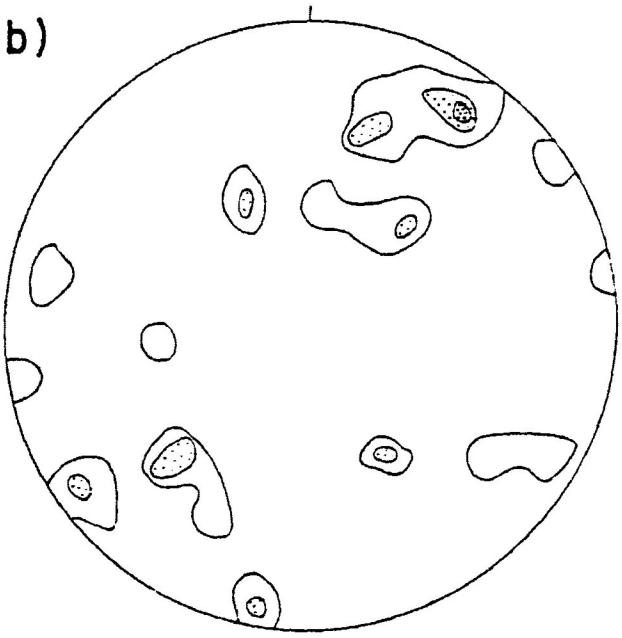

Turner's method for compression direction

contour interval = 1 (2,3,4)

n = 45 39 1 6 2 } e-twin planes

c)

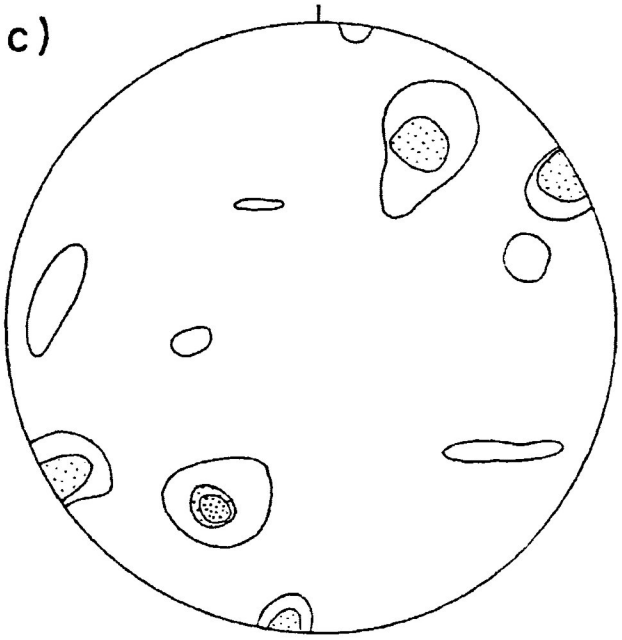

Lamellae Index spacing mm^{-1}

n = 45

contour interval = 20 (20, 40, 60)

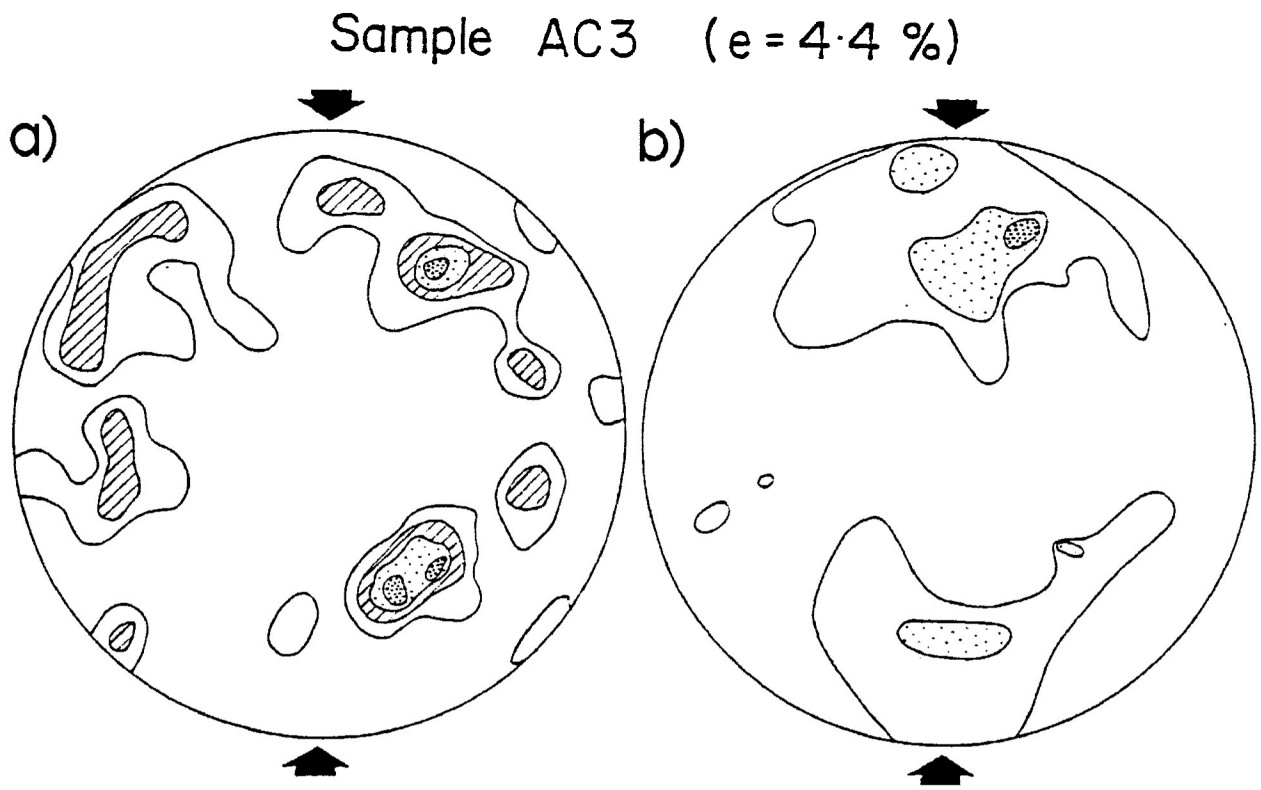

Figure 4.43 Preferred crystallographic and dynamic orientations in a sample (AC-3) shortened by 4.4% (R_s=1.070) by pure shear. The orientation of the σ_1 that existed during the triaxial rig tests is shown by the broad arrows. (Borradaile and McArthur, 1989)

a) Turner's method for the determination of the orientation of the compressive stress direction from individual twin sets in calcite grains. Figure shows spurious distribution of compression directions.

b) Lamellae index method for the determination of the orientation of the maximum principal compressive stress. Figure shows a distribution of compression direction lamellae index values which exhibits a better approximation of the σ_1 orientation.

majority of e_2-twin sets show less than 40 L/mm (Fig. 4.5). As the lamellae index value increases (*i.e.*, contour lines 80 and 120 L/mm) the orientation of the distribution permits an increasingly better approximation of the known σ_1 direction compared with that of Turner's method.

The contoured stereogram of the higher experimentally strained sample AC-8 (e=18.03% (R_s=1.347)) for Turner's method is presented in figure 4.44a. The distribution of compression axes for AC-8 exhibit a broad concentration about the known σ_1 direction. A point concentration of compression axes also occurs at 35 to 45° to the known σ_1 orientation. The majority of calcite grains that contribute to the point maximum have lamellae oriented parallel to the plane of foliation (Fig. 4.44c). This point distribution suggests that rigid body rotation of some calcite grains has occurred in the deformed sample, towards positions in which lamellae are perpendicular to the external shortening axis.

Figure 4.44c presents Dietrich and Song's dynamic analysis method. The stereogram illustrates the weak development of a small circle representing a cone with an opening of 26° around the known σ_1 orientation within which no *c*-axes (small arrowhead) are present. The axis of the small circle cone indicates that the orientation of the inferred σ_1 is within 15° of the known σ_1 orientation. It is also observed, that the characteristic direction of shear represented by the orientation of the arrows in figure 4.44c is directed away from the maximum compressive stress direction.

Contouring of the lamellae index values of the compression axes directions of figure 4.44b produces a well defined contour of high lamellae indices sub-parallel to the known σ_1 orientation. Again the higher lamellae index value locate, more precisely, the orientation of the known σ_1.

Figure 4.44 Preferred crystallographic and dynamic orientations in a sample (AC-8) shortened by 18.3% (R_s=1.347) by pure shear. The orientation of the maximum principle compressive stress that existed during the triaxial rig tests is shown by the broad arrows. (Borradaile and McArthur, 1989)

a) Turner's method for the determination of the orientation of the compressive stress direction from individual twin sets in calcite grains. Figure shows spurious distribution of compression directions.

b) Lamellae index method for the determination of the orientation of the maximum principal compressive stress. Figure shows a distribution of compression direction lamellae index values which exhibits a better approximation of the maximum principal compressive stress.

c) Dietrich and Song' method for the determination of the σ_1 orientation from preferred crystallographic orientation. The direction of shear is represented by the direction of arrowheads on the great circles containing the *c*-axis and the pole to the *e*-twin plain. This method is not completely successfully due to low strain of sample, however, poles to *e*-twin planes are located close to the known σ_1 direction.

Sample AC8 (e = 18·3 %)

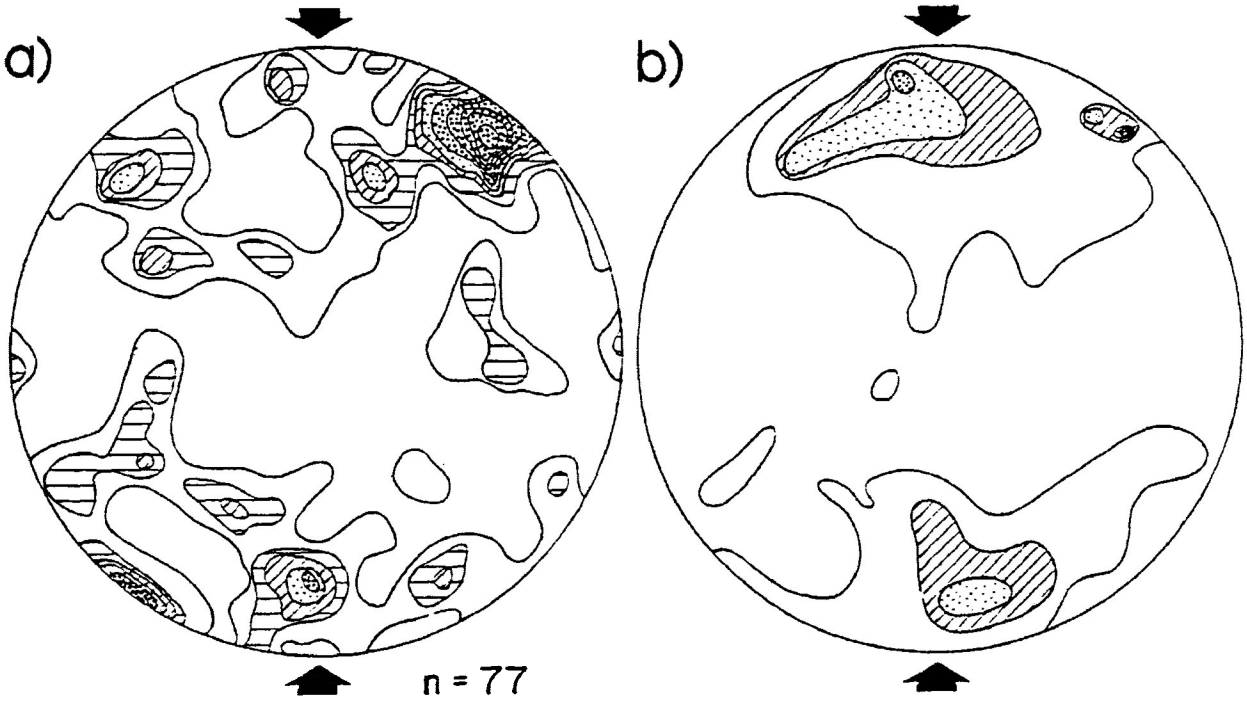

n = 77

Turner's method for compression direction
44 x 1
33 x 2
} e-twin planes
contour interval = 1 (2,3,4,5,6,7,8,9,10)

Lamellae Index
spacing mm^{-1}
n = 46
contour interval = 40
(40,80,120,160)

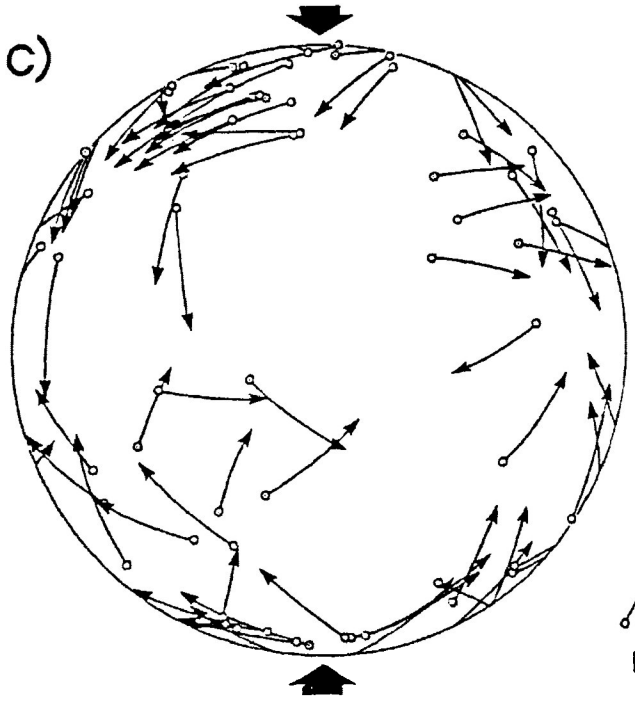

Dietrich and Song's method for compression axis

n = 59

c - axis

pole to e - twin plane

c) **Pure Shear (wet experimental conditions)**

In wet experimental conditions a large majority of twin lamellae become oriented perpendicular to the known σ_1 orientation. This distribution is clearly reflected in the stereographic projection of Dietrich and Song's Method (Fig. 4.45a). In the figure a well developed small circle distribution of *c*-axes has developed at 26° to the compressive stress and no *c*-axes are present within the small circle cone. Furthermore, many poles to *e*-twin planes are found to be oriented parallel to the axis of the small circle cone. The axis of the small circle cone locates the orientation of the known σ_1 quite precisely. The direction of shear, as expressed by the orientation of arrowheads in figure 4.45a, for each individual twin set point away from the orientation of known σ_1.

Turner's method yields a small circle girdle of compression axes at 45° to, and a point maximum parallel to, the known σ_1 orientation. This orientation is also indicated by the lamellae index method which exhibits the highest lamellae index values (>120 L/mm) approximately parallel to the known σ_1 orientation and surrounding this at 45° is a small circle distribution of lamellae index values between 80 and 100 L/mm (Fig. 4.45b).

Wet pure shear tests (Fig. 4.45b) show a more homogeneous compression axis distribution than those of the dry pure shear tests at equivalent experimental strains (Fig. 4.44a). It appears that the 45° small circle distribution observed in this sample is the result of controlled particulate flow (Borradaile, 1981) of calcite grains into orientations that have dominant twin sets parallel to the plane of foliation.

Figure 4.45 Preferred crystallographic and dynamic orientations in a sample (CPF-13) shortened by 17.8% (R_s=1.342) by pure shear. The orientation of the maximum principle compressive stress that existed during the triaxial rig tests is shown by the broad arrows. (Borradaile and McArthur, 1989)

a) Dietrich and Song' method for the determination of the σ_1 orientation. The direction of shear is represented by the direction of arrowheads on the great circles containing the *c*-axis and the pole to the e-twin plain (26° small circle girdle given). In this case the method is successfully due to the pore fluid pressure and its associated particulate flow.

b) Lamellae index method for the determination of the orientation of the σ_1. Figure shows a distribution of compression direction lamellae index values which exhibits a good approximation of the σ_1 direction. Also shown is the development of a small circle girdle at 45° to the known σ_1 direction due to particulate flow of grains in the presence of a pore fluid pressure approximately equal to the rock pressure.

a)

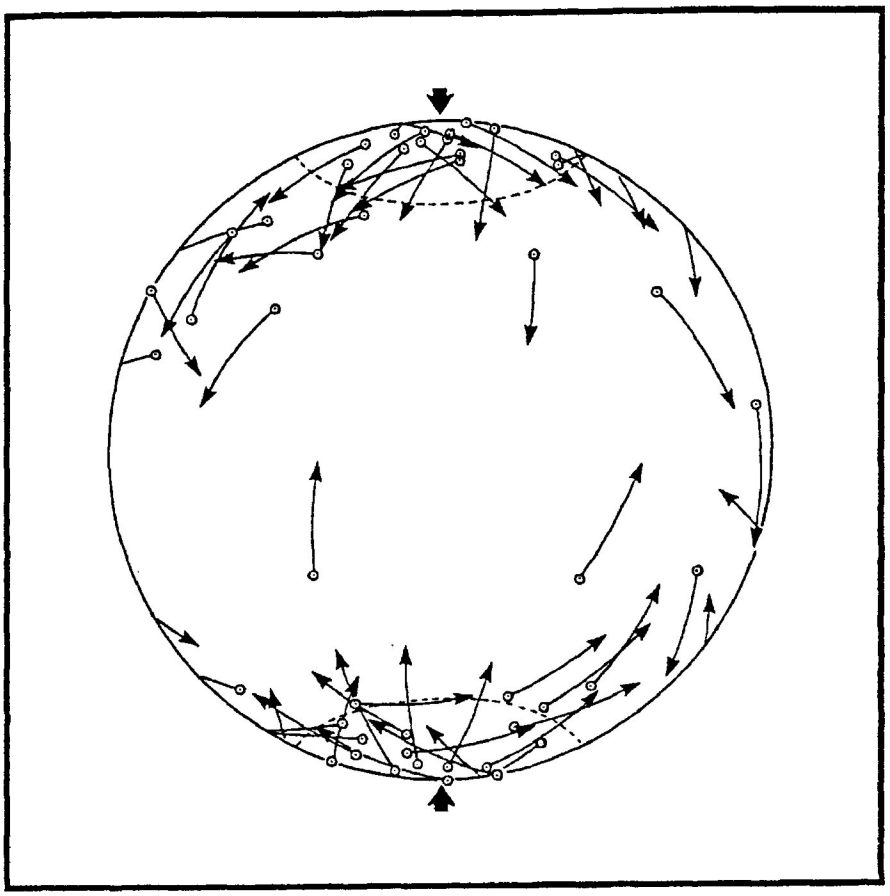

b)

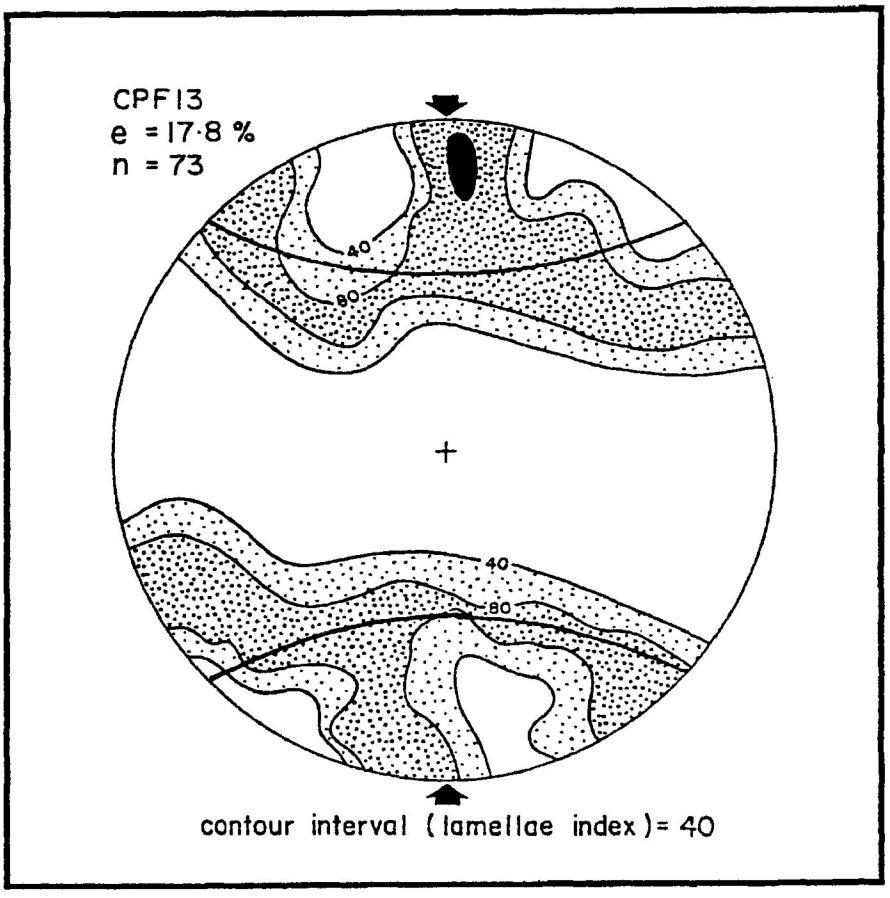
CPF13
e = 17·8 %
n = 73
40
80
40
80
contour interval (lamellae index) = 40

The point maximum parallel to the known σ_1 orientation is the result of those calcite grains that have rotated into orientations which are most favourable for the development of twin lamellae. These calcite grains may either be restricted from further rotation by neighbouring grains or are still in the process of rigid rotation towards an orientation in which twin lamellae become normal to the known σ_1 direction.

d) <u>Transpressional Shear (Dry tests) in oblique shear zones</u>

Interpretation of the σ_1 orientation was conducted on samples SZ-C1, SZ-C3, and SZ-C3-1 (with experimental shear strains of 0.111, 0.129 and 0.189, respectively) for dry transpressional shear tests. The contoured stereogram of sample SZ-C1 (shear strain=0.111) for Turner's method is presented in figure 4.46a. In the figure a point maximum occurs at approximately 35 to 45° to the known σ_1 direction approximately normal to the shear zone direction. Contouring of the lamellae index values yields a two-part broad maximum for values greater than 80 L/mm (Fig. 4.46b). The first part of this lamellae index maximum is located parallel to the known σ_1 direction and the second part appears to be approximately perpendicular to the shear zone wall.

The contoured stereogram of Turner's method for sample SZ-C3 (shear strain=0.129) is presented in figure 4.47a. The distribution of compression directions is not as well developed as that observed in the sample SZ-C1 (shear strain=0.111) or the preceding sample SZ-C3-1 (shear strain=0.189). This poor distribution of compression axes is also reflected in the lamellae index stereogram except for a small point maximum at the known σ_1 direction (Fig. 4.47b). The lack of any distinct maximum in either Turner's or lamellae index method may be the result of the lower preferred dimensional orientation observed in the sample SZ-C3 (Fig.

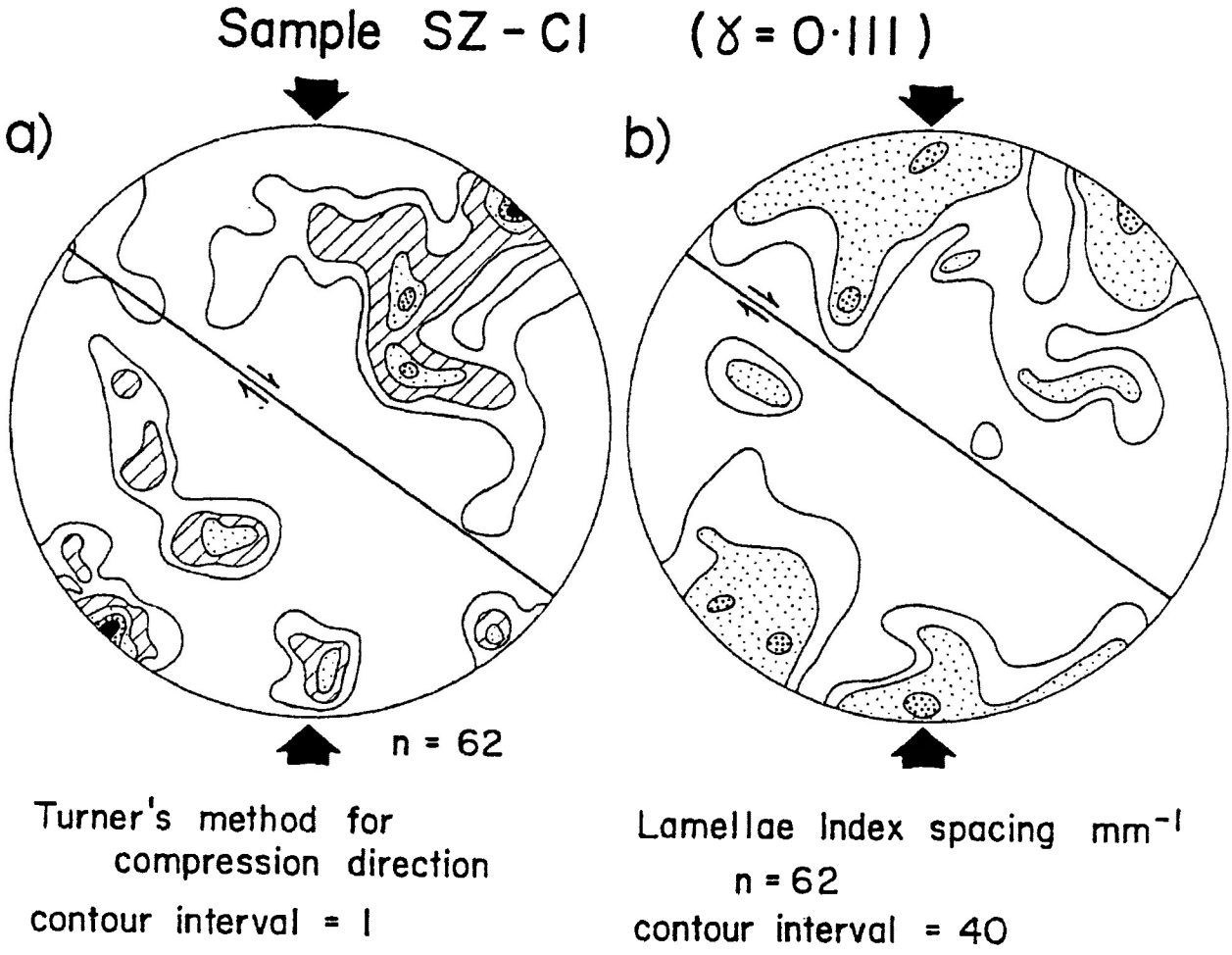

Figure 4.46 Preferred crystallographic and dynamic orientations in a sample (SZ-C1) deformed by transpressional shear in a oblique shear zone (shear strain 0.111). The orientation of the σ_1 that existed during the triaxial rig tests is shown by the broad arrows (Borradaile and M^{c}Arthur, 1989).

a) Turner's method for the determination of the orientation of the compressive stress direction from individual twin sets in calcite grains.

b) Lamellae index method for the determination of the orientation of the σ_1. Figure shows a distribution of compression direction lamellae index values which exhibits a better approximation of the σ_1 orientation.

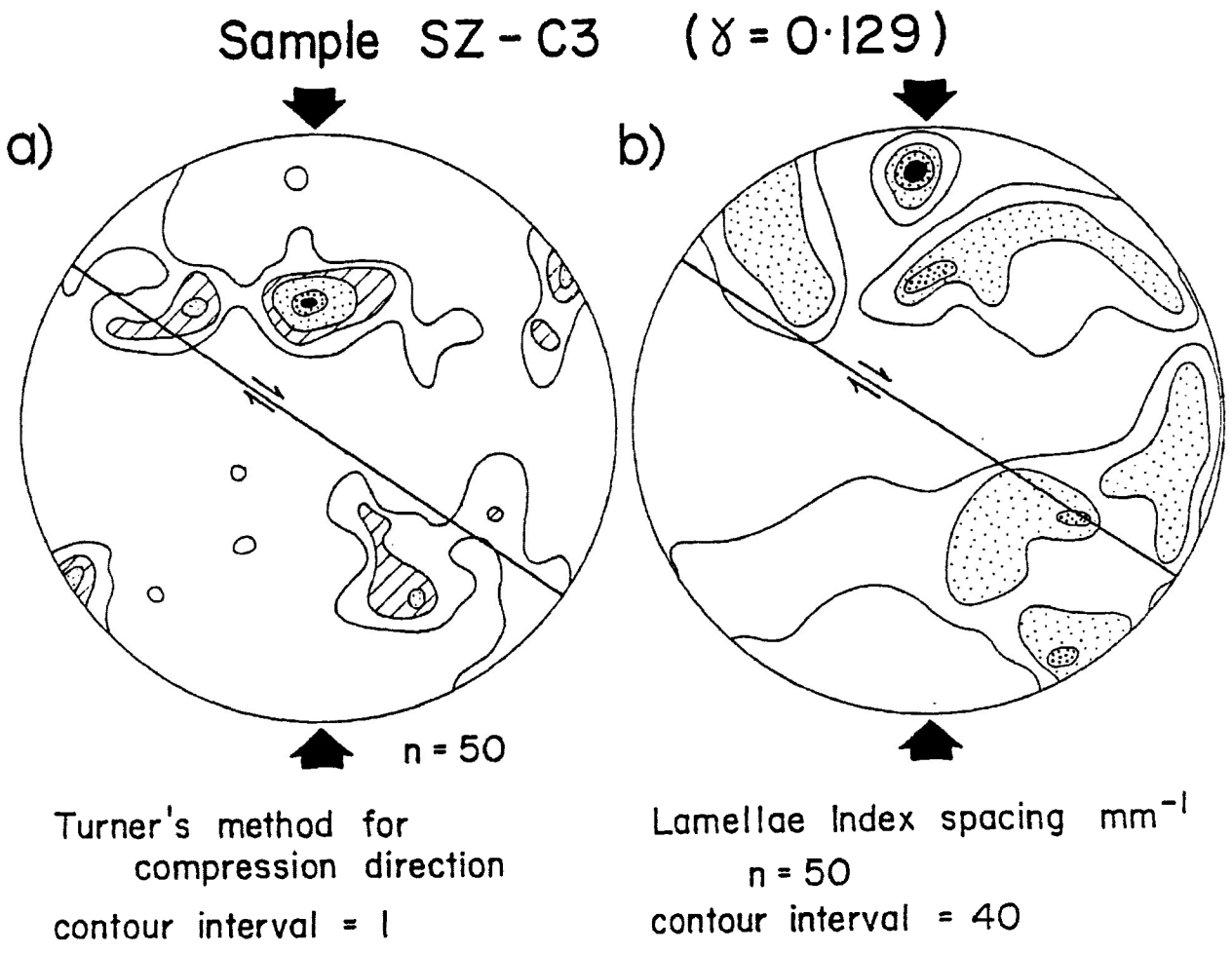

Figure 4.47 Preferred crystallographic and dynamic orientations in a sample (SZ-C3) deformed by transpressional shear in a oblique shear zone (shear strain 0.129). The orientation of the known σ_1 that existed during the triaxial rig tests is shown by the broad arrows. (Borradaile and McArthur, 1989)

a) Turner's method for the determination of the orientation of the compressive stress direction from individual twin sets in calcite grains. The distribution is not as well developed as that observed in SZ-C1 and SZ-C3-1.

b) Lamellae index method for the determination of the orientation of the σ_1. The distribution is not as well developed as that observed in SZ-C1 and SZ-C3-1.

Figure 4.48 Preferred crystallographic and dynamic orientations in a sample (SZ-C3-1) deformed by transpressional shear in a oblique shear zone (shear strain 0.189). The orientation of the known σ_1 that existed during the triaxial rig tests is shown by the broad arrows (Borradaile and McArthur, 1989).

a) Turner's method for the determination of the orientation of the compressive stress direction from individual twin sets in calcite grains.

b) Lamellae index method for the determination of the orientation of the σ_1.

c) Dietrich and Song' method for the determination of the σ_1 orientation. The 26° small circle girdle centred on σ_1 is given. The direction of shear is represented by the direction of arrowheads on the great circles containing the *c*-axis and the pole to the *e*-twin plain. In this case the method is successfully in deducing an orientation of the σ_1.

Sample SZ-C3-1 ($\gamma = 0.189$)

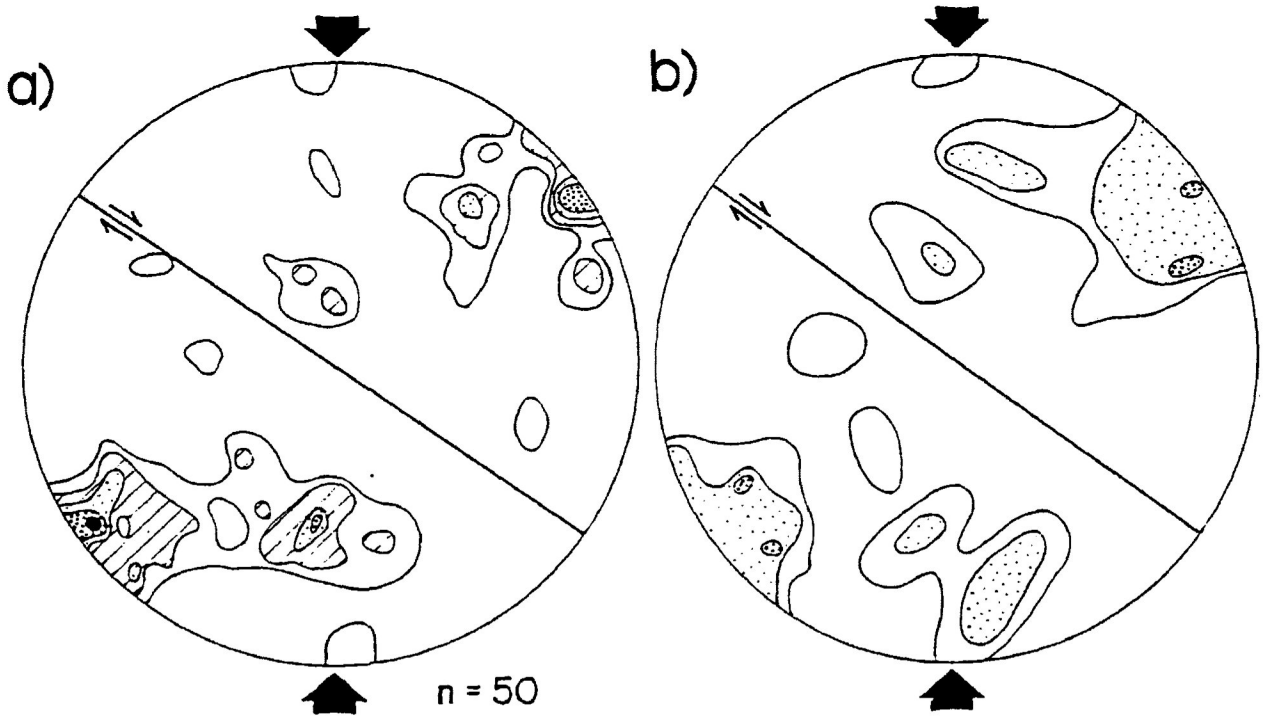

Turner's method for compression direction
contour interval = 1

Lamellae Index spacing mm^{-1}
n = 50
contour interval = 40

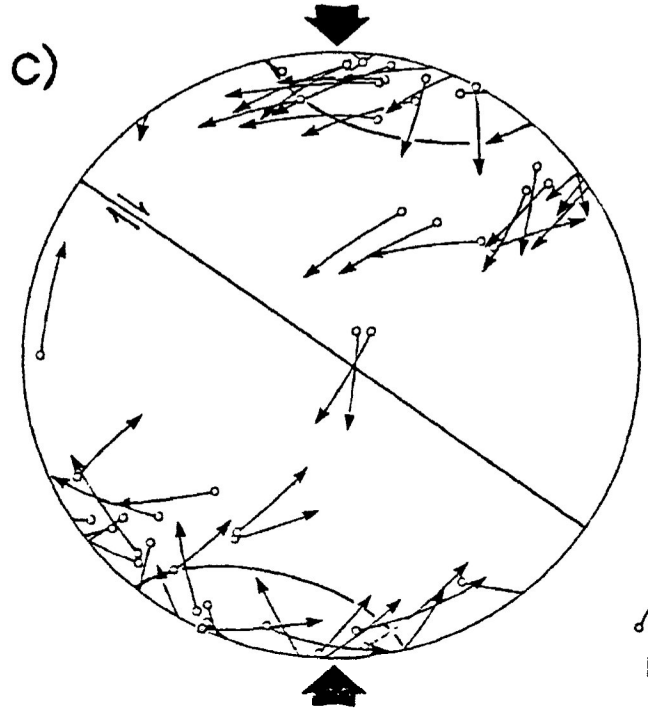

Dietrich and Song's method for compression axis

n = 45

c - axis

pole to e - twin plane

5.19a-e) and the lower average lamellae index value observed in figure 4.15c.

The contoured stereogram for Turner's method for sample SZ-C3-1 (shear strain=0.189) is presented in figure 4.48a. In the figure a point maximum is located approximately 50° from the known σ_1 direction. This point maximum is also reflected in the contoured lamellae index diagram (Fig. 4.48b) in which values of 80 and 120 L/mm are concentrated. Also present is a weaker distribution of high lamellae index values, in the southern half of the stereogram, parallel to the known σ_1 orientation.

Dietrich and Song's method for compression axes determination (Fig. 4.48c) yields a small circle with an open angle of 26° around the inferred σ_1 orientation. The cone axes is found to be oriented slightly oblique (15°) to the known σ_1 orientation in the direction of shear.

In sample SZ-C3-1 a large number of the twin sets operate in a shear direction which is opposite to that imposed by the oblique shear zone (Fig. 4.48c). This was also observed to a lesser degree by Schmid *et.al.* (1987). Their experiments were conducted at much higher temperatures, shear strains and much faster strain rates than those of this study. The increased number of calcite grains that exhibit the opposite direction of shear may be due to the difference in experimental conditions or possibly due to the large component of pure shear that is the result of the 55° oblique shear zone used in this study, as opposed to 35° in theirs.

e) <u>Simple Shear (2 mm thick longitudinal shear zone)</u>

Interpretation of the σ_1 orientation was conducted on samples LS8811 (shear strain=0.230) and LS8807 (shear

a)

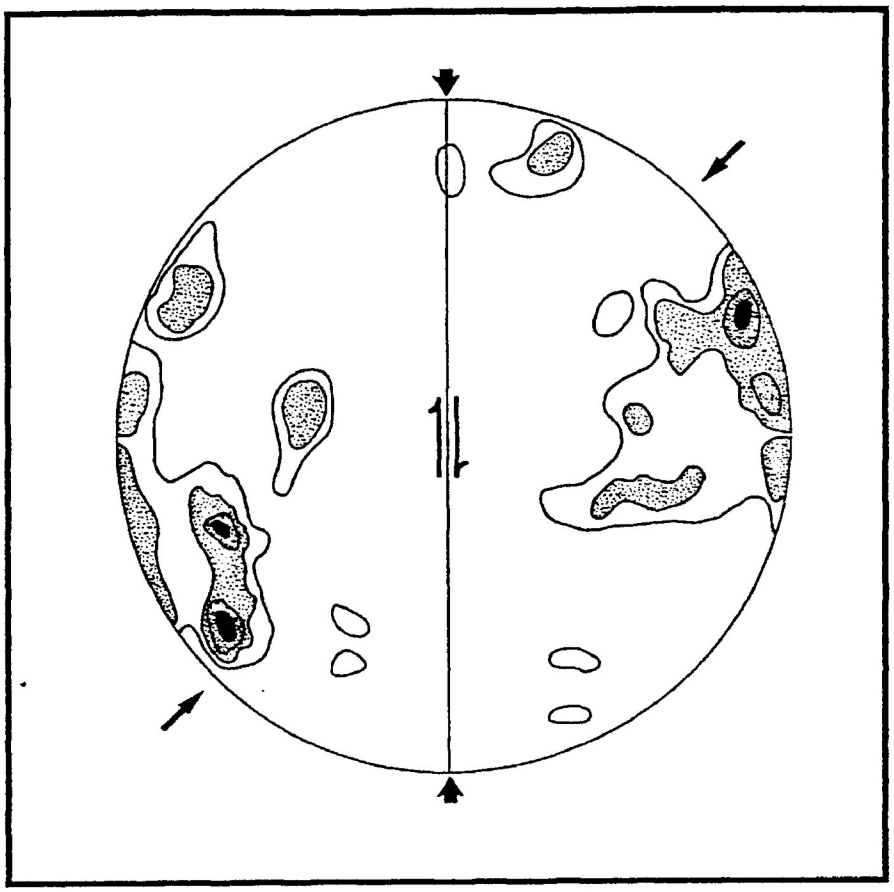

b)

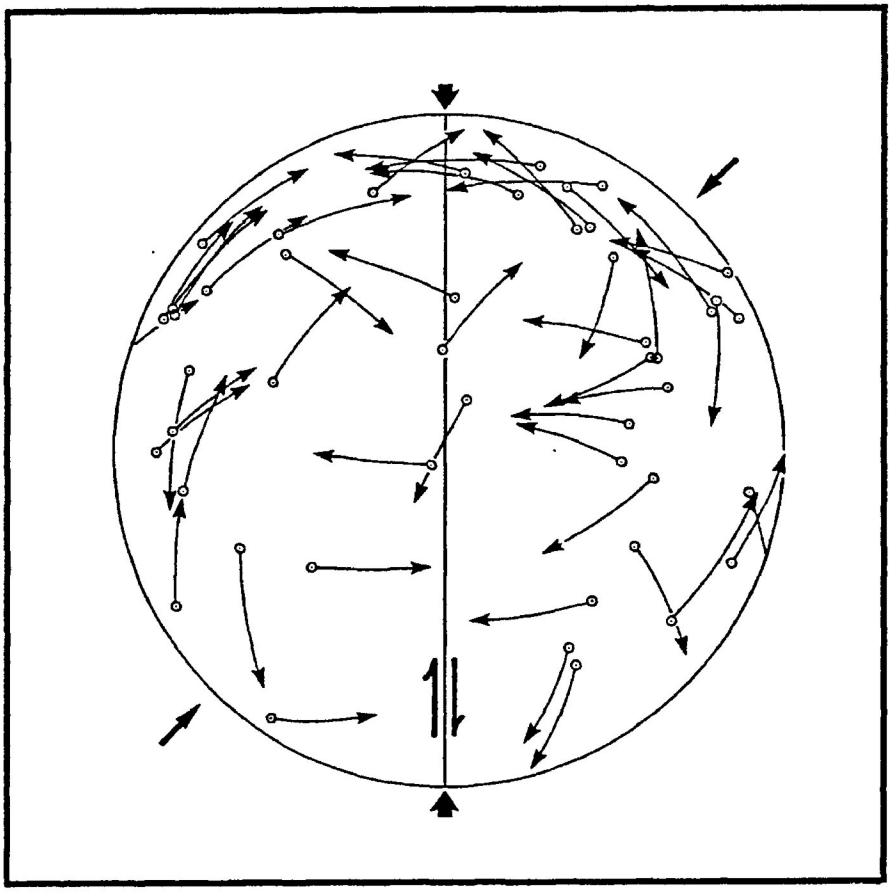

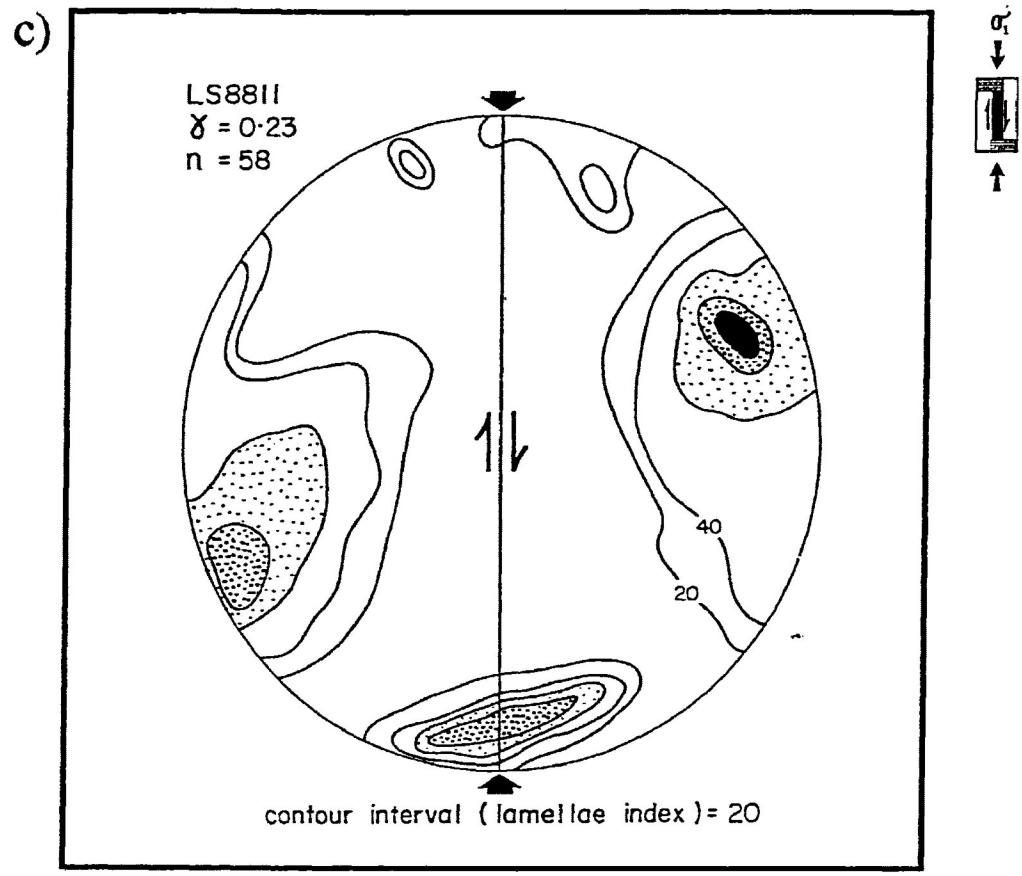

Figure 4.49 Preferred crystallographic and dynamic orientations in sample LS8811 deformed by "simple shear" in a 2mm thick longitudinal shear zone (shear strain=0.233). (Borradaile and McArthur, 1989).

a) Turner's method for the determination of the orientation of the compressive stress direction from individual twin sets in calcite grains. Figure presents a theoretical σ_1 orientation which is kinematically compatible with the sense of shear (thin arrows). Broad arrows represent the known σ_1 orientation.

b) Dietrich and Song' method for the determination of the σ_1 orientation. The direction of shear is represented by the direction of arrowheads on the great circles containing the *c*-axis and the pole to the *e*-twin plain. Figure presents a theoretical σ_1 orientation which is kinematically compatible with the sense of shear (thin arrows). Broad arrows represent the known σ_1 orientation.

c) Lamellae index method for the determination of the orientation of the σ_1. Determination of the σ_1 orientation for the 2mm thick longitudinal shear zone which is kinematically compatible with the sense of shear. Broad arrows represent the known σ_1 orientation.

strain=0.993) for 2 mm wide longitudinal simple shear. Figure 4.49a presents the contoured stereogram of Turner's method for sample LS8811. In the figure the maximum concentrations of compression axes are oriented at approximately 45° to the shear zone in a sense that is compatible with the observed shear zone (theoretical σ_1 orientation). There is also a small point maximum of compression axes parallel to the known σ_1 orientation. This distribution is reflected in the lamellae index diagram (Fig. 4.49c) which exhibits maximum twin lamellae values of 80 to 100 L/mm at 45° to the shear zone as well as a smaller maximum lamellae index distribution (80 L/mm) parallel to the known σ_1 orientation.

Dietrich and Song's method is presented in figure 4.49b. The figure does not exhibit a small circle girdle of *c*-axis around the known σ_1 orientation or the theoretical σ_1 orientation. Similar to transpressional shear, but to a lesser degree, the direction of shear (defined by small arrowheads) in many cases is also not compatible with the dextral shear sense.

A stereogram for Sample LS8807 (shear strain=0.933) for Lamellae index method is presented in figure 4.50a. From the figure it can be observed that the sample has experienced a higher degree of axial compression, represented by the point maximum of compression axes parallel to the known σ_1 direction. This is a result of the inability of the longitudinal shear assemblage to accommodate high experimental shear strains (a function of the compactability of the putty insert). It should also be noted that the lamellae index distribution no longer reflects the earlier simple shear strain history observed in the less strained sample.

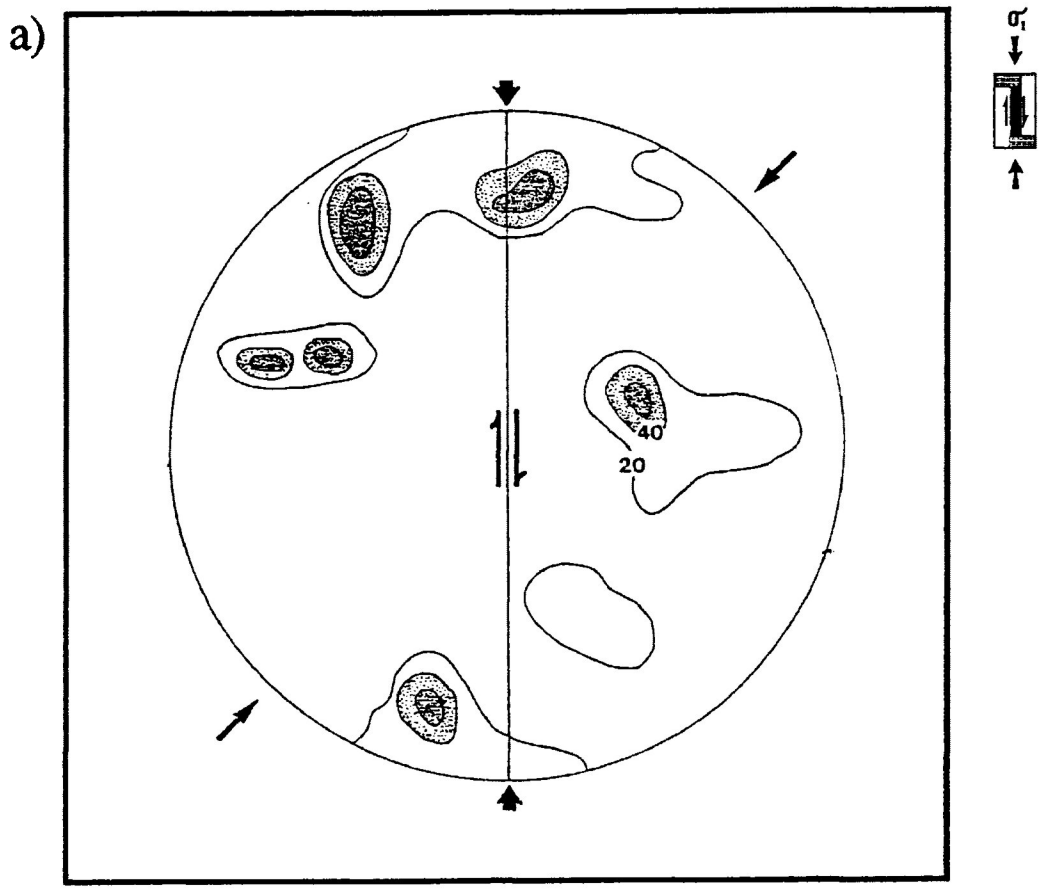

Figure 4.50 Preferred crystallographic and dynamic orientations in sample LS8811 deformed by "simple shear" in a 5mm thick longitudinal shear zone (shear strain 0.933) (Borradaile and McArthur, 1989).

a) Lamellae index method for the determination of the orientation of the σ_1. Figure shows a distribution of the highest lamellae index values parallel to the known σ_1 (broad arrows) suggesting a high degree of pure shear. Figure presents a theoretical σ_1 orientation which is kinematically compatible with the sense of shear (thin arrows).

4.5 Discussion of twin lamellae development for dry and wet pure shear, transpressional shear and simple shear

a) Variation in the percentage and degree of twinned calcite grains between deformation types

i) Transpressional shear and Pure shear (wet and dry)

Comparison of the percentage of calcite grains exhibiting microscopically visible twinning and average e_1-lamellae index with increasing experimental strain are presented in figure 4.51 and 4.52, respectively, for transpressional shear and pure shear (wet and dry experimental conditions). Shear strains have been converted to strain % from a formula developed by G.J Borradaile for 2 dimensional strain deformation (personal communication, see curve in Appendix B). The formula is % shortening = $(1-R^{-2/3})\cdot 100$, where R is equal to the finite strain ratio.

In figure 4.51 the majority of calcite grains exhibit twin lamellae development at much lower experimental strains in transpressional shear than in wet and dry pure shear. The calcite grains in transpressional shear also exhibit on average higher e_1-lamellae indices than the other forms of deformation at similar experimental strains (Fig. 4.52). Twinning in wet pure shear occurs more readily than dry pure shear with the majority of calcite grains exhibiting twinning at slightly higher experimental strains than transpressional shear (Fig. 4.51). However, the twinning is less pronounced than in transpressional shear or dry pure shear. In dry pure shear higher experimental strains are needed to cause the majority of the calcite grains to exhibit twinning. The average e_1-lamellae index values that occur in calcite grains deformed by dry pure shear, are higher than in the case of wet pure shear and lower than transpressional shear.

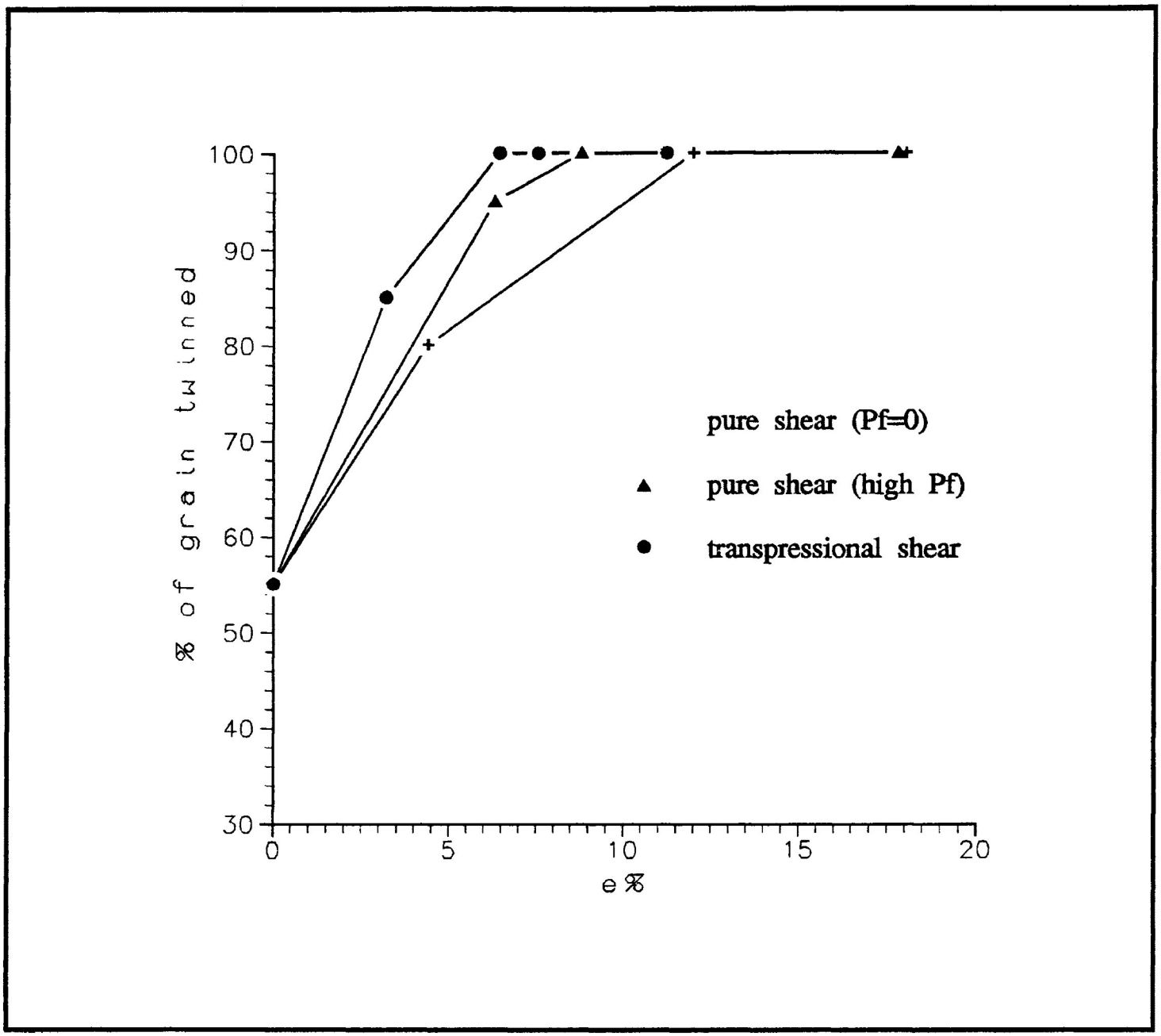

Figure 4.51 Variation in % of calcite grains in total aggregate that exhibit twinning in pure shear under dry and wet experimental conditions and transpressional shear as experimental strain increases (strain in % shortening) The shear strains values have been converted to an equivalent percent strains by a formula developed by G.B. Borradaile (personal communication, 1989).

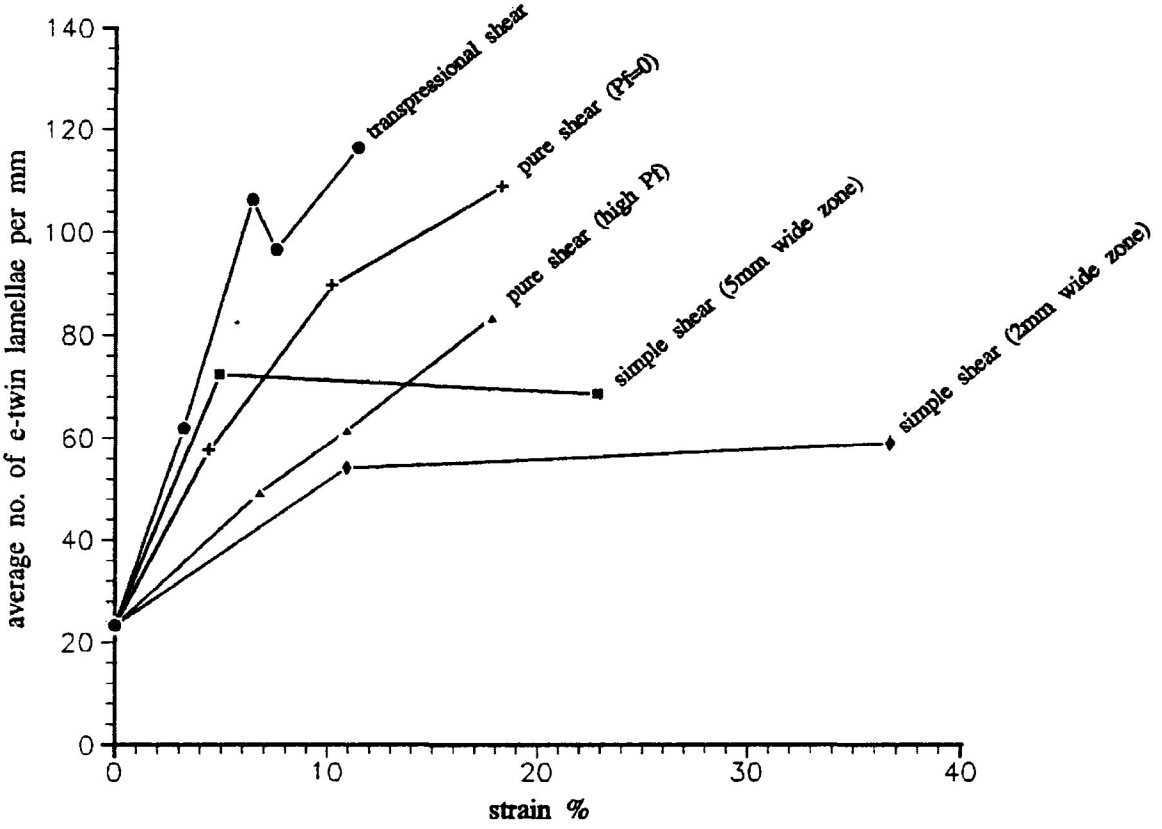

Figure 4.52 Variation in average e_1-lamellae index for the frequency distributions of measurements on individual calcite grains. The samples were deformed by pure shear (dry (P_f=0) and wet experimental conditions (high P_f), tranpressional shear and simple shear (2mm and 5mm thick shear zones). The shear strains values have been converted to an equivalent percent strains by a formula developed by G.B. Borradaile (personal communication, 1989).

Transpressional shear and wet pure shear exhibit the most rapid increase in the percentage of calcite grains that exhibit microscopically observable twinning with increasing experimental strain. As presented in the previous section (4.4) highly strained transpressional shear and wet pure shear samples (Fig. 4.48c and Fig. 4.45a, respectively) develop a distribution of *c*-axes for calcite grains, like that predicted by Dietrich and Song (1984). This reflects a moderate to strong PCO in calcite e_1-twin lamellae as expressed by the poles to the e_1-twin sets oriented parallel to the inferred σ_1 direction.

A moderate to strong PCO of e_1-twin lamellae is the result of the development of a moderate to strong preferred dimensional orientation (PDO, see Chapter 5 for discussion) in calcite grains. This can be described as a related preferred dimensional orientation/ preferred crystallographic orientation (PDO/PCO). The degree of PDO/PCO development is a function of the amount of experimental strain and the type of deformation occurring in the test specimen.

The preferred crystallographic orientation of the dominant e-lamellae in calcite grain, in a well developed PDO, is both a consequence of the initial calcite grain shape (R_i= 1.52, sample 7C-3C) and the deformation of the calcite grain by twinning, or a combination of the two. The R_i of calcite grain are controlled mostly by fracture along cleavage planes, produced during the crushing of calcite in the sample material preparation. This process produces a rhombohedral shaped calcite grains in which twin lamellae are parallel to the long diagonal of the grains (fig 4.53a).

Although calcite grain deformation is occurring through twinning on e_1 much of the PDO is produced by rigid body rotation of the calcite grains within the ductile cement

Figure 4.53a-d Schematic representation of the development of PDO/PCO in calcite grains.

a) Twin lamellae in the undeformed calcite cut the long diagonal of the cleavage defined grain shape. Strain by intense twinning and rigid body rotation are induced by an internally applied stress.

b) Development of the PDO/PCO in transpressional shear sub-parallel to the shear zone wall. (undeformed (left); deformed (right))

c) Development of the PDO/PCO in wet pure shear perpendicular to the experimental σ_1 orientation.(undeformed (left); deformed (right))

d) Development of the PDO/PCO in simple shear 45° to the shear zone wall. Development of the PDO/PCO perpendicular to the experimental σ_1 orientation as component of pure shear becomes dominant. (undeformed (left); deformed (right))

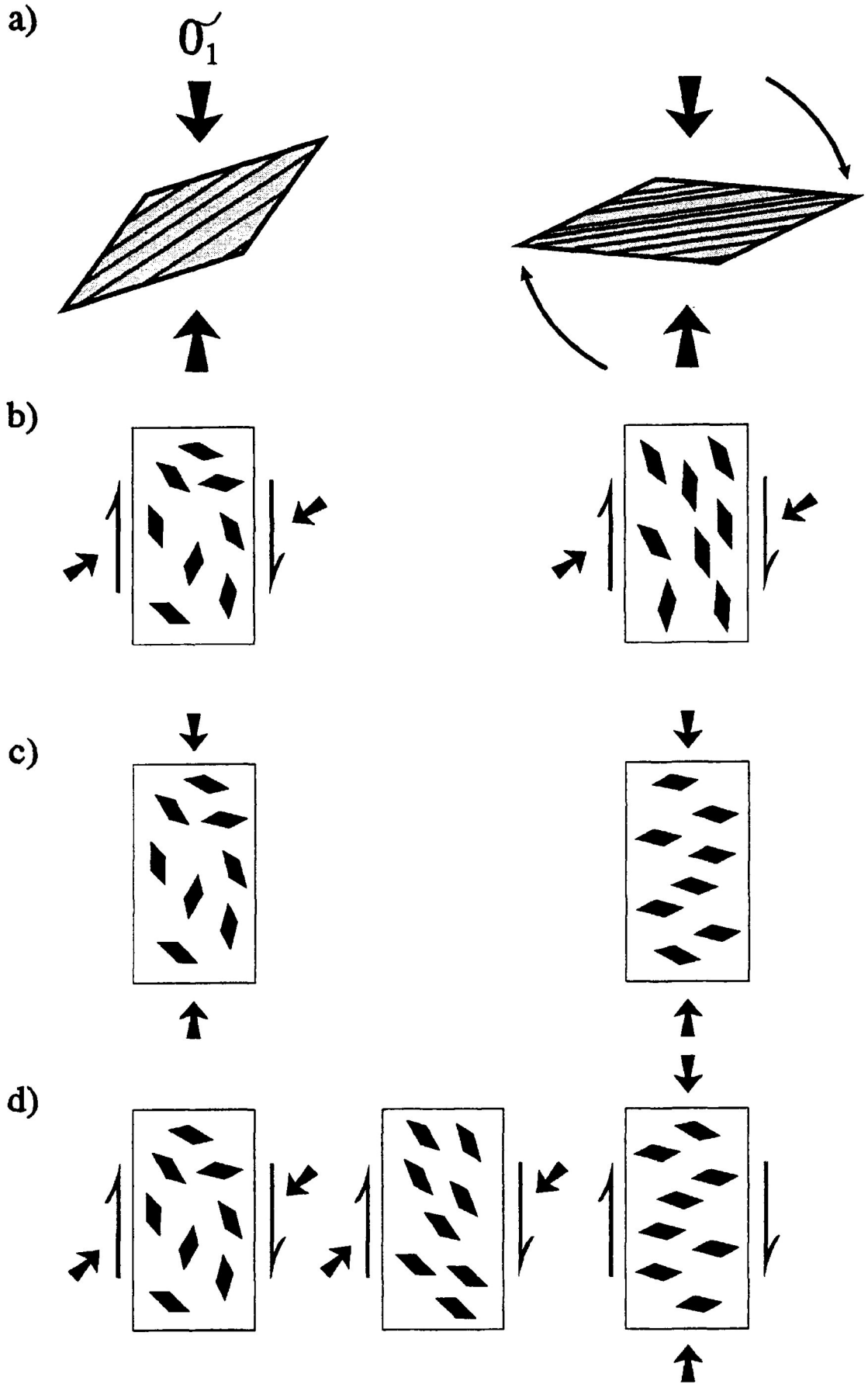
a)
σ_1
b)
c)
d)

matrix. The development and specific orientation of a PDO/PCO has a direct effect on the percentage of calcite grains exhibiting twin lamellae in the deformed specimen and the degree of twinning in individual calcite grains.

The intergranular deformation in transpressional shear produces calcite grain alignments which are favourably oriented for further twinning (Fig. 4.53b). The orientation of the PDO/PCO is at 55° to the known σ_1 direction. This allows for many of the calcite grains to become twinned at low experimental strains. High lamellae indices also develop in calcite grains that are favourably oriented increasing the average lamellae index value.

In the case of wet pure shear the calcite grain alignments are unfavourable for further twinning (Fig. 4.53c). The orientation of the PDO/PCO is perpendicular to the known σ_1 direction. The resolved shear stress on calcite grain contained within the PDO/PCO will be low and fewer twins will develop. However, during the development of the PDO/PCO some calcite grains may rotate through orientations more favourable for twinning. This would allow an increasing number of calcite grains to become twinned with lower lamellae indices than would be required in the absence of grain rotation. This allows for a more consistent lamellae index distributions reflected by a decreasing standard deviation.

The development of a strong PDO/PCO in dry pure shear occurs at much higher experimental strains and as a result calcite grains unfavourably oriented for twinning remain so until higher experimental strains are reached (e>18.30% (R_s=1.347)). At higher experimental strains calcite grains may begin to undergo rigid rotation so that e-twin lamellae become oriented perpendicular to known σ_1 orientation, similar to that observed in wet pure shear at low experimental strains.

ii) **Simple shear (2 mm and 5 mm thick longitudinal shear zones)**

Comparison of the percentage of calcite grains exhibiting twinning and average e_1-lamellae index with increasing experimental strain are presented in figure 4.54 and 4.52, respectively, for simple shear (2 mm and 5 mm thick longitudinal shear zones). Shear strains have been converted to strain % from a formula developed by G.J. Borradaile (personal communication).

In 2 mm thick longitudinal shear zones the PDO/PCO is low to moderate as a result the new twin lamellae are restricted to calcite grains that are favourably oriented (45° to the kinematically imposed σ_1 orientation necessary for shear zone development). This only allows for approximately 75% to 80% of the calcite grains to be visibly twinned. Also the average lamellae index and the standard deviation remains relatively constant as the experimental shear strain increases.

The development of a strong PDO/PCO in the calcite grains is not observed in the deformed specimens of this study. It would be expected that at higher experimental shear strains (>0.993) the development of a strong PDO/PCO may occur in the shear zone with calcite grain long axes oriented obliquely to the walls of the shear zone. This will subsequently allow for an increase in the number of calcite grains visibly twinned and an increase in the degree of twinning (higher lamellae index values).

For 5 mm thick longitudinal shear zones a strong PDO/PCO develops as a result of a combination of simple shear at low experimental shear strains and pure shear at higher experimental shear strains. The PDO/PCO rotates from an orientation oblique to the shear zone walls to an orientation that is perpendicular to the known σ_1 orientation as the

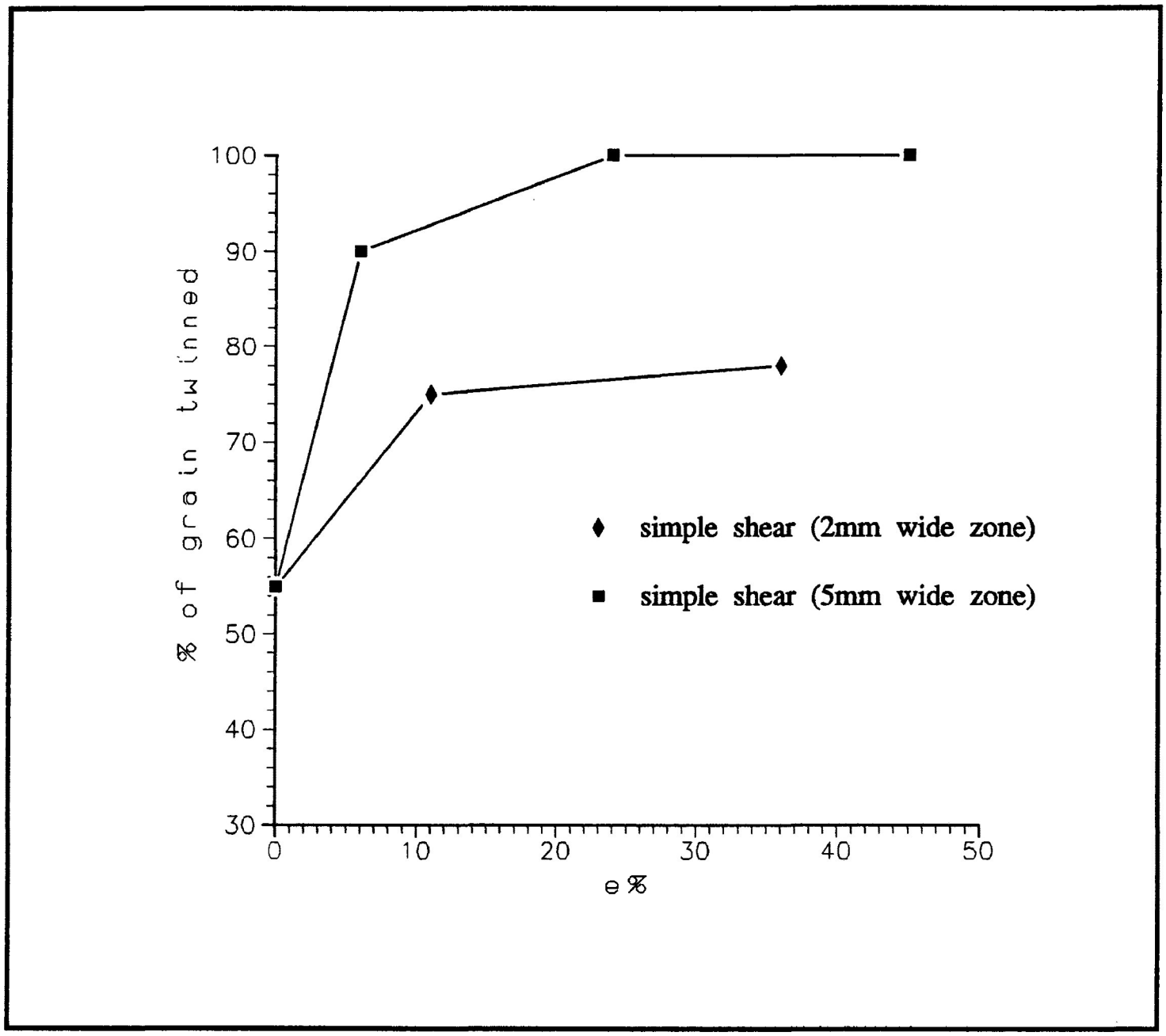

Figure 4.54 Variation in % of calcite grains in total aggregate that exhibit twinning in simple shear for 2mm and 5mm thick shear zones as experimental strain increases (strain in shortening). The shear strains values have been converted to an equivalent percent strains by a formula developed by G.B. Borradaile (personal communication, 1989 (see Appendix D).

component of pure shear becomes more dominant (Fig. 5.29a-c).

The intergranular deformation causing the rotation of calcite grains through orientations favourable for twinning subsequently allowing the majority of calcite grains to develop visible twin lamellae (Fig 4.53d). The higher average lamellae indices observed in the 5 mm thick shear zones, therefore, reflect the pure shear component on a well developed PDO/PCO in an orientation favourable for twinning in calcite grains.

b) Effect of a pore fluid pressure on the development of twin lamellae

In wet pure shear the rigid body rotation of calcite grains is greater than in dry pure shear because of the introduction of a pore fluid pressure equal to approximately 95% of the rock pressure. The presence of a pore fluid pressure influences the development of twin lamellae in calcite grains. A pore fluid pressure, during sample deformation, allows rigid body rotation and other complex intergranular motion to produce "particulate flow" (Borradaile, 1981) in the aggregate. As a result of "particulate flow" lower differential stresses are needed to deform the sample. This causes a decrease in the resolved shear stress values acting on *e*-twin planes in individual calcite grains. Both effects reduce the degree of twinning in the calcite grains compared to that of similarly strained samples deformed under dry pure shear.

i) Previous work

As discussed by Borradaile (1981) the presence of a fluid within the pore spaces of a grain aggregate (*i.e.*, a hydrostatic fluid pressure (P_f)) will reduce the normal stress across a grain surface from its value (σ_n) under dry

conditions. Also of importance is the degree of interconnection of the fluid medium within the pore system is a function of the compressibility of the aggregate and the type of grain material, given by the value *a* (Robin, 1973). The effective stress will, therefore, be given by the formula:

$$\text{effective pressure} = (\sigma_n - P_f(1-a))$$

Since the fluid pressure is hydrostatic, the normal stresses acting across grain contacts will all be reduced by the same amount ($P_f(1-a)$) regardless of the orientation of the grain to grain contact (Hubbert and Rubey, 1959). The sliding friction on a grain to grain contact is directly proportional to the normal stress acting across the contact. The total shearing resistance (t) offered by an isotropic material to failure is given by the following formula:

$$t = t_o + \sigma_n \mu$$

Where the parameters are t_o=cohesive strength, σ_n=normal stress, and μ=coefficient of internal friction (analogous with that of ordinary sliding friction). Therefore, since t_o and μ are constants for a given material, slip will be easier where the normal stress is reduced by the pore fluid pressure (Fig. 4.55).

Borradaile (1981) has classified three types of particulate flow. The first is independent particulate flow in which the grains are not deformed. The second is dependent particulate flow in which grain sliding is limited and dependent on the incompatible deformation of grains. The third is controlled particulate flow where grain sliding is encouraged by other factors (*eg.*, pore fluid pressure) but the rate of grain sliding is controlled by the deformation of grains.

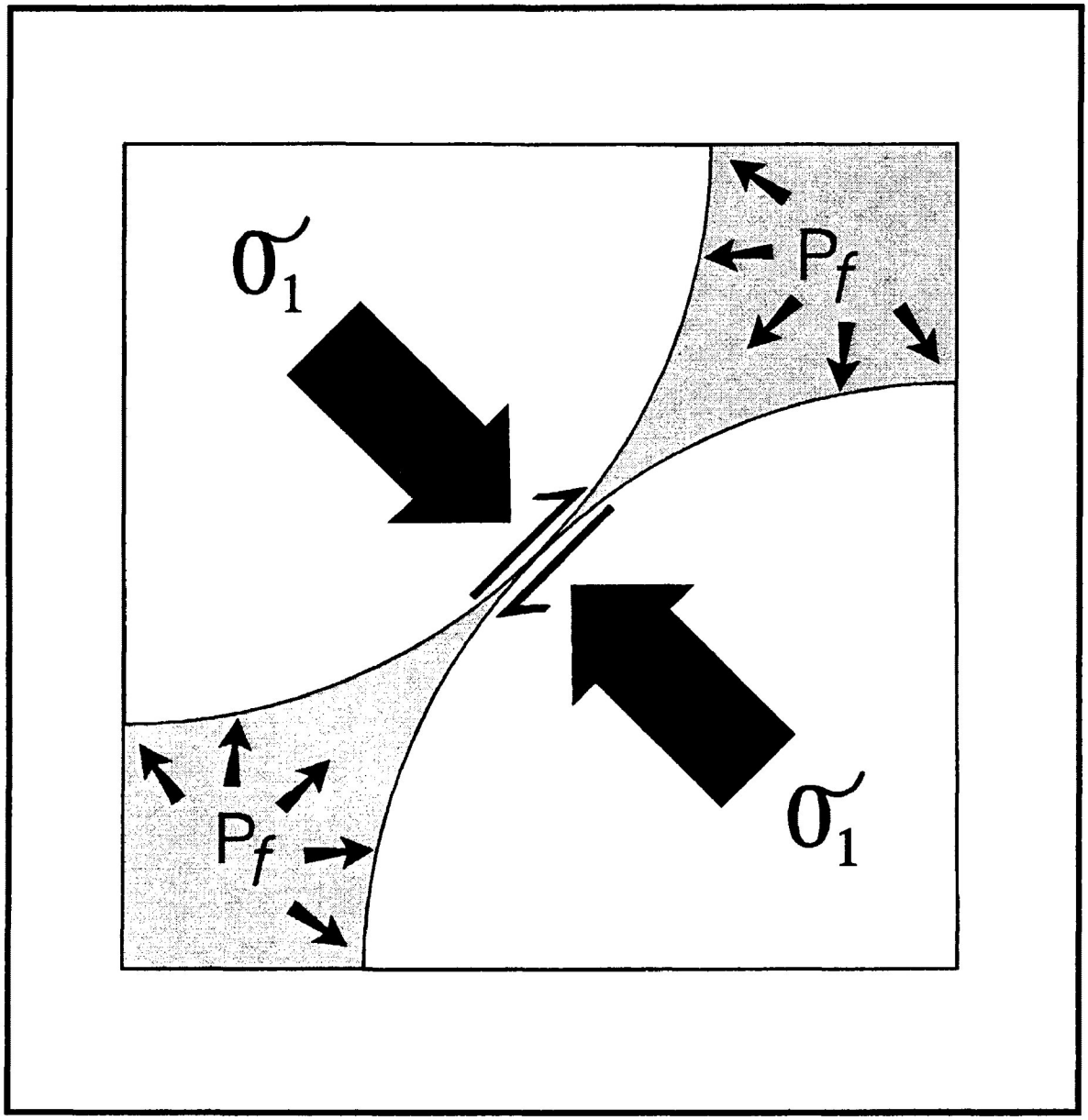

Figure 4.55 Pore fluid pressure reduces the stress value at grain contacts. At high pore fluid pressures (P_f) grain may slide past each other producing controlled particulate flow (Borradaile , 1988).

Deformation experiments by Handin *et.al.* (1963) on Berea Sandstone, with P_f equal to the confining pressure, produced experimental bulk strains of 9 to 24%. The textures observed in their deformed specimens were indistinguishable from the textures in the undeformed specimen suggesting that bulk deformation was exclusively the result of particulate flow.

ii) Calcite Portland-cement aggregate (wet experimental conditions)

In this study the P_f, approximately 95% of the confining pressure, permitted calcite grains to experience greater controlled particulate flow between neighbouring calcite grains and cement matrix so that the long axes of the grains developed a strong PDO/PCO.

The controlled particulate flow of the long axes of calcite grains into a foliation plane normal to the σ_1 orientation causes e_1-twin lamellae to align into a PCO. Subsequently, particulate flow will quickly accumulate twin lamellae into orientations of low resolved shear stress. This will have effect on the resolved shear stress acting on twin planes and will effect the development of twin lamellae as discussed in the previous section (4.5a).

As a result of controlled particulate flow a lower differential stress is needed to produce the observed deformation in the calcite grain aggregate (Borradaile and McArthur, 1990 Fig. 6). This effect has been observed by many authors including Handin *et.al.* (1963). This results in a direct reduction in the resolved shear stress acting on the calcite twin sets. Therefore, twinning in all calcite grains will be suppressed and lamellae index values will be lower than in dry pure shear.

As a result of the combination of controlled particulate

flow and a lower differential stress the average lamellae index is about 20% lower than that observed in samples deformed by dry pure shear for similar strain. The degree to which the suppression of twin lamellae occurs will depend on how closely the pore fluid pressure approximates the confining pressure (lithostatic pressure). The closer the approximation of the fluid pressure to the confining pressure, the lower the differential stress needed to produce deformation and the larger the degree of controlled particulate flow.

4.6 Discussion of dynamic analysis for the compression axis orientation for pure, transpressional and simple shear

a) Turner's Method

Dynamic analysis by Turner's method (1953) is based on an unique compressive stress necessary to produce twinning for a given calcite grain orientation. The overall spread of compressive stress directions that Turner's method can generate may be great, especially in the case of an initial random or weak preferred dimensional and crystallographic orientation. The spread of data is the result of the fact that the most effective shear stress direction (45° to σ_1) can differ significantly from the actual shear stress direction responsible for twinning in a given calcite grain.

The deformed calcite Portland-cement samples, with the exception of those deformed in 2 mm thick longitudinal shear zones, exhibited twinning in the majority of calcite grains within the range of experimental strain in this study. The lack of any well defined PDO/PCO in some of the samples studied, suggest that the interpretation of the σ_1 orientation may not be accurate. An example of this is sample AC-3 (e=4.4% (R_s=1.070)), deformed in dry pure shear under conditions of high stress at room temperature.

In sample AC-3 the large spread of orientations of e_1-twin lamellae results in a broad distribution of compression axes directions. Consequently, the interpretation of the σ_1 orientation from Turner's method cannot be accurately made, as demonstrated in figure 4.43a.

In pure shear intragranular deformation causes rotation of calcite grains into orientations perpendicular to the compression direction or parallel to the shear wall resulting in a well developed PDO/PCO. The formation of a PDO/PCO in

calcite grains allows for the development of a Dietrich and Song's distribution, which spreads compression axis away from the known σ_1 orientation into a 45° small circle distribution. Many of these compression axes have lamellae indices greater than 60 L/mm. As a result, in the calcite Portland-cement aggregate, the enhancement technique of Friedman and Conger (1964) cannot be used to accurately determine the orientation of the σ_1 stress by point concentrations of compression axes directions.

In the case of sample SZ-C1, deformed by transpressional shear, a good PDO and PCO exists in the calcite grains. As a result the distribution of compression axes is better developed. However, Turner's method does not yield an accurate determination of the known σ_1 orientation. In these deformed samples Turner's method produces compression axis distributions which are skewed away from orientation of the known σ_1 and towards the direction of shear. This is the result of calcite grain rotation during twin lamellae development in a non-coaxial stress field. The rigid rotation of calcite grains may, therefore, create inaccuracy in the determination of the σ_1 orientation.

An extreme effect of intragranular deformation is observed to an in the sample deformed by pure shear under wet experimental conditions. These samples have experienced a high degree of controlled particulate flow producing a moderate to good PDO. The ideal effect of this is to produce a Dietrich and Song distribution, with a 45° small circle girdle of compression axes (as inferred from Turner's Method (Fig. 4.48a)) about the known σ_1 orientation. As a result no point concentrations of compression axes exist.

Turner's method must, therefore, rely on those few calcite grains that are the most favourably oriented for twinning.

That is, with *e*-planes at 45° to the known σ_1 direction, which may be few in number, depending on how well the PDO/PCO has developed. If the 45° small circle is well developed the σ_1 direction may be determined from its axis or from the 26° small circle of *c*-axes or compression axes as observed in figure 4.44. The concentration of e_1-twin lamellae can also be used to determine the orientation of σ_1.

The degree to which this small circle girdle is developed may produce inaccuracies in the determination of the σ_1 orientation determined from Turner's method. Sample AC-8 has a compression axes concentration at 35 to 45° to the known σ_1 orientation (Fig. 4.44a). In this case the maximum is due to the rotation of some calcite long dimensional orientations into the foliation plane (Fig. 4.37b). This produces a weak Dietrich and Song distribution with a concentration of compression axes directions in the upper right hemisphere of the stereogram. Determination of the σ_1 direction from a point concentration derived from Turner's method would yield a 35 to 45° error in this particular case.

The use of the enhancement to Turner's method by Friedman and Conger (1964) does not remove this distribution since most of the calcite grains have lamellae indices greater that 60 L/mm (Fig. 4.3c). If a larger limit on the lamellae index is taken (*eg.*, 100 L/mm), the amount of data that can be used in the interpretation of the σ_1 orientation is reduced significantly.

As observed in other studies (Friedman (1963), Friedman and Conger (1964) and Friedman and Stearns (1971)) the inferred σ_1 orientation (maximum compression axes concentration) determined from Turner's method can be inaccurate. This has also been demonstrated in this study, especially in the case of dry pure shear and transpressional

shear. However, the axis of the 45° small circle cone as well as the point concentration of e_1-twin lamellae in wet pure shear could be used to interpret the orientation of the σ_1.

Samples in a 2 mm thick longitudinal assemblage were essentially deformed in an approximation of ideal simple shear. In this case Turner's method does yield a relatively good approximation of the orientation of the σ_1 necessary to produce a shear zone fabric (*i.e.*, 45° to the shear zone wall). In these deformed samples there is a weak to moderate PDO and PCO, even at an experimental shear strains of 0.993 (Fig 4.41, 5.27a-e).

The lack of high lamellae indices in these samples suggests that the component of the known σ_1 acting on the shear zone was low. As a result only those calcite grains that were the most favourably oriented (*i.e.* e_1 approximately 45° to the shear zone compressive stress) developed a high degree of twinning. This is apparent in samples deformed in 2 mm thick longitudinal shear zones which develop low PDO/PCO and lamellae indices compared to pure shear and transpressional shear, for experimental shear strains of 0.233 to 0.993.

A low compressive stress in the deforming calcite Portland-cement aggregate may be necessary for Turner's method to yield accurate determinations of the σ_1 orientation. This is the result the lack of rigid body rotation of calcite grains. Only those calcite grains that are favourably oriented for twinning will be used in the interpretation, subsequently giving a more accurate determination of the σ_1 direction. Calcite rock where neighbouring grains are more restricted to particulate flow such as in marbles, the use of Turner's method may be extended into higher strains.

b) Dietrich and Song's method

The use of Dietrich and Song's method in the determination of the σ_1 direction at low temperature is useful for samples deformed to large strains where large amounts of data can be obtained. Under the conditions of this study the Dietrich and Song's distributions result from rigid rotation of calcite grains into orientations in which the long axes and *e*-twin planes are positioned parallel\sub-parallel to the foliation plane. Axial symmetrical compression to high strains has been observed to result in the development of a preferred orientation of *e*-twin planes normal to the compression direction at 25°C in Carrara marble (Rutter and Rusbridge, 1977).

The rotation of the maximum calcite grain dimensions into orientations parallel to the foliation plane and the subsequent development of a Dietrich and Song distribution is observed to a smaller degree in dry pure shear (sample AC-8 (e=18.03% (R_s=1.347))). The compressive stress determined from this method is approximately parallel to the known σ_1 orientation. At higher experimental strains as the PDO/PCO becomes well developed the accuracy of this method will increase.

In transpressional shear the Dietrich and Song's method does produce a more consistent compressive stress orientation (Fig. 4.48c), but this orientation is not that of the experimentally imposed σ_1 direction (*i*.e., 15-20°). This is due to the fact that the foliation is parallel to the shear direction at 55° to the σ_1 direction. Therefore, the use of this method can only be made when the PDO/PCO is well developed and the stress is coaxial as observed in dry pure shear samples.

However, under wet experimental conditions the Dietrich and Song distribution becomes well developed as a result of controlled particulate flow in the calcite grains at low strains. This is observed in sample CPF-13 (Fig. 4.45a). The development of a good Dietrich and Song distribution and PDO may indicate that a pore fluid pressure was present in the rock during its deformation. At least in the case of wet pure shear the σ_1 orientation can either be determined by the axis of the 26° *c*-axis small circle girdle (Dietrich and Song's method (Fig. 4.45a)) or 45° compression axis (Lamellae Index method (Fig. 4.45b)). Also, it may be determined from the point concentration of the e_1-twin plane distribution (Figure 4.45a).

c) <u>Lamellae index method</u>

The new method proposed in this study for the determination of the maximum compressive stress direction has been used at various levels of experimental strain in the calcite Portland-cement aggregate. The lamellae index method does not rely on the interpretation of concentrations of compression axes directions that are derived from Turner's method. Instead the interpretation takes into account the significance of each datum point (*i*.e., lamellae index value). This is achieved by allowing for those calcite grains that are the most favourably oriented for twinning to be used in the interpretation of the σ_1 orientation. Those calcite grains that are not favourably oriented for twinning or have undergone rotation into orientation of low resolved shear stress (*i*.e., low L/mm value) may not make a significant contribution to the interpretation. This new method is useful in that only a small number of calcite grains are needed for the interpretation of the compression direction (approximately 50 grains).

In the case of dry pure shear (sample AC-8), figure 4.56b illustrates the lamellae index frequency distribution for each of the contour intervals in the stereogram. In the figure the percentage of calcite grains that contribute to each of the contour intervals decreases as the lamellae index increases. Twinned calcite grains with lamellae index values from 1 to 39 L/mm (28.87%) are randomly distributed about the stereogram (Fig. 4.56a) and, therefore, are not included as a contour interval.

The majority of twinned calcite grains are found to lie in the 40 to 79 L/mm contour range (46.39%). This contour interval is broadly distributed around the maximum principal compressive stress. The percentage of calcite grains decreases to 11.34% for the contour range of 80 to 119 L/mm, to 9.28% for the contour range of 120 to 159 L/mm and to 4.1% in the highest range of lamellae index contour values (160 to 270 L/mm). As the value of the contour interval range increases, the more localized the distribution of the lamellae index values become in the stereographic projection. The location of the inferred σ_1 direction is more accurately determined by these higher lamellae index contour intervals as demonstrated in figure 4.56a.

For Turner's method, as observed in sample AC-8 (Fig. 4.48a), the maximum concentration of compression axes is located 35 to 45° from the known σ_1 orientation as a result of rigid rotation of the calcite grains in the softer cement matrix. The lamellae index method for sample AC-8 removes the effect of the many of these calcite grains since they have lower lamellae indices than calcite grains more favourable oriented for twinning. As observed in figure 4.56b the majority of these calcite grains are found to have lamellae indices in the 40 to 79 L/mm contour interval.

Figure 4.56a-b a) Lamellae index method for the determination of the orientation of the maximum principal compressive stress. Figure shows a distribution of compression direction lamellae index values which exhibits a better approximation of the maximum principal compressive stress for a sample (AC-8) shortened by 18.3% (R_s=1.347) by pure shear. The orientation of the σ_1 that existed during the triaxial rig tests is shown by the broad arrows (Borradaile and M^{c}Arthur, 1989).

b) Comparison of the lamellae index values from calcite grains used in the above stereographic interpretation. Range and frequency of the calcite grains given.

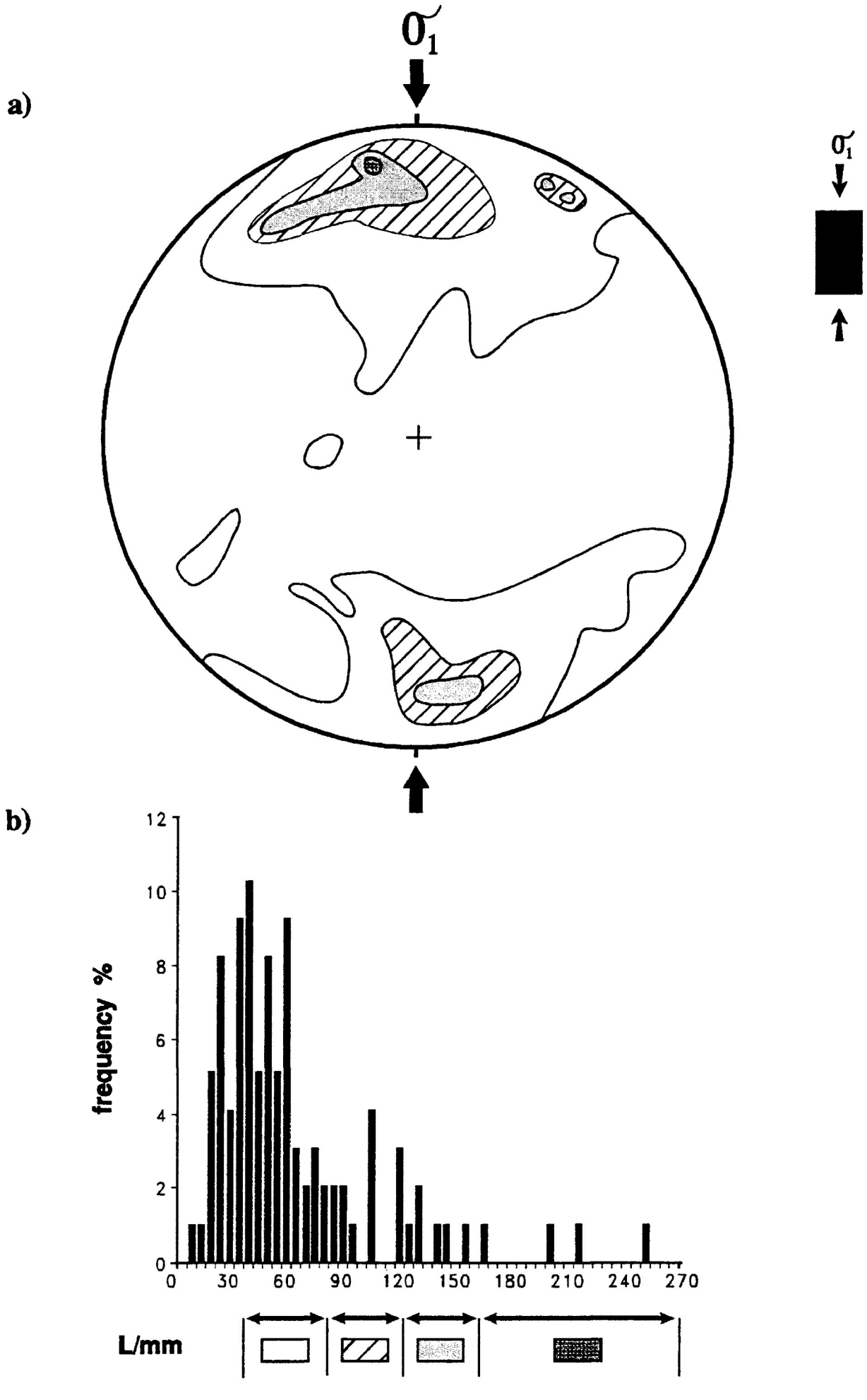
a)
σ1
σ1
b)
frequency %
12
10
8
6
4
2
0
0
30
60
90
120
150
180
210
240
270
L/mm

The rigid rotation of the calcite grains into the foliation plane, however, does produce a small lamellae index maximum at 40° to the σ_1 orientation in this sample. This contour maximum occupies 1.03% of the lamellae index data (in the contour interval 160 to 270 L/mm). The remaining 3.09% of the data is located approximately parallel to the σ_1 direction. The separation of the higher lamellae index contour distributions away from the exact location of the principal compressive stress, as observed in the upper and lower halves of the stereogram (Fig. 4.56a), may be the result of weak development of a Dietrich and Song distribution. The maximum effect of this is observed in the wet pure shear sample CPF-13 in which a 45° small circle girdle is developed (Fig. 4.45b).

The lamellae index method has been observed to yield more accurate determinations of the inferred σ_1 orientation in samples deformed by pure shear (dry and wet) and in simple shear. In the case of transpressional shear the interpretation does not accurately determine the orientation of the σ_1. The direction, as determined from the maximum lamellae index values, is skewed in the direction of shear. This is the result of the development of a strong PDO/PCO and subsequent development of a Dietrich and Song distribution. Contouring the lamellae indices is more consistent than contouring the compression axes concentration of Turner's method.

Chapter 5: Fabric analysis of experimentally deformed calcite-cement aggregate

5.1 Introduction

This chapter deals with the fabric analysis of experimental triaxial deformation of undeformed calcite-cement aggregate samples. The experimental tests consisted of deformation by pure shear (axial symmetrical compression for dry and wet experimental conditions), transpressional shear (oblique shear zone) and simple shear (longitudinal shear zone (2 and 5 mm in thickness)).

5.2 Fabric Analysis of calcite grains (coaxial deformation).

Orientational, dimensional and strain analyses (Robin's, linearization, and harmonic mean methods) were conducted on the calcite grains present in the undeformed and deformed X/Z principal plane of the calcite-cement aggregate samples. Also conducted was a Flinn diagram analysis of 3-dimensional strain ellipsoid development. The calcite grains used in these determinations were measured from the central portion of the thin sections to eliminate heterogeneous affect near the walls and top of the test cylinder.

a) Computer simulation ("forward modelling") of pure shear

For comparison with experimental results a calcite grain shape sample from an undeformed calcite-cement aggregate specimen ($n_{markers}$=250) was deformed by a "forward modelling" computer simulation of homogeneous pure shear by R_f/ϕ transformation. The calcite grain shapes were converted to best-fit ellipses based on their moment-of-inertia before "forward modelling" simulation were conducted. The computer simulation was conducted on an IBM computer using a strain analysis program (version 1.25) developed by Dr. G. Borradaile

(@1989). In the following computer simulations the maximum extension direction in the X/Z principal plane is oriented at 0°, perpendicular to the axial length of the undeformed test cylinder from which the initial undeformed grain sample was taken.

Figure 5.1a-f illustrates the orientational frequency distributions of the longest dimension (Angle Ax (ϕ)) of a sample of strain markers in the undeformed state for simulated strains increasing from 1.000 (e=0.00%) to 1.500 (e=23.69%). Calcite grains in the undeformed state exhibit a slight preferred dimensional orientation (PDO perpendicular to the long axis of the test cylinder (mean theta = 2.28° and angular deviation = 24.84°). The weak initial fabric is most likely the result of settling of the calcite grains prior to hardening of the Portland cement.

In the simulated deformed samples there is a tendency for the long axis of the initial markers to quickly align in an orientation perpendicular to the shortening direction ($\sigma_{(1sim)}$). The PDO begins to develop at low simulated strain ratios and becomes increasingly more well developed at higher simulated strains ratios. The fluctuation of the orientation distribution (F, Ramsay, 1967) remaining at approximately 180° as simulated strain increases from 0.00% to 23.69% shortening. Figure 5.2 presents the angular deviation of the long axes of calcite grains for 15 samples as the simulated bulk strain ratio increases from 1.000 (e=0.00%) to 1.700 (e=29.80%) in 0.5 intervals. The angular deviations decrease from 24.82 to 12.72 as the simulated strain ratio increases.

Figure 5.3 exhibits variations in the mean R_f as the simulated bulk strain increases. The range of R_f increases as the simulated strain ratios increase as presented in the frequency distribution diagrams of figure 5.4a-f. The R_f/ϕ

Figure 5.1a-f Forward modelling of frequency distribution of Angle Ax (ϕ) orientations of strain markers in undeformed and simulated deformed calcite-cement aggregate. Simulated strains ratios ranged from 1.000 (e=0.00%) to 1.500 (e=23.69%). Maximum extension direction orientated at 0°. Samples were deformed by a computer simulation of homogeneous pure shear.

a) UNDCAL (R_s=1.0 (e=0.0%))
b) CAL1 (R_s=1.1 (e=6.2%))
c) CAL2 (R_s=1.2 (e=11.5%))
d) CAL3 (R_s=1.3 (e=16.1%))
e) CAL4 (R_s=1.4 (e=20.1%))
f) CAL5 (R_s=1.5 (e=23.7%))

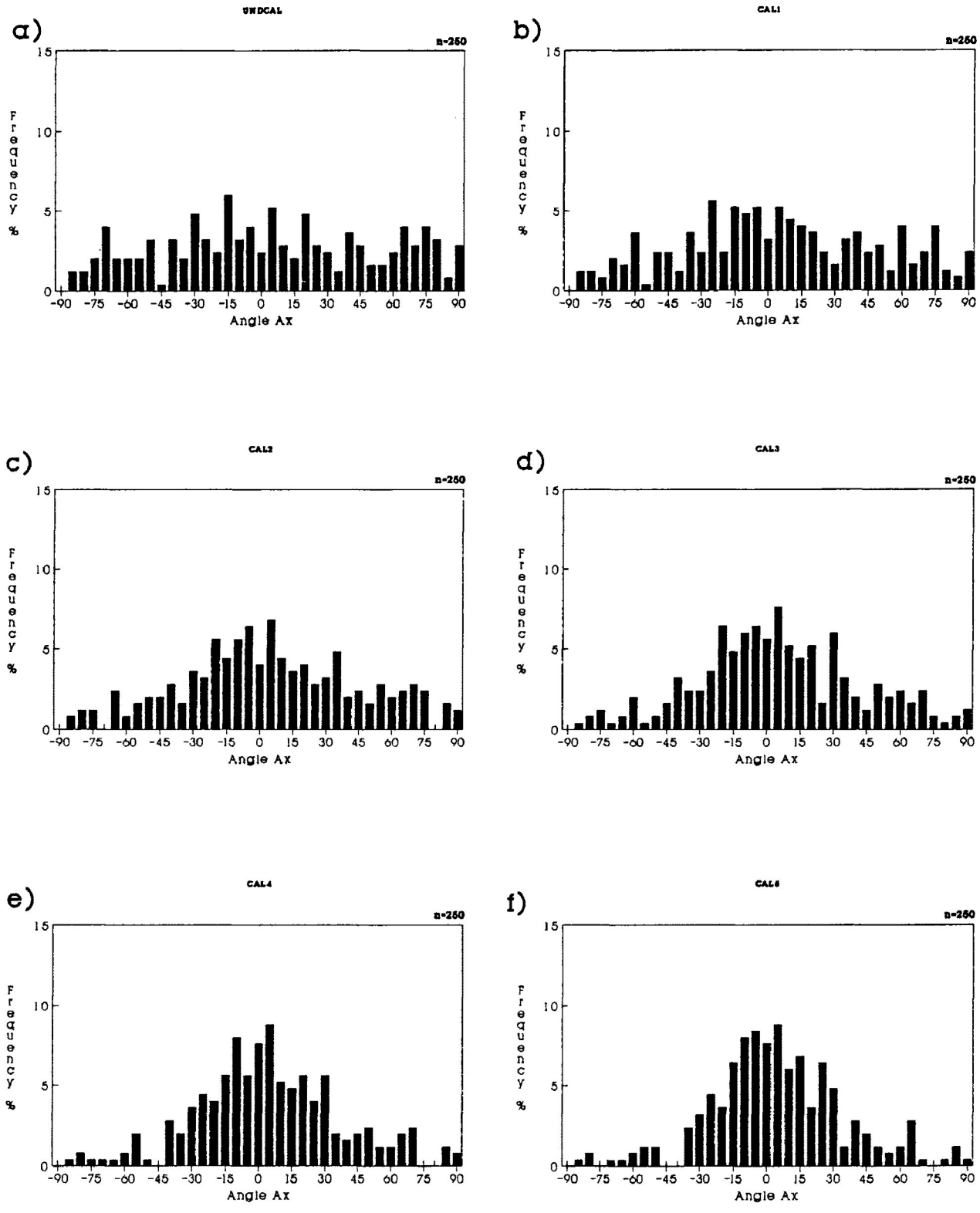
a)
UNDCAL
n=250
b)
CAL1
n=250
c)
CAL2
n=250
d)
CAL3
n=250
e)
CAL4
n=250
f)
CAL5
n=250
Frequency %
Angle Ax
0
5
10
15
-90 -75 -60 -45 -30 -15 0 15 30 45 60 75 90

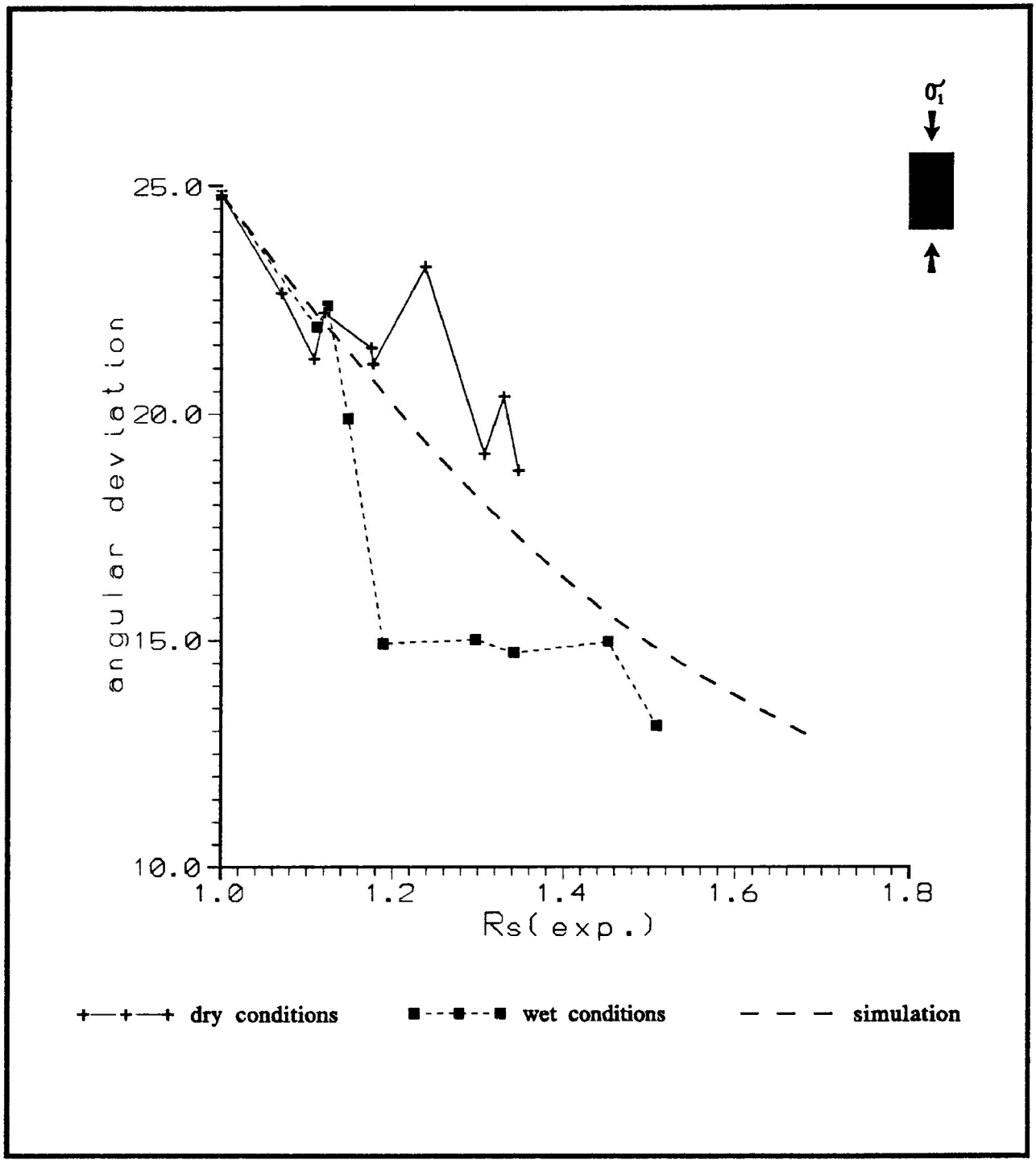

Figure 5.2 Variations in angular deviation of Angle Ax (ϕ) simulated deformation (thick dashed line), dry pure shear (square) and wet pure shear (plus) in the X/Z principal plane of calcite grains in undeformed and deformed calcite-cement aggregate.

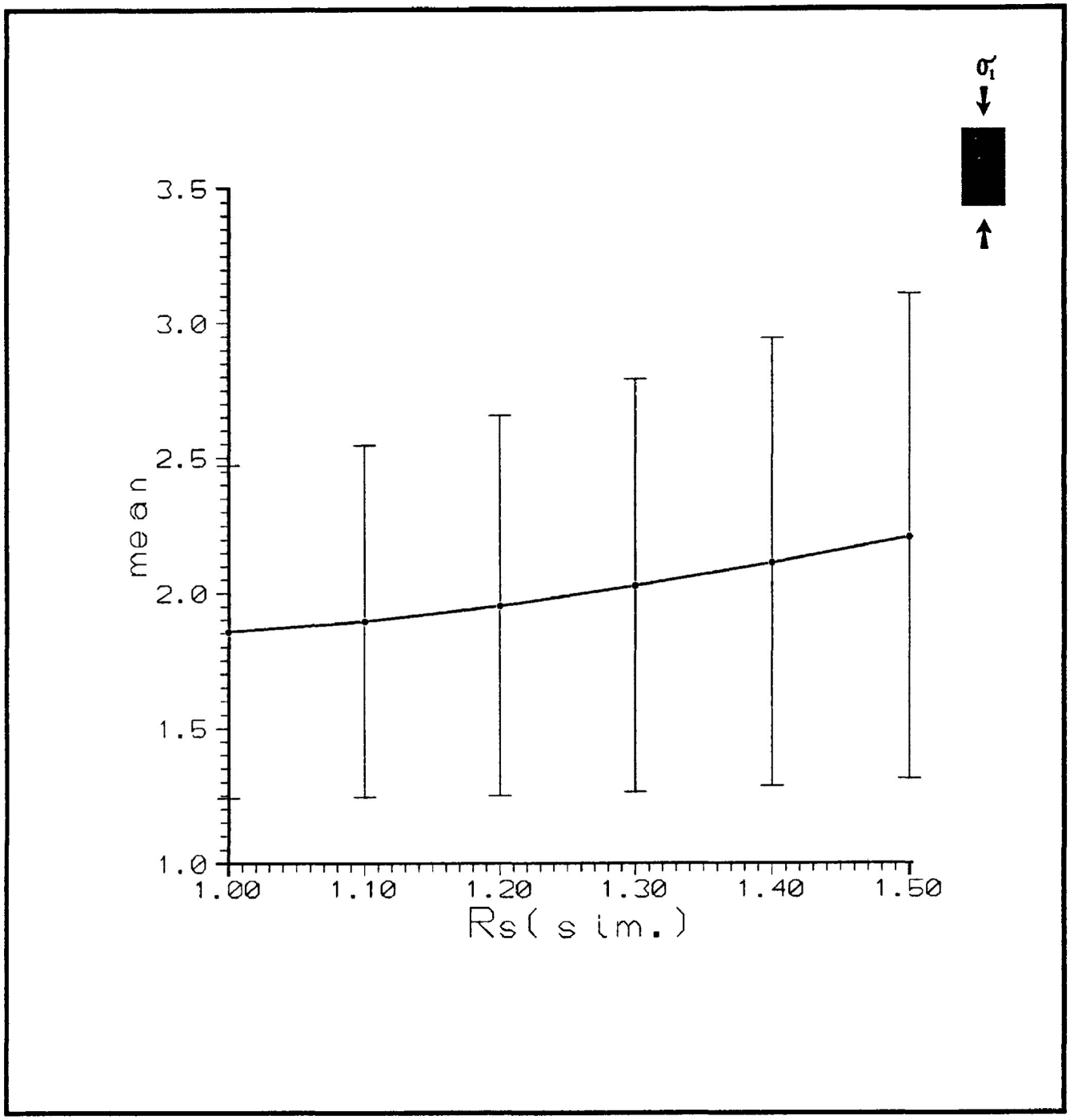

Figure 5.3 Variation in mean simulated R_f of strain markers in undeformed and simulated deformed calcite-cement aggregate against experimental strain, with standard deviation (error bar). Simulated strain ratios range from 1.000 (e=0.00%) to 1.500 (e=23.69%). Samples were deformed by a computer simulation of homogeneous pure shear.

Figure 5.4a-f Forward modelling of frequency distribution of R_i and R_f of strain markers in undeformed and simulated deformed calcite-cement aggregate. Simulated strain ratios ranged 1.000 (e=0.00%) to 1.500 (e=23.69%). Samples were deformed by a computer simulation of homogeneous pure shear.

a) UNDCAL (R_s=1.0 (e=0.0%))
b) CAL1 (R_s=1.1 (e=6.2%))
c) CAL2 (R_s=1.2 (e=11.5%))
d) CAL3 (R_s=1.3 (e=16.1%))
e) CAL4 (R_s=1.4 (e=20.1%))
f) CAL5 (R_s=1.5 (e=23.7%))

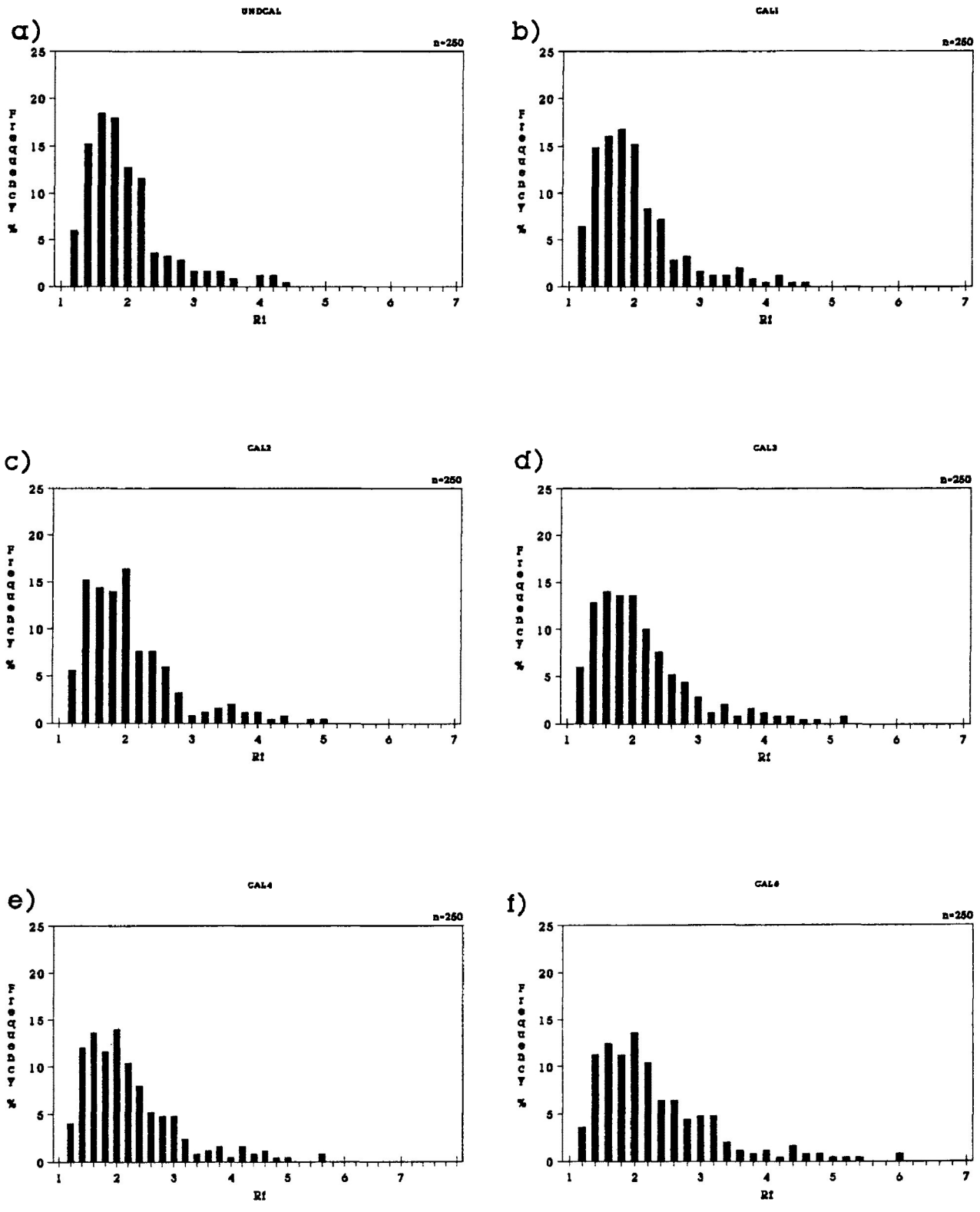
a)
UNDCAL
n=250
Frequency %
Rf
b)
CAL1
n=250
Frequency %
Rf
c)
CAL2
n=250
Frequency %
Rf
d)
CAL3
n=250
Frequency %
Rf
e)
CAL4
n=250
Frequency %
Rf
f)
CAL6
n=250
Frequency %
Rf

Figure 5.5a-f R_f/ϕ diagrams for strain markers in undeformed and simulated deformed calcite-cement aggregate. Maximum extension direction orientation orientated at 0°. Simulated strain ratios ranged from 1.000 (e=0.00%) to 1.500 (e=23.69%). Samples were deformed by a computer simulation of homogeneous pure shear.

a) UNDCAL (R_s=1.0 (e=0.0%))
b) CAL1 (R_s=1.1 (e=6.2%))
c) CAL2 (R_s=1.2 (e=11.5%))
d) CAL3 (R_s=1.3 (e=16.1%))
e) CAL4 (R_s=1.4 (e=20.1%))
f) CAL5 (R_s=1.5 (e=23.7%))

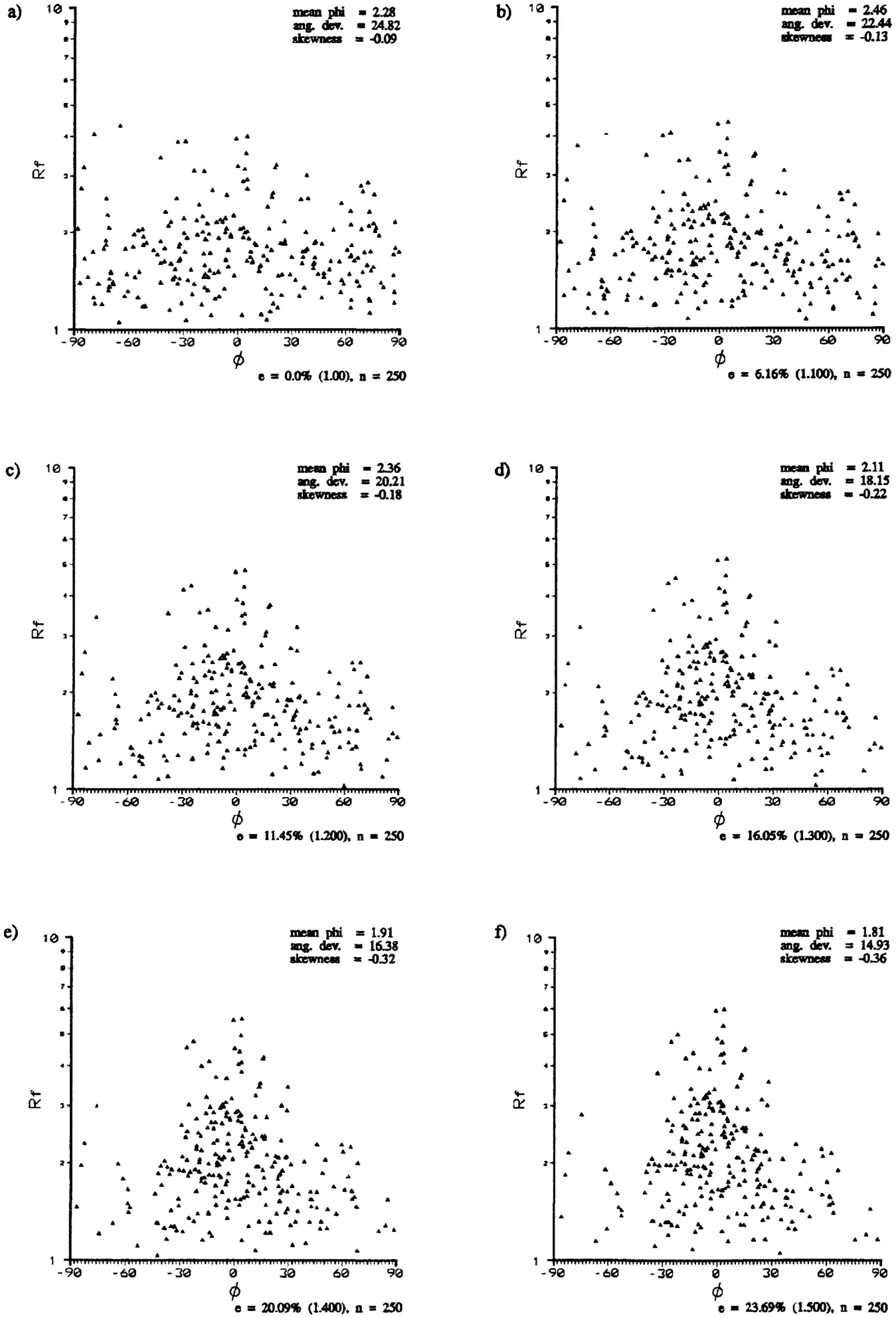
a)
mean phi = 2.28
ang. dev. = 24.82
skewness = -0.09
Rf
ϕ
e = 0.0% (1.00), n = 250
b)
mean phi = 2.46
ang. dev. = 22.44
skewness = -0.13
Rf
ϕ
e = 6.16% (1.100), n = 250
c)
mean phi = 2.36
ang. dev. = 20.21
skewness = -0.18
Rf
ϕ
e = 11.45% (1.200), n = 250
d)
mean phi = 2.11
ang. dev. = 18.15
skewness = -0.22
Rf
ϕ
e = 16.05% (1.300), n = 250
e)
mean phi = 1.91
ang. dev. = 16.38
skewness = -0.32
Rf
ϕ
e = 20.09% (1.400), n = 250
f)
mean phi = 1.81
ang. dev. = 14.93
skewness = -0.36
Rf
ϕ
e = 23.69% (1.500), n = 250

diagrams for the deformed marker grains are presented in figure 5.5a-f. These figures illustrate the development of a preferred dimensional orientation (PDO) of the strain markers attributed to R_f/ϕ transformation parallel to the simulated σ_1 direction.

Figure 5.6 presents the comparison of the Robin's, linearization and harmonic mean methods of strain analysis for the strain markers in the simulated deformation of the undeformed calcite grain shape sample. The samples were deformed between simulated strain ratios of 1.000 (e=0.0%) and 1.70 (e=29.80%). It is observed from the figure that there is a good correlation between Robin's method and the simulated strain ratio. The overestimate observed in Robin's method, which increases slightly as the simulated strain ratio increases, is the result of the weak initial fabric present in the undeformed sample.

The linearization method gives an increasing overestimate of the actual simulated strain, surpassing Robin's method at a low simulated strains ratio (≈1.06) and harmonic mean at a higher simulated strain ratio (≈1.54). The harmonic mean is a large overestimate of the simulated strain ratio. The overestimate decreases in value as the simulated strain ratio increases. The best of the three methods for the estimate of the actual simulated strain ratio is Robin's method.

Standard deviation (1 s.d.) for Robin's method, linearization method and the harmonic mean method were calculated and are presented in Table 5.1. For the linearization method the calculations of standard deviation that yield confidence brackets that extend into bulk strains estimates less than 1.000 are not given.

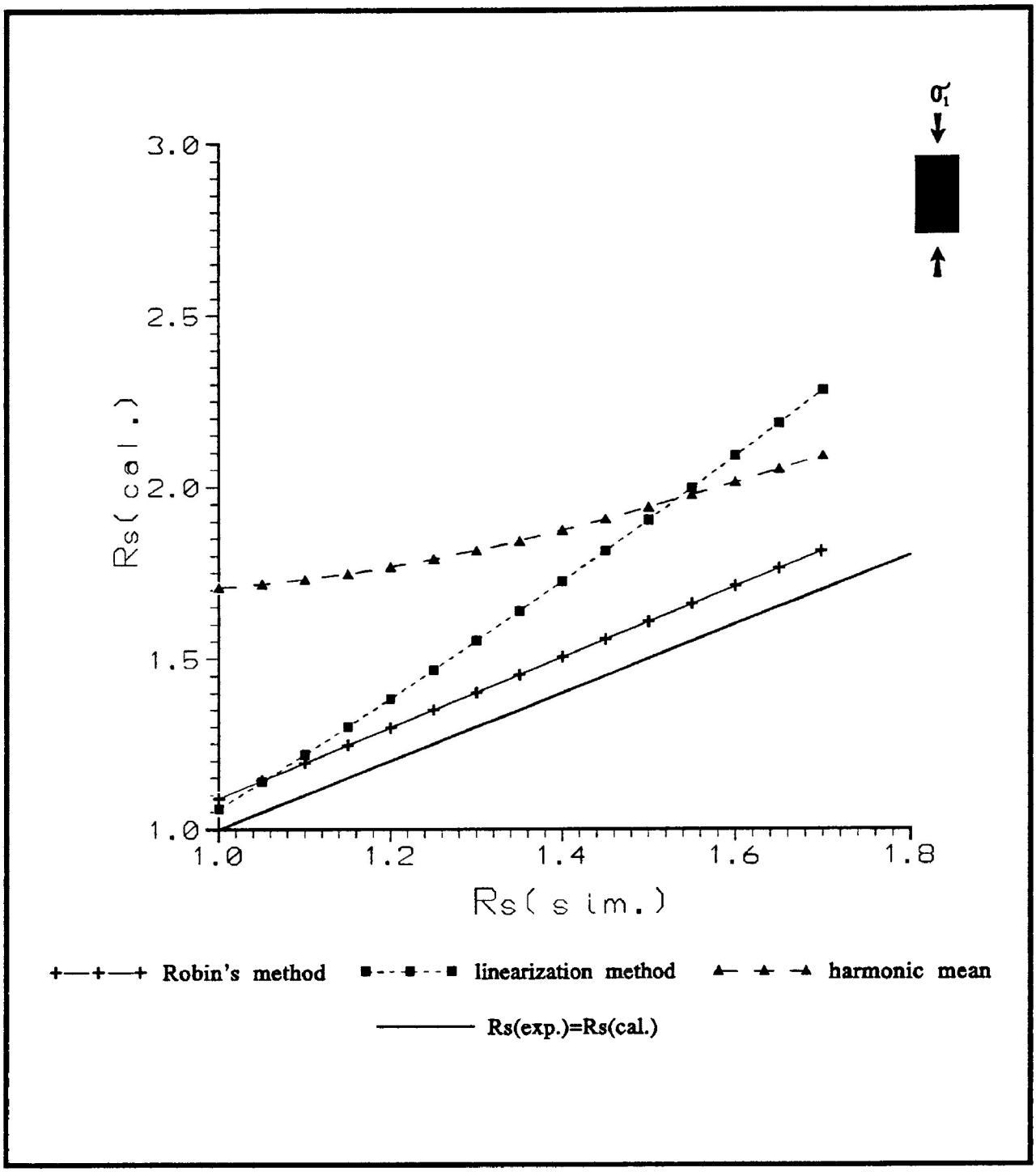

Figure 5.6 Comparison of strain estimates by Robin's method (1977), linearization method (Yu and Zheng, 1984) and harmonic mean method (Lisle, 1977) for strain markers in the X/Z principal plane of the undeformed and simulated deformed calcite-cement aggregate samples. Equivalent R_s is represented by the dark solid line. Strain ratios range from 1.000 (e=0.00%) to 1.500 (e=23.69%). Samples were deformed by a computer simulation of homogeneous pure shear.

TABLE 5.1

sample	e%	Rs(exp.)	Robin's error (s.d.)	Harmonic error (s.d.)	Linear error (s.d.)	n
UNCAL	0.00	1.000	0.100	0.155	n.a	93
CAL1	6.16	1.100	0.100	0.159	n.a	93
CAL2	11.45	1.200	0.100	0.165	n.a	93
CAL3	16.05	1.300	0.100	0.169	n.a	93
CAL4	20.09	1.400	0.100	0.171	n.a	93
CAL5	23.69	1.500	0.100	0.171	n.a	93

TABLE 5.2

sample	e%	Rs(exp.)	Robin's error (s.d.)	Harmonic error (s.d.)	Linear error (s.d.)	n
UNCAL	0.00	1.000	0.135	0.163	n.a	137
AC-3	4.44	1.070	0.131	0.174	n.a	250
AC-1	6.60	1.108	0.100	0.167	n.a	205
AC-4	7.30	1.120	0.096	0.147	n.a	222
AC-2	7.60	1.126	0.100	0.162	n.a	206
AC-5	10.20	1.175	0.110	0.152	n.a	189
BB8807	10.27	1.177	0.101	0.164	n.a	202
AC-6	12.00	1.211	0.102	0.160	n.a	211
AC-9	13.26	1.238	0.132	0.183	n.a	137
AC-11	17.30	1.330	0.097	0.165	n.a	229
AC-8	18.03	1.347	0.134	0.187	n.a	250
AC-10	18.30	1.354	0.110	0.152	n.a	178

TABLE 5.3

sample	e%	Rs(exp.)	Robin's error (s.d.)	Harmonic error (s.d.)	Linear error (s.d.)	n
UNCAL	0.00	1.000	0.135	0.163	n.a	137
CPF-12	6.80	1.111	0.090	0.162	n.a	250
CPF-11	7.50	1.124	0.092	0.168	n.a	250
CPF-08	8.80	1.148	0.106	0.187	n.a	225
CPF-09	9.60	1.163	0.095	0.182	n.a	250
CPF-04	10.90	1.189	0.096	0.169	n.a	235
CPF-10	15.90	1.297	0.094	0.167	n.a	241
CPF-01	16.36	1.307	0.093	0.164	n.a	250
CPF-13	17.8	1.342	0.085	0.167	n.a	250
CPF-02	22.00	1.452	0.102	0.175	n.a	227
CPF-03	24.00	1.509	0.098	0.164	n.a	237

b) Dry experimental pure shear (P_c=200 Mpa, de/dt=10^{-5}/s)

In dry experimental pure shear deformation a comparison of orientational and dimensional frequency distributions and R_f/ϕ diagrams were made from 6 samples increasing in experimental strain ratio from 1.000 (e=0.00%) to 1.347 (e=18.03%). Other figures and analysis involved all samples deformed by pure shear under dry conditions (see Appendix A).

Figure 5.7a-f illustrates the orientational frequency distribution of the longest dimension (Angle Ax (ϕ)) for the calcite grains of 6 samples increasing in experimental strain ratio. In the deformed samples there is a tendency for the long axis of the calcite grains to align quickly in an orientation perpendicular to the σ_1 (parallel to the long axis of the test cylinder). The PDO begins to develop at low experimental strain (e=4.4%) and becomes increasingly better developed at higher strains. At low experimental strains ratios the development of the PDO in calcite grains is similar to that observed in the simulated pure shear deformation of the previous section (Fig. 5.4b). However, the development of the PDO in calcite grains at higher experimental strains ratios is less pronounced than that generated by simulated R_f/ϕ transformation. The F remains at approximately 180° as experimental strain increases from 0.00% to 18.03% shortening.

Figure 5.2 presents the angular deviation of the long axes of calcite grains for 10 samples as the experimental strain ratio increases from 1.000 to 1.347. From the figure it is observed that the angular deviations decrease from 24.82 to 18.76 as the experimental strain ratio increases. The angular deviation of the developing PDO is similar to the simulated deformation for experimental strain ratios less than approximately 1.171 (10% shortening). As the percent strain increases the angular deviation deviates from the simulation,

Figure 5.7a-f Frequency distribution of Angle Ax (ϕ) orientations of calcite grains in undeformed and deformed calcite-cement aggregate. Experimental strain ratios range from 1.000 (e=0.00%) to 1.347 (e=18.03%). Maximum extension direction orientation orientated at 0°. Samples were deformed under dry experimental conditions with confining pressures of 200 Mpa, strain rate of 10^{-5}/s and temperatures of 25°C.

a) UNDCAL (R_s=1.000 (e=0.0%))
b) AC-3 (R_s=1.070 (e=4.44%))
c) AC-1 (R_s=1.108 (e=6.60%))
d) AC-5 (R_s=1.175 (e=10.20%))
e) AC-11 (R_s=1.330 (e=17.30%))
f) AC-8 (R_s=1.347 (e=18.03%))

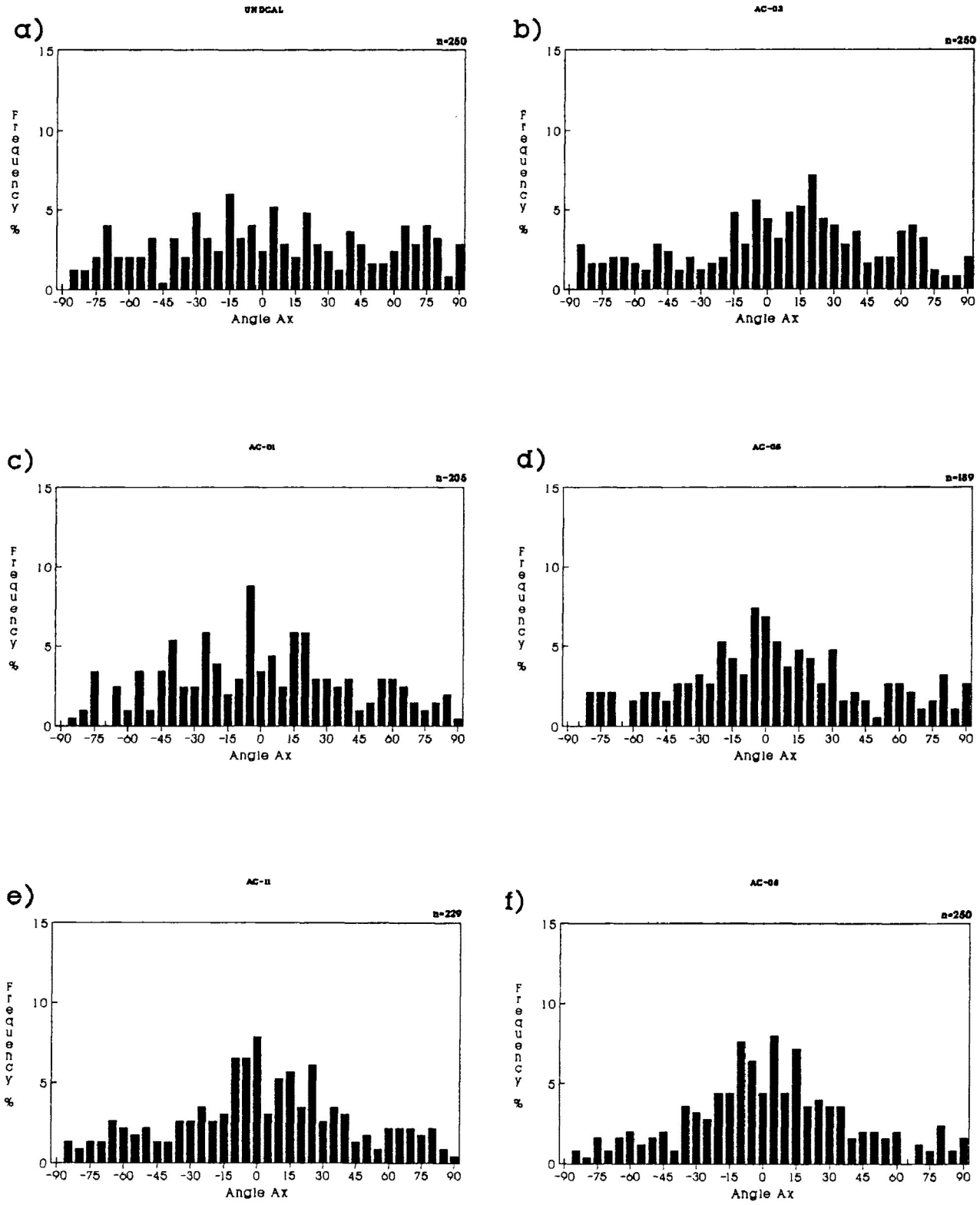
a)
UNSCAL
n=250
b)
AC-03
n=250
c)
AC-01
n=205
d)
AC-06
n=189
e)
AC-11
n=229
f)
AC-08
n=250
Frequency %
Angle Ax
0
5
10
15
-90 -75 -60 -45 -30 -15 0 15 30 45 60 75 90

becoming consistently greater in value. Therefore, the development of a preferred orientation is less than that predicted by passive R_f/ϕ transformation.

Figure 5.8 exhibits variations in the mean R_f as the experimental strain ratio increases, it is observed that the mean R_f remains relatively constant. Comparison of the variation of mean R_f between experimental and computer simulated data illustrates that, for dry pure shear deformation at low experimental strain ratios, the mean R_f of calcite grains are less than those generated by simulation. However, at higher experimental strains deformed samples (*eg.*, AC-08 (e=18.03%)) exhibit an increase in the mean R_f, represented by a larger range of R_f values as presented in the R_f frequency distributions of figure 5.9a-f.

The R_f/ϕ diagrams for calcite grains are presented in figure 5.10a-f. These figures suggest that there is little change in R_f at low experimental strains with the development of a PDO parallel to the σ_1 direction. The PDO is mainly defined by the concentration of calcite grains with low R_f (<2.2) with the incorporation of higher R_f grains as the experimental strain ratio increases. In the higher strained sample an increase in R_f is more noticeable, enhancing the development of a PDO.

The role of twinning in the plastic (heterogeneous) deformation of the calcite grains appears to be minor in the development of the PDO in the calcite-cement aggregate deformed by dry pure shear for low experimental strain ratios. The increase in R_f obtainable by twinning in calcite grains for an ideal situation is restricted to a limited degree (*i.e.*, total twinning of host lattice). However, in the deformed samples of this study the host lattice of the calcite grains are not observed to be completely twinned even in

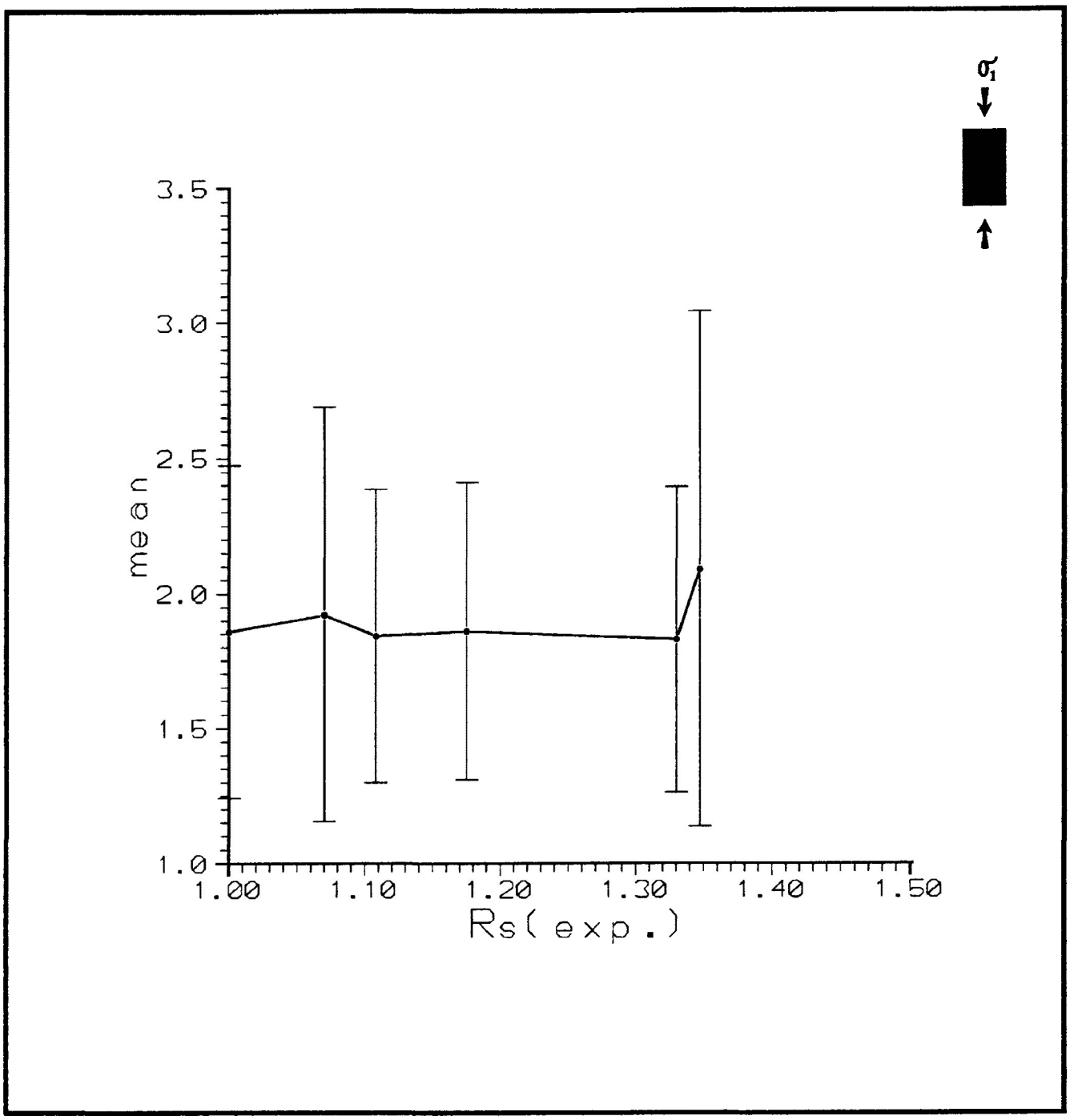

Figure 5.8 Variation in mean R_f of calcite grains in undeformed and deformed calcite-cement aggregate with standard deviation against experimental strain. Experimental strain ratios range from 1.000 (e=0.00%) to 1.347 (e=18.03%). Samples were deformed under dry experimental conditions with confining pressures of 200 Mpa, strain rate of 10^{-5}/s and temperatures of 25°C.

Figure 5.9a-f Frequency distribution of R_i and R_f for calcite grains in undeformed and deformed calcite-cement aggregate. Experimental strain ratios range from 1.000 (e=0.00%) to 1.347 (e=18.03%). Samples were deformed under dry experimental conditions with confining pressures of 200 Mpa, strain rate of 10^{-5}/s and temperatures of 25°C.

a) UNDCAL (R_s=1.000 (e=0.0%))
b) AC-3 (R_s=1.070 (e=4.44%))
c) AC-1 (R_s=1.108 (e=6.60%))
d) AC-5 (R_s=1.175 (e=10.20%))
e) AC-11 (R_s=1.330 (e=17.30%))
f) AC-8 (R_s=1.347 (e=18.03%))

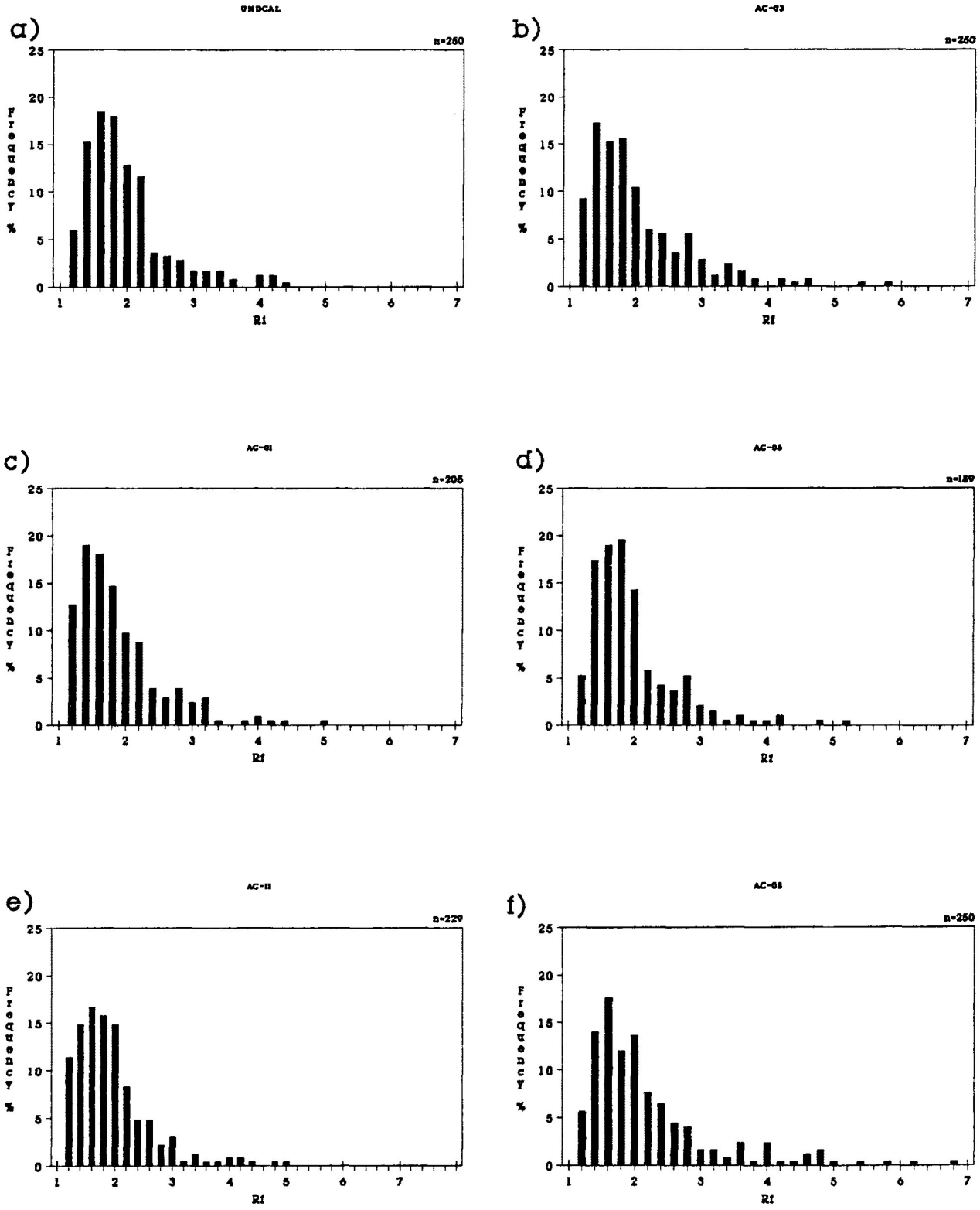
a)
UNDCAL
n=250
b)
AC-03
n=250
c)
AC-01
n=205
d)
AC-06
n=189
e)
AC-11
n=229
f)
AC-08
n=250
Frequency %
Rf

Figure 5.10a-f R_f/ϕ diagrams for calcite grains in undeformed and deformed calcite-cement aggregate. Experimental strain ratios range 1.000 (e=0.00%) to 1.347 (e=18.03%). Maximum extension direction orientation orientated at 0°. Samples were deformed under dry experimental conditions with confining pressures of 200 Mpa, strain rate of 10^{-5}/s and temperatures of 25°C.

a) UNDCAL (R_s=1.000 (e=0.0%))
b) AC-3 (R_s=1.070 (e=4.44%))
c) AC-1 (R_s=1.108 (e=6.60%))
d) AC-5 (R_s=1.175 (e=10.20%))
e) AC-11 (R_s=1.330 (e=17.30%))
f) AC-8 (R_s=1.347 (e=18.03%))

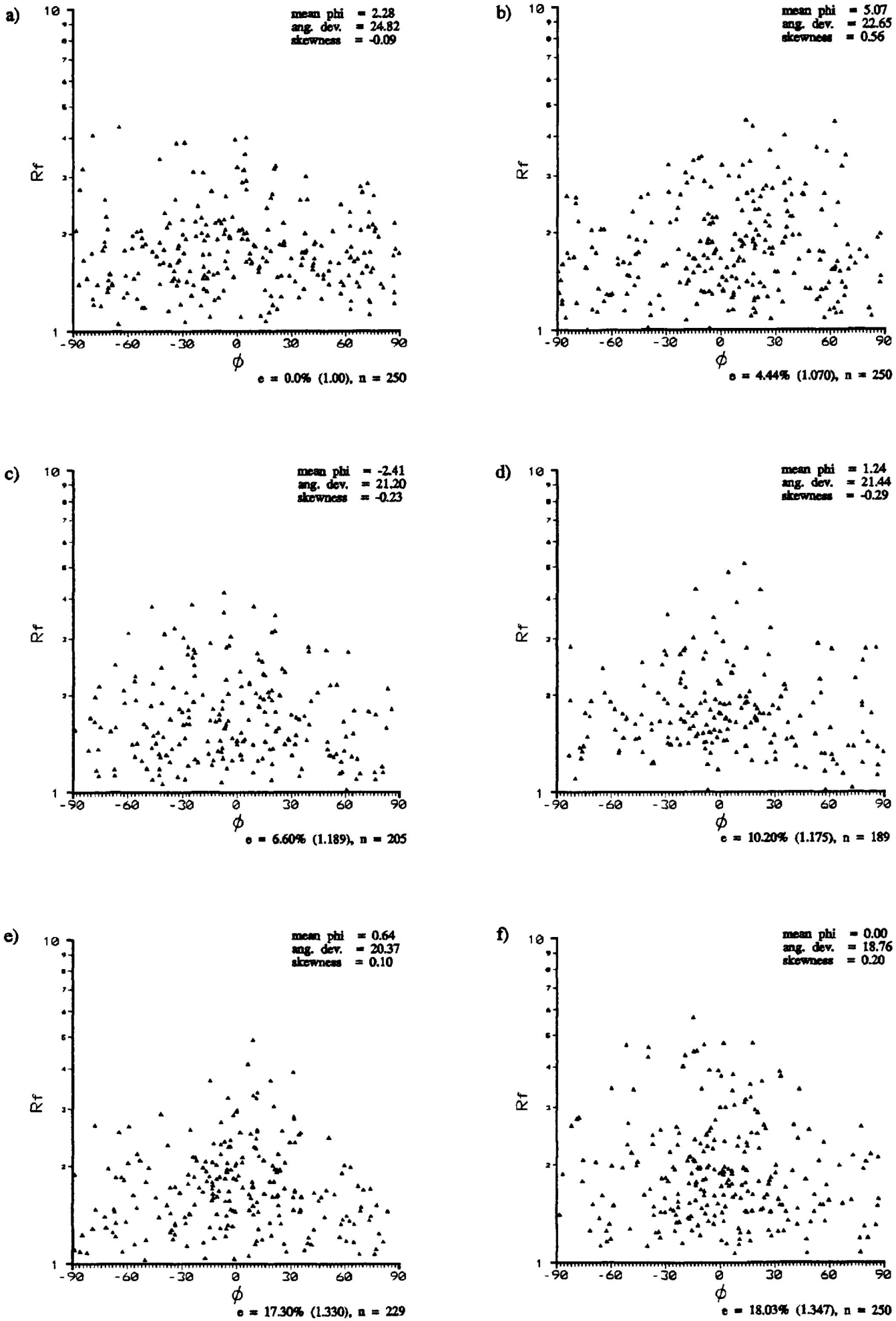
a)
mean phi = 2.28
ang. dev. = 24.82
skewness = -0.09
e = 0.0% (1.00), n = 250
b)
mean phi = 5.07
ang. dev. = 22.65
skewness = 0.56
e = 4.44% (1.070), n = 250
c)
mean phi = -2.41
ang. dev. = 21.20
skewness = -0.23
e = 6.60% (1.189), n = 205
d)
mean phi = 1.24
ang. dev. = 21.44
skewness = -0.29
e = 10.20% (1.175), n = 189
e)
mean phi = 0.64
ang. dev. = 20.37
skewness = 0.10
e = 17.30% (1.330), n = 229
f)
mean phi = 0.00
ang. dev. = 18.76
skewness = 0.20
e = 18.03% (1.347), n = 250
Rf
ϕ
-90 -60 -30 0 30 60 90
1 2 3 4 5 6 7 8 9 10

calcite grains which have high lamellae indices.

High lamellae indices in deformed calcite grains do not induce R_f/ϕ transformation under dry experimental conditions for pure shear. This is concordant with the fact that 5 independent slip systems are needed to allow homogeneous plastic deformation of a strain marker, where as calcite at low temperature only has 3 independent slip systems. It may be suggested that the fabric development is mainly the result of rigid rotation of the calcite grains with some strain produce by twinning for suitably oriented grains. This is suggested by the fact that the higher R_f grains do not necessarily exhibit large lamellae indices and by the relatively strong alinement of calcite grains with low R_f values.

Figure 5.11 presents the comparison of the Robin's, linearization, and harmonic mean methods of strain analysis for deformed calcite grains. It is observed from the figure, that there is a moderately good correlation between the experimental strain ratio estimates of the Robin's method and linearization method for low experimental strains, with the linearization method being consistently higher. However, at higher experimental strain there appears to be a large deviation of the linearization method from Robin's method and the actual R_s producing the deformation (AC-8, R_s(exp.)=1.347).

The small deviation at lower strains and the larger deviation at higher strains, between the linearization and Robin's method, may be the result of rigid rotation of calcite grains with high aspect ratios. For the linearization method these grains can significantly affect the linear regression through the linearization data producing an overestimate (see Chapter 3). Since Robin's method is an arithmetic average these values have less of an affect on the strain estimate.

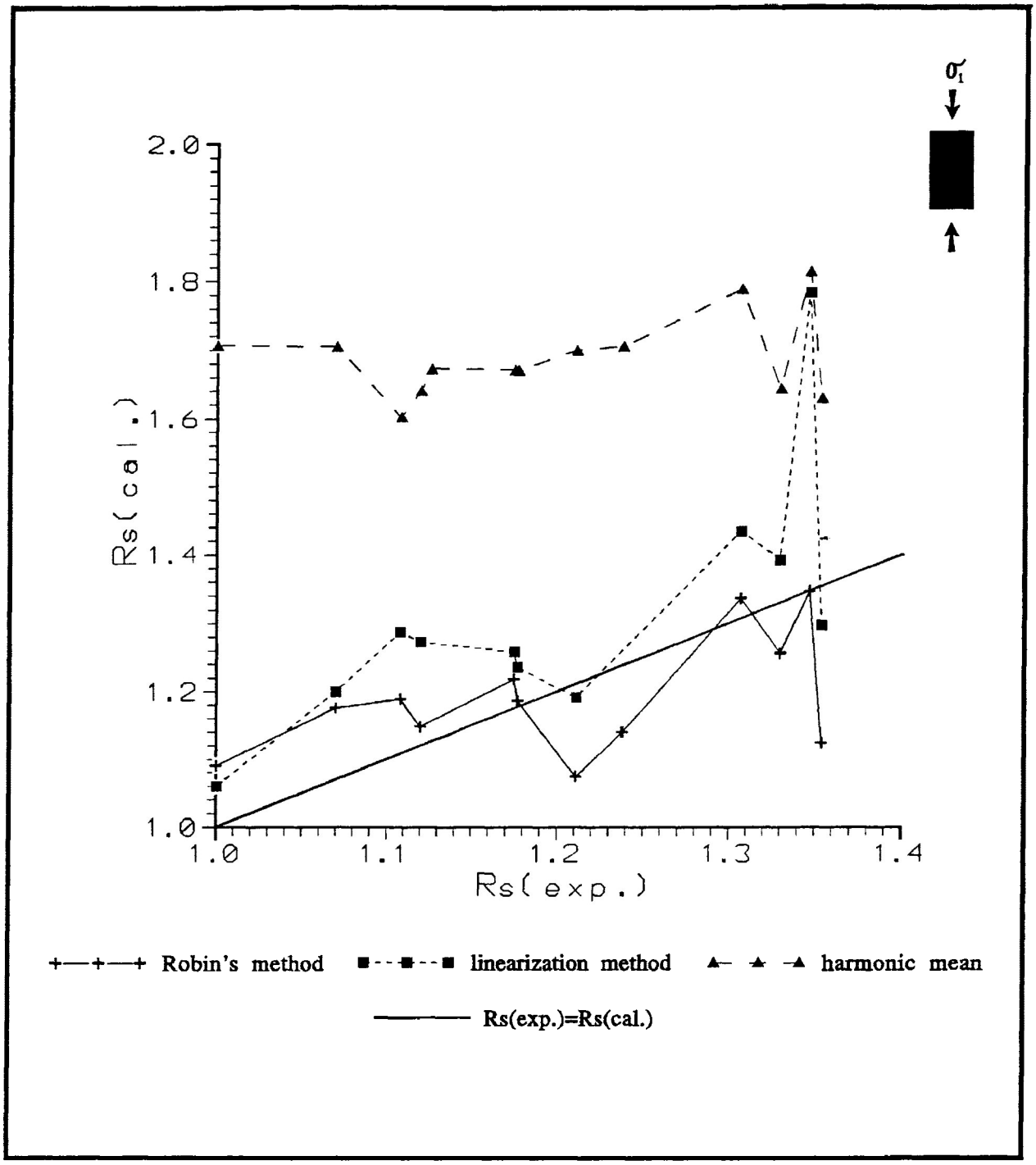

Figure 5.11 Comparison of strain estimates by Robin's method (1977), linearization method (Yu and Zheng, 1984) and harmonic mean method (Lisle, 1977) for calcite grains in the X/Z principal plane of undeformed and deformed calcite-cement aggregate. Equivalent R_s is represented by the dark solid line. Samples were deformed under dry experimental conditions with confining pressures of 200 Mpa, strain rate of 10^{-5}/s and temperatures of 25°C.

For the most part, the harmonic means appear to be a larger overestimate of the experimental strain ratio. Since only minor strain is reflected in the calcite grains the harmonic mean remains relatively constant (≈1.67) as the experimental strain ratio increases. However, at higher experimental strains (> R_s=1.2) the result of increased rigid rotation and strain by twinning causes an increase in the harmonic mean. For the three methods of strain analysis the best estimates of the actual experimental strain ratio is Robin's method.

For Robin's method comparison of the strain estimate with that of the actual experimental strain exhibits an overestimate of the experimental strain ratio in the first 10% shortening. This is possibly reflecting the slight preferred orientation that existed in the undeformed state. This type of overestimate is also observed in the simulated deformation. At higher experimental strains the estimates become more varying, however, many samples give reasonable estimates of the experimental bulk strain. The calculation of the strain estimate by Robin's method from calcite grains deformed by a combination of rigid rotation and minor strain by twinning approximately reflects the bulk strain of the sample

Standard deviation for Robin's method, linearization method and the harmonic mean method were calculated and are presented in Table 5.2. For the linearization method the calculations of standard deviation that yield confidence brackets that extend into bulk strains estimates less than 1.000 are not given.

Figure 5.12 presents the Flinn diagram for samples of calcite cement aggregate deformed under dry experimental conditions. The X/Y and Y/Z ratios are determined from the harmonic mean of the X/Z and X/Y principal plane sections.

Figure 5.12 Flinn diagram for samples of calcite-cement aggregate deformed under wet experimental conditions for experimental strain ratios between 1.000 (e=0.00%) to 1.347 (e=18.03%). The X/Y and Y/Z ratios are determined from the harmonic mean of the X/Z and X/Y principal plane sections. The overall trend for the calcite grains into the S>L field is represented by the dark arrow. Samples were deformed under dry experimental conditions with confining pressures of 200 Mpa, strain rate of 10^{-5}/s and temperatures of 25°C. Standard errors for each sample are given in the sub diagram.

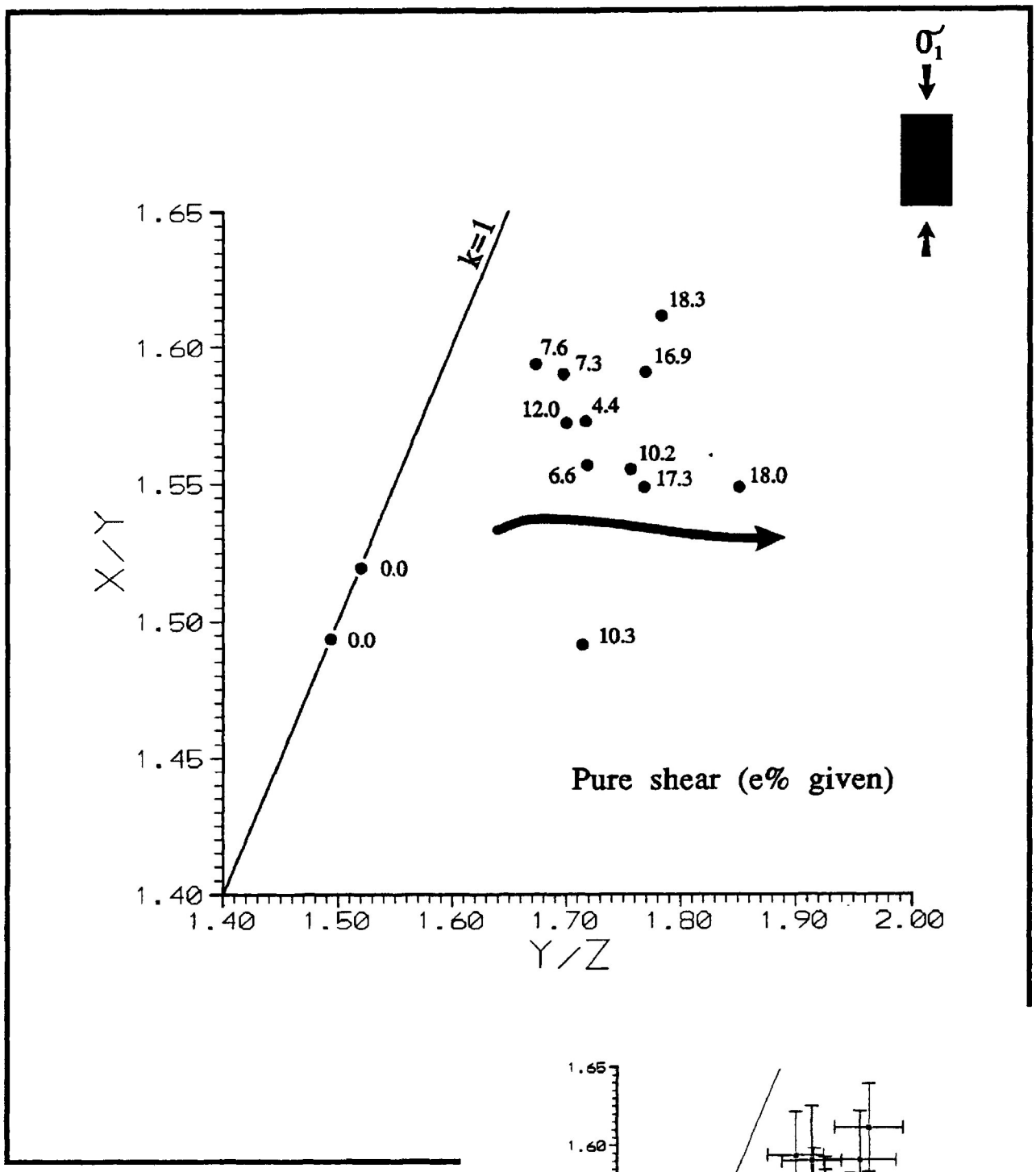
σ1
k=1
18.3
7.6
7.3
16.9
12.0
4.4
10.2
6.6
17.3
18.0
0.0
0.0
10.3
Pure shear (e% given)
X/Y
Y/Z
1.65
1.60
1.55
1.50
1.45
1.40
1.40
1.50
1.60
1.70
1.80
1.90
2.00

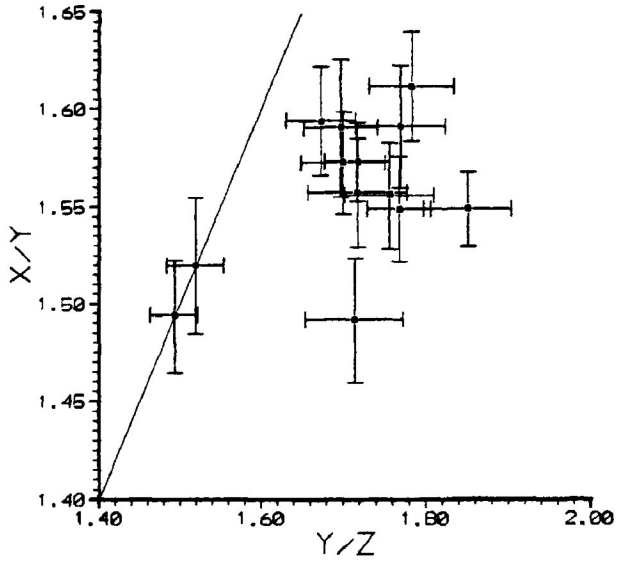
X/Y
Y/Z
1.65
1.60
1.55
1.50
1.45
1.40
1.40
1.60
1.80
2.00

From the figure is observed that there is much variation in the X/Y data of the Flinn data. However, there is an overall trend for the strain ellipsoid of the calcite grains to progress into the S>L field as illustrated by the dark arrow. The progression of the samples into the S>L field is the result of increased rigid rotation and strain by twinning as the experimental strain ratio is increased. Variation in the data may reflect the varying degree of rigid rotation that is occurring during dry experimental deformation. Standard errors for each sample are given in the sub diagram of figure 5.12.

c) Wet experimental pure shear (P_c=200 Mpa, $de/dt=10^{-5}$/s, P_f=195 Mpa)

In wet experimental pure shear deformation, a comparison of orientational and dimensional frequency distributions and R_f/ϕ diagrams were made from 6 samples increasing in experimental strain ratio from 1.000 (e=0.00%) to 1.509 (e=24.00%). Other figures and analysis involved all samples deformed by pure shear under dry conditions (see Appendix A).

Figure 5.13a-f illustrates the orientational frequency distribution of the longest dimension (Angle Ax (ϕ)) for the calcite grains of 6 samples increasing in strain ratio. In the deformed samples there is a tendency for the long axis of the calcite grains to align rapidly in an orientation perpendicular to the experimental σ_1. The PDO begins to develop at low experimental strain (e=6.8%) and becomes very well developed at slightly higher experimental strains (>e=10.9%). The rapid development of the PDO in calcite grains is greater than that observed in the simulated pure shear deformation of the previous section (Fig. 5.1b-f). The F remains at approximately 180° to 170° as the experimental strain increases. The slight decrease in the fluctuation occurs at relatively low experimental strains, R_s=1.189 (e=10.9%).

Figure 5.13a-f Frequency distribution of Angle Ax (ϕ) orientations of calcite grains in undeformed and deformed calcite-cement aggregate. Experimental strain ratios range from 1.000 (e=0.00%) to 1.509 (e=24.00%). Maximum extension direction orientation orientated at 0°. Samples were deformed under wet experimental conditions with confining pressures of 200 Mpa, strain rate of 10^{-5}/s and temperatures of 25°C. Pore fluid pressures were less than 195 Mpa.

a) UNDCAL (R_s=1.000 (e=0.0%))
b) CPF-12 (R_s=1.111 (e=6.8%))
c) CPF-08 (R_s=1.148 (e=8.8%))
d) CPF-04 (R_s=1.189 (e=10.9%))
e) CPF-13 (R_s=1.342 (e=17.8%))
f) CPF-03 (R_s=1.509 (e=24.0%))

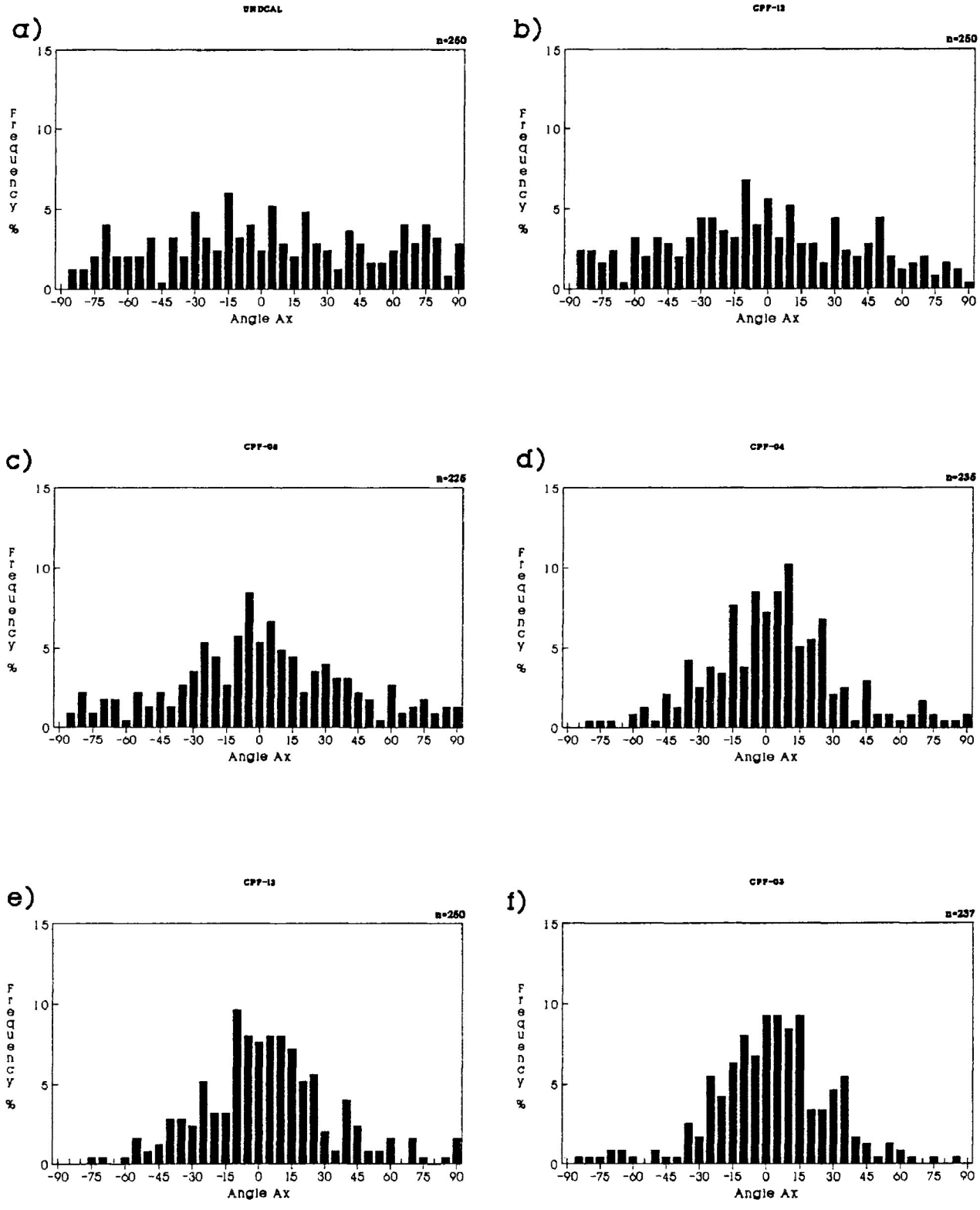
a)
UNDCAL
n=250
b)
CPF-13
n=250
c)
CPF-08
n=225
d)
CPF-04
n=235
e)
CPF-13
n=250
f)
CPF-03
n=237
Frequency %
Angle Ax
0
5
10
15
-90 -75 -60 -45 -30 -15 0 15 30 45 60 75 90

Figure 5.2 presents the angular deviation of the long axes of calcite grains for 9 samples, it is observed that the angular deviations decrease from 24.82 to 13.12 as the experimental strain ratio increases. The angular deviation of the developing PDO is similar to the simulated deformation for low experimental strain ratios, less than approximately 1.124 (≈7.5% shortening). As the percent strain increases the angular deviation rapidly departs from the simulation, becoming lower in value. The rapid decrease in angular deviation occurs between experimental strain ratios of 1.148 (e=8.80%) and 1.189 (e=10.90%). The angular deviation remains relatively constant as the experimental strain continues to increase, However, another decrease is observed at an experimental strain ratio of 1.509 (e=24.00%). The development of a PDO is greater than that predicted by passive R_f/ϕ transformation.

Figure 5.14 exhibits variations in the mean R_f. It is observed that the mean R_f in the plane of observation increases as strain increases. This is reflected in the R_f frequency distributions of figure 5.15a-f. Comparison of the variation of mean R_f between experimental and computer simulated data illustrates that, for wet pure shear deformation, the mean R_f of calcite grains are slightly greater than those generated by simulation. However, the role of twinning in the plastic (heterogeneous) deformation of the calcite grains plays a minor role in the increase of the mean R_f since the lamellae indices are less than that observed in dry pure shear. The increase in the R_f in the plane of observation must, therefore, be the result of rigid rotation of the calcite grains into a PDO.

The R_f/ϕ diagrams for calcite grains are presented in figure 5.16a-f. These figures suggest that there is a change in R_f as experimental strain increases, with the development

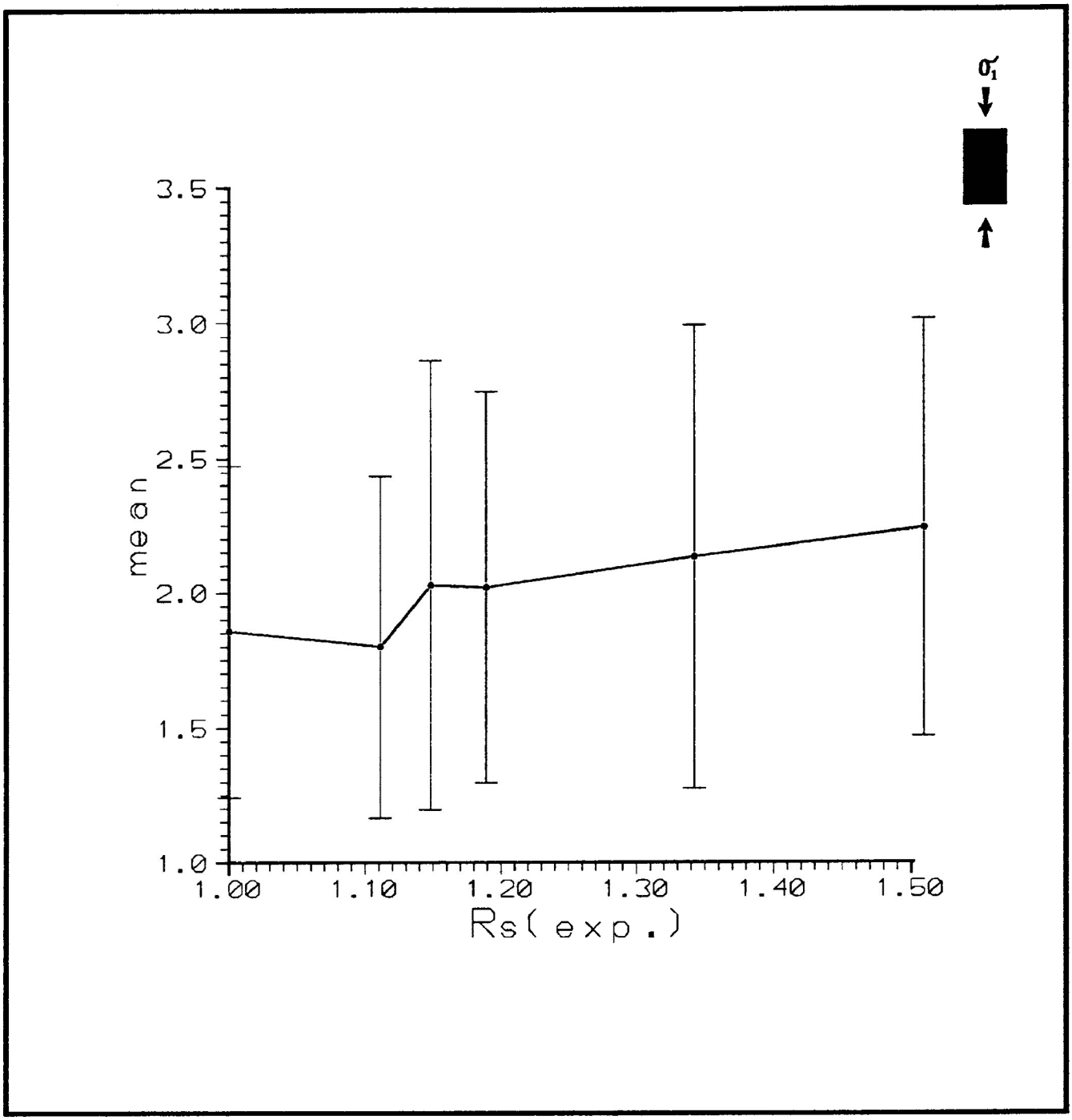

Figure 5.14 Variation in mean R_f of calcite grains in undeformed and deformed calcite-cement aggregate with standard deviation against experimental strain. Experimental strain ratios range from 1.000 (e=0.00%) to 1.509 (e=24.00%). Samples were deformed under dry experimental conditions with confining pressures of 200 Mpa, strain rate of 10^{-5}/s and temperatures of 25°C. Pore fluid pressures were less than 195 Mpa.

Figure 5.15a-f Frequency distribution of R_i and R_f for calcite grains in undeformed and deformed calcite-cement aggregate. Experimental strain ratios range from 1.000 (e=0.00%) to 1.509 (e=24.00%). Samples were deformed under dry experimental conditions with confining pressures of 200 Mpa, strain rate of 10^{-5}/s and temperatures of 25°C. Pore fluid pressures were less than 195 Mpa.

a) UNDCAL (R_s=1.000 (e=0.0%))
b) CPF-12 (R_s=1.111 (e=6.8%))
c) CPF-08 (R_s=1.148 (e=8.8%))
d) CPF-04 (R_s=1.189 (e=10.9%))
e) CPF-13 (R_s=1.342 (e=17.8%))
f) CPF-03 (R_s=1.509 (e=24.0%))

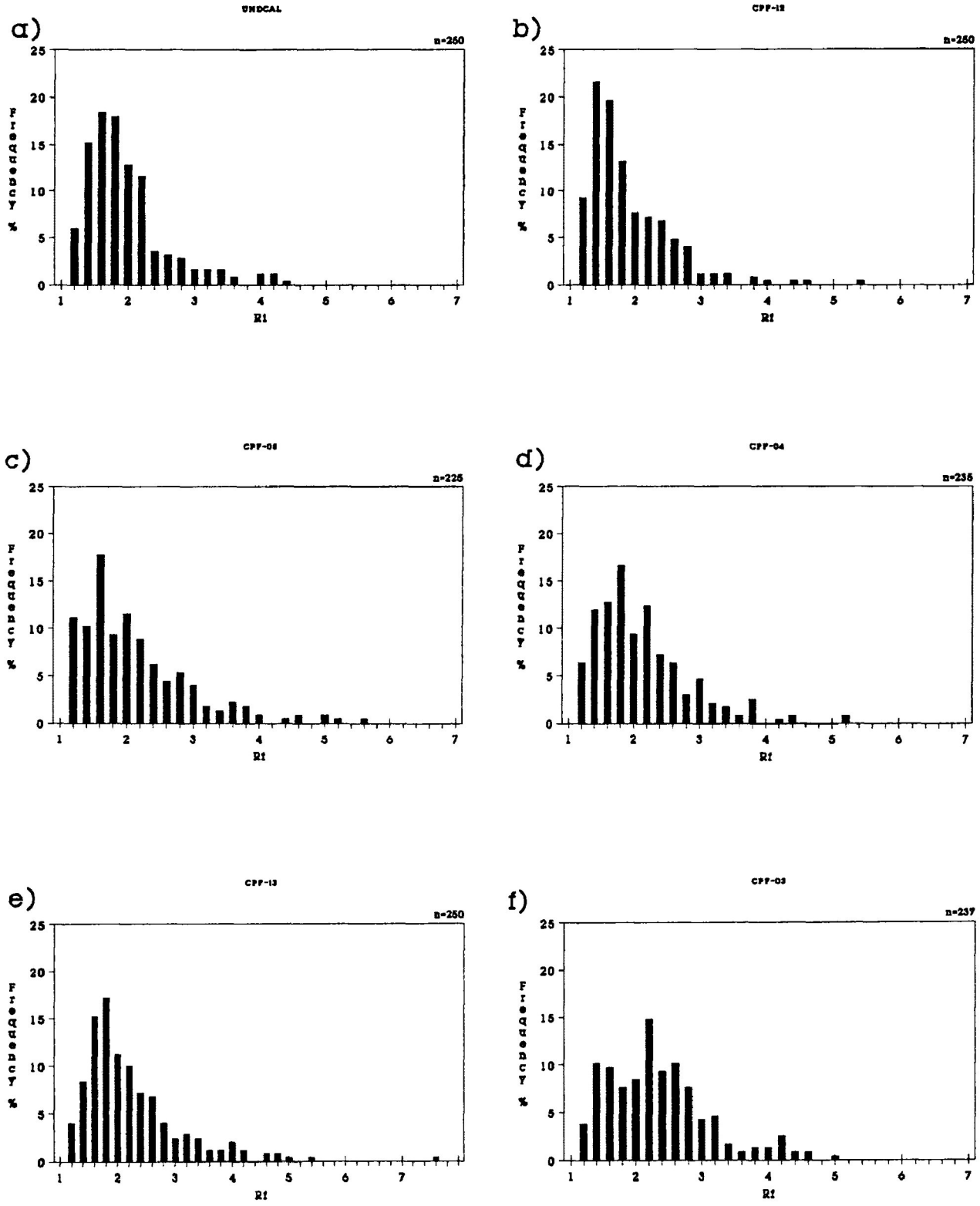
a)
UNDCAL
n=250
b)
CPF-12
n=250
c)
CPF-08
n=225
d)
CPF-04
n=235
e)
CPF-13
n=250
f)
CPF-03
n=237
Frequency %
Rf

Figure 5.16a-f R_f/ϕ diagrams for calcite grains in undeformed and deformed calcite-cement aggregate. Experimental strain ratios range from 1.000 (e=0.00%) to 1.509 (e=24.00%). Maximum extension direction orientation orientated at 0°. Samples were deformed under wet experimental conditions with confining pressures of 200 Mpa, strain rate of 10^{-5}/s and temperatures of 25°C. Pore fluid pressures were less than 195 Mpa.

a) UNDCAL (R_s=1.000 (e=0.0%))
b) CPF-12 (R_s=1.111 (e=6.8%))
c) CPF-08 (R_s=1.148 (e=8.8%))
d) CPF-04 (R_s=1.189 (e=10.9%))
e) CPF-13 (R_s=1.342 (e=17.8%))
f) CPF-03 (R_s=1.509 (e=24.0%))

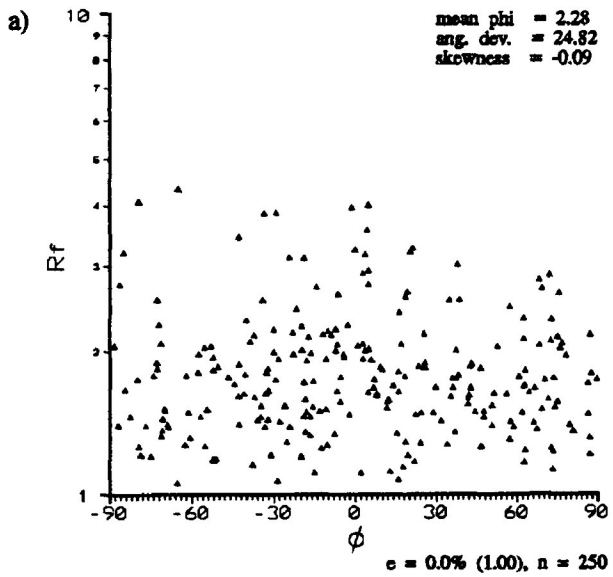
a)
mean phi = 2.28
ang. dev. = 24.82
skewness = -0.09
Rf
ϕ
e = 0.0% (1.00), n = 250

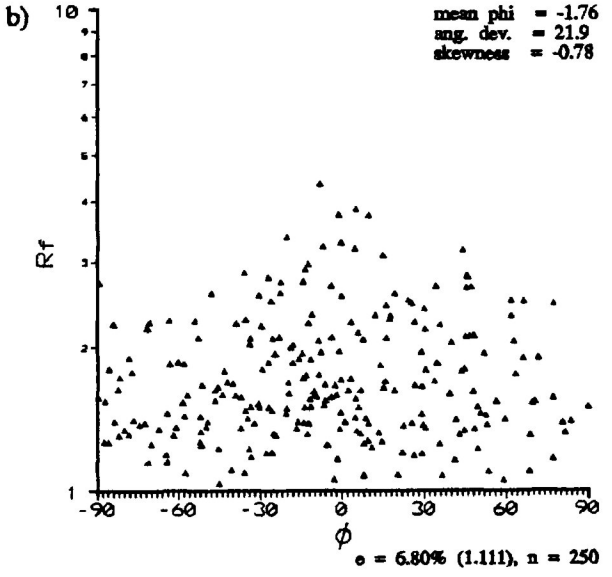
b)
mean phi = -1.76
ang. dev. = 21.9
skewness = -0.78
Rf
ϕ
e = 6.80% (1.111), n = 250

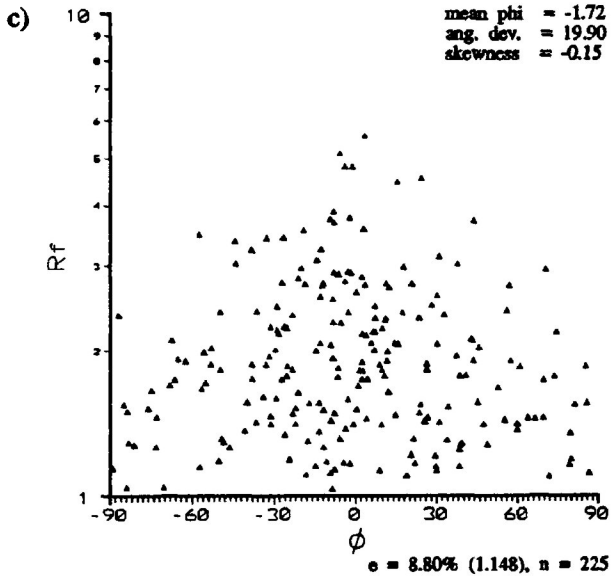
c)
mean phi = -1.72
ang. dev. = 19.90
skewness = -0.15
Rf
ϕ
e = 8.80% (1.148), n = 225

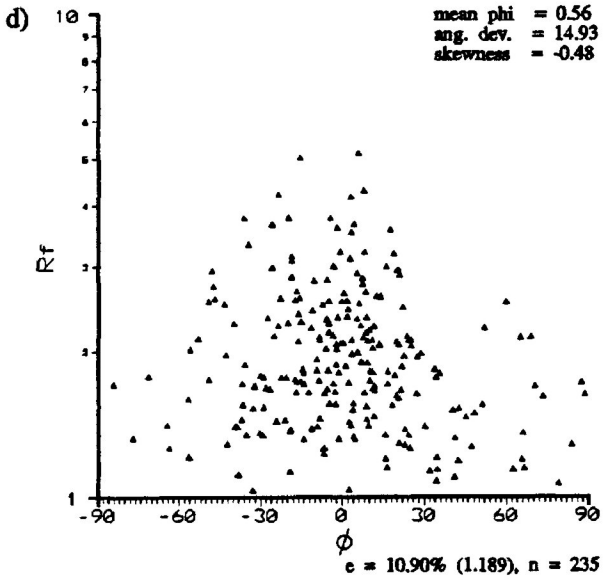
d)
mean phi = 0.56
ang. dev. = 14.93
skewness = -0.48
Rf
ϕ
e = 10.90% (1.189), n = 235

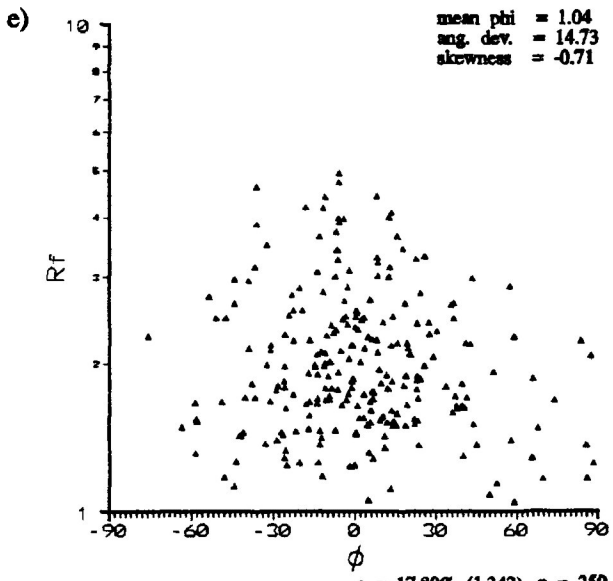
e)
mean phi = 1.04
ang. dev. = 14.73
skewness = -0.71
Rf
ϕ
e = 17.80% (1.342), n = 250

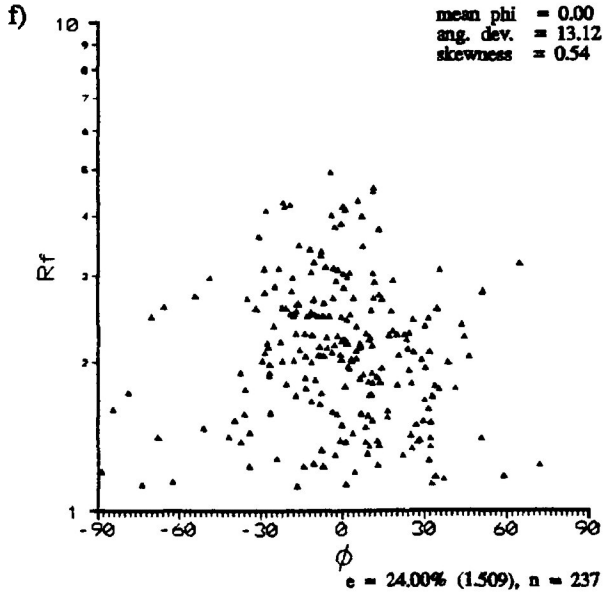
f)
mean phi = 0.00
ang. dev. = 13.12
skewness = 0.54
Rf
ϕ
e = 24.00% (1.509), n = 237

of a PDO parallel to the σ_1 direction. The PDO is defined by the concentration of calcite grains over the total range of R_f. The R_f/ϕ distribution is enhanced by the concentration of high R_f calcite grains at low experimental strains. At higher experimental strains the majority of calcite grains appear to be localized in the centre of the R_f/ϕ distribution with less grains of low R_f than observed in dry pure shear. The R_f/ϕ distributions are similar in appearance to those produced by simulated pure shear deformation.

It may be suggested that the fabric development is mainly the result of rigid rotation of the calcite grains with minor strain produce by twinning in suitably oriented grains. This is suggested by the fact that the higher R_f grains do not necessarily exhibit large lamellae indices and by the relatively strong alinement of calcite grains with low R_f values at very low experimental strains, where deformation by twinning is very low.

Figure 5.17 presents the comparison of the Robin's, linearization and harmonic mean methods of strain analysis for deformed calcite grains. All three methods of strain analysis give overestimates of the strain ratio. Robin's method is the closest approximation of the actual R_s. The linearization method yields a poor correlation with Robin's method. The deviation of the linearization method from that of the calculated strain ratio by Robin's method increases as strain increases. For lower strains (<1.3) the linearization method yields estimates of strain that are less than the strain estimate of the harmonic mean method. At higher strains the estimates by the linearization method become greater than the harmonic mean strain ratio estimate.

The development of the large deviation in the strain ratio estimate (observed even at low strains) may be the result of

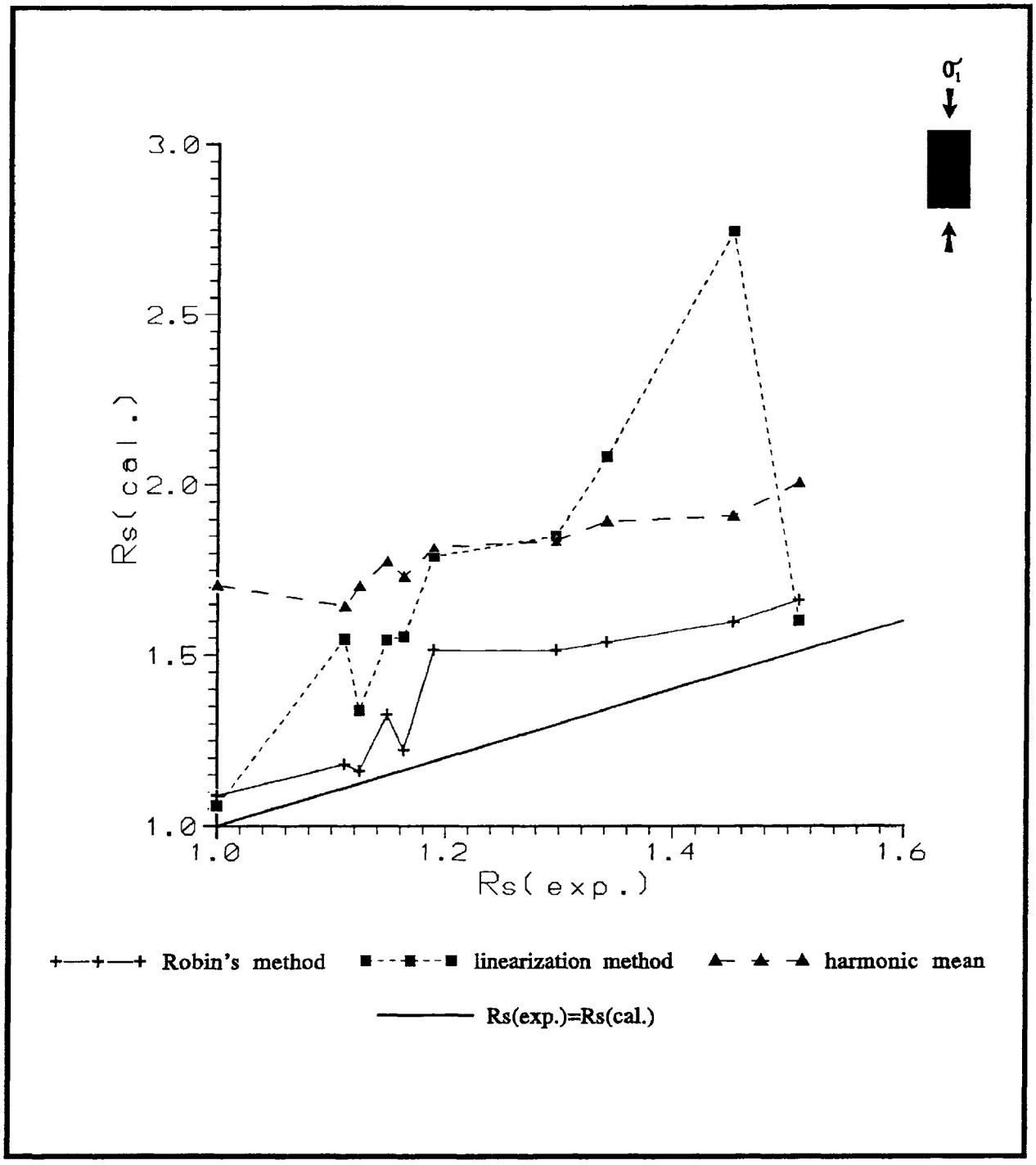

Figure 5.17 Comparison of strain estimates by Robin's method (1977), linearization method (Yu and Zheng, 1984) and harmonic mean method (Lisle, 1977) for calcite grains in the X/Z principal plane of undeformed and deformed calcite-cement aggregate. Equivalent R_s is represented by the dark solid line. Samples were deformed under wet experimental conditions with confining pressures of 200 Mpa, strain rate of 10^{-5}/s and temperatures of 25°C. Pore fluid pressures were less than 195 Mpa.

controlled particulate flow. At low strains controlled particulate flow is characterized by the rigid rotation of calcite grains with high aspect ratios and at higher strains by the rotation of lower R_f grains. For the linearization method high R_f grains aligned parallel to the PDO can significantly affect the linear regression through the linearization data producing an overestimate (see Chapter 3). For Robin's method the rigid rotation of the majority of calcite grains at higher strains ratios causes the arithmetic mean of the a_j/c_j ratios to become an overestimate of the strain.

At low experimental strain ratios the harmonic means appear to be a larger overestimate of the strain ratio. The harmonic mean does not remains constant, as in the case of dry pure shear, but increases steadily as the experimental strain ratio increases. Since twinning is not a major factor in increasing the R_f of calcite grains, under wet conditions, the above observation must be the result of rigid rotation of grains into a PDO. For the three methods of strain analysis the best estimates of the actual experimental strain ratio is Robin's method.

For Robin's method comparison of the strain estimate with that of the actual experimental strain exhibits an overestimate of experimental strain ratio in the first 10% shortening. This is possibly reflecting the slight preferred orientation that existed in the undeformed state. This type of overestimate is also observed in the simulated deformation. As the experimental strain ratio becomes greater, a rapid increase in strain by Robin's method is observed. The strain ratio estimate increases slightly as the experimental strain ratio increases. The calculation of the strain estimate by Robin's method from calcite grains in an aggregate mainly deformed by particulate flow does not reflect the bulk strain

of the sample. The grain strain is less than that of the bulk strain of the sample.

Standard deviation for Robin's method, linearization method and the harmonic mean method were calculated and are presented in Table 5.3. For the linearization method the calculations of standard deviation that yield confidence brackets extending into bulk strains estimates less than 1.000 are not given.

Figure 5.18 presents the Flinn diagram for samples of calcite cement aggregate deformed under wet experimental conditions. The X/Y and Y/Z ratios are determined from the harmonic mean of the X/Z and X/Y principal plane sections. From the figure is observed that there is an overall trend for the strain ellipsoid of the calcite grains to progress into the S>L field as illustrated by the dark arrow. The progression of the samples into the S>L field is the result of rigid rotation of the calcite grains as the experimental strain ratio is increased. The variation in X/Y data that is observed in the dry pure shear experiments is not observed in the wet experimental conditions suggesting that variations in the degree of rigid rotation are consistent as strain increases. Standard errors for each sample are given in the sub diagram of figure 5.18.

Figure 5.18 Flinn diagram for samples of calcite-cement aggregate deformed under wet experimental conditions for experimental strain ratios between 1.000 (e=0.00%) to 1.509 (e=24.00%). The X/Y and Y/Z ratios are determined from the harmonic mean of the X/Z and X/Y principal plane sections. The overall trend for the calcite grains into the S>L field is represented by the dark arrow. Samples were deformed under dry experimental conditions with confining pressures of 200 Mpa, strain rate of 10^{-5}/s and temperatures of 25°C. Pore fluid pressures were less than 195 Mpa. Standard errors for each sample are given in the sub diagram.

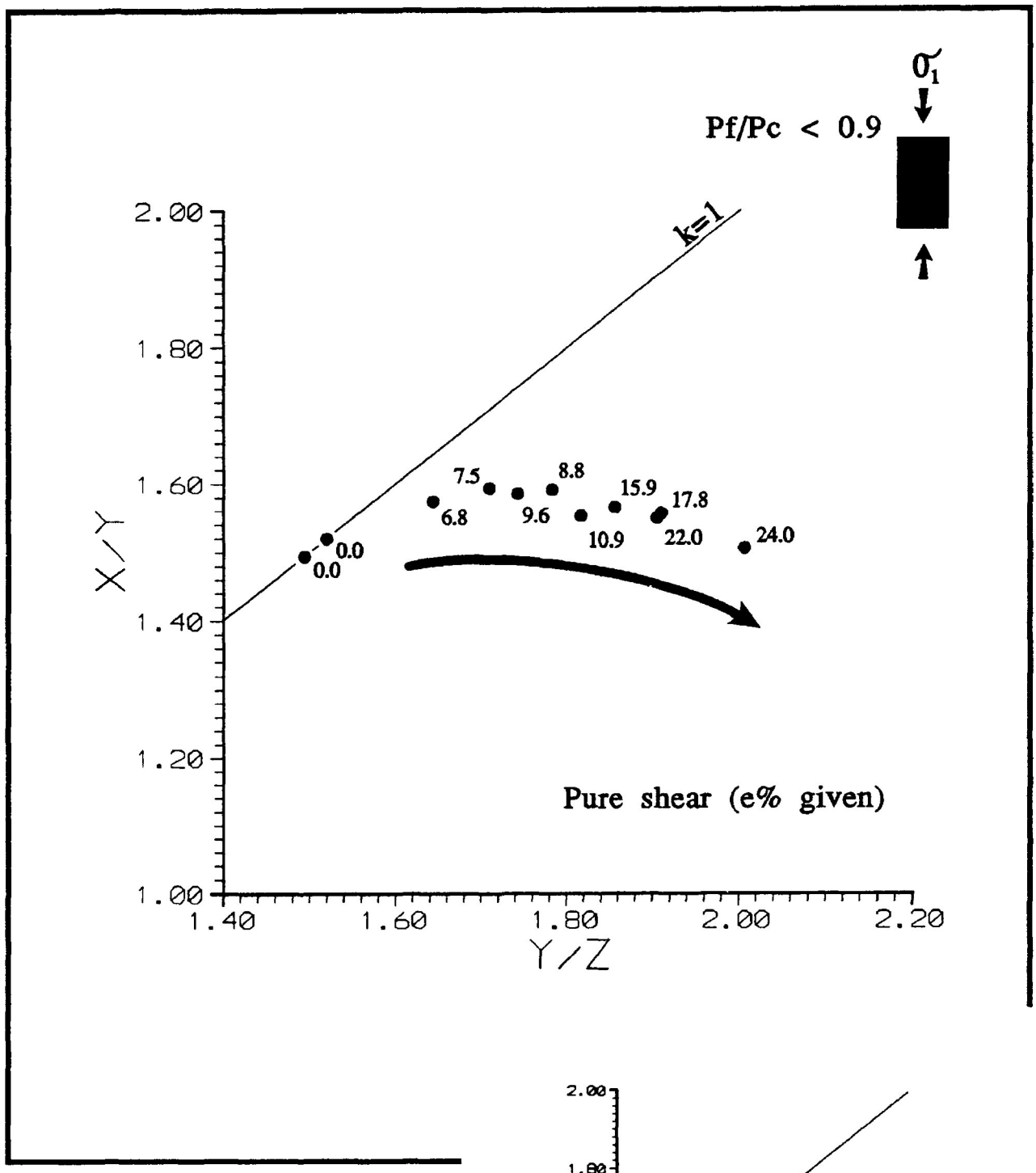
σ1
Pf/Pc < 0.9
k=1
2.00
1.80
1.60
1.40
1.20
1.00
X/Y
1.40
1.60
1.80
2.00
2.20
Y/Z
0.0
0.0
6.8
7.5
8.8
9.6
10.9
15.9
17.8
22.0
24.0
Pure shear (e% given)

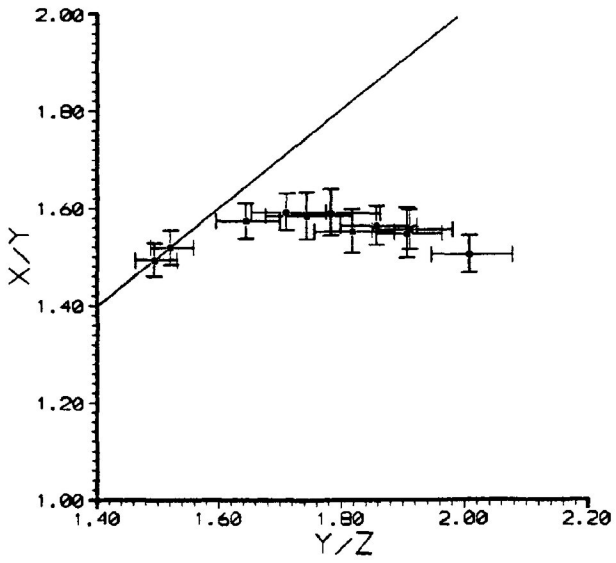
2.00
1.80
1.60
1.40
1.20
1.00
X/Y
1.40
1.60
1.80
2.00
2.20
Y/Z

5.3 Fabric Analysis of calcite grains (non-coaxial deformation)

Orientational and dimensional analyses were conducted on the calcite grains present in the undeformed and deformed X/Z principal plane of the calcite-cement aggregate samples. The samples were deformed by experimental approximations of transpressional shear and simple shear. Also conducted was a Flinn diagram analysis of 3-dimensional strain ellipsoid development. The calcite grains used in these determinations were measured from the central portion of the thin sections to eliminate heterogeneous affect near the walls and top of the test cylinder. Thin sections of the samples were cut to obtain the X/Z and X/Y principal plane for transpressional shear. In the case of longitudinal shear the thin section were cut parallel and perpendicular to the shear zone wall as well as perpendicular to the shear direction.

b) Transpressional Shear (Oblique shear zone (P_c= 200Mpa, $de/dt=10^{-5}/s$))

In dry experimental transpressional (oblique) shear deformation a comparison of orientational and dimensional frequency distributions and R_f/ϕ diagrams were made from 5 samples increasing in experimental shear strain from 0.000 (e=0.00%) to 0.189 (e=11.45%). For all orientational diagrams the shear zones and σ_1 are oriented at 0° and 55°, respectively. These orientations will generate a dextral shear sense in the experimental shear zone during deformation. Other figures and analysis involved all samples deformed by transpressional shear under dry conditions (see Appendix A).

Figure 5.19a-e illustrates the orientational frequency distribution of the longest dimension (Angle Ax (ϕ)) for the calcite grains of 5 samples increasing in experimental shear strain. from 0.000 to 0.189. As discussed in a previous

Figure 5.19a-e Frequency distribution of Angle Ax (ϕ) orientations of calcite grains in undeformed and deformed calcite-cement aggregate deformed by transpressional (oblique) shear. Experimental shear strain range from 0.000 to 0.189. The σ_1 direction orientated at 55°. Shear direction orientated at 0° with dextral sense of shear. Samples were deformed under dry experimental conditions with confining pressures of 200 Mpa, slip rates of 0.73×10^{-4} mm/s and temperatures of 25°C.

a) Undeformed
b) SZ-C4 (shear strain= 0.051)
c) SZ-C1 (shear strain= 0.111)
d) SZ2-C2 (shear strain= 0.129)
e) SZ-C3 (shear strain= 0.189)

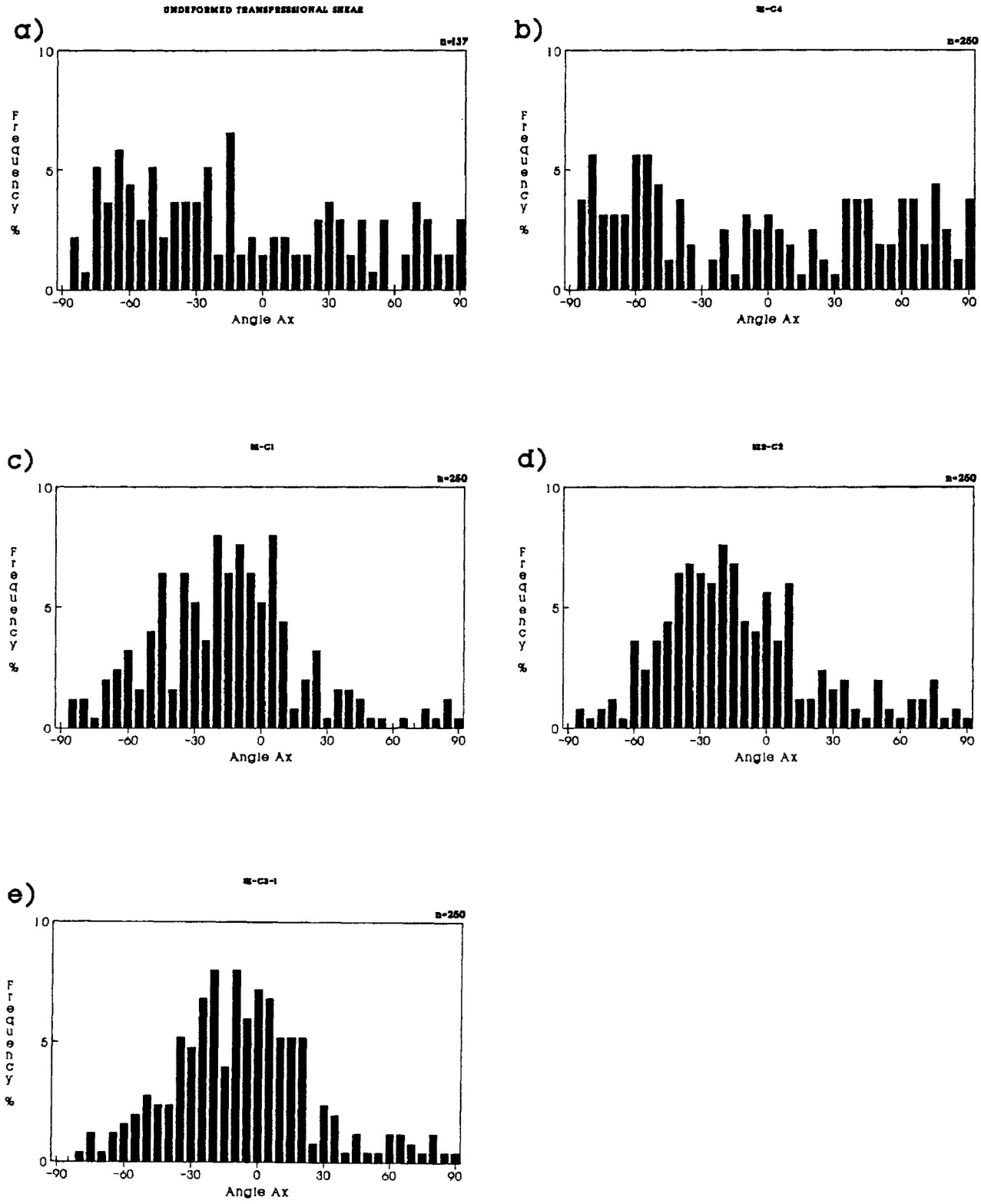
a)
UNDEFORMED TRANSPRESSIONAL SHEAR
n=137
b)
n=250
c)
n=250
d)
n=250
e)
n=250
Frequency %
Angle Ax
0
5
10
-90
-60
-30
0
30
60
90

section, the calcite grains in the undeformed shear zone assemblage exhibit a slight PDO perpendicular to the long axis of the test cylinder (*i.e.*, 35° from the shear direction, 90° from the σ_1 orientation).

In the deformed samples (Fig. 5.19b-e) there is a tendency for the long axis of the calcite grains to align quickly in an orientation oblique to the σ_1 direction. The PDO begins to develop at low experimental shear strains and becomes increasingly more pronounced at higher shear strains. Figure 5.20a presents the angular deviation of the PDO of calcite grains for 6 shear zone samples, it is observed that the angular deviations of the PDO decrease from 26.27 to 13.77 as the experimental shear strain increases.

However, as deformation in the shear zone increases the mean PDO of calcite grains rotates towards an orientation parallel to the shear direction in a clockwise (dextral) sense. The rotational development of the PDO is presented in figure 5.21 and 5.22. Figure 5.21 illustrates the rapid rotation of the developing PDO towards the shear zone with increasing deformation at low shear strains. In figure 5.22 a comparison of the reduction in angle between schistosity and the shear zone can be made to the development of a theoretical schistosity in ideal simple shear. For transpressional shear, the reduction in the angle between schistosity and the shear zone does not conform to ideal simple shear. This is true for all samples deformed by transpressional shear, except possibly for samples deformed by low shear strains (<0.051). The F remaining at approximately 180° as experimental shear strain increases from 0.000 to 0.189.

Figure 5.23 exhibits variations in the mean R_f, it is observed that the mean R_f in the plane of observation increases as the experimental shear strains increase. This

Figure 5.20a-c Variations in angular deviation of PDO for Angle Ax (ϕ) of samples deformed by transpressional shear (a) and 2 mm and 5 mm thick longitudinal simple shear (b (2 mm), c (5 mm)) in the X/Z principal plane of calcite grains in undeformed and deformed calcite-cement aggregate. Sub-figures give deformation assemblages. Samples were deformed under dry experimental conditions with confining pressures of 200 Mpa, slip rates of 0.73×10^{-4} mm/s and temperatures of 25°C. (modified from Borradaile and McArthur (1990))

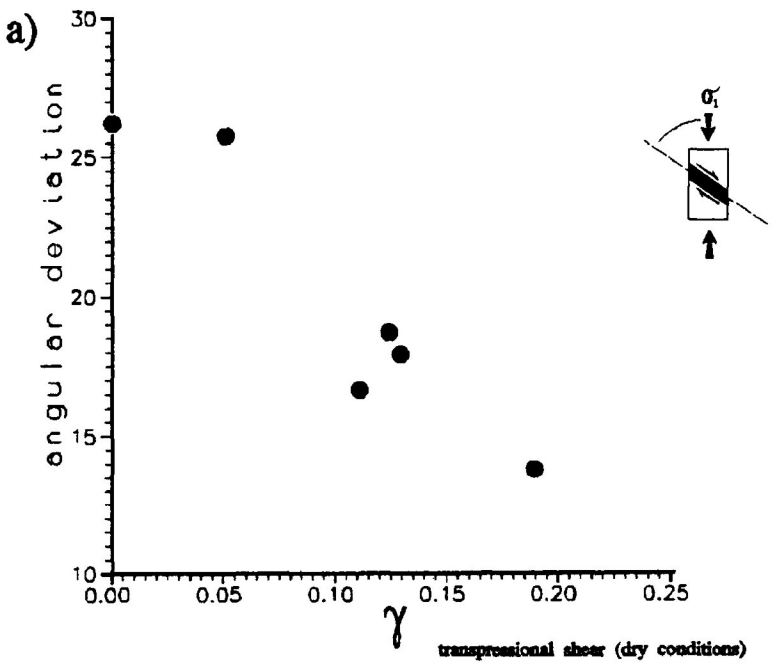
a)
angular deviation
30
25
20
15
10
0.00
0.05
0.10
0.15
0.20
0.25
γ
σ1
transpressional shear (dry conditions)

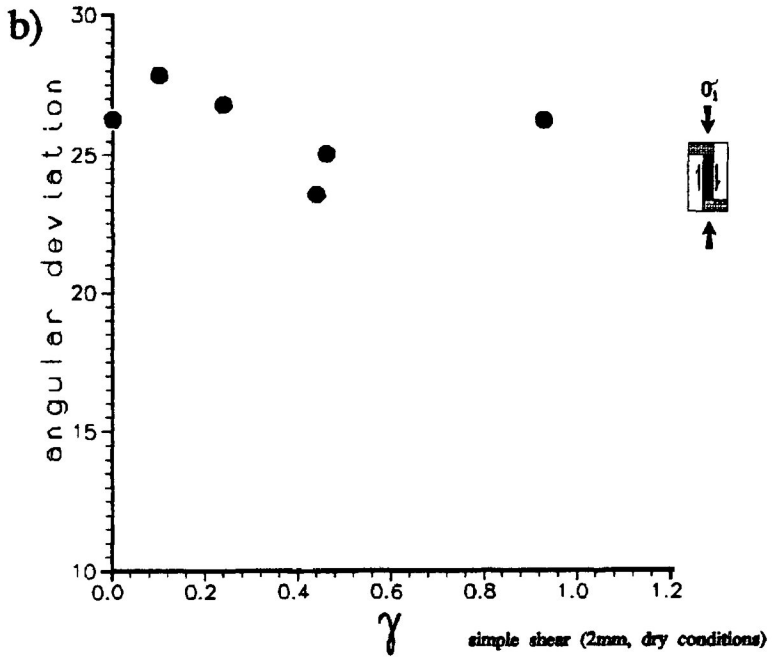
b)
angular deviation
30
25
20
15
10
0.0
0.2
0.4
0.6
0.8
1.0
1.2
γ
σ1
simple shear (2mm, dry conditions)

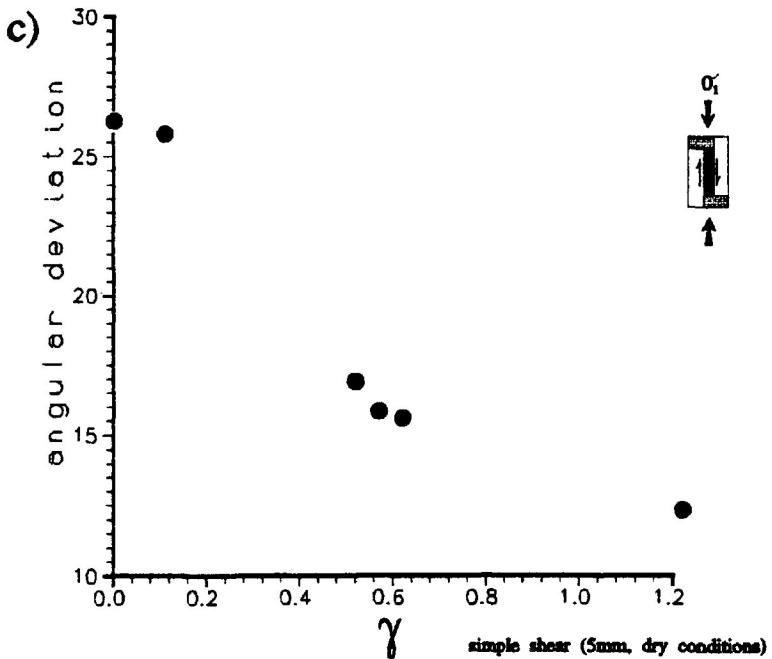
c)
angular deviation
30
25
20
15
10
0.0
0.2
0.4
0.6
0.8
1.0
1.2
γ
σ1
simple shear (5mm, dry conditions)

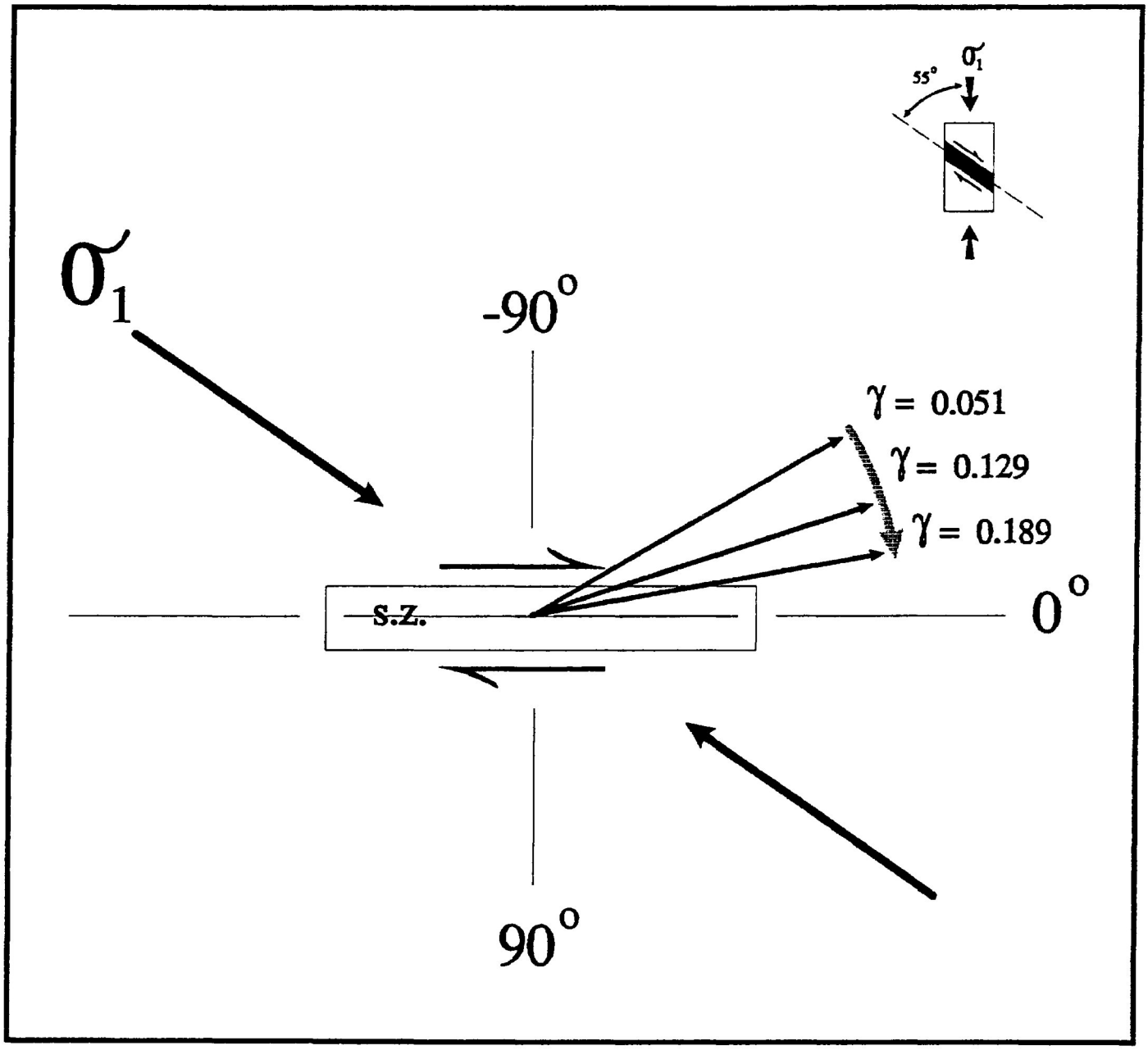

Figure 5.21 Rapid rotation of the developing PDO towards the shear zone with increasing deformation for low experimental shear strains. Angle between schistosity and the shear zone decreases from 35° to 13° as the experimental shear increases. The σ_1 direction orientated at 55°. Shear direction orientated at 0° with dextral sense of shear. Samples were deformed under dry experimental conditions with confining pressures of 200 Mpa, slip rates of 0.73×10^{-4} mm/s and temperatures of 25°C.

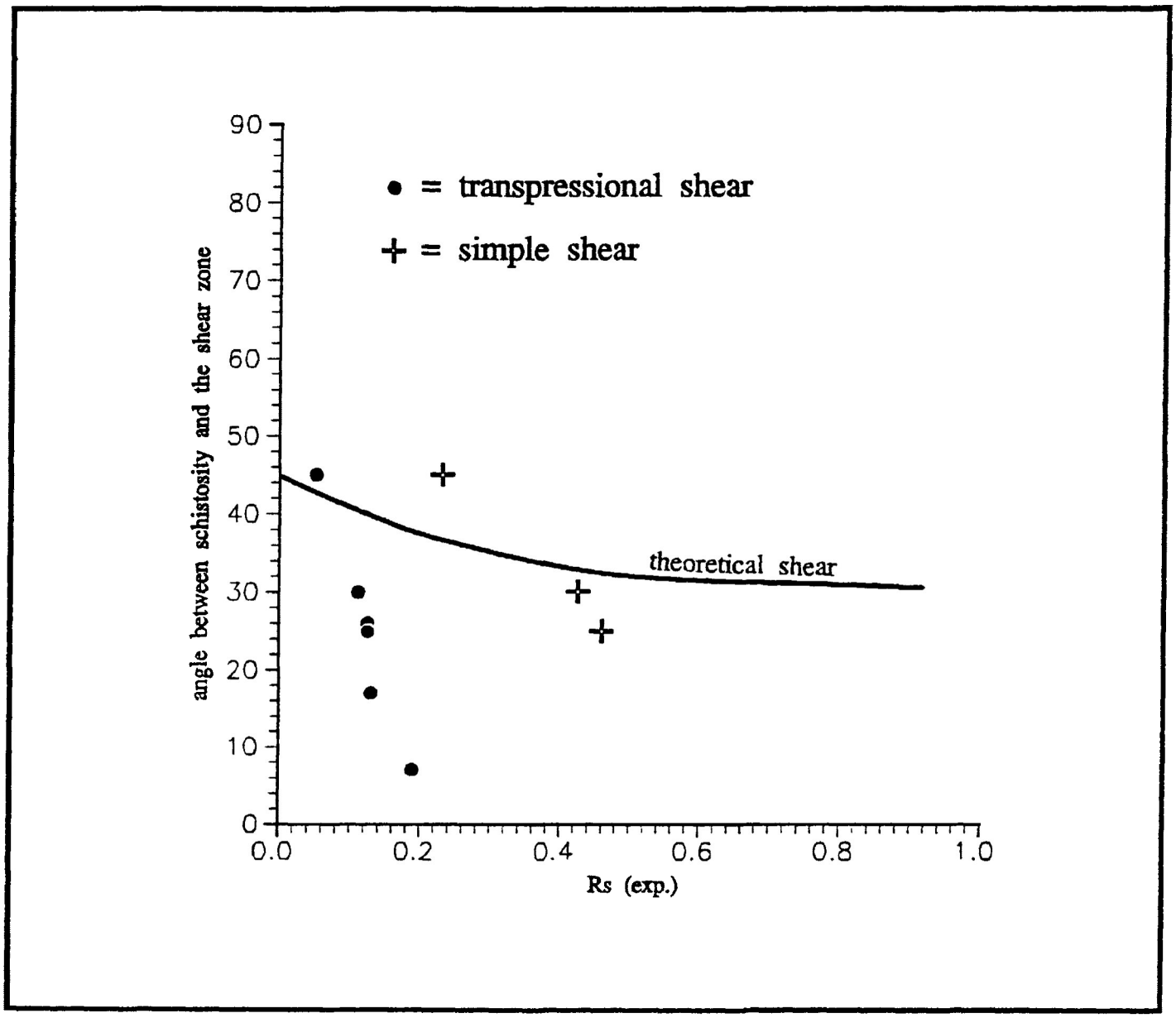

Figure 5.22 A comparison of the reduction in angle between schistosity and the shear zone for transpressional (oblique) shear (closed circle), longitudinal simple shear (cross) and that predicted by theoretical ideal simple shear (broad line). Shear direction orientated at 0°. Experimental samples were deformed under dry experimental conditions with confining pressures of 200 Mpa, slip rates of 0.73×10^{-4} mm/s and temperatures of 25°C. (modified from Borradaile and McArthur (1990))

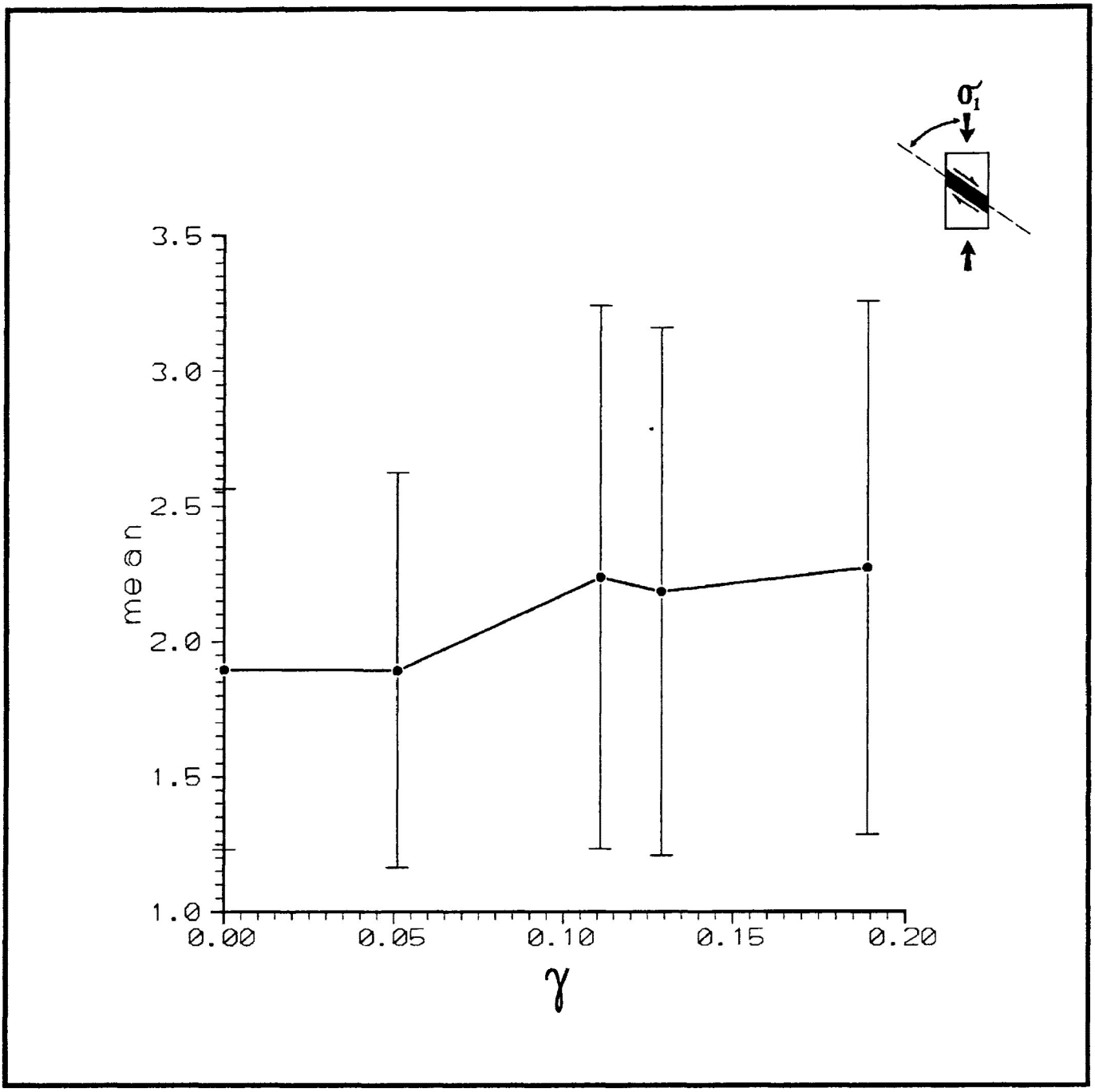

Figure 5.23 Variation in mean R_f of calcite grains in undeformed and deformed calcite-cement aggregate by transpressional (oblique) shear with increasing experimental strain. Standard deviation of the mean R_f is also given. Experimental shear strains range from 0.000 to 0.189. Samples were deformed under dry experimental conditions with confining pressures of 200 Mpa, slip rates of 0.73×10^{-4} mm/s and temperatures of 25°C.

Figure 5.24a-e Frequency distribution of R_i and R_f for calcite grains in undeformed and deformed calcite-cement aggregate by transpressional (oblique) shear. Experimental shear strains range from 0.000 to 0.189. Samples were deformed under dry experimental conditions with confining pressures of 200 Mpa, slip rates of 0.73×10^{-4} mm/s and temperatures of 25°C.

a) Undeformed
b) SZ-C4 (shear strain= 0.051)
c) SZ-C1 (shear strain= 0.111)
d) SZ2-C2 (shear strain= 0.129)
e) SZ-C3 (shear strain= 0.189)

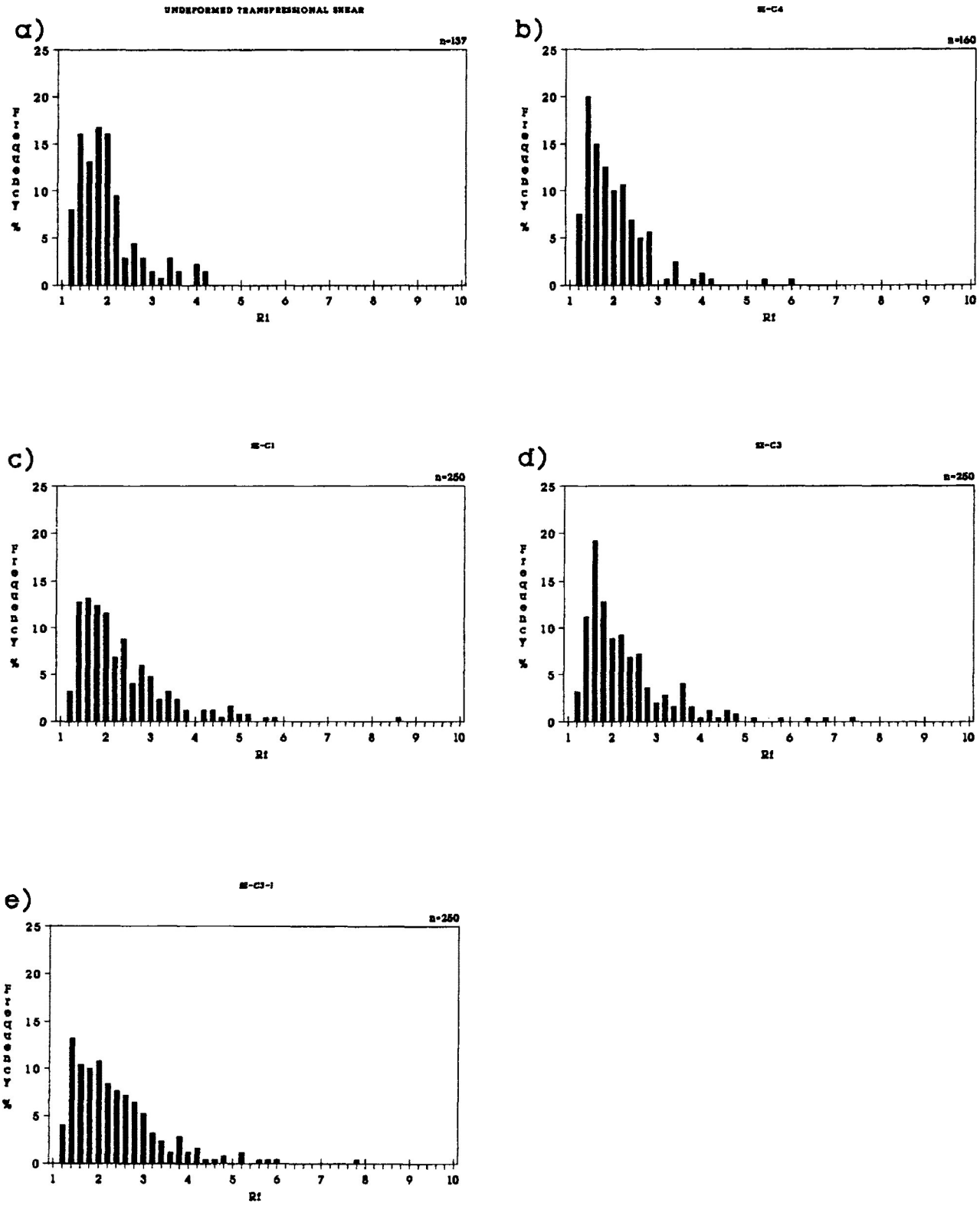
a)
UNDEFORMED TRANSPRESSIONAL SHEAR
n=137
b)
n=160
c)
n=250
d)
n=250
e)
n=250
Frequency %
Rf

trend is reflected in the increase in the range of R_f values as presented in the R_f frequency distributions of figure 5.24a-e. Comparison of the variation of mean R_f between transpressional and pure shear (dry and wet) illustrates that, for transpressional shear deformation, the mean R_f of calcite grains in the plane of observation increases more rapidly than in pure shear.

The R_f/ϕ diagrams for calcite grains are presented in figure 5.25a-f. These figures suggest an increase in R_f at low experimental shear strains with the development of a PDO oblique to the σ_1 direction in a sense compatible with the shear direction. The PDO is mainly defined by the concentration of calcite grains over the full range of R_f as experimental shear strain increases. The increasingly better developed R_f/ϕ distribution is observed to rotate towards the shear direction as the experimental shear strain becomes higher in value. The R_f/ϕ distribution is enhance at high shear strains by the alignment of grains with large R_f values.

Twinning in the plastic deformation of the calcite grains appears to play a role in the development of the PDO in samples deformed by transpressional shear. This is suggested by the high average lamellae index exhibited in the calcite grains of the deformed calcite-cement aggregate. However, calcite grains do not exhibit complete twinning. The strain expressed in calcite grain shape change is restricted to lower values.

It may be suggested that the fabric development is mainly the result of rapid rigid rotation of the calcite grains with strain produce by twinning for suitably oriented grains. The rapid rotation of the grains into a PDO approximately parallel to the shear zone causes many calcite grains to be in an orientation that is favourable for twinning.

Figure 5.25a-e R_f/ϕ diagrams for calcite grains in undeformed and deformed calcite-cement aggregate. Experimental shear strains range from 0.000 to 0.189. The σ_1 direction orientated at 55°. Shear direction orientated at 0° with dextral sense of shear. Samples were deformed under dry experimental conditions with confining pressures of 200 Mpa, slip rates of 0.73×10^{-4} mm/s and temperatures of 25°C.

a) Undeformed
b) SZ-C4 (shear strain= 0.051)
c) SZ-C1 (shear strain= 0.111)
d) SZ2-C2 (shear strain= 0.129)
e) SZ-C3 (shear strain= 0.189)

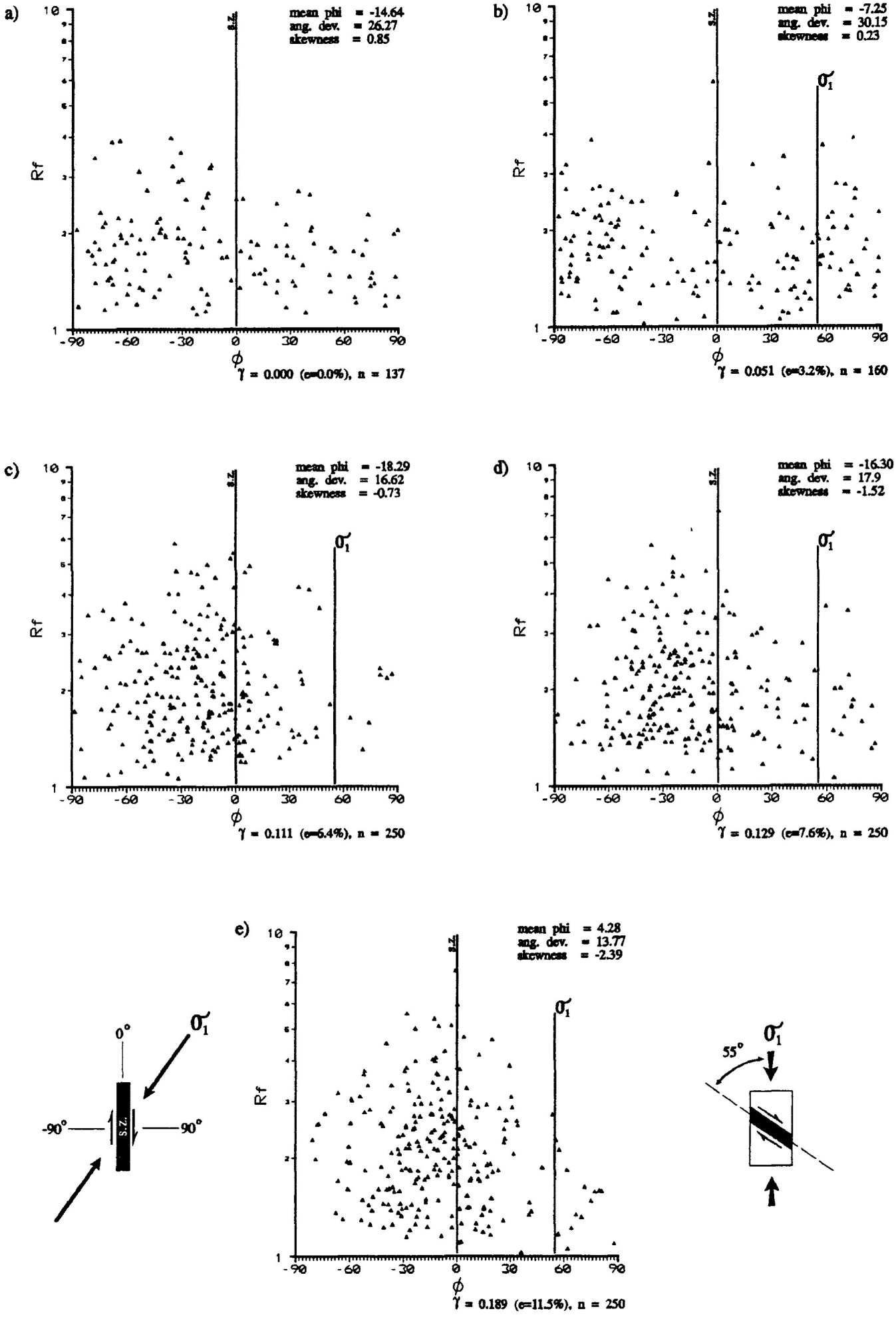
a)
mean phi = -14.64
ang. dev. = 26.27
skewness = 0.85
γ = 0.000 (e=0.0%), n = 137
b)
mean phi = -7.25
ang. dev. = 30.15
skewness = 0.23
γ = 0.051 (e=3.2%), n = 160
c)
mean phi = -18.29
ang. dev. = 16.62
skewness = -0.73
γ = 0.111 (e=6.4%), n = 250
d)
mean phi = -16.30
ang. dev. = 17.9
skewness = -1.52
γ = 0.129 (e=7.6%), n = 250
e)
mean phi = 4.28
ang. dev. = 13.77
skewness = -2.39
γ = 0.189 (e=11.5%), n = 250
Rf
φ
S.Z.
σ1
0°
-90°
90°
55°

Figure 5.26 presents the Flinn diagram for samples of calcite cement aggregate deformed under transpressional shear. The X/Y and Y/Z ratios are determined from the harmonic mean of the X/Z and X/Y principal plane sections. From the figure is observed that the three-dimensional strain ellipsoid of the calcite grains quickly enter into the S-field of the Flinn diagram. The rapid progression of the samples into the S-field is the result of increased rigid rotation and strain by twinning as the experimental shear strain is increased. There also appears to be a slight trend in the data to increase in Y/Z as the experimental shear strain increases. Standard errors for each sample are given in the sub diagram of figure 5.26.

Figure 5.26 Flinn diagram for samples of calcite-cement aggregate deformed under transpressional (oblique) shear for experimental shear strains between 0.000 and 0.189. The X/Y and Y/Z ratios are determined from the harmonic mean of the X/Z and X/Y principal plane sections. Samples were deformed under dry experimental conditions with confining pressures of 200 Mpa, slip rates of 0.73×10^{-4} mm/s and temperatures of 25°C. Standard errors for each sample are given in the sub diagram. (modified from Borradaile and McArthur (1990))

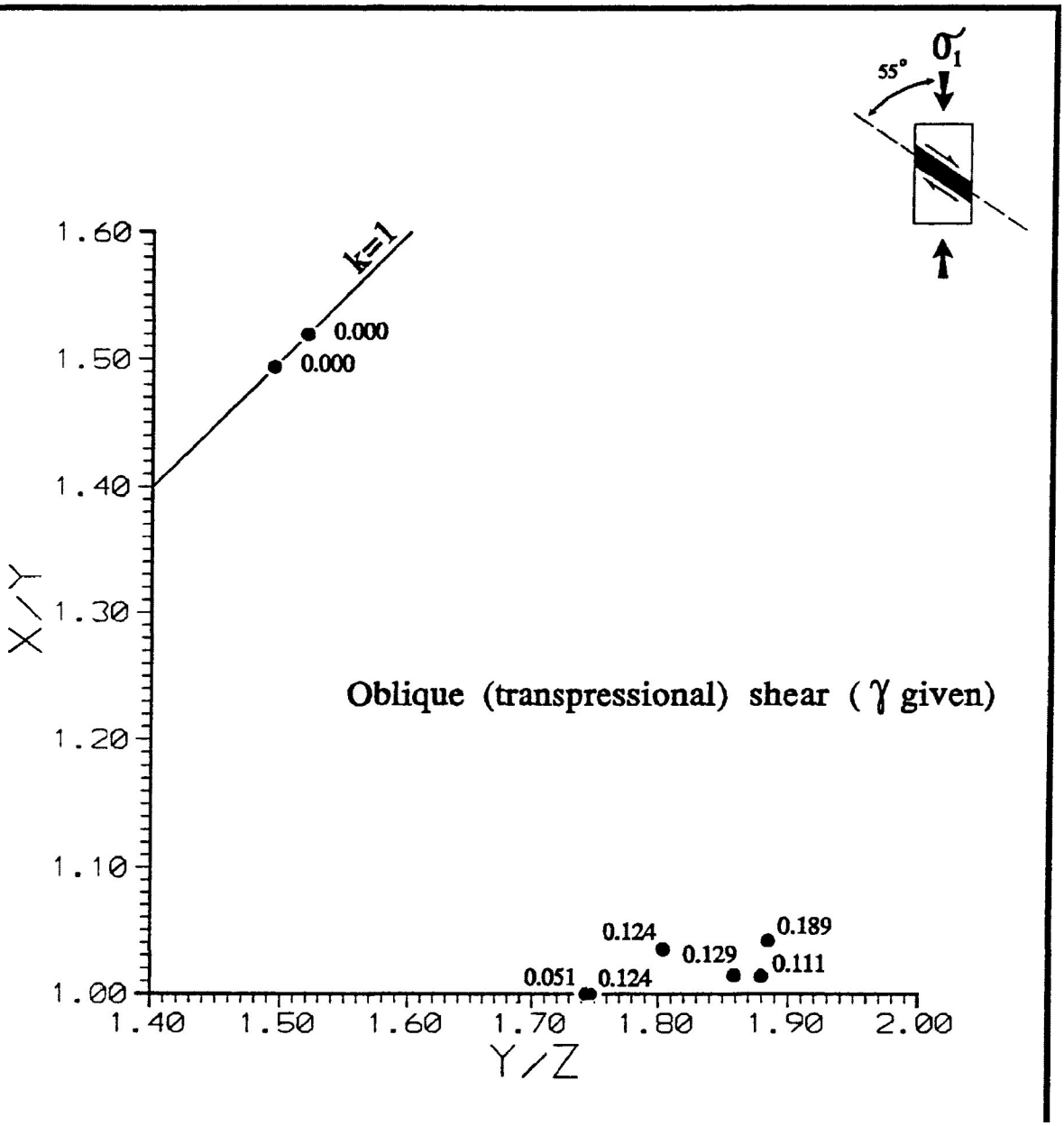

Oblique (transpressional) shear (γ given)

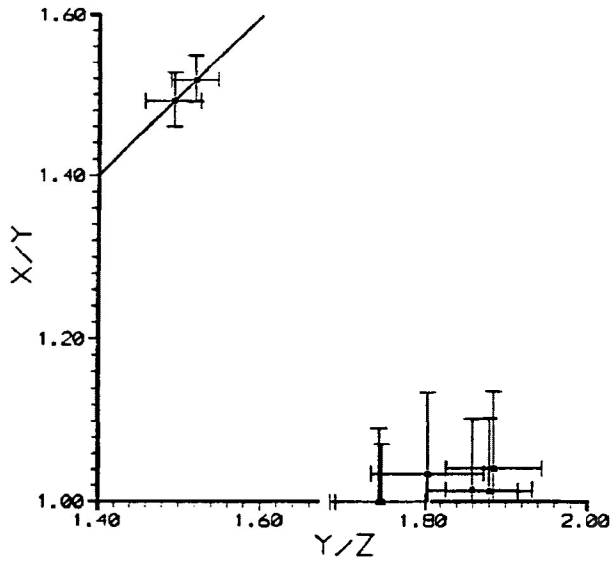

b) Simple shear (Longitudinal shear zone (P_c= 200Mpa, $de/dt=10^{-5}/s$))

In dry experimental simple (longitudinal) shear deformation a comparison of orientational and dimensional frequency distributions and R_f/ϕ diagrams were made from 5 samples of 2 mm thick shear zones only, increasing in experimental shear strain from 0.000 (e=0.00%) to 0.933 (e=36.45%). For all orientational diagrams the shear zones and σ_1 are oriented at 0°. These orientations will generate a dextral shear sense in the experimental longitudinal shear zone during deformation. Other figures and analysis involved all samples deformed by longitudinal shear under dry conditions (see Appendix A). The reason only 2 mm shear zones were used was that 5 mm shear zones experience large component of pure shear due to the limitations of the shear assemblage. Interpretation of the strain history is, therefore, very complex. However, comparisons are made to these sample when information is warranted.

Figure 5.27a-e illustrates the orientational frequency distribution of the longest dimension (Angle Ax (ϕ)) for the calcite grains of 5 samples increasing in experimental shear strain from 0.000 to 0.933. As discussed in a previous section the calcite grains in the undeformed shear zone assemblage exhibit a slight PDO perpendicular to the long axis of the test cylinder and the shear direction.

In the deformed samples (Fig. 5.27b-e) there is a tendency for the long axis of the calcite grains to align at moderate shear strains (>0.4) in an orientation oblique to the experimental σ_1 direction (approximately 45°). The PDO is weakly developed at low experimental shear strains and becomes better developed at higher shear strains. Figure 5.20b presents the angular deviation of the PDO of calcite grains for 6 shear zone samples, it is observed that the angular

Figure 5.27a-e Frequency distribution of Angle Ax (ϕ) orientations of calcite grains in undeformed and deformed calcite-cement aggregate deformed by 2mm thick longitudinal simple shear. Experimental shear strain range from 0.000 to 0.933. The σ_1 direction and shear direction orientated at 0° with dextral sense of shear. Samples were deformed under dry experimental conditions with confining pressures of 200 Mpa, slip rates of 0.73×10^{-4} mm/s and temperatures of 25°C.

a) Undeformed
b) LS8803 (shear strain= 0.101)
c) LS8811 (shear strain= 0.230)
d) LS8810 (shear strain= 0.425)
e) LS8807 (shear strain= 0.933)

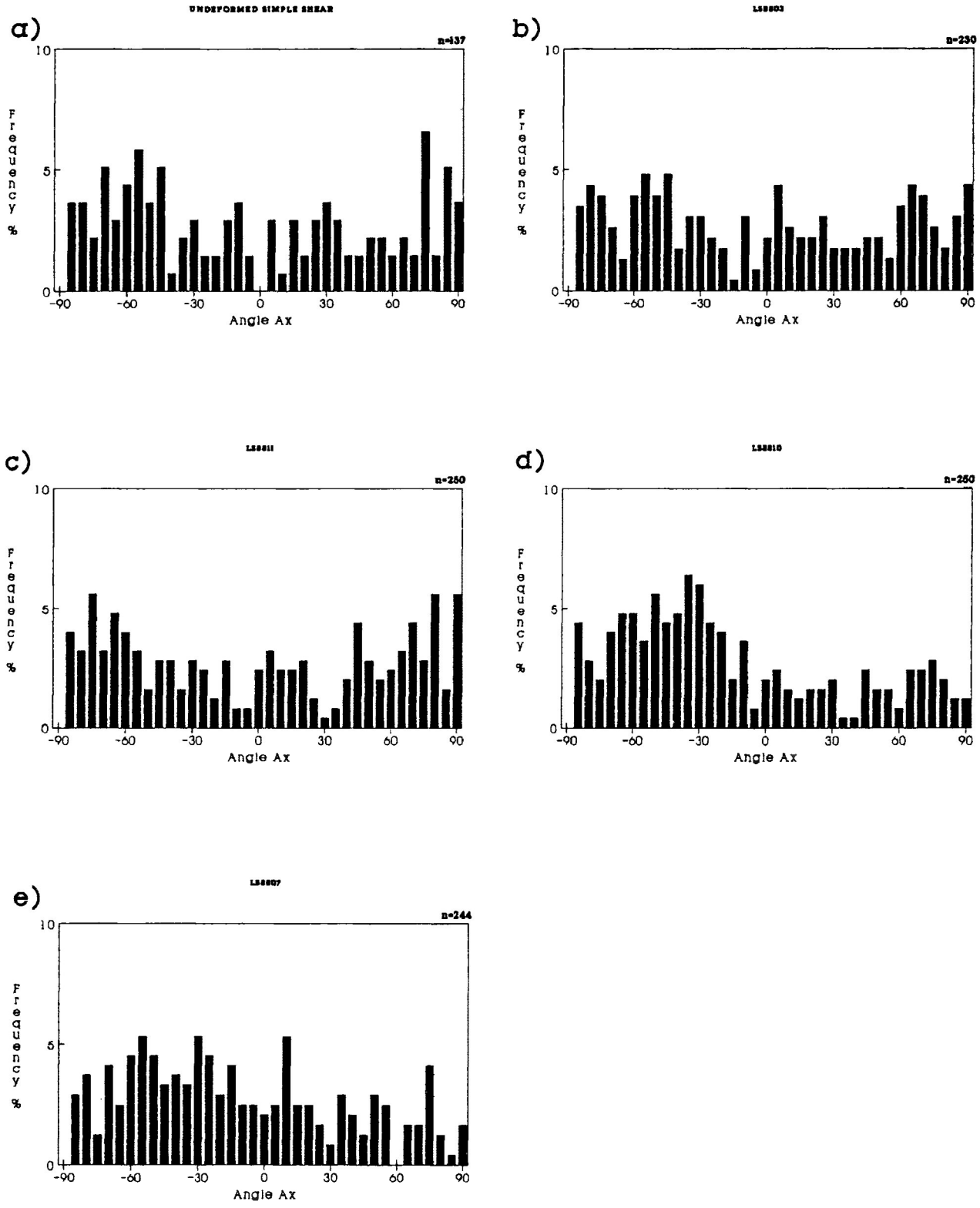
a)
UNDEFORMED SIMPLE SHEAR
n=437
b)
n=230
c)
n=250
d)
n=250
e)
n=244
Frequency %
Angle Ax
0
5
10
-90
-60
-30
0
30
60
90

deviations of the PDO slowly decrease from 26.27 to 23.45 as the experimental shear strain increases to a shear strain of 0.425.

As deformation in the shear zone increases the mean PDO in calcite grains rotates towards the orientation approximately 45° to the shear direction in a clockwise (dextral) sense. However, the effect of the shear limitations of the longitudinal assemblage causes an increasing in the pure shear component imposed on the samples. As the pure shear component increases the PDO rotates towards the perpendicular to the experimental σ_1 direction (perpendicular to the shear zone). This trend is illustrated in figure 5.28a-c for 5 mm shear zones. The rapid decrease of the angular deviation of the PDO in 5 mm thick longitudinal shear as pure shear becomes more dominant with increasing shear strain is exhibited in figure 5.20c.

The rotational development of the PDO is presented in figure 5.22. In figure 5.22 a comparison of the angle between schistosity and the shear zone can be made to the development of a theoretical schistosity in ideal simple shear. For the longitudinal shear in this experimental study the reduction in angle between schistosity and the shear zone does conform moderately to ideal simple shear. This suggests that the process of deformation in the experimental shear zone is producing an orientational fabric that is similar to that of simple shear. The F remains constant at approximately 180° as experimental shear strain increases from 0.000 to 0.933.

Figure 5.29 exhibits variations in the mean R_f for 2 mm thick longitudinal shear, it is observed that the mean R_f remains relatively constant as the experimental strain ratios increase. The lack of an increase in the mean R_f, represented by a constant range of R_f values, is presented in the R_f

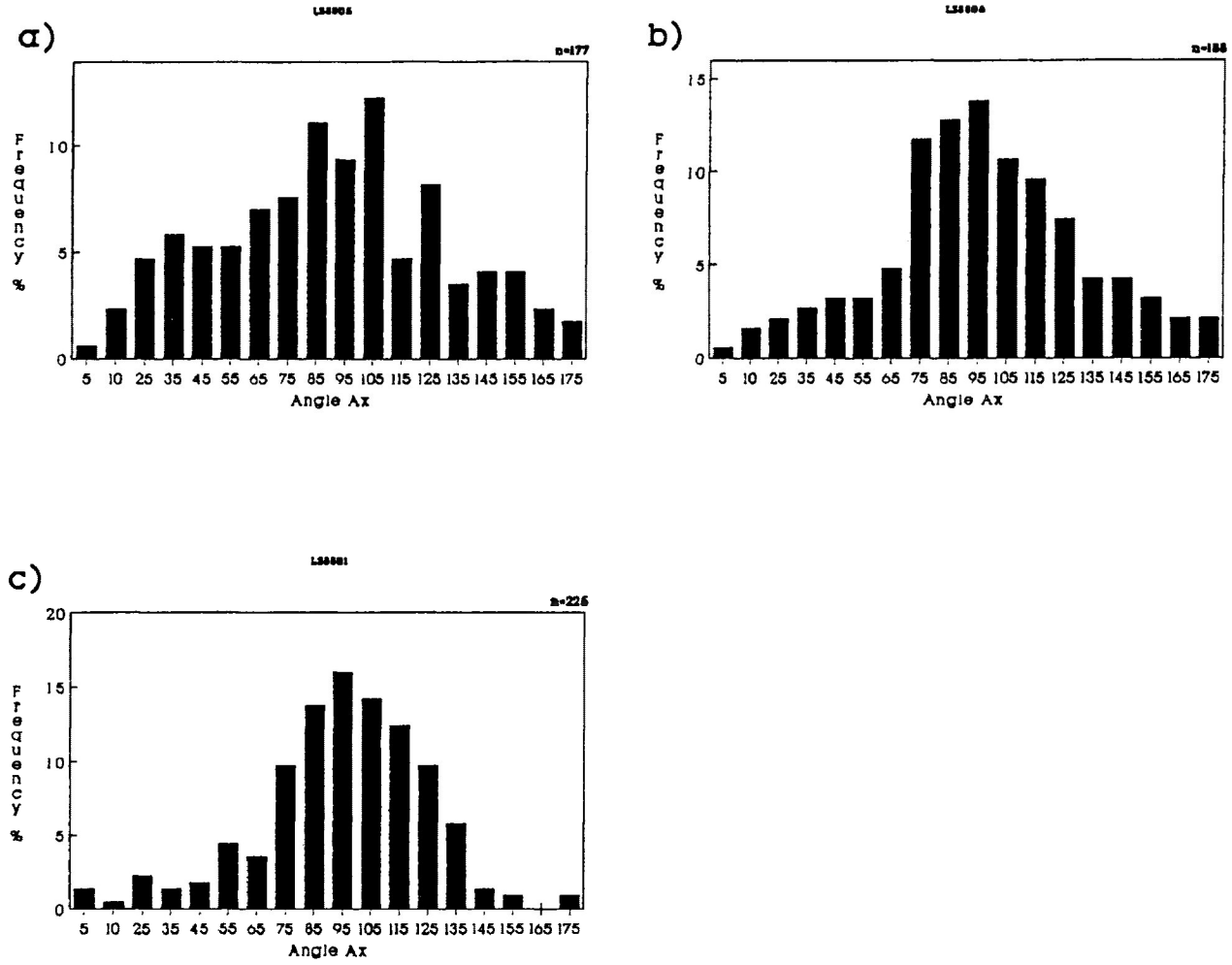

Figure 5.28a-g Frequency distribution of a_j/c_j ratios for lithic fragments in the X/Z principal plane of the deformed China Beach sandstone samples. Experimental strain ratios range from 1.000 (e=0.0%) to 1.637 (e=28.0%). Samples were deformed under dry experimental conditions with confining pressures of 200 Mpa, strain rate of 10^{-5}/s and temperatures of 135°C. Measurements taken from the X/Z principal plane of the deformed test cylinder.

a) e=0.0% (R_s=1.000)
b) e=8.0% (R_s=1.133)
c) e=12.0% (R_s=1.211)
d) e=25.0% (R_s=1.540)
e) e=28.0% (R_s=1.637)

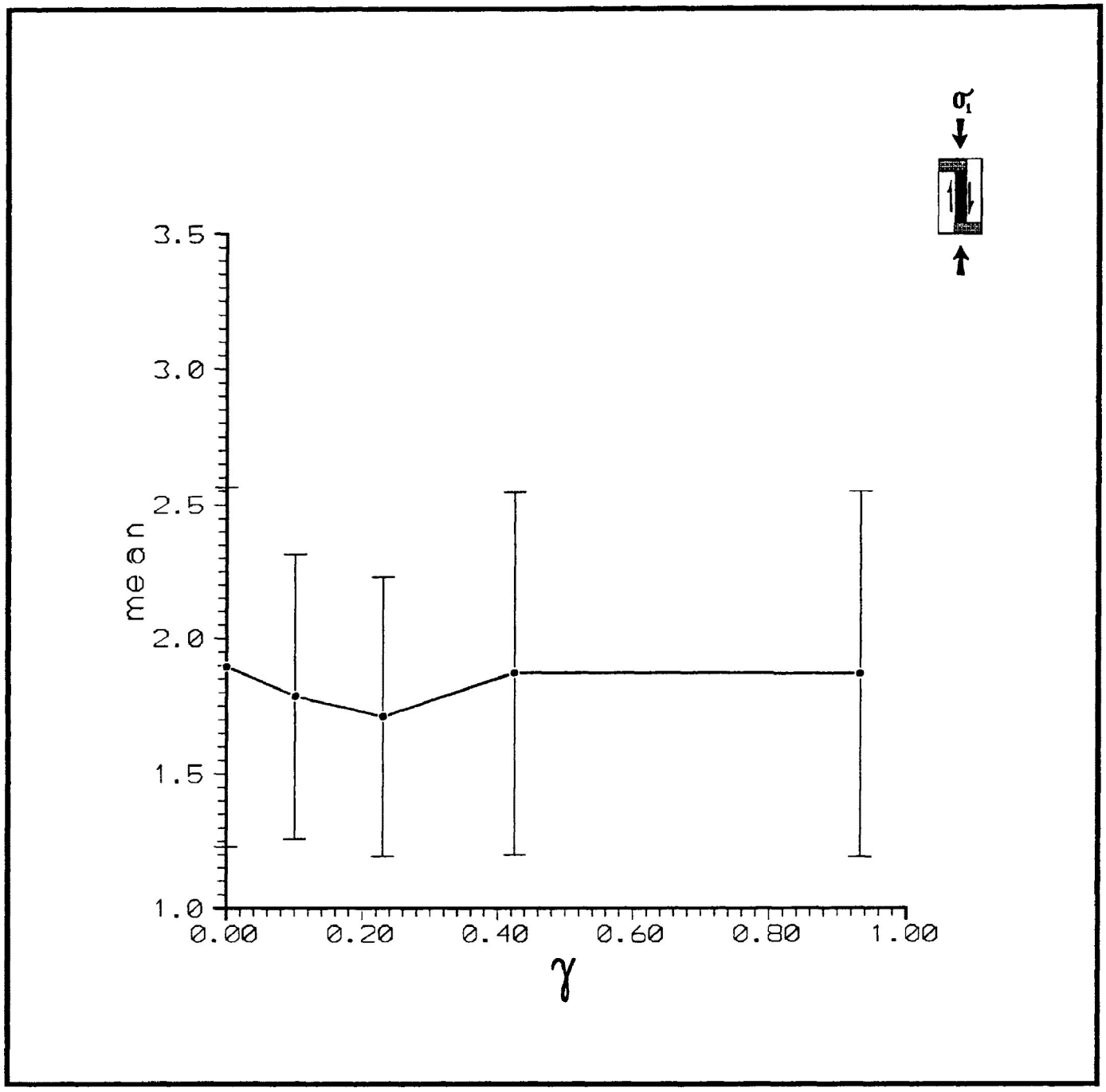

Figure 5.29 Variation in mean *R*f of calcite grains in undeformed and deformed calcite-cement aggregate by 2mm thick longitudinal simple shear with increasing experimental strain. Standard deviation of the mean R_f is also given. Experimental shear strains range from 0.000 to 0.922. Samples were deformed under dry experimental conditions with confining pressures of 200 Mpa, slip rates of 0.73×10^{-4} mm/s and temperatures of 25°C.

Figure 5.30a-e Frequency distribution of R_i and R_f for calcite grains in undeformed and deformed calcite-cement aggregate by 2mm thick longitudinal simple shear. Experimental shear strains range from 0.000 to 0.933. Samples were deformed under dry experimental conditions with confining pressures of 200 Mpa, slip rates of 0.73×10^{-4} mm/s and temperatures of 25°C.

a) Undeformed
b) LS8803 (shear strain= 0.101)
c) LS8811 (shear strain= 0.230)
d) LS8810 (shear strain= 0.425)
e) LS8807 (shear strain= 0.933)

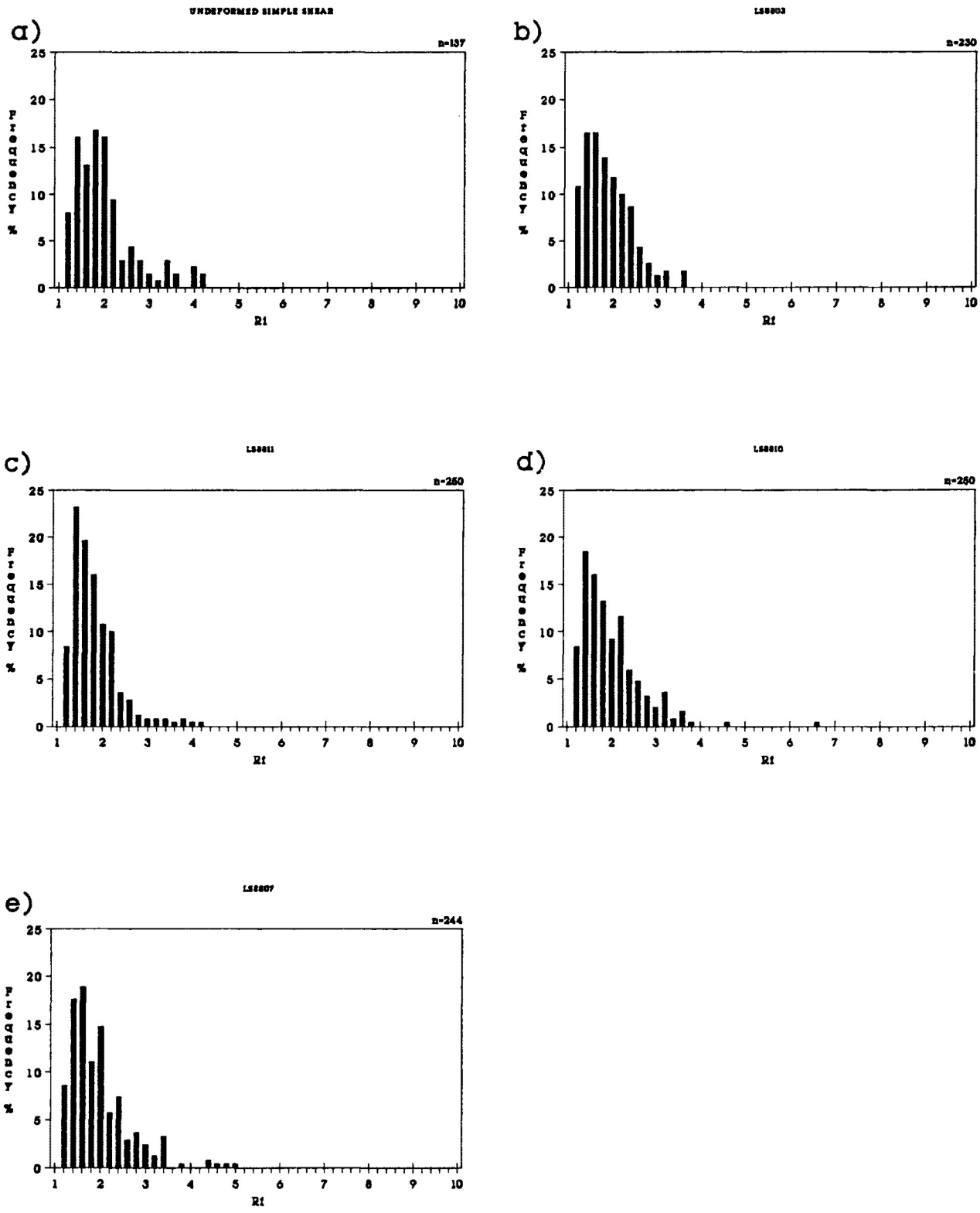
a)
UNDEFORMED SIMPLE SHEAR
n=137
b)
n=230
c)
n=250
d)
n=250
e)
n=244
Frequency %
Rf

Figure 5.31a-e R_f/ϕ diagrams for calcite grains in undeformed and deformed calcite-cement aggregate. Experimental shear strains range from 0.000 to 0.933. The σ_1 direction and shear direction orientated at 0° with dextral sense of shear. Samples were deformed under dry experimental conditions with confining pressures of 200 Mpa, slip rates of 0.73×10^{-4} mm/s and temperatures of 25°C.

a) Undeformed
b) LS8803 (shear strain= 0.101)
c) LS8811 (shear strain= 0.230)
d) LS8810 (shear strain= 0.425)
e) LS8807 (shear strain= 0.933)

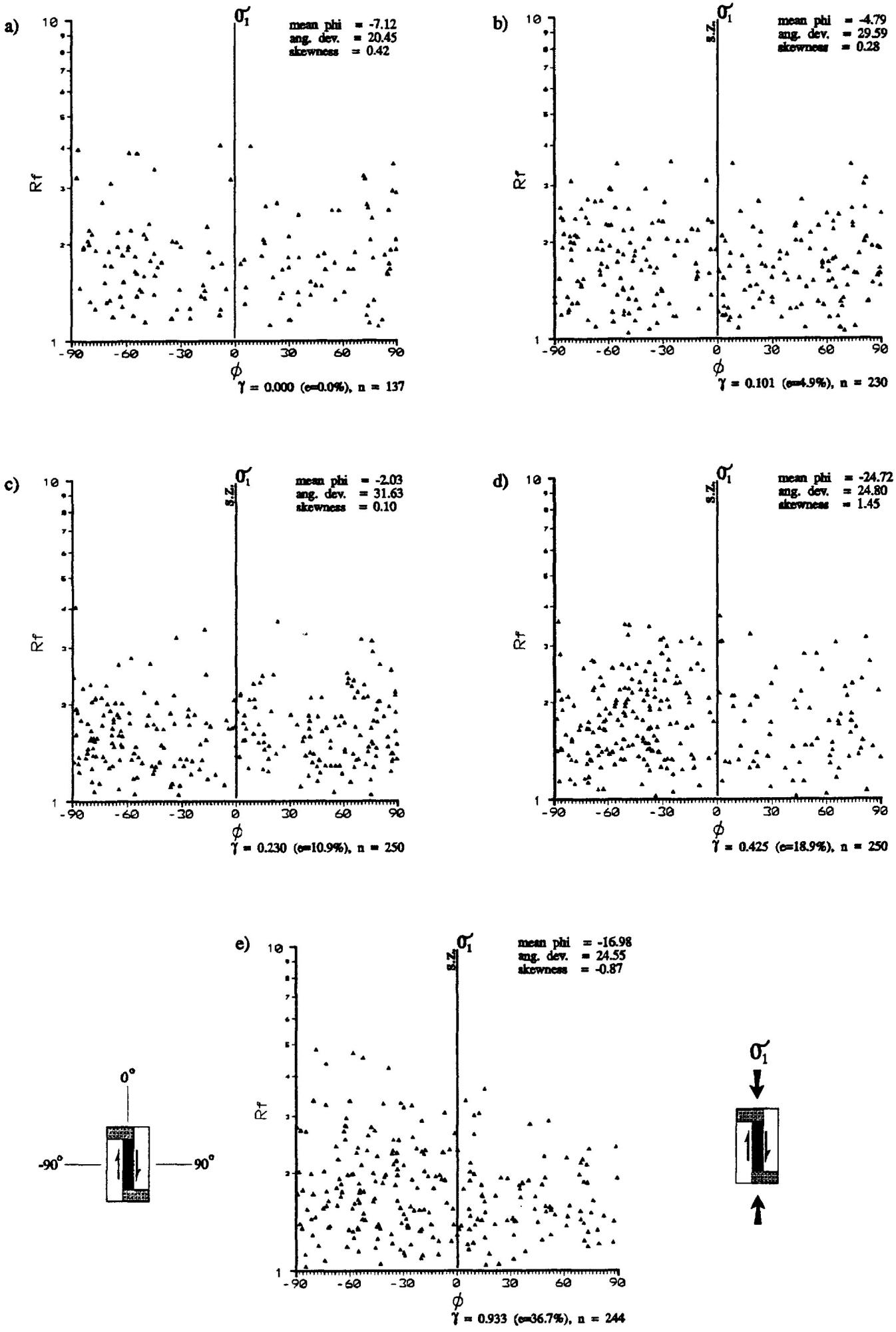
a)
mean phi = -7.12
ang. dev. = 20.45
skewness = 0.42
γ = 0.000 (c=0.0%), n = 137
b)
mean phi = -4.79
ang. dev. = 29.59
skewness = 0.28
γ = 0.101 (c=4.9%), n = 230
c)
mean phi = -2.03
ang. dev. = 31.63
skewness = 0.10
γ = 0.230 (c=10.9%), n = 250
d)
mean phi = -24.72
ang. dev. = 24.80
skewness = 1.45
γ = 0.425 (c=18.9%), n = 250
e)
mean phi = -16.98
ang. dev. = 24.55
skewness = -0.87
γ = 0.933 (c=36.7%), n = 244
Rf
φ
S.Z.
0°
-90°
90°

frequency distributions of figure 5.30a-e.

The R_f/ϕ diagrams for calcite grains are presented in figure 5.31a-e. These figures suggest little increase in R_f for increasing shear strains with the development of a moderate PDO oblique to the experimental σ_1 direction in a sense compatible with the shear direction. At low strains the PDO is approximately 45° to the shear zone and begins to rotate towards the perpendicular to the shear zone at higher shear strains. The PDO of the R_f/ϕ distribution is mainly defined by the concentration of calcite grains over the full range of R_f as experimental shear strain increases. The PDO is enhanced by calcite grains of large R_f values at higher shear strains.

The role of twinning in the plastic (heterogeneous) deformation of the calcite grains appears to be very minor in the development of the PDO in the calcite-cement aggregate deformed by 2 mm thick longitudinal simple shear. This is suggested by low average lamellae index occurring in the deformed calcite grains. It may be suggested that the fabric development is the result of rigid rotation of calcite grains in suitably orientation. Observation of the scatter of the R_f/ϕ distribution (high angular deviation) suggests that selective rotation of grains of over the complete range R_f values is occurring in the deforming shear zone.

Figure 5.32 presents the Flinn diagram for samples of calcite cement aggregate deformed under longitudinal shear. The X/Y and Y/Z ratios are determined from the harmonic mean of the X/Z and X/Y principal plane sections. From the figure is observed that the three-dimensional strain ellipsoid quickly enter into the S-field. The rapid progression of the samples into the S-field is the result of rigid rotation as the experimental shear strain is increased. It can be

Figure 5.32 Flinn diagram for samples of calcite-cement aggregate deformed under 2mm thick longitudinal simple shear for experimental shear strains between 0.000 and 0.933. The X/Y and Y/Z ratios are determined from the harmonic mean of the X/Z and X/Y principal plane sections. Samples were deformed under dry experimental conditions with confining pressures of 200 Mpa, slip rates of 0.73×10^{-4} mm/s and temperatures of 25°C. Standard errors for each sample are given in the sub diagram. (modified from Borradaile and McArthur (1990))

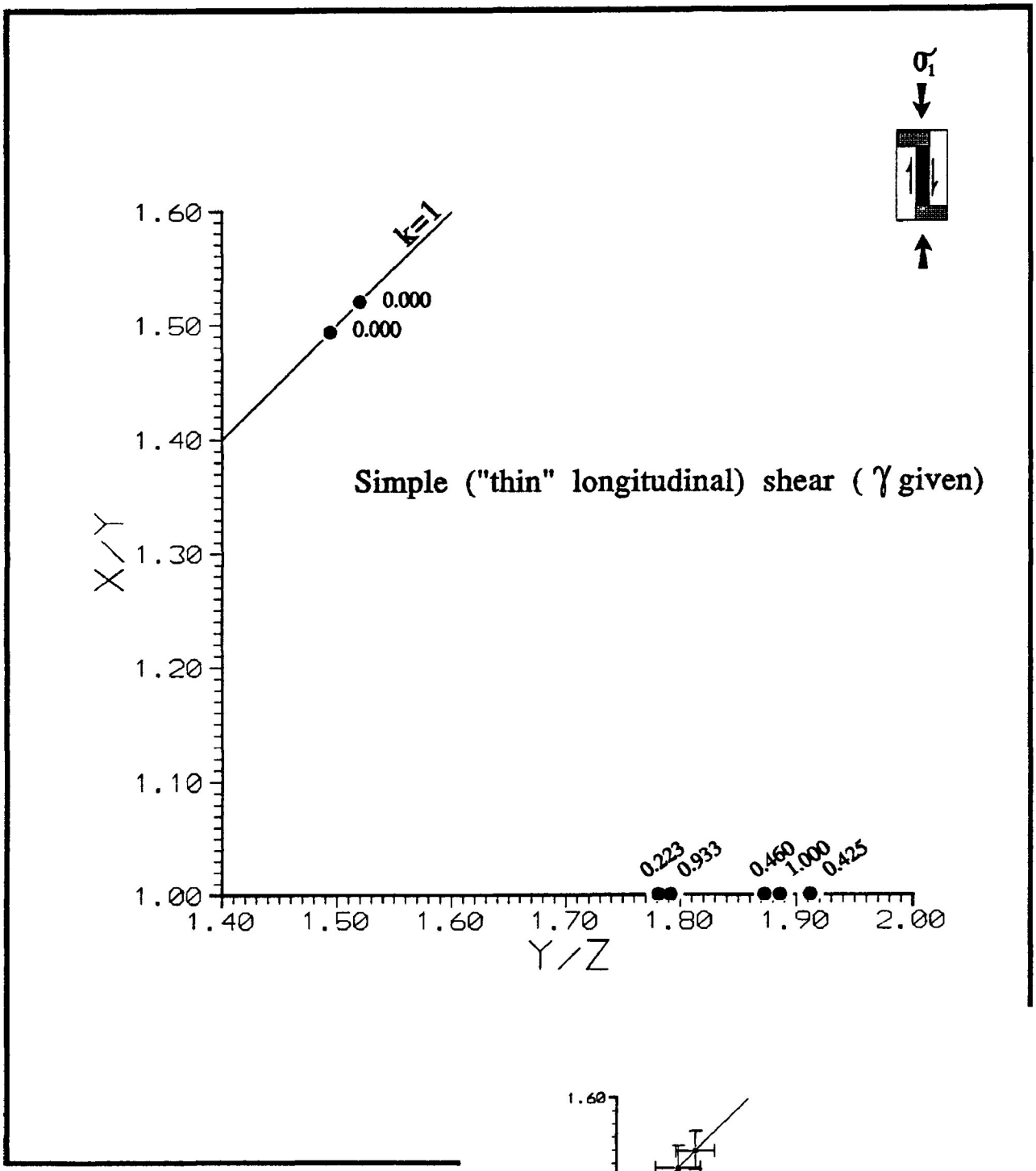
σ1
k=1
0.000
0.000
Simple ("thin" longitudinal) shear (γ given)
X/Y
Y/Z
1.60
1.50
1.40
1.30
1.20
1.10
1.00
1.40
1.50
1.60
1.70
1.80
1.90
2.00
0.223
0.933
0.460
1.000
0.425

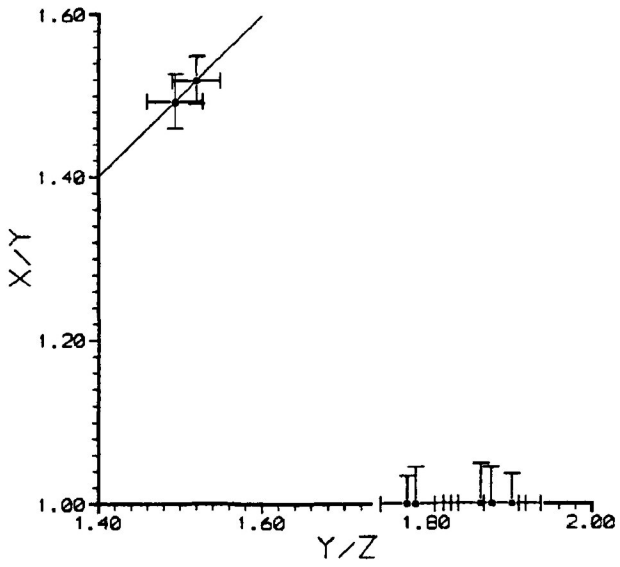
X/Y
Y/Z
1.60
1.40
1.20
1.00
1.40
1.60
1.80
2.00

suggested that the grain shape fabric does not conform to the symmetry of the bulk deformation of the longitudinal shear deformation. No trend is observed in the Y/Z values of the deformed specimens as was observed in the transpressional samples.

Figure 5.33 presents samples deformed in 5 mm thick longitudinal shear zones. The strain ellipsoids of the deformed samples plot on the Flinn diagram in the S>>L field and also the S-field. At higher shear strains (*eg.*, 1.22) the sample plots in the S>L field. This may be the result of the deformation of the calcite-cement aggregate by an increasing component of pure shear and subsequent rigid rotation in to a PDO perpendicular to the σ_1 direction. The Flinn diagram data may be partially repositioning into a similar field as that observed in the pure shear experiments. Calcite grains in the highly deformed 5 mm thick shear zones exhibit very large lamellae indices, higher than in other forms of deformation. No trend is observed in the Y/Z values of the deformed specimens as observed in transpressional shear. Standard errors for each sample are given in the sub diagram of figure 5.32 and 5.33.

Figure 5.33 Flinn diagram for samples of calcite-cement aggregate deformed under 5mm thick longitudinal simple shear for experimental shear strains between 0.000 and 1.220. The X/Y and Y/Z ratios are determined from the harmonic mean of the X/Z and X/Y principal plane sections. Samples were deformed under dry experimental conditions with confining pressures of 200 Mpa, slip rates of 0.73×10^{-4} mm/s and temperatures of 25°C. Standard errors for each sample are given in the sub diagram. (modified from Borradaile and McArthur (1990))

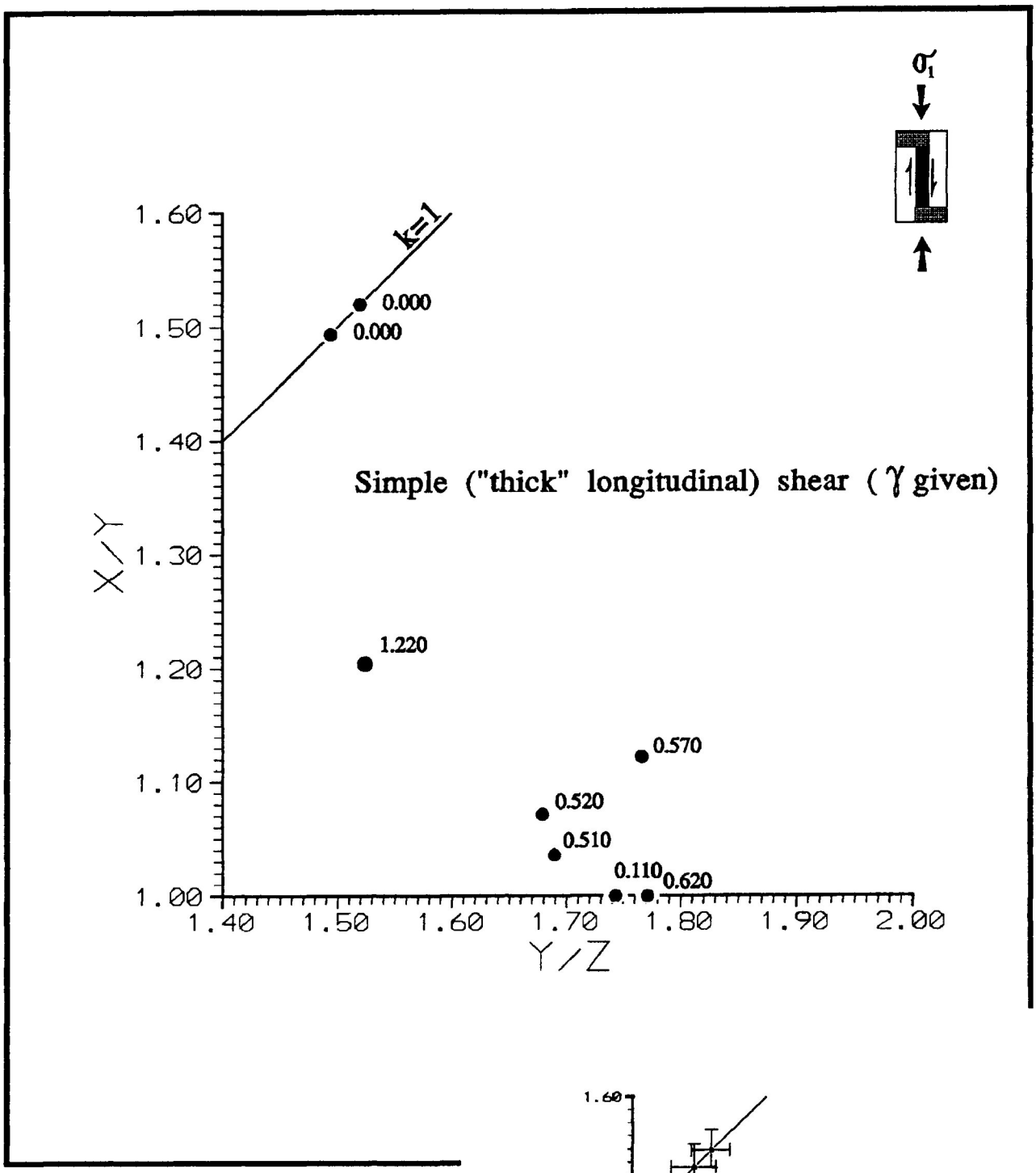

Simple ("thick" longitudinal) shear (γ given)

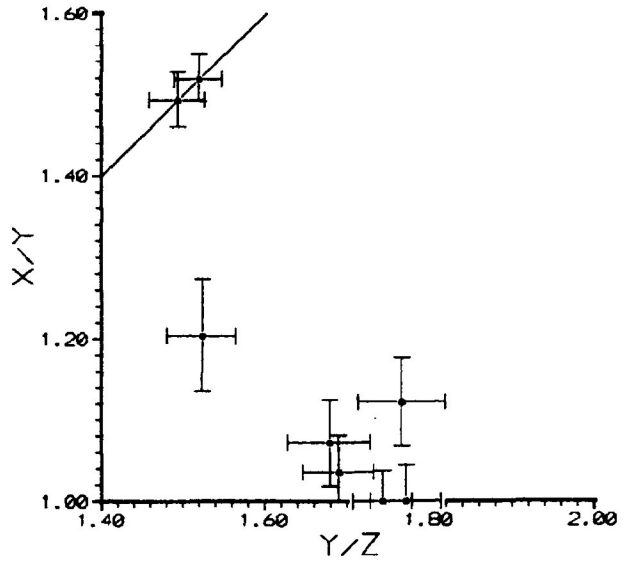

5.4 Compaction of the calcite cement matrix during experimental deformation

As discussed in Borradaile and McArthur (1990) the properties of the Portland cement and its deformation mechanisms are not well understood. However, the deformation of the portland cement is characterized by the collapse of pore space at low shear strains and destruction of delicate crystal forms which are replaced by more amorphous grain shapes after a few percent strain. This was attributed to the micro-cataclasis of the cement's crystal aggregate and is presented in the electron microphotographs of Borradaile and McArthur (1990, Fig. 3a-b).

Figure 5.34a-e illustrate the percent compaction of the portland cement by variation in the volume percent of mineral grains (calcite and magnetite) with increasing deformation. For the case of pure shear, wet experimental condition produce the greatest amount of compaction in the deformed aggregate than that of dry experimental conditions. Similar compaction is observed in the transpressional shear, but high compaction occurs at much lower axial compression. Compaction is not observed in the 2 and 5 mm thick simple shear experiments, except in those samples that have experienced a large component of pure shear (highly deformed 5 mm thick shear zones).

Figure 5.34 Variation on volume % of the calcite-cement sample consisting of mineral grains (calcite and magnetite).

a) pure shear (dry conditions)
b) pure shear (wet conditions)
c) transpressional shear (dry conditions)
d) 2mm thick longitudinal simple shear
e) 5mm thick longitudinal simple shear

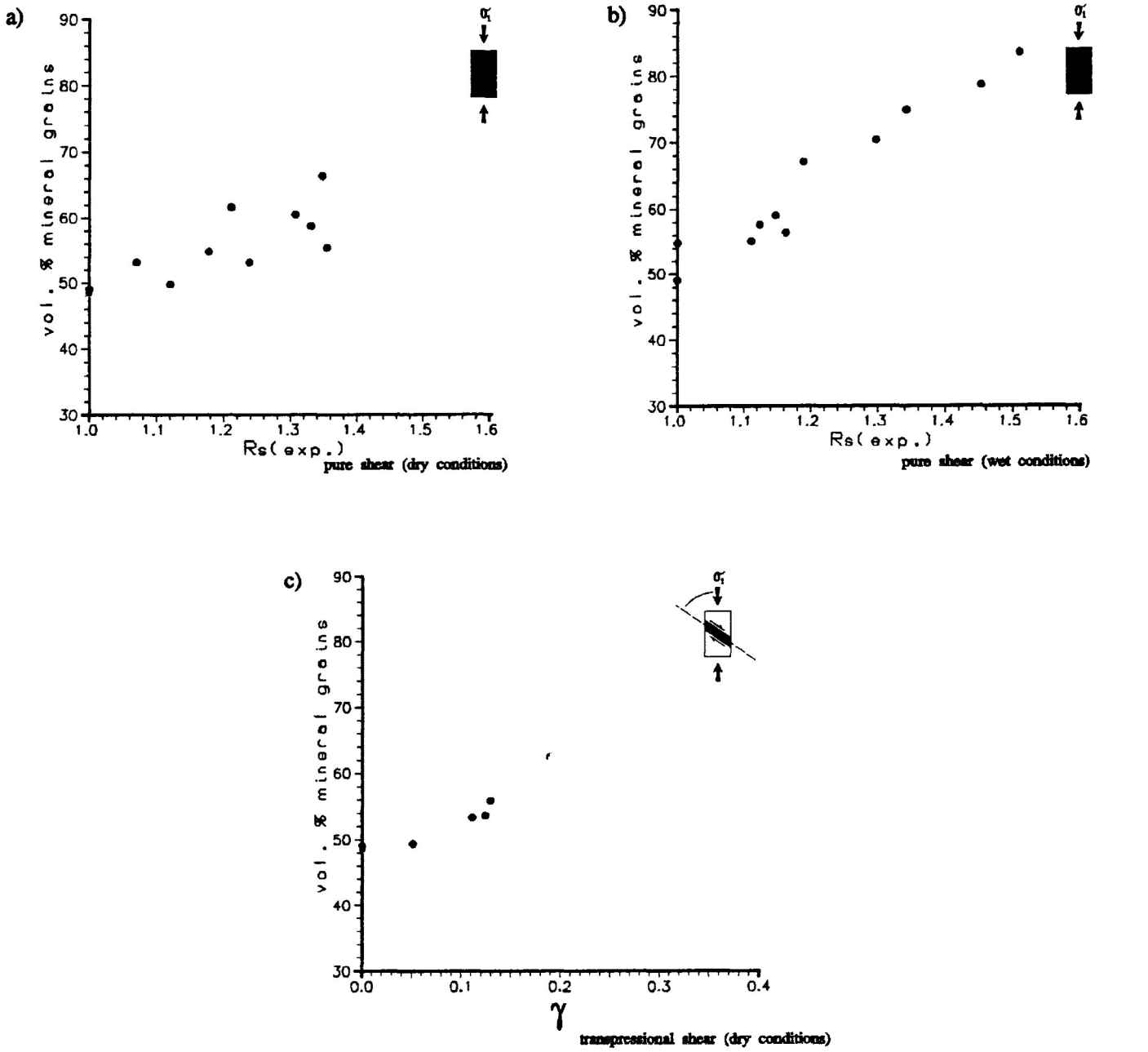
a)
b)
c)
d)
e)
vol. % mineral grains
Rs(exp.)
γ
σ1
pure shear (dry conditions)
pure shear (wet conditions)
transpressional shear (dry conditions)
simple shear (2mm, dry conditions)
simple shear (5mm, dry conditions)

5.5 Discussion of dimensional fabric development in deformed calcite-cement aggregate

From the previous sections it can be suggested that the fabric development in the deformed calcite-cement aggregate is the result of extensive calcite grain rigid rotation accompanied by heterogeneous plastic deformation of the calcite grains by twinning. The bulk strain in the deformed sample will depend on the degree to which the above mechanisms are involved in the deformation process. The different types of assemblages vary in their behaviour with respect to the degree of deformation and the development of the dimensional fabric for equivalent bulk strains.

It is apparent from this study that for the experimental approximation of pure shear (dry and wet conditions) the development of a PDO occurs perpendicular to the σ_1 orientation producing an embryonic schistosity. The PDO increases in strength as the bulk strain increases in the deforming aggregate. The presence of a pore fluid pressure, in the deforming calcite-cement aggregate, induces controlled particulate flow in the calcite grains. The pore fluid pressure allows for the development of a strong PDO which occurs at lower bulk strains than in the case of pure shear under dry conditions. The development of a strong PDO in the calcite-cement aggregate deformed under wet experimental conditions occurs at approximately 10% shortening or a finite strain ratio of 1.170. The degree to which a pore fluid pressure influences the deformation of a calcite-cement aggregate may depend on how closely its magnitude compares to that of the confining pressure.

In non-coaxial deformation it is apparent that for the experimental approximation of transpressional shear, with a strong component of pure shear, the PDO develops parallel to sub-parallel to the shear direction. The development of a

strong PDO occurs at lower equivalent bulk strains than for either dry or wet pure shear. The PDO in simple shear deformation developed oblique to the shear zone wall, approximately 45° in an orientation kinematically related to the sense of shear. In the simple shear deformation the development of a strong PDO may occur at much higher bulk strain than in the case of either transpressional or pure shear. The orientation of the PDO in the different types of deformation are, therefore, reliable kinematic indicators under the experimental conditions studied (Borradaile and McArthur, 1990).

As suggested in the last chapter (section 4.5) heterogeneous plastic deformation of calcite grains by twinning in the X/Z principal plane is controlled by the different deformation assemblages and the conditions of deformation. The increase in the R_f of calcite grains due to heterogeneous plastic deformation by twinning is higher in transpressional shear than in pure shear and simple shear. This is a result of the development of a strong PDO parallel to the shear zone wall (a direction favourable for twinning in calcite grains).

For dry pure shear the change in R_f due to twinning is less than in transpressional shear, but greater than that of pure shear under wet experimental conditions. The development of a strong PDO (an orientation unfavourable for twinning) in wet pure shear prevents a significant increase in R_f due to twinning. No detectable change in R_f is observed in the 2 mm thick simple shear tests. However, in 5 mm thick simple shear tests, when a large component of pure shear is added to the specimen, the change in R_f as a result heterogeneous plastic deformation is greater than the other types of deformation. Furthermore, the overall bulk of the observed change in the R_f for the calcite grains shapes in the plane of observation

(X/Z principal plane) of samples deformed in the different assemblies is the result of rigid body rotation of the grains into a PDO as strain increases.

The R_f/ϕ distributions for wet pure shear and the computer simulated R_f/ϕ transformations are similar in appearance. However, each distribution is produced by different processes and deformed to different strains. Figure 5.35 presents a comparison of two R_f/ϕ distributions one for a wet pure shear sample and another for a computer simulated R_f/ϕ transformations. The finite strain ratios for each of these samples are 1.189 (e=10.9%) and 1.500 (e=23.7%), respectively. Calculation of bulk strain by Robin's method yield values of 1.515 (±0.081 s.d.) for the wet pure shear sample and 1.607 (±0.010 s.d.) for the computer simulation. The overestimate of the bulk strain in the case of the wet pure shear sample suggests that deformation by processes that are not continuum behaviour such as particulate flow can produce overestimates of strain when the strain analysis method assumes a continuum process such as R_f/ϕ transformations. The non-continuum process of deformation (rigid rotation and particulate flow) in this study is characterized by the observed grain strain being less than the bulk strain of the sample.

This effect is observed in the comparison of dry and wet pure shear strain estimates by Robin's method. Dry pure shear strain estimate are relatively good approximations of the estimates of bulk strain. Here, the process of deformation is the result of rigid rotation and heterogeneous plastic deformation by twinning of the calcite grains. For wet pure shear the estimates of bulk strain become large overestimates for samples deformed above 10% shortening. This occurs when the effects particulate flow become the most noticeable in the calcite-cement aggregate with the development of a good PDO. The overestimate of bulk strain in the wet pure shear samples

a) grain strain << bulk strain

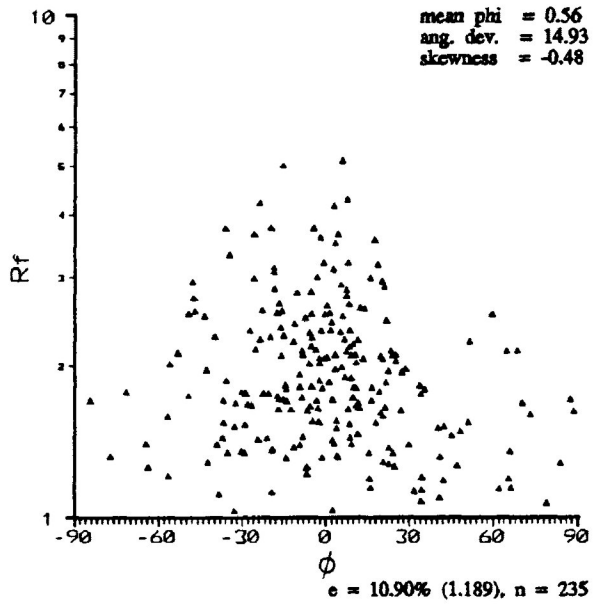

b) grain strain = bulk strain

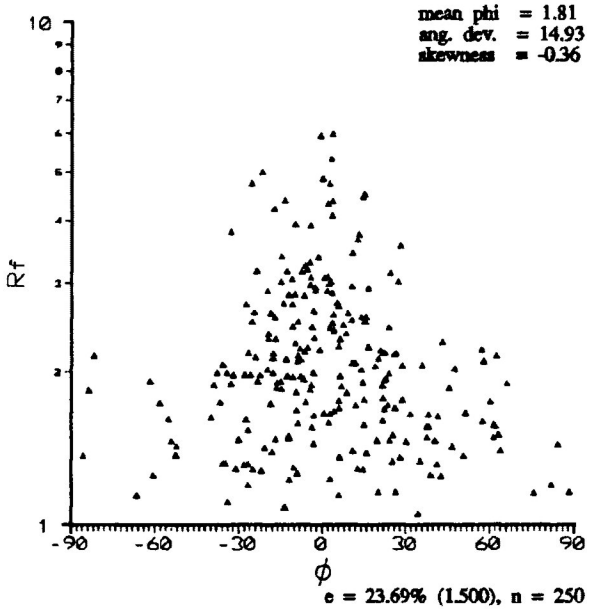

Figure 5.35 Comparison of the R_f/ϕ distribution for samples deformed by a) wet pure shear (e=10.9%) and b) computer simulation of R_f/ϕ distribution (e=23.7%). For a) the grain strain of the deformed particles is less than the bulk strain of the sample as a result of particulate flow induced by the presence of a pore fluid pressure. For b) the grain strain of the deformed particles is equal to than the bulk strain of the sample as a result of R_f/ϕ transformation. Bulk strain estimate by Robin's method are 1.515 (±0.081) for wet pure shear and 1.607 (±0.1) for R_f/ϕ transformation.

increases as strain increases, but the increase is less pronounced compared the rapid increase observed at 10% shortening.

The data presented in the Flinn diagrams for the different forms of deformation lie in different fields. In the case of pure shear, both wet and dry, conditions the strain ellipsoid calculated from harmonic means plot in the S>L field. Since the change in calcite grain shape was not the result of twinning the trend in the strain ellipsoid position on the Flinn diagram is the result of particulate flow and rigid body rotation of the grains in response to the development of a PDO. This is especially true in wet pure shear where a more consistent trend is observed in the data, particulate flow is the most prevalent deformation process in these samples.

For transpressional shear, where a strong component of pure shear is added to the system, the strain ellipsoids plot in the S-field. This is a result of the development of a strong PDO and heterogeneous plastic deformation by twinning. Simple shear deformation data plots in the S-field as well, however, this is related to rigid rotation and not the result of any deformation of the calcite grain by twinning. It may be suggested from these observations that the grain shape fabric observed in the calcite grains of the different deformation assemblages do not conform to the symmetry of the bulk strain of the sample for the experimental conditions of this study (Borradaile and McArthur, 1990).

CHAPTER 6: Strain Analysis of Experimentally Deformed Ancaster Oolitic Limestone

6.1 Introduction

The deformation of initially spherical and elliptical particles in natural rocks provides a useful means for structural geologist to study the distortions which have taken place in rocks subject to deformation processes. For the analysis of finite strain in deformed rocks, oolites are a suitable choice. Oolites have properties, that would appear to make them nearly ideal for strain analysis. In particular, the original shape of the ooid is usually nearly spherical, and many oolites are monomineralic rocks, essentially uniform in composition.

The monomineralic character of oolites suggests passive homogeneous deformation of the strain markers (fine grained) and matrix (coarse grained), and this homogeneity is usually assumed. However, it has been observed experimentally that the rheological behaviour of different types of calcite rocks, Solenhofen Limestone (Schmid, 1976), Carrara Marble (Schmid, 1976) and Yule Marble (Heard and Raleigh, 1972) can vary under similar conditions of deformation. This is believed to be the result of grain size, which can have a dramatic affect on flow stress of calcite rocks, especially at low geologically realistic stresses.

Given the emphasis on grain size as an important material parameter in rock deformation, and the fact that ooids often have a different grain size from the matrix, doubts arise about the validity of the assumption of homogeneous passive deformation between the markers and the matrix. The effect of these considerations on strain analysis of naturally deformed may be significant.

This chapter deals with the experimental triaxial deformation of an undeformed Ancaster oolitic limestone sample. The experimental tests consisted of deformation by pure shear (axial symmetrical compression) for dry and wet experimental conditions. The temperature was held constant at 135°C during deformation, with computer controlled natural strain rates of 10^{-5}/s. The confining pressure during each experiment was 200 Mpa. Pore fluid pressures used throughout the wet experimental tests were less than 60% of the confining pressure. The undeformed oolitic limestone was deformed to strains of 0.0% to 20.0% axial shortening in the dry experimental test and 0.0% to 26.4% axial shortening in the wet experimental tests. Errors on the calculation of experimental strain from the test cylinder shortening after triaxial deformation are considered to be negligible. For comparison a computer simulation ("forward modelling") of passive homogeneous deformation was conducted for the undeformed oolitic R_f/ϕ data. The ooid grain shapes were converted to best-fit ellipses based on their moment-of-inertia before "forward modelling" simulation were conducted.

Orientational, dimensional and strain analyses (Robin's, linearization, and harmonic mean methods) were conducted on the ooid grains present in the undeformed and deformed X/Z principal plane of the Ancaster oolitic samples. The ooids used in these determinations were measured from the central portion of the thin sections to eliminate heterogeneous effects near the walls and top of the test cylinder.

6.2 Sample Material in the undeformed state

The sample material used in this experimental study consisted of an undeformed oolite of Jurassic age (Ancaster oolitic limestone) from Lincolnshire county, U.K.. The secondary calcite matrix of the limestone is sparitic, consisting of blocky calcite cement with drusy calcite cement located around the periphery of uniformly distributed ooids and isolated fossil fragments.

The calcite cement matrix consists of approximately 39.3% of the limestone by volume. The grain size in thin section of the calcite cement is on the order of 0.1 mm to 1.75 mm in diameter, with a typical grain size of 0.75 mm in diameter. The drusy cement consists of clear acicular calcite crystals with an average thickness of 0.025 mm around the rim of the ooids. The drusy cement appears to have been the first to form, followed by the precipitated of blocky calcite cement at some later time, filling the vug porosity between ooid grains. Individual grains of calcite cement are usually in contact with < 40% of the drusy/ooid periphery. In the case of the largest grains size the calcite cement encompass 3 to 5 ooids. However, these large grains are few in number. Very little twinning is observed in the blocky cement and drusy cement.

The undeformed ooids occupy approximately 58.2% of the sample material by volume and are uniformly distributed throughout the specimen. The ooids have a range of initial R_i between 1.02 and 2.34 with an average value of 1.38 (±0.26 s.d.) as presented in figure 6.1. Sectional diameters range from 0.26 mm to 1.43 mm. No apparent preferred dimensional orientation or bedding fabric is observed in the undeformed sample. Figure 6.2 presents the distribution of the long axis of the ooids for the undeformed sample in which the angular

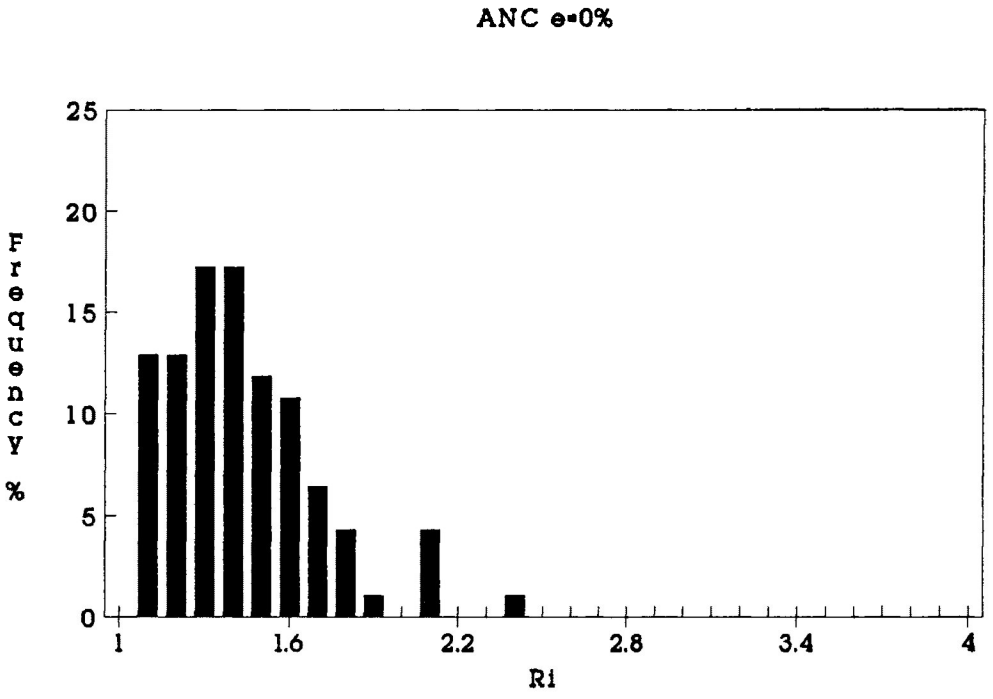

Figure 6.1 Frequency distribution of the initial R_i ratios of ooids in undeformed Ancaster Limestone.

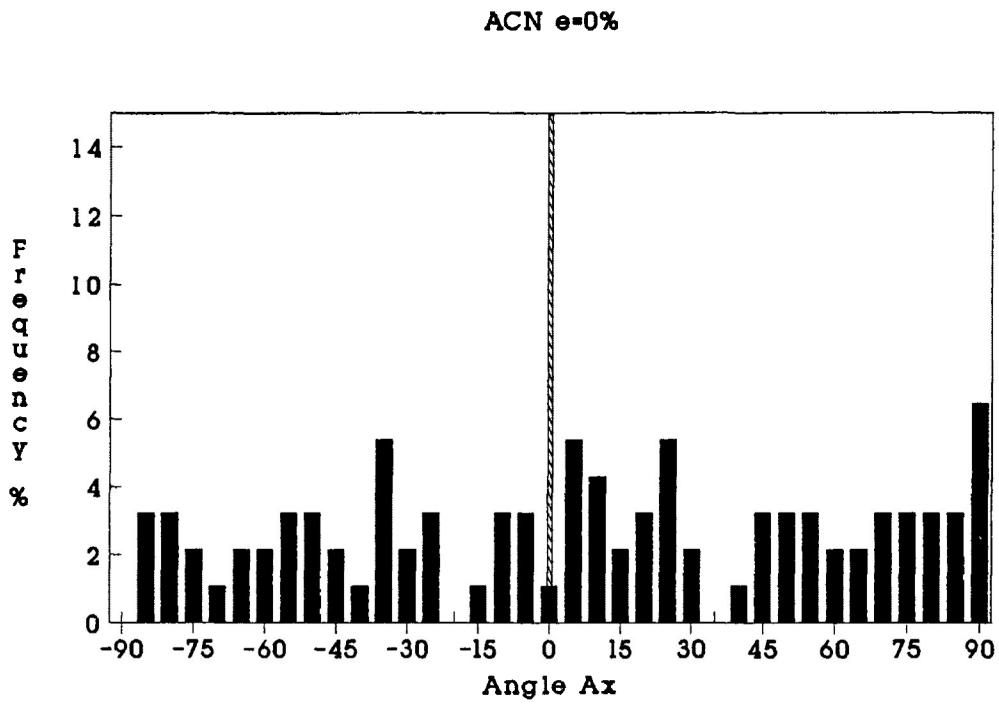

Figure 6.2 Frequency distribution of the initial Angle Ax (ϕ) orientations of ooids in undeformed Ancaster Limestone. Bedding surface orientation given by striped line.

6.3 Tracings of microphotograph of undeformed and deformed Ancaster oolitic limestone (X/Z principal plane). a) undeformed sample b) dry experimental conditions. Sample was deformed to 8.0% shortening under dry experimental conditions with confining pressures of 200 Mpa, strain rate of 10^{-5}/s and temperature of 135°C. c) wet experimental conditions. Sample was deformed to 8.0% shortening under wet experimental conditions with confining pressures of 200 Mpa, strain rate of 10^{-5}/s and temperature of 135°C. Pore fluid pressures were less than 60% of the confining pressure. (scale 10:1)

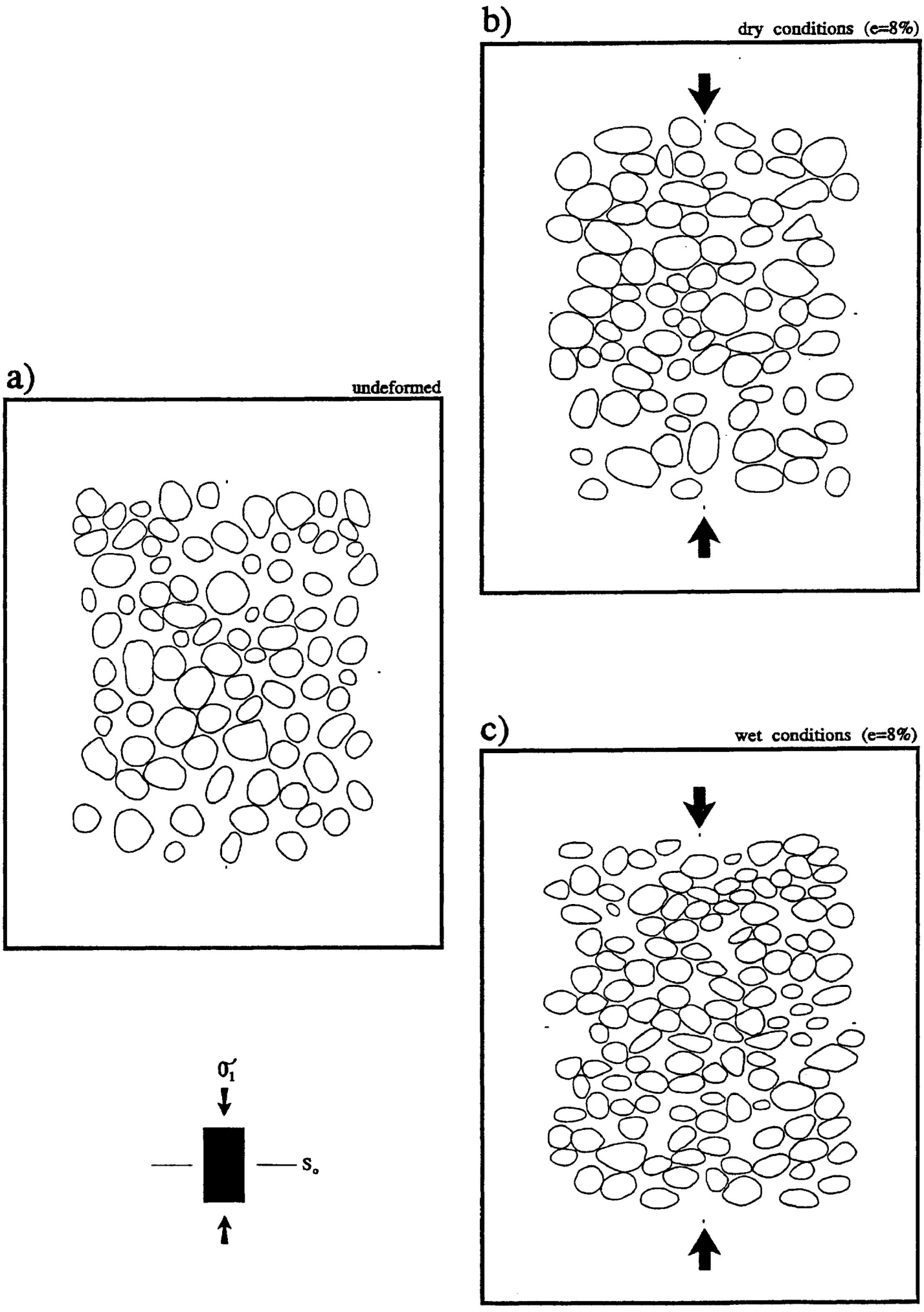
a)
undeformed
b)
dry conditions (e=8%)
c)
wet conditions (e=8%)
σ'1
S₀

deviation is 28.10. The bedding direction is perpendicular to the long axis of the test specimen (represented by the striped line in figure 6.2). A tracing of ooids in a section of the undeformed Ancaster oolitic limestone sample is presented in figure 6.3a.

The matrix of the ooids consists of a fine grained mosaic of equant calcite crystals, with a grain sizes as large as 0.008 mm in diameter, however, the typical grain size is less than 0.003 mm in diameter. There are also small (approximately 0.003 mm to 0.010 mm in diameter) opaque and translucent impurities dispersed through individual ooids. These are possibly carbon of organic origin and iron oxide (*i*.e., hematite).

Approximately 36.0% of the ooids (approximately 20.7% by sample volume) in the undeformed specimen are observed to have formed around fossil debris, displaced sedimentary fragments and quartz sand grains. Ooids, in which the nucleus has a high aspect ratio, can deviate substantially from the ideal spherical form, especially in the case of fossilized shell fragments. These large aspect ratio grains comprise approximately 5.0% of the grains (approximately 2.9% by sample volume). Non-oolitic material in also present in the sample (approximately 2.5% by volume) consisting mainly consisting of fragments of fossilized remains.

6.3 Microscopic observations in the deformed state

a) Dry experimental conditions

Microscopic investigation of the Ancaster oolitic limestone, deformed under dry experimental conditions, yields the following observations. Twinning in the calcite matrix increases as strain increases during deformation. Approximately 100% of the calcite grains in the cement matrix exhibit twinning at 8.0% (R_s=1.133) shortening. The lamellae indices are moderate to high in grains which are the most suitably oriented for twinning (*i*.e., e_1-twin plane $\approx 45^\circ$ to the σ_1 orientation).

At higher strains the lamellae indices in the cement grains increase in all grain orientations and bending of twin lamellae and kink band development is observed. This is reflected in the slight flattening of the calcite cement grain in the highest strained samples. Undulose extinction and brittle behaviour (minor crack development along cleavage planes) are also observed at higher strains. There is a notable decrease in the amount of large optically continuous cement grains which were observed in the undeformed sample. The deformed grains of this type show undulose extinction and in some cases a 10° to 30° rotation of the extinction direction between neighbouring parts of the same grain, which are separated by ooids.

No twinning deformation is observed in the fine grained ooid matrix for all levels of strain studied. Rowe and Rutter (1990) have suggested, from experimental studies of deformed marbles, that twinning activity is reduced in calcite grains of small diameter. This is a result of the fact that grain boundaries impede the spreading and widening of twin lamellae. However, the ooids of this study exhibit a slight change in

grain shape as strain increases. Figure 6.3b illustrates this shape change from the undeformed state to a sample deformed to a strain of 8.0% shortening under dry conditions.

Considerable deformation is observed in the drusy cement around the periphery of the ooid grains at low strain. The deformation is characterized by intense twinning and kinking in an orientational range of 20° to 30° around the periphery of the ooid in a direction perpendicular to the σ_1 orientation (Fig.6.4). This is a result of the orientation of the *c*-axes in the drusy cement crystals, which are perpendicular to the ooid surface. As strain increases many ooid grains exhibit highly deformed drusy cement deformed around the entire periphery.

The observed deformation of the cement matrix under dry conditions suggests that it was deformed by intense twinning and by grain boundary sliding between other cement grains and ooid particles. The observed deformation of the ooid grains suggests that they were deforming as semi-rigid particles in which the ooid marker deformed by rigid body rotation with some shape change due to particulate flow in the fine grained matrix of the ooid. Observation of bent twin lamellae and deformed drusy cement supports this conclusion (Fig. 6.5a-b). In figure 6.5a the drusy cement is deformed in a way that suggests a shearing motion between the ooid grain and the cement matrix in response to rigid rotation. In figure 6.5b twin lamellae are bent in response to the rotation of an ooid grain into a PDO perpendicular to the f_1 orientation.

b) <u>Wet experimental conditions</u>

Microscopic investigation of the Ancaster oolitic limestone, deformed under wet experimental conditions, yields the following observations. The number of grains twinned in

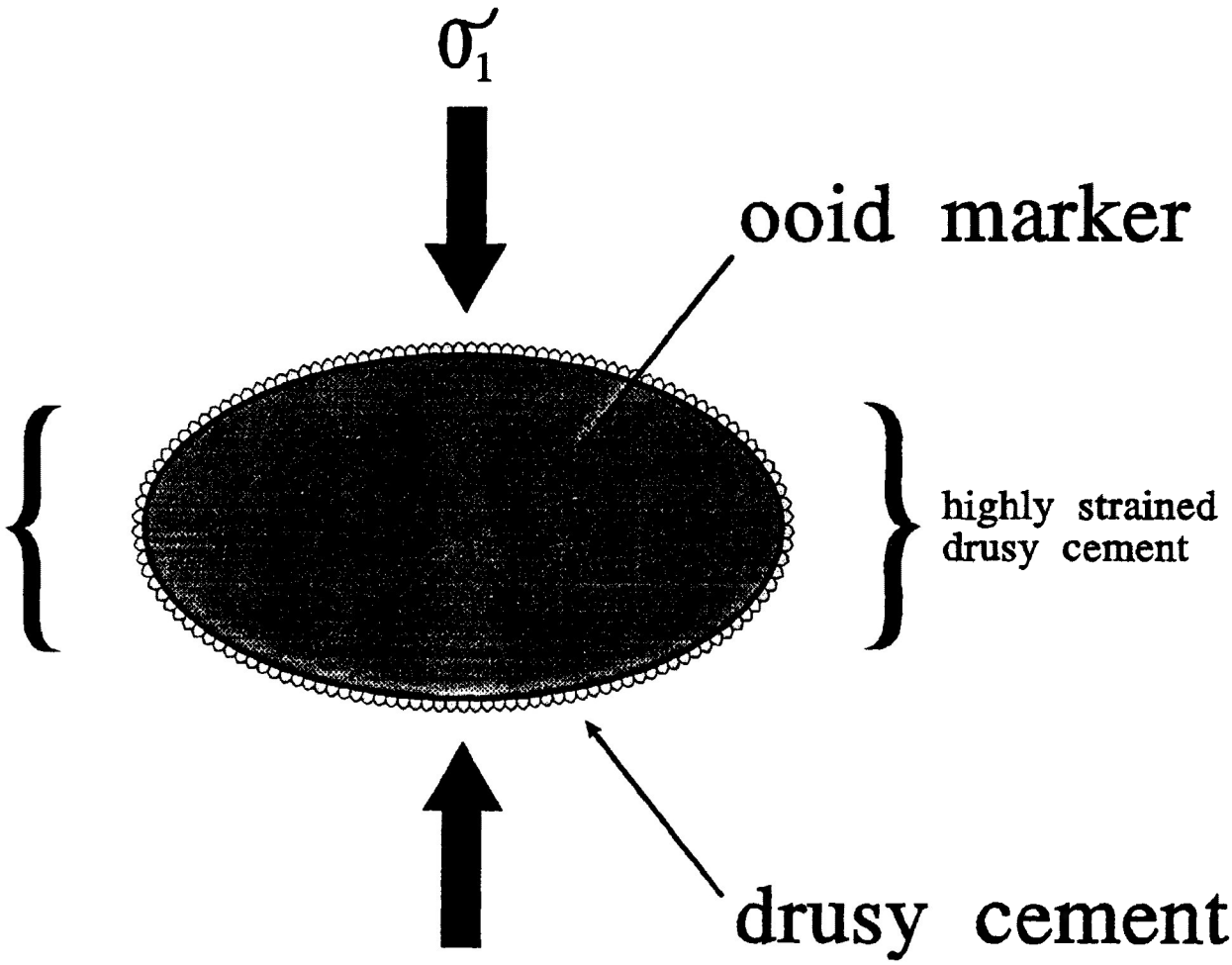

Figure 6.4 The deformation of the drusy cement at low experimental strains. The deformation is characterized by intense twinning and kinking in an orientational range of 20° to 30° around the periphery of the ooid in a direction perpendicular to the σ_1 orientation.

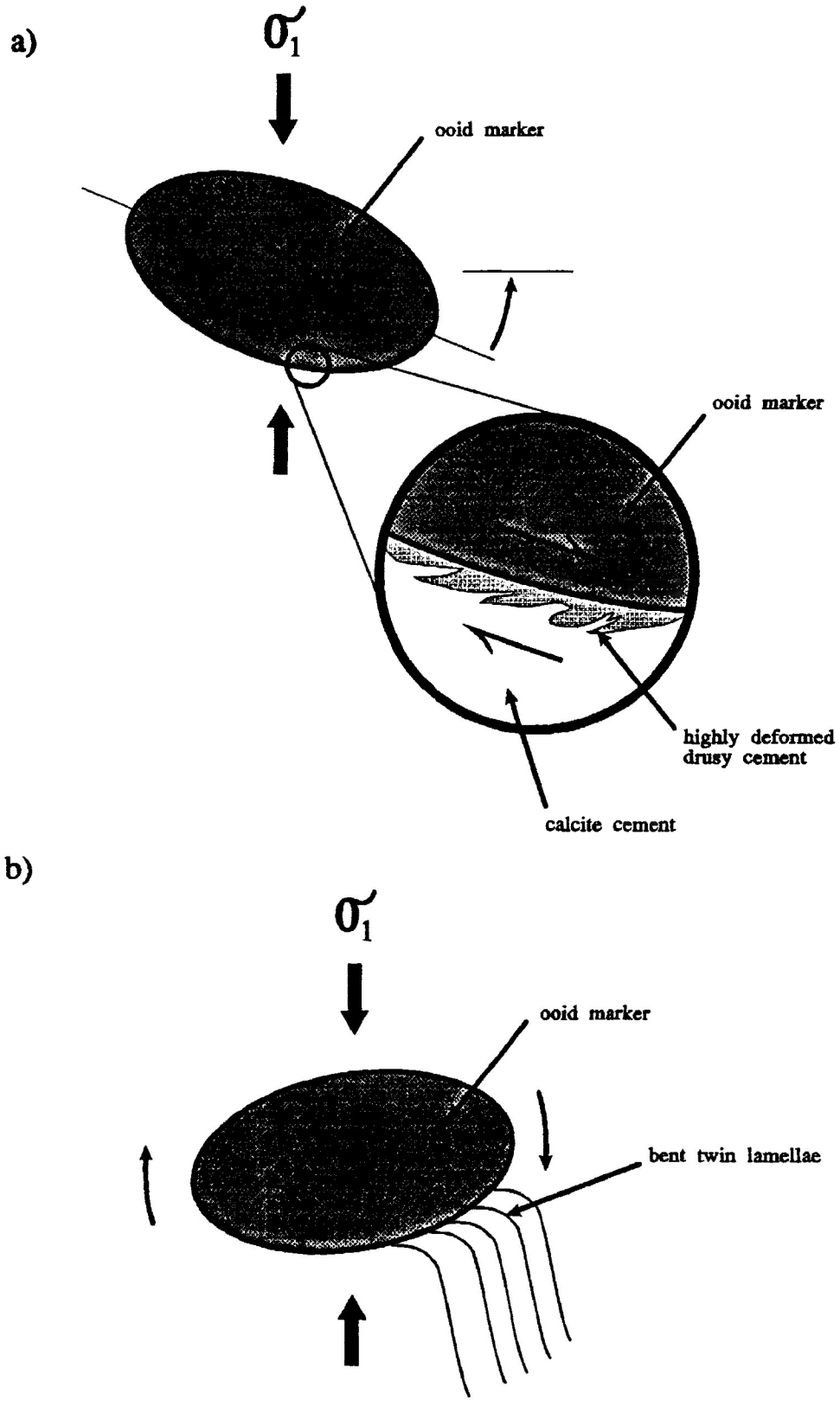

Figure 6.5a-b Two example of deformation that suggest rigid body rotation of the ooid grains. a) the drusy cement is deformed in a way that suggests a shearing motion between the ooid grain and the cement matrix. b) twin lamellae are bent in response to the rotation of an ooid grain into a PDO.

the calcite matrix increases as strain increases during deformation. However, the value of the lamellae index is observed to be approximately 10% to 15% less in the wet experimental test compared with that of the dry experimental tests. At high strains (*eg.*, 17.5% shortening (R_s=1.335)) approximately 100% of the calcite grains of the cement matrix are twinned. The lamellae indices are low to moderate in most calcite-cement grains and are high only in the most suitably oriented calcite grains.

Strained extinction and brittle behaviour (minor crack development along cleavage planes) are observed at higher strains. There is also a notable decrease in the amount of large optically continuous grains that encompass many ooids. The deformed grains of this type show strained extinction and a 10° to 30° rotation of the extinction direction between neighbouring parts of the same grain, which were separated by ooids.

No twinning deformation is observed in the fine grained ooid matrix at all levels of strain studied. However, a change in grain shape is observed as strain increases. Figure 6.3c illustrates this shape change from the undeformed state to a sample deformed to a strain of 8.0% shortening under wet experimental conditions. The overall change in ooid grain shape and development of a PDO is greater compared with dry experimental conditions. Deformation is observed in the drusy cement around the periphery of the ooid grains similar to that observed under dry conditions at low strains. Only at very high strain do ooid grains exhibit highly deformed drusy cement deformed around the entire periphery.

The observed deformation of the cement matrix under wet conditions suggests that the calcite cement appears to deform by grain boundary sliding between other cement grains and ooid

particles. Dilation along some calcite-cement grain boundaries suggest that this is the case. Impingement of the calcite grains into the ooids at high strains may suggest particulate flow of the smaller calcite cement gains. The larger grains are less likely to undergo particulate flow because of the constriction of neighbouring grains.

The observed deformation of the ooid grains suggests that they were deforming as ductile particles with their matrices deforming by particulate flow. Rigid body rotation may also occur in the ooid grains. The lack of highly deformed drusy cement supports this conclusion.

6.4 Strain contribution of the deformed calcite grains in the cement matrix

The cement matrix strain (e_m) was calculated from the bulk strain of the sample (e_b), the ooid strain (e_{oo}, Robin's method), and the volume fraction of ooids (f_{oo}, taken from the X/Z principal plane). The formula used to calculate the cement matrix strain was developed by Schmid and Paterson (1977) and is as follows:

$$e_m=(e_b-f_{oo}e_{oo})/(1-f_{oo})$$

The calculated values of e_m is presented in Table 6.1. A correction was made to sample JL-8, which experienced faulting during deformation. As a result of faulting in the sample the experimental bulk strain was calculated to be an overestimate. Assuming that no matrix strain (e_m=0) existed in this sample (lack of observed intensive deformation (twinning) in the calcite-cement grains) the bulk strain can be recalculated based on the ooid strain and the volume fraction of ooids. The recalculation of the bulk strain reduces the value from 1.232 (e=13.0%) to 1.083 (e=5.2%). This was considered to be a more realistic bulk strain for the observed deformation in the sample.

Figures 6.6 and 6.7 present the comparison of the matrix strain to that of the known bulk strain of the sample. It is apparent from the figures that at low strains the matrix contributes little to the overall bulk strain of the sample. As deformation continues the matrix strain of the calcite cement increases in its contribution to the bulk strain. This may be the result of an increase in the role of grain boundary sliding in the matrix grains.

Overall, the matrix strain in both wet and dry experimental deformation is less than the bulk strain of the

Table 6.1

Sample	Rs(Robin)	f%	e(matrix)	Rs(matrix)	s.d.
ANC-87 (e=0%)	1.002	0.58	0	1	0.14
JL-1 (e=5.6%)	1.167	0.55	0.00	1.007	0.10
JL-5 (e=8%)	1.328	0.58	-0.05	0.934	0.10
JL-6 (e=11.4%)	1.284	0.61	0.05	1.083	0.11
JL-3 (e=16.7%)	1.489	0.62	0.06	1.096	0.10
JL-4 (e=17.6%)	1.545	0.64	0.04	1.063	0.09
JL-7 (e=20%)	1.490	0.64	0.14	1.256	0.13
ANC-87 (e=0%)	1.002	0.58	0.00	1.000	0.14
JL-8 (e=5.2%)	1.132	0.58	0.00	1.000	0.12
Jl-13 (e=5.5%)	1.379	0.61	0.02	1.028	0.13
JL-10 (e=8%)	1.148	0.52	-0.04	0.943	0.10
JL-9 (e=14%)	1.569	0.53	0.00	1.006	0.15
JL-11 (e=17.5%)	1.569	0.51	0.09	1.146	0.14
JL-12 (e=26.4%)	1.911	0.54	0.16	1.305	0.14

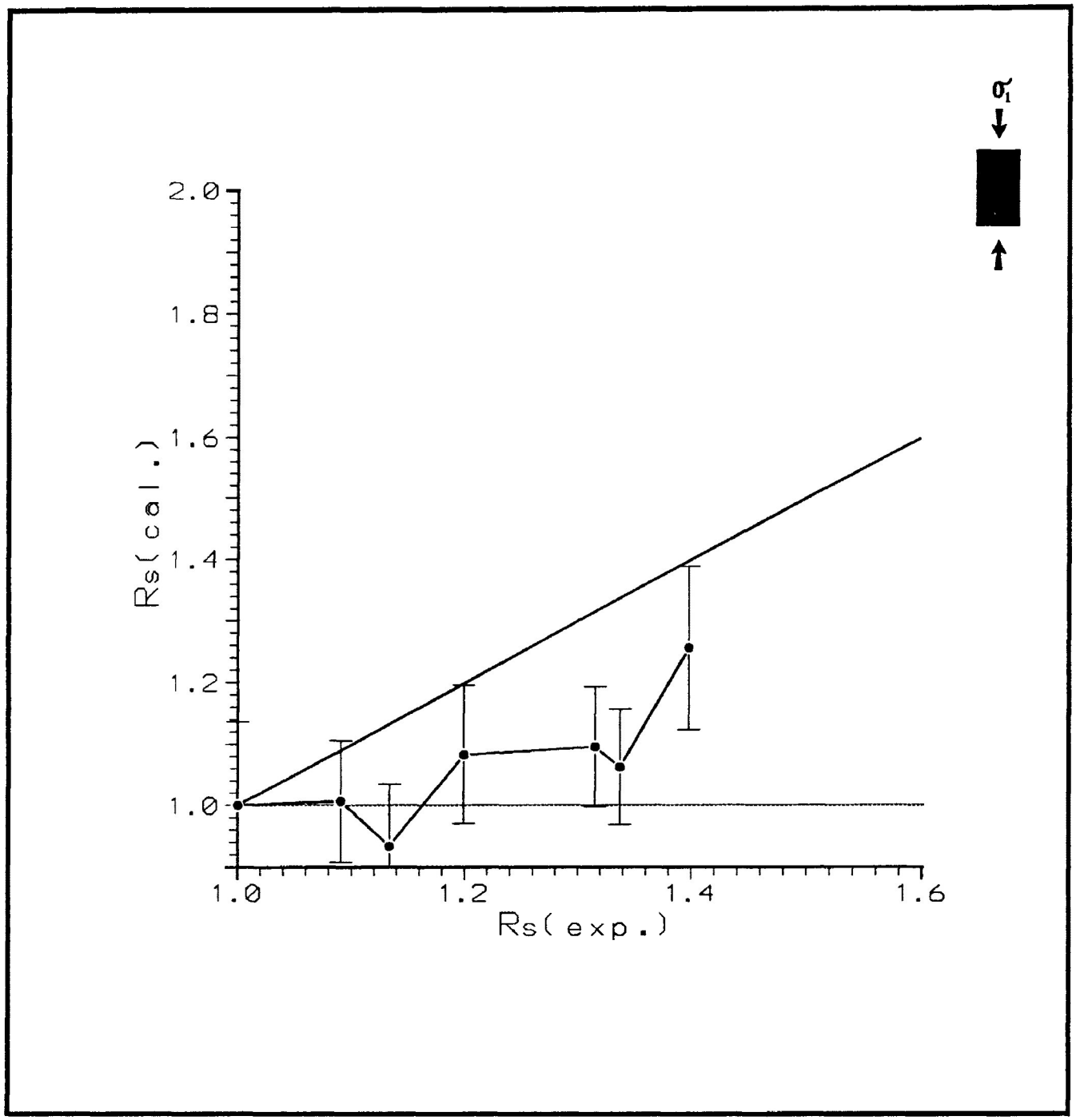

Figure 6.6 Comparison of matrix strain to bulk experimental strain. Equivalent R_s is represented by the dark solid line, R_s=1.0 is represented by light solid line. Experimental strain ratios range from 1.000 (e=0.0%) to 1.389 (e=20.0%). Samples were deformed under dry experimental conditions with confining pressures of 200 Mpa, strain rate of 10^{-5}/s and temperature of 135°C. Error bars represent one standard deviation.

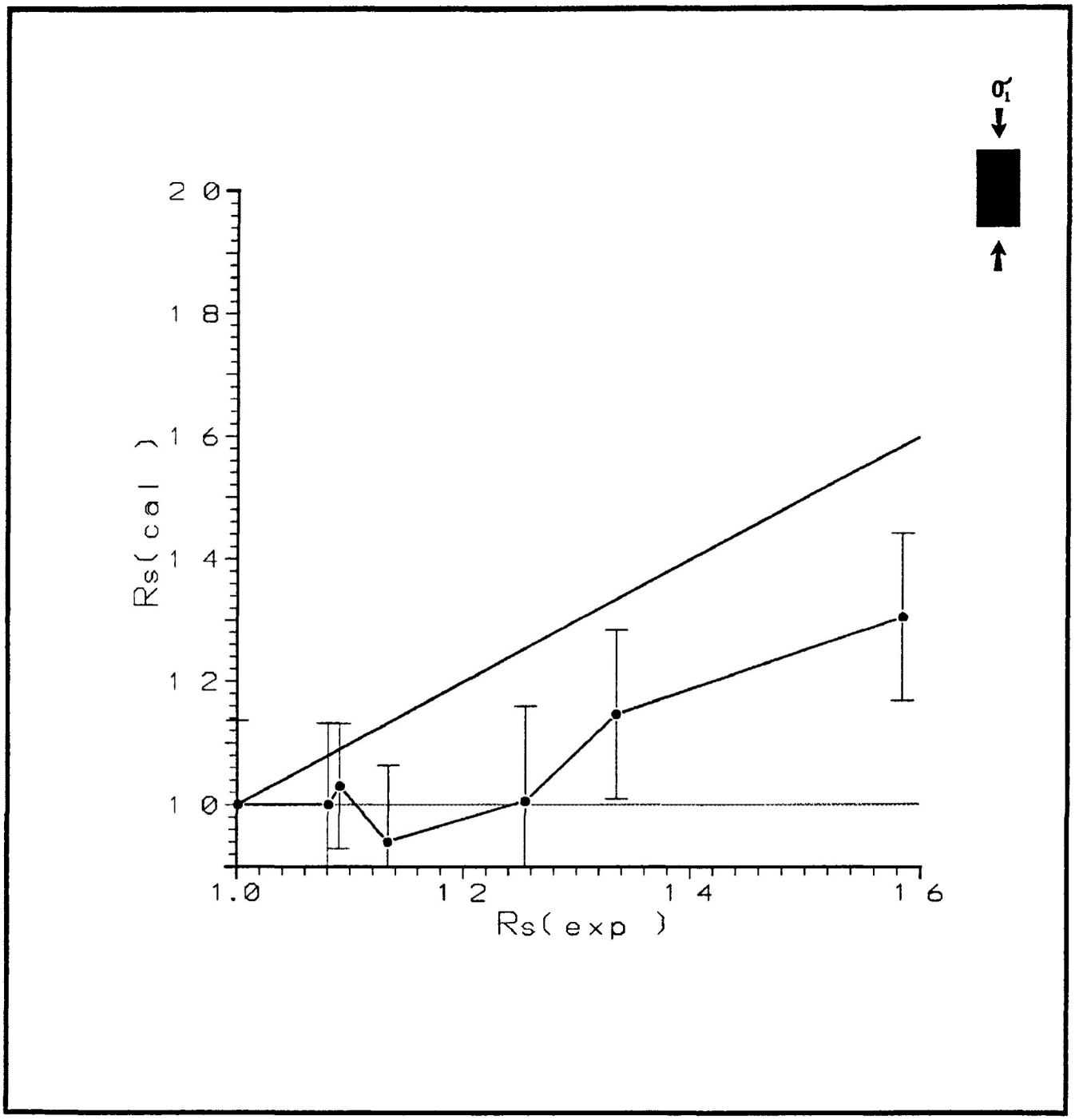

Figure 6.7 Comparison of matrix strain to bulk experimental strain. Equivalent R_s is represented by the dark solid line, R_s=1.0 is represented by light solid line. Experimental strain ratios range from 1.000 (e=0.0%) to 1.584 (e=26.4%). Samples were deformed under wet experimental conditions with confining pressures of 200 Mpa, strain rate of 10^{-5}/s and temperature of 135°C. Pore fluid pressures were less than 60% of the confining pressure. Error bars represent one standard deviation.

sample. As presented in the following sections the main contribution to the bulk strain is taken up by the ooids in the deforming limestone.

6.5 Analysis of a computer simulation ("Forward Modelling") of homogeneous deformation of undeformed oolitic data

For the purpose of comparison an ooid grain shape sample from an undeformed Ancaster oolitic limestone specimen ($n_{markers}$=93) was deformed by a "forward modelling" computer simulation of homogeneous pure shear by R_f/ϕ transformation. The computer simulation was conducted on an IBM computer using a strain analysis program (version 1.25) developed by Dr. G. Borradaile (@1989). In the following computer simulation the maximum extension direction in the X/Z principal plane is oriented at 0°, perpendicular to the axial length of the undeformed test cylinder and parallel to the bedding surface from which the initial undeformed grain sample was taken.

a) Frequency distributions of strain marker ϕ with increasing simulated strain

Figure 6.8a-h present the orientational frequency distribution of Angle Ax (ϕ) for the deformation of strain markers. In the undeformed state no PDO was apparent in the ooids grain shapes (mean theta=6.82° and angular deviation =28.10°). In figure 6.8a-h there is observed, in the long dimension of the strain markers, an increasing development of a PDO for sampled deformed to simulated strains from 0.0% (R_s=1.000) to 23.7% (R_s=1.500) shortening. The PDO aligns into an orientation perpendicular to simulated σ_1 (parallel to the long axis of the test cylinder). This is first observable at low simulated strains (e=5.6% (R_s=1.090)) and is continually observed as simulated strain increases.

The developing PDO is characterized by a slight decrease in the fluctuation (F) of the frequency distribution of ϕ for strains of samples deformed from 0.0% (R_s=1.000) to 17.6% (R_s=1.337) shortening. As strain increases from 17.6% (R_s=1.337) to 23.7% (R_s=1.500) shortening, there is observed

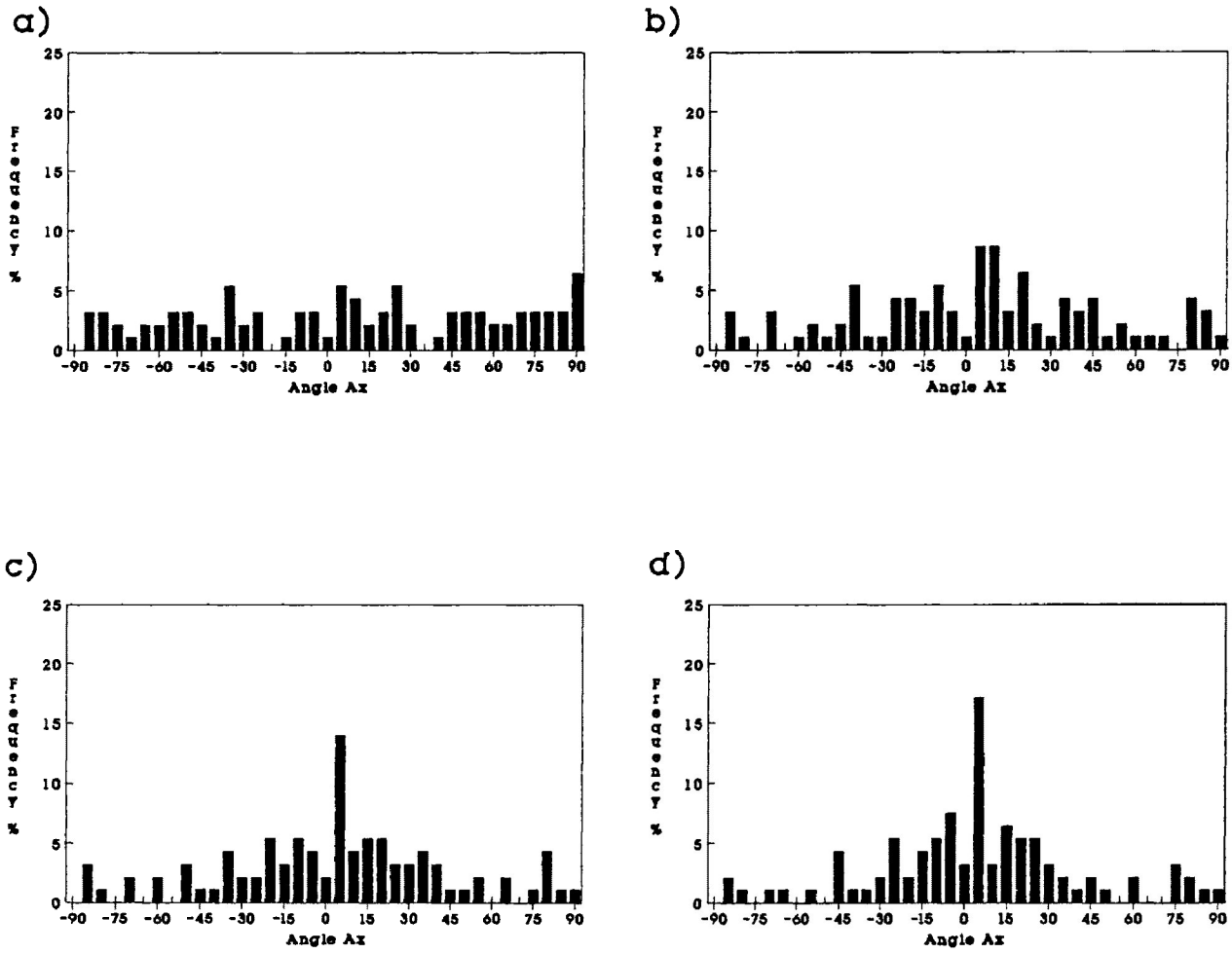

Figure 6.8a-h Frequency distribution of Angle Ax (ϕ) orientations of strain markers (originally undeformed ooid R_f/ϕ data). Simulated strain ratios range from 1.000 (e=0.0%) to 1.500 (e=23.7%). Maximum extension direction oriented at 0°. Samples were deformed by a computer simulation of homogeneous pure shear. Measurements taken from the X/Z principal plane.

a) ANC-87 (R_s=1.000 (e=0.0%))
b) ANC-1 (R_s=1.090 (e=5.6%))
c) ANC-5 (R_s=1.133 (e=8.0%))
d) ANC-6 (R_s=1.199 (e=11.4%))
e) ANC-3 (R_s=1.315 (e=16.7%))
f) ANC-4 (R_s=1.337 (e=17.6%))
g) ANC-7 (R_s=1.398 (e=20.0%))
h) ANC-8 (R_s=1.500 (e=23.7%))

e)

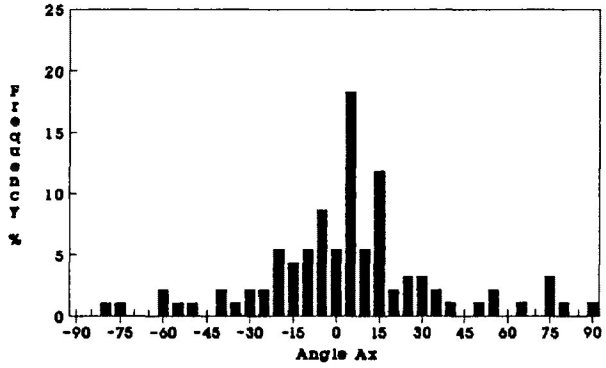
Frequency %
25
20
15
10
5
0
-90 -75 -60 -45 -30 -15 0 15 30 45 60 75 90
Angle Ax

f)

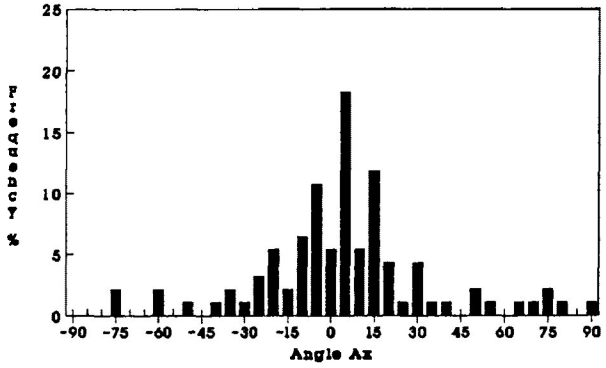
Frequency %
25
20
15
10
5
0
-90 -75 -60 -45 -30 -15 0 15 30 45 60 75 90
Angle Ax

g)

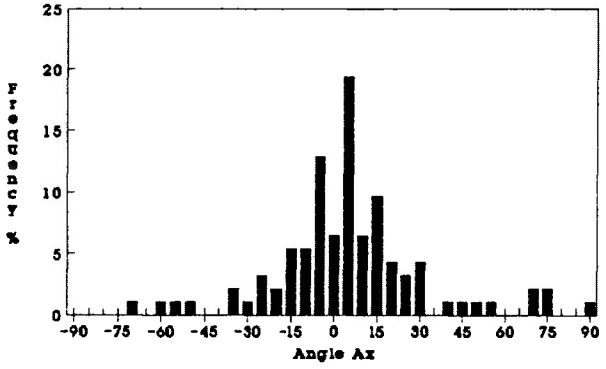
Frequency %
25
20
15
10
5
0
-90 -75 -60 -45 -30 -15 0 15 30 45 60 75 90
Angle Ax

h)

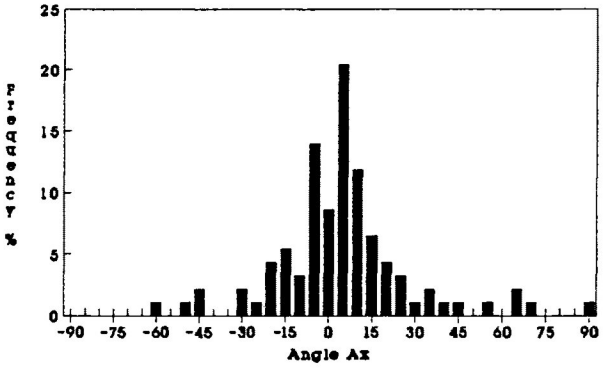
Frequency %
25
20
15
10
5
0
-90 -75 -60 -45 -30 -15 0 15 30 45 60 75 90
Angle Ax

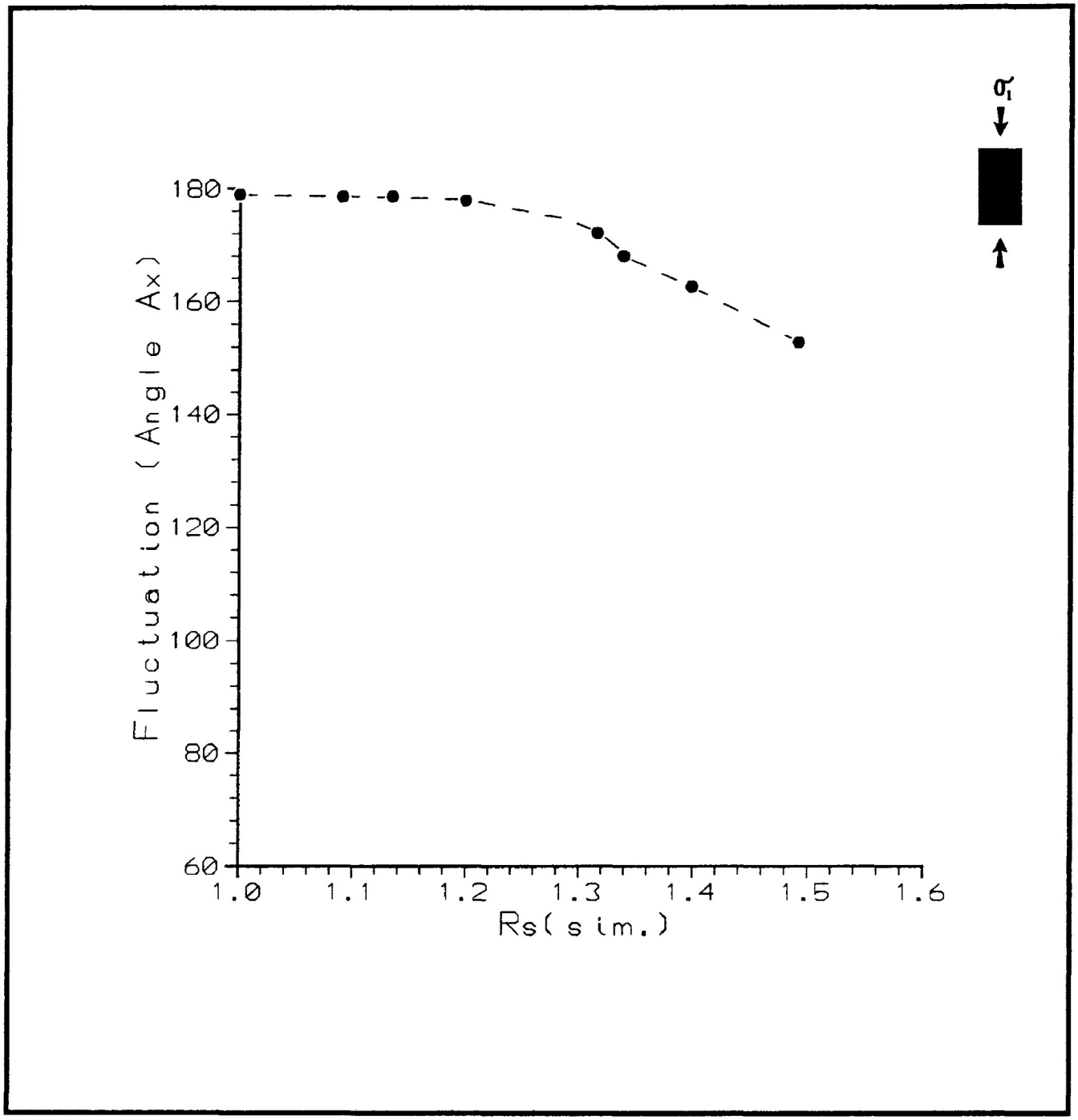

Figure 6.9 Variations in fluctuation of Angle Ax with increasing strain. Simulated strain ratios range from 1.000 (e=0.0%) to 1.500 (e=23.7%). Maximum extension direction oriented at 0°. Samples were deformed by a computer simulation of homogeneous pure shear.

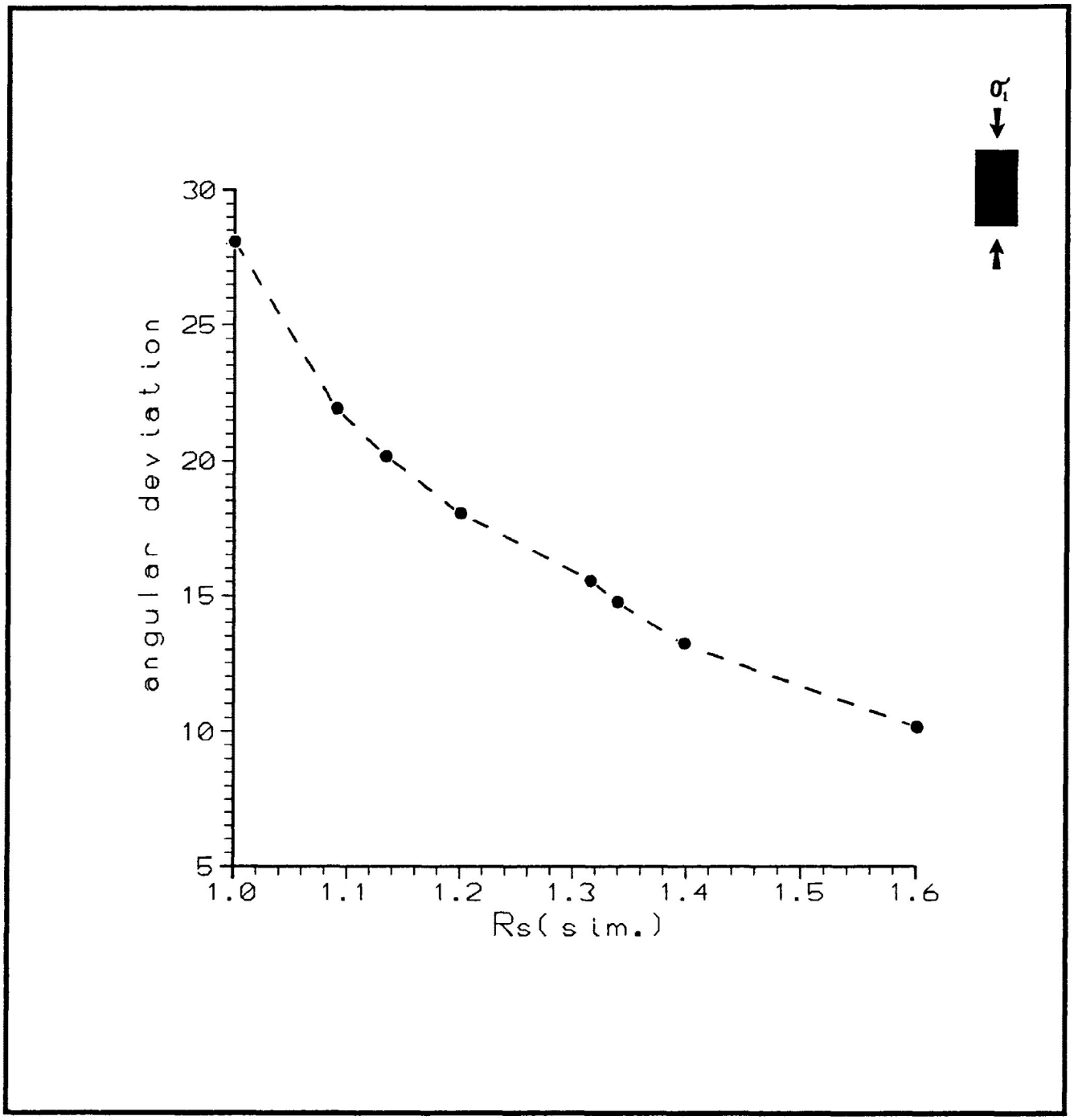

Figure 6.10 Variations in angular deviation of Angle Ax (ϕ) with increasing strain. Simulated strain ratios range from 1.000 (e=0.0%) to 1.500 (e=23.7%). Samples were deformed by a computer simulation of homogeneous pure shear.

a more noticeable decrease in F (Fig. 6.9).

A change in angular deviation is observed with increasing simulated strain and is presented in figure 6.10. In the figure there is a consistent decrease in angular deviation between simulated strains ratios 1.000 and 1.500. The decrease in angular deviation becomes less as simulated strain increases. The consistent decrease in angular deviation is reflected in a slow formation of a well developed PDO of the long axis of strain markers, with increasing simulated strain.

b) R_f frequency distributions of strain markers with increasing simulated strain

Changes in R_f of the strain markers with simulated strain are presented in figure 6.11a-h. As simulated strain increases the distribution of R_f becomes slightly more lognormal. The range of R_f values increase from 1.1 to 2.0 in the undeformed state to 1.1 to 2.6 at 23.7% shortening. The mean R_f of the strain markers and standard deviation of the R_f distribution are presented in figure 6.12.

c) R_f/ϕ diagrams for deformed strain markers

R_f/ϕ distributions of the deformed strain markers are presented in figure 6.13a-h. The R_f/ϕ diagrams are characterized by the slow development of a moderate R_f/ϕ distributions as simulated strain increases from 0.0% to 23.7% shortening. The distributions remain symmetrical about the known principal extension direction for all simulated strains.

d) Comparison between strain analysis methods for deformed strain markers in the "forward modelling" simulation

Figure 6.14 presents the comparison of the Robin's, linearization and harmonic mean methods of strain analysis

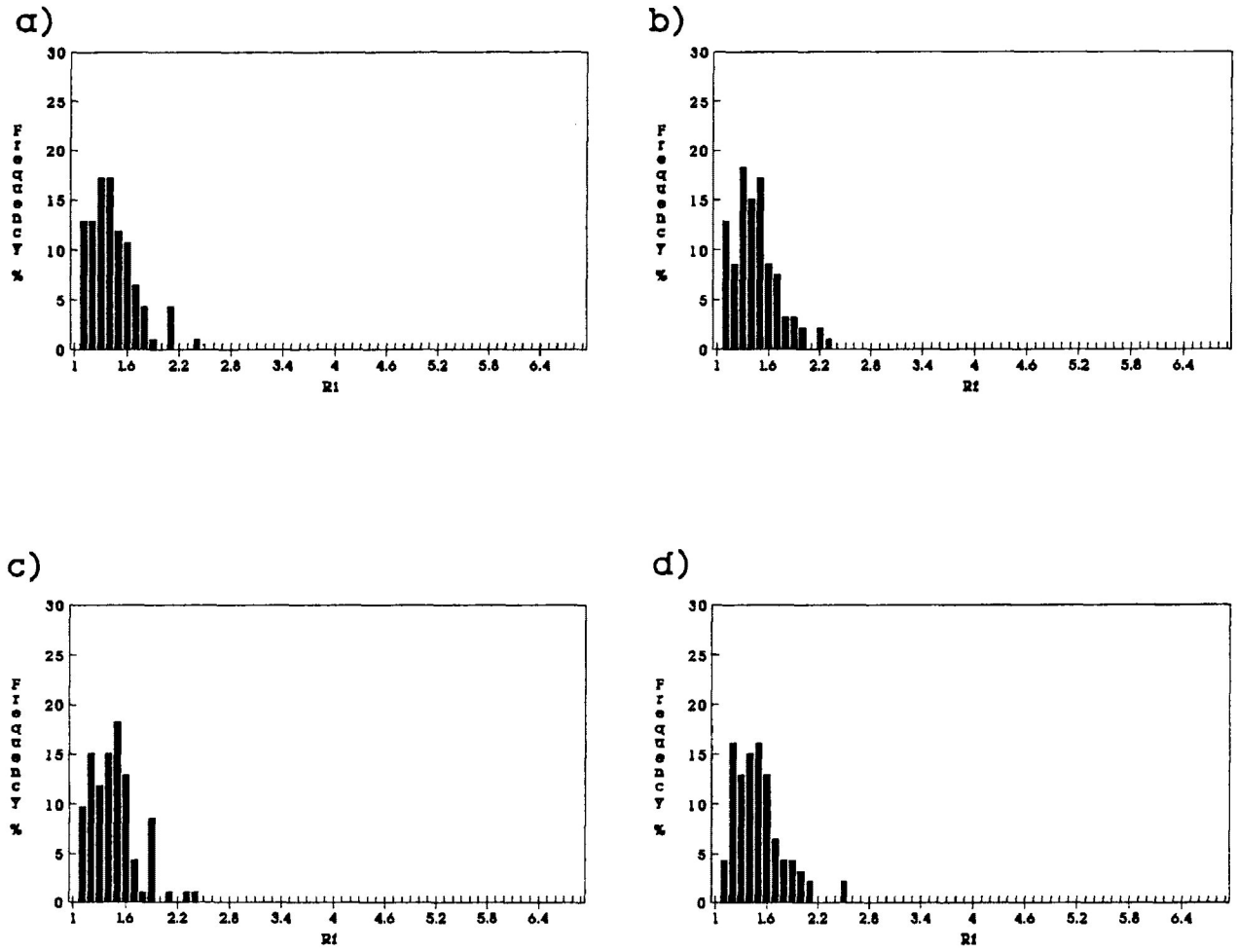

Figure 6.11a-h Frequency distribution of R_f for strain markers (originally undeformed ooid R_f/ϕ data). Simulated strain ratios range from 1.000 (e=0.0%) to 1.500 (e=23.7%). Samples were deformed by a computer simulation of homogeneous pure shear. Measurements taken from the X/Z principal plane.

a) ANC-87 (R_s=1.000 (e=0.0%))
b) ANC-1 (R_s=1.090 (e=5.6%))
c) ANC-5 (R_s=1.133 (e=8.0%))
d) ANC-6 (R_s=1.199 (e=11.4%))
e) ANC-3 (R_s=1.315 (e=16.7%))
f) ANC-4 (R_s=1.337 (e=17.6%))
g) ANC-7 (R_s=1.398 (e=20.0%))
h) ANC-8 (R_s=1.500 (e=23.7%))

e)

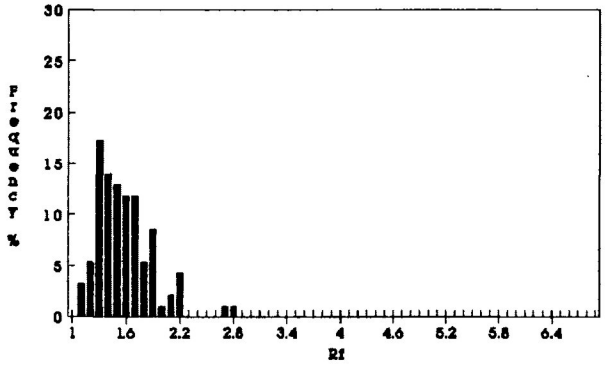
Frequency %
30
25
20
15
10
5
0
1
1.6
2.2
2.8
3.4
4
4.6
5.2
5.8
6.4
Rf

f)

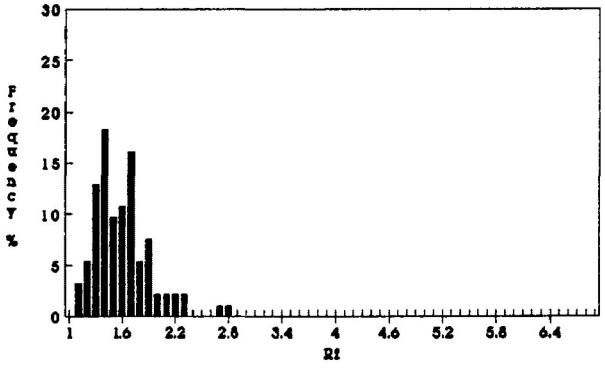
Frequency %
30
25
20
15
10
5
0
1
1.6
2.2
2.8
3.4
4
4.6
5.2
5.8
6.4
Rf

g)

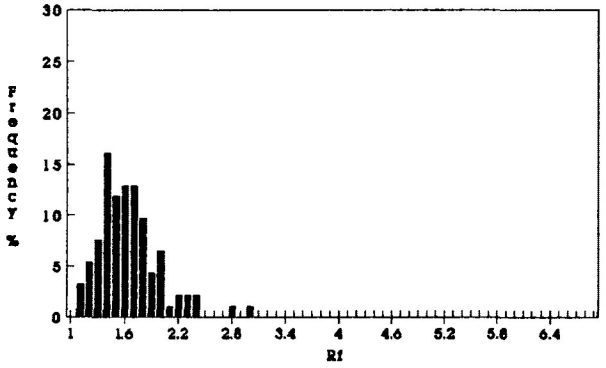
Frequency %
30
25
20
15
10
5
0
1
1.6
2.2
2.8
3.4
4
4.6
5.2
5.8
6.4
Rf

h)

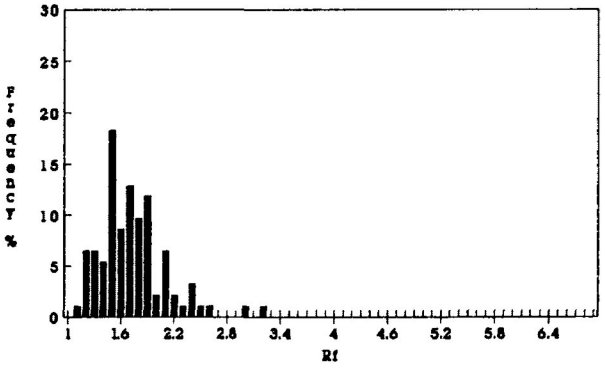
Frequency %
30
25
20
15
10
5
0
1
1.6
2.2
2.8
3.4
4
4.6
5.2
5.8
6.4
Rf

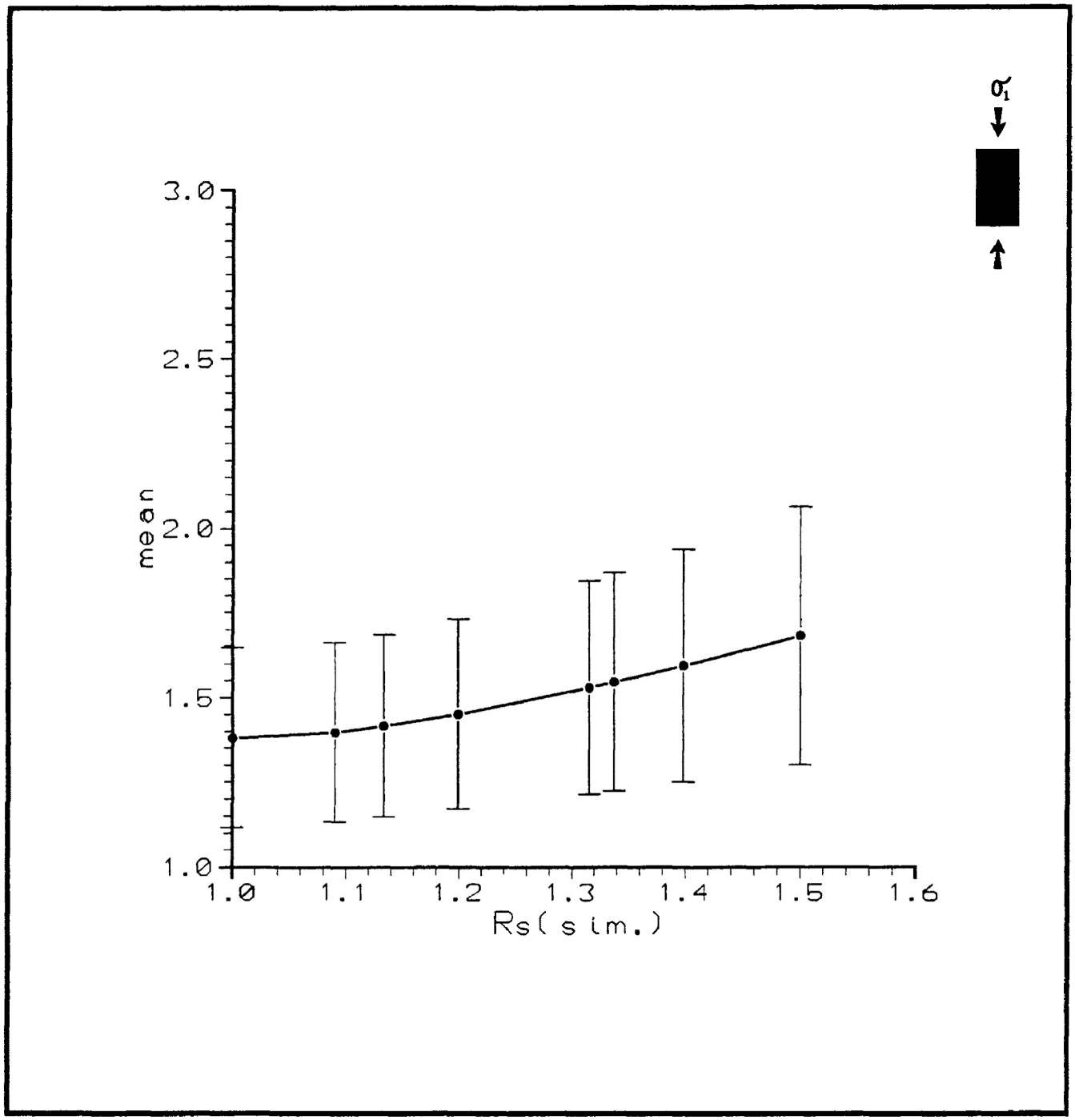

Figure 6.12 Variations in mean and standard deviation of R_f with increasing strain. Simulated strain ratios range from 1.000 (e=0.0%) to 1.500 (e=23.7%). Samples were deformed by a computer simulation of homogeneous pure shear.

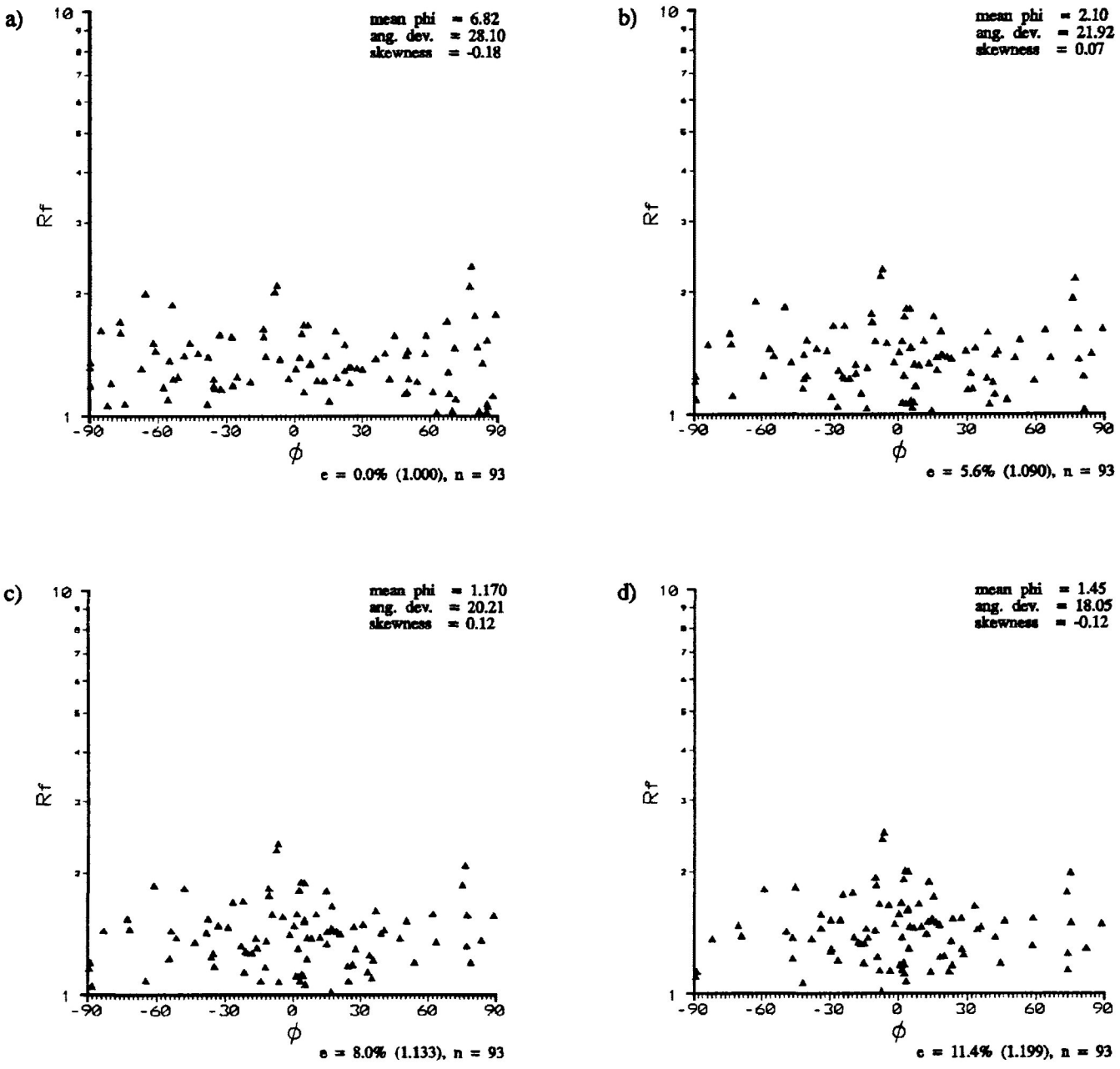

Figure 6.13a-h R_f/ϕ diagrams for strain markers (originally undeformed ooid R_f/ϕ data). Simulated strain ratios range from 1.000 (e=0.0%) to 1.500 (e=23.7%). Maximum extension direction oriented at 0°. Samples were deformed by a computer simulation of homogeneous pure shear. Measurements taken from the X/Z principal plane.

a) ANC-87 (R_s=1.000 (e=0.0%))
b) ANC-1 (R_s=1.090 (e=5.6%))
c) ANC-5 (R_s=1.133 (e=8.0%))
d) ANC-6 (R_s=1.199 (e=11.4%))
e) ANC-3 (R_s=1.315 (e=16.7%))
f) ANC-4 (R_s=1.337 (e=17.6%))
g) ANC-7 (R_s=1.398 (e=20.0%))
h) ANC-8 (R_s=1.500 (e=23.7%))

e)

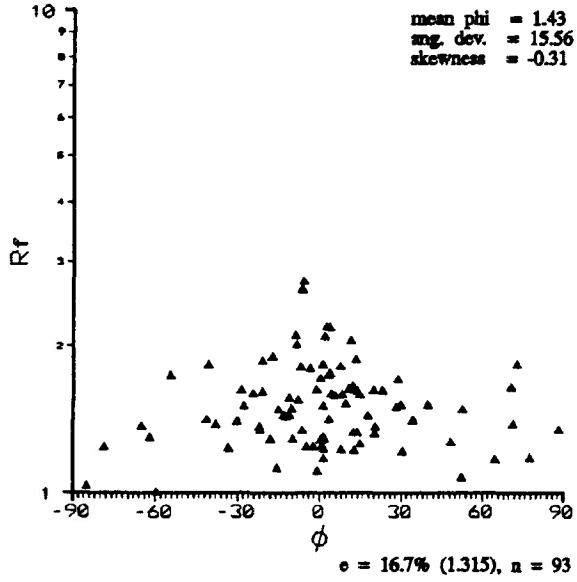

e = 16.7% (1.315), n = 93

f)

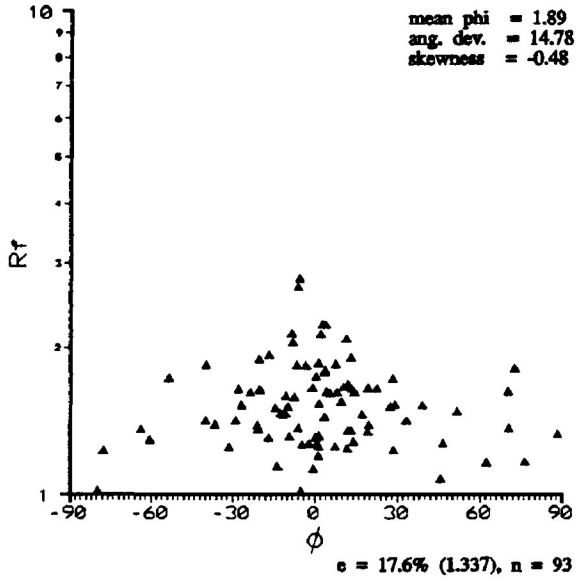

e = 17.6% (1.337), n = 93

g)

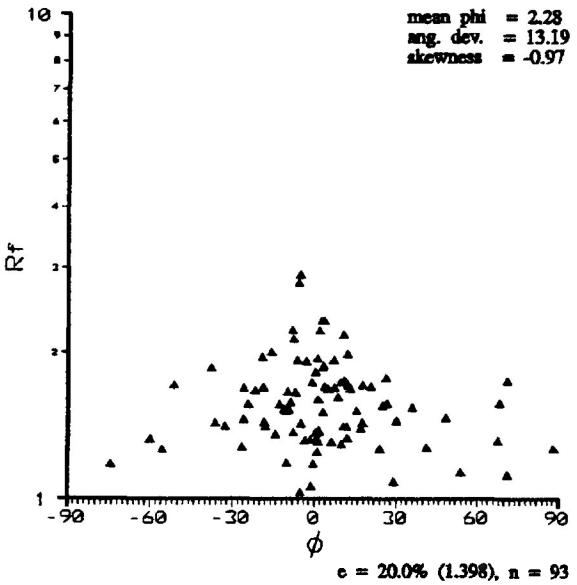

e = 20.0% (1.398), n = 93

h)

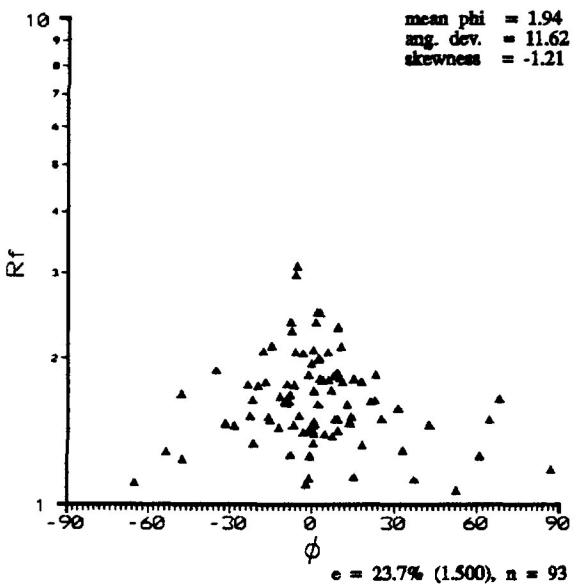

e = 23.7% (1.500), n = 93

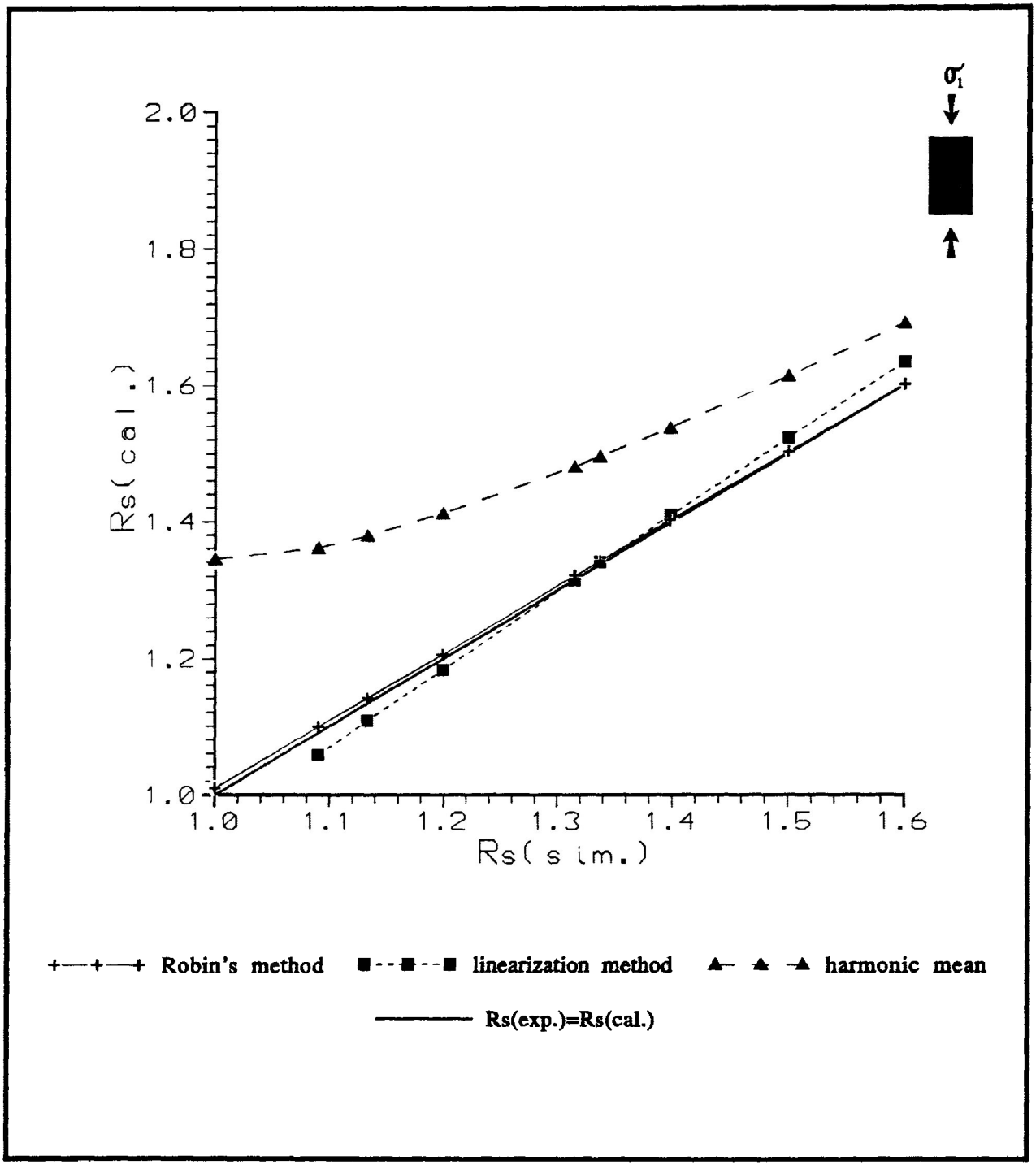

Figure 6.14 Comparison of the estimate of strain ratio (R_s(cal.)) calculated from Robin's method (cross), linearization method (square) and harmonic mean (triangle) to the simulated strain (R_s(sim.)) for a "forward modelling" simulation of the deformation of ooid R_f/ϕ data (ANC-87, n =93) by a computer simulation of homogeneous pure shear in the X/Z principal plane. Simulated strain ratios range from 1.000 (e=0.0%) to 1.500 (e=23.7%). Broad line represents the line of (R_s(sim.)) =(R_s(cal.)).

TABLE 6.2

sample	e%	Rs(exp.)	Robin's error (s.d.)	Harmonic error (s.d.)	Linear error (s.d.)	n
ANC-87	0	1.000	0.136	0.127	n.a	93
asc2	5.6	1.090	0.136	0.127	n.a	93
asc3	8	1.133	0.136	0.127	n.a	93
asc4	11.4	1.199	0.136	0.125	1.220	93
asc5	16.7	1.315	0.136	0.123	1.398	93
asc6	17.6	1.337	0.136	0.125	1.436	93
asc7	20	1.398	0.136	0.125	1.550	93
asc8	23.7	1.500	0.136	0.126	1.813	93
asc9	37.0	2.000	0.136	0.128	n.a	93

TABLE 6.3

sample	e%	Rs(exp.)	Robin's error (s.d.)	Harmonic error (s.d.)	Linear error (s.d.)	n
ANC-87 (e=0%)	0	1.000	0.136	0.127	n.a	93
JL-1 (e=5.6%)	5.6	1.090	0.099	0.110	1.273	119
JL-5 (e=8%)	8	1.133	0.102	0.129	1.766	116
JL-6 (e=11.4%)	11.4	1.199	0.112	0.131	1.616	93
JL-3 (e=16.7%)	16.7	1.315	0.097	0.115	1.901	125
JL-4 (e=17.6%)	17.6	1.337	0.094	0.121	n.a	140
JL-7 (e=20%)	20	1.398	0.133	0.140	n.a	72

TABLE 6.4

sample	e%	Rs(exp.)	Robin's error (s.d.)	Harmonic error (s.d.)	Linear error (s.d.)	n
ANC-87 (e=0%)	0	1.000	0.136	0.127	n.a	93
Jl-13 (e=5.5%)	5.5	1.089	0.132	0.116	n.a	86
JL-10 (e=8%)	8	1.133	0.101	0.111	1.373	147
JL-8 (e=13%)	13	1.232	0.124	0.122	1.230	97
JL-9 (e=14%)	14	1.254	0.154	0.134	n.a	70
JL-11 (e=17.5%)	17.5	1.335	0.137	0.144	n.a	92
JL-12 (e=26.4%)	26.4	1.584	0.136	0.171	n.a	103

for the simulated homogeneous deformation of strain marker data (ooids). It is observed in the figure, that Robin's method is a slight overestimate of the experimental bulk strain at low strains. The overestimate of bulk strain decreases as strain increases and becomes a slight underestimate of the bulk strain above 10% shortening. For passive homogeneous deformation Robin's method yield a good approximation of the simulated bulk strain.

Similar estimates of bulk strain are calculated from the linearization method compared to that of Robin's method. The linearization method is represented by a decreasing underestimate of the actual R_s, for strain ratios up to 1.350 and becomes an increasing overestimate as simulated strain ratio increases from 1.350 to 1.5. Harmonic mean is the largest overestimate of strain for the range of deformation presented in figure 6.14. At bulk strain above 1.890 the linearization method generates a larger strain estimates than the harmonic mean. The most consistent and best estimate of the actual strain ratio is Robin's method.

Standard deviation for Robin's method, linearization method and the harmonic mean method were calculated and are presented in table 6.2. For the linearization method the calculations of standard deviation that yield confidence brackets that extend into bulk strains estimates less than 1.000 are not given.

Comparison of the a_j/c_j ratio necessary to calculate Robin's method for a computer simulation of homogeneous strain is presented in figure 6.15a-h. It is observed from the figures that the a_j/c_j ratio distributions are approximately normal for all simulated strains. The range of a_j/c_j increases as simulated strain increases from a range of 0.5-1.7 in the undeformed state to a range of 0.8-2.5 at 23.7% shortening.

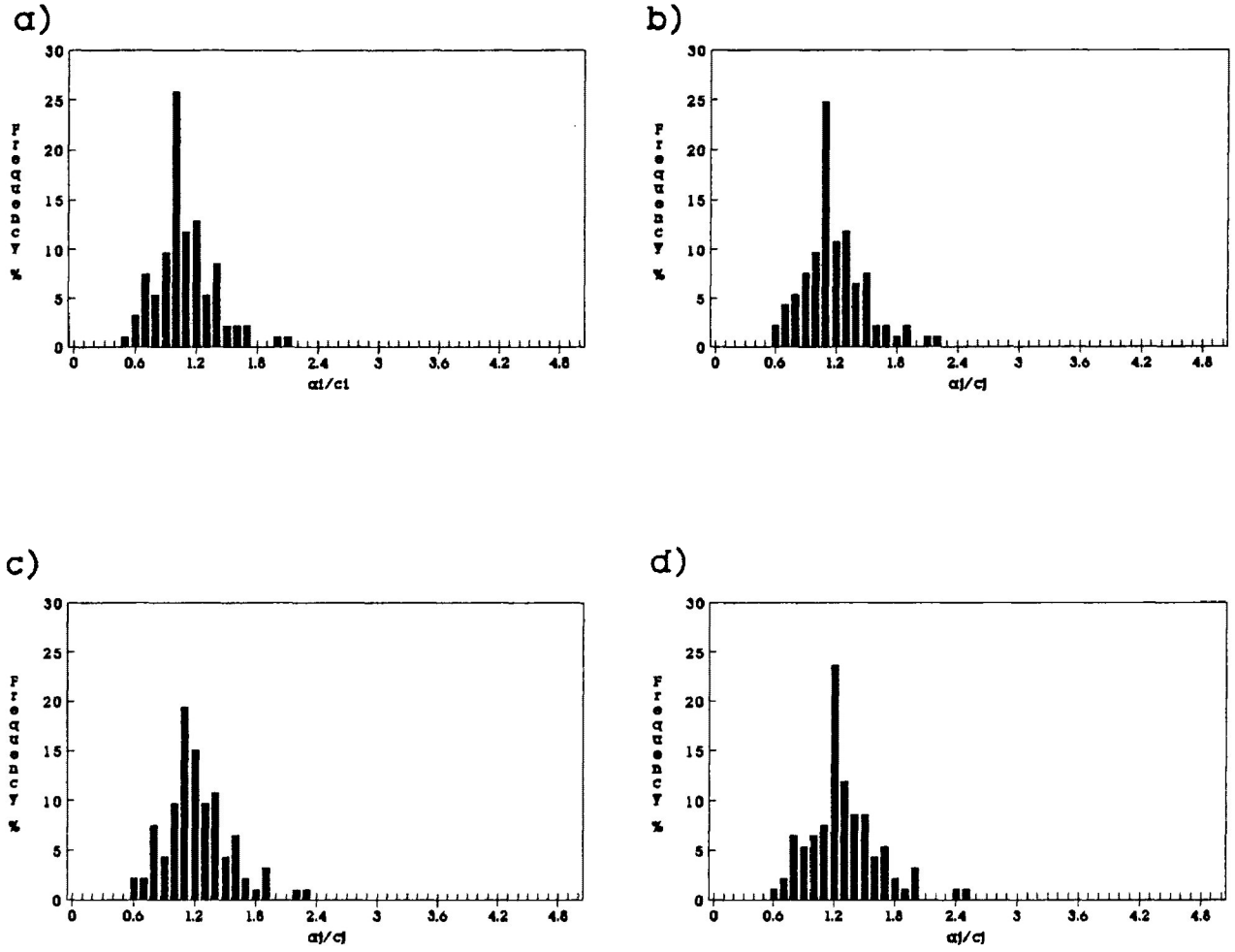

Figure 6.15a-h Frequency distribution of a_j/c_j ratios for strain markers (originally undeformed ooid R_f/ϕ data). Simulated strain ratios range from 1.000 (e=0.0%) to 1.500 (e=23.7%). Samples were deformed by a computer simulation of homogeneous pure shear. Measurements taken from the X/Z principal plane.

a) ANC-87 (R_s=1.000 (e=0.0%))
b) ANC-1 (R_s=1.090 (e=5.6%))
c) ANC-5 (R_s=1.133 (e=8.0%))
d) ANC-6 (R_s=1.199 (e=11.4%))
e) ANC-3 (R_s=1.315 (e=16.7%))
f) ANC-4 (R_s=1.337 (e=17.6%))
g) ANC-7 (R_s=1.398 (e=20.0%))
h) ANC-8 (R_s=1.500 (e=23.7%))

e)

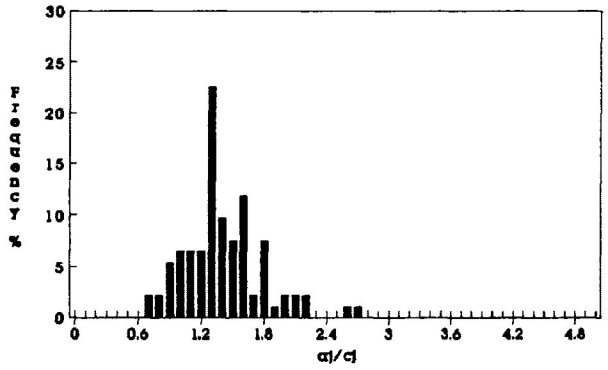
Frequency %
30
25
20
15
10
5
0
0
0.6
1.2
1.8
2.4
3
3.6
4.2
4.8
αj/cj

f)

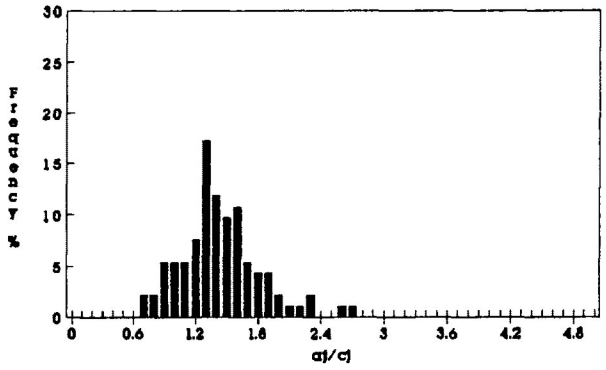
Frequency %
30
25
20
15
10
5
0
0
0.6
1.2
1.8
2.4
3
3.6
4.2
4.8
αj/cj

g)

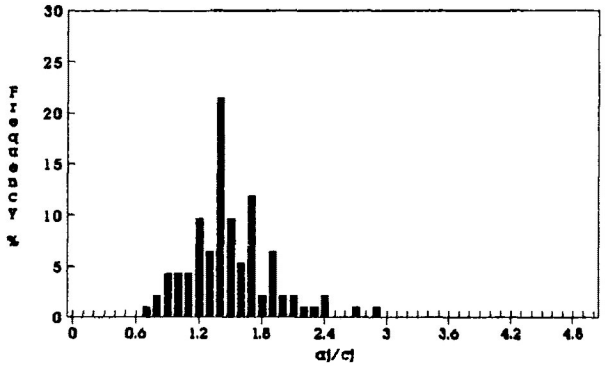
Frequency %
30
25
20
15
10
5
0
0
0.6
1.2
1.8
2.4
3
3.6
4.2
4.8
αj/cj

h)

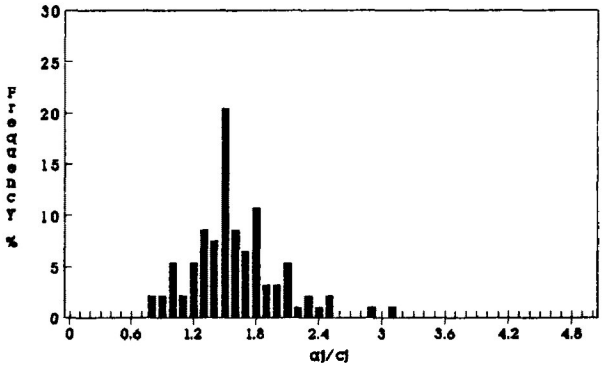
Frequency %
30
25
20
15
10
5
0
0
0.6
1.2
1.8
2.4
3
3.6
4.2
4.8
αj/cj

The best estimates of tectonic strain are at low bulk deformations (<20% shortening), as a result of the normal distributions of the a_j/c_j ratios, a condition necessary for the determination of tectonic strain by Robin's method.

6.6 Analysis of deformed ooids under dry experimental conditions (P_c=200 Mpa)

In dry experimental pure shear deformation a comparison of orientational and dimensional frequency distributions and R_f/ϕ diagrams were made from 7 samples increasing in experimental strain ratio from 1.000 (e=0.0%) to 1.584 (e=26.4%).

a) Frequency distributions of ϕ for ooid grains with increasing strain

Figure 6.16a-g present the orientational frequency distribution of Angle Ax (ϕ) for ooid grains. In each diagram the maximum extension direction is oriented at 0°, perpendicular to the axial length of the undeformed test cylinder and parallel to the bedding surface. In figure 6.16a-g there is observed, in the long dimension of the ooid grains, an increasing formation of a well developed PDO for samples experimentally deformed from 0.0% (R_s=1.000) to 20.0% (R_s=1.398) shortening. The PDO aligns quickly into an orientation perpendicular to experimental σ_1 (parallel to the long axis of the test cylinder). This is first observable at low strains (e=5.6% (R_s=1.090)) and is continually observed as strain increases.

The developing PDO is characterized by the decrease in F for samples experimentally deformed from 0.0% (R_s=1.000) to 16.7% (R_s=1.315) shortening. As strain increases from 16.7% to 20.0% (R_s=1.398) shortening, there is observed an increase in the F and the development of a skewness (+ve) in the distribution (Fig. 6.17). The increase in fluctuation and increasing skewness (+ve) at high strains may be the attributed to bulging of the specimen cylinder and the development of embryonic conjugate fractures at 30° to 40° to the σ_1 orientation.

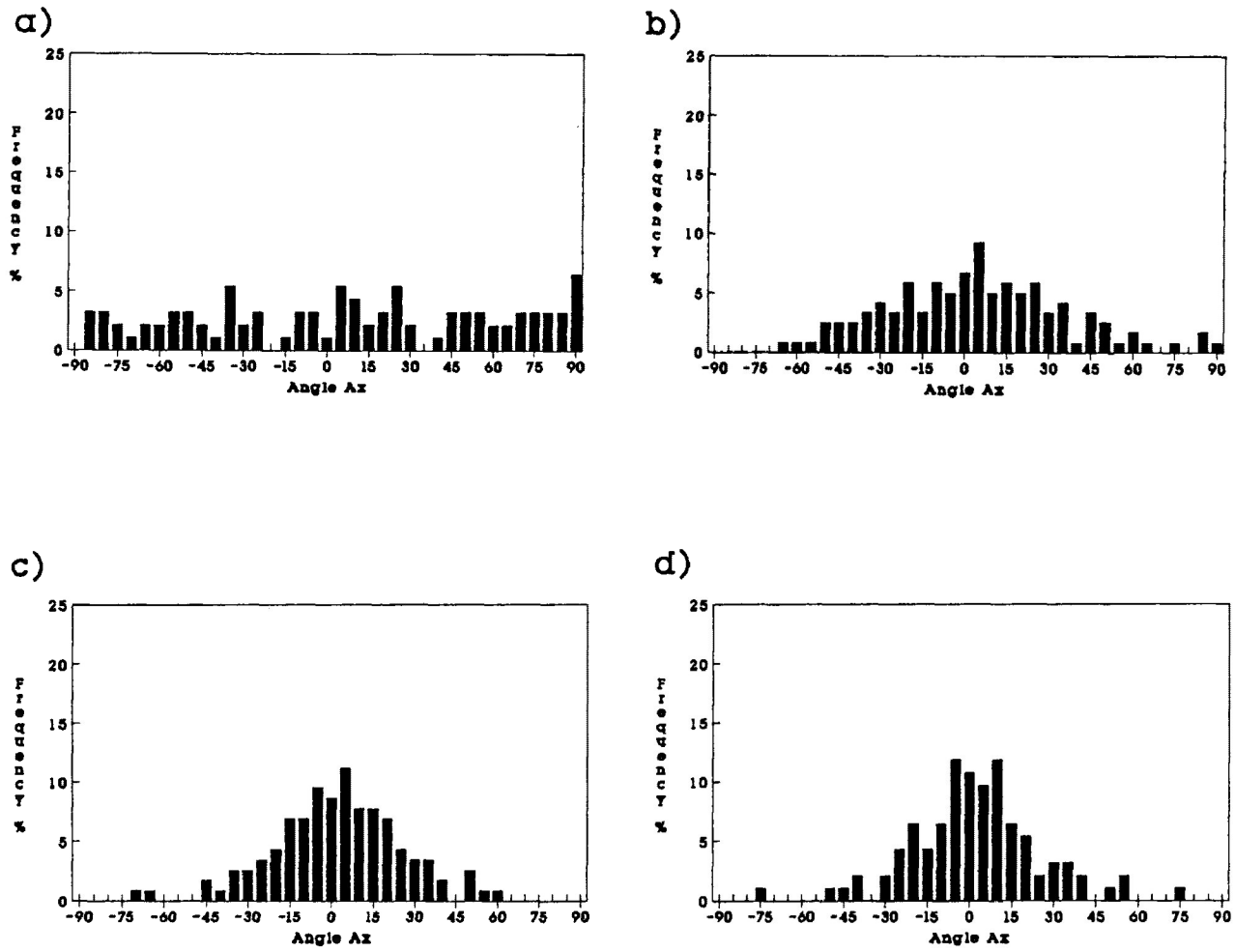

Figure 6.16a-g Frequency distribution of Angle Ax (ϕ) orientations of ooids in undeformed and deformed Ancaster Limestone. Experimental strain ratios range from 1.000 (e=0.0%) to 1.389 (e=20.0%). Maximum extension direction oriented at 0°. Samples were deformed under dry experimental conditions with confining pressures of 200 Mpa, strain rate of 10^{-5}/s and temperatures of 135°C. Measurements taken from the X/Z principal plane.

a) ANC-87 (R_s=1.000 (e=0.0%))
b) JL-1 (R_s=1.090 (e=5.6%))
c) JL-5 (R_s=1.133 (e=8.0%))
d) JL-6 (R_s=1.199 (e=11.4%))
e) JL-3 (R_s=1.315 (e=16.7%))
f) JL-4 (R_s=1.337 (e=17.6%))
g) JL-7 (R_s=1.398 (e=20.0%))

e)

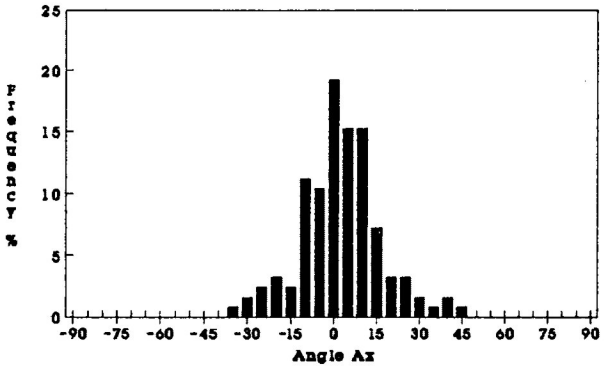
Frequency %
25
20
15
10
5
0
-90 -75 -60 -45 -30 -15 0 15 30 45 60 75 90
Angle Ax

f)

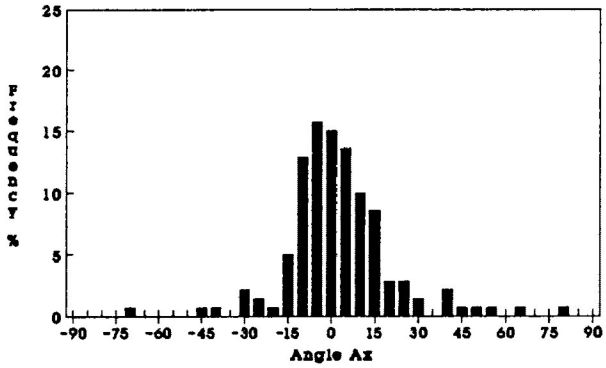
Frequency %
25
20
15
10
5
0
-90 -75 -60 -45 -30 -15 0 15 30 45 60 75 90
Angle Ax

g)

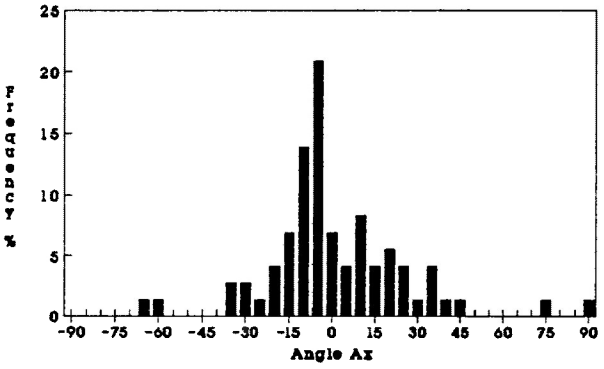
Frequency %
25
20
15
10
5
0
-90 -75 -60 -45 -30 -15 0 15 30 45 60 75 90
Angle Ax

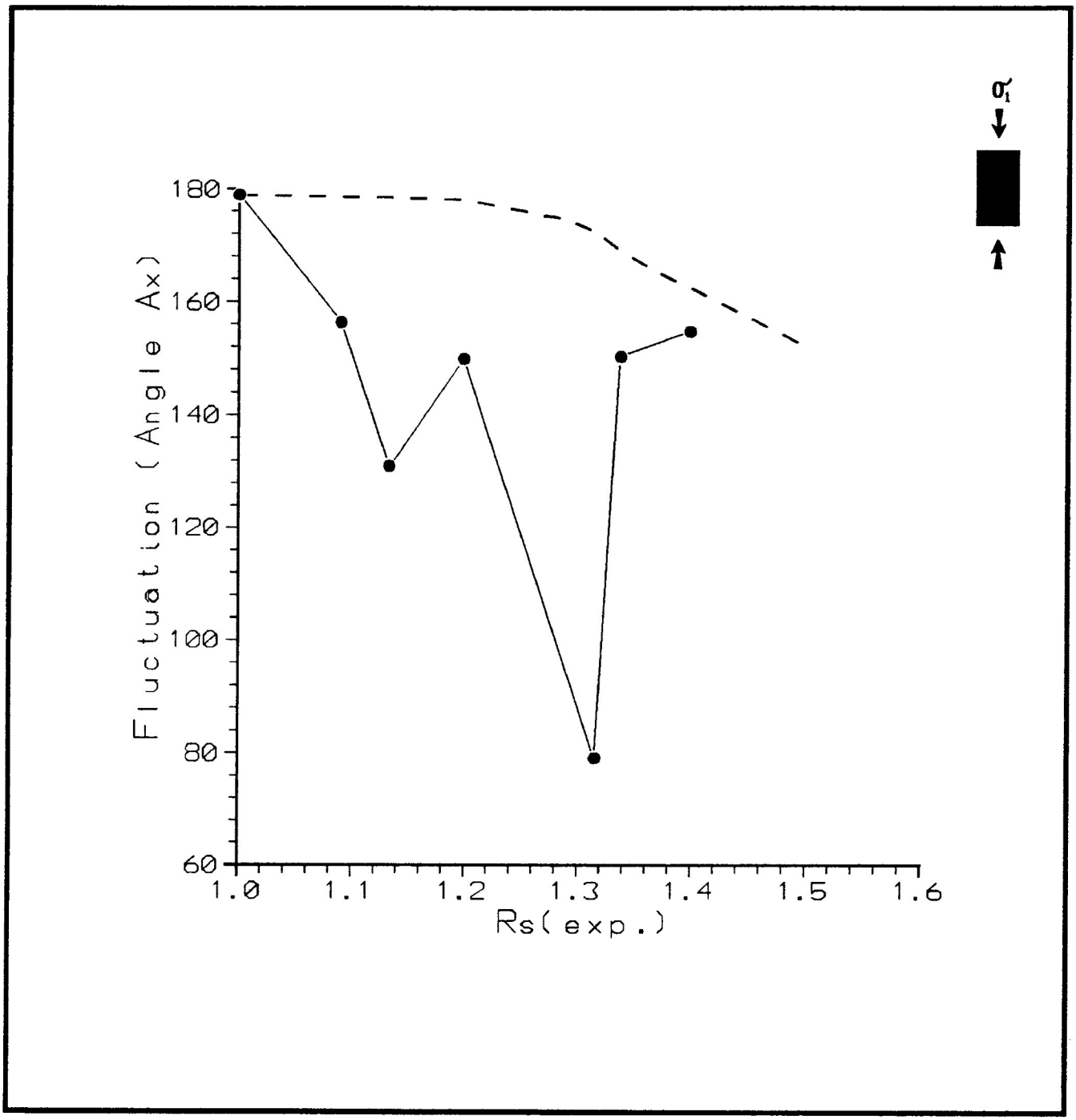

Figure 6.17 Variations in fluctuation of Angle Ax with increasing experimental strain. Experimental strain ratios range from 1.000 (e=0.0%) to 1.389 (e=20.0%). Maximum extension direction oriented at 0°. Dash line is for simulated deformation. Samples were deformed under dry experimental conditions with confining pressures of 200 Mpa, strain rate of 10^{-5}/s and temperatures of 135°C.

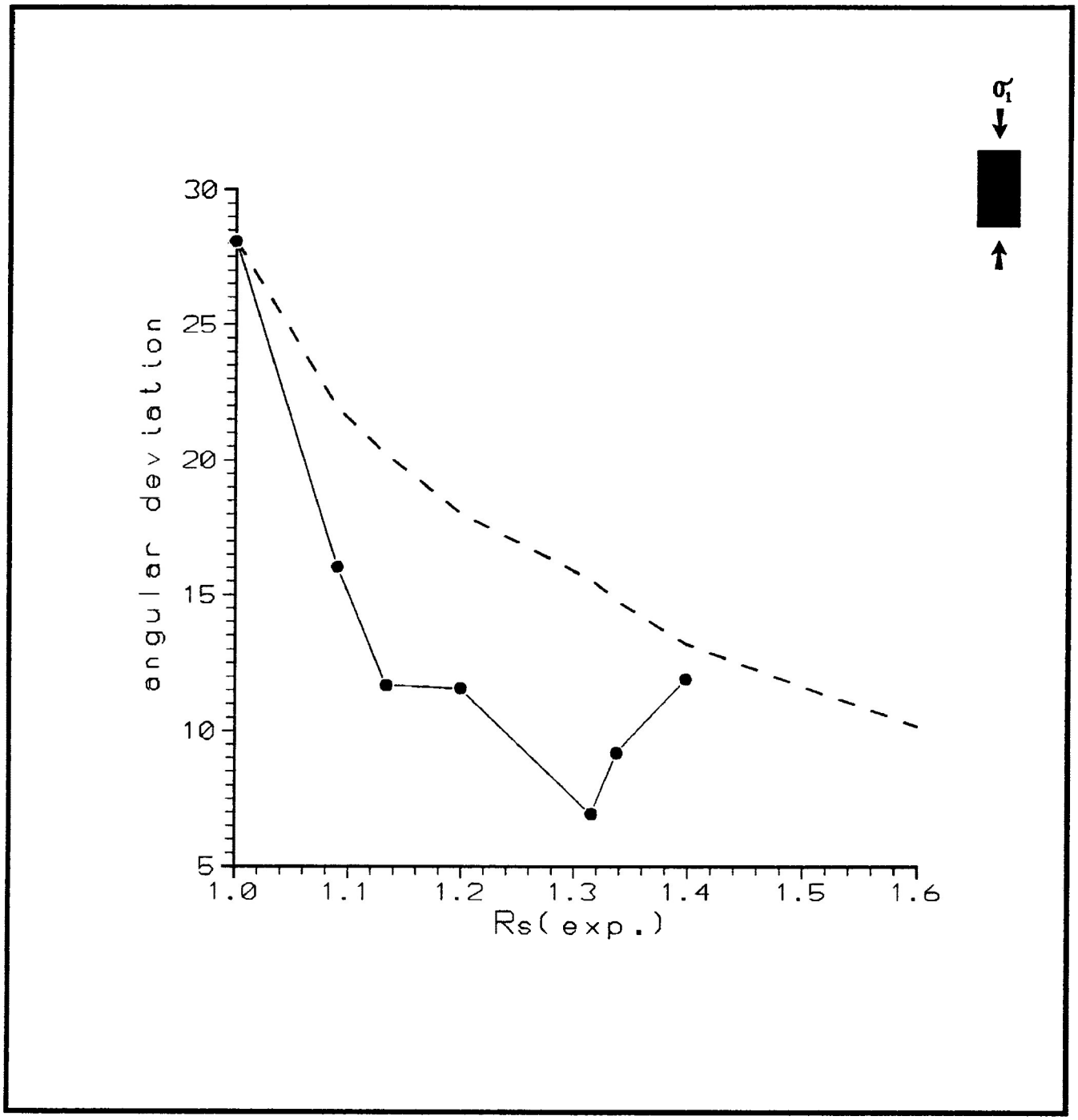

Figure 6.18 Variations in angular deviation of Angle Ax (ϕ) with increasing experimental strain. Experimental strain ratios range from 1.000 (e=0.0%) to 1.389 (e=20.0%). Dash line is for simulated deformation. Samples were deformed under dry experimental conditions with confining pressures of 200 Mpa, strain rate of 10^{-5}/s and temperatures of 135°C.

A change in angular deviation is observed with increasing strain and is presented in figure 6.18. In the figure there is a rapid decrease in angular deviation between experimental strain ratios of 1.000 and 1.133, and a less dramatic decrease between experimental strain ratios of 1.133 and 1.315. The decrease in angular deviation is reflected in a rapid development of a PDO at low strain, with respect to the long axis of deformed ooids. At higher strains there is an increase in angular deviation reflecting the development of late stage heterogeneous strain.

b) R_f frequency distributions of ooids grains with increasing strain.

Changes in R_f with strain is presented in figure 6.19a-g. As strain increases the distribution of R_f becomes more lognormal. The range of R_f values increase from 1.1 to 2 in the undeformed state to 1.1 to 2.9 at 20.0% shortening. The mean R_f and standard deviation of the R_f distribution are presented in figure 6.20. The increase in R_f in the plane of observation is similar to that observed in the simulated deformation of the previous section.

c) R_f/ϕ diagrams for deformed ooids

R_f/ϕ distributions of ooid grains are presented in figure 6.21a-g for dry experimental conditions. The R_f/ϕ diagrams are characterized by the rapid development of moderate to good R_f/ϕ distributions as strain increases. The R_f/ϕ distributions involve the concentration of ooid grain for all R_f values in the development of the PDO, especially for ooids of low R_f values. The distribution is enhanced by the alignment of ooid grains with high R_f values at moderate strains perpendicular to σ_1 orientation.

The distributions remain symmetrical about the known

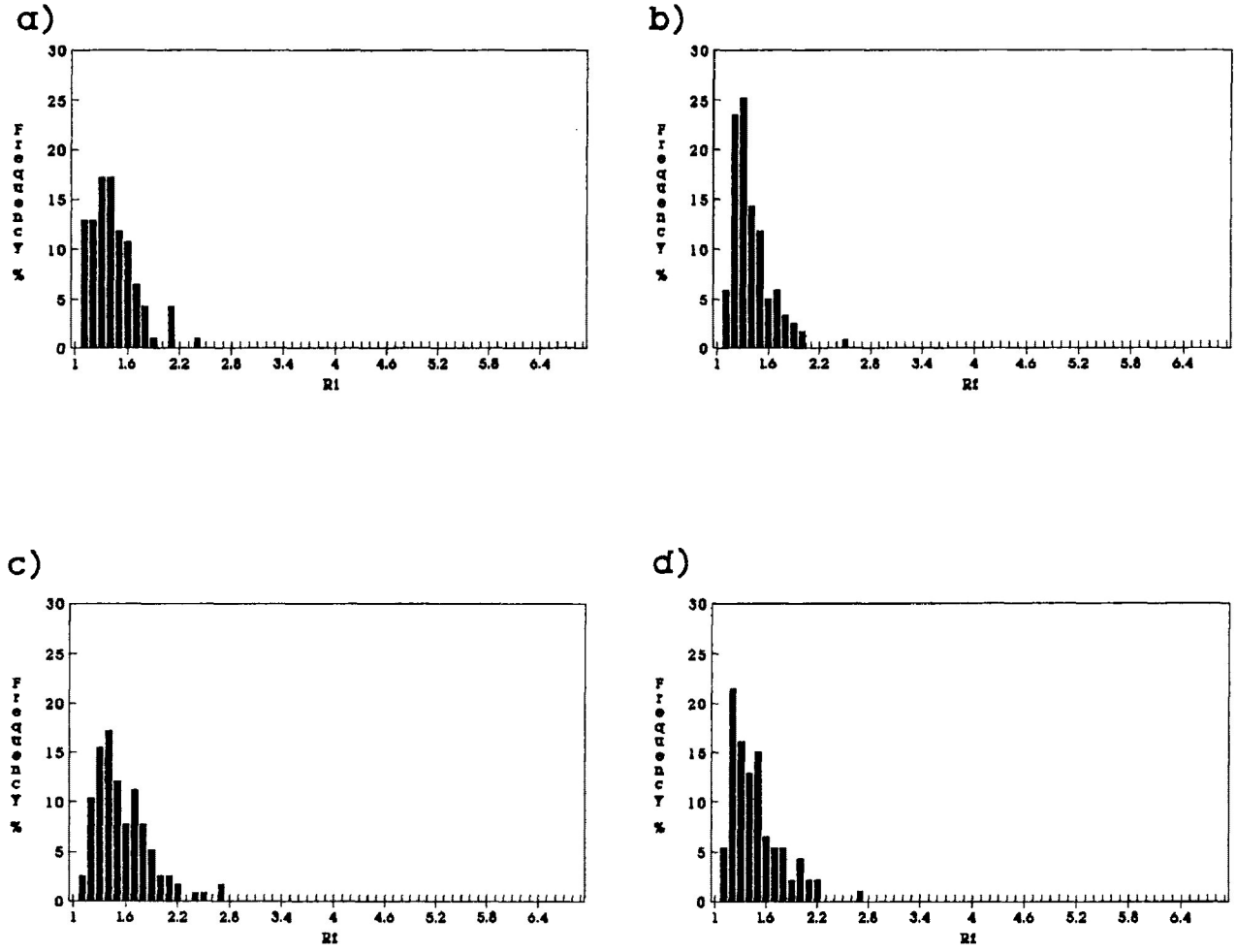

Figure 6.19a-g Frequency distribution of R_f for ooids in undeformed and deformed Ancaster Limestone. Experimental strain ratios range from 1.000 (e=0.0%) to 1.389 (e=20.0%). Samples were deformed under dry experimental conditions with confining pressures of 200 Mpa, strain rate of 10^{-5}/s and temperatures of 135°C. Measurements taken from the X/Z principal plane.

a) ANC-87 (R_s=1.000 (e=0.0%))
b) JL-1 (R_s=1.090 (e=5.6%))
c) JL-5 (R_s=1.133 (e=8.0%))
d) JL-6 (R_s=1.199 (e=11.4%))
e) JL-3 (R_s=1.315 (e=16.7%))
f) JL-4 (R_s=1.337 (e=17.6%))
g) JL-7 (R_s=1.398 (e=20.0%))

e)

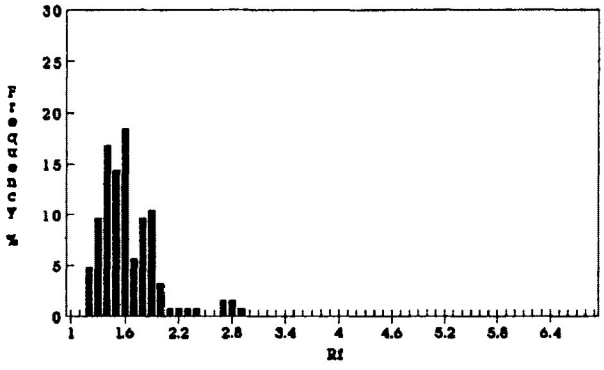
Frequency %
30
25
20
15
10
5
0
1
1.6
2.2
2.8
3.4
4
4.6
5.2
5.8
6.4
Rf

f)

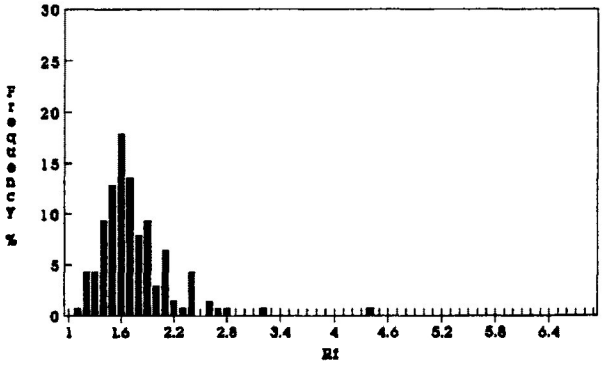
Frequency %
30
25
20
15
10
5
0
1
1.6
2.2
2.8
3.4
4
4.6
5.2
5.8
6.4
Rf

g)

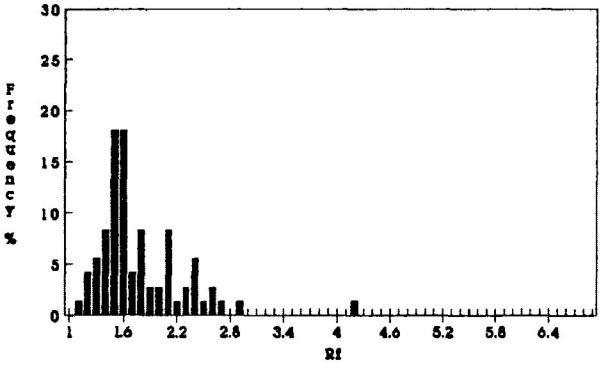
Frequency %
30
25
20
15
10
5
0
1
1.6
2.2
2.8
3.4
4
4.6
5.2
5.8
6.4
Rf

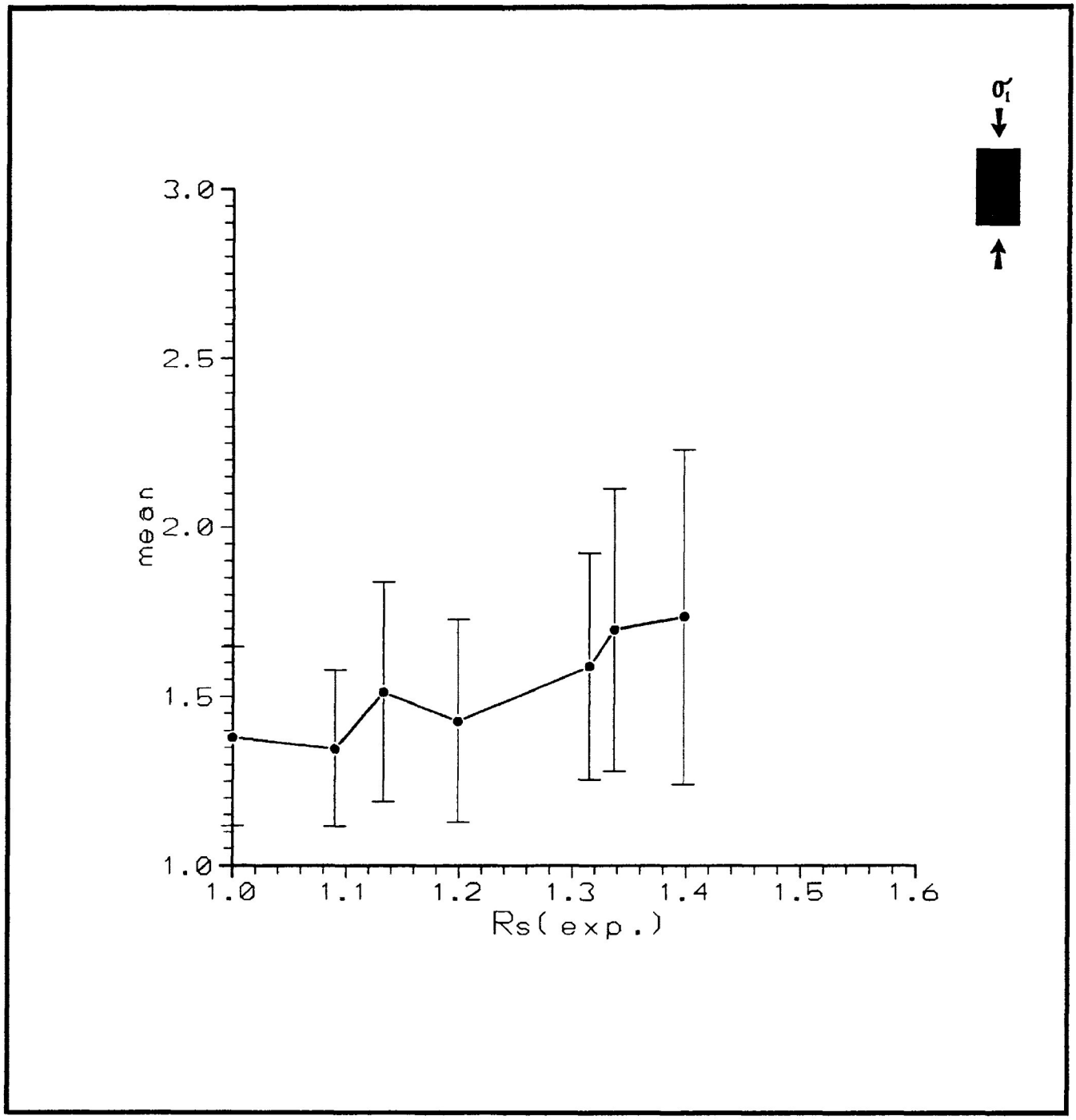

Figure 6.20 Variations in mean and standard deviation of R_f with increasing experimental strain. Experimental strain ratios range from 1.000 (e=0.0%) to 1.389 (e=20.0%). Samples were deformed under dry experimental conditions with confining pressures of 200 Mpa, strain rate of 10^{-5}/s and temperatures of 135°C.

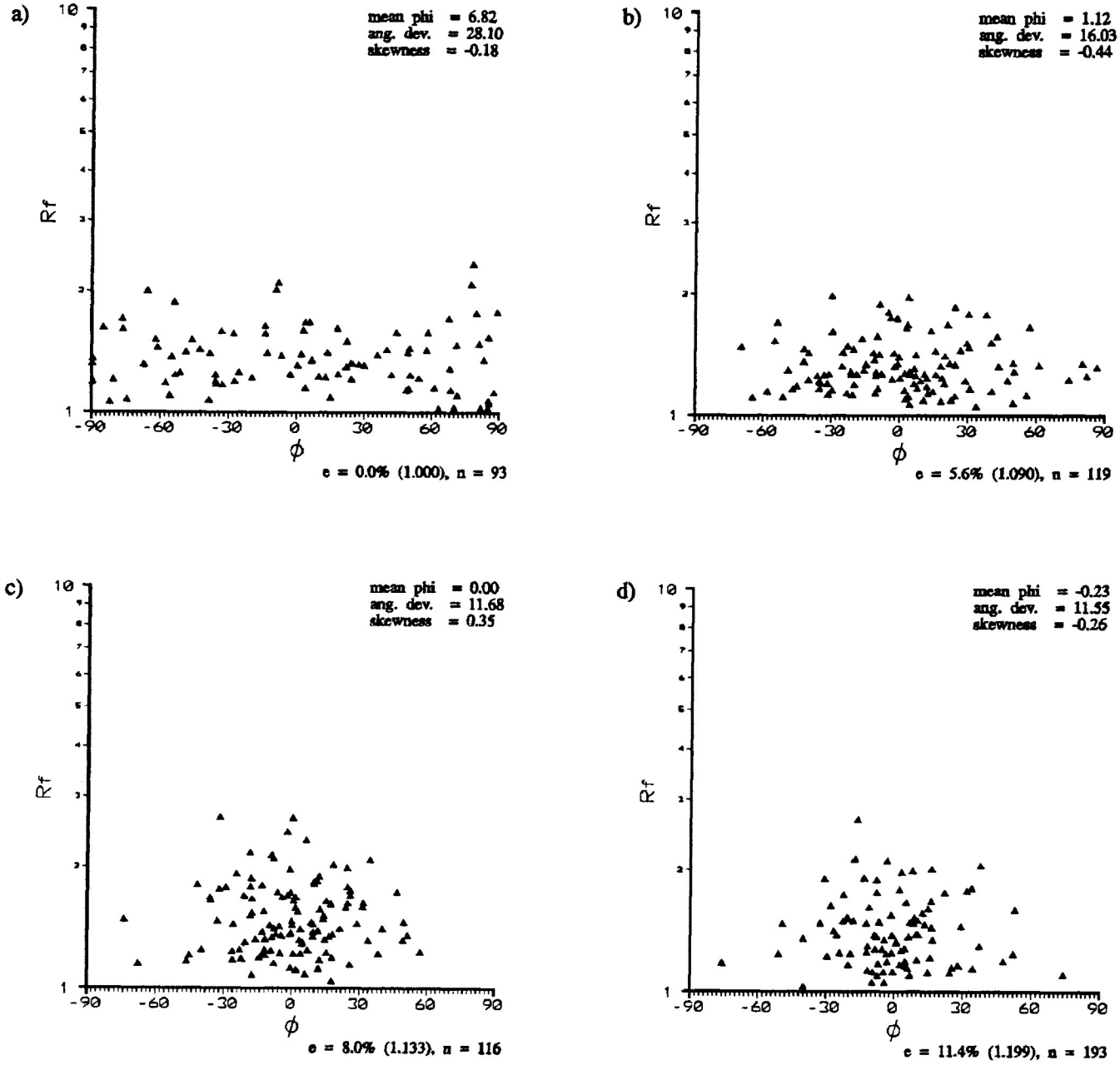

Figure 6.21a-g R_f/ϕ diagrams for ooids in undeformed and deformed Ancaster Limestone. Experimental strain ratios range from 1.000 (e=0.0%) to 1.389 (e=20.0%). Maximum extension direction oriented at 0°. Samples were deformed under dry experimental conditions with confining pressures of 200 Mpa, strain rate of 10^{-5}/s and temperatures of 135°C. Measurements taken from the X/Z principal plane.

a) ANC-87 (R_s=1.000 (e=0.0%))
b) JL-1 (R_s=1.090 (e=5.6%))
c) JL-5 (R_s=1.133 (e=8.0%))
d) JL-6 (R_s=1.199 (e=11.4%))
e) JL-3 (R_s=1.315 (e=16.7%))
f) JL-4 (R_s=1.337 (e=17.6%))
g) JL-7 (R_s=1.398 (e=20.0%))

e)

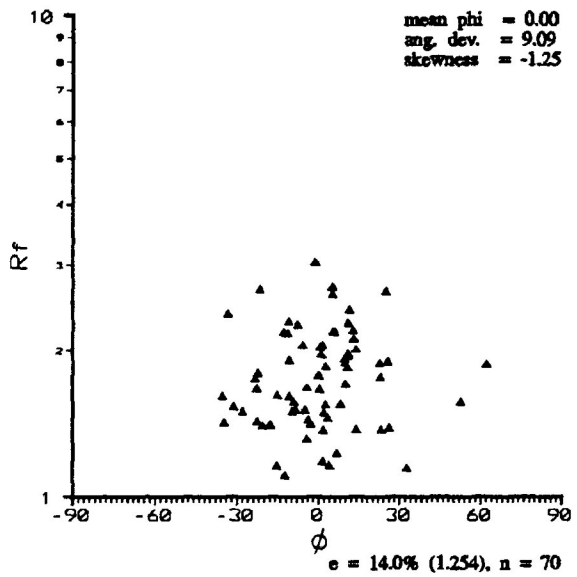
mean phi = 0.00
ang. dev. = 9.09
skewness = -1.25
Rf
ϕ
e = 14.0% (1.254), n = 70

f)

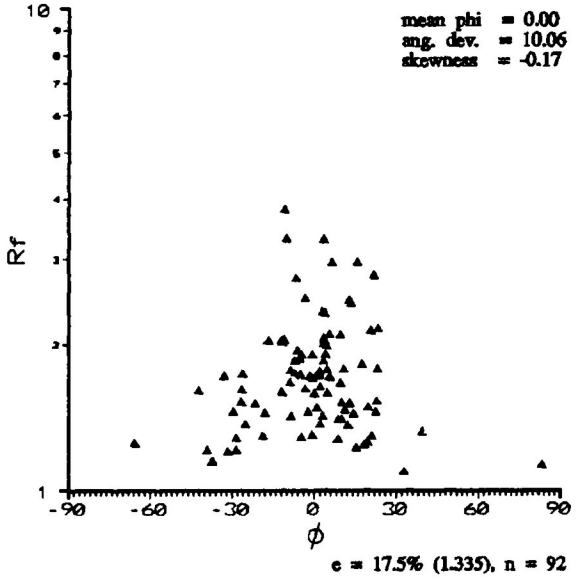
mean phi = 0.00
ang. dev. = 10.06
skewness = -0.17
Rf
ϕ
e = 17.5% (1.335), n = 92

g)

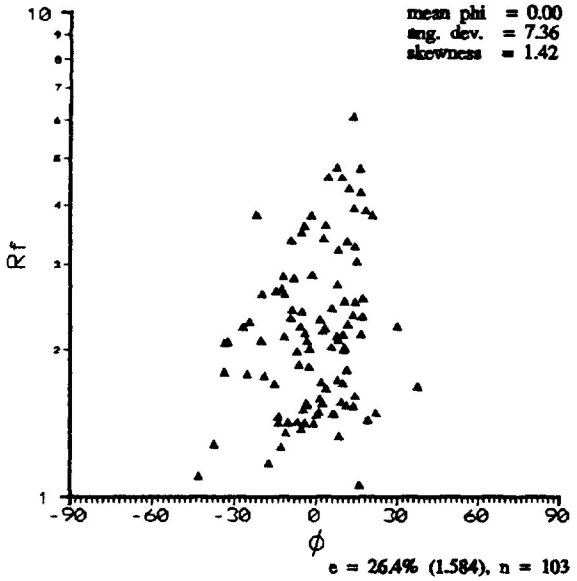
mean phi = 0.00
ang. dev. = 7.36
skewness = 1.42
Rf
ϕ
e = 26.4% (1.584), n = 103

principal extension direction for strains below 17.6% shortening. At higher strains the R_f/ϕ distribution begins to spread out and become slightly asymmetric. This is most likely the result of the embryonic development of conjugate fractures at 30 to 40° to the σ_1 direction.

d) Comparison between strain analysis methods based on ooid grains in the dry experimental studies

Figure 6.22 presents the comparison of the Robin's method, linearization method and harmonic mean methods of strain analysis for ooid grains. Since most of the strain in the experimentally deformed limestone is taken up by the ooids (the matrix, at least at low strains, is relatively undeformed and characterized by large grains with thin lamellae of low to moderate lamellae index) the estimates of strain are overestimates of the experimental bulk strain.

Robin's method exhibits an overestimate of strain as the experimental bulk strain increases. For the linearization method the estimate of strain is a larger overestimate than Robin's method. The overestimate by the linearization method increases as strain increases. At all strains there is a large difference between the linearization method and the Robin's method, and this difference increases as strain increases. The estimate of the strain ratio by the linearization method become greater than that of the harmonic mean for experimental bulk strains above 1.15. The reasons for the overestimate and the large difference between the Robin's and linearization methods may be the result of rigid body rotation of the ooid particles into a strong PDO at low bulk strains and strain heterogeneity between ooid and matrix. Robin's method gives the best approximations of the experimental strain ratios for the three methods studied.

Standard deviation for Robin's method, linearization

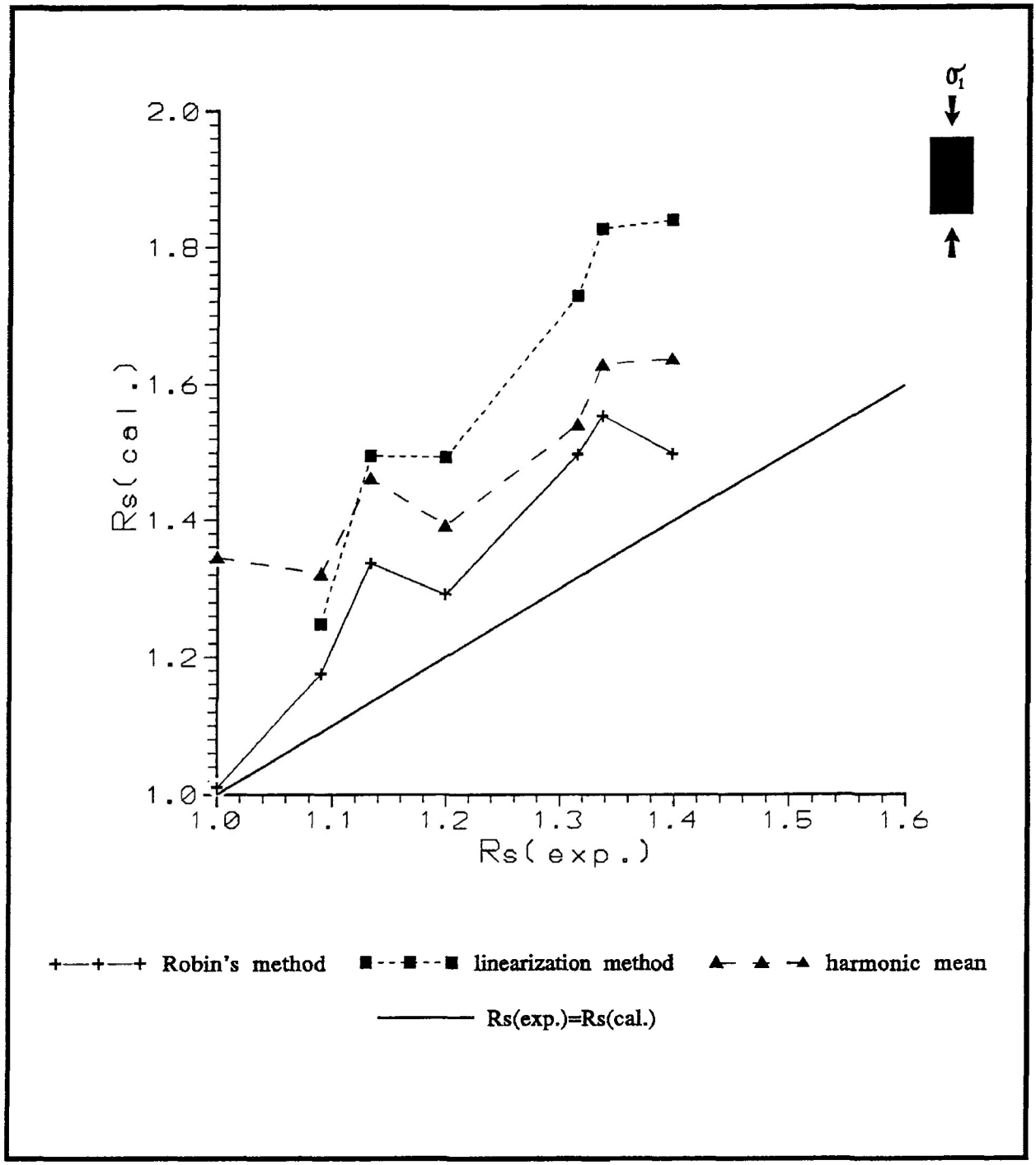

Figure 6.22 Comparison of the estimate of strain ratio (R_s (cal.)) calculated from Robin's method (cross), linearization method (square) and harmonic mean (triangle) to the experimental strain (R_s (exp.)) from ooids in samples of deformed Ancaster Oolitic limestone. The Ancaster Oolitic limestone has been deformed to experimental strain ratios less than 1.398 under dry experimental conditions (P_c=200 Mpa, strain rate of 10^{-5}/s) at a temperature of approximately 135°C. Broad line represents the line of (R_s(exp.))=(R_s(cal.)).

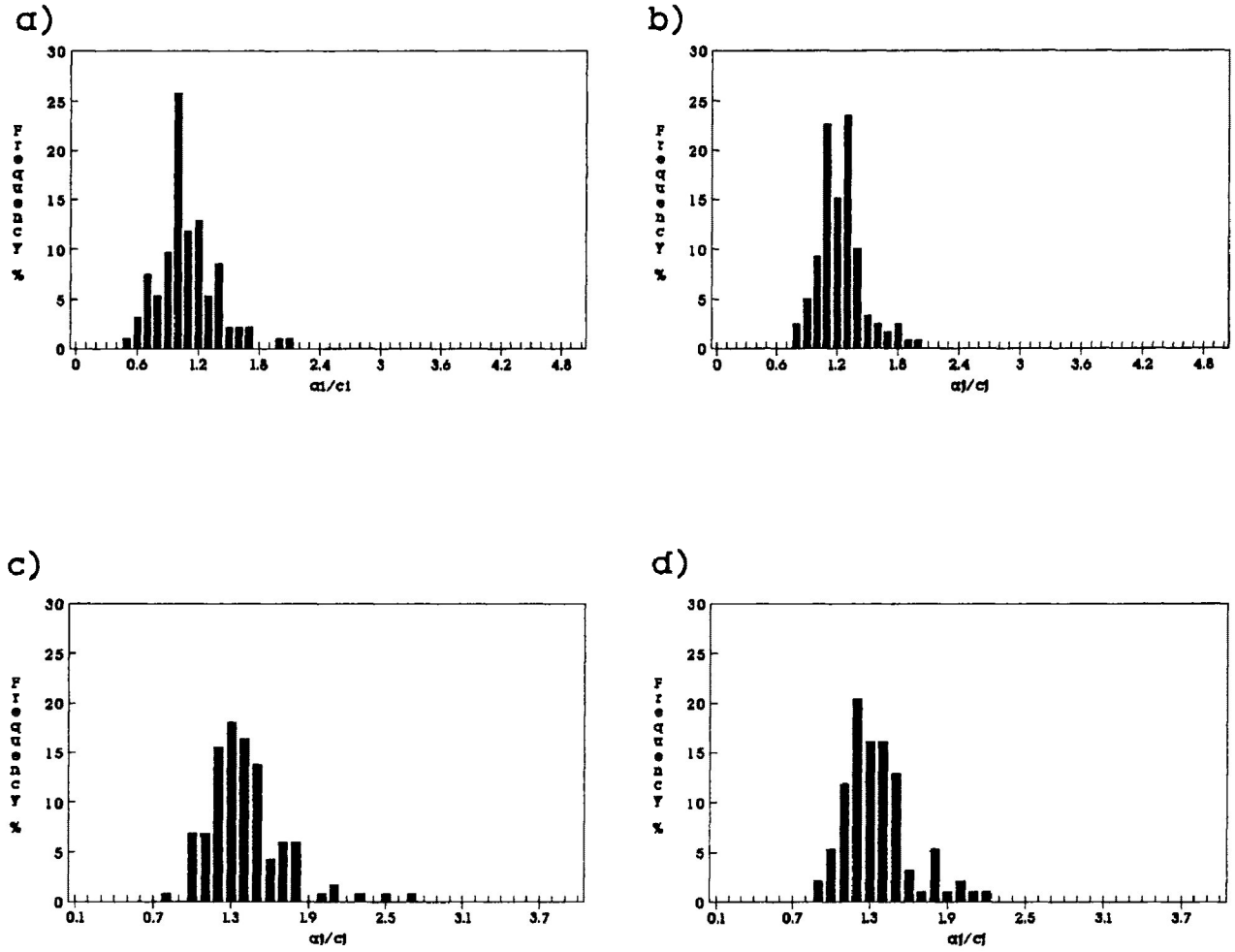

Figure 6.23a-g Frequency distribution of a_j/c_j ratios for ooids in undeformed and deformed Ancaster Limestone. Experimental strain ratios 1.000 (e=0.0%) to 1.389 (e=20.0%). Samples were deformed under dry experimental conditions with confining pressures of 200 Mpa, strain rate of 10^{-5}/s and temperatures of 135°C. Measurements taken from the X/Z principal plane.

a) ANC-87 (R_s=1.000 (e=0.0%))
b) JL-1 (R_s=1.090 (e=5.6%))
c) JL-5 (R_s=1.133 (e=8.0%))
d) JL-6 (R_s=1.199 (e=11.4%))
e) JL-3 (R_s=1.315 (e=16.7%))
f) JL-4 (R_s=1.337 (e=17.6%))
g) JL-7 (R_s=1.398 (e=20.0%))

e)

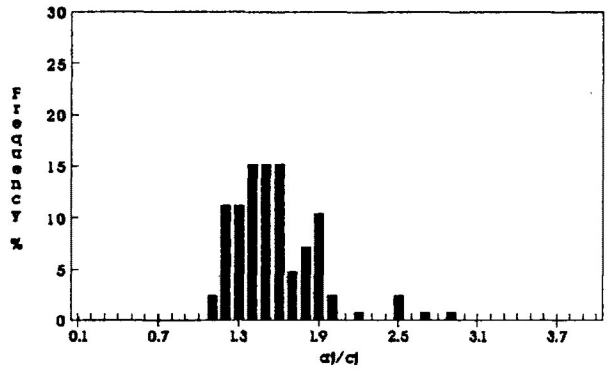
Frequency %
30
25
20
15
10
5
0
0.1
0.7
1.3
1.9
2.5
3.1
3.7
αj/cj

f)

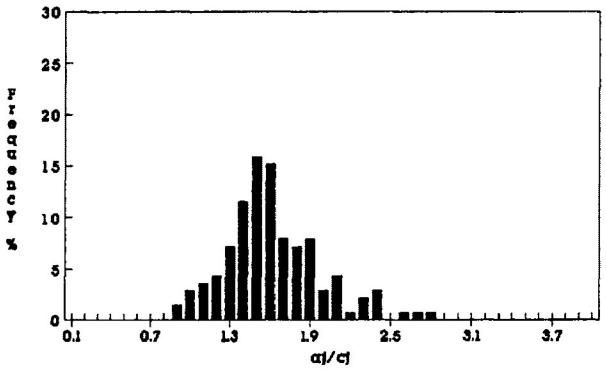
Frequency %
30
25
20
15
10
5
0
0.1
0.7
1.3
1.9
2.5
3.1
3.7
αj/cj

g)

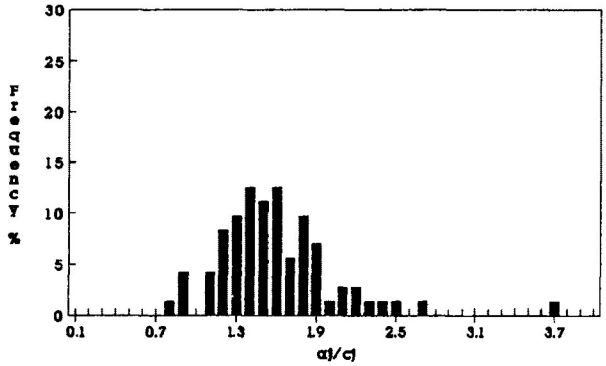
Frequency %
30
25
20
15
10
5
0
0.1
0.7
1.3
1.9
2.5
3.1
3.7
αj/cj

method and the harmonic mean method were calculated and are presented in table 6.3. For the linearization method the calculations of standard deviation that yield confidence brackets that extend into bulk strains estimates less than 1.000 are not given.

Comparison of the a_j/c_j ratio necessary to calculate Robin's method of strain for dry experimental conditions is presented in figure 6.23a-g. It is observed from the figures that the a_j/c_j becomes increasingly lognormal in distribution as strain increases. However, for the first few % strain this distribution is approximately normal in distribution. The best estimates of tectonic strain are at low bulk deformations (<10% shortening), as a result of the normal distributions of the a_j/c_j ratios, a condition necessary for the determination of tectonic strain by Robin's method.

e) <u>Homogeneity coefficient for ooid grains</u>

The homogeneity coefficient r^2 was calculated as the best fit straight line through the point distribution of long vs. short axis of the deformed ooids of the data presented in figure 6.24a-g. The variation in homogeneity coefficient with increasing bulk experimental strain is presented in figure 6.25. It is observed in the figure that there is a decrease in the homogeneity coefficient with strain. The values range from 0.74 in the undeformed state to the lowest value of 0.29 at 17.6% shortening. These r^2 values are similar to those determined by Wood and Holm (1980). Calculation of strain by the axial ratio method (Ramsay, 1969) is presented in figure 6.26. The strain estimate from this method is a 13% to 23% overestimate of the actual experimental bulk strain.

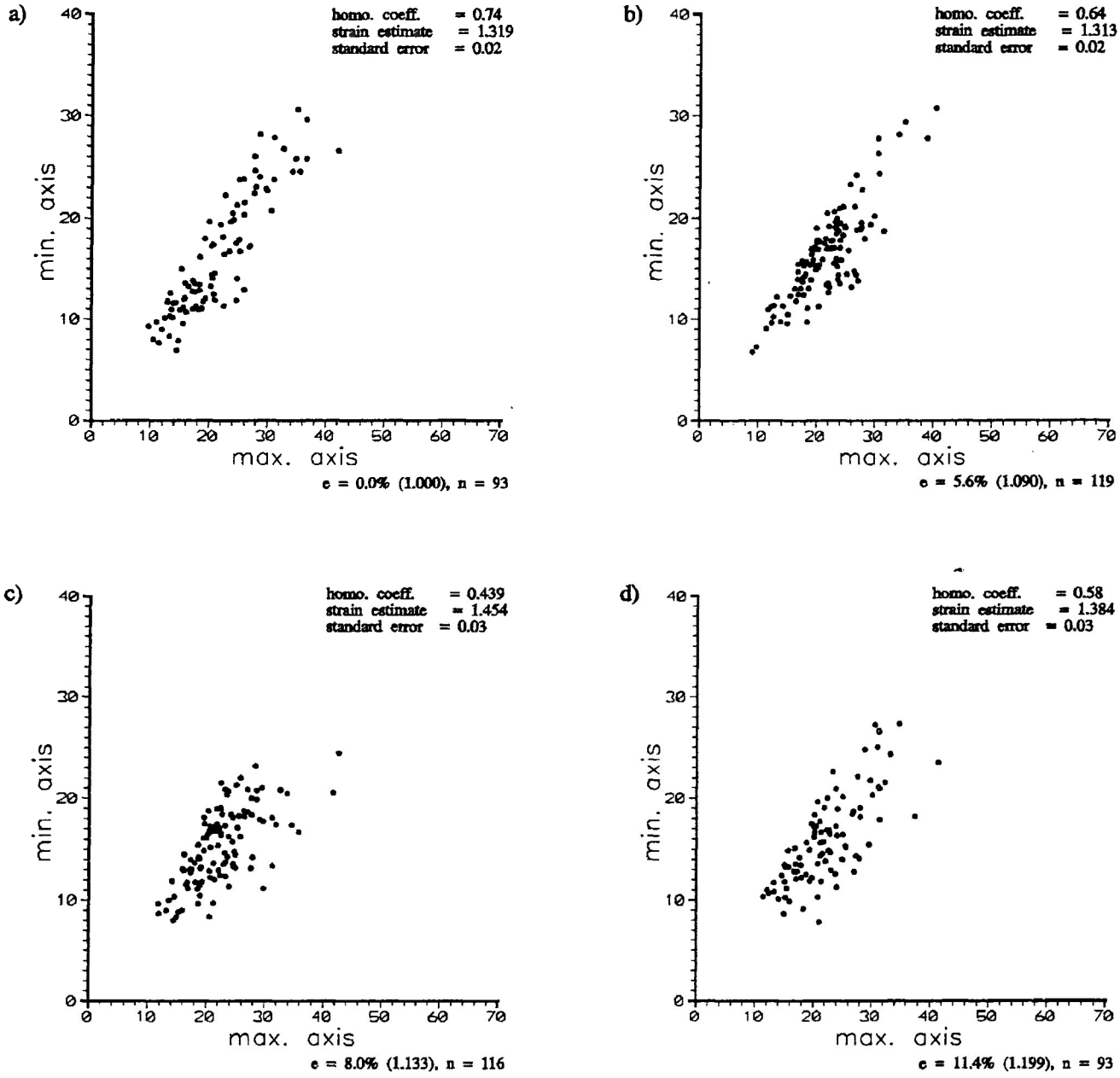

Figure 6.24a-g Distribution of maximum and minimum axis for ooids in undeformed and deformed Ancaster Limestone. Experimental strain ratios range from 1.000 (e=0.0%) to 1.389 (e=20.0%). Samples were deformed under dry experimental conditions with confining pressures of 200 Mpa, strain rate of 10^{-5}/s and temperatures of 135°C. Measurements taken from the X/Z principal plane. Homogeneity coefficient, strain estimate from Max/Min method (Ramsay, 1969) and error are also given.

a) ANC-87 (R_s=1.000 (e=0.0%))
b) JL-1 (R_s=1.090 (e=5.6%))
c) JL-5 (R_s=1.133 (e=8.0%))
d) JL-6 (R_s=1.199 (e=11.4%))
e) JL-3 (R_s=1.315 (e=16.7%))
f) JL-4 (R_s=1.337 (e=17.6%))
g) JL-7 (R_s=1.398 (e=20.0%))

e)

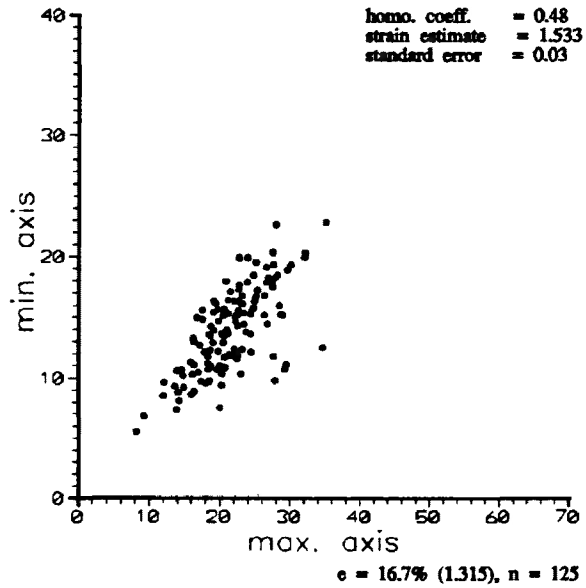

e = 16.7% (1.315), n = 125

f)

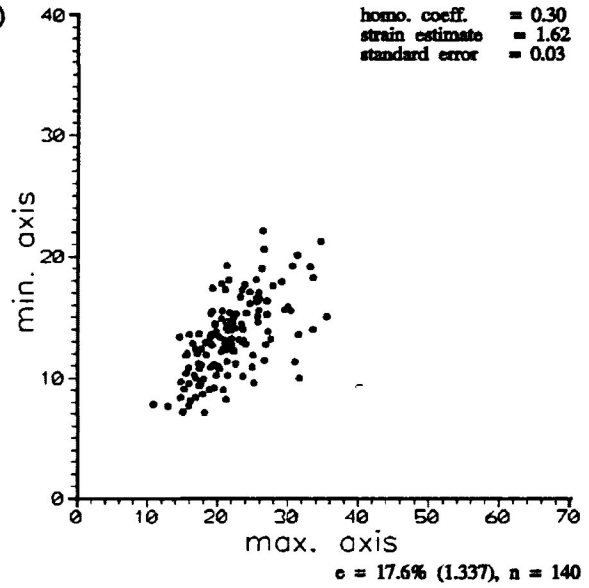

e = 17.6% (1.337), n = 140

g)

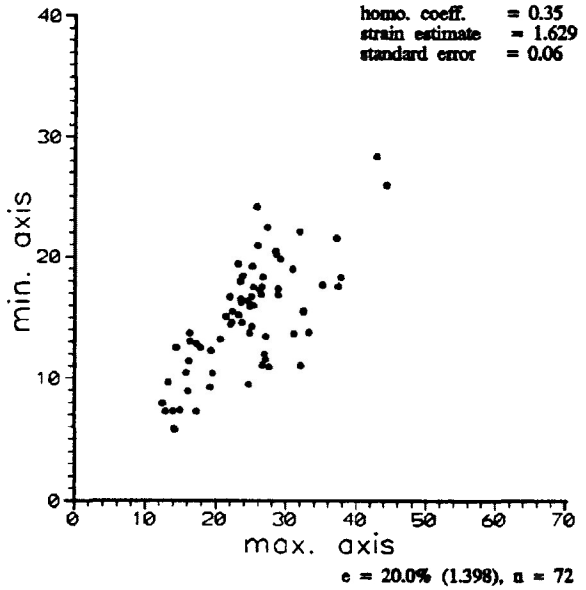

e = 20.0% (1.398), n = 72

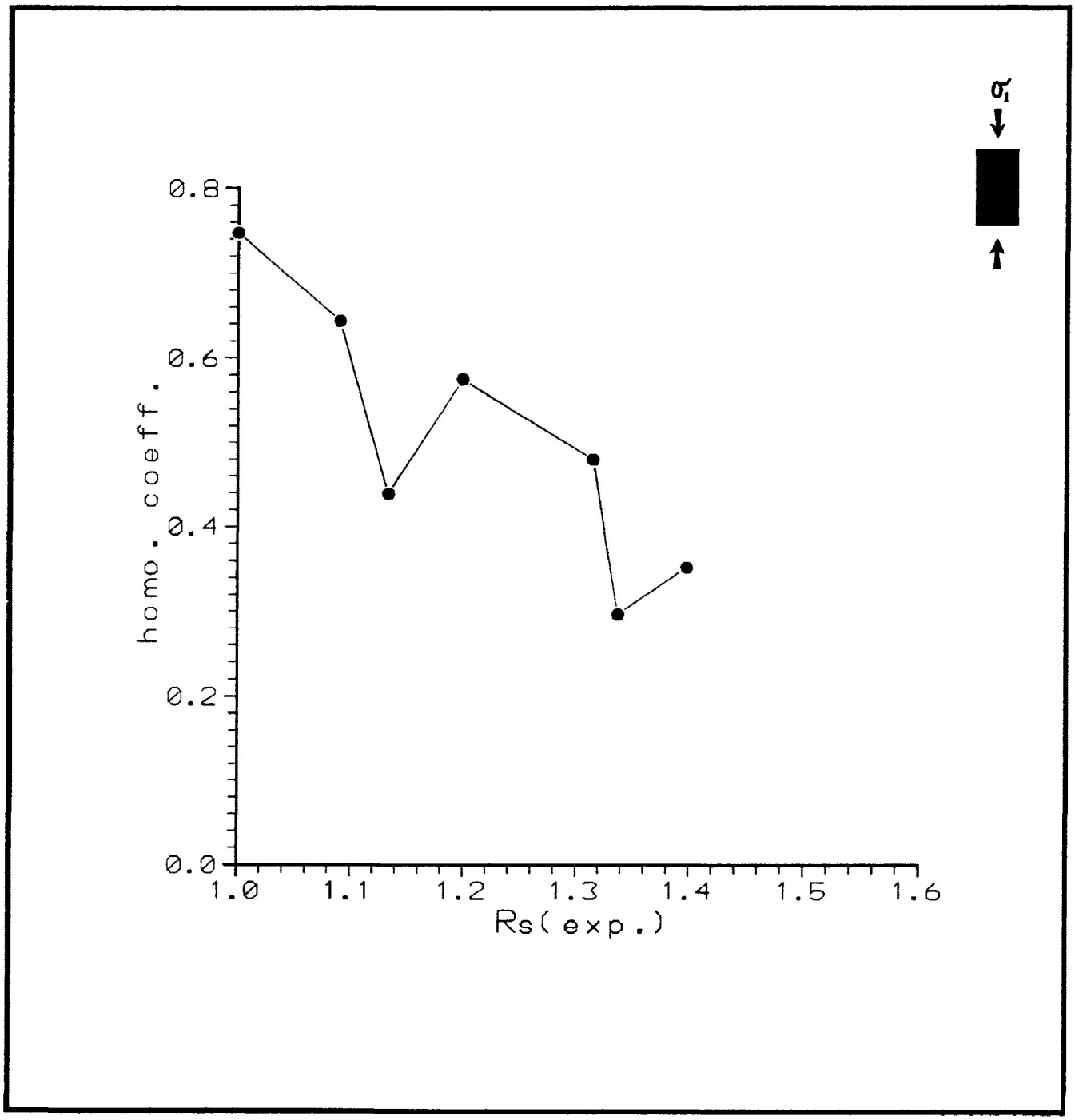

Figure 6.25 Variations homogeneity coefficient increasing experimental strain. Experimental strain ratios range from 1.000 (e=0.0%) to 1.389 (e=20.0%). Samples were deformed under dry experimental conditions with confining pressures of 200 Mpa, strain rate of 10^{-5}/s and temperatures of 135°C.

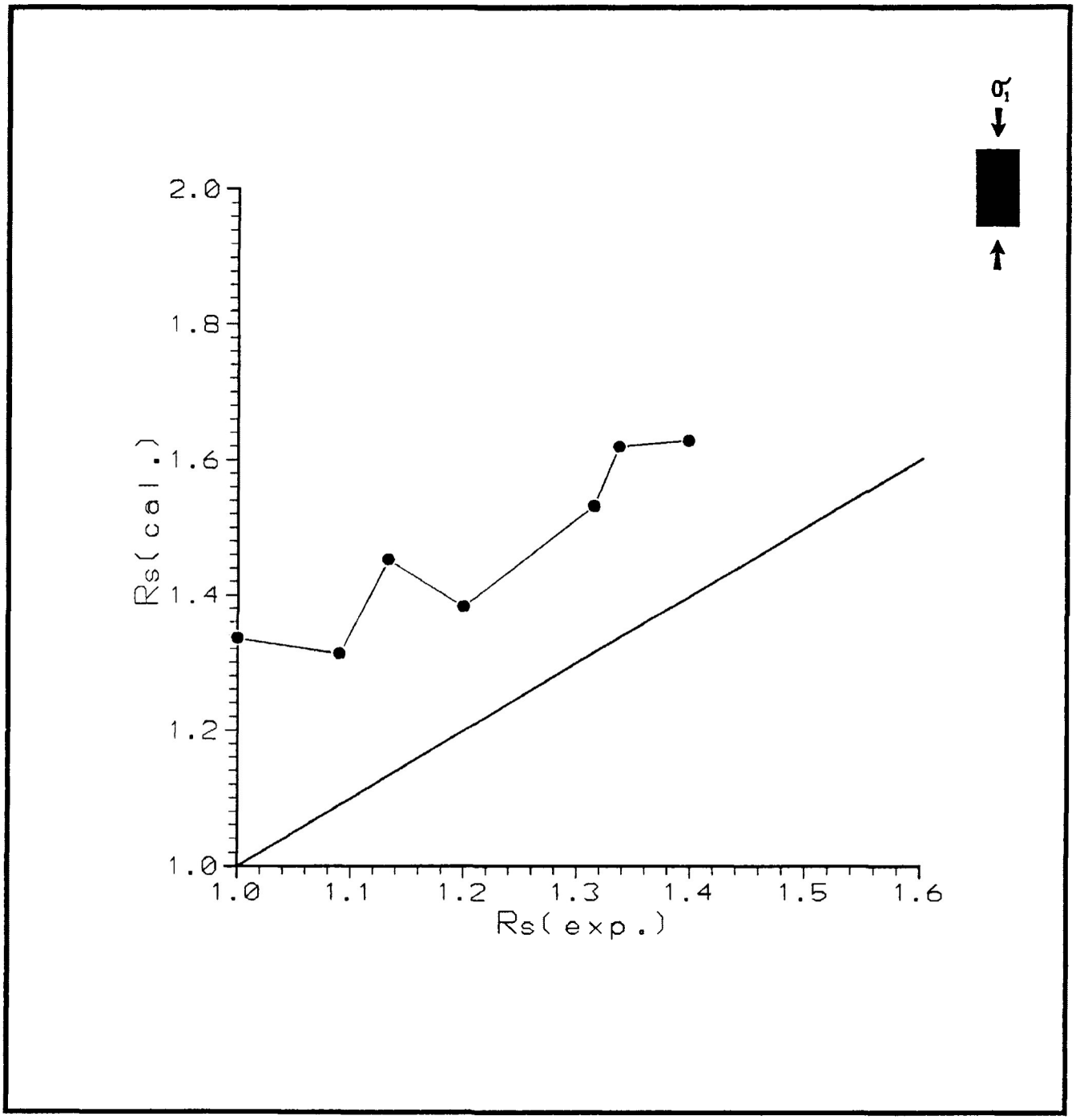

Figure 6.26 Estimate of strain by Max/Min method (Ramsay, 1969). Equivalent Rs is represented by the dark solid line. Experimental strain ratios range from 1.000 (e=0.0%) to 1.389 (e=20.0%). Samples were deformed under dry experimental conditions with confining pressures of 200 Mpa, strain rate of 10^{-5}/s and temperatures of 135°C.

f) Deformation mechanism of ooid grains

It may be suggested that a major component of the deformation of the ooids in the limestone, under dry experimental conditions, is the result of rigid rotation of smaller ooid grains in the coarser calcite cement. No twinning is observable in the fine grain matrix of the ooid grain. Bent twinning and intense deformation of the drusy cement around the ooid periphery may suggest rigid body rotation of these particles. The small change in the range of R_f, rapid decrease in the fluctuation of ϕ and angular deviation as strain increases also suggests that this is the case. Some strain observed in the ooids may be expressed by particulate flow in the fine grain ooid matrix as strain increases. The rigid rotation of ooids may cause many grains to become oriented parallel to the extension direction subsequently generating an overestimate of strain by the Robin's and especially the linearization method.

6.7 Analysis of deformed ooids under wet experimental conditions (P_c=200 Mpa, P_f=180 to 195 Mpa)

In wet experimental pure shear deformation a comparison of orientational and dimensional frequency distributions and R_f/ϕ diagrams were made from 7 samples increasing in experimental strain ratio from 1.000 (e=0.0%) to 1.584 (e=26.4%) (Appendix A).

a) Frequency distributions of ϕ for ooid grains with increasing strain

Figure 6.27a-g present the orientational frequency distribution of ϕ (Angle Ax) for ooid grains. In each diagram the maximum extension direction is oriented at 0°, perpendicular to the axial length of the undeformed test cylinder and parallel to the bedding surface. In figure 6.27a-g there is observed, in the long dimension of the ooid grains, an increasing development of a strong PDO for samples experimentally deformed from 0.0% (R_s=1.000) to 26.4% (R_s=1.584) shortening. The PDO aligns into an orientation perpendicular to experimental σ_1 (parallel to the long axis of the test cylinder). This is first observable at low strains (e=5.2% (R_s=1.083)) and is continually observed as strain increases.

The developing PDO is characterized by the overall decrease in F. A rapid decrease in the fluctuation is observed to occur between 5 and 10% shortening from 170° to 100°. As strain increases from 14.0% to 26.4% shortening, there is observed a continued decrease in F and the development of a noticeably skewness (-ve) in the distribution of highly strained samples (*i*.e., Sample J1-12 (e=26.4%)) (Fig. 6.28). The increase in skewness at high strains may be attributed to the development of embryonic conjugate ductile shear zones at 30° to 40° to the experimental σ_1 orientation.

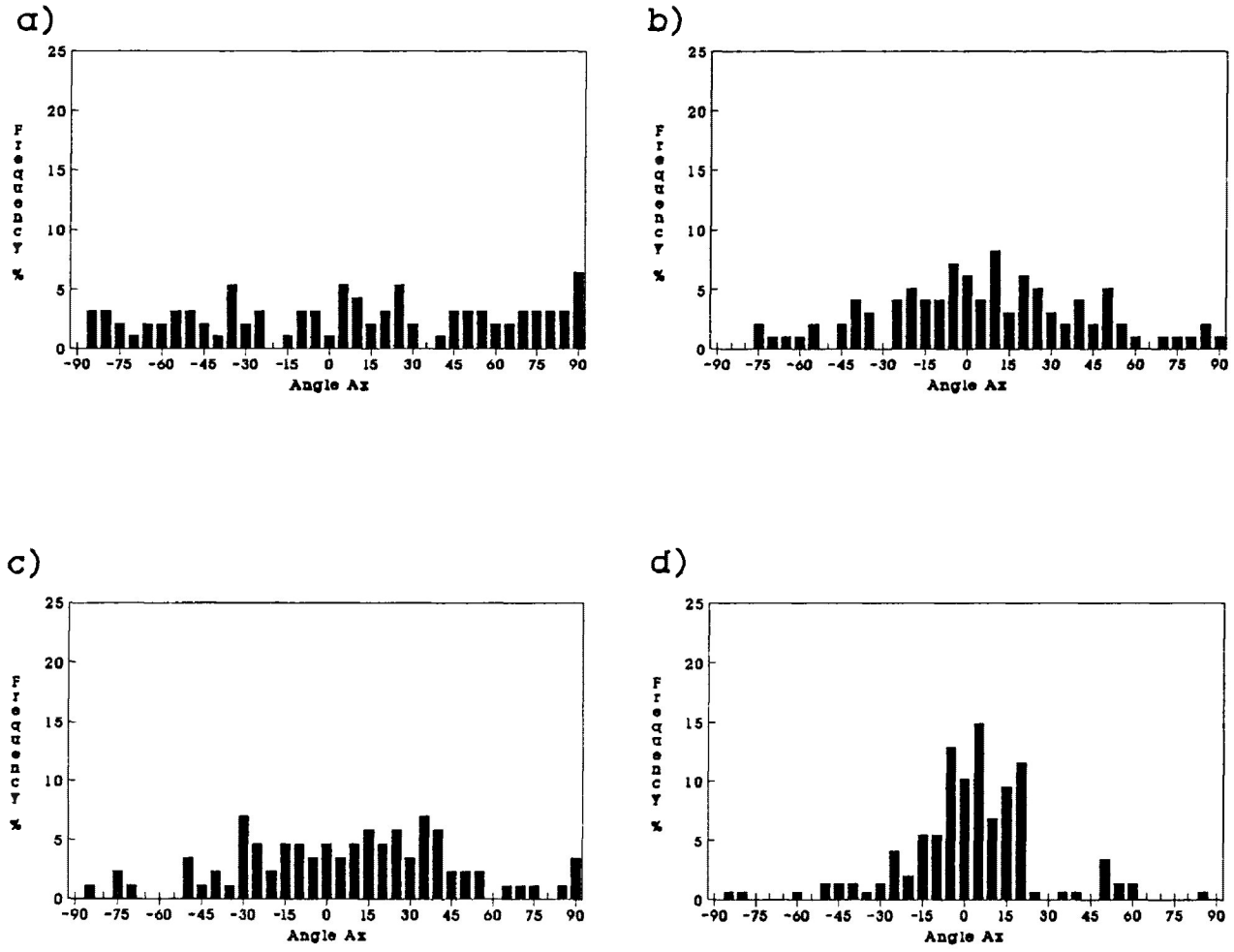

Figure 6.27a-g Frequency distribution of Angle Ax (ϕ) orientations of ooids in undeformed and deformed Ancaster Limestone. Experimental strain ratios range from 1.000 (e=0.0%) to 1.584 (e=26.4%). Maximum extension direction oriented at 0°. Samples were deformed under wet experimental conditions with confining pressures of 200 Mpa, strain rate of 10^{-5}/s and temperatures of 135°C. Pore fluid pressures were less than 60% of the confining pressure. Measurements taken from the X/Z principal plane.

a) ANC-87 (R_s=1.000 (e=0.0%))
b) JL-8 (R_s=1.083 (e=5.2%))
c) JL-13 (R_s=1.089 (e=5.5%))
d) JL-10 (R_s=1.133 (e=8.0%))
e) JL-9 (R_s=1.254 (e=14.0%))
f) JL-11 (R_s=1.335 (e=17.5%))
g) JL-12 (R_s=1.584 (e=26.4%))

e)

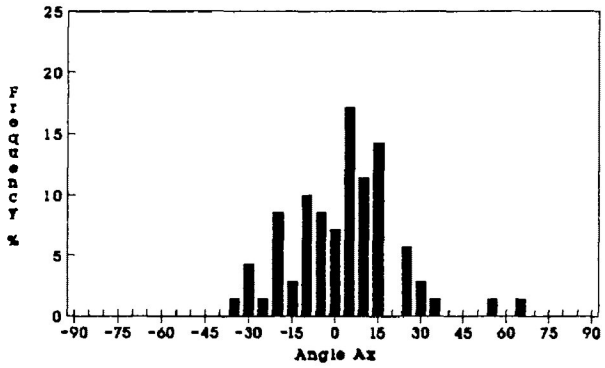
25
20
15
10
5
0
Frequency %
-90 -75 -60 -45 -30 -15 0 15 30 45 60 75 90
Angle Ax

fig35f

f)

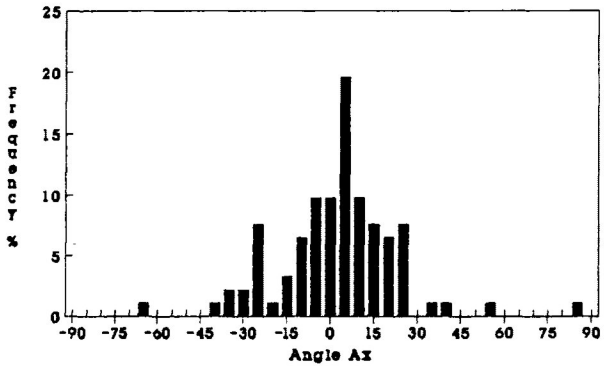
25
20
15
10
5
0
Frequency %
-90 -75 -60 -45 -30 -15 0 15 30 45 60 75 90
Angle Ax

g)

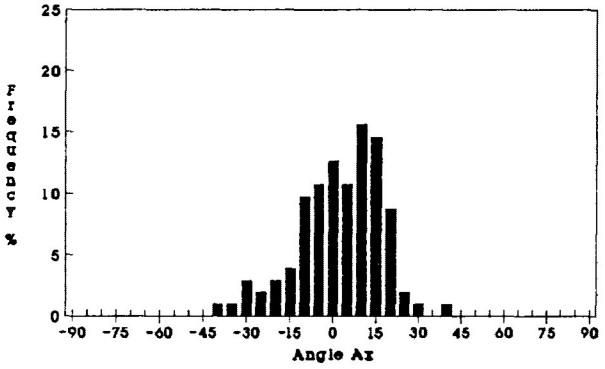
25
20
15
10
5
0
Frequency %
-90 -75 -60 -45 -30 -15 0 15 30 45 60 75 90
Angle Ax

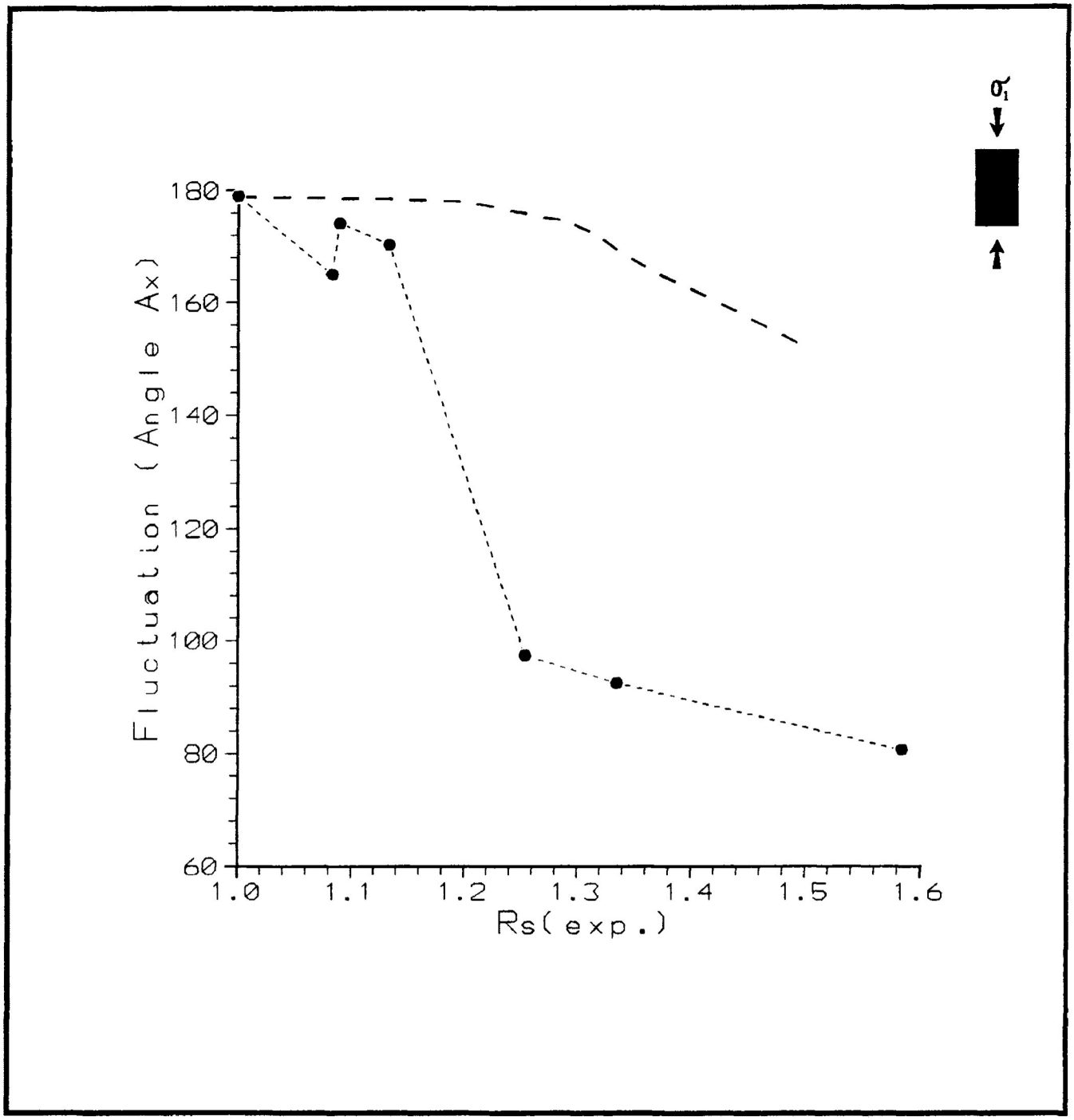

Figure 6.28 Variations in fluctuation of Angle Ax with increasing experimental strain. Experimental strain ratios range from 1.000 (e=0.0%) to 1.584 (e=26.4%). Maximum extension direction oriented at 0°. Dashed line is for simulated strain. Samples were deformed under wet experimental conditions with confining pressures of 200 Mpa, strain rate of 10^{-5}/s and temperatures of 135°C. Pore fluid pressures were less than 60% of the confining pressure.

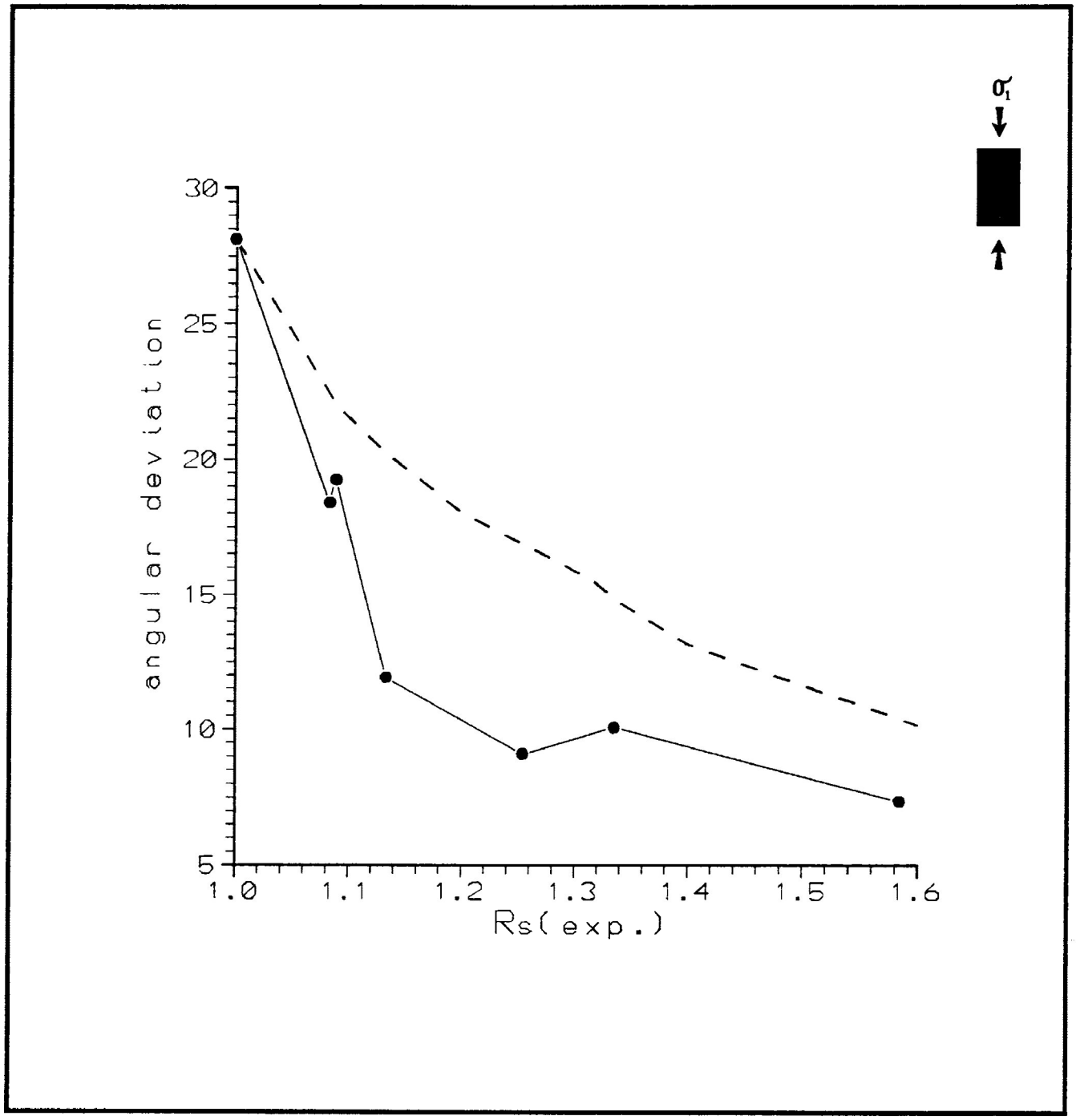

Figure 6.29 Variations in angular deviation of Angle Ax (ϕ) with increasing experimental strain. Experimental strain ratios range from 1.000 (e=0.0%) to 1.584 (e=26.4%). Dashed line is for simulated strain. Samples were deformed under wet experimental conditions with confining pressures of 200 Mpa, strain rate of 10^{-5}/s and temperatures of 135°C. Pore fluid pressures were less than 60% of the confining pressure.

In figure 6.29 there is a rapid overall decrease in angular deviation between experimental bulk strains of 1.000 and 1.133. A less dramatic decrease in angular deviation is observed between experimental bulk strains of 1.133 and 1.59. This overall decrease in angular deviation is reflecting a strong development of a PDO at low strain, with respect to the long axes of the deformed ooids.

b) R_f frequency distributions of ooid grains with increasing strain

Changes in R_f of ooid grains with strain is presented in figure 6.30 a-g. As strain increases the distribution of R_f becomes more lognormal. The range of R_f values increase from 1.1 to 2 in the undeformed state to 1.1 to 4.8 at 26.4% shortening. The mean R_f and standard deviation of the R_f distribution are presented in figure 6.31. The change in ooid shape as experimental strain increases in greater than that of the dry deformation conditions presented in the previous section.

c) R_f/ϕ diagrams for deformed ooids

The development of moderate R_f/ϕ distributions of ooid grains are presented in figure 6.32a-g for wet experimental conditions. The R_f/ϕ distributions are characterized by the concentration of ooid grain for medium to high R_f values in the development of the PDO. The distribution is enhanced by the alignment of elongated ooid grains of large R_f values at high strains perpendicular to σ_1 orientation.

The distributions remain reasonably symmetrical about the known principal extension direction for strains below 17.6% shortening. At higher strains the R_f/ϕ distribution begins to be slightly spread out and become asymmetric. This is most likely the result of the embryonic development of conjugate

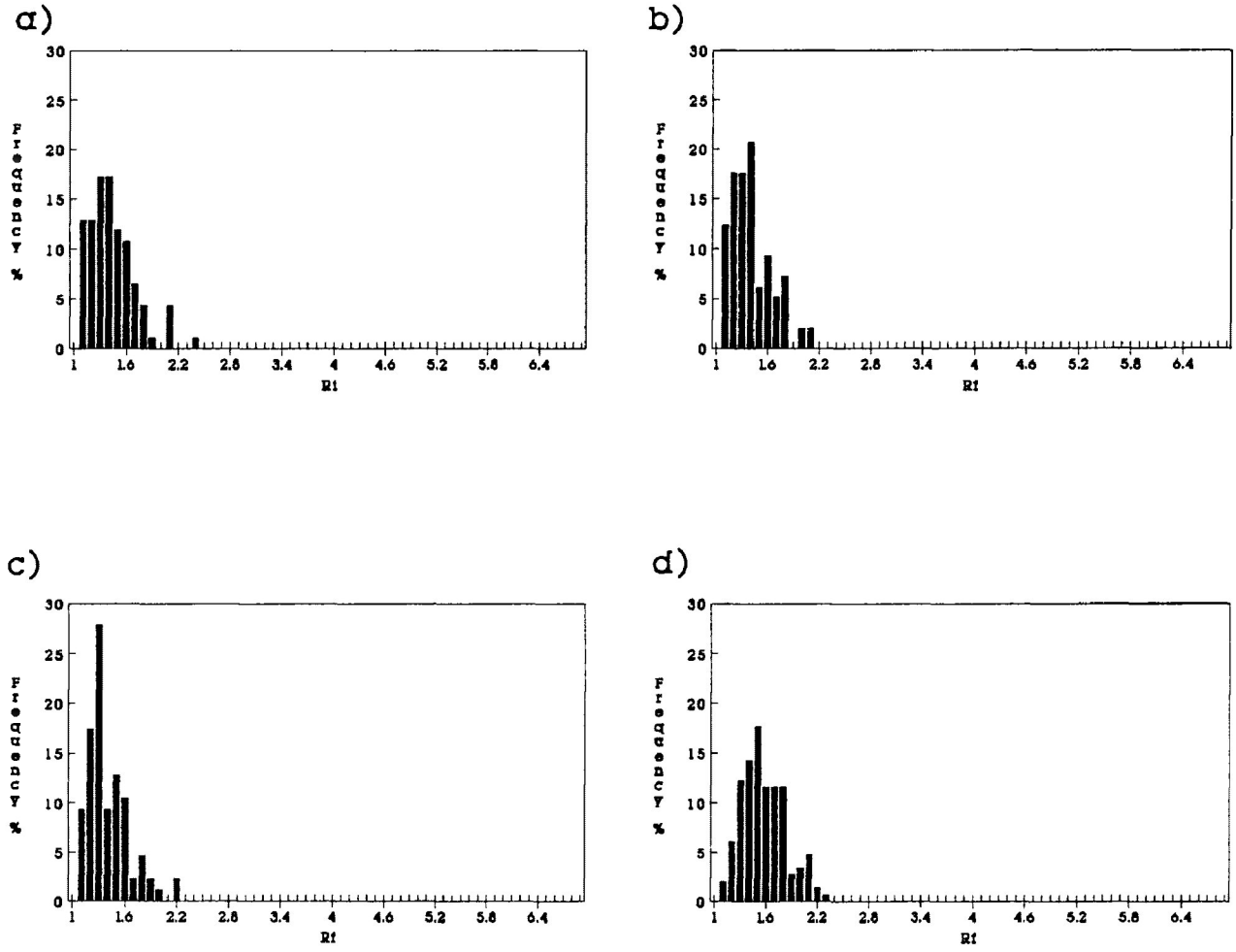

Figure 6.30a-g Frequency distribution of R_f for ooids in undeformed and deformed Ancaster Limestone. Experimental strain ratios range from 1.000 (e=0.0%) to 1.584 (e=26.4%). Samples were deformed under wet experimental conditions with confining pressures of 200 Mpa, strain rate of 10^{-5}/s and temperatures of 135°C. Pore fluid pressures were less than 60% of the confining pressure. Measurements taken from the X/Z principal plane.

a) ANC-87 (R_s=1.000 (e=0.0%))
b) JL-8 (R_s=1.083 (e=5.2%))
c) JL-13 (R_s=1.089 (e=5.5%))
d) JL-10 (R_s=1.133 (e=8.0%))
e) JL-9 (R_s=1.254 (e=14.0%))
f) JL-11 (R_s=1.335 (e=17.5%))
g) JL-12 (R_s=1.584 (e=26.4%))

e)

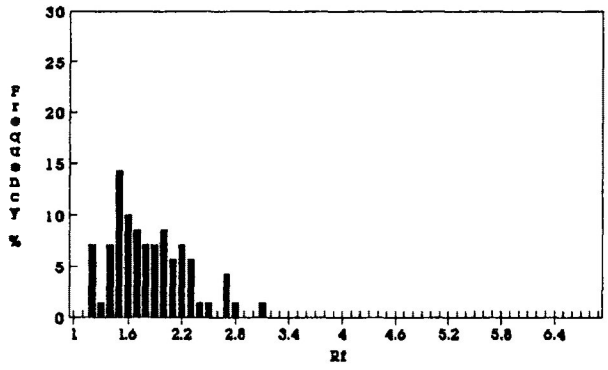
30
25
20
15
10
5
0
Frequency %
1
1.6
2.2
2.8
3.4
4
4.6
5.2
5.8
6.4
Rf

f)

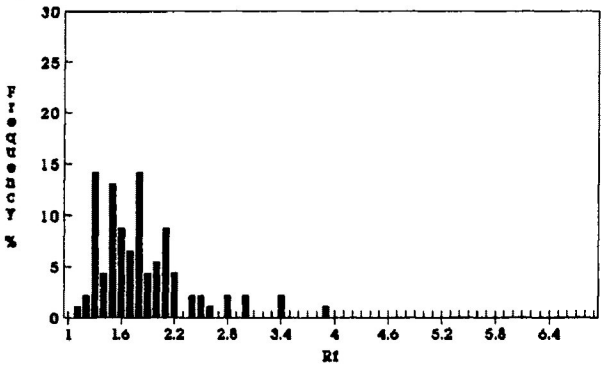
30
25
20
15
10
5
0
Frequency %
1
1.6
2.2
2.8
3.4
4
4.6
5.2
5.8
6.4
Rf

g)

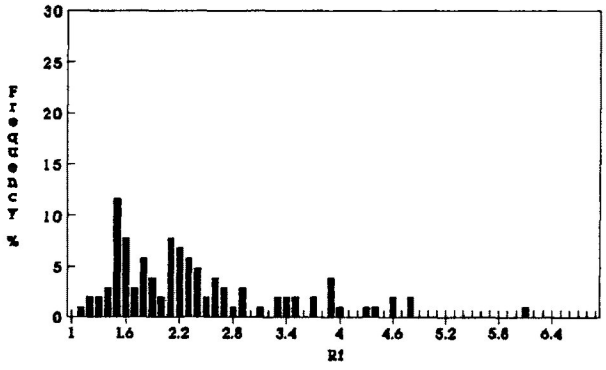
30
25
20
15
10
5
0
Frequency %
1
1.6
2.2
2.8
3.4
4
4.6
5.2
5.8
6.4
Rf

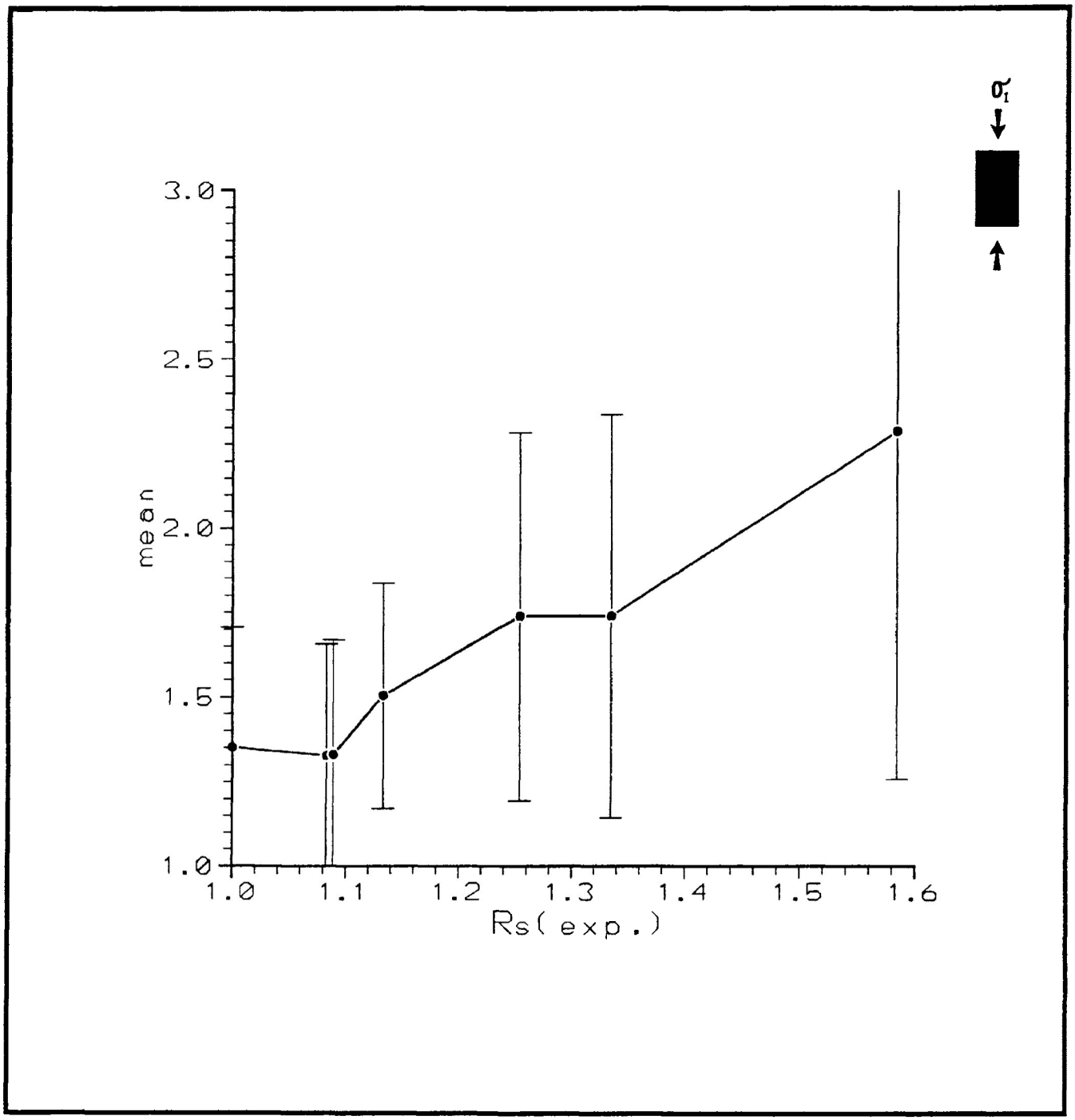

Figure 6.31 Variations in mean and standard deviation of R_f with increasing experimental strain. Experimental strain ratios range from 1.000 (e=0.0%) to 1.584 (e=26.4%). Samples were deformed under wet experimental conditions with confining pressures of 200 Mpa, strain rate of 10^{-5}/s and temperatures of 135°C. Pore fluid pressures were less than 60% of the confining pressure.

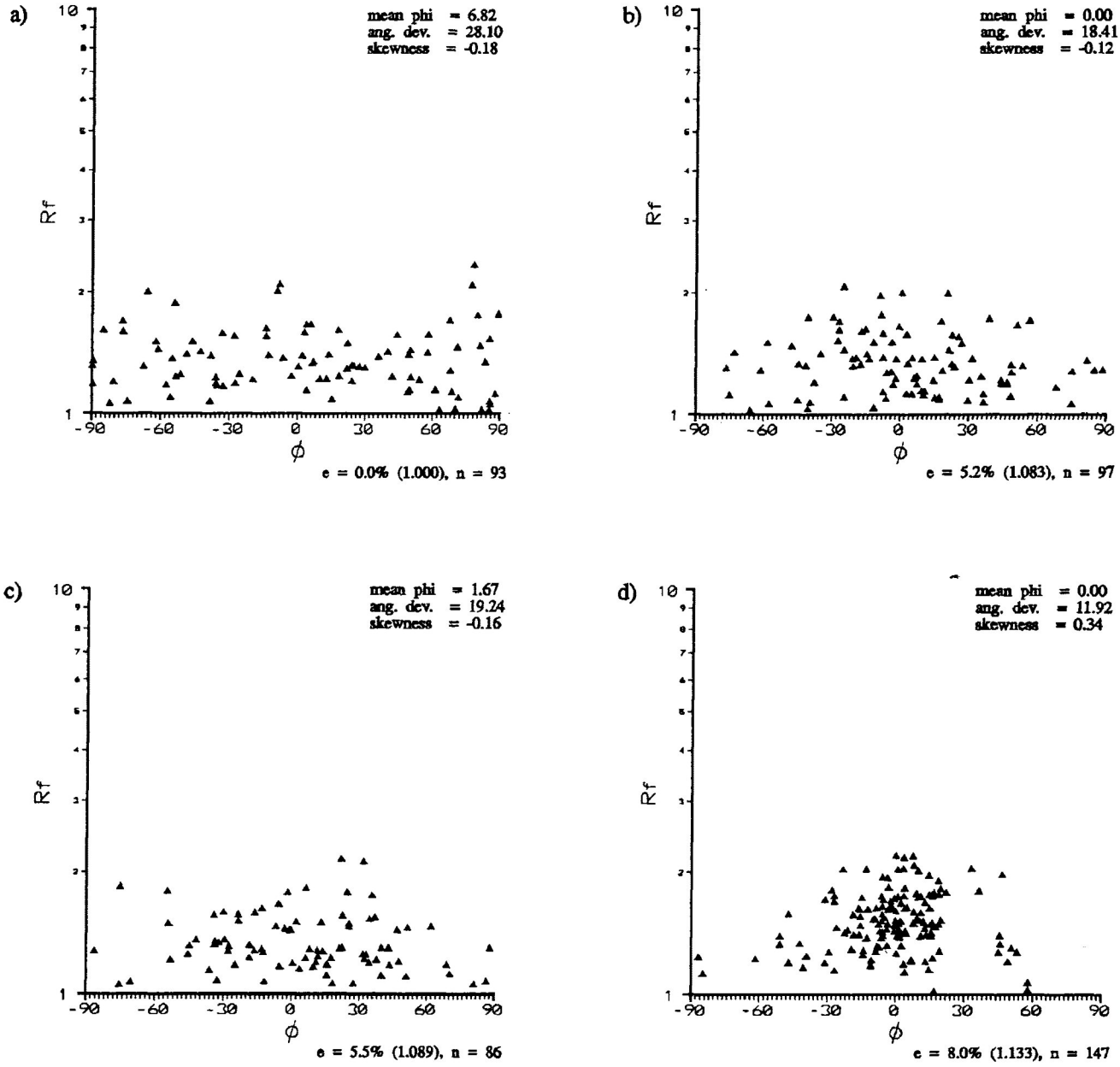

Figure 6.32a-g R_f/ϕ diagrams for ooids in undeformed and deformed Ancaster Limestone. Experimental strain ratios range from 1.000 (e=0.0%) to 1.584 (e=26.4%). Maximum extension direction oriented at 0°. Samples were deformed under wet experimental conditions with confining pressures of 200 Mpa, strain rate of 10^{-5}/s and temperatures of 135°C. Pore fluid pressures were less than 60% of the confining pressure. Measurements taken from the X/Z principal plane.

a) ANC-87 (R_s=1.000 (e=0.0%))
b) JL-8 (R_s=1.083 (e=5.2%))
c) JL-13 (R_s=1.089 (e=5.5%))
d) JL-10 (R_s=1.133 (e=8.0%))
e) JL-9 (R_s=1.254 (e=14.0%))
f) JL-11 (R_s=1.335 (e=17.5%))
g) JL-12 (R_s=1.584 (e=26.4%))

e)

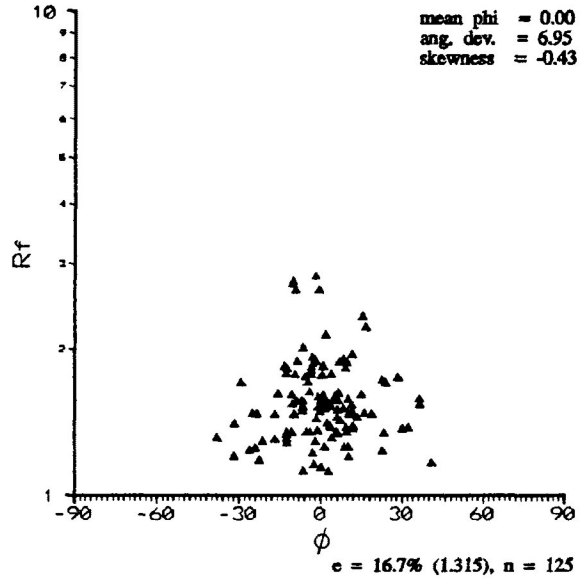

e = 16.7% (1.315), n = 125

f)

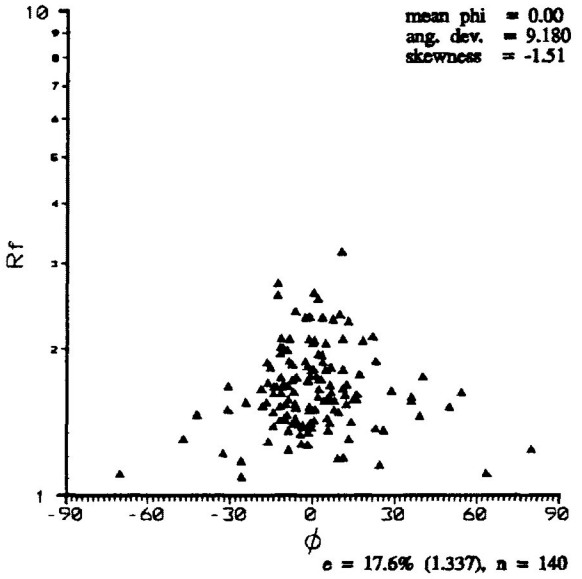

e = 17.6% (1.337), n = 140

g)

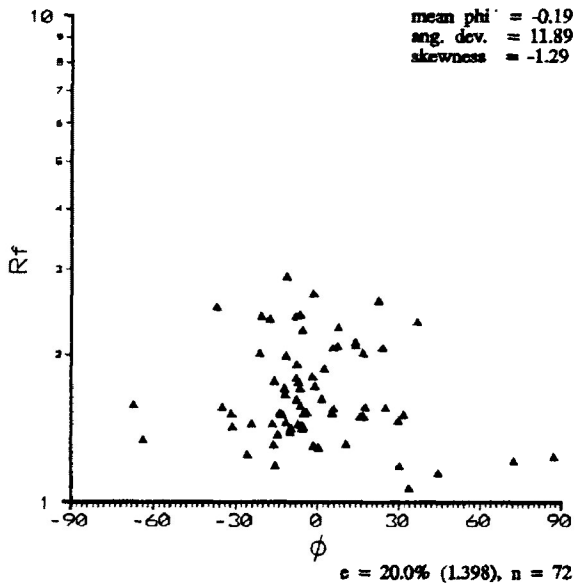

e = 20.0% (1.398), n = 72

fractures at 30 to 40° to the principal compressive stress direction.

d) Comparison between strain analysis methods based on ooid grains in the dry experimental studies

Figure 6.33 presents the comparison of the Robin's, linearization and harmonic mean methods of strain analysis for ooid grains. Since most of the strain in the experimentally deformed limestone is taken up by the ooids (the matrix, at least at low strains, is relatively undeformed) the estimates of strain ratio are overestimates of the actual calculate experimental bulk strains. It is apparent, from the figure, that the estimate of strain from the linearization method is in close correlation with that of Robin's method, except at high strains where a large deviation is observed. The strain estimate from harmonic mean method is a larger overestimate of bulk experimental strain for each deformed sample. In this study Robin's method gives the best approximations of the experimental strain ratios for the three methods.

Standard deviation for Robin's method, linearization method and the harmonic mean method were calculated and are presented in table 6.4. For the linearization method the calculations of standard deviation that yield confidence brackets that extend into bulk strains estimates less than 1.000 are not given.

Comparison of the a_j/c_j ratio necessary to calculate Robin's method of strain for wet experimental conditions is presented in figure 6.34a-g. It is observed from the figures that the a_j/c_j is essentially normal in distribution, as strain increases in the deformed sample between 0.0% and 8.0% shortening. A strain increases, between 14.0% and 24.6% shortening, there is observed a development of a bimodal distribution of a_j/c_j ratios (Fig. 6.34 e-g). The range of

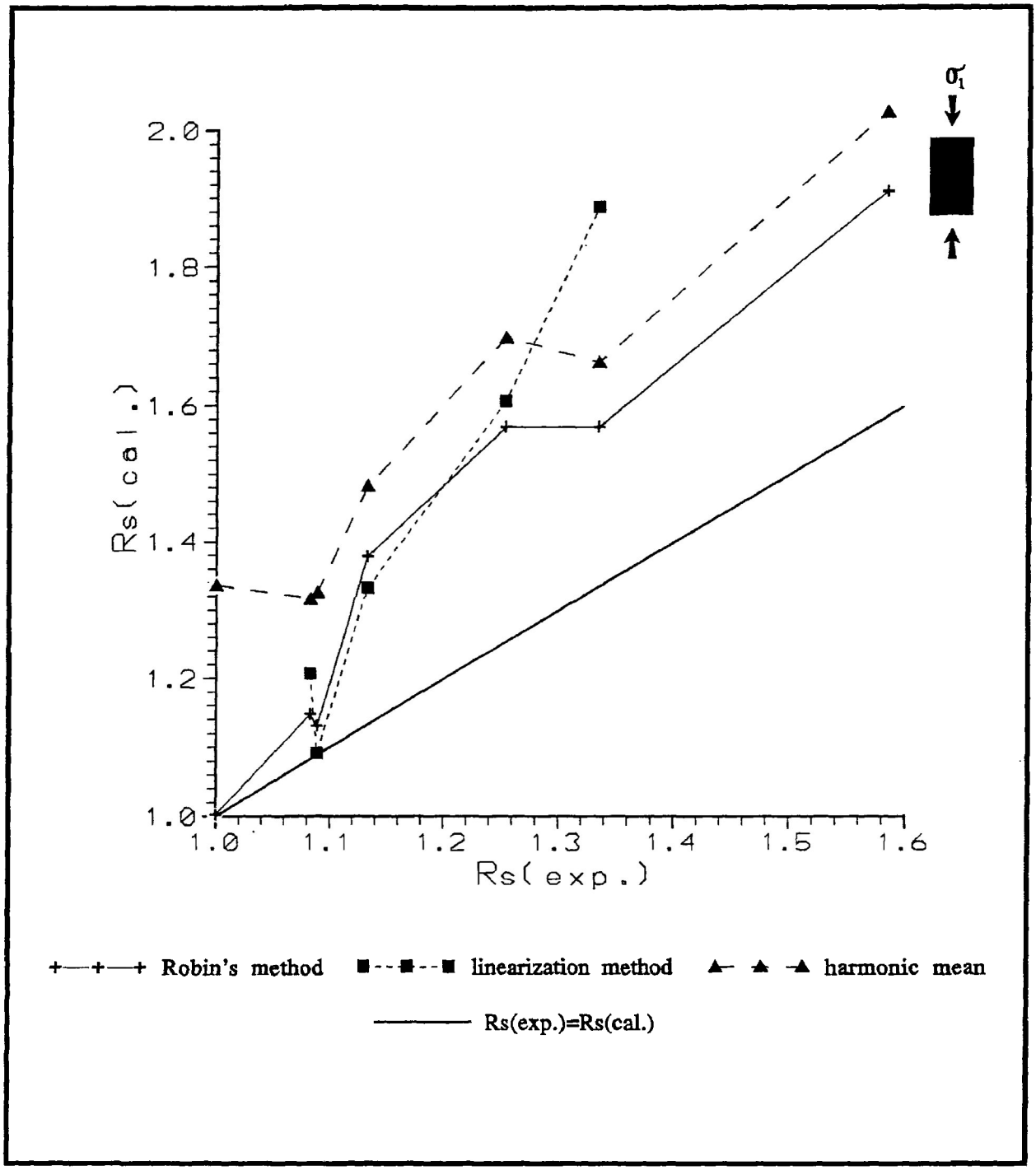

Figure 6.33 Comparison of the estimate of strain ratio (R_s (cal.)) calculated from Robin's method (cross), linearization method (square), and harmonic mean (triangle) to the experimental strain (R_s (exp.)) from ooids in samples of deformed Ancaster Oolitic limestone. The Ancaster Oolitic limestone has been deformed to strain ratio less than 1.584 in the X/Z principal plane under wet experimental conditions (P_c=200 Mpa, strain rate of 10^{-5}/s) at a temperature of approximately 130°C. Pore fluid pressures were less than 60% of the confining pressure. Broad line represents the line of (R_s(exp.))=(R_s(cal.)).

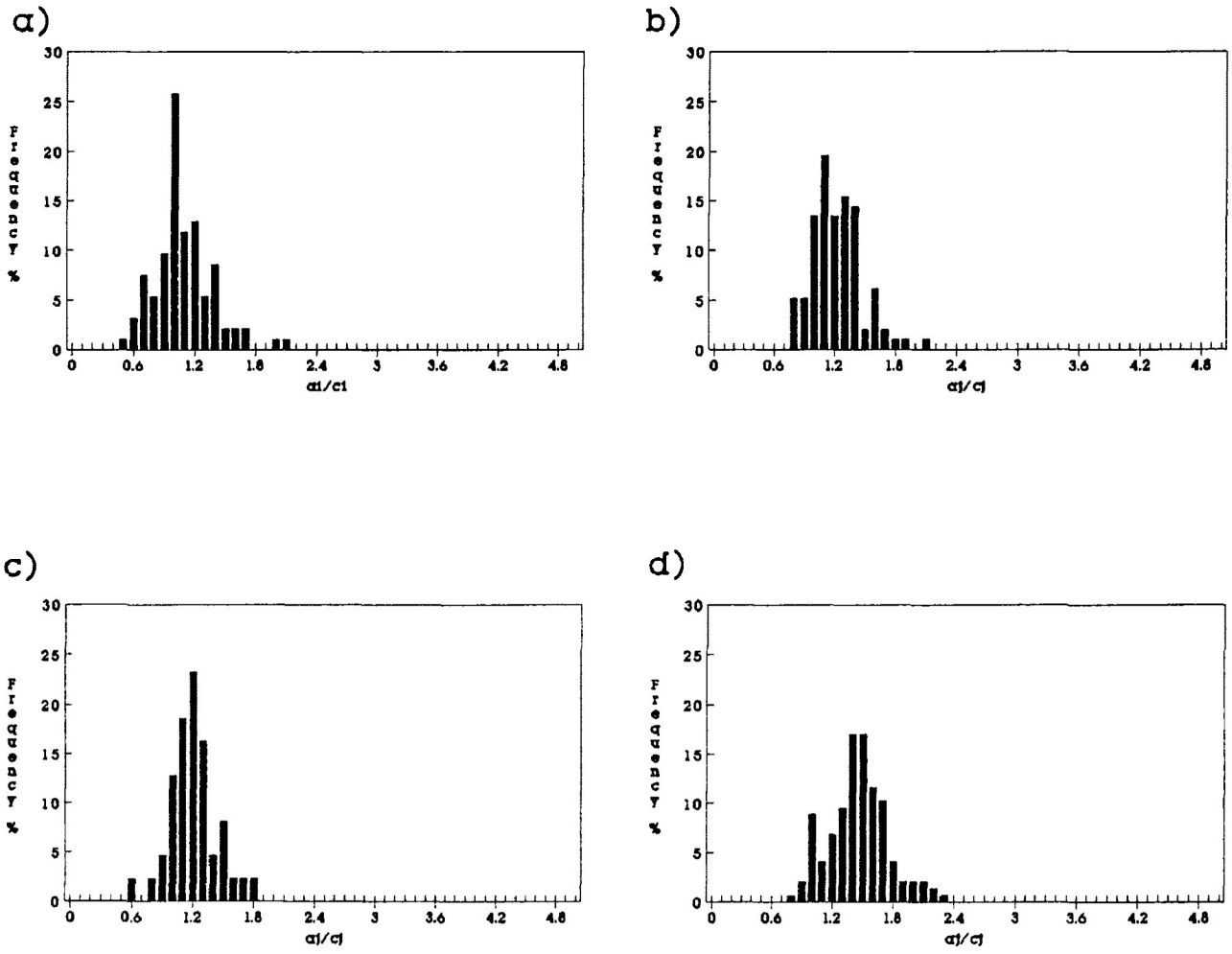

Figure 6.34a-g Frequency distribution of a_j/c_i ratios for ooids in undeformed and deformed Ancaster Limestone. Experimental strain ratios range from 1.000 (e=0.0%) to 1.584 (e=26.4%). Samples were deformed under wet experimental conditions with confining pressures of 200 Mpa, strain rate of 10^{-5}/s and temperatures of 135°C. Pore fluid pressures were less than 60% of the confining pressure. Measurements taken from the X/Z principal plane.

a) ANC-87 (R_s=1.000 (e=0.0%))
b) JL-8 (R_s=1.083 (e=5.2%))
c) JL-13 (R_s=1.089 (e=5.5%))
d) JL-10 (R_s=1.133 (e=8.0%))
e) JL-9 (R_s=1.254 (e=14.0%))
f) JL-11 (R_s=1.335 (e=17.5%))
g) JL-12 (R_s=1.584 (e=26.4%))

e)

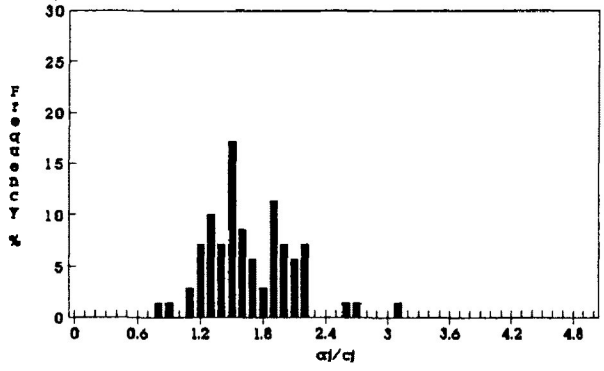
Frequency %
30
25
20
15
10
5
0
0
0.6
1.2
1.8
2.4
3
3.6
4.2
4.8
αj/cj

f)

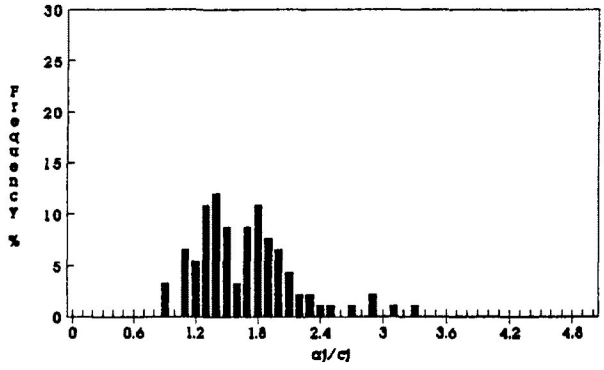
Frequency %
30
25
20
15
10
5
0
0
0.6
1.2
1.8
2.4
3
3.6
4.2
4.8
αj/cj

g)

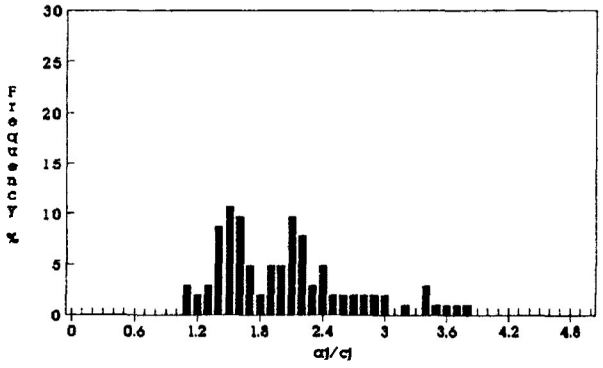
Frequency %
30
25
20
15
10
5
0
0
0.6
1.2
1.8
2.4
3
3.6
4.2
4.8
αj/cj

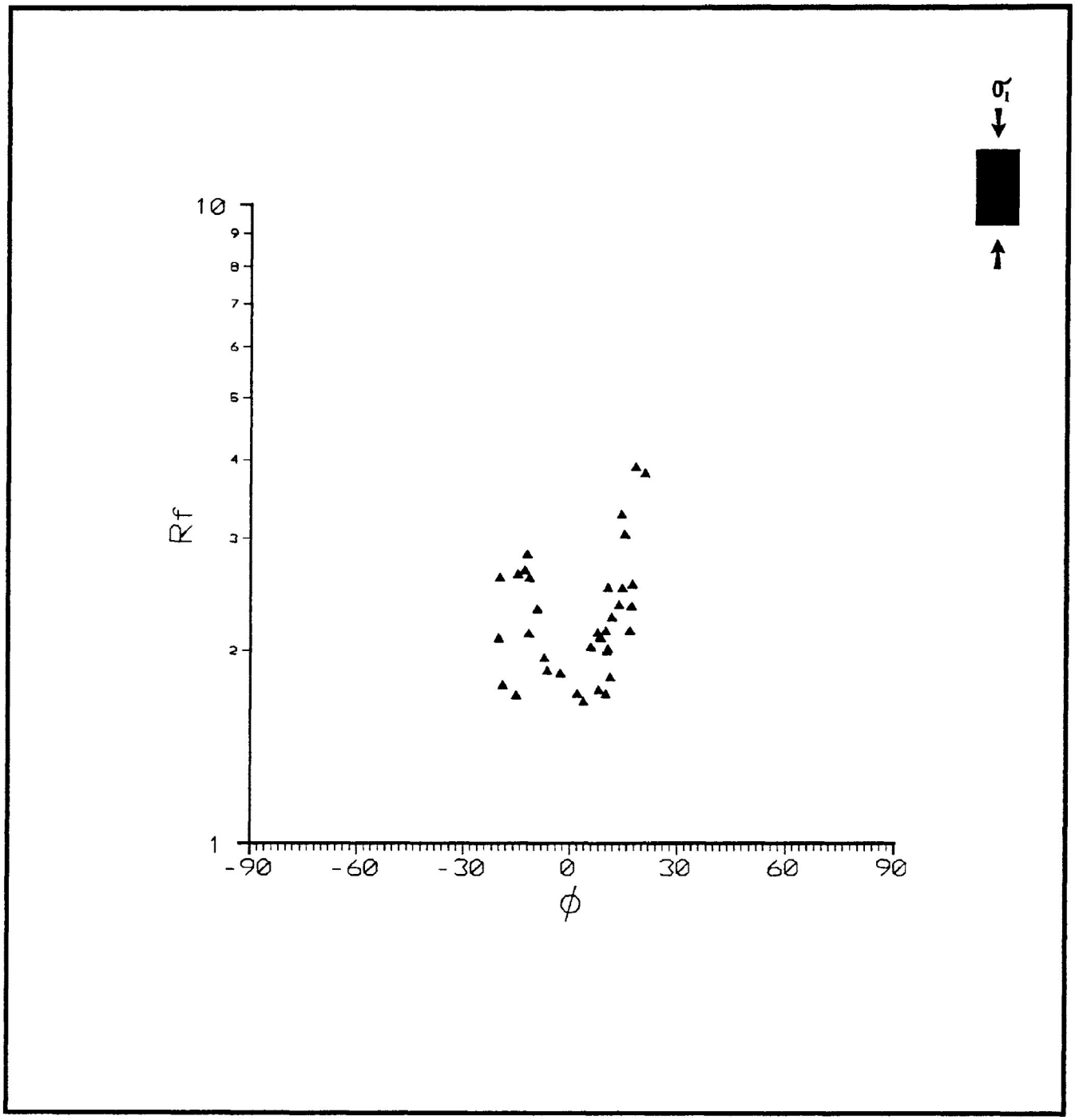

Figure 6.35 R_f/ϕ diagram for ooids data with a_j/c_j ratios in the second mode of figure 6.34g. Maximum extension direction oriented at 0°. Samples were deformed under wet experimental conditions with confining pressures of 200 Mpa, strain rate of 10^{-5}/s and temperatures of 135°C. Pore fluid pressures were less than 60% of the confining pressure.

a_j/c_j increases as strain increases from a range of 0.5-1.7 in the undeformed state to a range of 1.1-3.8 at 26.4% shortening.

If the bimodal distribution of a_j/c_j ratios are divided into the two modes, the first gives a much better estimate of strain by Robins's method where as the second gives an overestimate of strain. The second mode may be the result of the embryonic development of conjugate ductile shear zones. Figure 6.35 exhibits the corresponding R_f/ϕ diagram for the a_j/c_j data making up the second mode. It is observed that the R_f/ϕ data is concentrated at 20° to 30° on either side of the extension direction.

The development of ductile conjugate zones in these samples are similar to that, developed at higher strain (e=40%, dry conditions), in the study by Donath and Wood (1980). Donath and Wood observed that the development of ductile faulting is obscure in thin section, however, the concentration of relatively high compressional strain in conjugate zones is obvious in the strain contour diagrams. This suggests that the ooids in the immediate vicinity of the faults are being subjected to high, localized heterogeneous strain.

For Robin's method the best estimates of tectonic strain are at low bulk deformations (<10% shortening), as a result of the normal distributions and lake of a bimodal distribution of the a_j/c_j ratios, a condition necessary for the determination of tectonic strain by Robin's method.

e) <u>Homogeneity coefficient for ooid grains</u>

The homogeneity coefficient r^2 was calculated as the best fit straight line through the point distribution of long vs.

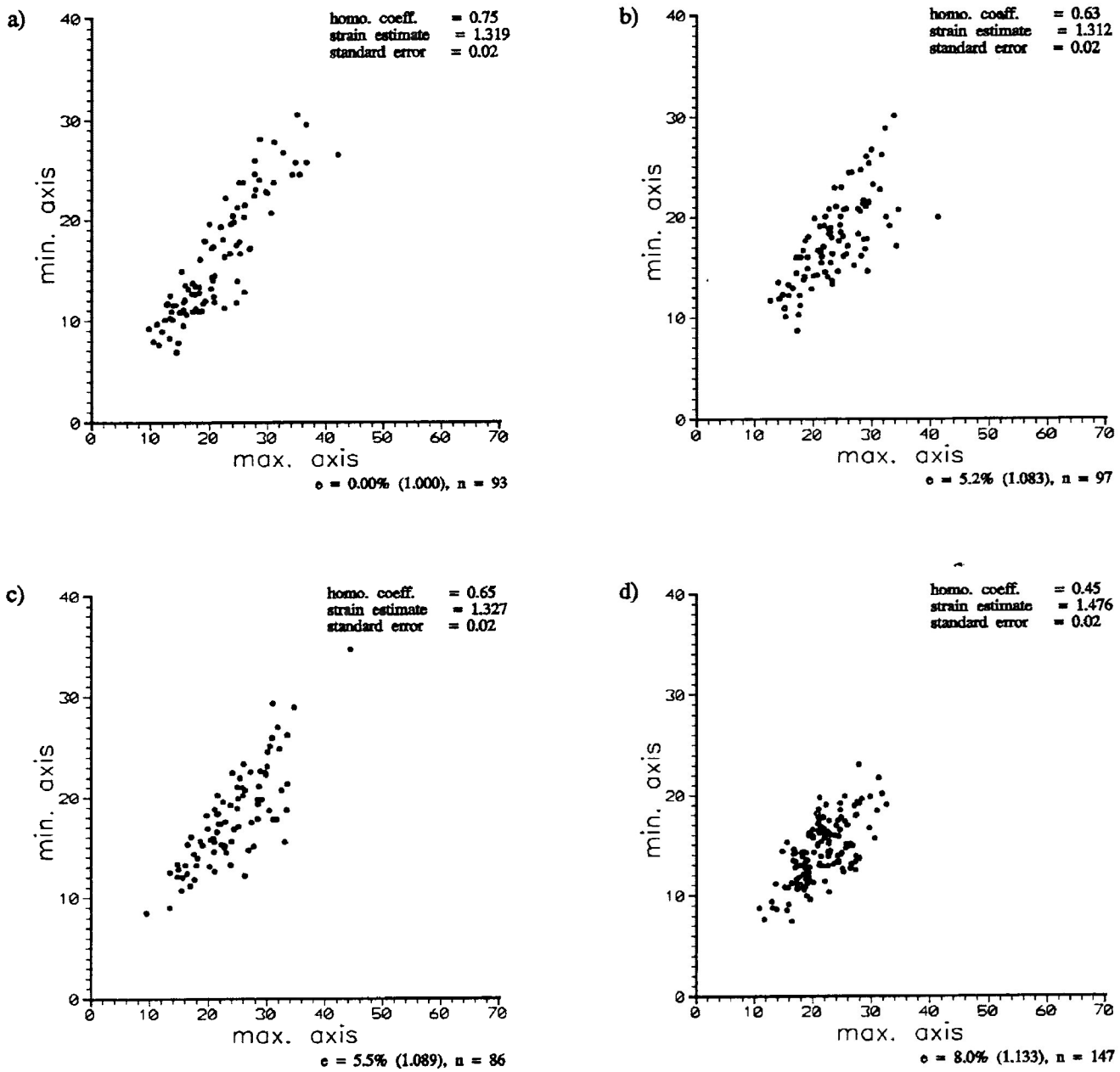

Figure 6.36a-g Distribution of maximum and minimum axis for ooids in undeformed and deformed Ancaster Limestone. Experimental strain ratios range from 1.000 (e=0.0%) to 1.584 (e=26.4%). Samples were deformed under wet experimental conditions with confining pressures of 200 Mpa, strain rate of 10^{-5}/s and temperatures of 135°C. Pore fluid pressures were less than 60% of the confining pressure. Homogeneity coefficient, strain estimate from Max/Min method (Ramsay, 1969) and error are also given. Measurements taken from the X/Z principal plane.

a) ANC-87 (R_s=1.000 (e=0.0%))
b) JL-8 (R_s=1.083 (e=5.2%))
c) JL-13 (R_s=1.089 (e=5.5%))
d) JL-10 (R_s=1.133 (e=8.0%))
e) JL-9 (R_s=1.254 (e=14.0%))
f) JL-11 (R_s=1.335 (e=17.5%))
g) JL-12 (R_s=1.584 (e=26.4%))

e)

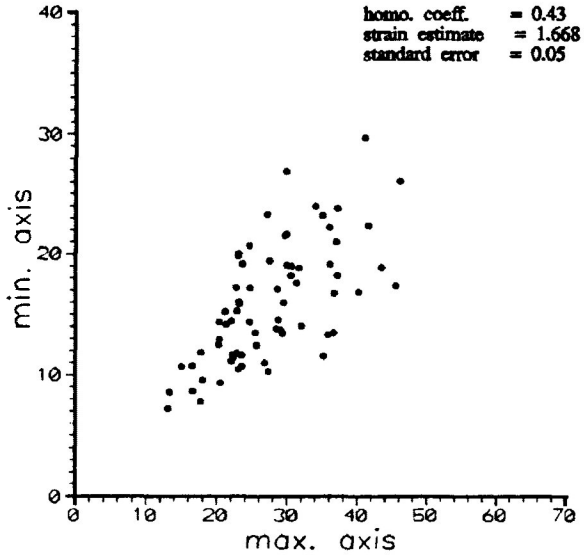

e = 14.0% (1.254), n = 70

f)

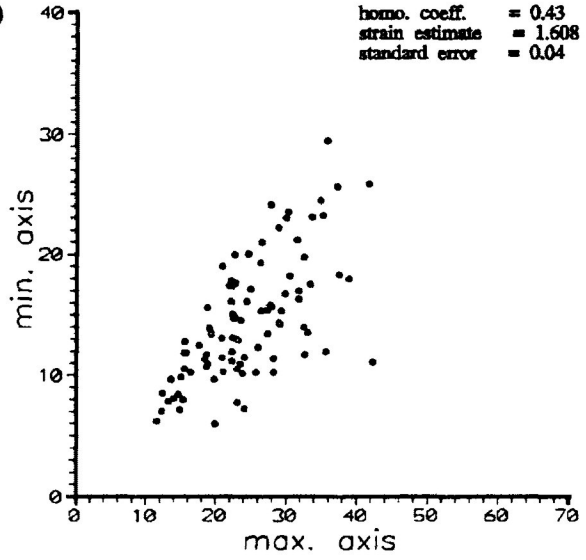

e = 17.5% (1.335), n = 92

g)

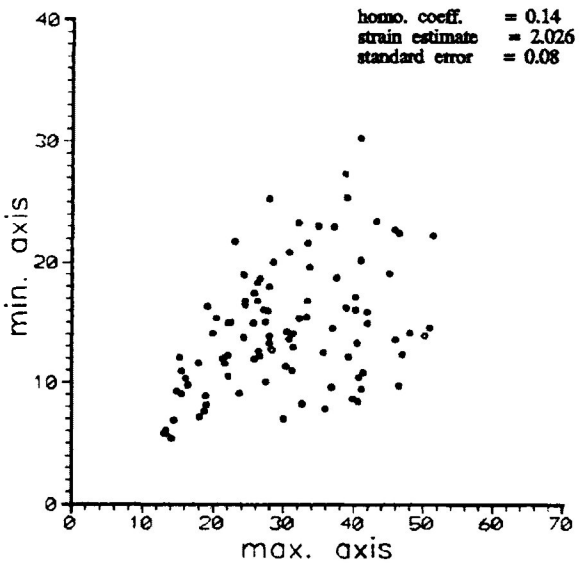

e = 26.4% (1.584), n = 103

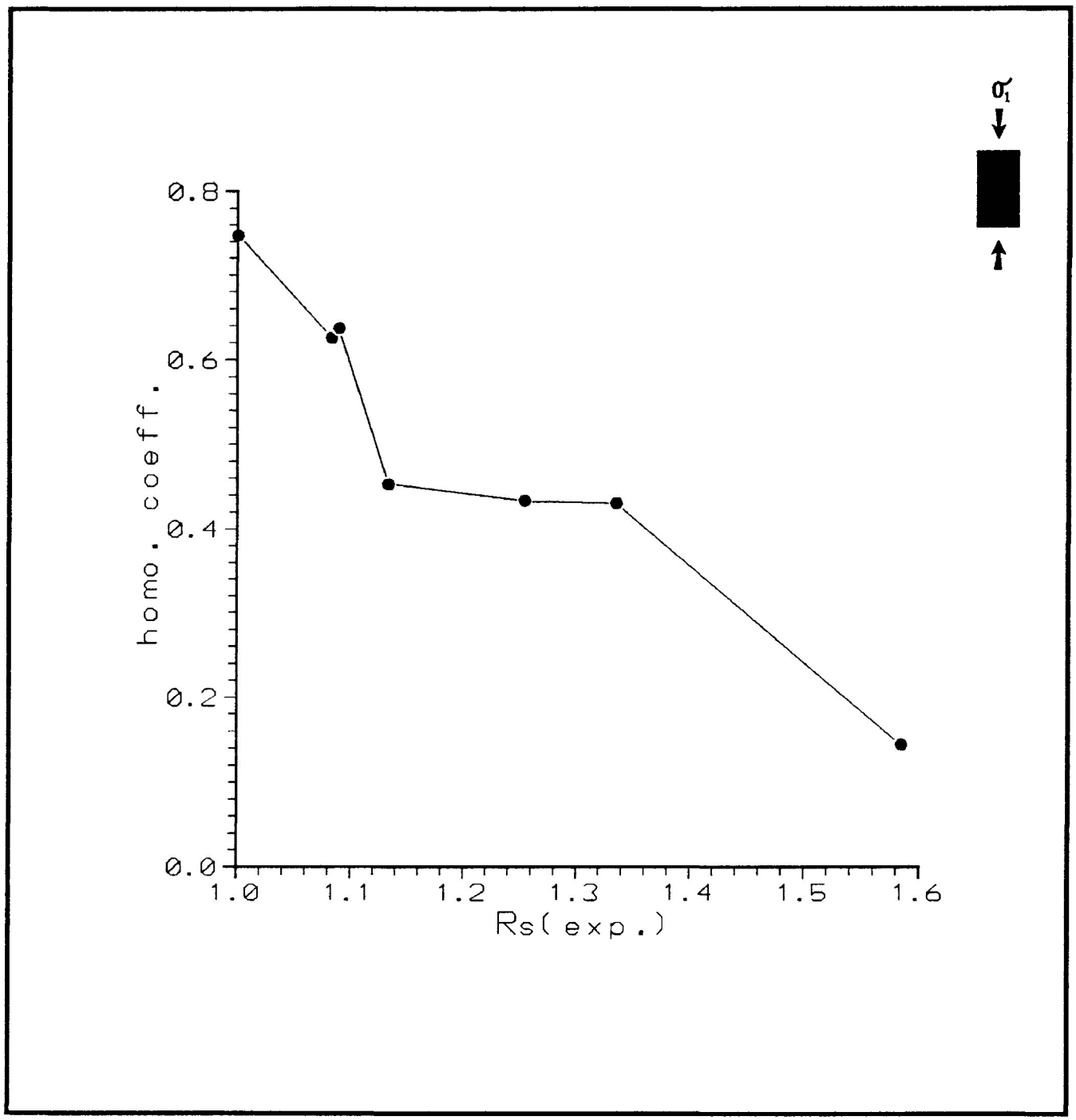

Figure 6.37 Variations homogeneity coefficient increasing experimental strain. Experimental strain ratios range from 1.000 (e=0.0%) to 1.584 (e=26.4%). Samples were deformed under wet experimental conditions with confining pressures of 200 Mpa, strain rate of 10^{-5}/s and temperatures of 135°C. Pore fluid pressures were less than 60% of the confining pressure.

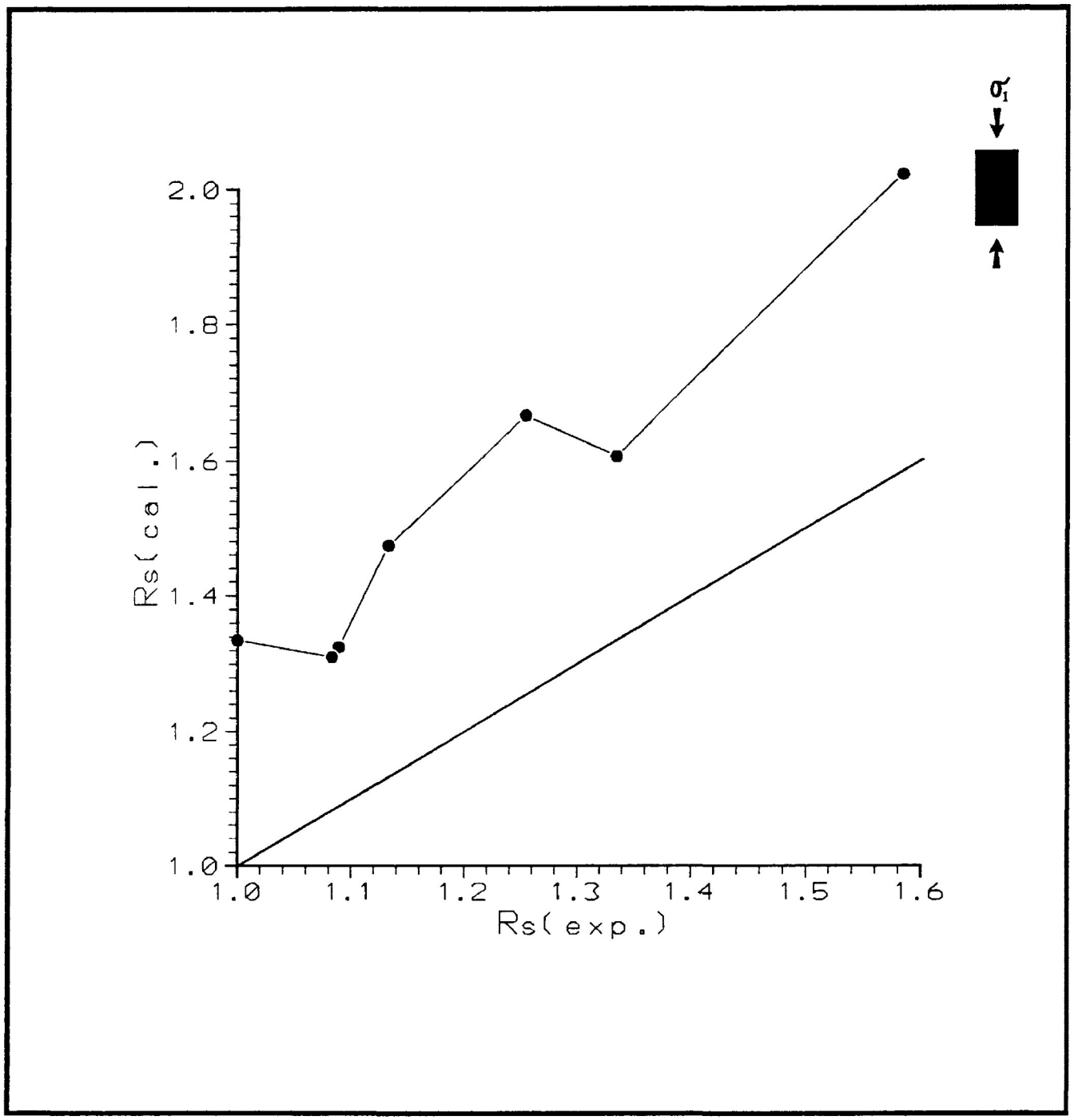

Figure 6.38 Estimate of strain by Max/Min method (Ramsay, 1969). Equivalent Rs is represented by the dark solid line. Experimental strain ratios range from 1.000 (e=0.0%) to 1.584 (e=26.4%). Samples were deformed under wet experimental conditions with confining pressures of 200 Mpa, strain rate of 10^{-5}/s and temperatures of 135°C. Pore fluid pressures were less than 60% of the confining pressure.

short axis of the deformed ooids from data presented in figure 6.36a-g. The variation in homogeneity coefficient with increasing bulk experimental strain is presented in figure 6.37. It is observed in the figure that there is a decrease in the homogeneity coefficient with strain. The values range from 0.74 in the undeformed state to the lowest value of 0.14 at 26.4% shortening. Calculation of strain by the axial ratio method (Ramsay, 1969) is presented in figure 6.38. The strain estimate from this method are a 6% to 15% overestimate of the actual experimental bulk strain.

f) <u>Deformation mechanism of ooid grains</u>

It may be suggested that a greater component of the deformation of the ooids in the limestone, under wet experimental conditions, is the result of homogenous strain. The greater homogeneous deformation may be the result of controlled particulate flow within the fine grain matrix of the ooid. This is an effect of the pore fluid pressure in the deforming samples. The pore fluid pressure at 60% of the confining pressure reduces the effective stress allowing grains of the fine grained ooid matrix to slide past one another. The ooids behave as ductile particle, represented by the large increase in R_f, forming a strong PDO as the sample experiences strain. This may reduce the role of rigid rotation of the ooid grains observed in dry experimental conditions.

6.8 Discussion of ooid and calcite-cement matrix for wet and dry experimental deformation

It is apparent from the previous sections that a more substantial amount of deformation is expressed in the ooid particles than in the calcite cement matrix of the deformed Ancaster oolitic limestone. Ooids deform, under the experimental conditions of this study, mainly by rigid body rotation and by controlled particulate flow for dry and wet experimental conditions, respectively. The calcite-cement matrix deforms by rigid rotation and twinning in the case of dry conditions and by controlled particulate flow in the case of wet experimental conditions. Twinning in the wet experimental tests was observed to be approximately 10% to 15% less than in the case of dry experimental conditions. The more intense twinning observed in the dry tests is reflected in a noticeable flattening of the calcite-cement grains at higher bulk strains.

Figure 6.39 presents a comparison of the ooid derived strain ratio (Robin's method) and the calcite cement strain ratio calculated in section 6.4 for the deformed Ancaster oolitic limestone. From the figure it is observed that a significant amount of the deformation departs from the homogeneity between the ooid and matrix strain. Most of the deformation is expressed in the ooid, which is true even at low strains. The larger strain heterogeneity (viscosity contrast) is observed in the wet experimental conditions. This may be the result of the fact that particulate flow is a grain size dependent process, the finer grain ooid being the most significantly affected.

This large difference in strain between ooid and matrix was also observed in the study by Schmid and Paterson (1977) at deformation temperatures of 900°C. However, the larger deformation of the ooids was the result of superplastic flow

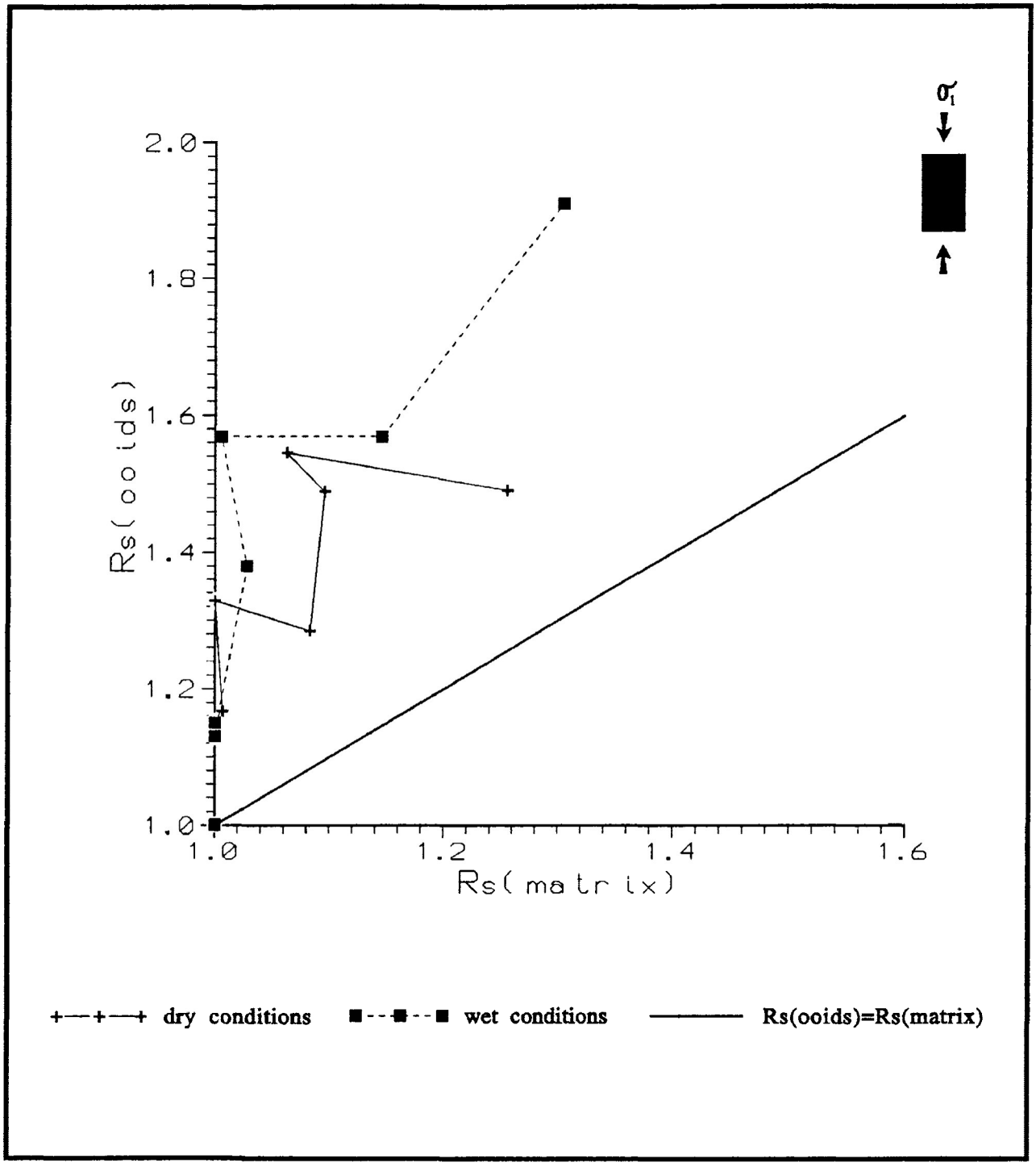

Figure 6.39 Plot of ooid strain ratio estimate (Robin's method) versus the calculated calcite-cement matrix strain ratio estimate (Schmid and Paterson, 1977) for both dry experimental conditions (cross) and wet experimental conditions (square). Solid line represent homogeneity between the strain of the ooids and the cement matrix.

of the ooid's fine grain matrix, a deformation process in which particulate flow plays an important role.

The large deviations in the comparison of strain ratios, observed at high strains, are the result of the development of ductile shears at 30° to the σ_1 orientation in the wet experimental tests and brittle faulting in the case of the dry experimental conditions. The ductile shear zones that develop in the wet experimental tests developed at much lower bulk strains than in the case of the study by Donath and Wood (1976), which was conducted under dry experimental conditions. In their tests the ductile faulting occurred at strains of 30% to 40%; in the case of this study the ductile fractures occurred at much lower bulk strains approximately 17.5% shortening.

A large viscosity contrast exist between the two parts of the deforming limestone. This leads to large overestimate of the bulk strain when the strain analysis estimate relies on ooid shape change as presented in the previous sections. This suggest that ooids deformed at low temperatures are not useful for the determination of the finite strain.

6.9 Discussion of the use of Robin's method for the determinations of strain from ooids from wet, dry and computer simulated experimental deformation

It is apparent from the data that the ooid are exhibiting a much higher strain than the calcite cement matrix, as a result of different deformation processes. The result of the different deformation processes is to produce a viscosity contrast between the matrix and the ooid. This invalidates one of the principal assumptions of Robin's method of strain analysis in that there must be no significant competency contrast between the markers and the host rock. Competency differences between marker and matrix can cause considerable error in the determination of the tectonic strain. This is reflected in the comparison of the calculated Robin's method strain estimate for dry and wet to that of simulated deformation in figures 6.22, 6.33 and 6.14, respectively.

There is, however, a use for the strain value calculated by Robin's method even though it is not a true estimate of strain. The strain value can be used as an indicator of progressive shape change as deformation increases systematically in the deformed samples. Even though there may be a competency contrast between the ooid and the host rock, ooid in general, may be used to determine fabric changes as a result of systematic variation in strain over large areas in natural situation such as in the case of Cloos (1947) and Tan (1976).

Chapter 7: Strain Analysis of Experimentally Deformed China Beach Sandstone

7.1 Introduction

In a sandstone, grains of differing lithology will most likely vary in rheological behaviour, which may be expressed in the rock as a large heterogeneity of strain. This heterogeneity is the result of different deformation process or combinations of processes. For example, at low temperature, grains may deform by strictly plastic deformation, rigid body rotation or by cataclasis, other grains may deform by some combination of the above. In other words, the grain strains of varying lithologies may be greater or less than the bulk strain of the deformed rock. The bulk strain of the sample will, therefore, reflect the overall influence of the varying rheological behaviour of all grain types.

Strain analysis based on grain strain measurements and assuming passive R_f/ϕ transformation will be influenced by the rheological behaviour of each grain group. The variation in the degree of deformation between different grain types, in a sandstone aggregate, may lead to a large deviation of the strain estimate from the actual R_s producing the deformation. The degree of deviation from the actual R_s will depend on the lithology of grains present in the deformed material and the volume percentage of each lithologic group.

This chapter deals with the experimental triaxial deformation of five undeformed China Beach sandstone samples. The experimental tests consisted of deformation by pure shear (axial symmetrical compression) for dry experimental conditions. The temperature was held constant at room temperature ($25^{\circ}C$) during deformation, with computer controlled natural strain rates of $10^{-5}/s$. The confining pressure during each experiment was 200 Mpa. The five

undeformed sandstone samples were deformed to strains of 0.0% (R_s=1.000) to 28.0% (R_s=1.637) axial shortening. Errors on the calculation of experimental strain from the test cylinder shortening after triaxial deformation are considered to be negligible.

7.2 Undeformed China Beach Sandstone

The China Beach sandstone is an arkosic sandstone of the Oligocene epoch and is a part of the Sooke Formation. The sandstone is located in the south western portion of Vancouver island, British Columbia, Canada. The sandstone shows no evidence of deformation at the outcrop scale.

The majority of undeformed detrital grains of the China Beach sandstone can be subdivided into 5 groups. These groups consist of quartz (undeformed, undulose and fractured), feldspar (unaltered and altered) and lithic fragments (igneous, sedimentary and metamorphic). There are also minor amounts of muscovite, amphibole (hornblende) and opaque (magnetite) clasts. The sandstone grains are angular to subangular in shape with average longest dimension (in thin section) being approximately 0.57mm. The cement is mainly limonite, present as a fine grain brownish yellow precipitate at grain to grain contacts and on the walls of vugs. A small amount of the cement is also present in the sandstone as hematite.

The quartz grains of the undeformed China Beach sandstone consist mainly of grains that are clear and undulose. As presented in figure 7.1 approximately 23.1% of the sample is clear quartz and 13.5% is that of undulose. A small amount of fractured quartz (approximately 0.6%) is also present. Unaltered and altered feldspars are present in the undeformed sandstone sample as approximately 31.1% and 8.0%,

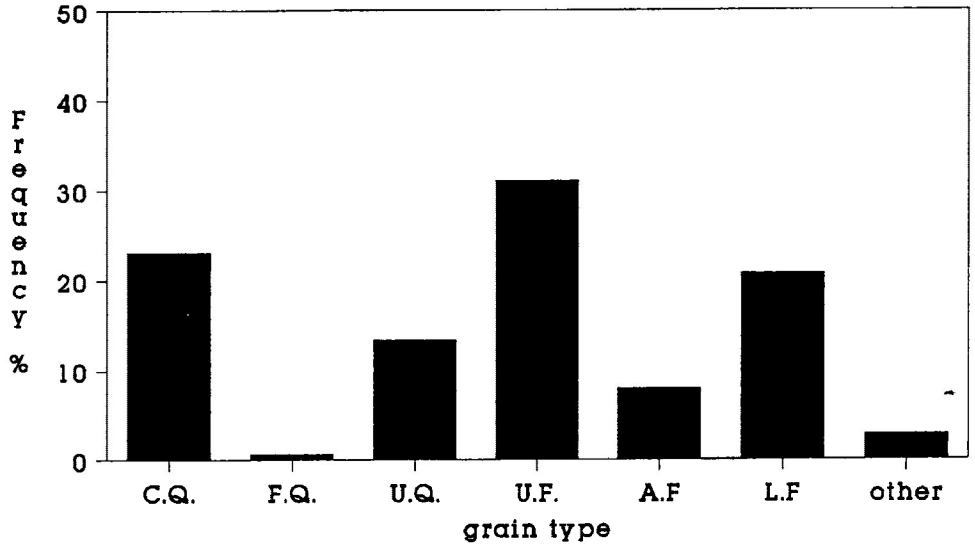

Figure 7.1 Volume % of the 5 major grain types present in the undeformed and deformed China Beach sandstone samples. The grain types consist of quartz (undeformed (C.Q.), fractured (F.Q.) and undulose (U.Q.)), feldspar (unaltered (U.F.) and altered (A.F.) and lithic fragments (L.F.). The subtype "other" consists of muscovite, biotite, hornblende, opaque grains (magnetite), porosity and cement.

respectively. The alteration is mainly that of saussurization with alteration to clay minerals. Some of the altered feldspar grains exhibit sericitic alteration. The feldspar alteration is observed to range in degree from small traces to the nearly complete alteration of the grain. Muscovite, biotite, hornblende and opaque grains (possibly magnetite) are present in the sample as minor detrital fragments and occupy approximately 2.0% of the sample. Porosity, present in the undeformed sample as small vugs, occupies approximately 2.0% of the sample.

Lithic fragments occur as igneous, sedimentary and metamorphic grain and occupy approximately 15.6%, 4.2% and 1.0% of the sample, respectively (Fig. 7.1). The largest group of lithic fragments is of igneous lithology, consisting almost entirely of basalt. The largest percentage of these basaltic grains (55%) are porphyritic and microporphyritic dominated by laths of feldspars with minor augite.

The basaltic grains mainly exist in the sample as two types. The first consists of a fine grained matrix with slender feldspar laths (approximately 50% of the grain) with longest dimension less than 0.15 mm in length. The second group, which occurs to a lesser degree, consists of approximately 70% to 85% feldspar laths, which are stubby in appearance, with longest dimension less than 0.25 mm in length. The matrix of these porphyritic grains is very fine grained. The remaining 45% of the basalt grains are not porphyritic and are fine grained. Approximately 30% of the basaltic fragments exhibit a small to moderate degree of alteration. The second largest group of lithic fragments is of sedimentary origin, consisting mainly of shale fragments. The remaining lithic fragments are metamorphic, in which the majority of grains are quartzite in nature. There is also minor amounts of a quartz hornblende schist.

Figure 7.2a-e illustrates the grain type distribution of the clear quartz, undulose quartz, unaltered feldspar, altered feldspar and lithic fragments in a plane parallel to the long axis of the test cylinder for the undeformed China Beach sandstone sample. The figure 7.2a represents grain distribution of all recognized grain types in the sample (spaces indicate the presents of very small grains, minor amounts of mica (biotite and muscovite), amphibole (hornblende) and opaque minerals (magnetite), cement (limonite and hematite), and porosity). Figure 7.2b-e represents individual grain groups in the undeformed sample. From the figures it can be observed that the distribution of grain types are approximately randomly positioned in the specimen and no major centre of high or low density is observed. A slight PDO of long dimensions of grains can be observed parallel to the bedding direction (the normal of the bedding direction is parallel to the long axis of the test cylinder).

The orientational frequency distribution of the long axis (Angle Ax (ϕ)) of all recognized grains in the undeformed China Beach sandstone sample is presented in figure 7.3a. From the figure it is apparent that, for the overall undeformed sample a weak, PDO is observed approximately parallel to the bedding direction. The distribution has a mean theta of -0.07° and an angular deviation of 45.34. A break down of the dimensional analysis of each grain group is presented in figure 7.4a-f. The strongest PDO development is in the undeformed quartz grains. The remaining grain groups of figure 7.4 illustrates less well developed PDO.

Figure 7.3b presents the total range of R_i for all recognized grains in the undeformed China Beach sandstone. The distribution has a mean R_i of 1.94 (±0.69 s.d.). A break down of the R_i distributional range in the different grain groups is presented in figure 7.5a-f. It is apparent from the figures

Figure 7.2a-e Grain type distribution of the clear quartz, undulose quartz, unaltered feldspar, altered feldspar and lithic fragments in a plane parallel to the long axis of the test cylinder for the undeformed China Beach sandstone sample. a) represents grain distribution of all recognized grain types (spaces indicate the presents of very small grains, minor amounts of mica (biotite and muscovite), amphibole (hornblende) and opaque minerals (magnetite), cement (limonite and hematite), and porosity). b) undeformed quartz. c) undulose quartz. d) altered (shaded) and unaltered feldspar. e) lithic fragments. Dark solid line illustrates the bedding direction (S_0). Tracings are from the central portion of the thin section.

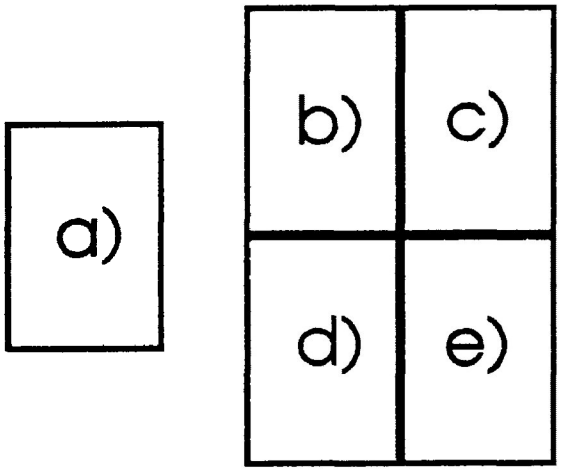

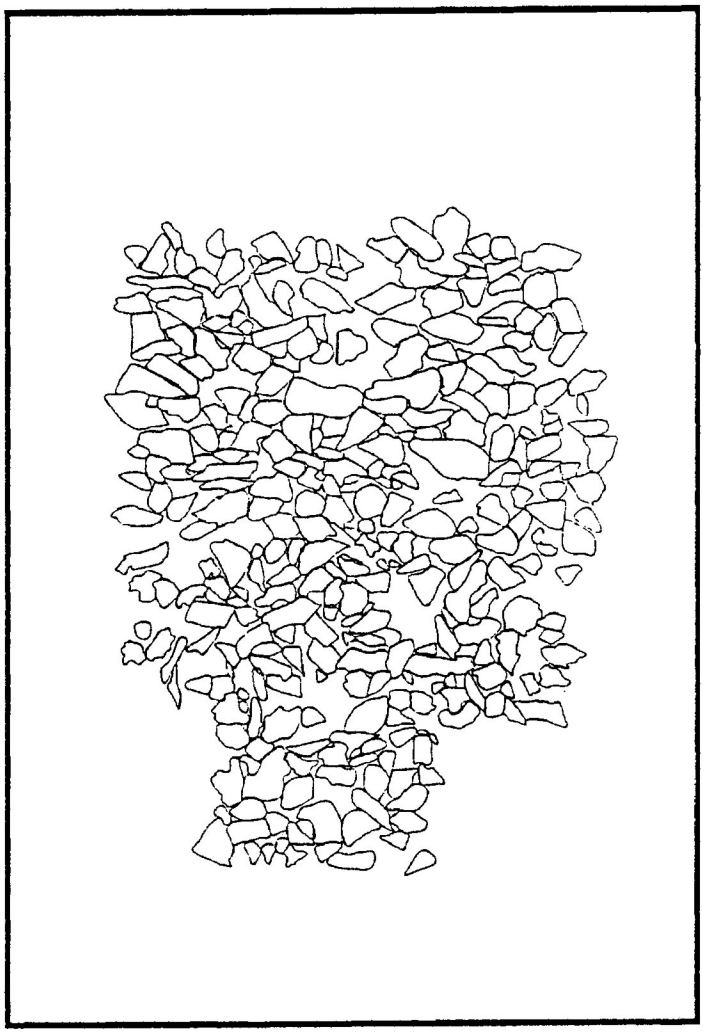

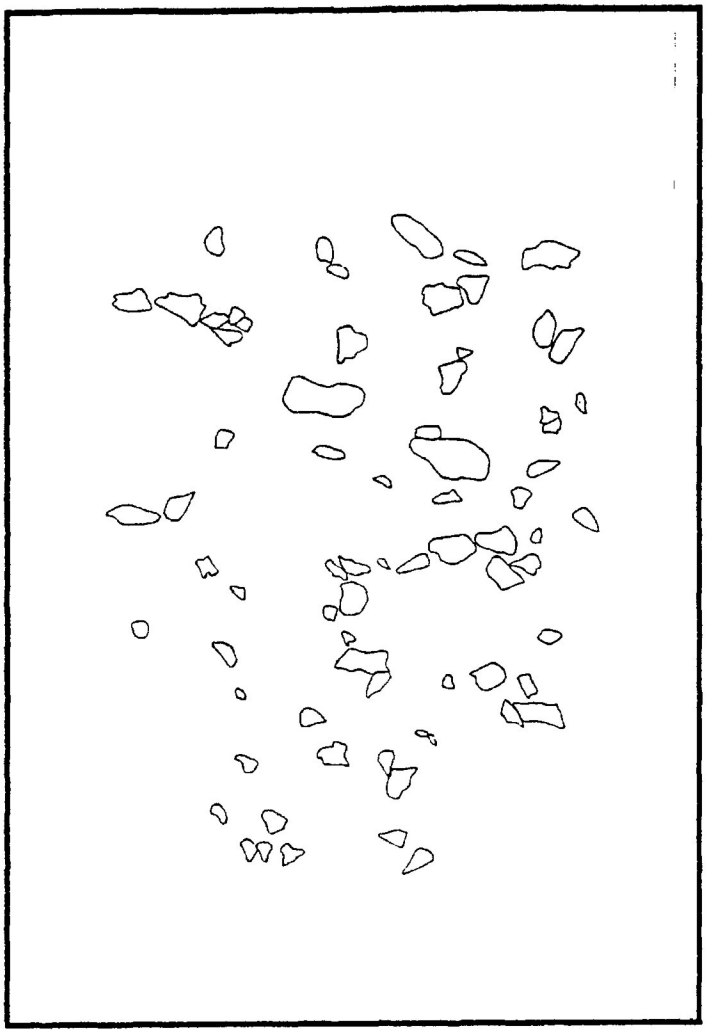

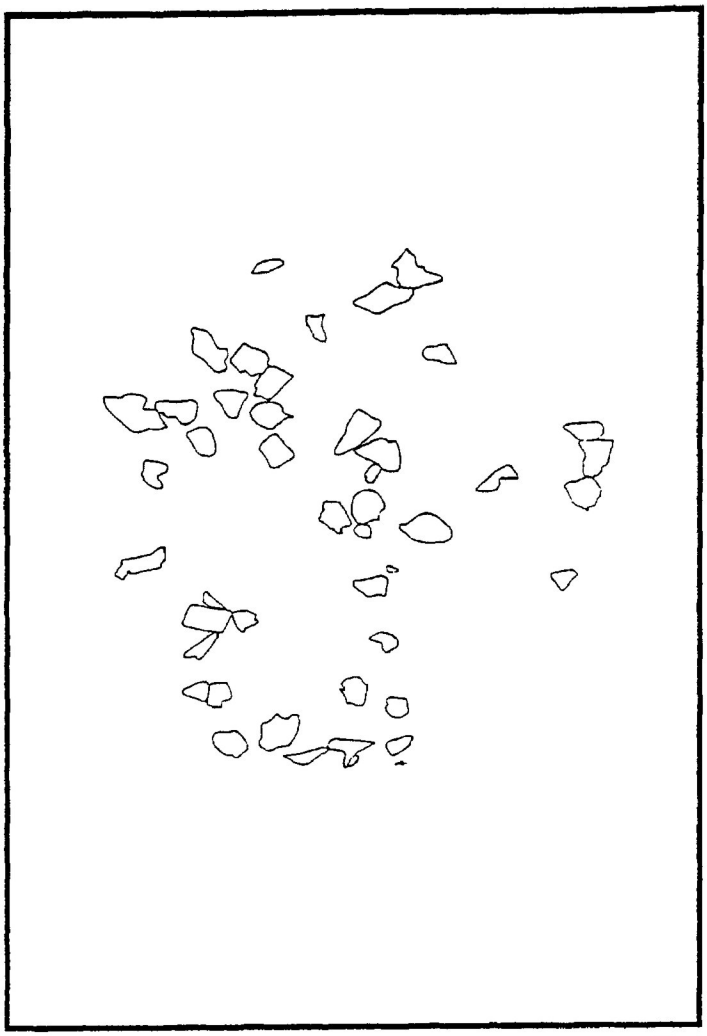

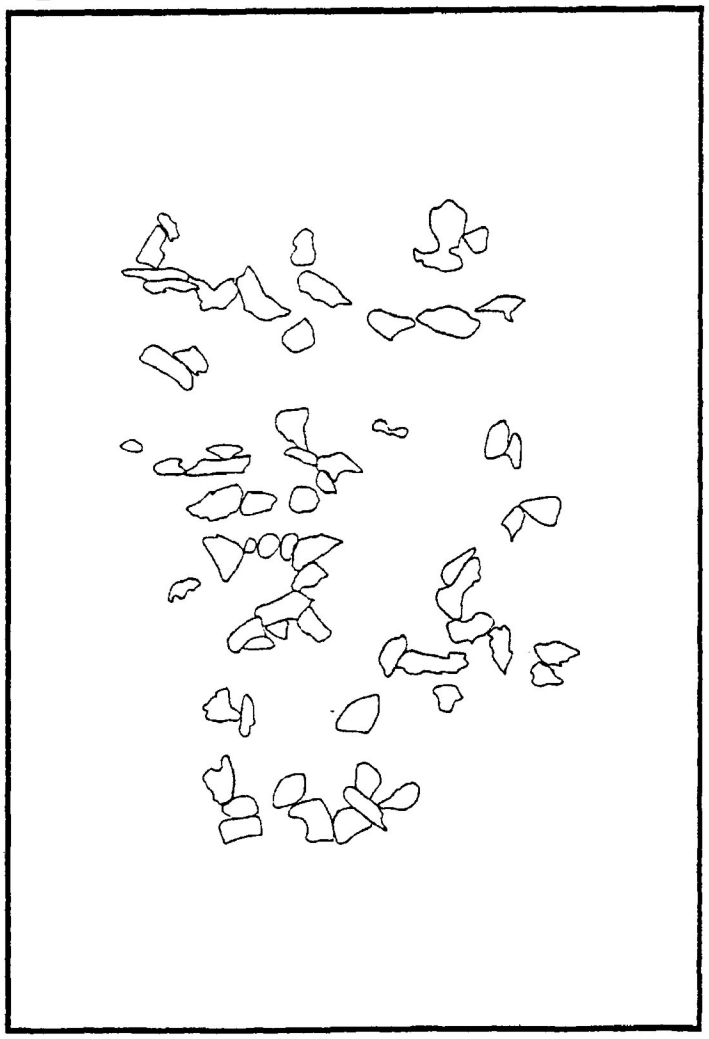

a)

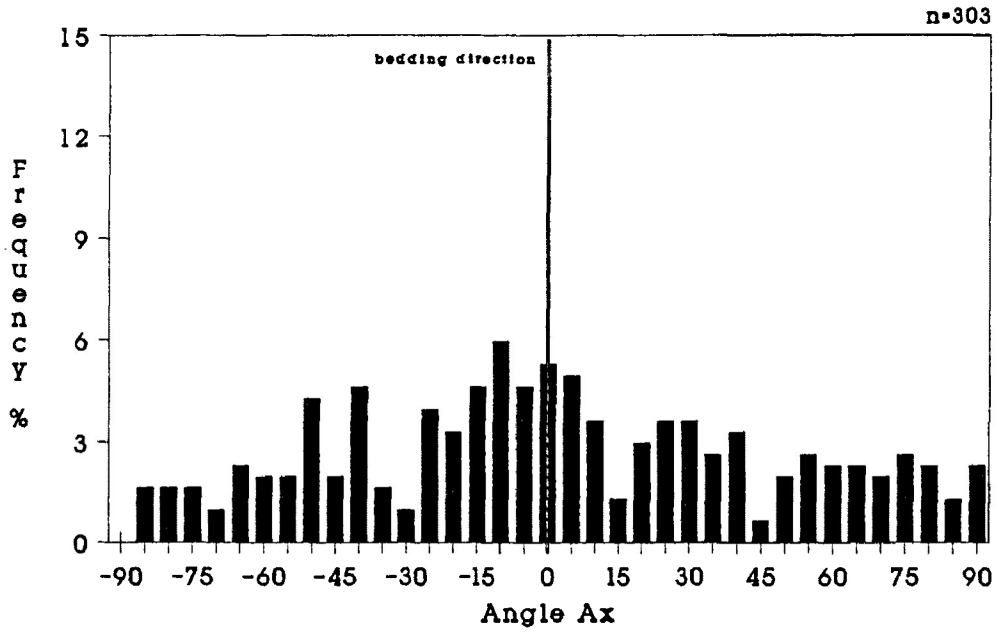

b)

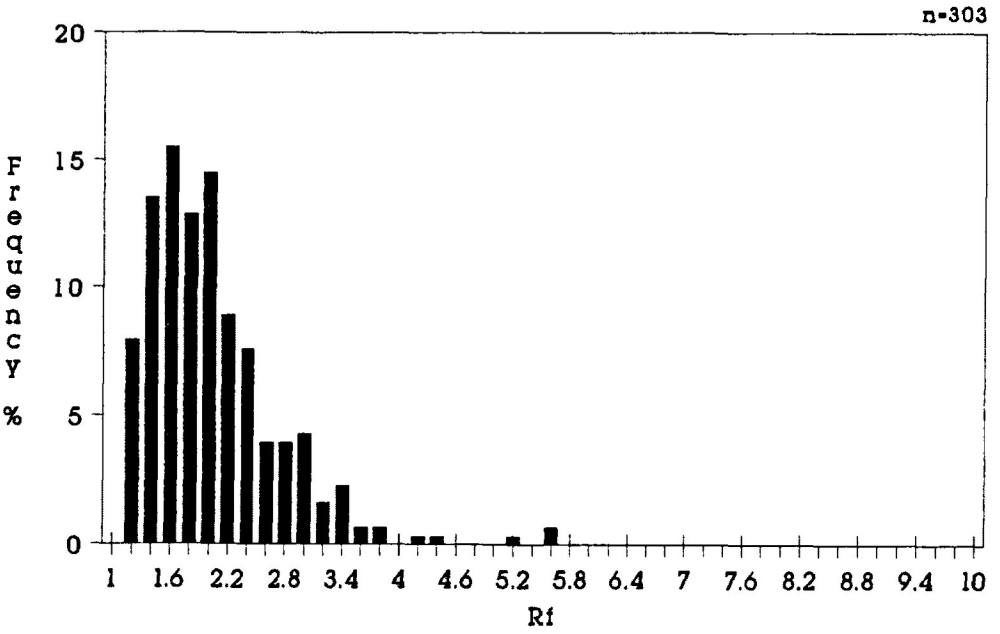

Figure 7.3a-b a) Angular frequency distribution of the long axis of all recognized grains in the undeformed China Beach Sandstone sample. b) Frequency distribution of total range of R_i for all recognized grains in the undeformed China Beach sandstone. Measurements taken from a plane parallel to the long axis of the test cylinder.

Figure 7.4a-e Frequency distribution of Angle Ax (ϕ) orientations of each grain type in the undeformed China Beach Sandstone sample. Measurements taken from a plane parallel to the long axis of the test cylinder.

a) undeformed quartz.
b) undulose quartz.
c) unaltered feldspar.
d) altered feldspar.
e) lithic fragments.

a)

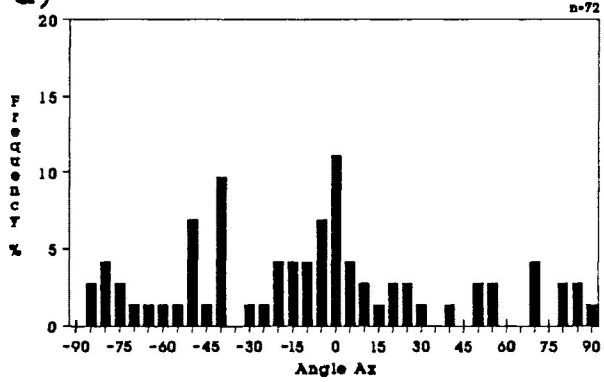
n=72
Frequency %
20
15
10
5
0
-90 -75 -60 -45 -30 -15 0 15 30 45 60 75 90
Angle Ax

b)

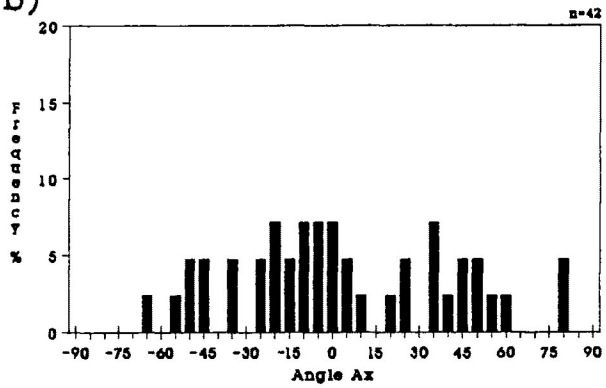
n=42
Frequency %
20
15
10
5
0
-90 -75 -60 -45 -30 -15 0 15 30 45 60 75 90
Angle Ax

c)

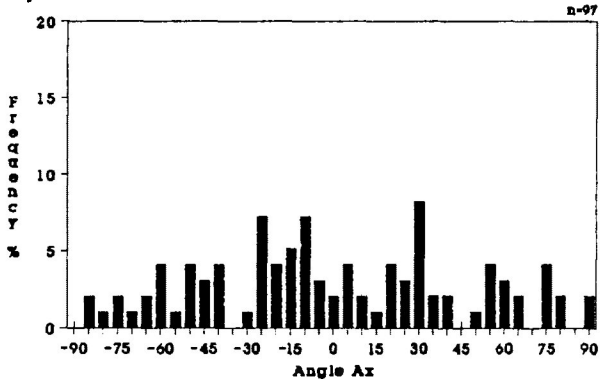
n=97
Frequency %
20
15
10
5
0
-90 -75 -60 -45 -30 -15 0 15 30 45 60 75 90
Angle Ax

d)

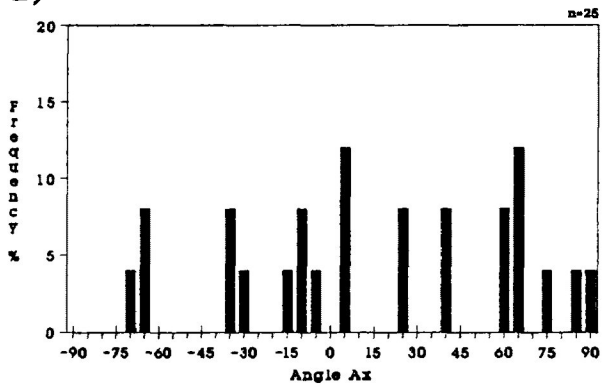
n=25
Frequency %
20
15
10
5
0
-90 -75 -60 -45 -30 -15 0 15 30 45 60 75 90
Angle Ax

e)

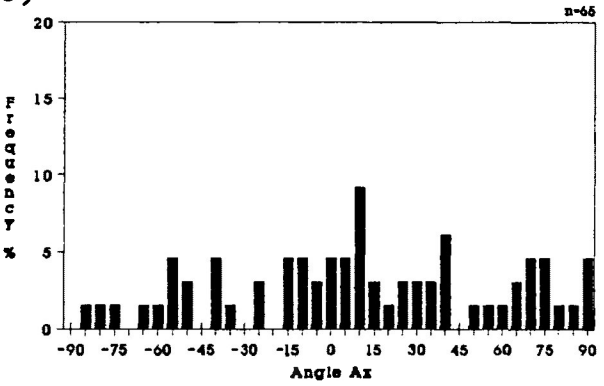
n=65
Frequency %
20
15
10
5
0
-90 -75 -60 -45 -30 -15 0 15 30 45 60 75 90
Angle Ax

Figure 7.5a-e Frequency distribution of range of R_i for each grain type in the undeformed China Beach sandstone. Measurements taken from a plane parallel to the long axis of the test cylinder.

a) undeformed quartz.
b) undulose quartz.
c) unaltered feldspar.
d) altered feldspar.
e) lithic fragments.

a)

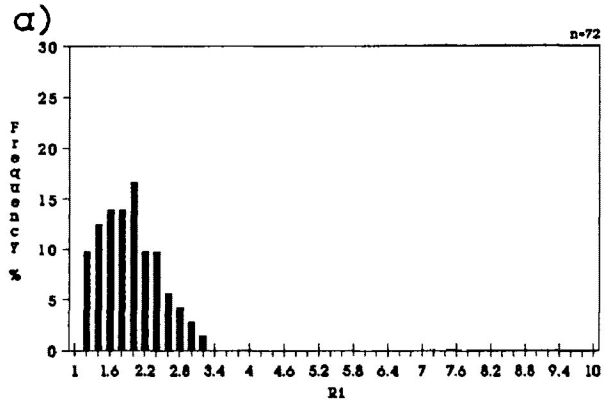
n=72
Frequency %
0
5
10
15
20
25
30
1 1.6 2.2 2.8 3.4 4 4.6 5.2 5.8 6.4 7 7.6 8.2 8.8 9.4 10
R1

b)

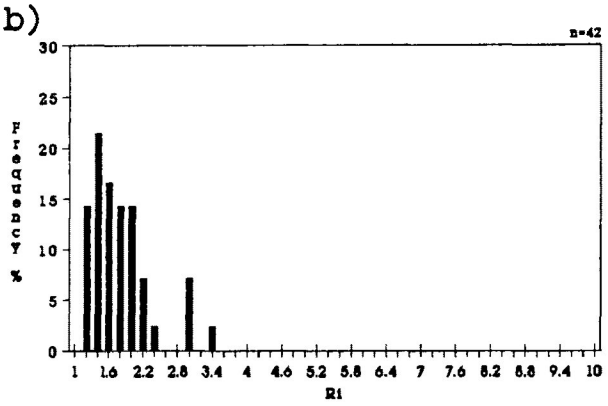
n=42
Frequency %
0
5
10
15
20
25
30
1 1.6 2.2 2.8 3.4 4 4.6 5.2 5.8 6.4 7 7.6 8.2 8.8 9.4 10
R1

c)

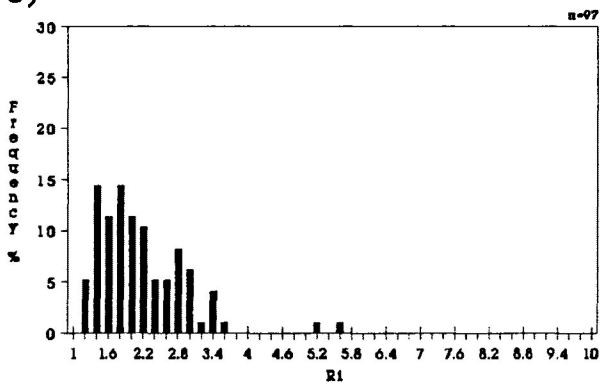
n=97
Frequency %
0
5
10
15
20
25
30
1 1.6 2.2 2.8 3.4 4 4.6 5.2 5.8 6.4 7 7.6 8.2 8.8 9.4 10
R1

d)

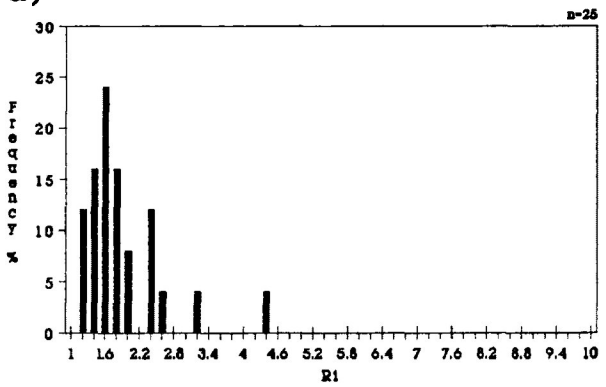
n=25
Frequency %
0
5
10
15
20
25
30
1 1.6 2.2 2.8 3.4 4 4.6 5.2 5.8 6.4 7 7.6 8.2 8.8 9.4 10
R1

e)

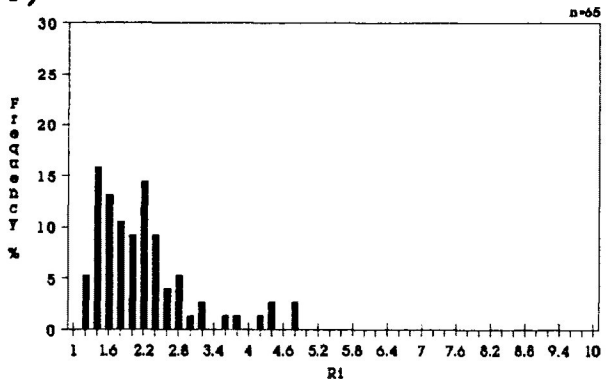
n=65
Frequency %
0
5
10
15
20
25
30
1 1.6 2.2 2.8 3.4 4 4.6 5.2 5.8 6.4 7 7.6 8.2 8.8 9.4 10
R1

that the R_i distributions are approximately lognormal, both for the entire sample and for each individual grains. The lowest and highest range of R_i is exhibited in undeformed quartz (Fig. 7.5a) and lithic fragments (Fig.7.5e), respectively.

7.3 Analysis of the China Beach sandstone

Orientational, dimensional and strain analysis (Robin's, linearization, and harmonic mean methods) was conducted on the 5 major grain types present in the undeformed and deformed China Beach sandstone samples. The grain types consist of quartz (undulose and fractured), feldspar (unaltered and altered) and lithic fragments.

a) Quartz grains

Detrital quartz grains in the deformed China Beach sandstone occur as two types. The two types consist of fractured and undulose quartz. However, the presence of fractured quartz becomes dominant at low strains (<8.0% (R_s=1.133) shortening) in the deformation experiments (figure 7.6). It is apparent from the undeformed state that the majority of these two grain types are derived mainly from quartz grains that exhibited little deformation at the microscopic scale (*i.e.*, undeformed quartz). At the temperature of triaxial deformation in this experiment (25°C), the quartz grain are expected to behave as rigid particles.

i) fractured quartz

At low strains the percentage of the sample that consists of quartz grains that exhibit fracturing becomes greater (Figure 7.6). The fractures present in the quartz grains are of three types. The first appears to be extensional fractures,

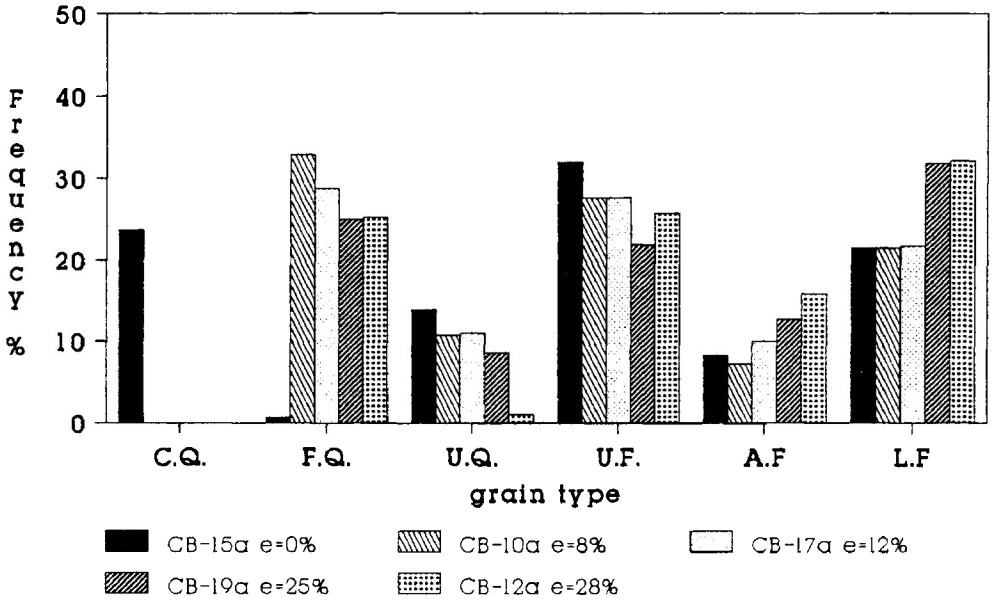

Figure 7.6 Volume % of the 5 major grain types present in the undeformed and undeformed and deformed China Beach sandstone samples. The grain types consist of quartz (undeformed (C.Q.), fractured (F.Q.) and undulose (U.Q.)), feldspar (unaltered (U.F.) and altered (A.F.) and lithic fragments (L.F.). Measurements taken from a plane parallel to the long axis of the test cylinder.

with fracture planes approximately perpendicular to the extension direction (σ_3). The second is present in quartz grains as shear fractures, with fracture planes inclined to the principal compressive stress (σ_1). Minor slip is observed on these shear fractures. The third observed type is that of radial fractures caused by grain to grain contact of rigid grains, such as other quartz grains and unaltered feldspars. In the cases extensional and radial types many of the fracture planes exhibit dilation in the principal extension direction.

Figure 7.7a-d illustrates the orientational frequency distribution of the longest dimension (Angle Ax (ϕ)) of fractured quartz grains for increasing strain. From the figure it is observed that there is a moderately good development of a PDO with a decrease in angular deviation from 21.0 (e=8.0%) to 14.31 (e=28.0%). The fluctuation of the orientation distribution is reduced by a small amount as strain increases from 0% to 28% shortening (approximately 180° (e=0%) to 160° (e=28%)).

In the R_f frequency distributions, as presented in figure 7.8a-e, there is observed very little increase in the maximum R_f of the quartz grains. However, there is a tendency for the grains to become less spherical. It is believed that this increase in R_f probably reflects the pulling apart of the fracture quartz grain, by dilation normal to fracture planes, into slightly elongated grains which may then under go rotation into a weak PDO. The R_f/ϕ diagrams for fractured quartz grains is presented in figure 7.9a-e. These figures suggest that there is only a small change in R_f, but a development of a PDO.

Strain analysis of fractured quartz grains is presented in figure 7.10 for the Robin's, linearization, and harmonic mean methods. From the figure it is observed that there is a

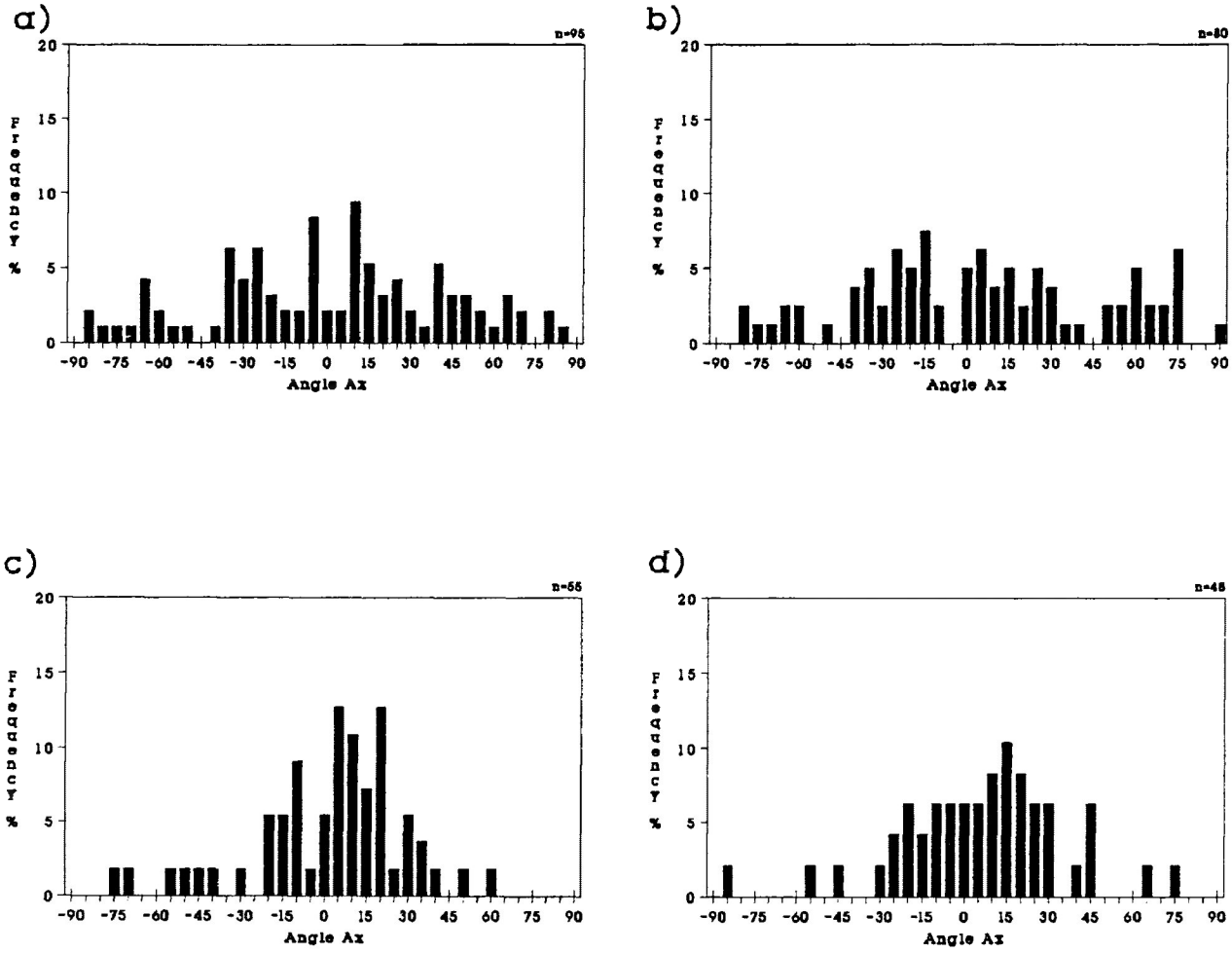

Figure 7.7a-d Frequency distribution of Angle Ax (ϕ) orientations of fractured quartz in the X/Z principal plane of the deformed China Beach sandstone samples. Experimental strain ratios range from 1.133 (e=8.0%) to 1.637 (e=28.0%). Maximum extension direction oriented at 0°. Samples were deformed under dry experimental conditions with confining pressures of 200 Mpa, strain rate of 10^{-5}/s and temperatures of 25°C. Measurements taken from the X/Z principal plane of the deformed test cylinder.

a) e=8.0% (R_s=1.133)
b) e=12.0% (R_s=1.211)
c) e=25.0% (R_s=1.540)
d) e=28.0% (R_s=1.637)

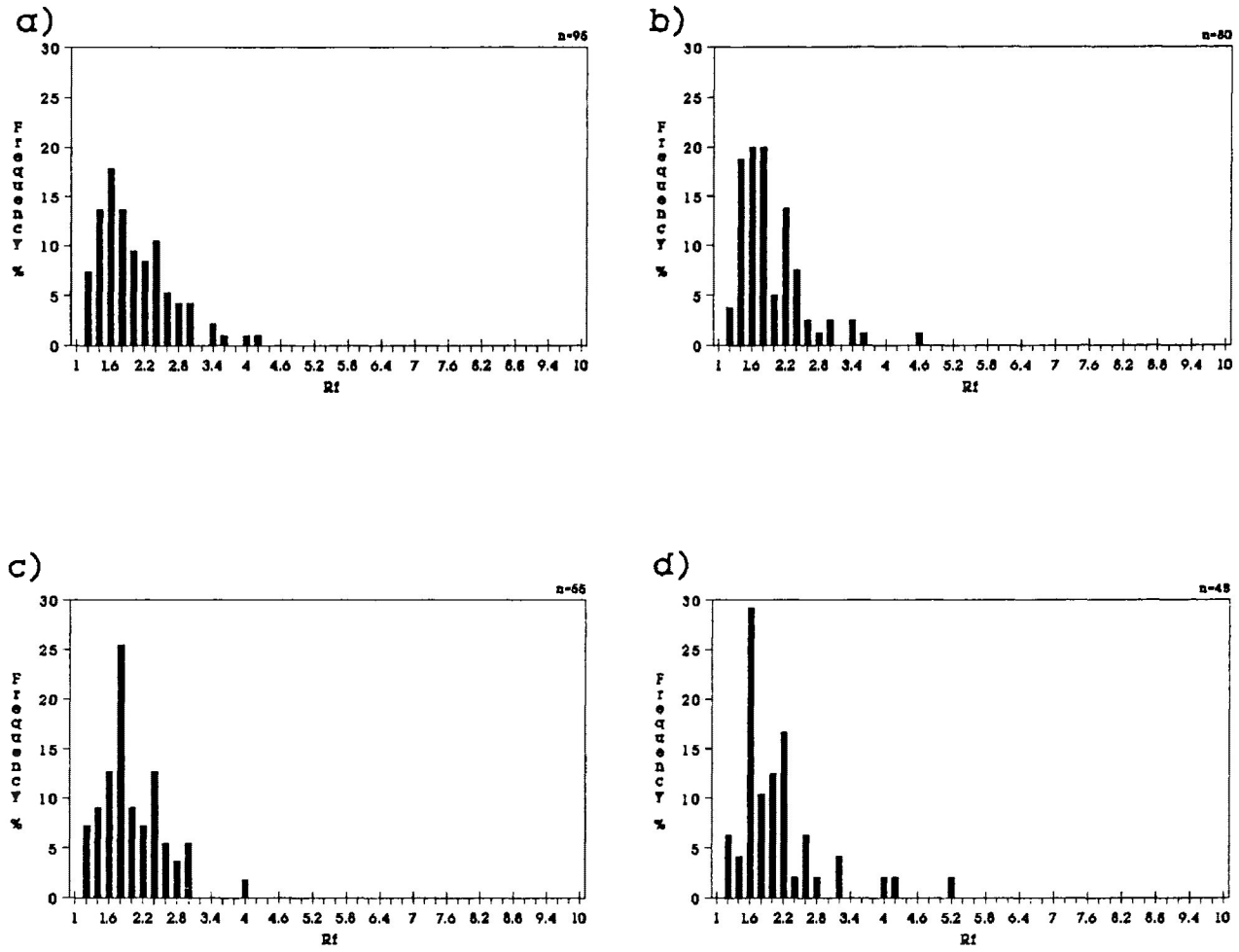

Figure 7.8a-d Frequency distribution of R_f for fractured quartz in the X/Z principal plane of the deformed China Beach sandstone samples. Experimental strain ratios range from 1.133 (e=8.0%) to 1.637 (e=28.0%). Samples were deformed under dry experimental conditions with confining pressures of 200 Mpa, strain rate of 10^{-5}/s and temperatures of 25°C. Measurements taken from the X/Z principal plane of the deformed test cylinder.

a) e=8.0% (R_s=1.133)
b) e=12.0% (R_s=1.211)
c) e=25.0% (R_s=1.540)
d) e=28.0% (R_s=1.637)

Figure 7.9a-e R_f/ϕ diagrams for fractured quartz in the X/Z principal plane of the deformed China Beach sandstone samples. Experimental strain ratios range from 1.000 (e=0.0%) to 1.637 (e=28.0%). Maximum extension direction oriented at 0°. Samples were deformed under dry experimental conditions with confining pressures of 200 Mpa, strain rate of 10^{-5}/s and temperatures of 25°C. Note statistical information given in the upper right hand corner of each R_f/ϕ diagram. Measurements taken from the X/Z principal plane of the deformed test cylinder.

a) e=0.0% (R_s=1.000)
b) e=8.0% (R_s=1.133)
c) e=12.0% (R_s=1.211)
d) e=25.0% (R_s=1.540)
e) e=28.0% (R_s=1.637)

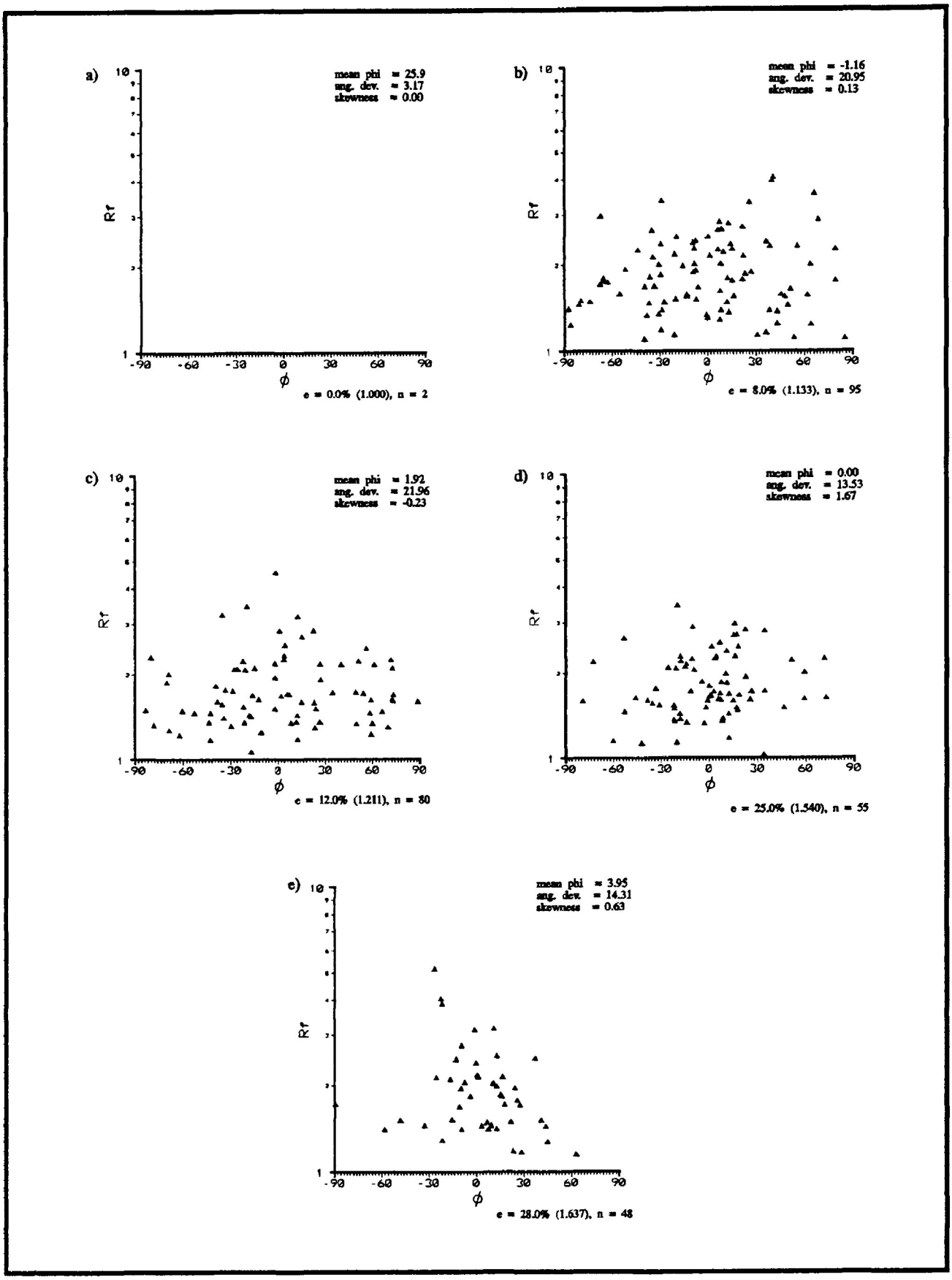
a)
mean phi = 25.9
ang. dev. = 3.17
skewness = 0.00
Rr
ϕ
e = 0.0% (1.000), n = 2
b)
mean phi = -1.16
ang. dev. = 20.95
skewness = 0.13
Rr
ϕ
e = 8.0% (1.133), n = 95
c)
mean phi = 1.92
ang. dev. = 21.96
skewness = -0.23
Rr
ϕ
e = 12.0% (1.211), n = 80
d)
mean phi = 0.00
ang. dev. = 13.53
skewness = 1.67
Rr
ϕ
e = 25.0% (1.540), n = 55
e)
mean phi = 3.95
ang. dev. = 14.31
skewness = 0.63
Rr
ϕ
e = 28.0% (1.637), n = 48

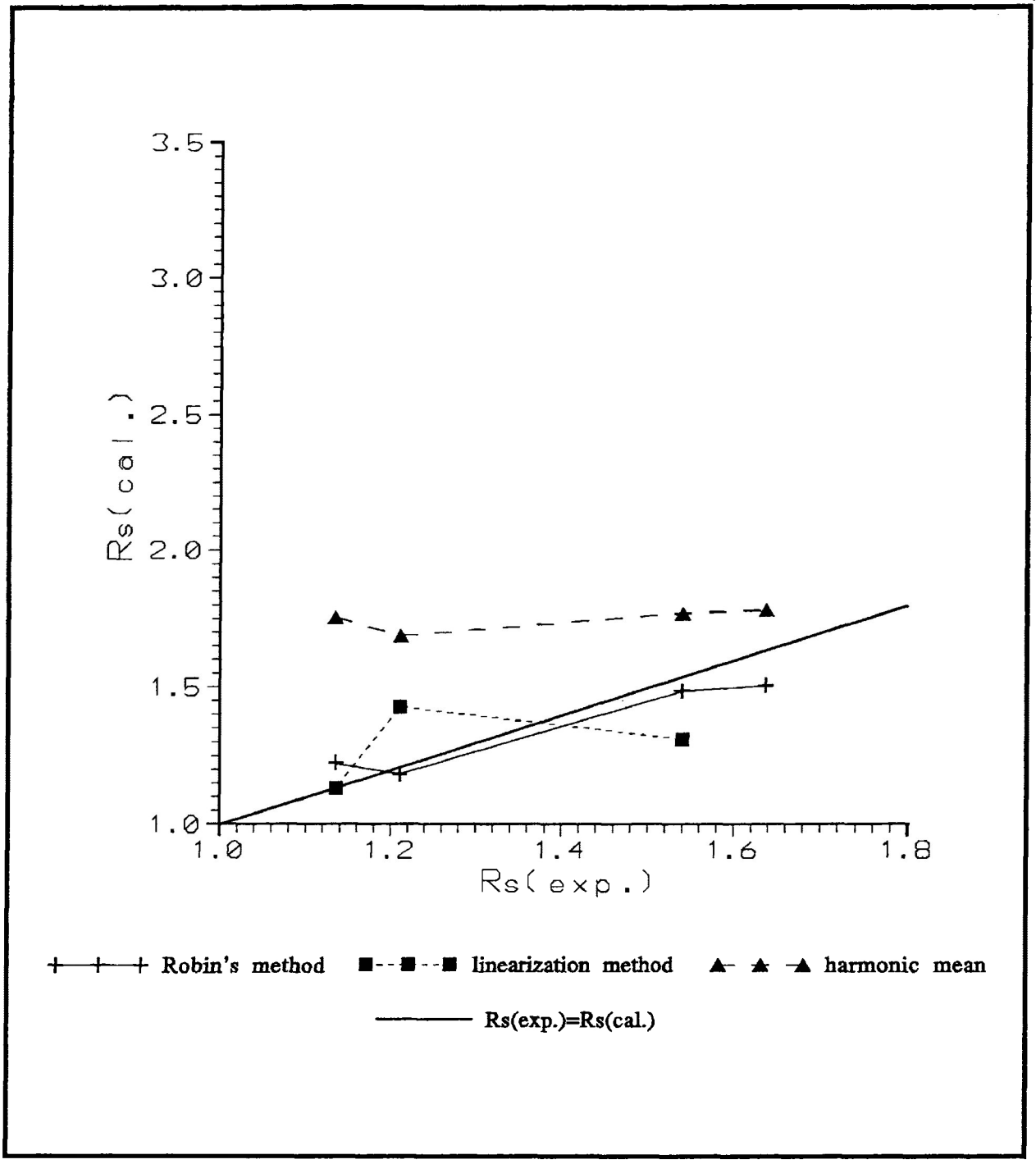

Figure 7.10 Comparison of strain estimates by Robin's method (1977), linearization method (Yu and Zheng, 1984) and harmonic mean method (Lisle, 1977) for fractured quartz in the X/Z principal plane of the deformed China Beach sandstone samples. Equivalent R_s is represented by the dark solid line. Experimental strain ratios range 1.133 (e=8.0%) to 1.637 (e=28.0%). Samples were deformed under dry experimental conditions with confining pressures of 200 Mpa, strain rate of 10^{-5}/s and temperatures of 25°C.

TABLE 7.1

sample	e%	Rs(exp.)	Robin's error (s.d.)	Harmonic error (s.d.)	Linear error (s.d.)	n
FRACTURED QTZ.						
CB-15A	0	1.000	0.109	0.935	n.a	2
CB-17A	12	1.211	0.146	0.182	n.a	80
CB-10A	18	1.347	0.121	0.154	n.a	95
CB-19A	25	1.540	0.157	0.188	n.a	55
CB-12A	28	1.637	0.767	0.799	n.a	48
UNDULOSE QTZ.						
CB-15A	0	1.000	0.162	0.206	n.a	42
CB-17A	12	1.211	0.146	0.182	n.a	63
CB-10A	18	1.347	0.206	0.255	n.a	31
CB-19A	25	1.540	0.273	0.303	n.a	19
CB-12A	28	1.637	0.767	0.799	n.a	31
UNALTERED FELD.						
CB-15A	0	1.000	0.168	0.158	n.a	97
CB-17A	12	1.211	0.120	0.156	n.a	97
CB-10A	18	1.347	0.130	0.171	n.a	80
CB-19A	25	1.540	0.169	0.216	n.a	48
CB-12A	28	1.637	0.174	0.224	n.a	49
ALTERED FELD.						
CB-15A	0	1.000	0.172	0.319	n.a	25
CB-17A	12	1.211	0.204	0.251	n.a	35
CB-10A	18	1.347	0.265	0.367	n.a	21
CB-19A	25	1.540	0.219	0.288	n.a	28
CB-12A	28	1.637	0.221	0.347	n.a	30
LITHIC FRAG.						
CB-15A	0	1.000	0.162	0.214	n.a	65
CB-17A	12	1.211	0.137	0.165	n.a	76
CB-10A	18	1.347	0.152	0.198	n.a	62
CB-19A	25	1.540	0.139	0.183	n.a	70
CB-12A	28	1.637	0.151	0.211	n.a	61

weak correlation between the actual strain and the strain estimate of Robin's and the linearization method (more so in Robin's method). In most cases the strain estimates are slight underestimates of the actual strain. The harmonic mean exhibits a slight increase as strain increases and is an overestimate of strain. However, the overestimate of strain becomes less as strain increases.

Standard deviation for Robin's method, linearization method and the harmonic mean method were calculated and are presented in Table 7.1. For the linearization method the calculations of standard deviation that yield confidence brackets that extend into bulk strains estimates less than 1.000 are not given.

It is believed that the deformation expressed in the grains of fractures quartz is the result of a combination of rigid rotation and dilation and minor slip on fracture surfaces. In the case of extensional and radial fractures the deformation results in a small amount of grain extension in an orientation approximately parallel to the extension direction of the deforming sandstone. For shear fractures slip may produce elongation of the grain, which may induce rigid body rotation into a weak PDO.

ii) Undulose Quartz

Detrital quartz that exhibits only undulose extinction (no visible fracturing) in the deformed China Beach sandstone decreases in sample percentage at higher strains (Fig. 7.6). Many of the undulose quartz grains become fractured as strain increases. The undulose extinction is low to moderate for all strains and is most likely detrital in origin.

Figure 7.11a-d illustrates the orientational frequency distribution (Angle Ax (ϕ)) of the longest dimension of undulose quartz grains for increasing experimental strain. From the figure it is observed that there is a very weak development of a PDO with a decrease in the angular deviation from 18.6 (e=0%) to 17.2 (e=25% (R_s=1.540)). Fluctuation of the orientational distribution remains high as experimental strain increases.

As presented in figure 7.12a-d there is observed little change in the R_f distribution of the quartz grains. This suggests that these grains are most likely part of the original undulose grains present in the undeformed state. The R_f/ϕ diagrams for undulose quartz grains is presented in figure 7.13a-e. These figures again suggest that there is little change in the undulose quartz fabric as strain increases. This is not to say that a fabric may have existed if many of quartz grains had not fractured as strain increased.

Strain analysis of undulose quartz grains is presented in figure 7.14 for the Robin's, linearization, and harmonic mean methods. From the figure it is observed that there is a poor correlation between the actual strain and the strain estimate of Robin's and the linearization method. In both cases the estimates of strain are underestimates of the actual strain producing the deformation. The harmonic mean exhibits little variation as strain increases suggesting a lack of any grain shape change in the undulose quartz grains. The harmonic mean is also an overestimate, which decreases in as strain increases.

Standard deviation for Robin's method, linearization method and the harmonic mean method were calculated and are presented in Table 7.1. For the linearization method the

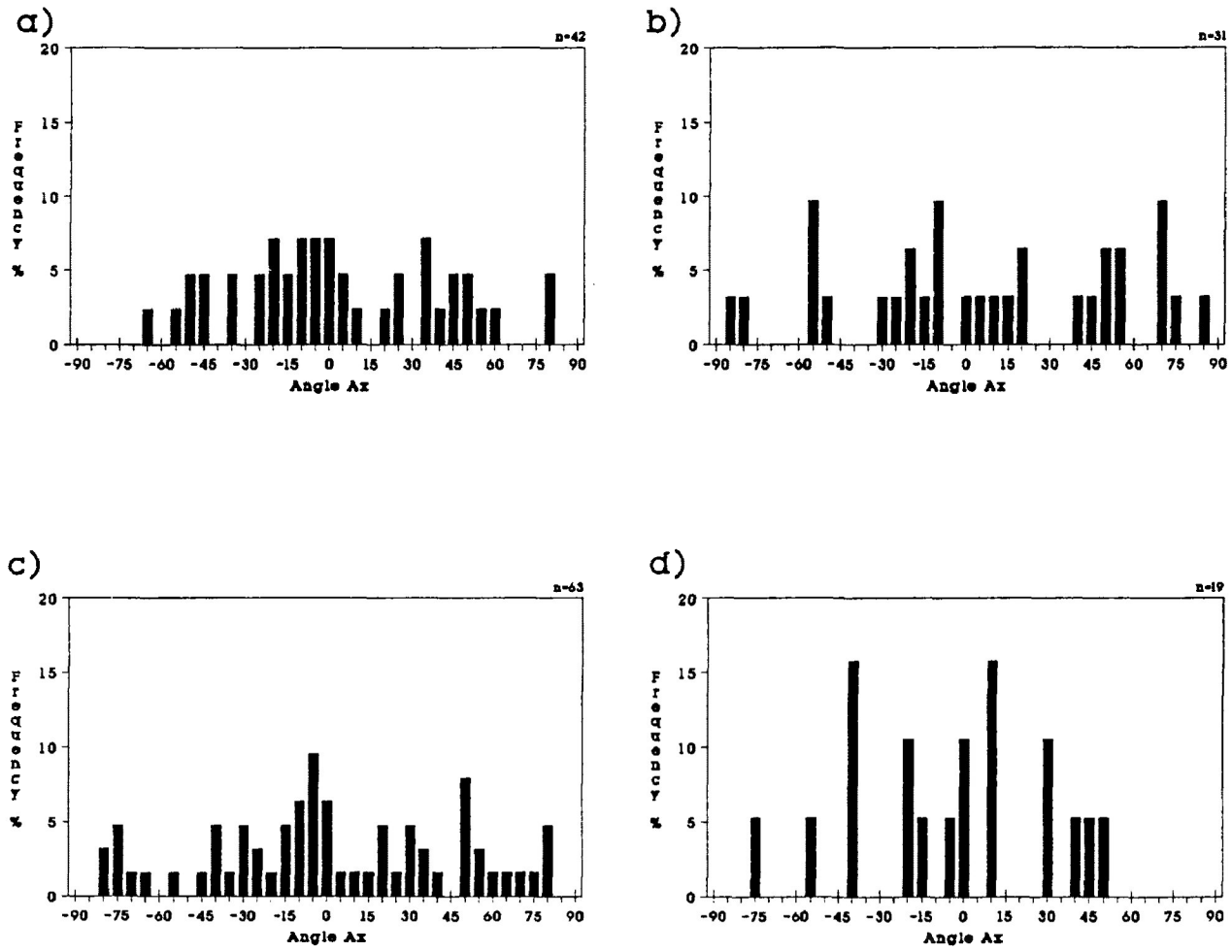

Figure 7.11a-d Frequency distribution of Angle Ax (ϕ) orientations of undulose quartz in the X/Z principal plane of the deformed China Beach sandstone samples. Experimental strain ratios range from 1.000 (e=0.0%) to 1.637 (e=28.0%). Maximum extension direction oriented at 0°. Samples were deformed under dry experimental conditions with confining pressures of 200 Mpa, strain rate of 10^{-5}/s and temperatures of 25°C. Measurements taken from the X/Z principal plane of the deformed test cylinder.

a) e=0.0% (R_s=1.000)
b) e=8.0% (R_s=1.133)
c) e=12.0% (R_s=1.211)
d) e=25.0% (R_s=1.540)

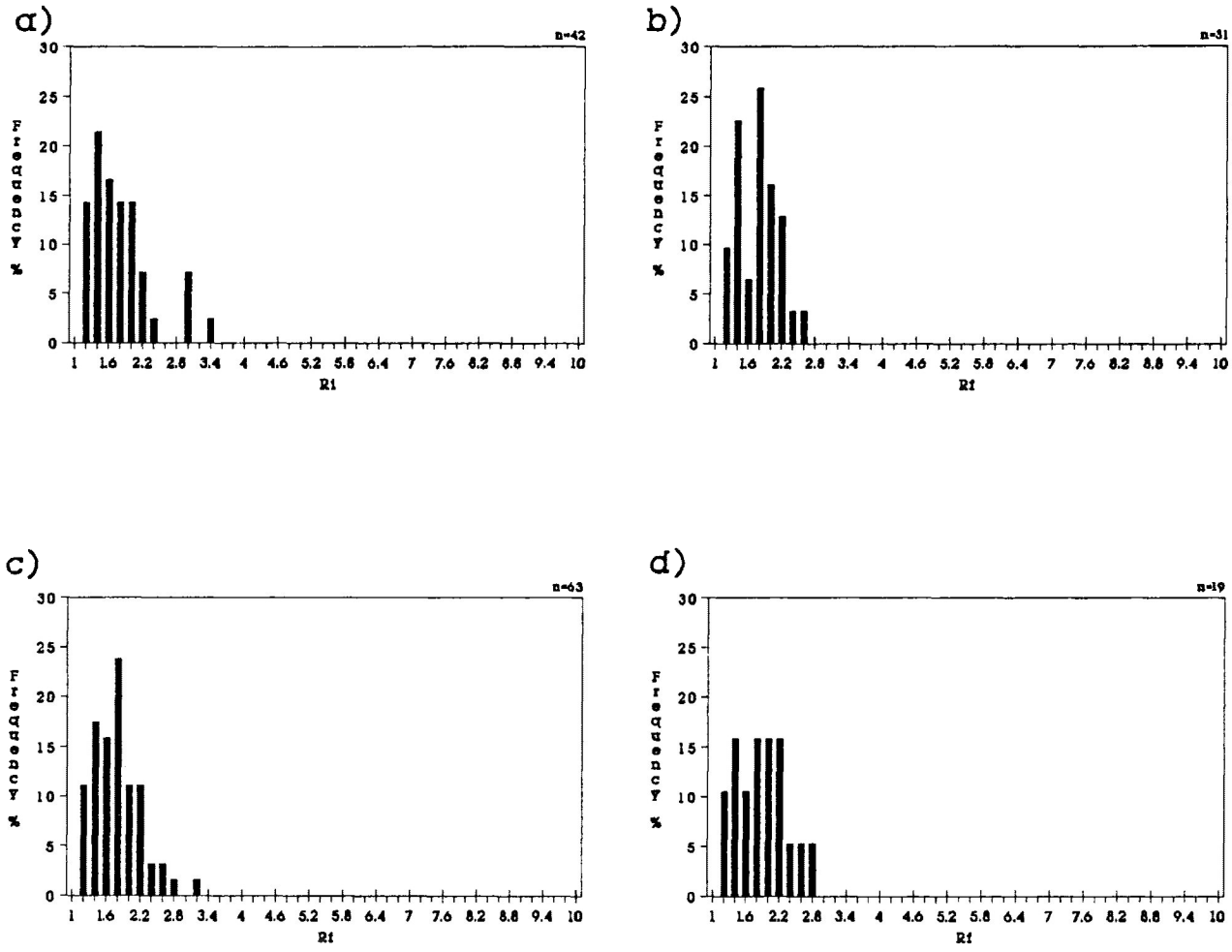

Figure 7.12a-d Frequency distribution of R_f for undulose quartz in deformed in the X/Z principal plane of the China Beach sandstone samples. Experimental strain ratios range from 1.000 (e=0.0%) to 1.637 (e=28.0%). Samples were deformed under dry experimental conditions with confining pressures of 200 Mpa, strain rate of 10^{-5}/s and temperatures of 25°C. Measurements taken from the X/Z principal plane of the deformed test cylinder.

a) e=0.0% (R_s=1.000)
b) e=8.0% (R_s=1.133)
c) e=12.0% (R_s=1.211)
d) e=25.0% (R_s=1.540)

Figure 7.13a-e R_f/ϕ diagrams for undulose quartz in the X/Z principal plane of the deformed China Beach sandstone samples. Experimental strain ratios range from 1.000 (e=0.0%) to 1.637 (e=28.0%). Maximum extension direction oriented at 0°. Samples were deformed under dry experimental conditions with confining pressures of 200 Mpa, strain rate of 10^{-5}/s and temperatures of 25°C. Note statistical information given in the upper right hand corner of each R_f/ϕ diagram. Measurements taken from the X/Z principal plane of the deformed test cylinder.

a) e=0.0% (R_s=1.000)
b) e=8.0% (R_s=1.133)
c) e=12.0% (R_s=1.211)
d) e=25.0% (R_s=1.540)
e) e=28.0% (R_s=1.637)

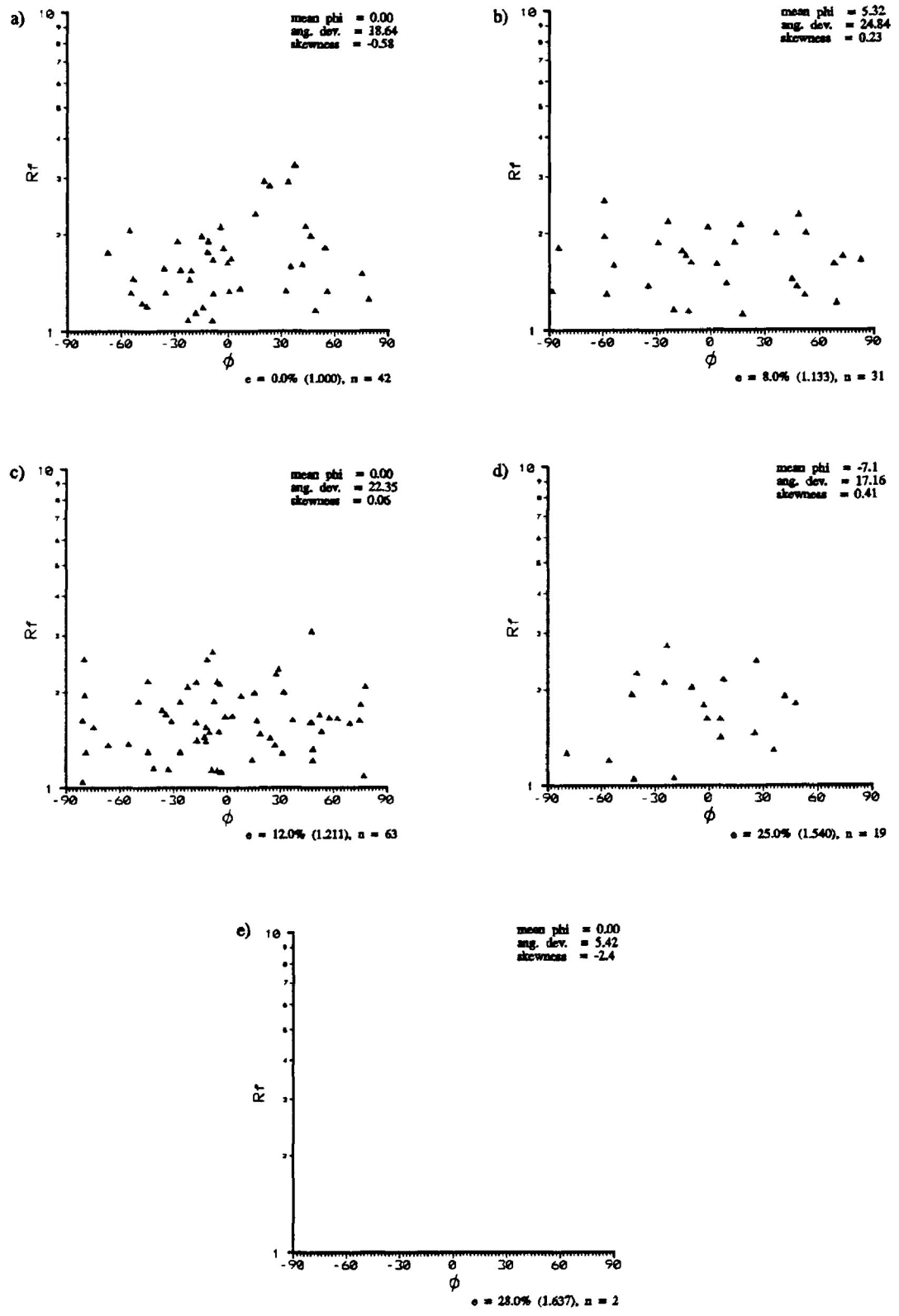
a)
mean phi = 0.00
ang. dev. = 18.64
skewness = -0.58
Rf
ϕ
e = 0.0% (1.000), n = 42
b)
mean phi = 5.32
ang. dev. = 24.84
skewness = 0.23
Rf
ϕ
e = 8.0% (1.133), n = 31
c)
mean phi = 0.00
ang. dev. = 22.35
skewness = 0.06
Rf
ϕ
e = 12.0% (1.211), n = 63
d)
mean phi = -7.1
ang. dev. = 17.16
skewness = 0.41
Rf
ϕ
e = 25.0% (1.540), n = 19
e)
mean phi = 0.00
ang. dev. = 5.42
skewness = -2.4
Rf
ϕ
e = 28.0% (1.637), n = 2

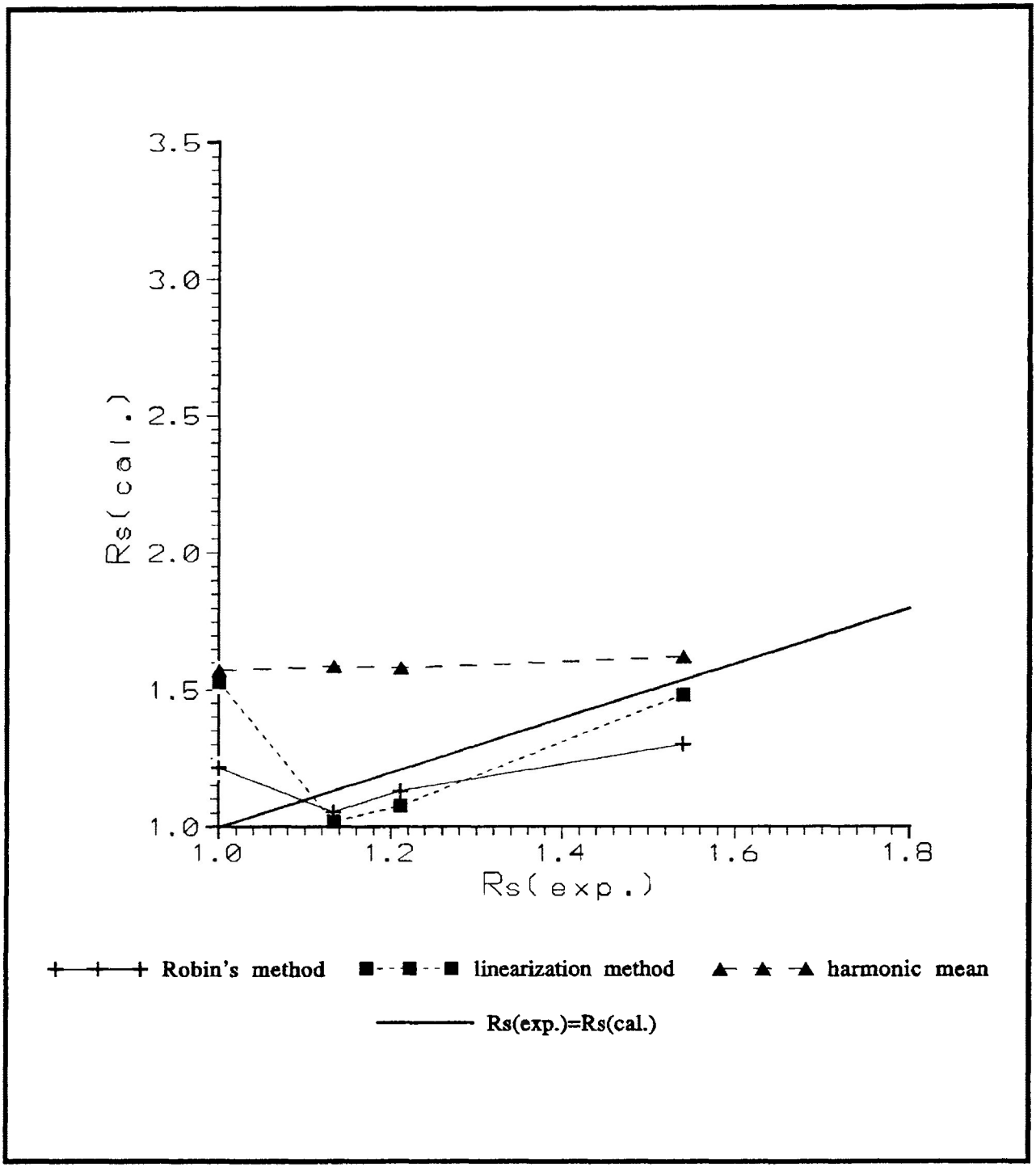

Figure 7.14 Comparison of strain estimates by Robin's method (1977), linearization method (Yu and Zheng, 1984) and harmonic mean method (Lisle, 1977) for undulose quartz in the X/Z principal plane of the China Beach sandstone samples. Equivalent R_s is represented by the dark solid line. Experimental strain ratios range from 1.133 (e=8.0%) to 1.637 (e=28.0%). Samples were deformed under dry experimental conditions with confining pressures of 200 Mpa, strain rate of 10^{-5}/s and temperatures of 25°C.

calculations of standard deviation that yield confidence brackets that extend into bulk strains estimates less than 1.000 are not given.

It is believed that most of the crystallographic deformation expressed in the grain of the undulose quartz is detrital. However, rigid rotation of these grains may be occurring in response to the deformation of more ductile neighbouring grains. Most of the undulose quartz grains undergo fracturing as strain increases.

b) Feldspar grains

Detrital feldspar grains in the deformed China Beach sandstone can be subdivided into two types. These two types consist of unaltered and altered feldspar. Each of these types of grains exhibit very different rheological behaviour.

i) unaltered feldspar.

Detrital undeformed feldspar in the deformed China Beach sandstone exhibits no deformation textures. However, in the deformed state a small number of unaltered feldspar exhibits bending of twin lamellae in a sigmoidal sense, representing either dextral or sinistral shear along shear surfaces against ductile grains. Strained extinction is also observed in some grains. Extensional fractures are also observed is some of the unaltered feldspar grains. The fracturing is much less in sample percentage than in the case of fractured quartz.

Figure 7.15a-e illustrates the orientational frequency distribution of the longest dimension (Angle Ax (ϕ)) of unaltered feldspar grains for increasing experimental strain. From the figure it is observed that there is a relatively good development of a PDO with a decrease in the angular deviation

Figure 7.15a-e Frequency distribution of Angle Ax (ϕ) orientations of unaltered feldspar in the X/Z principal plane of the deformed China Beach sandstone samples. Experimental strain ratios range from 1.000 (e=0.0%) to 1.637 (e=28.0%). Maximum extension direction oriented at 0°. Samples were deformed under dry experimental conditions with confining pressures of 200 Mpa, strain rate of 10^{-5}/s and temperatures of 25°C. Measurements taken from the X/Z principal plane of the deformed test cylinder.

a) e=0.0% (R_s=1.000)
b) e=8.0% (R_s=1.133)
c) e=12.0% (R_s=1.211)
d) e=25.0% (R_s=1.540)
e) e=28.0% (R_s=1.637)

a)

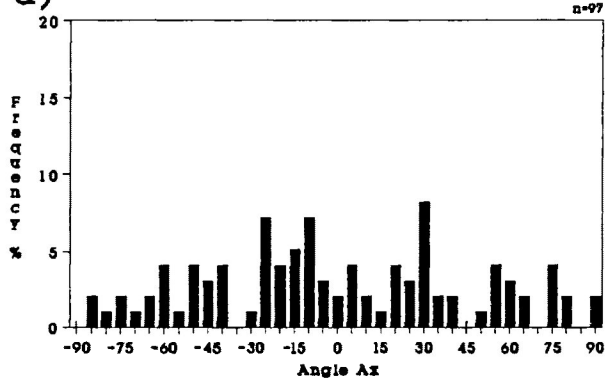
n=97
Frequency %
20
15
10
5
0
-90 -75 -60 -45 -30 -15 0 15 30 45 60 75 90
Angle Ax

b)

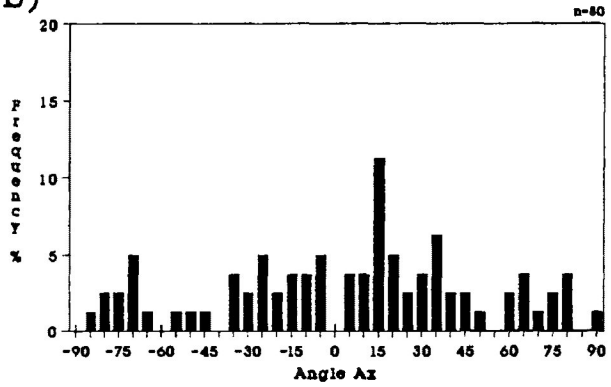
n=80
Frequency %
20
15
10
5
0
-90 -75 -60 -45 -30 -15 0 15 30 45 60 75 90
Angle Ax

c)

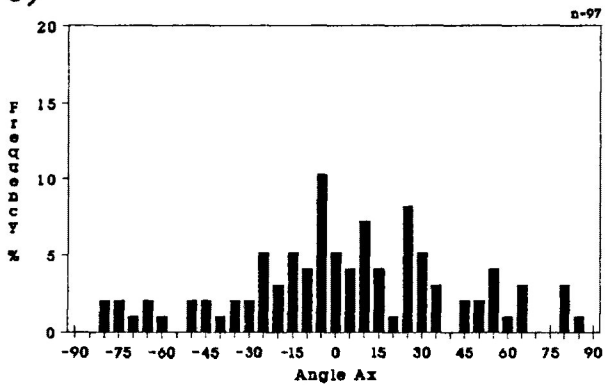
n=97
Frequency %
20
15
10
5
0
-90 -75 -60 -45 -30 -15 0 15 30 45 60 75 90
Angle Ax

d)

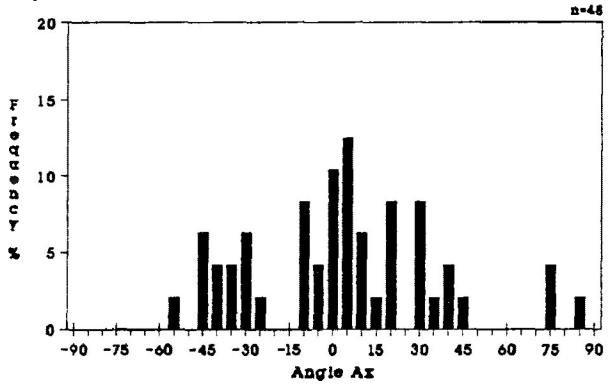
n=48
Frequency %
20
15
10
5
0
-90 -75 -60 -45 -30 -15 0 15 30 45 60 75 90
Angle Ax

e)

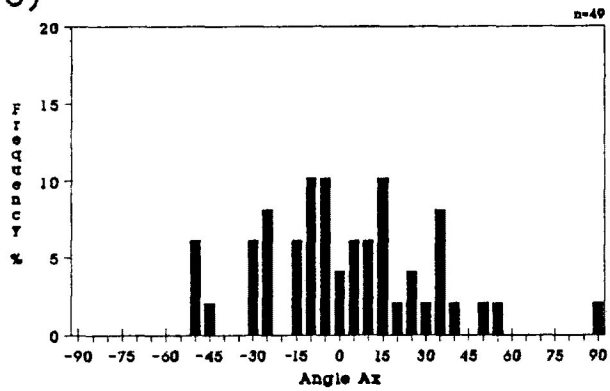
n=49
Frequency %
20
15
10
5
0
-90 -75 -60 -45 -30 -15 0 15 30 45 60 75 90
Angle Ax

from 23.0 (e=0%) to 14.0 (e=28%). Fluctuation of the orientation distribution decreases considerably as strain increases (180° (e=0%) to 105° (e=28%)).

As presented in figure 7.16a-e there is observed a small increase in the R_f of the unaltered feldspar grains. However, this increase is only observed at high strains. The R_f/ϕ diagrams for unaltered feldspar grains is presented in figure 7.17a-e. These figures suggest that there is little change in R_f and a good development of a PDO.

Strain analysis of unaltered feldspar grains is presented in figure 7.18 for the Robin's, linearization, and harmonic mean methods. From the figure it is observed that there is a good correlation between the actual strain producing the deformation and the strain estimate of Robin's method. The strain estimate by Robin's method becomes increasingly better as strain increases. The linearization method exhibits a poor correlation with the R_s and becomes an increasing overestimate as strain increases. The harmonic mean exhibits an increase as strain increases and is an overestimate of strain. The harmonic mean is a better estimate of strain than the linearization method at high strains. Robin's method generates the best estimate of the experimental strain ratio.

Standard deviation for Robin's method, linearization method and the harmonic mean method were calculated and are presented in Table 7.1. For the linearization method the calculations of standard deviation that yield confidence brackets that extend into bulk strains estimates less than 1.000 are not given.

It is believed that most of the deformation expressed in the grains of the unaltered feldspar is the result of rigid rotation. Those grains with the highest R_i (*i.e.*, higher

Figure 7.16a-e Frequency distribution of R_f for unaltered feldspar in the X/Z principal plane of the deformed China Beach sandstone samples. Experimental strain ratios range from 1.000 (e=0.0%) to 1.637 (e=28.0%). Samples were deformed under dry experimental conditions with confining pressures of 200 Mpa, strain rate of 10^{-5}/s and temperatures of 25°C. Measurements taken from the X/Z principal plane of the deformed test cylinder.

a) e=0.0% (R_s=1.000)
b) e=8.0% (R_s=1.133)
c) e=12.0% (R_s=1.211)
d) e=25.0% (R_s=1.540)
e) e=28.0% (R_s=1.637)

a)

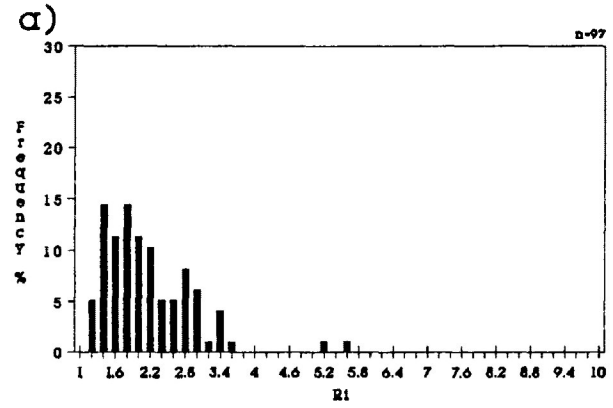
n=97
Frequency %
Rf

b)

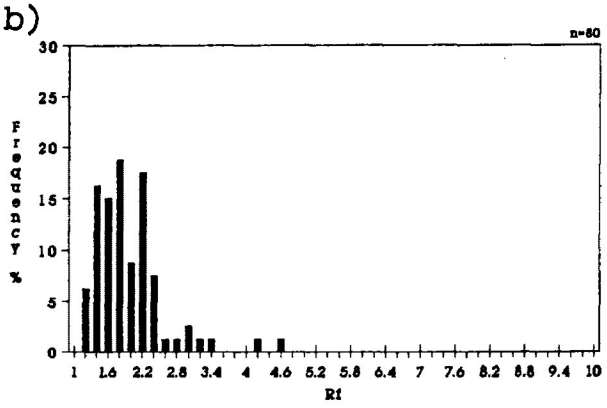
n=80
Frequency %
Rf

c)

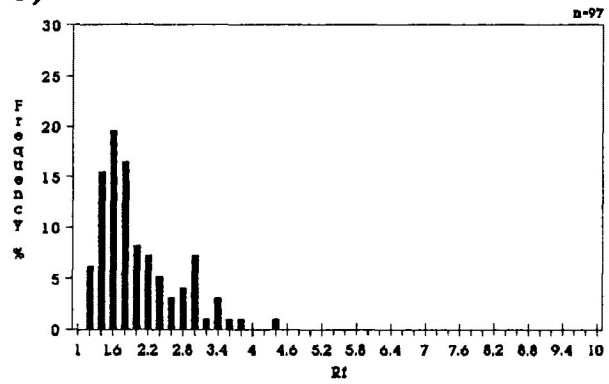
n=97
Frequency %
Rf

d)

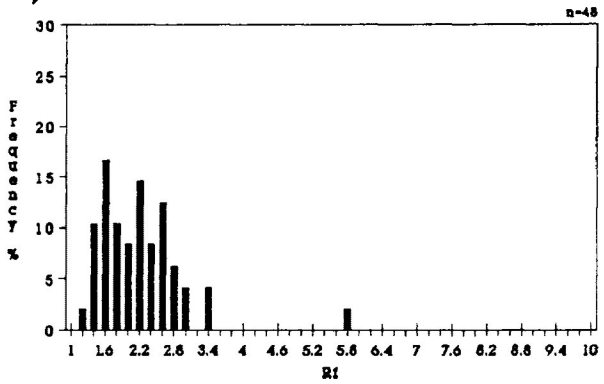
n=48
Frequency %
Rf

e)

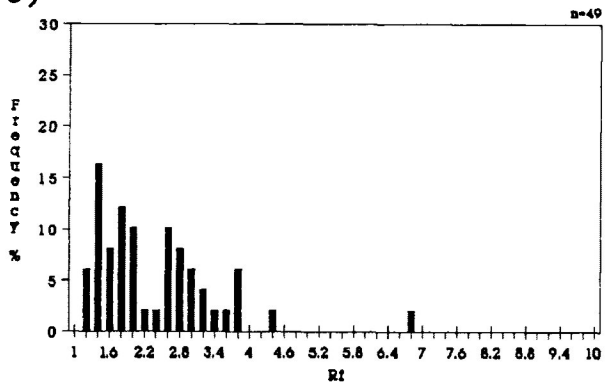
n=49
Frequency %
Rf

Figure 7.17a-e R_f/ϕ diagrams for unaltered feldspar in the X/Z principal plane of the deformed China Beach sandstone samples. Experimental strain ratios range from 1.000 (e=0.0%) to 1.637 (e=28.0%). Maximum extension direction oriented at 0°. Samples were deformed under dry experimental conditions with confining pressures of 200 Mpa, strain rate of 10^{-5}/s and temperatures of 25°C. Note statistical information given in the upper right hand corner of each R_f/ϕ diagram. Measurements taken from the X/Z principal plane of the deformed test cylinder.

a) e=0.0% (R_s=1.000)
b) e=8.0% (R_s=1.133)
c) e=12.0% (R_s=1.211)
d) e=25.0% (R_s=1.540)
e) e=28.0% (R_s=1.637)

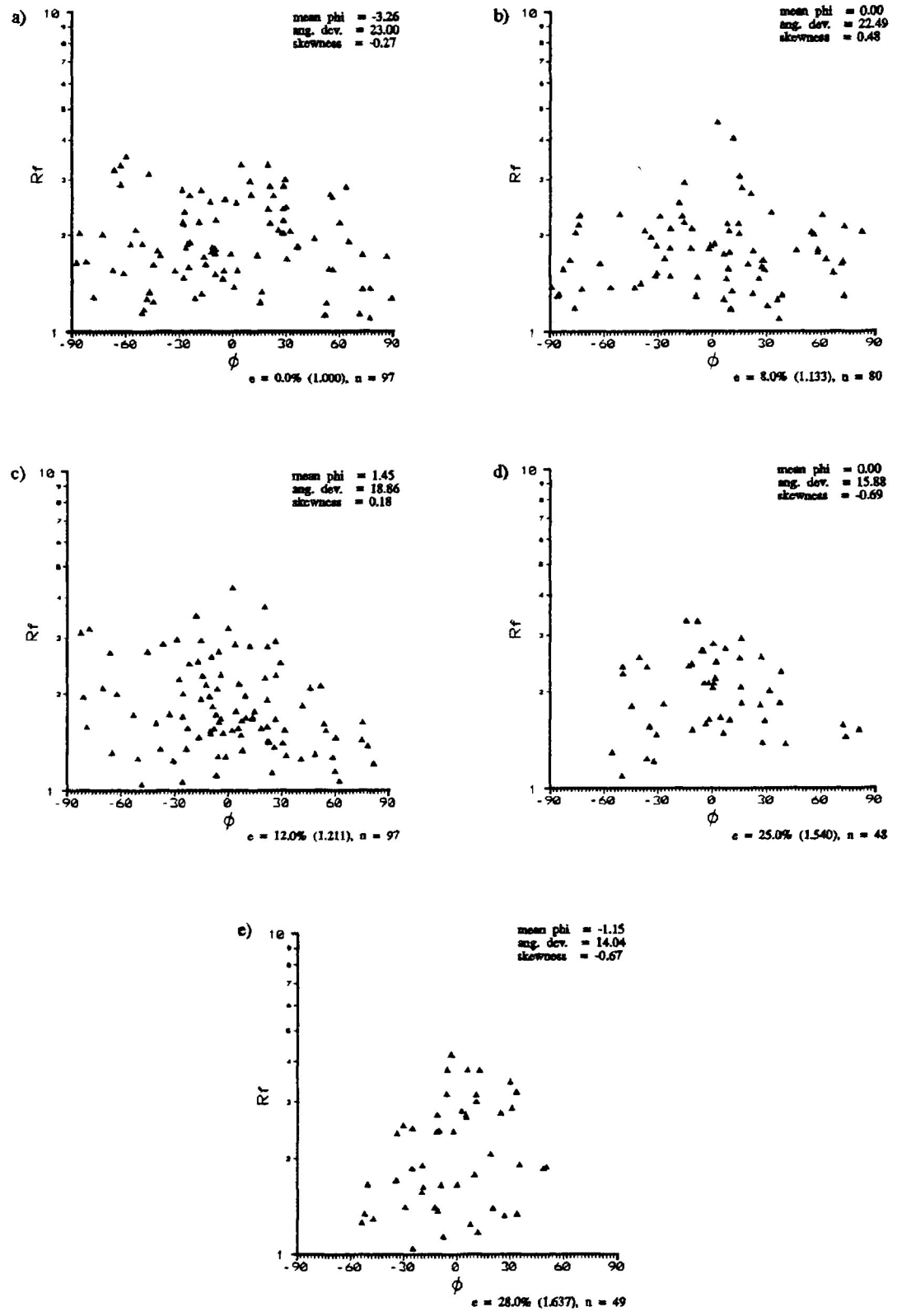
a)
mean phi = -3.26
ang. dev. = 23.00
skewness = -0.27
Rf
ϕ
e = 0.0% (1.000), n = 97
b)
mean phi = 0.00
ang. dev. = 22.49
skewness = 0.48
Rf
ϕ
e = 8.0% (1.133), n = 80
c)
mean phi = 1.45
ang. dev. = 18.86
skewness = 0.18
Rf
ϕ
e = 12.0% (1.211), n = 97
d)
mean phi = 0.00
ang. dev. = 15.88
skewness = -0.69
Rf
ϕ
e = 25.0% (1.540), n = 48
e)
mean phi = -1.15
ang. dev. = 14.04
skewness = -0.67
Rf
ϕ
e = 28.0% (1.637), n = 49

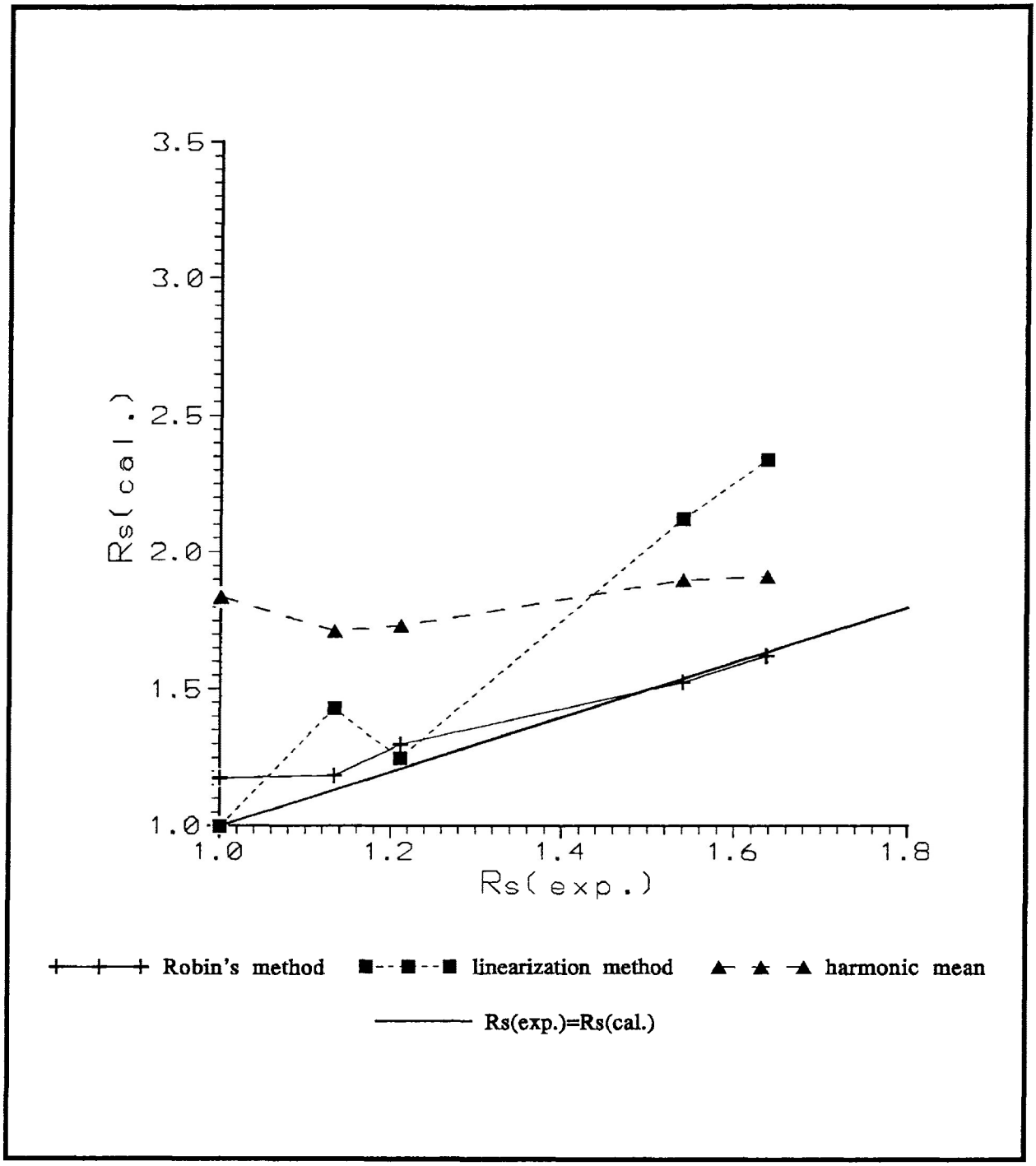

Figure 7.18 Comparison of strain estimates by Robin's method (1977), linearization method (Yu and Zheng, 1984) and harmonic mean method (Lisle, 1977) for unaltered feldspar in the X/Z principal plane of the China Beach sandstone samples. Equivalent R_s is represented by the dark solid line. Experimental strain ratios range from 1.133 (e=8.0%) to 1.637 (e=28.0%). Samples were deformed under dry experimental conditions with confining pressures of 200 Mpa, strain rate of 10^{-5}/s and temperatures of 25°C.

rotational inertia) are aligning quickly with the extension direction as strain increases. The rigid rotation of these grains may be enhanced by the deformation of more ductile neighbouring grains. It is possible that some plastic deformation is occurring in grains with polysynthetic twinning (expressed by bending of the twin lamellae and undulose extinction) or in the case of grains with slight alteration. Some unaltered feldspar grains exhibit fracturing.

ii) altered feldspar

Detrital altered feldspar grain in the deformed China Beach sandstone are observed to have varying degrees of alteration. Those grains that are the most altered exhibit the largest strain.

Figure 7.19a-e illustrates the orientational frequency distribution of the longest dimension (Angle Ax (ϕ)) of altered feldspar grains for increasing experimental strain. From the figure it is observed that there is a well developed PDO with a decrease in the angular deviation from 24.5 (e=0%) to 13.8 (e=28%). Fluctuation of the orientational distribution decreases considerably as strain increases (180° (e=0%) to 125° (e=28%)).

As presented in figure 7.20a-e there is observed a large increase in the range of R_f for altered feldspar grains as strain increases suggesting ductile behaviour. The R_f/ϕ diagrams for altered feldspar grains are presented in figure 7.21a-e. These figures suggest that the altered feldspar grain are behaving ductilely with a large increase in R_f and a well developed PDO parallel to the extension direction.

Strain analysis of altered feldspar grains is presented in figure 7.22 for the Robin's, linearization, and harmonic

Figure 7.19a-e Frequency distribution of Angle Ax (ϕ) orientations of altered feldspar in the X/Z principal plane of the deformed China Beach sandstone samples. Experimental strain ratios range from 1.000 (e=0.0%) to 1.637 (e=28.0%). Maximum extension direction oriented at 0°. Samples were deformed under dry experimental conditions with confining pressures of 200 Mpa, strain rate of 10^{-5}/s and temperatures of 25°C. Measurements taken from the X/Z principal plane of the deformed test cylinder.

a) e=0.0% (R_s=1.000)
b) e=8.0% (R_s=1.133)
c) e=12.0% (R_s=1.211)
d) e=25.0% (R_s=1.540)
e) e=28.0% (R_s=1.637)

a)

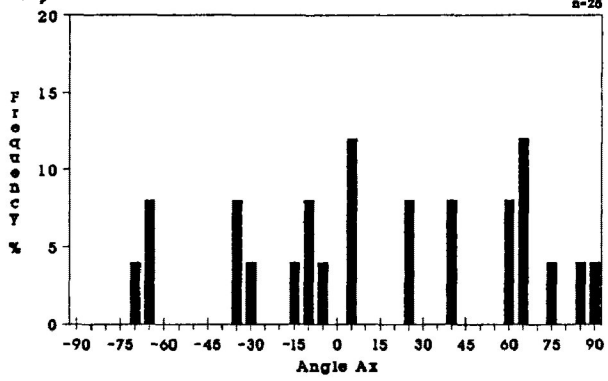
n=25
Frequency %
0
5
10
15
20
-90 -75 -60 -45 -30 -15 0 15 30 45 60 75 90
Angle Ax

b)

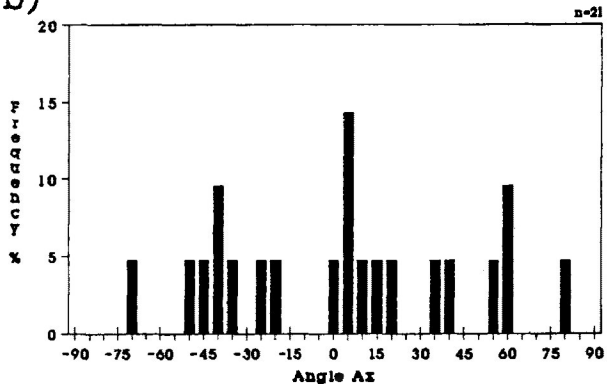
n=21
Frequency %
0
5
10
15
20
-90 -75 -60 -45 -30 -15 0 15 30 45 60 75 90
Angle Ax

c)

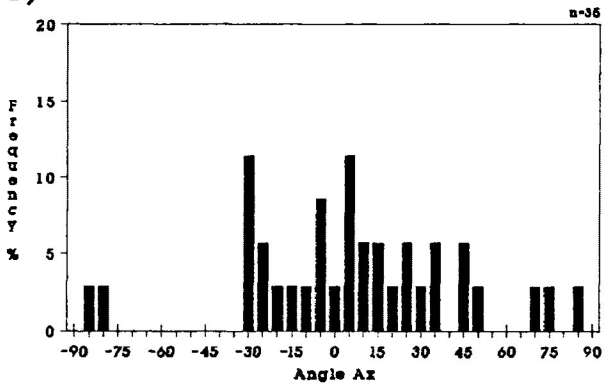
n=35
Frequency %
0
5
10
15
20
-90 -75 -60 -45 -30 -15 0 15 30 45 60 75 90
Angle Ax

d)

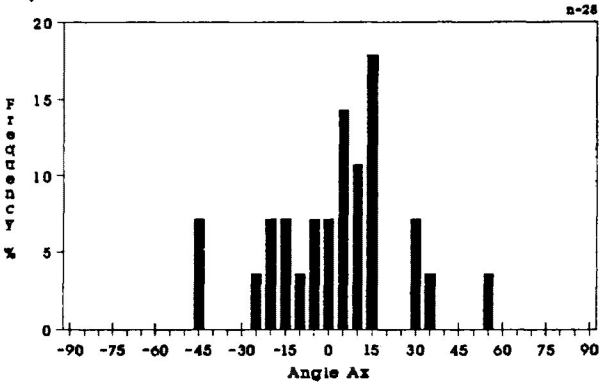
n=28
Frequency %
0
5
10
15
20
-90 -75 -60 -45 -30 -15 0 15 30 45 60 75 90
Angle Ax

e)

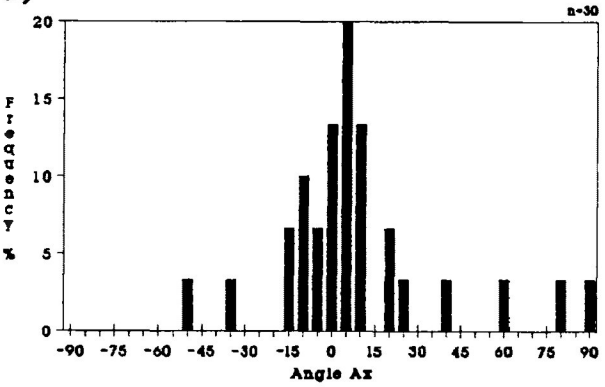
n=30
Frequency %
0
5
10
15
20
-90 -75 -60 -45 -30 -15 0 15 30 45 60 75 90
Angle Ax

Figure 7.20a-e Frequency distribution of R_f for altered feldspar in the X/Z principal plane of the deformed China Beach sandstone samples. Experimental strain ratios range from 1.000 (e=0.0%) to 1.637 (e=28.0%). Samples were deformed under dry experimental conditions with confining pressures of 200 Mpa, strain rate of 10^{-5}/s and temperatures of 25°C. Measurements taken from the X/Z principal plane of the deformed test cylinder.

a) e=0.0% (R_s=1.000)
b) e=8.0% (R_s=1.133)
c) e=12.0% (R_s=1.211)
d) e=25.0% (R_s=1.540)
e) e=28.0% (R_s=1.637)

a)

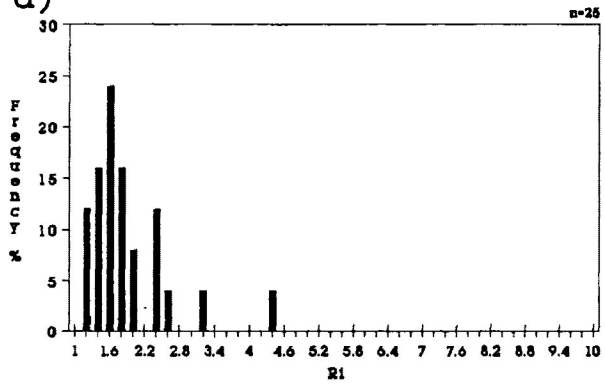
n=25
Frequency %
Rf

b)

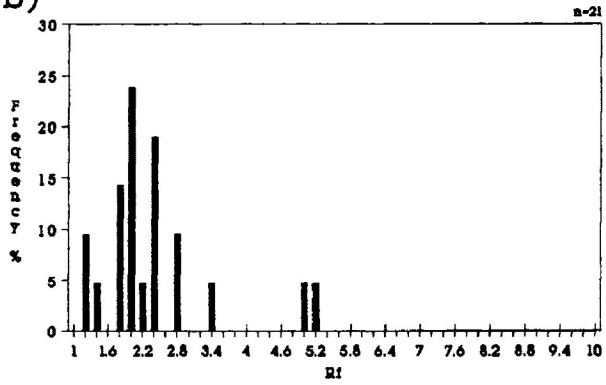
n=21
Frequency %
Rf

c)

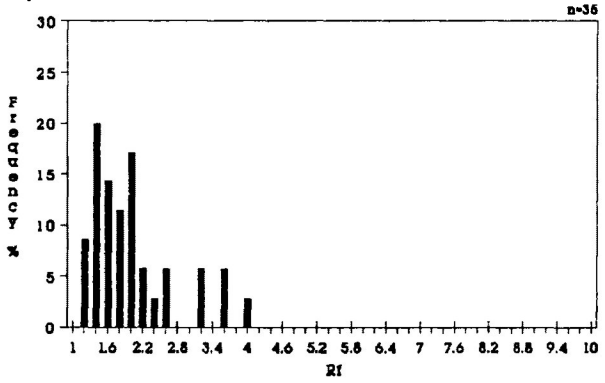
n=35
Frequency %
Rf

d)

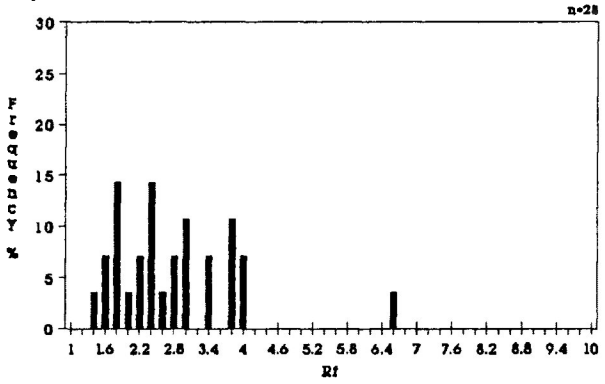
n=28
Frequency %
Rf

e)

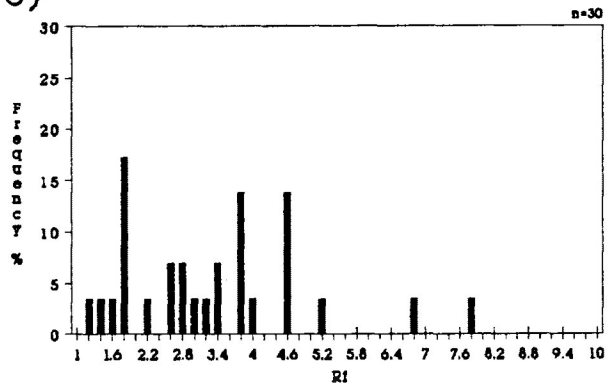
n=30
Frequency %
Rf

Figure 7.21a-e R_f/ϕ diagrams for altered feldspar in the X/Z principal plane of the deformed China Beach sandstone samples. Experimental strain ratios range from 1.000 (e=0.0%) to 1.637 (e=28.0%). Maximum extension direction oriented at 0°. Samples were deformed under dry experimental conditions with confining pressures of 200 Mpa, strain rate of 10^{-5}/s and temperatures of 25°C. Note statistical information given in the upper right hand corner of each R_f/ϕ diagram. Measurements taken from the X/Z principal plane of the deformed test cylinder.

a) e=0.0% (R_s=1.000)
b) e=8.0% (R_s=1.133)
c) e=12.0% (R_s=1.211)
d) e=25.0% (R_s=1.540)
e) e=28.0% (R_s=1.637)

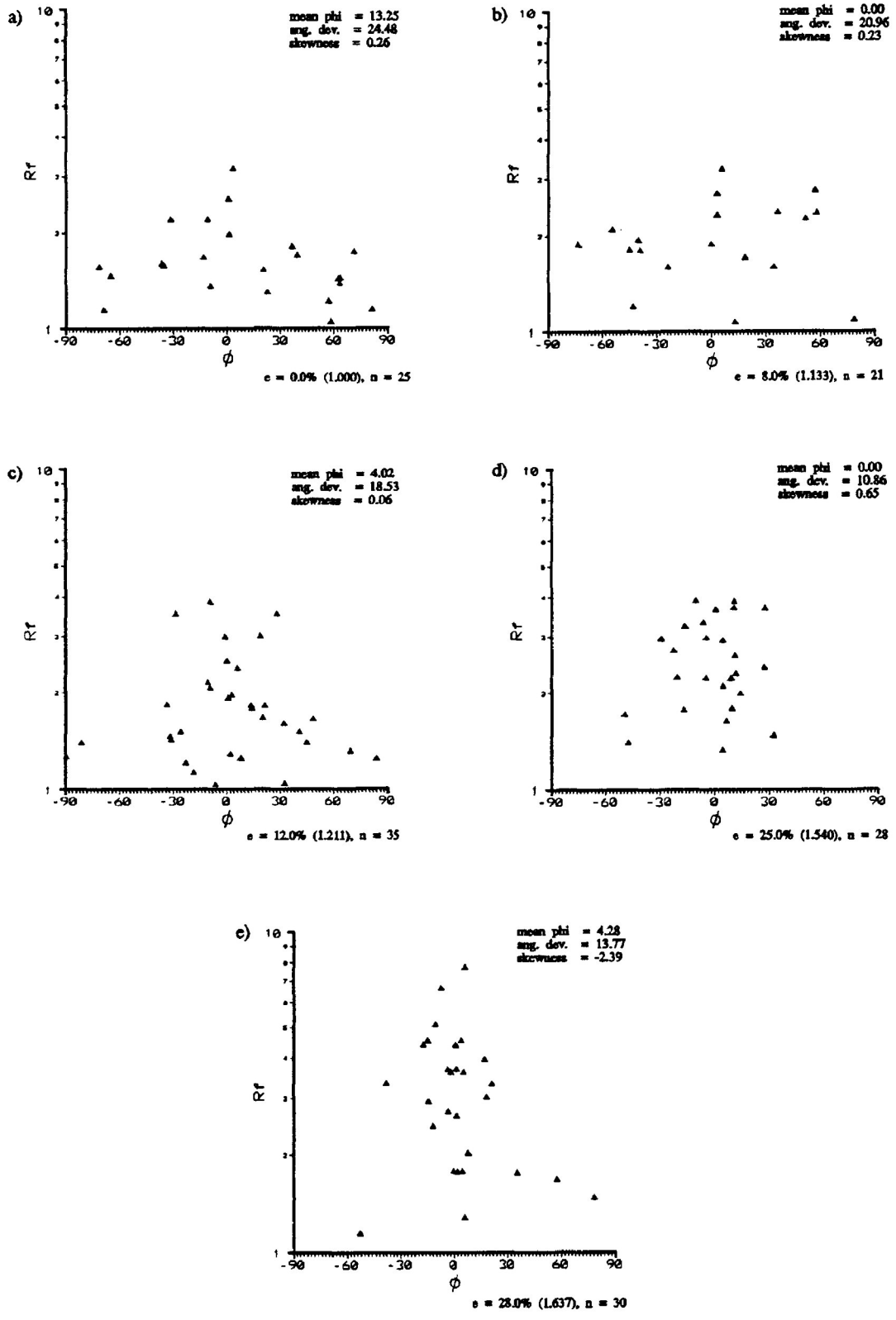
a)
mean phi = 13.25
ang. dev. = 24.48
skewness = 0.26
Rf
ϕ
e = 0.0% (1.000), n = 25
b)
mean phi = 0.00
ang. dev. = 20.96
skewness = 0.23
Rf
ϕ
e = 8.0% (1.133), n = 21
c)
mean phi = 4.02
ang. dev. = 18.53
skewness = 0.06
Rf
ϕ
e = 12.0% (1.211), n = 35
d)
mean phi = 0.00
ang. dev. = 10.86
skewness = 0.65
Rf
ϕ
e = 25.0% (1.540), n = 28
e)
mean phi = 4.28
ang. dev. = 13.77
skewness = -2.39
Rf
ϕ
e = 28.0% (1.637), n = 30

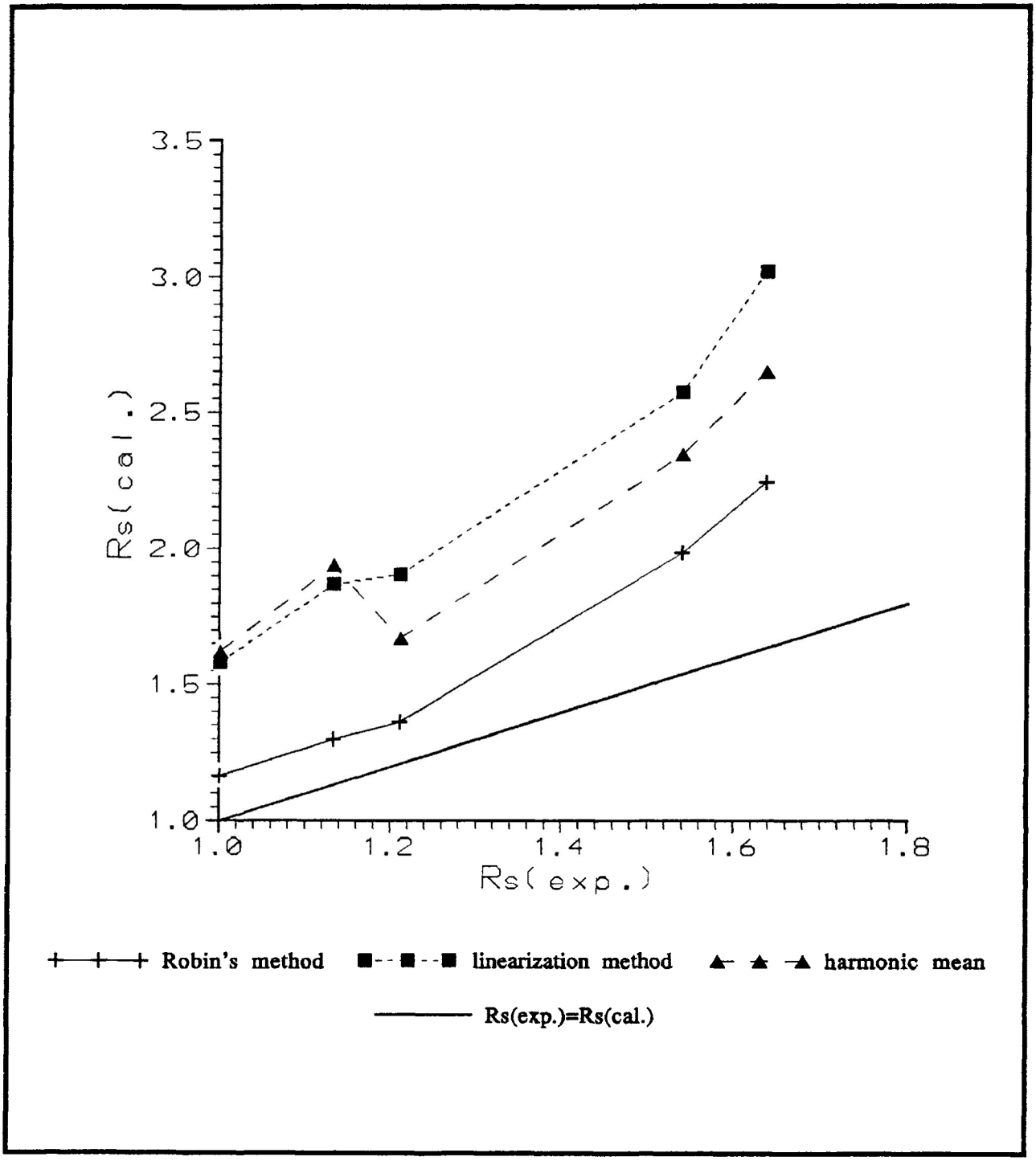

Figure 7.22 Comparison of strain estimates by Robin's method (1977), linearization method (Yu and Zheng, 1984) and harmonic mean method (Lisle, 1977) for altered feldspar in the X/Z principal plane of the China Beach sandstone samples. Equivalent R_s is represented by the dark solid line. Experimental strain ratios range from 1.133 (e=8.0%) to 1.637 (e=28.0%). Samples were deformed under dry experimental conditions with confining pressures of 200 Mpa, strain rate of 10^{-5}/s and temperatures of 25°C.

mean methods. From the figure it is observed that a poor correlation exists between the actual strain and the strain estimate of Robin's and linearization method. In both cases there is a large deviation between strain estimate and the actual strain, especially in the case of the linearization method. The overestimates of strain increase as strain increases. The harmonic mean exhibits an increase as strain increases similar to the other two methods and is an overestimate of strain, although at higher strains it is a better estimate than the linearization method. Robin's method generates the best estimate of the experimental strain ratio.

Standard deviation for Robin's method, linearization method and the harmonic mean method were calculated and are presented in Table 7.1. For the linearization method the calculations of standard deviation that yield confidence brackets that extend into bulk strains estimates less than 1.000 are not given.

Figure 7.23 presents the a_j/c_j ratio used to calculate strain from Robin's method from altered feldspar grains. It is observed from the figure that the frequency distributions are increasingly lognormal and spread out as strain increases, subsequently causing the arithmetic average of the a_j/c_j ratios to be an overestimate of strain. The larger overestimate of strain produced by the linearization method is the result of high R_f grains parallel to the principal extension direction.

It is believed that most of the deformation expressed in the grains of the altered feldspar is the result of ductile deformation because of the weakening of the feldspar lattice as a result of saussuritic and sericitic alteration and associated collapse of grain pore space. This ductile deformation is not, however, representative of passive R_f/ϕ transformations. The strain expressed in the altered feldspar

Figure 5.23a-g Frequency distribution of a_j/c_j ratios for altered feldspar in the X/Z principal plane of the deformed China Beach sandstone samples. Experimental strain ratios range from 1.000 (e=0.0%) to 1.637 (e=28.0%). Samples were deformed under dry experimental conditions with confining pressures of 200 Mpa, strain rate of 10^{-5}/s and temperatures of 135°C. Measurements taken from the X/Z principal plane of the deformed test cylinder.

a) e=0.0% (R_s=1.000)
b) e=8.0% (R_s=1.133)
c) e=12.0% (R_s=1.211)
d) e=25.0% (R_s=1.540)
e) e=28.0% (R_s=1.637)

a)

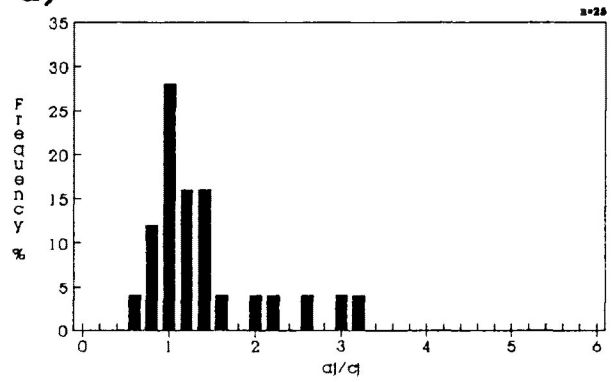
n=25
Frequency %
0
5
10
15
20
25
30
35
0
1
2
3
4
5
6
aj/ai

b)

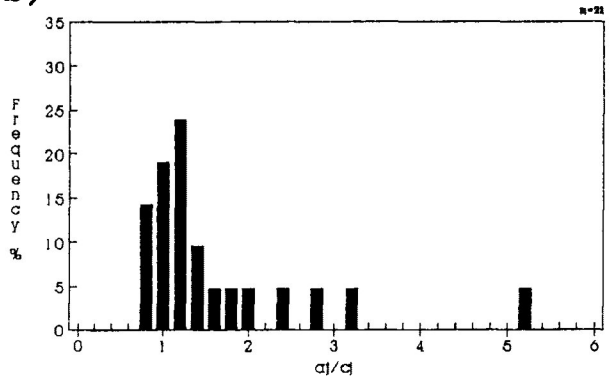
n=21
Frequency %
0
5
10
15
20
25
30
35
0
1
2
3
4
5
6
aj/ai

c)

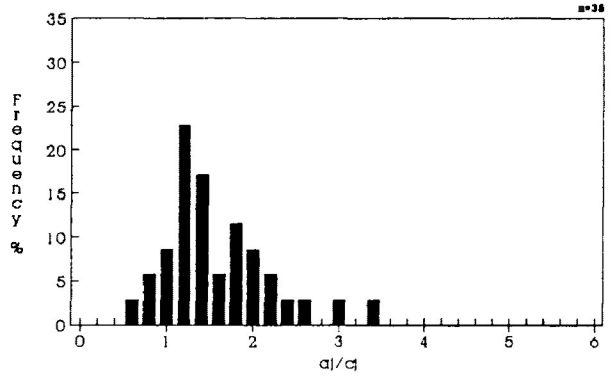
n=35
Frequency %
0
5
10
15
20
25
30
35
0
1
2
3
4
5
6
aj/ai

d)

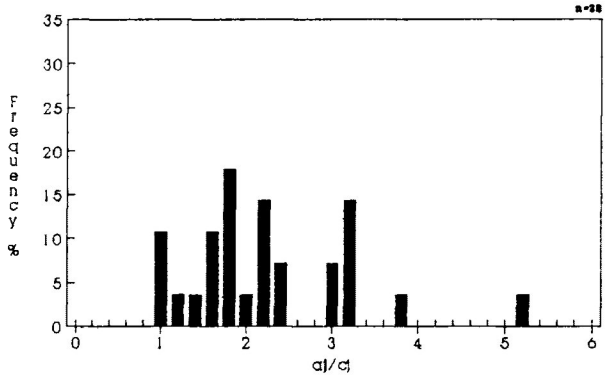
n=28
Frequency %
0
5
10
15
20
25
30
35
0
1
2
3
4
5
6
aj/ai

e)

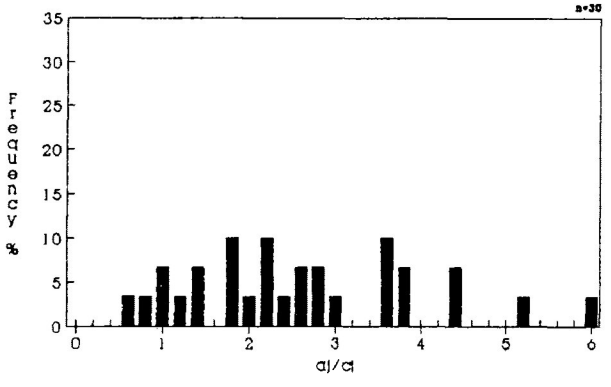
n=30
Frequency %
0
5
10
15
20
25
30
35
0
1
2
3
4
5
6
aj/ai

is greatly influenced by the rheological behaviour of neighbouring grains, which may consist of varying grain lithology. This is expressed in the indentation of more rigid particles into the deformed altered feldspar grains. The ductile altered feldspar grains are flowing into available space and in some cases are wrapping around more rigid grains.

c) <u>lithic fragments</u>

Detrital lithic fragments in the deformed China Beach sandstone deform through a range of rheological behaviour depending on their lithology. The most deformed of the lithic fragments with increasing strain is the shale fragments. Following shale as the second most deformed is basalt grain (with or without phenocryst), especially those grains that exhibit some degree of alteration. Metamorphic grains (quartzite and schists) are the lowest strained lithic fragments. For the purpose of fabric development all lithic grain types were grouped together.

Figure 7.24a-e illustrates the orientational frequency distribution of the longest dimension (Angle Ax (ϕ)) of lithic fragments grains for increasing strain. From the figure it is observed that there is a well developed PDO with a decrease in the angular deviation from 24.1 (e=0%) to 8.4 (e=28%). The fluctuation of the orientational distribution decreases considerably as strain increases (180° (e=0%) to 95° (e=28%)).

As presented in figure 7.25a-e there is observed a very large increase in the R_f of the lithic fragment grains as strain increases suggesting ductile behaviour. The R_f/ϕ diagrams for lithic fragments is presented in figure 7.26a-e. These figures suggest that the lithic fragments are ductile producing a large increase in the range of R_f and a very good development of a PDO parallel to the extension direction.

Figure 7.24a-e Frequency distribution of Angle Ax (ϕ) orientations of lithic fragments in the X/Z principal plane of the deformed China Beach sandstone samples. Experimental strain ratios range from 1.000 (e=0.0%) to 1.637 (e=28.0%). Maximum extension direction oriented at 0°. Samples were deformed under dry experimental conditions with confining pressures of 200 Mpa, strain rate of 10^{-5}/s and temperatures of 25°C. Measurements taken from the X/Z principal plane of the deformed test cylinder.

a) e=0.0% (R_s=1.000)
b) e=8.0% (R_s=1.133)
c) e=12.0% (R_s=1.211)
d) e=25.0% (R_s=1.540)
e) e=28.0% (R_s=1.637)

a)

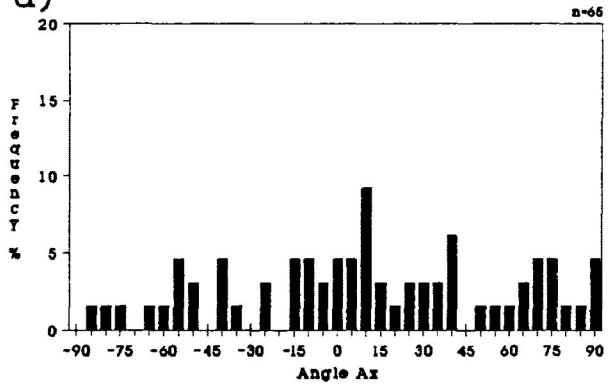
n=66
20
15
10
5
0
Frequency %
-90 -75 -60 -45 -30 -15 0 15 30 45 60 75 90
Angle Ax

b)

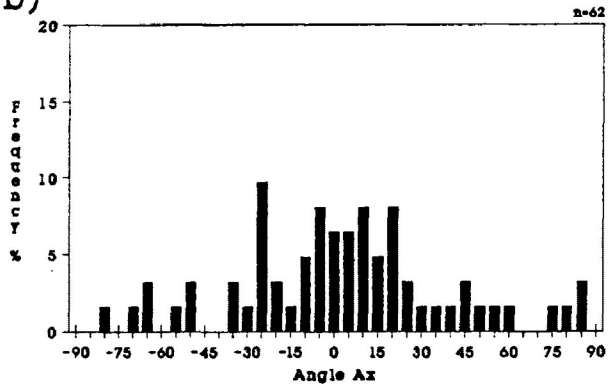
n=62
20
15
10
5
0
Frequency %
-90 -75 -60 -45 -30 -15 0 15 30 45 60 75 90
Angle Ax

c)

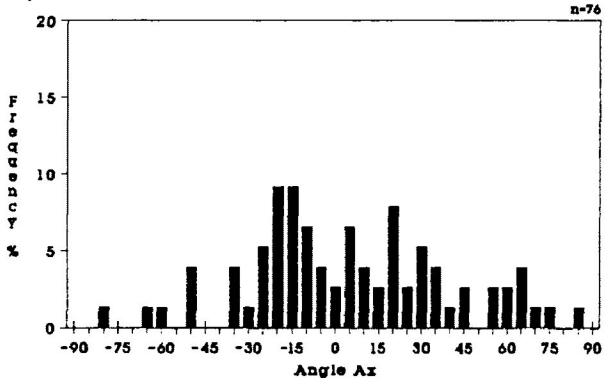
n=76
20
15
10
5
0
Frequency %
-90 -75 -60 -45 -30 -15 0 15 30 45 60 75 90
Angle Ax

d)

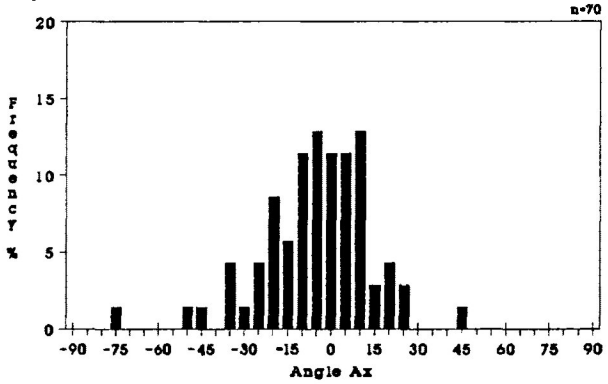
n=70
20
15
10
5
0
Frequency %
-90 -75 -60 -45 -30 -15 0 15 30 45 60 75 90
Angle Ax

e)

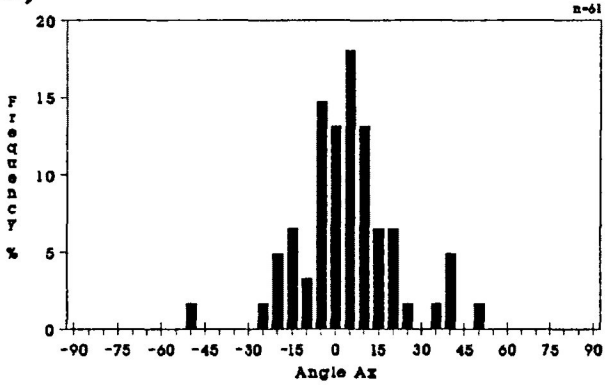
n=61
20
15
10
5
0
Frequency %
-90 -75 -60 -45 -30 -15 0 15 30 45 60 75 90
Angle Ax

Figure 7.25a-e Frequency distribution of R_f for lithic fragments in the X/Z principal plane of the deformed China Beach sandstone samples. Experimental strain ratios range from 1.000 (e=0.0%) to 1.637 (e=28.0%). Samples were deformed under dry experimental conditions with confining pressures of 200 Mpa, strain rate of 10^{-5}/s and temperatures of 25°C. Measurements taken from the X/Z principal plane of the deformed test cylinder.

a) e=0.0% (R_s=1.000)
b) e=8.0% (R_s=1.133)
c) e=12.0% (R_s=1.211)
d) e=25.0% (R_s=1.540)
e) e=28.0% (R_s=1.637)

a)

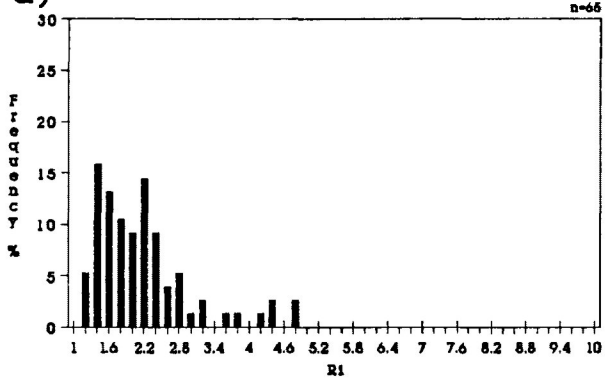
n=65
Frequency %
Rf

b)

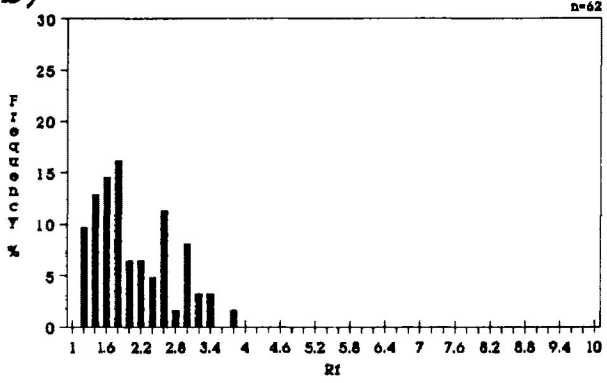
n=62
Frequency %
Rf

c)

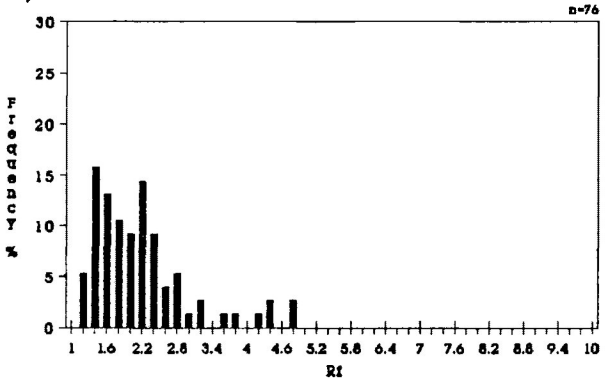
n=76
Frequency %
Rf

d)

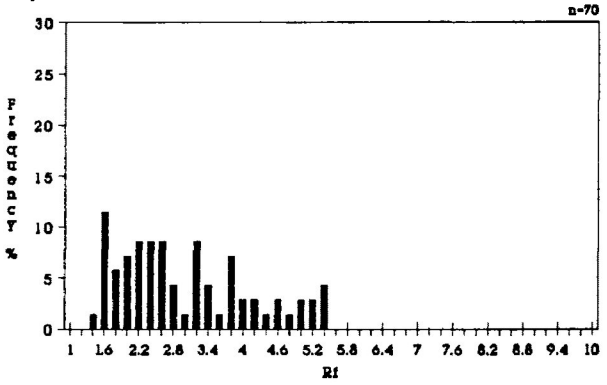
n=70
Frequency %
Rf

e)

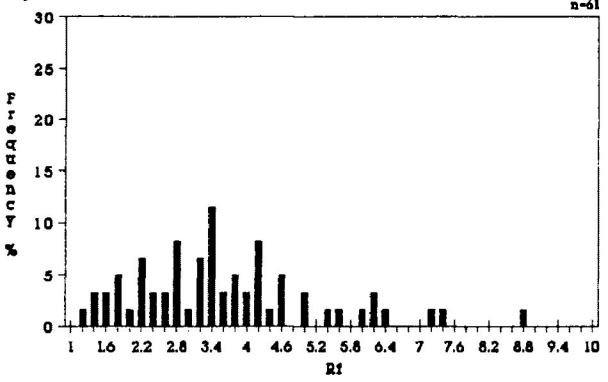
n=61
Frequency %
Rf

Figure 7.26a-e R_f/ϕ diagrams for lithic fragments in the X/Z principal plane of the deformed China Beach sandstone samples. Experimental strain ratios range from 1.000 (e=0.0%) to 1.637 (e=28.0%). Maximum extension direction oriented at 0°. Samples were deformed under dry experimental conditions with confining pressures of 200 Mpa, strain rate of 10^{-5}/s and temperatures of 25°C. Note statistical information given in the upper right hand corner of each R_f/ϕ diagram. Measurements taken from the X/Z principal plane of the deformed test cylinder.

a) e=0.0% (R_s=1.000)
b) e=8.0% (R_s=1.133)
c) e=12.0% (R_s=1.211)
d) e=25.0% (R_s=1.540)
e) e=28.0% (R_s=1.637)

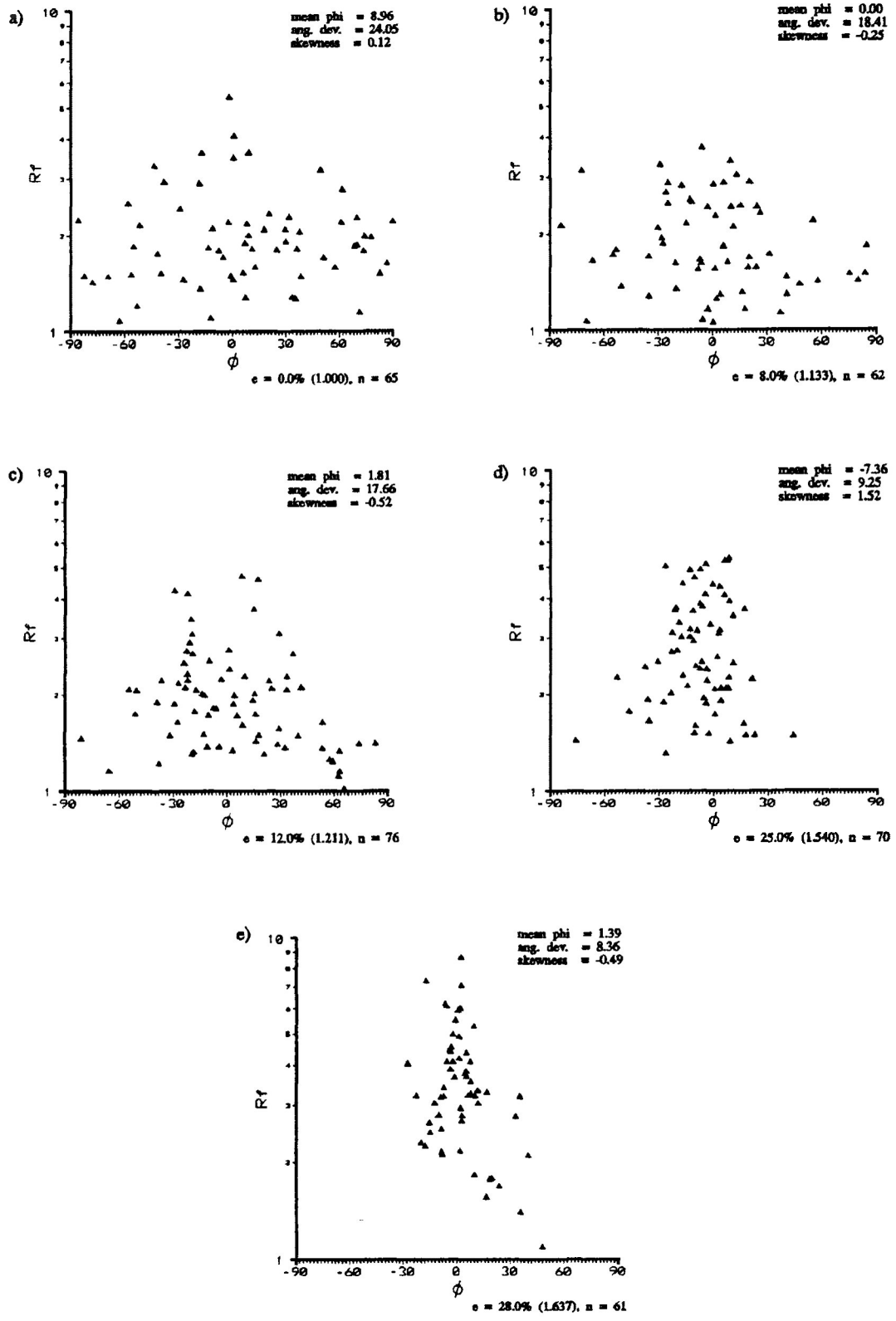
a)
mean phi = 8.96
ang. dev. = 24.05
skewness = 0.12
Rf
ϕ
e = 0.0% (1.000), n = 65
b)
mean phi = 0.00
ang. dev. = 18.41
skewness = -0.25
Rf
ϕ
e = 8.0% (1.133), n = 62
c)
mean phi = 1.81
ang. dev. = 17.66
skewness = -0.52
Rf
ϕ
e = 12.0% (1.211), n = 76
d)
mean phi = -7.36
ang. dev. = 9.25
skewness = 1.52
Rf
ϕ
e = 25.0% (1.540), n = 70
e)
mean phi = 1.39
ang. dev. = 8.36
skewness = -0.49
Rf
ϕ
e = 28.0% (1.637), n = 61

Strain analysis of lithic fragments grains is presented in figure 7.27 for the Robin's, linearization, and harmonic mean methods. From the figure it is observed that a poor correlation exists between the actual strain and the strain estimate of Robin's and linearization method. In both cases there is a large deviation between strain estimate and the actual strain, especially in the case of the linearization method. The overestimate of strain increases as strain increases for both methods and exhibits an increasing difference between the two estimates of strain. There is, however, a similar strain estimate at low strains. The harmonic mean increases as strain increases and is an overestimate of strain. It is, however, a smaller oyerestimate of strain at higher strains than the linearization method. Robin's method generates the best estimate of the experimental strain ratio.

Standard deviation for Robin's method, linearization method and the harmonic mean method were calculated and are presented in Table 7.1. For the linearization method the calculations of standard deviation that yield confidence brackets that extend into bulk strains estimates less than 1.000 are not given.

Figure 7.28 presents the a_j/c_j ratios used to calculate strain from Robin's method from lithic fragments. It is observed from the figure that these frequency distributions are increasingly lognormal and spread out as strain increases, subsequently causing the geometric average of the a_j/c_j ratios to be an overestimate of strain. The larger overestimate of strain of the linearization method is the result of high R_f grains parallel to the principal extension direction.

It is believed that most of the deformation expressed in the lithic fragments is the result of particulate flow of

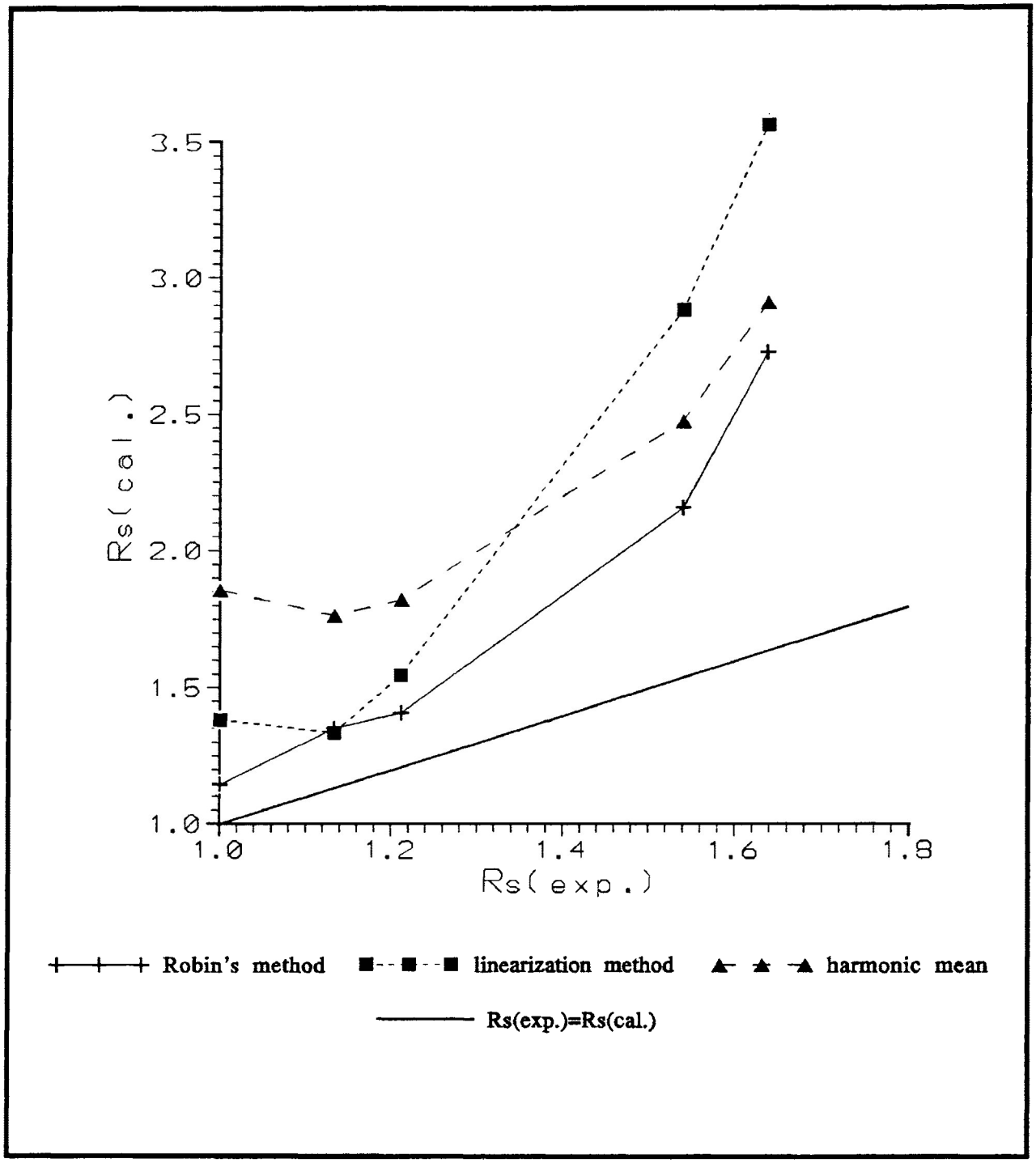

Figure 7.27 Comparison of strain estimates by Robin's method (1977), linearization method (Yu and Zheng, 1984) and harmonic mean method (Lisle, 1977) for lithic fragments in the X/Z principal plane of the China Beach sandstone samples. Equivalent R_s is represented by the dark solid line. Experimental strain ratios range from 1.133 (e=8.0%) to 1.637 (e=28.0%). Samples were deformed under dry experimental conditions with confining pressures of 200 Mpa, strain rate of 10^{-5}/s and temperatures of 25°C.

Figure 7.28a-g Frequency distribution of a_j/c_j ratios for lithic fragments in the X/Z principal plane of the deformed China Beach sandstone samples. Experimental strain ratios range from 1.000 (e=0.0%) to 1.637 (e=28.0%). Samples were deformed under dry experimental conditions with confining pressures of 200 Mpa, strain rate of 10^{-5}/s and temperatures of 135°C. Measurements taken from the X/Z principal plane of the deformed test cylinder.

a) e=0.0% (R_s=1.000)
b) e=8.0% (R_s=1.133)
c) e=12.0% (R_s=1.211)
d) e=25.0% (R_s=1.540)
e) e=28.0% (R_s=1.637)

a)

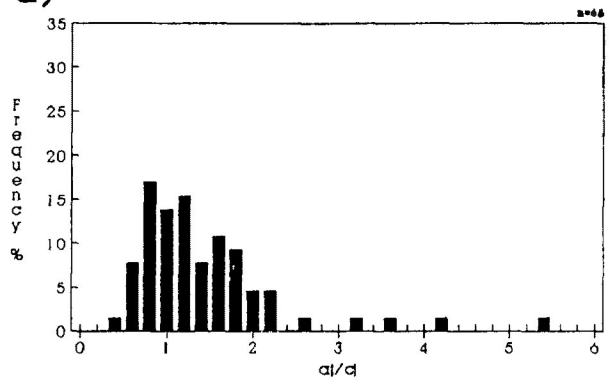
n=45
Frequency %
35
30
25
20
15
10
5
0
0 1 2 3 4 5 6
a1/a

b)

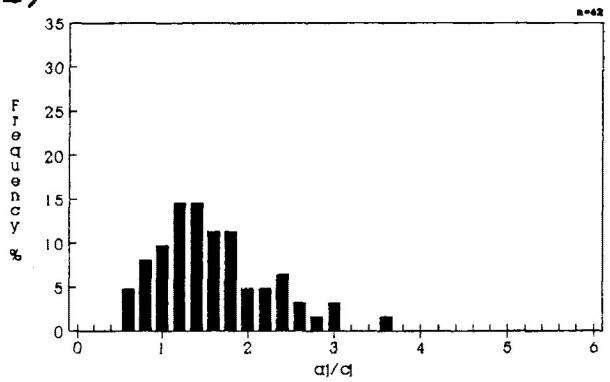
n=42
Frequency %
35
30
25
20
15
10
5
0
0 1 2 3 4 5 6
a1/a

c)

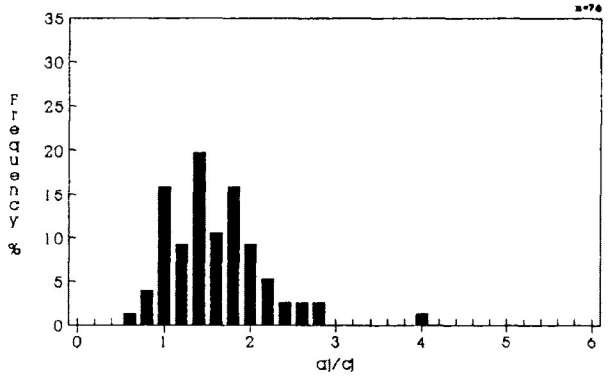
n=74
Frequency %
35
30
25
20
15
10
5
0
0 1 2 3 4 5 6
a1/a

d)

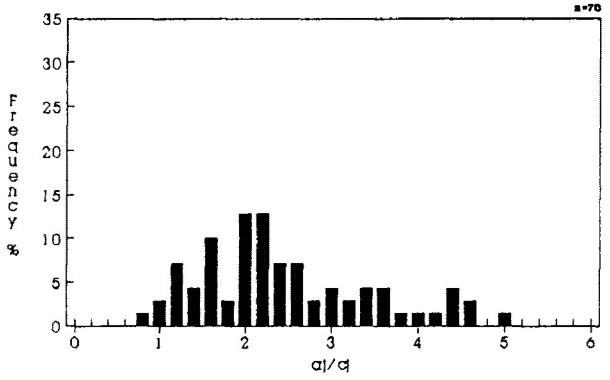
n=70
Frequency %
35
30
25
20
15
10
5
0
0 1 2 3 4 5 6
a1/a

e)

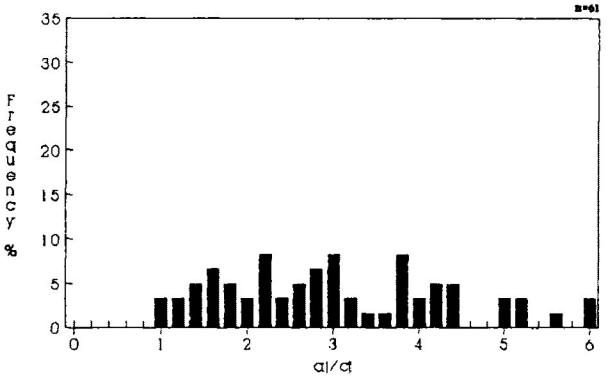
n=61
Frequency %
35
30
25
20
15
10
5
0
0 1 2 3 4 5 6
a1/a

grains within the rock aggregates. The presence of alteration minerals enhances the process of dependent particulate flow. There is observed in some of the porphyritic basalt grains the alinement of feldspar laths in the direction of elongation. The dependent particulate flow of particles within the grain aggregate results in the ductile deformation of the lithic fragment. The grain strains, however, are not representative of R_f/ϕ transformations. The strain expressed in the altered feldspar is greatly influenced by the rheological behaviour of neighbouring grains, which may consist of varying grain lithology. This is expressed in the indentation of more rigid particles into the deformed altered feldspar grain. The altered feldspar grains and lithic fragments are flowing into available space and in some cases are wrapping around more rigid grains.

d) <u>Whole rock strain analysis</u>

Figure 7.29 through 7.32 illustrates the grain type distribution of undulose quartz, unaltered feldspar, altered feldspar and lithic fragments in the central portion of the X/Z principal plane of the deformed China Beach sandstone test cylinders. The figures represent grain distribution of all recognized grain types (spaces indicate the presents of very small grains, minor amounts of mica, amphibole (hornblende) and opaque minerals, cement). Observed in the figures is the progressive development of cleavage as experimental strain increases in the china Beach sandstone.

From the figures it is apparent that the large heterogeneity of strain exhibited between the different grain types plays an important role in the development of cleavage parallel to the extension direction. The most ductile grains, which include lithic fragments and altered feldspar, are deformed to high aspect ratios and define the development of

Figure 7.29-32a-d Grain type distribution of the fractured quartz, undulose quartz, unaltered feldspar, altered feldspar and lithic fragments in the X/Z principal plane of the China Beach sandstone test cylinder. a) represents grain distribution of all recognized grain types (spaces indicate the presents of very small grains, minor amounts of mica (biotite and muscovite), amphibole (hornblende) and opaque minerals (magnetite) and cement (limonite and hematite)). b) undulose quartz. c) altered (shaded) and unaltered feldspar. d) lithic fragments. Solid arrows indicate the principal compressive stress direction (σ_1) and dark solid line illustrates the extension direction (σ_3). The sample was deformed under dry experimental conditions with confining pressures of 200 Mpa, strain rate of 10^{-5}/s and temperatures of 25°C. Tracings are from the central portion of the thin section.

7.29) e=8.0% (R_s=1.133)
7.30) e=12.0% (R_s=1.211)
7.31) e=25.0% (R_s=1.540)
7.32) e=28.0% (R_s=1.637)

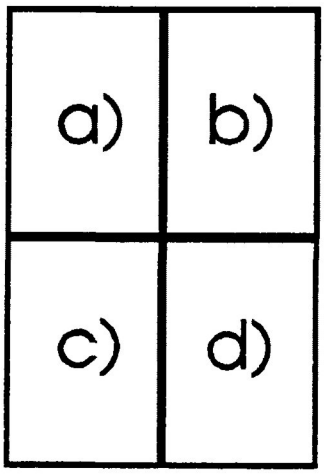

Figure 7.29a-d

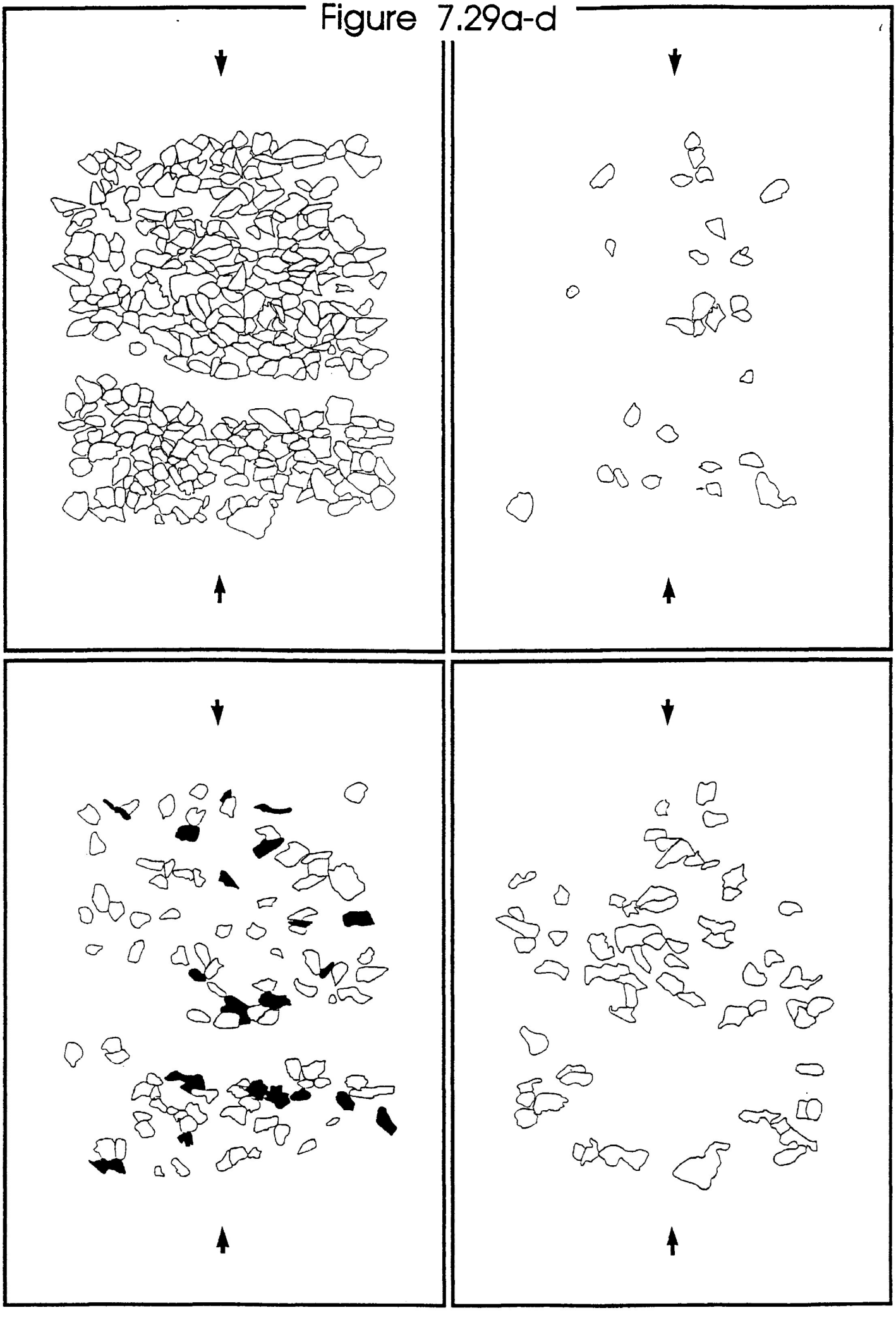

Figure 7.30a-d

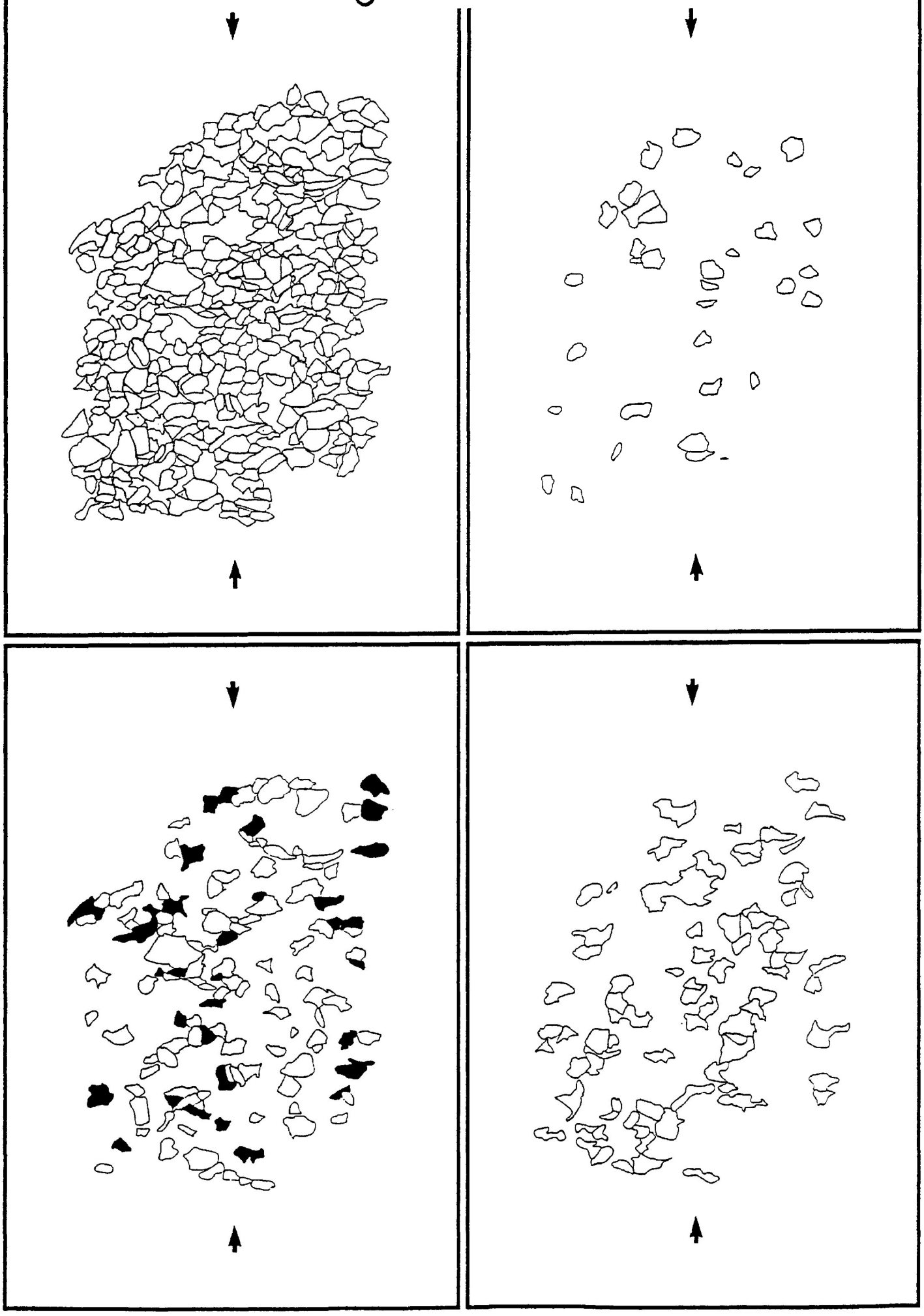

Figure 7.31a-d

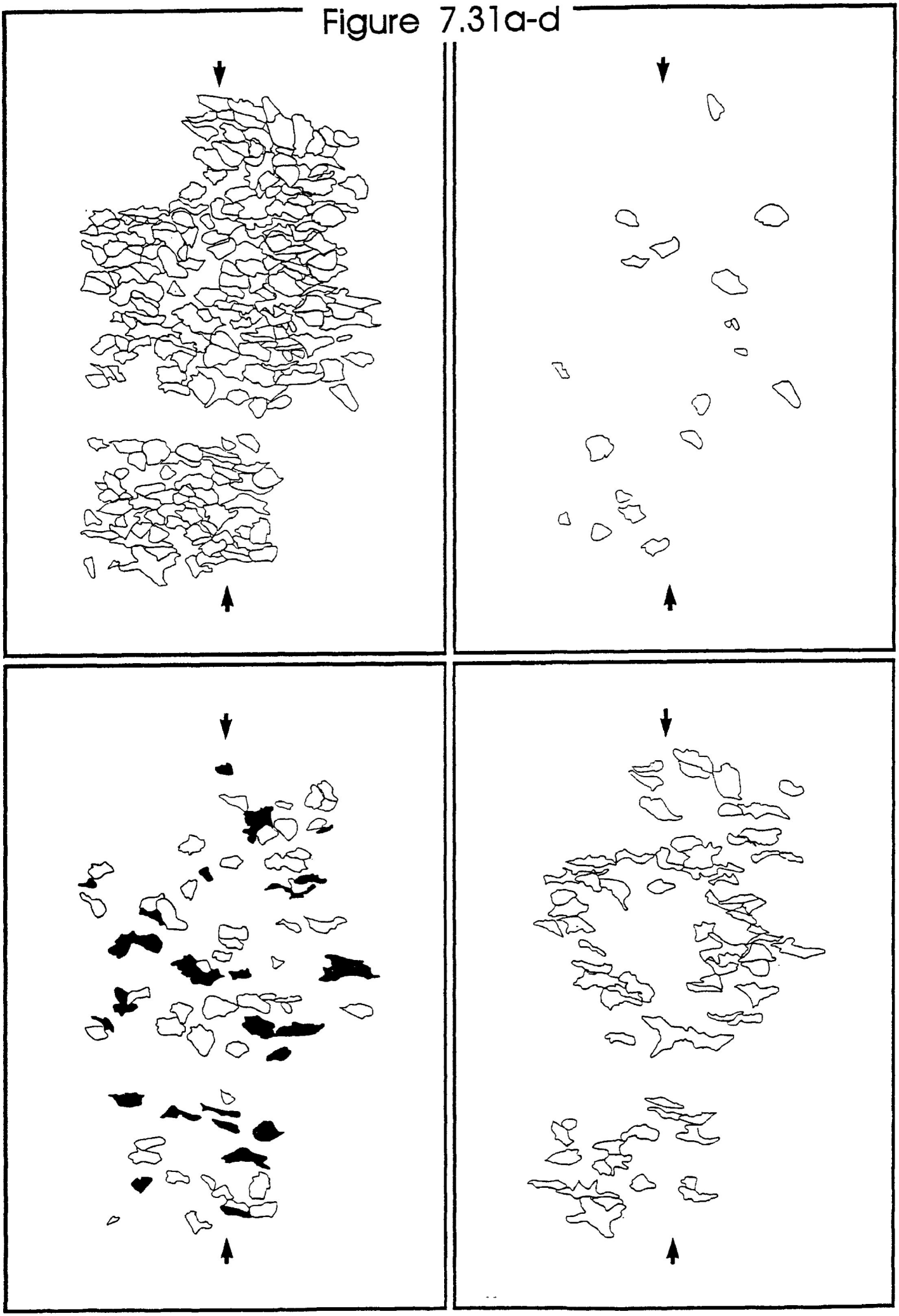

Figure 7.32a-d

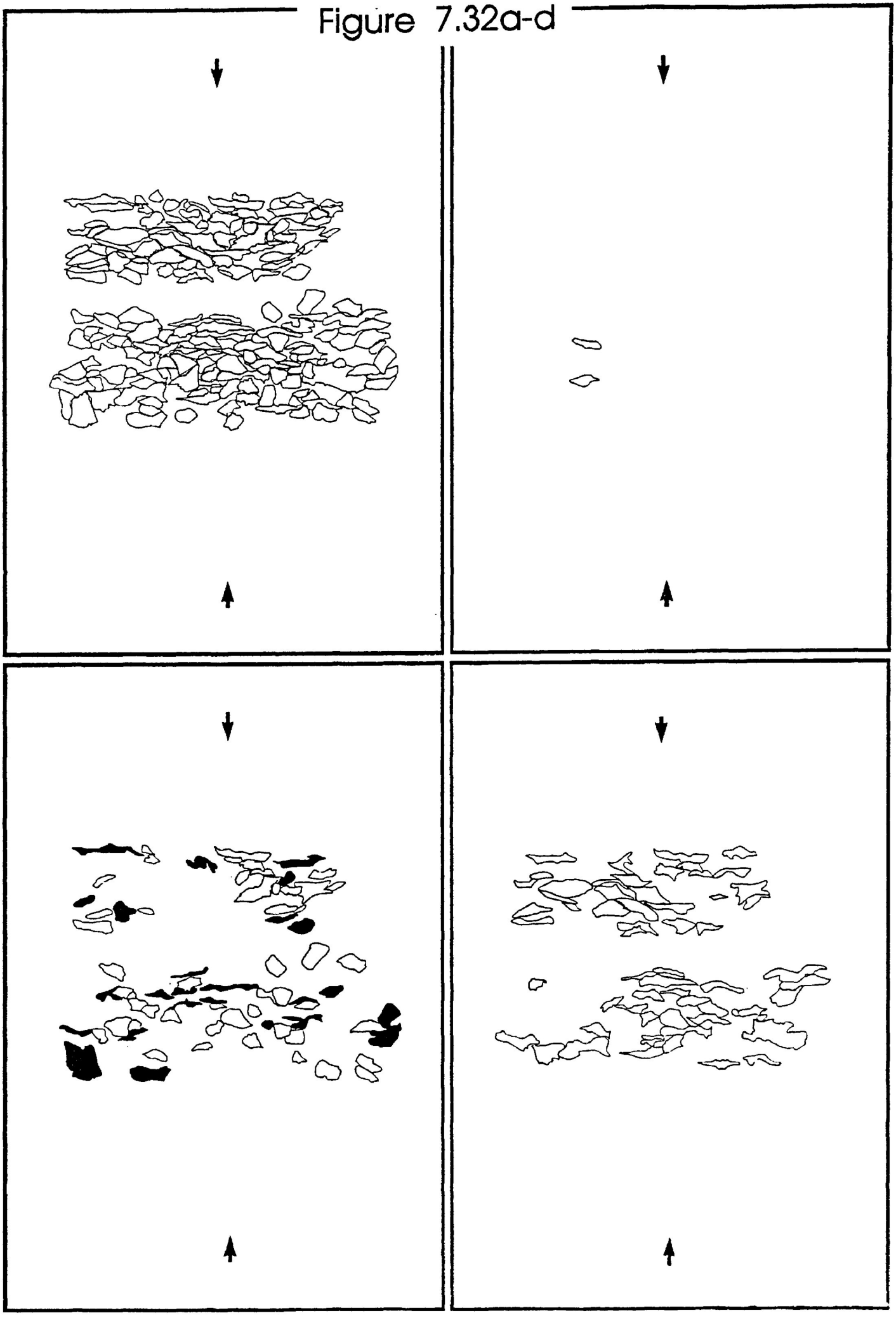

Figure 7.33-36a-b a) Angular frequency distribution of the long axis of all recognized grains in the China Beach Sandstone sample deformed to strains of e=8.0% (R_s=1.133) to e=28.0% (R_s=1.637). b) Frequency distribution of total range of R_i for all recognized grains in the China Beach sandstone sample deformed to strains of e=8.0% (R_s=1.133) to e=28.0% (R_s=1.637). The sample was deformed under dry experimental conditions with confining pressures of 200 Mpa, strain rate of 10^{-5}/s and temperatures of 25°C. Tracings are from the central portion of the thin section. Measurements taken from the X/Z principal plane of the deformed test cylinder.

7.33) e=8.0% (R_s=1.133)
7.34) e=12.0% (R_s=1.211)
7.35) e=25.0% (R_s=1.540)
7.36) e=28.0% (R_s=1.637)

Figure 7.33a-b

a)

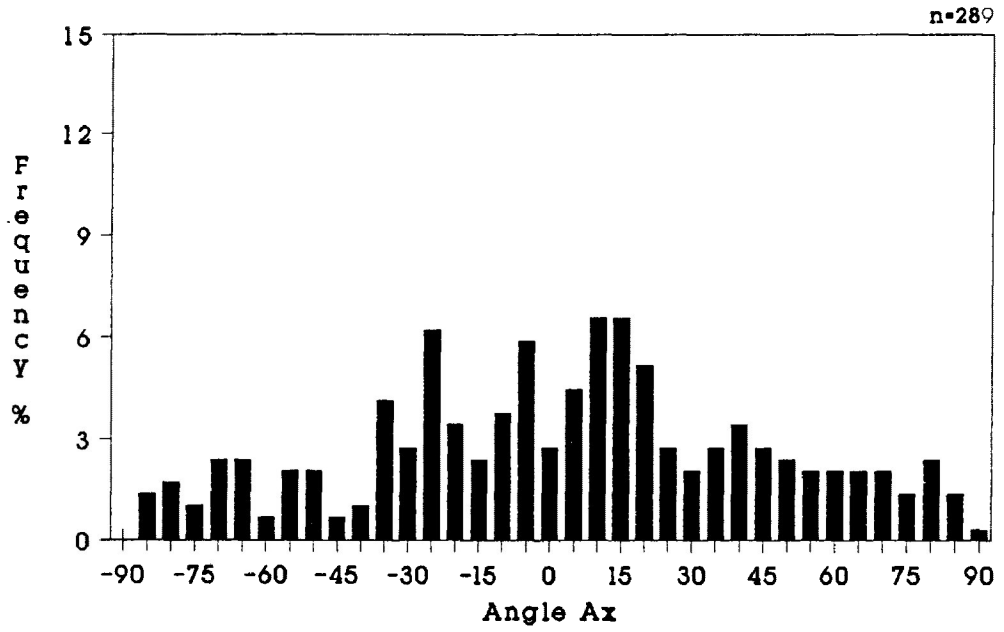

b)

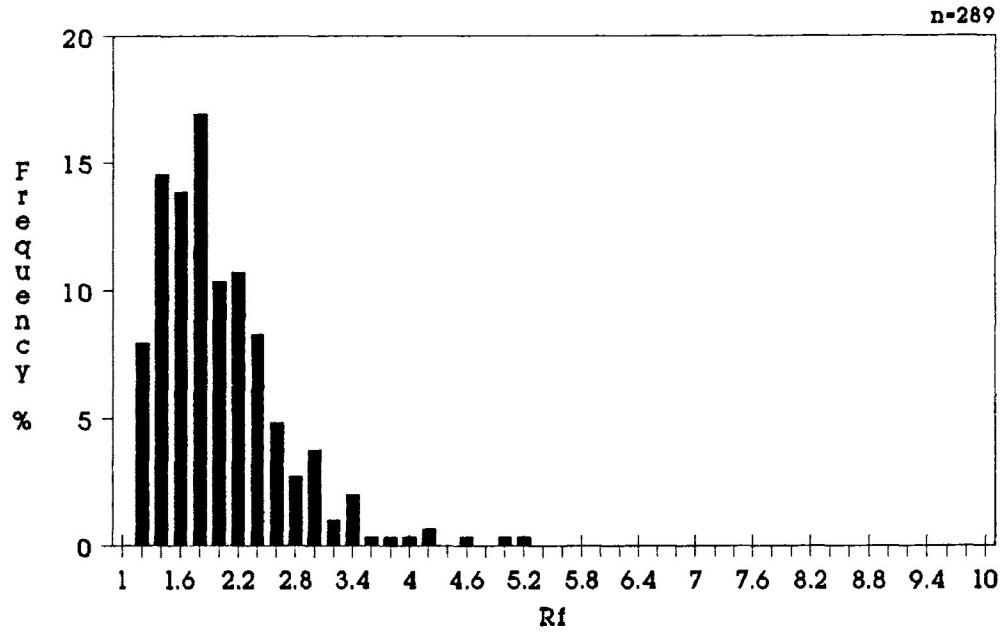

Figure 7.34a-b

a)

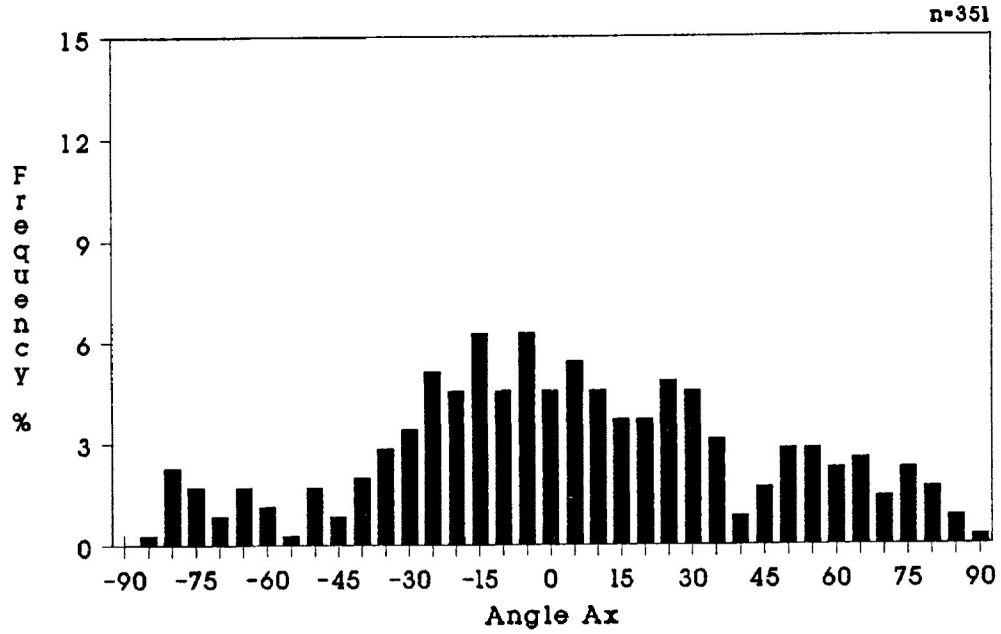

b)

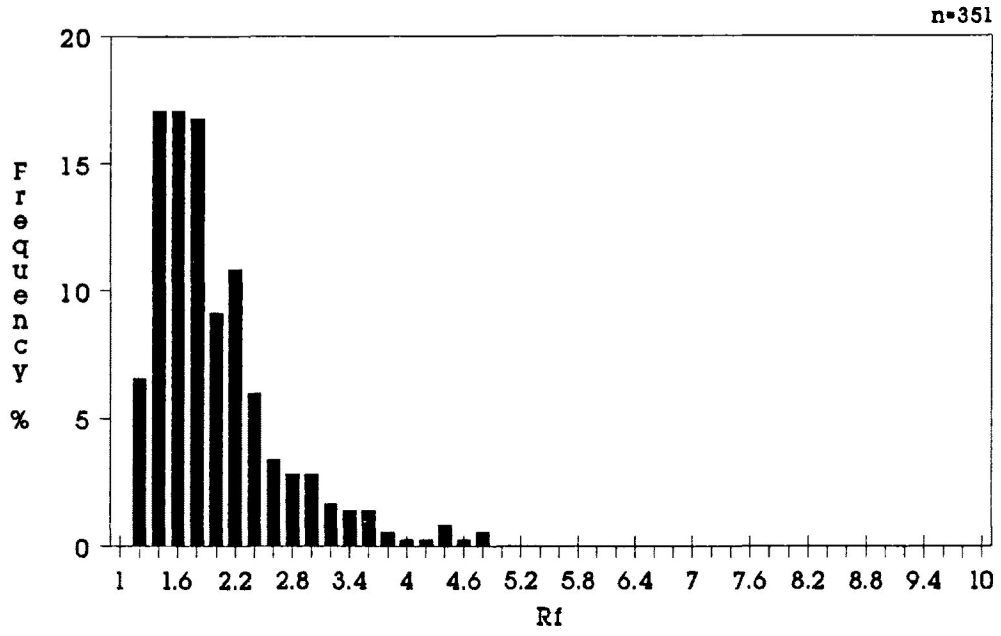

Figure 7.35a-b

a)

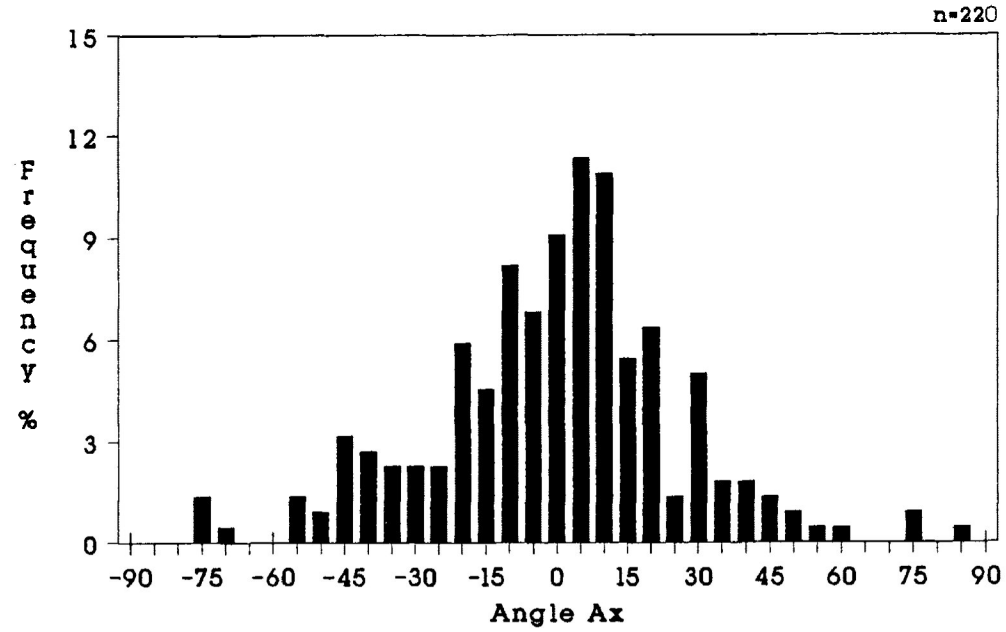

b)

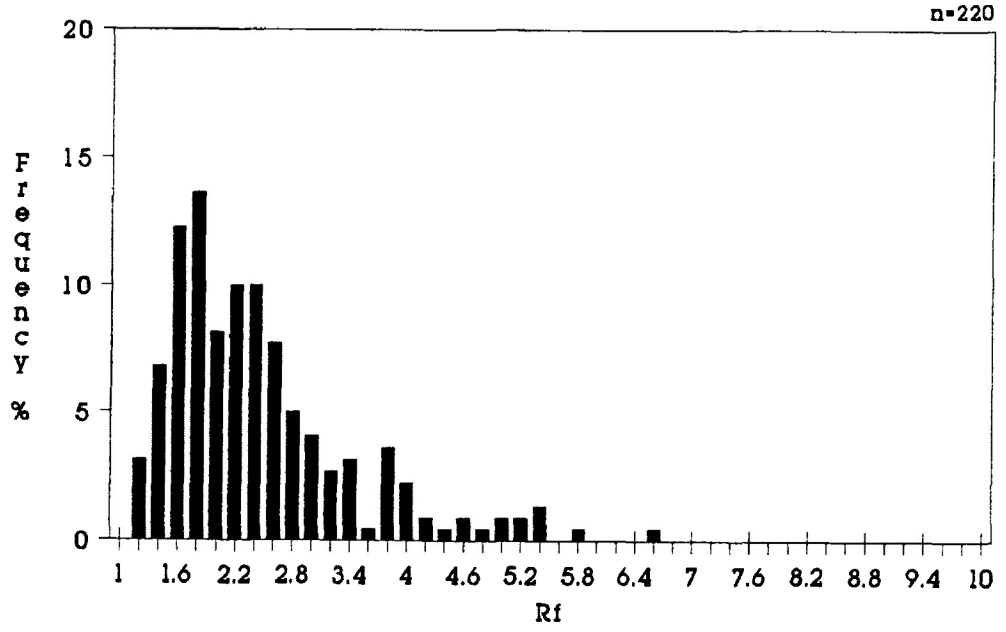

Figure 7.36a-b

a)

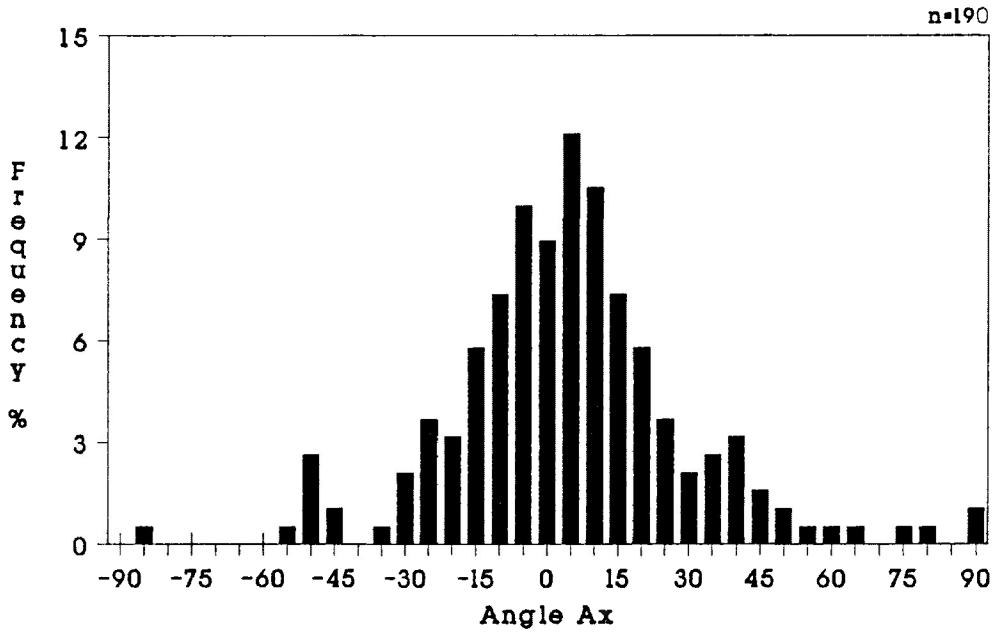

b)

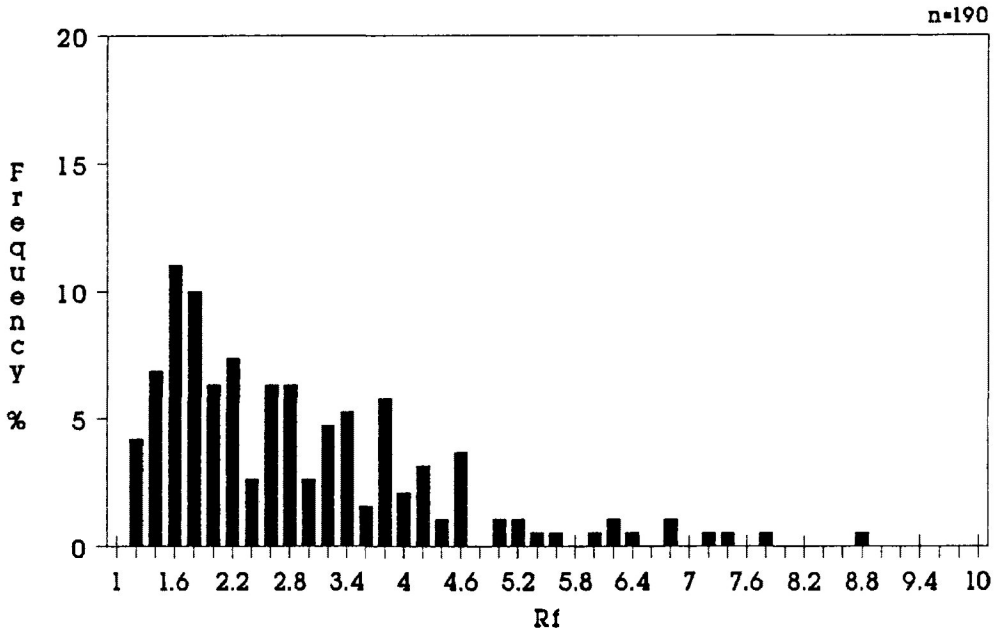

cleavage planes. The ductile nature of these fragments possibly allows for the increased development of PDO in more rigid quartz and feldspar grains. Rigid rotation of the quartz and feldspar grains may be the result of the ductile behaviour of neighbouring grains similar to rigid rotation in a flowing ductile matrix. Many of the rigid quartz and feldspar grains indent into ductile lithic fragments and altered feldspar grains.

The significance of mechanical heterogeneities in the formation of cleavage was discussed by Lebedeva (Borradaile *et.al.*, 1982). Lebedeva conducted experiments that confirmed the significance of viscosity contrasts in the development of cleavage using oils and resins. The experiment were conducted to 75% shortening with the development of cleavage surfaces similar to natural cleavage surfaces.

The orientational frequency distribution of the longest dimension (Angle Ax (ϕ)) of all measured grains in the deformed samples of deformed China Beach sandstone is presented in figure 7.33a through 7.36a. The R_f frequency distributions of all grains measured in the deformed samples of deformed China Beach sandstone is presented in figure 7.33b through 7.36b. These whole sample comparison are characterized by increasing PDO and increasing range of R_f as strain increases.

The angular deviation of the orientation distribution of each grain group in the deformed China Beach sandstone is presented in figure 7.37. The decrease in the angular deviation of lithic fragments occurs rapidly as strain increases and appears to be almost linear (except at high strains for altered feldspar). This most likely reflect the ductile behaviour of these grains. The angular deviations of unaltered feldspar, fractured quartz and undulose quartz

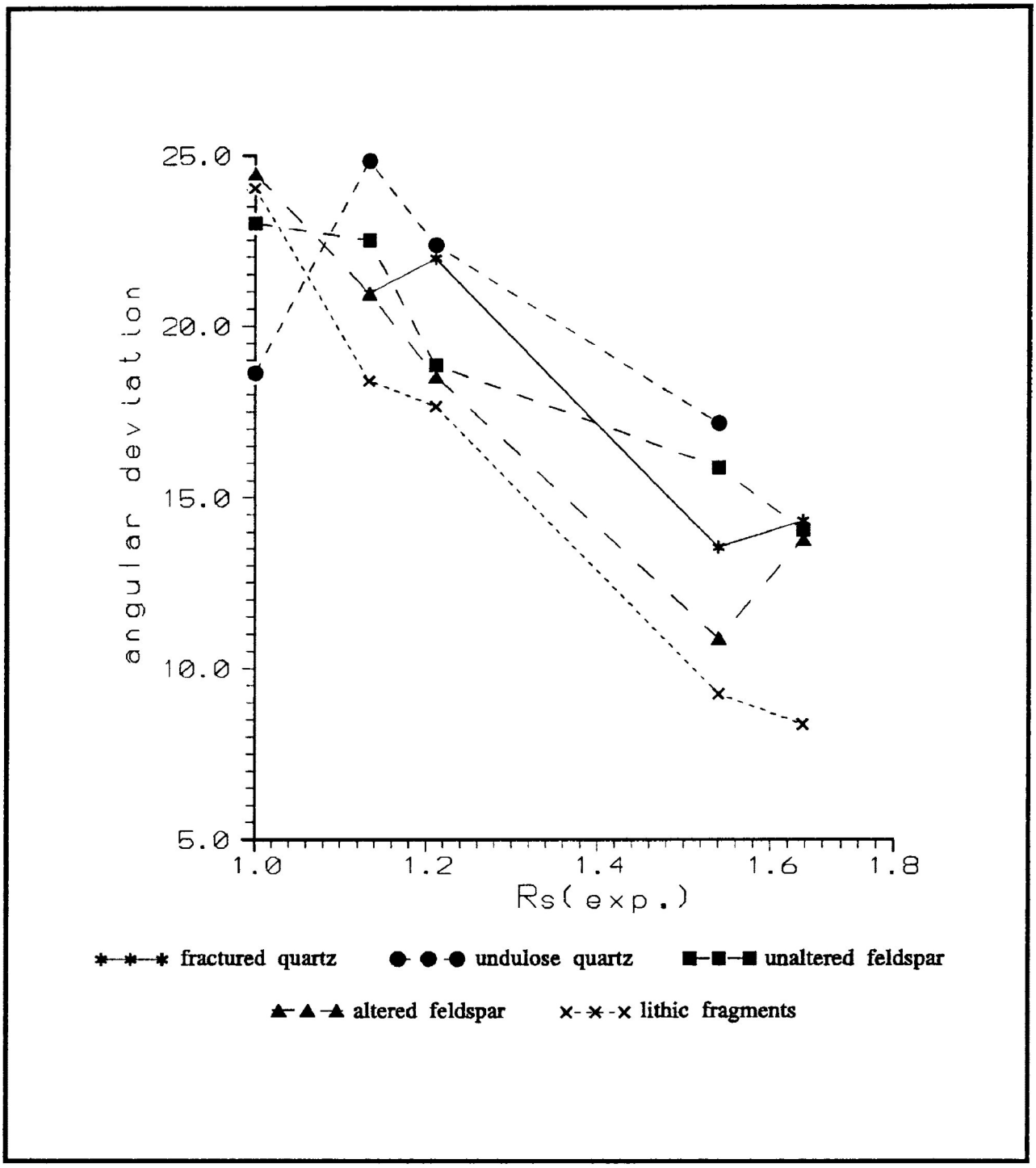

Figure 7.37 Variations in angular deviation of Angle Ax (ϕ) for fractured quartz (star), undulose quartz (circle), unaltered feldspar (square), altered feldspar (triangle) and lithic fragments (X) in the X/Z principal plane of the China Beach sandstone with increasing experimental strain ratio. Samples were deformed under dry experimental conditions with confining pressures of 200 Mpa, strain rate of 10^{-5}/s and temperatures of 25°C. Measurements taken from the X/Z principal plane of the deformed test cylinder.

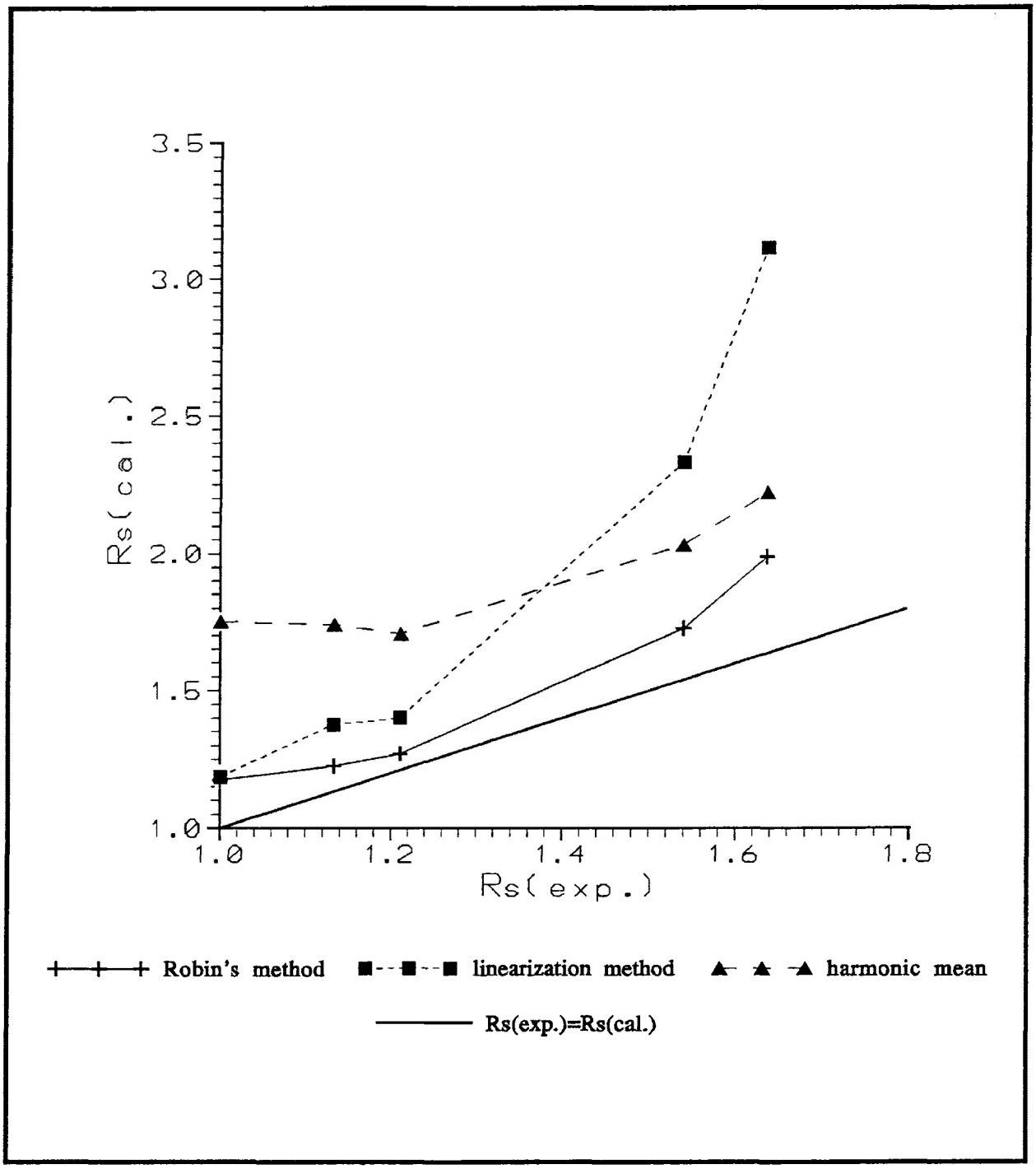

Figure 7.38 Comparison of strain estimates by Robin's method (1977), linearization method (Yu and Zheng, 1984) and harmonic mean method (Lisle, 1977) for all 5 grain types in the China Beach sandstone. Equivalent R_s is represented by the dark solid line. Experimental strain ratios range from 1.133 (e=8.0%) to 1.637 (e=28.0%). Samples were deformed under dry experimental conditions with confining pressures of 200 Mpa, strain rate of 10^{-5}/s and temperatures of 25°C. Measurements taken from the X/Z principal plane of the deformed test cylinder.

decrease to a less amount as strain increases, possibly reflecting deformation dominated by rigid rotation and fracturing.

Strain analysis of all measured grain type in the China Beach sandstone is presented in figure 7.38 for the Robin's, linearization, and harmonic mean methods. From the figure it is observed that Robin's method yields the best estimate of strain of the three methods. However, it is an overestimate of strain which appears to increase as strain increases. The linearization method is also an overestimate of strain which dramatically increases as strain increases. The deviation of the strain estimate of both methods is the result of the high grain strain exhibited in the ductile lithic fragments and altered feldspar. The harmonic mean is the largest overestimate of strain at low strains but becomes a better estimate of strain at higher strains.

Comparison of the strain analysis of each grain group with the whole rock strain analysis for Robin's and linearization methods are presented in figure 7.39 and 7.40. From the figures it is observed that Robin's method is a more consistent tool for the analysis of strain of different grain groups than in the case of the linearization method, which is less consistent. Even if the deformation, expressed in the grain of the deforming aggregate, is heterogeneous, Robin's method is useful as an indication of progressive fabric development in deforming aggregates. Comparison of the harmonic mean for different grain type and the whole rock is presented in figure 7.41.

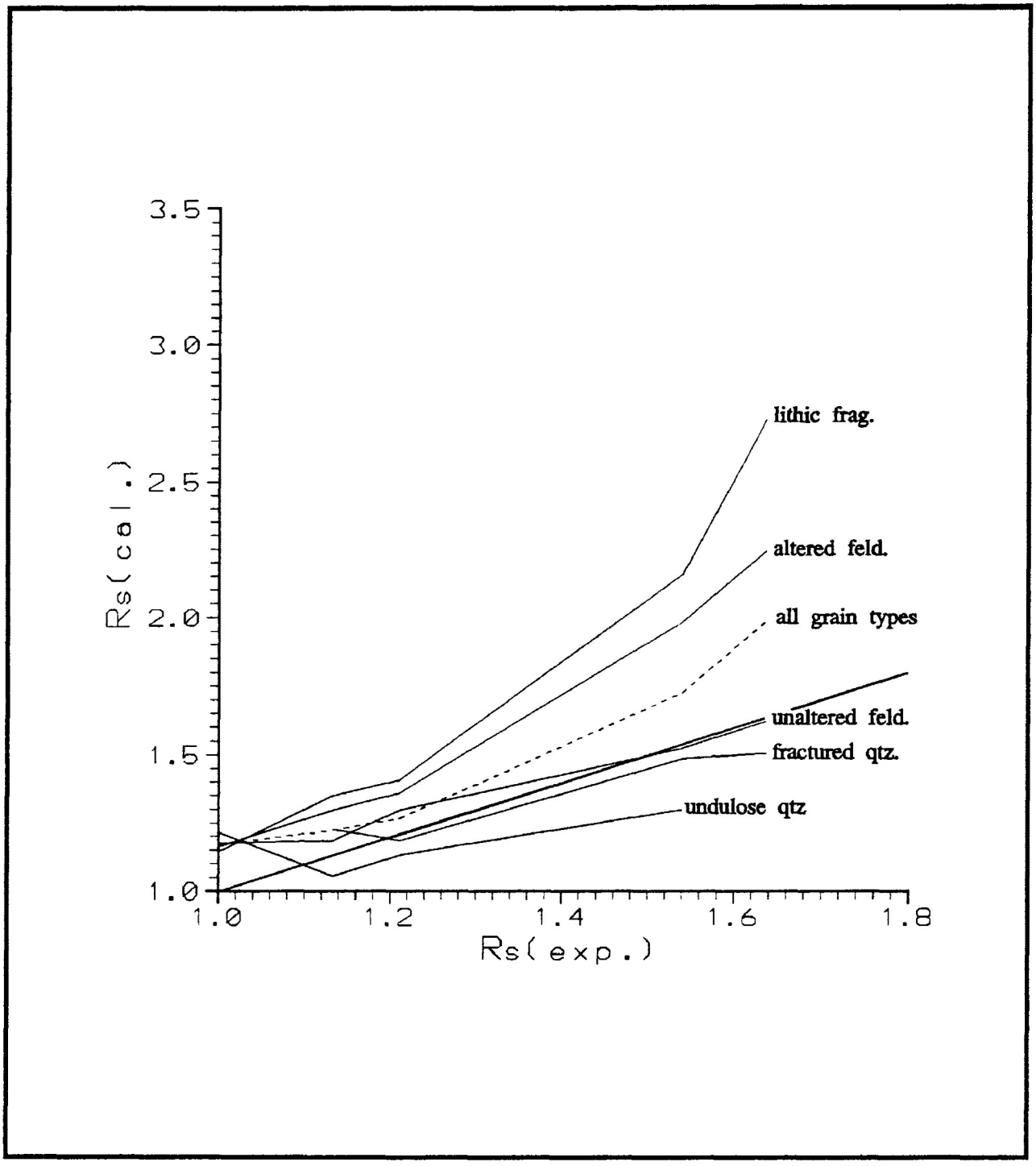

Figure 7.39 Comparison of strain estimates of Robin's method for fractured quartz, undulose quartz, unaltered feldspar, altered feldspar, lithic fragments to the strain estimate of all grain types in the China Beach sandstone. Equivalent R_s is represented by the dark solid line. Experimental strain ratios range from 1.133 (e=8.0%) to 1.637 (e=28.0%). Samples were deformed under dry experimental conditions with confining pressures of 200 Mpa, strain rate of 10^{-5}/s and temperatures of 25°C.

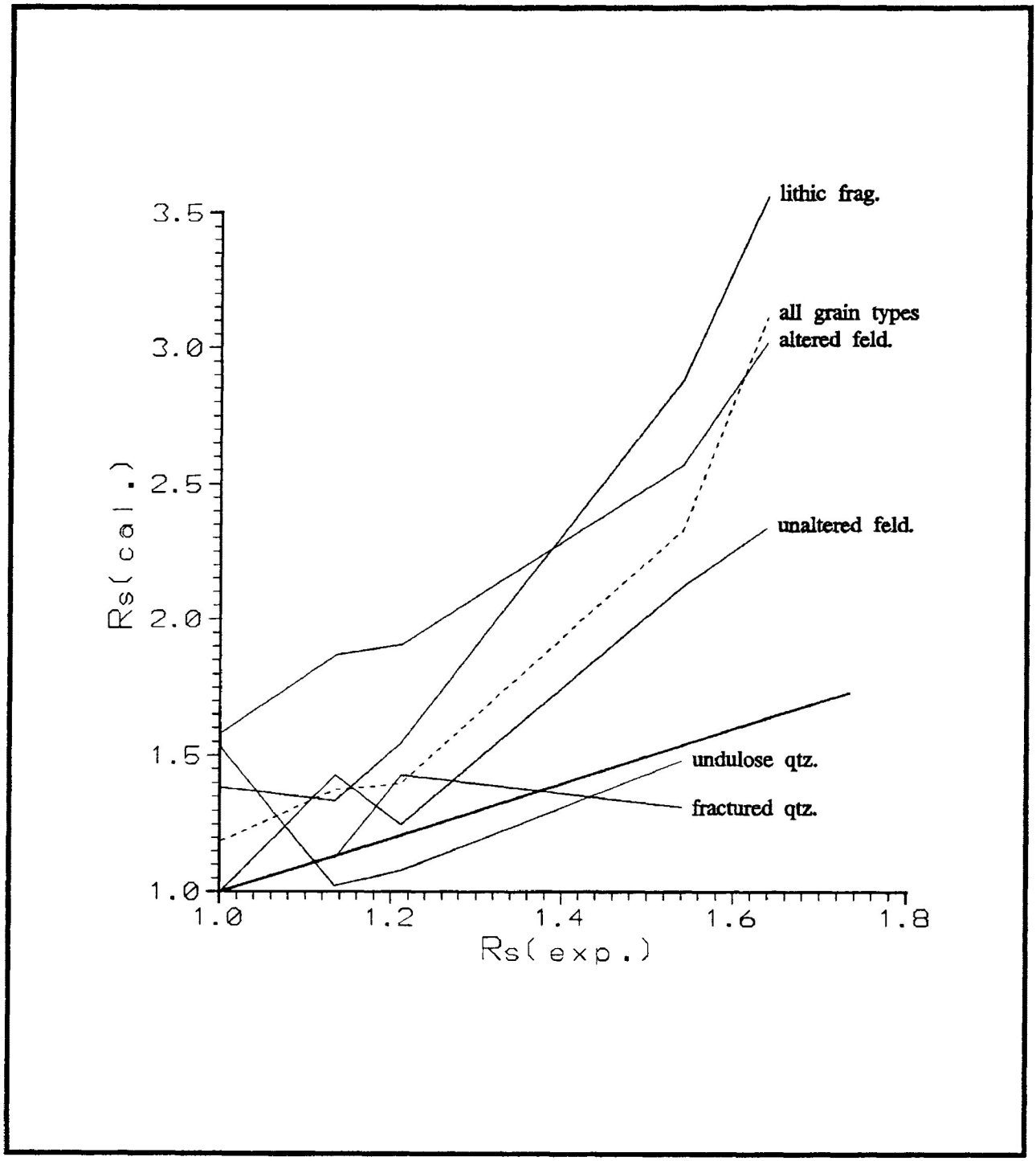

Figure 7.40 Comparison of strain estimates of the linearization method for fractured quartz, undulose quartz, unaltered feldspar, altered feldspar, lithic fragments to the strain estimate of all grain types in the China Beach sandstone. Equivalent R_s is represented by the dark solid line. Experimental strain ratios range from 1.133 (e=8.0%) to 1.637 (e=28.0%). Samples were deformed under dry experimental conditions with confining pressures of 200 Mpa, strain rate of 10^{-5}/s and temperatures of 25°C.

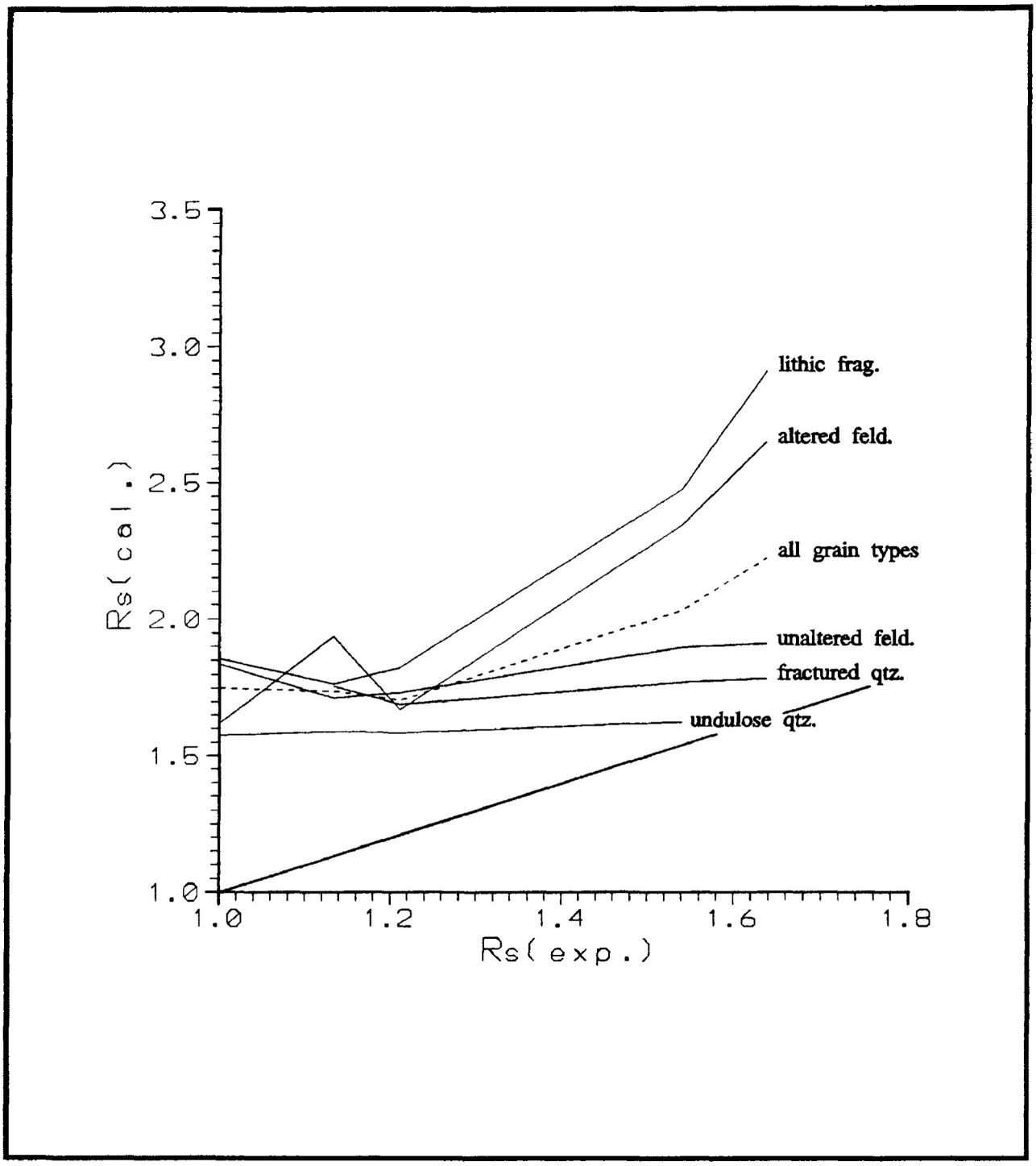

Figure 7.41 Comparison of strain estimates of the harmonic mean method for fractured quartz, undulose quartz, unaltered feldspar, altered feldspar, lithic fragments to the strain estimate of all grain types in the China Beach sandstone. Equivalent R_s is represented by the dark solid line. Experimental strain ratios range from 1.133 (e=8.0%) to 1.637 (e=28.0%). Samples were deformed under dry experimental conditions with confining pressures of 200 Mpa, strain rate of 10^{-5}/s and temperatures of 25°C.

Summation

Under the experimental conditions of this study:

a) Calcite Portland-Cement Aggregate

1) Calcite grains of the synthetic aggregate deform by extensive rigid rotation accompanied by twinning. This produces PDO/PCO in the calcite grains, which are characteristic of each deformation assemblage (Fig.1.2).

2) The effects of particulate flow during high pore fluid pressure in pure shear tests are detectable from both dimensional and crystallographic fabrics. In pure shear, PDO of the calcite grains are produced more efficiently in the present of a pore fluid pressure.

3) Transpressional shear is more effective in producing a PDO in the calcite grain than either pure shear or simple shear.

4) Grain shape fabrics do not conform to the symmetry of the bulk deformation when extensive rotation of calcite grains is involved. Calcite grain shape fabrics produced in pure shear lie in the L<S field, near the plane strain line. Simple shear and transpressional shear produce S-type grain shape fabrics.

5) Mean grain alignment is perpendicular to the shortening in pure shear, initially inclined and later parallel to the shear zone wall in transpressional shear, and inclined to the shear zone wall in simple shear. The mean orientation of the grain-alignment fabrics is a reliable kinematic indicator under the conditions investigated.

6) A new method has been successfully used to determine the σ_1 orientation. The method uses contouring of the lamellae

index associated with the compression direction determine from Turner's Dynamic analysis method. Stress orientations in the deformed specimens agree well with the externally imposed stresses in pure shear and simple shear at low experimental strains.

7) The intensity of twinning in wet pure shear is reduced in the presence of a pore fluid pressure. Transpressional shear and dry pure shear exhibit higher lamellae indices than either pure shear or simple shear.

8) Strain analysis of calcite grains by various numerical methods yield overestimates of the experimental bulk strain in wet pure shear. These methods fail to take into account interparticle motions that occur in the presence of a high pore fluid pressure.

9) Compaction of the cement matrix is achieved more completely in pure shear than in transpressional shear and simple shear. The compaction is more effective in the presence of a pore fluid pressure for pure shear.

b) <u>Ancaster Oolitic Limestone</u>

1) At low temperatures (135°C) the deformation process of ooids in the dry experimental test is rigid rotation of the ooid particles.

2) At low temperatures (135°C) under wet experimental conditions, it appears that the pore fluid pressure produces particulate flow in the fine grained ooid matrix. The ooids deform by ductile flow.

3) Viscosity contrast, between ooids and cement matrix, causes strain analysis on the ooids to exhibit an overestimate

of strain compared with the experimental bulk strain. This holds true for both wet and dry experimental conditions.

c) China Beach Sandstone

1) Mechanical heterogeneities in the different grain types of the China Beach sandstone samples play an important role in the development of cleavage at low strain and temperature under pure shear deformation.

2) Altered feldspar grains and lithic fragments deform by ductile processes, while unaltered feldspar and quartz grain deform by rigid rotation and brittle processes.

3) Strain analysis of each grain type in the China Beach sandstone yield a range of strain estimates depending on the deformation process compared with the experimental bulk strain.

d) Strain analysis

1) Comparison of Robin's method, the linearization method and Harmonic mean method suggest that Robin's method generates the best estimates of the bulk experimental strain ratio.

2) The linearization method yields poor finite strain estimates when the R_i was not constant in value.

References

Alford C. (1988) "Tectonic" magnetic fabrics in pure shear and simple shear: Experimental Investigation. Unpublished M.Sc. Thesis., Lakehead University, Ont.

Babaie H.A. (1986) A comparison of two-dimensional strain analysis methods using elliptical grains. J. Struct. Geol., 8, 585-587.

Bau A. (1979) History of the regional deformation of the Archean rocks in the Kashbowiw Lake-Lac des mille lacs area, Northwest Ontario. Unpublished Ph.D Thesis, Univ. of Toronto, Ont.

Borg I. and Turner F.J. (1953) Deformation of Yule Marble, Part VI. Geol. Soc. Am. Bull., 64, 1343-1352.

Borradaile G.J. (1981) Particulate flow and the formation of cleavage. Tectonophysics, 72, 117-136.

Borradaile G.J. (1984) Strain analysis of passive elliptical markers: success of the de-straining methods. J. Struct. Geol., 6, 433-437.

Borradaile G.J. (1987) Analysis of strained sedimentary fabrics: review and tests. Canadian. Jour. Earth Sc., 24, 442-455.

Borradaile G.J. and Alford C. (1988) Experimental shear zones and magnetic fabrics. J. Struct. Geol., 10, 895-904.

Borradaile G.J. and McArthur J. (1990). Experimental calcite fabrics in a synthetic soft aggregate by coaxial and non-coaxial deformation. J. Structural Geol., 12, 351-363.

Borradaile G.J., Bayly M.B. and Powell C.M. (1982) Atlas of deformational and metamorphic fabrics. Springer-Verlag, New York, 551p.

Clark R.H. (1954) A study of calcite twinning in the Strathavon marble, Banffshire. Geol. Magazine, 91, 121-128.

Conel J.E. (1962) Studies of the development of fabrics in some naturally deformed limestones. Unpublished Ph.D Thesis, Pasadena, California Inst Technology, 257p.

Dietrich D. and Song H. (1984) Calcite fabrics in a natural shear environment, the Helvetic nappes of the western Switzerland. J. Struct. Geol., 6, 19-32.

Reference-2

Donath F.A. and Wood D.S. (1976) Experimental evaluation of the deformation path concept. Phil. Trans. R. Soc. London Ser. A., 283, 187-201.

Dunnet D. (1969) A technique of finite strain analysis using elliptical particles. Tectonophysics, 7, 117-136.

Elliot D. (1970) Determination of finite strain and initial shape from deformed elliptical objects. Geol. Soc. Am. Bull., 81, 2221-2236.

Friedman M. (1963) Petrofabric analysis of experimentally deformed calcite-cemented sandstone. Jour. Geol. 71, 12-37.

Friedman M. (1964) Petrofabric techniques for the determination of the principal stress directions in rocks, in State of Stress in the Earth Crust. edited by W.R. Judd. Elsevier, New York, 451-552.

Friedman M. and Conger F.B. (1964) Dynamic interpretation of calcite twin lamellae in a naturally deformed fossil. Jour. Geol. 72, 361-368.

Friedman M. and Stearns D.W. (1971) Relationship between stresses inferred from calcite twin lamellae and microfractures. Teton Anticline, Montana. Geol. Soc. Am. Bull., 82, 1855-1864.

Friedman M. and Higgs N.G. (1981) Calcite fabrics in experimental shear zones. In: Mechanical Behaviour of Crustal Rocks, The Handing Volume. edited by N.L. Carter et al. Am. Geophys. Union Monograph, 24, 11-27

Gilmour P. and Carman M. (1954) Petrofabrics analysis of the Loch Tray limestone from Strachur Argyll. Geol. Magazine, 91, 41-60.

Griggs D.T. (1936) Deformation of rock under high confining pressures. Jour. Geol. 44, 541-577.

Griggs D.T. (1938) Deformation of single crystal under high confining pressure. Am. Mineral. 23/1, 28-33.

Griggs D.T., Turner F.J., Borg I., (1953) Deformation of Yule marble. Part V: Effects at 300° C. Geol. Soc. Am. Bull., 64, 1327-1342.

Griggs D.T., Turner F.J., Borg I., and Sosoka J. (1951) Deformation of Yule marble. Part IV: Effects at 150° C. Geol. Soc. Am. Bull., 62, 1385-1406.

Reference-3

Griggs D.T., Paterson M.S, Heard H.C. and Turner F.L. (1960) Annealing recrystallization in calcite crystals and aggregates. In: Rock deformation. Edited by D.T. Griggs and J.W Handin. Geol. Soc. Am. Mem., 79, 21-37.

Groshong R.H., Jr. (1972) Strain calculated from twinning in calcite. Geol. Soc. Am. Bull., 83, 2025-2038.

Handin J.W. and Griggs D.T. (1951) Deformation of Yule marble. Part II: Predicted fabric changes. Geol. Soc. Am. Bull., 62, 863-886.

Hansen and Borg (1962) The dynamic significance of deformation lamellae in quartz of a calcite-cement sandstone. Am. Journal Sci., 260, 321-336.

Heard H.C. (1963) Effect of large changes in strain rate in experimentally deformed Yule marble. Jour. Geol. 71, 162-195.

Heard H.C. and Raleigh C.B. (1972) Steady state flow in marble at 500° to 800° C. Geol. Soc. Am. Bull., 83, 935-956.

Hubbert M.K. and Rubey W.W. (1959) Role of fluid pressure in mechanism of overthrust faulting. Geol. Soc. Am. Bull, 70, 115-166.

Jackson M., Craddock J.P., Ballard M., Van der Voo R. and McCabe C. (1989) Anhysteretic remanent magnetic anisotropy and calcite strains in Devonian carbonates from the Appalachian Plateau, New York. Tectonophysics, 161, 43-51.

Lisle R.J. (1977a) Clastic grain shape and orientation in relation to cleavage from the Aberystwyth Grits, Wales. Tectonophysics, 39, 381-395.

Lisle R.J. (1977b) Estimation of the tectonic strain ratio from the mean shape of deformed elliptical markers. Geol Mijnbouw, 56, 140-144.

Lisle R.J. (1979) Strain analysis using deformed pebbles: the influence of initial pebble shape. Tectonophysics, 60, 263-277.

McIntyre D.B. and Turner F.J. (1953) Petrofabric analysis of marbles from mid-Strathspey and Strathavan. Geol. Magazine, 90, 225-240.

Nissen H.D. (1964a) Calcite fabric analysis of deformed oolites from the South Mountains Fold, Maryland. Amer. J. Science, 262, 892-903.

Reference-4

Nissen H.D. (1964b) Analysis of strained crinoid stems in sandstone from Lindar near Cologne, Germany. Geol. Magazine, 90, 346-360.

Paterson M.S. and Turner F.J. (1970) Experimental deformation of constrained crystals of calcite in extension. In: Experimental and natural rock deformation. Edited by Paulitsch. Springer Verlag, 109-141.

Paterson M. S. (1983) A comparison of the methods used in the measuring of finite strain from ellipsoidal objects. J. Struct. Geol., 5, 611-618.

Pfiffner, O.A. (1977) Tektonishe Untersuchungen im Infrahelvetikum der Ostschweiz. Mitt. Geol. Inst. ETH and Univ. ZUrich, N.F., 217, 1-432.

Ramsay J.G. (1969) Folding and fracturing of rocks. McGraw-Hill, New York, 568pp.

Robin P.-Y.F. (1973) Note on effective pressure. J. Geophys. Res., 78, 2434-2437.

Robin P.-Y.F. (1977) Determination of the geological strain using randomly oriented strain markers of any shape. Tectonophysics, 42, T7-T16.

Robin P.-Y.F. (1977) Torrance J.G. (1987) Statistical analysis of the effect of sample size on paleostrain calculation. I. Single face measurements. Tectonophysics, 138, 311-317.

Rutter E.H. and Rusbridge H. (1977) The effect of non-coaxial strain paths on the crystallographic preferred orientation developed in the experimental deformation of marble. Tectonophysics, 39, 73-86.

Rowe K.J. and Rutter E.H. (1990) Palaeostress estimation using calcite twinning: experimental calibration and application to nature. J. Struct. Geol., 12, 1-17.

Schnorr P. and Schwerdtner W.M. (1981) An empiricical test of sample size and precision of Robin's method of strain analysis. Tectonophysics, 73, T1-T8.

Schmid S.M., (1976) Rheological evidence for changes in the deformation mechanism of Solenhofen limestone towards low stresses. Tectonophysics, 31, T21-T28.

Schmid S.M., Boland J.N., and Paterson M.S. (1977) Superplastic flow in fine grained limestone. Tectonophysics, 43, 257-291.

Reference-5

Schmid S.M., Paterson M.S. (1977) Strain analysis in an experimentally deformed oolitic limestone. In: S.K. Saxena and S. Bhattacharji (Editors), Energetics of geological Processes. Springer, New York, 473p.

Schmid S.M., Paterson M.S. and Boland J.N. (1980) High temperature flow and dynamic recrystallization in Carrara Marble. Tectonophysics, 65, 245-280.

Schmid S.M., Panozzo R. and Bauer S. (1987) Simple shear experiments on calcite rocks: rheology and microfabrics. J. Struct. Geol., 9, 747-778.

Schwerdtner W.M., Stott G.M. and Sutcliffe R.H. (1983) Strain patterns of crescentic granitoid plutons in the Archean greenstone terrain of Ontario. J. Struct. Geol., 5, 419-430.

Shelley d. (1983) Manual of optical mineralogy. Elsevier Science Publishers, New York, 239p.

Spang J.H. (1972) Numerical method for dynamic analysis of calcite twin lamellae. Geol. Soc. Am. Bull., 83, 467-472.

Spiers C.J. (1979) Fabric development in polycrystals deformed a 400$\underline{o}$C. Bull. Minéral, 102, 282-289.

Tan B.K. (1976) Oolite deformation in Windgallen, Canton Uri. Tectonophysics, 31, 157-174.

Teufel L.W. (1980) Strain analysis of experimentally superposed deformation using calcite twin lamellae. Tectonophysics, 65, 291-309.

Turner F.J. (1953) Nature and Dynamic interpretation of deformation lamellae in calcite of three marbles. Am. Bull. J. Sci., 251, 276-298.

Turner F.J. and Ch'ih C.S. (1951) Deformation of Yule marble, Pt. III: Observed fabric changes. Geol. Soc. Am. Bull., 62, 887-905.

Turner F.J. and Weiss L.E. (1963) Structural analysis of metamorphic tectonites. Structural analysis of metamorphic tectonites. McGraw-Hill, Toronto, 435 pp.

Turner F.J., Griggs D.T, and Heard H.C. (1954) Experimental deformation of calcite crystals. Geol. Soc. Am. Bull., 65, 883-934.

Van Berkel J.T., Torrance J.G and Schwerdtner (1986) Deformed anhydrite nodules: a new type of finite strain gauge in sedimentary rocks. Tectonophysics, 124, 309-323.

Reference-6

Weiss L.E. (1954) A study of tectonic style-structural investigation of a marble-quartzite complex in southern California. Univ. Calif., Geol. Sci., 30, 1-102.

Wood D.S. and Holm P.E., (1980) Quantitative analysis of strain heterogeneity as a function of temperature and strain rate. In: W.M. Schwerdtner, P.J. Hudleston and J.M. Dixon (Editors), Analytical Studies in Structural Geology. Tectonophysics, 66, 1-14.

Yu H. and Zheng Y. (1984) A statistical analysis applied to the Rf/ϕ method. Tectonophysics, 110, 151-155.

Appendix A-1

Calcite Portland-Cement Aggregate

	e%	EXP. STRAIN	ROBIN METHOD	HARM. METHOD	LINEAR METHOD	Ri (Linear)	SKEW.	ANG. DEV.	PHI MEAN	n
Dry										
B8808	0.00	1.000	1.046	1.668	1.034	1.879	0.290	25.4	6.9	137
7C-3C	0.00	1.000	1.131	1.722	1.074	2.020	-0.430	23.8	-2.4	137
AC3	4.44	1.070	1.176	1.705	1.200	2.070	0.560	22.7	5.1	250
AC1	6.60	1.108	1.189	1.602	1.287	1.827	-0.230	21.2	-2.4	205
B8804 ol	7.03	1.116	1.117	1.621	1.250	1.881	-0.310	23.0	-0.7	212
AC4	7.30	1.120	1.148	1.641	1.272	1.857	-0.500	22.2	-2.1	222
AC2	7.60	1.126	0.920	1.673	n.a	n.a	0.210	29.8	-6.9	206
AC5	10.20	1.175	1.218	1.671	1.258	1.860	-0.290	21.4	1.2	189
B8807	10.27	1.177	1.186	1.670	1.235	1.921	-0.510	21.1	9.6	202
AC6	12.00	1.211	1.074	1.700	1.191	1.851	0.190	25.0	0.5	211
AC9	13.26	1.238	1.140	1.705	n.a	n.a	0.410	23.2	-1.2	137
AC11	17.30	1.330	1.256	1.644	1.392	1.839	0.100	20.4	0.6	229
AC8	18.03	1.347	1.346	1.814	1.784	2.421	-0.200	18.8	0.0	250
AC10	18.30	1.354	1.124	1.630	1.297	1.800	-0.180	23.1	-3.6	178
B8805 ol	21.70	1.443	1.462	1.884	2.050	2.319	-0.520	16.0	1.2	115
Wet										
BB8808	0.00	1.000	1.046	1.668	1.034	1.879	0.290	25.4	6.9	137
7C-3C	0.00	1.000	1.131	1.722	1.074	2.020	-0.430	23.8	-2.4	137
CPF-12	6.80	1.111	1.181	1.645	2.008	2.032	-0.110	21.9	-1.8	250
CPF-11	7.50	1.124	1.162	1.706	1.340	2.035	-0.110	22.4	0.6	250
CPF-08	8.80	1.148	1.327	1.778	1.544	2.163	-0.150	19.9	-1.7	225
CPF-09	9.60	1.163	1.223	1.733	1.554	2.230	0.000	21.4	-0.7	250
CPF-04	10.90	1.189	1.515	1.818	1.791	1.791	-0.480	14.9	0.6	235
CPF-10	15.90	1.297	1.514	1.838	1.851	2.056	0.710	15.0	1.8	241
CPF-01 d	16.36	1.307	1.336	1.789	1.435	2.005	-0.130	19.1	0.7	250
CPF-13	17.8	1.342	1.538	1.894	2.082	2.082	-0.710	14.7	1.0	250
CPF-02	22.00	1.452	1.598	1.910	2.746	2.746	0.210	15.0	0.6	227
CPF-03	24.00	1.509	1.663	2.007	1.601	2.058	0.540	13.1	0.0	237

ol=oil leak
d=dry

Appendix A-2

Ancaster Oolitic Limestone

	e%	EXP. STRAIN	ROBIN METHOD	HARM. METHOD	LINEAR METHOD	Ri (Linear)	SKEW.	ANG. DEV.	PHI MEAN	n
Dry										
ANC-87	0	1.000	1.002	1.337	n.a	n.a	-0.180	28.1	6.8	93
JL-1	5.6	1.090	1.167	1.313	1.240	1.351	-0.440	16.0	1.1	119
JL-5	8	1.133	1.328	1.454	1.487	1.459	0.350	11.7	0.0	116
JL-6	11.4	1.199	1.284	1.384	1.485	1.416	-0.260	11.6	-0.2	93
JL-3	16.7	1.315	1.489	1.533	1.720	1.387	-0.430	7.0	0.0	125
JL-4	17.6	1.337	1.545	1.620	1.819	1.493	-1.510	9.2	0.0	140
JL-7	20	1.398	1.490	1.629	1.832	1.666	-1.290	11.9	-0.2	72
Wet										
ANC-87	0	1.000	1.002	1.337	n.a	n.a	-0.180	28.1	6.8	93
Jl-13	5.5	1.089	1.132	1.326	1.092	1.381	-0.160	19.2	1.7	86
JL-10	8	1.133	1.379	1.483	1.333	1.366	0.340	11.9	0.0	147
JL-8	13	1.232	1.148	1.317	1.207	1.370	-0.120	18.4	0.0	97
JL-9	14	1.254	1.569	1.698	1.606	1.538	-1.250	9.1	0.0	70
JL-11	17.5	1.335	1.569	1.662	1.888	1.615	-0.170	10.1	0.0	92
JL-12	26.4	1.584	1.911	2.027	n.a	n.a	1.420	7.4	0.0	103

Appendix A-3

China Beach Sandstone

Fractured Quartz

Sample	e%	EXP. STRAIN	ROBIN METHOD	HARM. METHOD	LINEAR METHOD	SKEW.	ANG. DEV.	PHI MEAN	n
CB-15A	0	1.000	1.150	2.522	1.000	0.000	3.7	25.9	2
CB-17A	12	1.211	1.151	1.689	1.390	-0.230	22.0	1.9	80
CB-10A	18	1.347	1.228	1.758	1.126	0.130	21.0	-1.2	95
CB-19A	25	1.540	1.415	1.772	1.339	1.670	13.5	0.0	55
CB-12A	28	1.637	1.508	1.785	n.a	0.630	14.3	4.0	48

Undulose Quartz

Sample									
CB-15A	0	1.000	1.210	1.574	1.439	-0.580	18.6	0.0	42
CB-17A	12	1.211	1.091	1.584	1.009	0.060	22.4	0.0	63
CB-10A	18	1.347	1.055	1.592	1.021	0.230	24.8	5.3	31
CB-19A	25	1.540	1.160	1.624	1.029	0.410	17.2	-7.1	19
CB-12A	28	1.637	2.465	2.825	n.a	0.230	24.8	5.3	31

Unaltered Feldspar

Sample									
CB-15A	0	1.000	1.182	2.053	n.a.	-0.270	23.0	-3.3	97
CB-17A	12	1.211	1.285	1.733	1.259	0.180	18.9	1.5	97
CB-10A	18	1.347	1.181	1.714	1.445	0.480	22.5	0.0	80
CB-19A	25	1.540	1.521	1.899	1.927	-0.690	15.9	0.0	48
CB-12A	28	1.637	1.622	1.913	2.340	-0.670	14.0	-1.2	49

Altered Feldspar

Sample									
CB-15A	0	1.000	1.140	1.622	1.549	0.260	24.5	13.2	25
CB-17A	12	1.211	1.335	1.672	1.765	0.060	18.5	4.0	35
CB-10A	18	1.347	1.280	1.939	1.871	0.230	21.0	0.0	21
CB-19A	25	1.540	1.972	2.346	3.098	0.650	10.9	0.0	28
CB-12A	28	1.637	2.182	2.651	3.013	-2.390	13.8	4.3	30

Lithic Fragments

Sample								
CB-15A	0	1.000	1.147	1.858	1.385	0.120	24.1	9.0	65
CB-17A	12	1.211	1.396	1.824	1.768	-0.520	17.7	1.8	76
CB-10A	18	1.347	1.355	1.765	1.365	-0.250	18.4	0.0	62
CB-19A	25	1.540	2.158	2.478	2.886	1.520	9.3	-7.4	70
CB-12A	28	1.637	2.730	2.912	3.564	-0.490	8.4	1.4	61

Appendix B-1

Appendix B can be used to compare the macroscopic strain estimates for "pure shear" and "simple shear". In this the shear strain value (gamma) for the tests on sheared wafers can be assigned a finite strain ellipse ratio (R) assuming perfect simple shear (Ramsay, 1967). In the case of a plane strain history, like simple shear, the strain would be essentially 2-dimensional and the % shortening in the maximum shortening direction is given by the 2-D curve (below). In pure shear, approximately achieved by the compression tests of solid cylinders, the same strain ratio corresponds to a greater percentage shortening as shown by the 3-D curve (below).